Transactions of the ASME®

Transactions of the ASME, Journal of Turbomachinery (ISSN 0889-504X) is published quarterly (Jan., Apr., July, Oct.) by The American Society of Mechanical Engineers, Three Park Avenue, New York, NY 10016. Periodicals postage paid at New York, NY and additional mailing offices. POSTMASTER: Send address changes to Transactions of the ASME, Journal of Turbomachinery, c/o THE AMERICAN SOCIETY OF MECHANICAL ENGINEERS, 22 Law Drive, Box 2300, Fairfield, NJ 07007-2300.
CHANGES OF ADDRESS must be received at Society headquarters seven weeks before they are to be effective. Please send old label and new address.
STATEMENT from By-Laws. The Society shall not be responsible for statements or opinions advanced in papers or ... printed in its publications (B7.1, Par. 3).

INDEXED by Applied Mechanics Reviews and Engineering Information, Inc. Canadian Goods & Services Tax Registration #126148048

Journal of Turbomachinery

Published Quarterly by The American Society of Mechanical Engineers

VOLUME 124 • NUMBER 1 • JANUARY 2002

TECHNICAL PAPERS

(**Contents continued on inside back cover**)

This journal is printed on acid-free paper, which exceeds the ANSI Z39.48-1992 specification for permanence of paper and library materials. ♾™
♻ 85% recycled content, including 10% post-consumer fibers.

(**Contents continued**)

2000 Heat Transfer Committee Best Paper Award

Effects of Reynolds Number and Free-Stream Turbulence on Boundary Layer Transition in a Compressor Cascade

Heinz-Adolf Schreiber

Wolfgang Steinert

German Aerospace Center (DLR),
Institute of Propulsion Technology,
51170 Köln, Germany

Bernhard Küsters
Siemens AG,
Power Generation (KWU),
45466 Mülheim a.d. Ruhr, Germany

An experimental and analytical study has been performed on the effect of Reynolds number and free-stream turbulence on boundary layer transition location on the suction surface of a controlled diffusion airfoil (CDA). The experiments were conducted in a rectilinear cascade facility at Reynolds numbers between 0.7 and 3.0×10^6 and turbulence intensities from about 0.7 to 4 percent. An oil streak technique and liquid crystal coatings were used to visualize the boundary layer state. For small turbulence levels and all Reynolds numbers tested, the accelerated front portion of the blade is laminar and transition occurs within a laminar separation bubble shortly after the maximum velocity near 35–40 percent of chord. For high turbulence levels (Tu>3 percent) and high Reynolds numbers, the transition region moves upstream into the accelerated front portion of the CDA blade. For those conditions, the sensitivity to surface roughness increases considerably; at Tu=4 percent, bypass transition is observed near 7–10 percent of chord. Experimental results are compared to theoretical predictions using the transition model, which is implemented in the MISES code of Youngren and Drela. Overall, the results indicate that early bypass transition at high turbulence levels must alter the profile velocity distribution for compressor blades that are designed and optimized for high Reynolds numbers. [DOI: 10.1115/1.1413471]

Introduction

The aerodynamic performance of turbomachinery blading is strongly dependent on the nature of boundary layer development on the blades. The blade boundary layer is responsible for the airfoil aerodynamic efficiency and thus for the overall performance of the machine. Several previous investigations in turbomachinery test facilities have shown that, in spite of the high free-stream turbulence and the unsteady periodic wakes of the upstream blade rows, the boundary layer is laminar along the forward parts of the blade surface. This is true especially for turbine blade sections, which usually operate at low Reynolds numbers. Also the boundary layers on compressor blades are observed to be laminar in wide areas along the accelerated blade front region. Most blade designers take advantage of the laminar boundary layer on the front and set the maximum suction side velocity around 15–30 percent of blade chord. This allows high blade loading in combination with low losses. Beyond the velocity maximum, the suction surface flow is decelerated with a relatively steep gradient and then—to keep the boundary layer slightly apart from separation—decreased monotonically in strength toward the trailing edge. These ''controlled diffusion airfoils'' (CDA) are widely in use in multistage compressors.

Several experimental investigations have provided evidence of the existence of partial laminar boundary layers on compressor blades. Studies in cascade facilities with different free-stream turbulence levels and wakes, which have been produced by moving bars, showed laminar flow on the suction side and final transition within a laminar separation bubble shortly after the velocity maximum [1,2]. In real compressor environments, detailed measurements on stator blades showed extended laminar boundary layers up to 30–50 percent of blade chord. At very low Reynolds numbers, transition occurred even further downstream [3,4]. Transition is induced in rather complex modes that depend on the incoming wakes that impinge on the blade surface boundary layers, on the profile velocity distribution, and the Reynolds number. Behind the turbulent wakes so-called calmed ''laminar-like'' regions are observed, which are followed by transition either in bypass modes or in laminar separation bubbles aft of the suction side maximum. In case of separated-flow transition the separation bubble and its extension oscillates with the blade passing frequency [5]. The turbulence level between the wakes was determined by Halstead et al. [4] to be about 2.5–3 percent and within the wake region about 5.5–6 percent. All these complex transition modes are excellently described by Halstead et al. [4], or in the paper of Cumpsty et al. [6], for example.

Essential for the above-described observations is that the corresponding tests, both in cascade facilities and in compressor test rigs, have been performed at blade chord Reynolds numbers ranging from about 0.05 to 0.45×10^6. Even tests with a special Reynolds number variation did not exceed this range. Real compressors in aeroengines, however, operate at $Re=0.6–1.2\times10^6$ even at cruise altitude [7], and industrial compressors or compressors in heavy-duty gas turbines have blade chord Reynolds numbers roughly from 2 to 6×10^6 (Fig. 1). At these realistic turbomachinery conditions with high Reynolds numbers, the calmed regions after wake passing, the laminar boundary layers and, particularly, the laminar separation bubbles will play a less important role.

Recent blade design and optimization studies by Köller et al. [8] and Küsters et al. [9] showed that under high free-stream turbulence levels, boundary layer transition on the blade suction side successively propagated forward into the accelerated front region

Contributed by the International Gas Turbine Institute and presented at the 45th International Gas Turbine and Aeroengine Congress and Exhibition, Munich, Germany, May 8–11, 2000. Manuscript received by the International Gas Turbine Institute February 2000. Paper No. 2000-GT-263. Review Chair: D. Ballal.

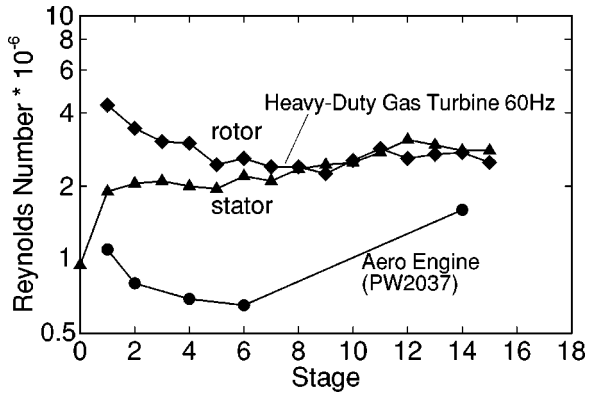

Fig. 1 Typical blade chord Reynolds number of a heavy-duty gas turbine compressor

of the blades when the Reynolds number was increased. The blade profile optimization algorithm employed considered this early transition location and set the velocity maximum on the blade suction side much further upstream than is common in so-called controlled diffusion designs, which assume at least partly laminar flow up to about 20–30 percent of chord [10]. It was clearly shown that the location of transition onset has a considerable influence on the blading design process. Conversely, the results of new blading designs depend strongly on the reliability of the transition models employed in the boundary layer codes. Therefore, it is essential that the transition models have been validated thoroughly for all turbomachinery relevant flow conditions with realistic turbulence levels and pressure gradients.

One correlation for transition onset, frequently used in numerical boundary layer codes and embedded in many design tools, is the correlation of Abu-Ghannam and Shaw [11]. It has been comprehensively verified for tests at lower turbulence levels for zero, adverse, and slightly favorable pressure gradients on flat plates. For high turbulence levels (>2 percent) there is little information and Gostelow and Bluden [12] emphasized that uncertainty exists for favorable gradients. Mayle [13] pointed out that, especially for favorable pressure gradients, there are only two data points from Blair [14] from a flat plate experiment with $Tu=2$ and 5 percent that give sufficient information on transition onset and length.

In this present study, experiments have been conducted in a linear cascade facility to give specific evidence that for higher turbulence levels and increasing Reynolds number, transition onset on real compressor blades moves upstream into the region of strong favorable pressure gradients. The test model used was a controlled diffusion airfoil with suction surface acceleration along a relatively long distance. This paper focuses on the investigation of the transition location for different levels of nearly *isotropic* turbulence and Reynolds numbers, a first step in which the complex mechanism of wake passing was neglected. The Reynolds number was increased beyond levels investigated so far. An oil flow technique and liquid crystal coatings have been used to visualize boundary layer state on the blade suction side.

Compressor Airfoil: Analytical Study

To study the effect of free-stream turbulence and Reynolds number on transition onset, a blade profile was selected that was designed for an inlet Mach number of 0.6 and a flow turning of 16 deg. Its profile pressure distribution is typical of controlled diffusion airfoils (CDA) with a favorable pressure gradient on the suction surface to 30 percent of chord and beyond the station of the maximum velocity, where the boundary layer is turbulent, a steep ''controlled diffusion'' with decreasing pressure gradient toward the trailing edge. Its profile Mach number distribution is shown in the upper part of Fig. 2.

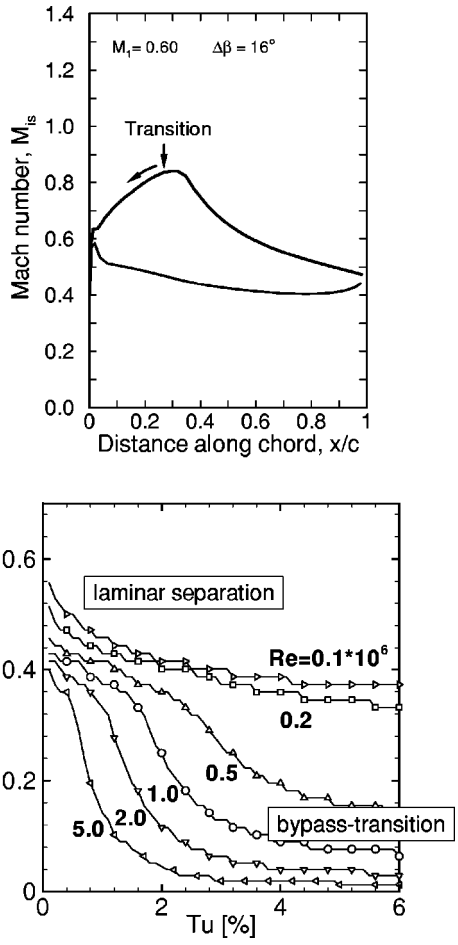

Fig. 2 Influence of Reynolds number and free-stream turbulence on suction side transition onset (MISES simulation)

The blade-to-blade solver MISES of Drela and Youngren [15] was used for the numerical study of boundary layer transition behavior. It is a coupled inviscid/viscous interaction method that employs integral boundary layer equations for boundary layer and wake development. Boundary layer transition is predicted employing the criterion of Abu-Ghannam/Shaw [11], which has been slightly modified by Drela [16] to achieve a more stable convergence during the coupling process.

Basically, transition can occur in three different modes; in a natural transition mode (Tollmien/Schlichting (TS) wave instabilities), in the ''bypass'' mode, or in the separated mode via a laminar separation bubble with turbulent reattachment. All these modes depend on the Reynolds number, the pressure gradient at the edge of the boundary layer, and the free-stream turbulence level. For high free-stream turbulence levels, transition primarily is induced from outside of the boundary layer and the stages of the natural transition process (TS instabilities) are ''bypassed''. For many practical flows TS wave transition and bypass transition both are often at work, but for favorable pressure gradients and higher turbulence levels, bypass transition is relevant exclusively.

For the present study, boundary layer transition is calculated for Reynolds numbers from 0.1 to 5×10^6 and different turbulence levels using the suction side Mach number distribution of Fig. 2. The results in Fig. 2 bottom show a tremendous influence on the suction side transition onset of both the Reynolds number and the turbulence level. For small turbulence levels ($Tu<1.5$ percent) and low Reynolds numbers, laminar separation is calculated after the velocity maximum and transition with turbulent reattachment is predicted to occur beyond 35 to 50 percent of chord. A stepwise

increase of the turbulence level up to 6 percent reduces the extent of the separation bubble, but as long as the Reynolds number does not exceed values of about 0.2×10^6, transition remains behind the velocity maximum ($x_t/c>0.3$). With increasing Reynolds numbers the bubble finally disappears and transition onset propagates upstream into the accelerated front portion of the blade. For example, at a Reynolds number of 2.0×10^6 and a turbulence level of 3 percent, transition onset is located near 6.1 percent of chord. Here the momentum thickness Reynolds number Re_θ, which is used as the criterion for transition onset, is calculated to be 220.

Overall, the curves in Fig. 2 illustrate that the transition onset location is most sensitive on the Reynolds number when the turbulence levels are between about 2 and 4 percent. Beyond $Tu=4$ percent the transition onset location for a given Reynolds number is more or less insensitive to higher *Tu* levels.

A further relevant influence parameter for boundary layer transition is the streamwise pressure gradient. Mayle [13] pointed out that for favorable pressure gradients, the flow acceleration parameter is the appropriate parameter to correlate transition onset

$$K=\frac{\nu}{U^2}\frac{dU}{ds}$$

To illustrate the acceleration rate on the blade surface of the present cascade, the calculated parameter *K* for the blade suction and pressure side is shown in Fig. 3. Calculations are presented for both a low and a high Reynolds number, the range in which the following experiments have been performed. On the front portion of the suction side this parameter exceeds values of 3×10^{-6} but the value successively falls toward zero near the velocity maximum. According to the definition of the acceleration parameter, it is obvious that *K* is inversely proportional to the chord Reynolds number. Therefore, the magnitude of this parameter becomes smaller when the Reynolds number is increased. The correlation of the momentum thickness Reynolds number at transition onset against the acceleration parameter (Mayle [13], Fig. 16) claims that for free-stream turbulence levels beyond 3 percent, the acceleration parameter *K* has no influence on the momentum thickness Reynolds number $\mathrm{Re}_{\theta t}$. As there is little experimental information on transition with accelerated boundary layers ($K>0$) and high turbulence levels, the following experiments will provide further insight to this transition process and help to confirm or correct the transition correlation.

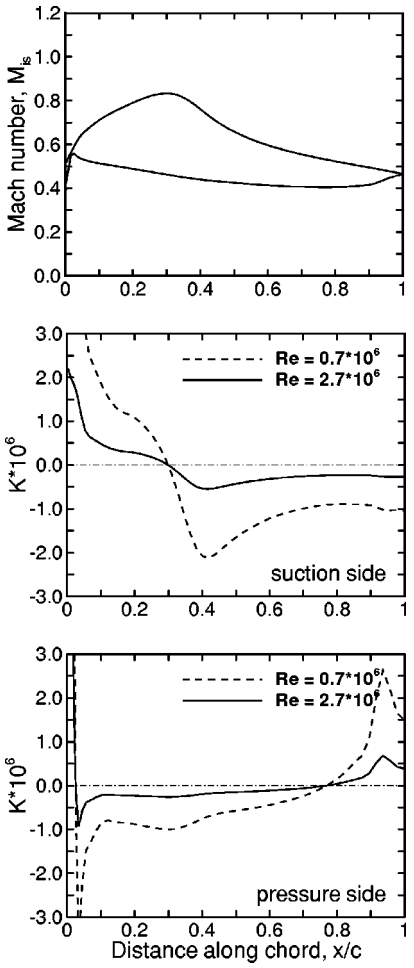

Fig. 3 Acceleration parameter for suction and pressure side for two different Reynolds numbers

Test Setup

The experiments were performed in the transonic cascade tunnel of the DLR Cologne [17]. This tunnel is a closed-loop, continuously running facility with a variable nozzle, an upper transonic wall, and a variable test section height. The air supply system enables an inlet Mach number range from 0.2 to 1.4 and a Mach number independent variation of the Reynolds number from about $1\times10^{*5}$ to $3\times10^{*6}$. Tunnel sidewall boundary layers ahead of the cascade are removed through protruding slots. Within the blade pack aft of the minimum pressure region, endwall boundary layers and AVDR are controlled by suction through chordwise slots. Tailboards combined with throttles are used to control inlet and exit boundary conditions.

To allow tests with high Reynolds numbers and to have a sufficient resolution of the blade surface, the cascade blade chord was enlarged to 150 mm. Three blades were installed in the test section, with the center blade instrumented on the pressure and suction side. A cross-sectional view of the test section and a photograph of the cascade model are shown in Figs. 4 and 5. For visualization tests using liquid crystal coating, the center blade was fabricated from a carbon-fiber-reinforced epoxy material to reduce a chordwise heat flux within the blade contour.

Most tests were run at an inlet Mach number of 0.6 with total pressures from 0.42 to 1.7 bar and total temperatures from about 306 to 310 Kelvin, giving blade chord Reynolds numbers from 0.7 to 2.8×10^6. Some tests at $M_1=0.7$ allowed Reynolds numbers around $3\times10^{*6}$. To increase the turbulence level, three different turbulence grids constructed from rectangular bars were installed near the entrance to the main tunnel contraction, one about 1.9 m and an even more coarse grid 1.55 m upstream of the test section.

Experimental Results

Two main test series with different turbulence levels have been performed: The first one used a standard oil flow technique and the second one employed liquid crystal coatings. The minimum

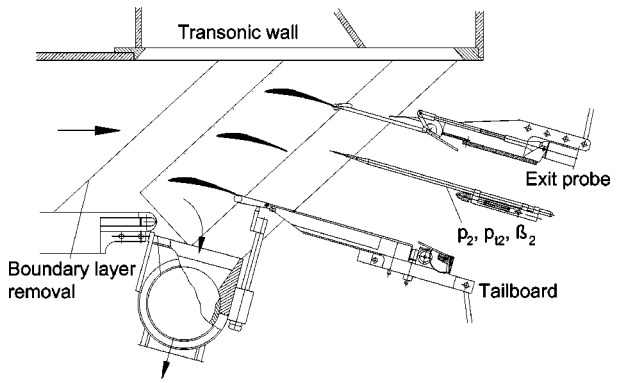

Fig. 4 Test section of the DLR Transonic Cascade Tunnel

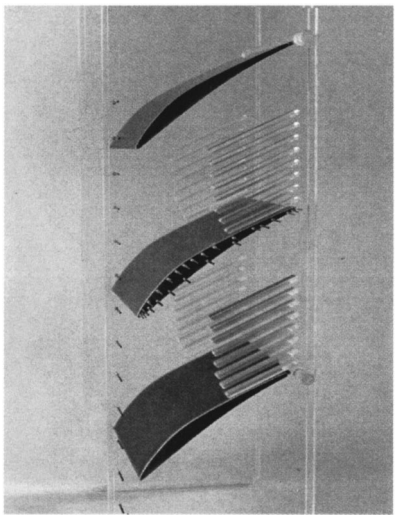

Fig. 5 Photograph of cascade and endwalls

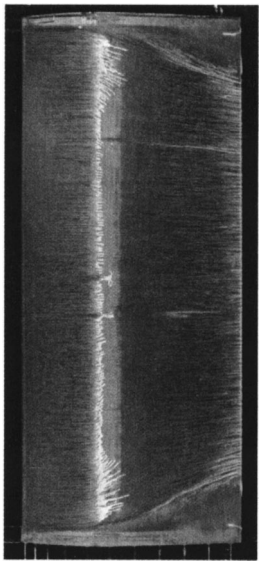

Fig. 6 Oil streak lines on suction side, $M_1=0.6$, $Re=0.8\times10^6$

turbulence level without a grid installed was measured to be 0.7 percent. Two grids were located near the entrance of the tunnel contraction; the first one, denoted ''screen 1.9'' with rectangular bars of about 20 mm, generated a turbulence level of about 2.5–3 percent and the second one, ''screen 1.9+4,'' had bars of 20 mm with four additional bars of 6 mm, generated slightly higher frequencies.

During the course of the investigations it turned out that the turbulence level of the first two grids was not sufficient to induce the expected upstream propagation of transition onset. Therefore, an even coarser grid (''screen 2.6'' with 25 mm bars) was located slightly closer to the test blade, generating a turbulence level of about 4–5 percent.

Oil Flow Visualization. In a preceding test series with blades of 70 mm chord an oil flow picture (Fig. 6) was obtained at a low Reynolds number of 0.8×10^6 and a turbulence level of 0.7 percent (no grid installed). Figure 6 shows the oil traces on this blade, which had an aspect ratio of 2.4. Due to a distinct suction side velocity maximum around 30 percent of chord, which is followed by a relatively strong diffusion, the laminar separation is well developed and establishes as a short bubble between about 34 to 41 percent.

All further experiments presented here were performed using a blade chord of 150 mm. Keeping the Reynolds number at the same low level (0.7×10^6) as in Fig. 6, but increasing the turbulence level, the laminar separation behavior does not change considerably. The blade Mach number distribution and the oil traces in Fig. 7 both again indicate a separation bubble for a *Tu* level of 2.5 percent and a Reynolds number of 0.7×10^6. This separation bubble, however, disappeared when the Reynolds number was increased to $Re=2.0\times10^6$. At this high Reynolds number and *Tu* level the oil traces do not show a specific change of their structure along the blade suction side (Fig. 8). Obviously, the discontinuity in c_f is not sufficiently distinct to show an essential difference on the blade surface, at least downstream of about 15 percent of chord. As at high Reynolds numbers the boundary layer is thinner, the measured total pressure losses are lower compared to those of the low Reynolds number tests and the experimental blade Mach number distribution does not show the separation bubble. A numerical simulation employing the blade to blade solver MISES nearly exactly matches the measured surface Mach number distribution, as shown in Fig. 8.

Further high Reynolds number tests with oil flow visualization and even higher turbulence levels ($Tu=4-5$ percent) did not provide a clear c_f-induced change in the surface flow structure within

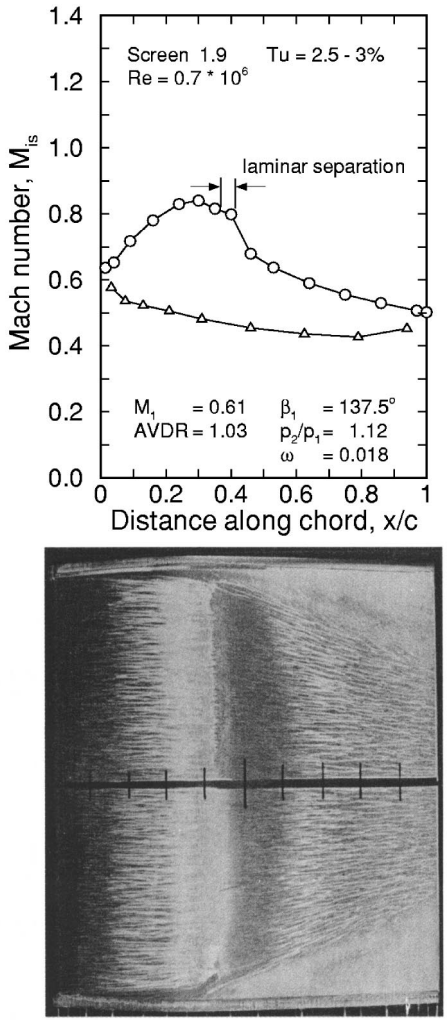

Fig. 7 Mach number distribution and oil streak lines at Re $=0.7\times10^6$ and $Tu\approx2.5-3$ percent, 1 tick approximately 10 percent of chord

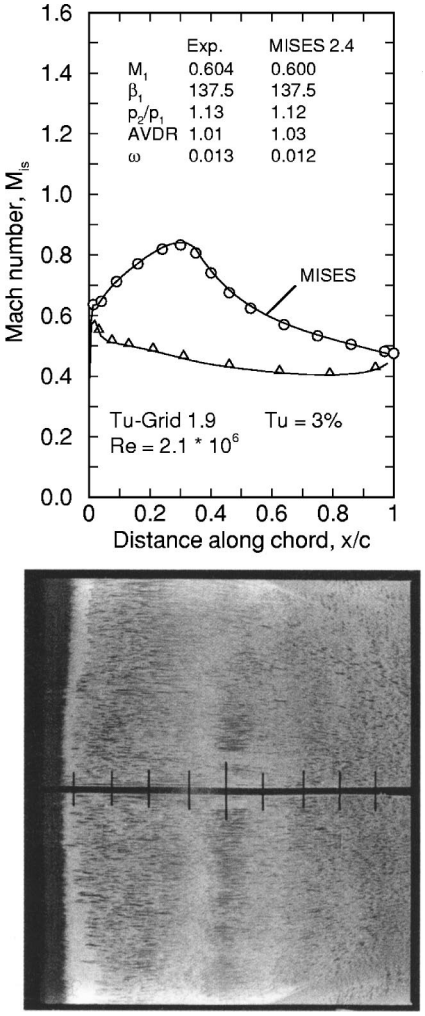

Fig. 8 Mach number distribution and oil streak lines at Re $=2.1\times10^6$ and $Tu\approx3$ percent, 1 tick approximately 10 percent of chord

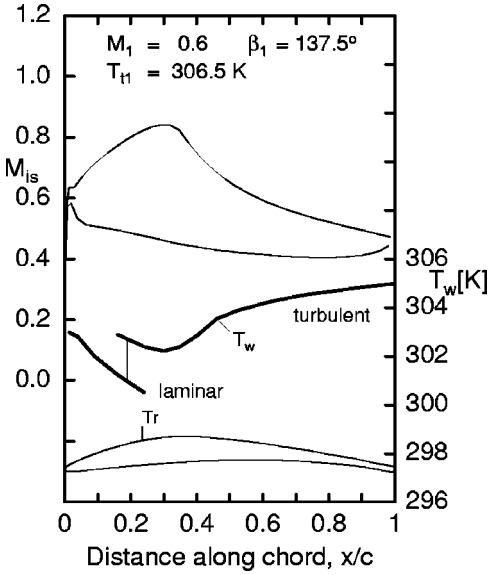

Fig. 9 Predicted blade Mach number distribution and calculated adiabatic wall temperature on suction side

the accelerated front portion of the blade and thus no evidence regarding transition in this region. Therefore, the tests have been repeated using sensitive liquid crystal coatings.

Visualization Using Liquid Crystal Coatings. Liquid crystal coatings have been used to detect transition by visualizing the difference in adiabatic wall temperature between laminar and turbulent boundary layers. This technique requires a relatively sensitive mixture of liquid crystals that is sprayed on the black colored blade surface. To achieve a sufficient contrast in wall temperature as reflected through colors of the liquid crystals, it was necessary to use a thermally insulated test blade that was made completely out of carbon fiber composite. The event temperature of the liquid crystals is selected to be approximately 4–5°C lower than the total temperature and within the sensitive temperature range (about 2°C) the colors of the scattered light are red, yellow, and green. Before approaching this range the liquid crystals are transparent and the blade surface looks black. A fine tuning of the total temperature in steps of about 0.1 deg allows an adjustment of the wall temperature to the event temperature of the liquid crystals (303–305 K). More information on this visualization technique is given in a previous report by Steinert and Starken [18] and a recent measurement technique paper by Bize et al. [19] for example.

The adiabatic surface temperature T_w, which depends on the type of boundary layer and the Mach number at the boundary layer edge, is calculated for the present cascade from its surface Mach number distribution using the different recovery factors for laminar and turbulent flow ($r=0.836$ and 0.89, respectively). Figure 9 shows that in the front portion of the suction side a maximum temperature difference of about 2 K can be expected between laminar and turbulent flow. Prior to the tests, a numerical parameter study was performed for a high Reynolds number and four different turbulence levels to estimate the expected location and magnitude of the temperature difference across transition. The model used for prediction of transition again was the modified correlation of Abu-Ghannam and Shaw [16]. Figure 10 shows the calculated suction side temperatures for the tests at the Reynolds number of $2.6\times10^6$and turbulence levels from 0.5 to 3 percent. The highest temperature difference across transition can be expected for the low turbulence level test. That case results in the lowest temperatures for the laminar flow at velocity maximum and a theoretical temperature increase of more than 2 K near 40

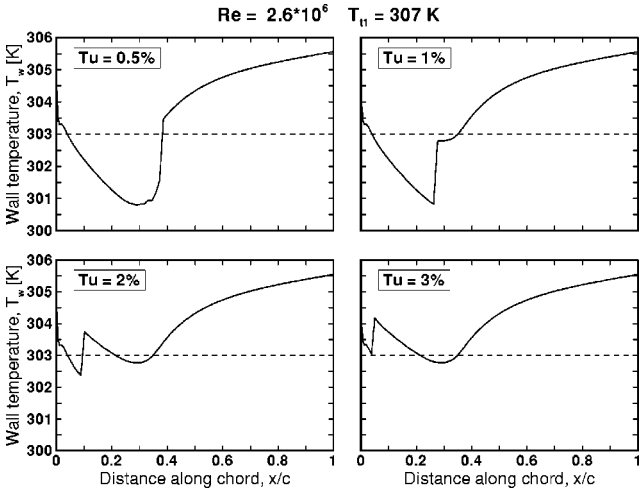

Fig. 10 Simulated surface temperature distribution on blade suction side, influence of free-stream turbulence on temperature discontinuity near transition for $M_1=0.6$ and $Re=2.6\times10^6$

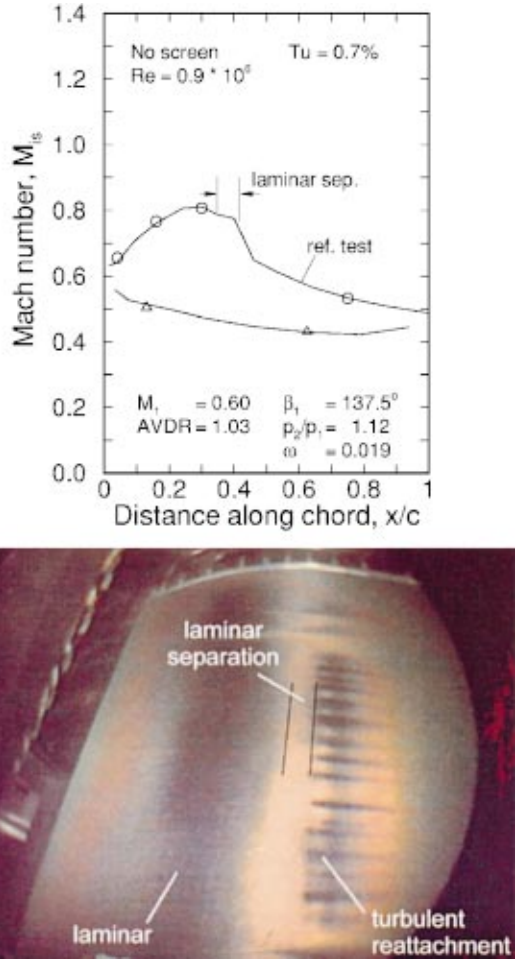

Fig. 11 Mach number distribution and liquid crystal picture of suction side at Re=0.9×10^6 and *Tu*≈0.7 percent showing laminar separation and turbulent reattachment

percent of chord. When transition propagates upstream with increasing *Tu* levels, this temperature difference unfortunately becomes somewhat less.

As transition in reality is a three-dimensional and more gradual process, the temperature increase on the surface will not be as pronounced and clear as predicted in Fig. 10, especially for the high-turbulence-level tests. The transition-induced change in surface temperature for those conditions, however, is still more pronounced than the gradual temperature variation that is caused by the local change of the surface Mach number. Certainly, some uncertainty remains concerning the precise experimental determination of the transition location. The theory (with $Tu=3$ percent) would expect early transition within the accelerated front portion around 5 percent of chord. The position of laminar separation and reattachment from the experiment, however, is quite accurate.

The first test presented in Fig. 11 shows a low-Reynolds-number test without a turbulence grid upstream ($Tu\approx 0.7$ percent). Black regions in the blade front portion indicate a cold laminar boundary layer. The ''warm'' laminar separation bubble to be seen between 34 and 41 percent of chord, is yellow-red followed by a streaky ''partly cold'' turbulent reattachment zone. Evidently, turbulent reattachment takes place in combination with longitudinal vortices, which produce a streaky temperature distribution. The rear turbulent blade surface shows increasing temperatures with yellow-red-green colors. Similar observations at such low Reynolds number tests had been shown previously by Steinert and Starken [18].

When increasing the Reynolds number to about 2.2×10^6 but keeping the turbulence level as low as before (no turbulence grid), the liquid crystal picture again showed laminar flow in the front portion; the yellow stripe, that indicates laminar separation, practically disappeared, but again or still, the streaky turbulent ''reattachment zone'' remained (Fig. 12). The blade Mach number distribution in Fig. 12 (top) provides no clear indication for a laminar separation bubble. Due to the increased Reynolds number, the thinner boundary layer now starts to become sensitive to certain roughness particles. Therefore, first yellow ''turbulence wedges,'' located downstream of isolated small grains or excrescencies, become visible within the laminar front portion.

Increasing the turbulence level to about 2.5 percent, one sees the weak laminar separation bubble completely disappears and boundary layer transition starts around 30 percent of chord, i.e., near the suction side velocity maximum (Fig. 13). A slightly higher turbulence level ($Tu\approx 3$ percent) provides only a marginal upstream shift of transition and the liquid crystal picture in Fig. 14 does not confirm the forward transition location that was predicted by the MISES code near 5 percent of chord (see Fig. 2 or for a similar condition Fig. 10 bottom right). However, the number of roughness-induced turbulence wedges increases considerably so that wide areas of the laminar flow effectively become turbulent. On the other hand, these turbulence wedges provide a clear evidence that the suction surface flow beside these wedges is *laminar.*

A final upstream movement of the transition process could be achieved only with a coarser turbulence grid. At about 4–5 percent turbulence intensity the bypass mechanism becomes dominant, and transition is observed upstream of 10 percent of chord (Fig. 15). A test with an even more increased Reynolds number could be achieved at an inlet Mach number of 0.7. Figure 16 provides the liquid crystal visualization for a Reynolds number of 3.1×10^6 and a turbulence level of about 3.5 percent generated by the turbulence grid denoted ''screen 1.9+4.'' About 70 percent of the blade front portion is covered with turbulence wedges, revealing the increasing sensitivity to surface roughness.

A comparison of the transition locations derived from the visualization experiments to the predicted locations, employing the criterion of the MISES code [16], is shown in Fig. 17 for a constant Reynolds number of 2×10^6. Overall, the forward movement of transition onset with rising turbulence level can be confirmed qualitatively; but around $Tu=3$ percent the Abu-Ghannam and Shaw/Drela correlation slightly overpredicts the forward movement of transition into the accelerated blade front portion. Some uncertainties remain because within the domain of higher Reynolds numbers surface roughness seems to play an additional, but essential, role.

Surface Roughness

The foregoing observations clearly show that both free-stream turbulence and surface roughness have a considerable influence on transition. At low Reynolds numbers, roughness is relatively harmless, but the boundary layer becomes very sensitive when the Reynolds number is increased. The test blade, which is covered with liquid crystals, has a certain roughness that probably could induce premature transition before the bypass transition process becomes dominant. To ensure that the surface roughness remains below the critical roughness height and that the global spanwise transition onset either is natural transition or really is induced by free-stream turbulence, a theoretical estimation was performed, the results of which are presented in Fig. 18. This figure, derived from a diagram in Mayle [13], presents a correlation of the momentum thickness Reynolds number at the onset of transition plotted against a roughness parameter (from Mick [20], upper dashed-dotted line). If Re_θ lies above this curve, surface roughness would induce transition. The nearly straight lines in Fig. 18 represent calculated Re_θ developments along the blade surface of the

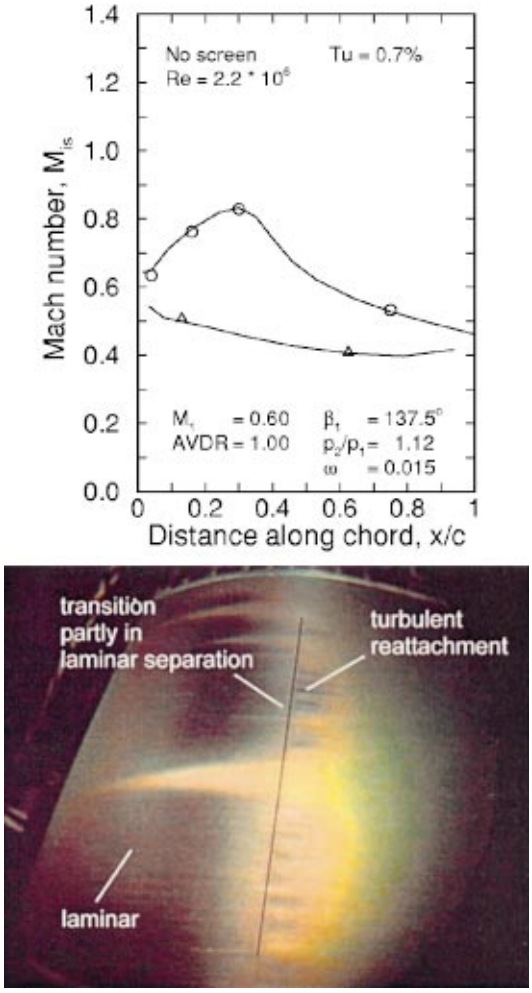

Fig. 12 Mach number distribution and liquid crystal picture of suction surface at Re=2.2×10^6 and *Tu*≈0.7 percent (no screen)

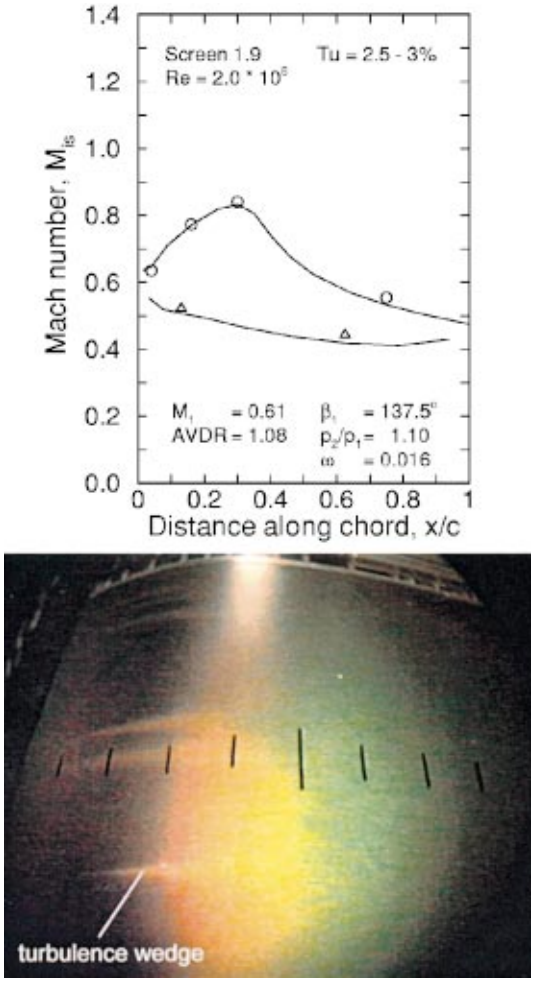

Fig. 13 Mach number distribution and liquid crystal picture of suction surface at Re=2.0×10^6 and *Tu*≈2.5–3 percent (screen 1.9)

present cascade for sand roughness heights of 5, 10, and 20 μm. Roughness measurements of the tested blade surface yielded sand roughness heights not greater than $k_s=10$ μm (with $k_s=8.6\times Ra$, following Schäffler [21]). As the curve with $k_s=10$ μm does not intersect the limiting curve for Re_θ transition, it can be concluded, or at least suspected, that transition at the high Reynolds numbers and high turbulence level is bypass transition, and not roughness, induced transition.

A further interesting and essential finding of these visualization experiments can be seen in Figs. 12–15. These figures again show

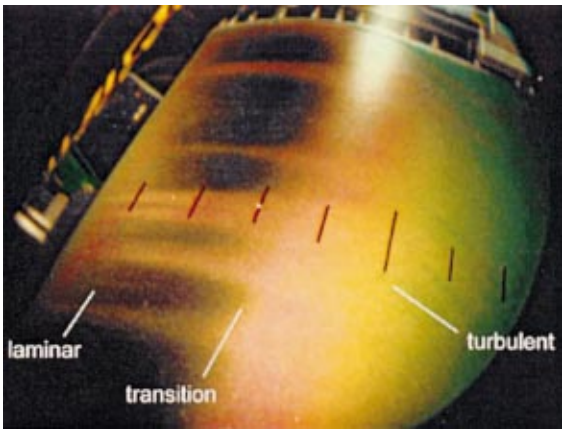

Fig. 14 Liquid crystal picture of suction surface at Re=2.0×10^6 and *Tu*≈3–3.5 percent (screen 1.9+4)

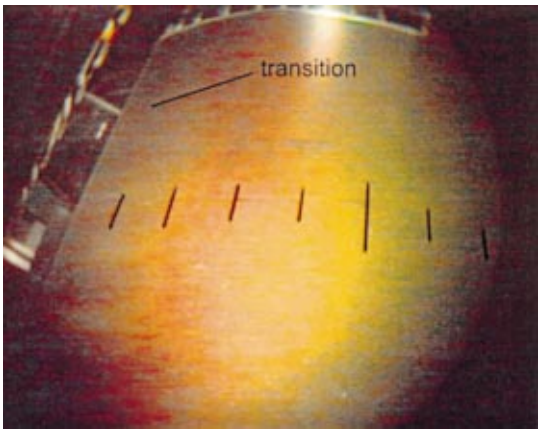

Fig. 15 Liquid crystal picture of suction surface at Re≈2.0×10^6 and *Tu*≈4–5 percent (screen 2.6)

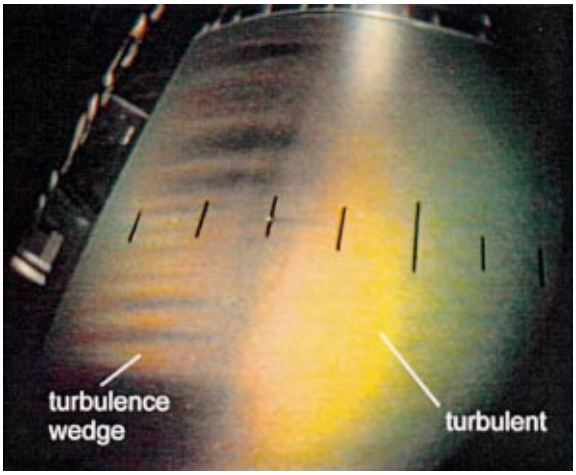

Fig. 16 Liquid crystal picture of suction surface at $M_1=0.7$, $Re=3.1\times10^6$ and $Tu\approx3-3.5$ percent

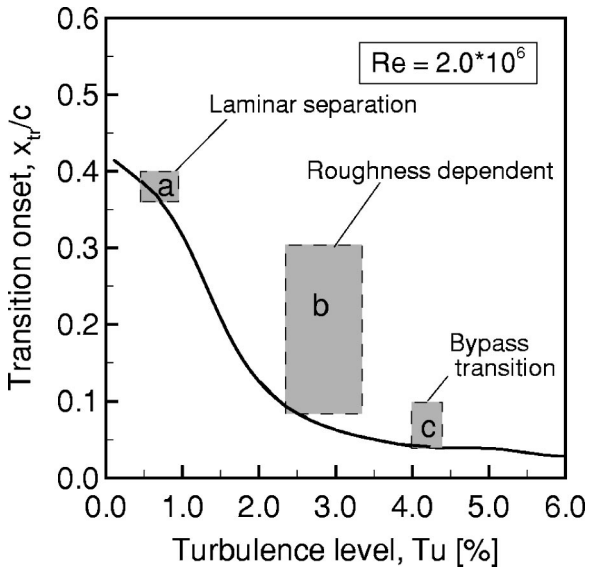

Fig. 17 Experimental (shaded area) and predicted (solid line) suction side transition onset at $Re=2\times10^6$

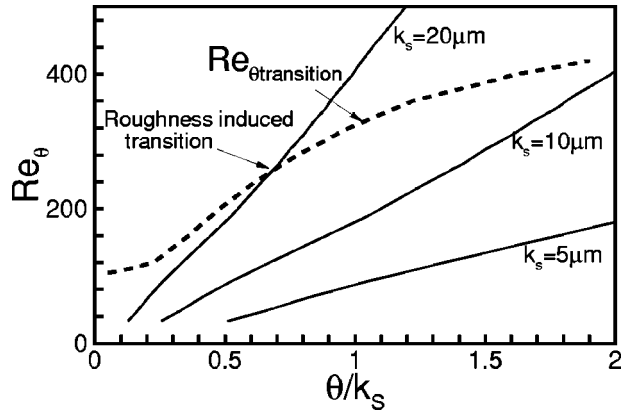

Fig. 18 Momentum thickness Reynolds number Re_θ calculated for three different roughness heights in comparison to Re_θ transition (dashed line from [20]) against the roughness parameter θ/k_s

tests for increasing turbulence levels at a high, but practically constant, Reynolds number of 2×10^6. As the turbulence level was raised, more and more turbulence wedges on the blade surface become visible originating with small roughness particles. Evidently, the particles alone are not able to produce turbulence, but the interaction of the particle-induced instabilities inside the boundary layer with disturbances of sufficient strength from the outer free-stream turbulence seems to initiate turbulence in the boundary layer. This interaction of surface particle-induced instabilities with the disturbances coming from outside of the boundary layer is a complex, but rather important, mechanism that must be considered in future research work on transition onset.

Conclusions

Surface flow visualization tests have been performed on the blade suction side of a controlled diffusion compressor blade to show the effect of Reynolds number and free-stream turbulence on transition location. At the low Reynolds number of 0.8×10^6, a clear laminar separation bubble with turbulent reattachment is visible on the suction side, which does not disappear when free-stream turbulence is increased to 3 percent.

The main focus, however, was on suction side transition onset at high Reynolds number ($Re>2\times10^6$) and accelerated boundary layers ($K>0$). A numerical study employing a modified Abu-Ghannam and Shaw correlation indicated that for high Reynolds numbers and an increasing turbulence level ($Tu\geqslant3$ percent), transition propagates far forward into the accelerated region of the suction side. The experiments qualitatively confirmed an upstream movement of transition, but a slightly higher *Tu* level was necessary to induce early bypass transition. Additionally, the tests clearly showed, that besides both increasing Reynolds number and turbulence level, the *surface roughness* plays an essential role. At high Reynolds numbers, roughness-induced turbulence wedges cover wide areas of the blade front portion so that laminar flow has a less important influence.

The results of both the numerical study and experiment suggest that for high Reynolds numbers, blading design has to consider the effect of early transition onset. Compressor blades with a transition location shortly after the blade leading edge should obtain a front-loaded blade pressure distribution at least for subsonic flows with a forward-located suction side velocity maximum.

When considering the more complex unsteady effects of wake-blade boundary layer interaction, one should consider that for high Reynolds numbers, laminar boundary layers are less important, and that the calming effects after wake-induced transition may be altered considerably. Furthermore, the combined effect of surface roughness at high Reynolds numbers and high turbulence level is an important field for future research work on boundary layer development in turbomachinery blading.

Nomenclature

AVDR = axial velocity density ratio $=(\rho_2 w_2 \sin\beta_2)/(\rho_1 w_1 \sin\beta_1)$
k_s = height of standard sand roughness, μm
K = acceleration parameter $\nu/U^2*(dU/ds)$
M = Mach number
M_{is} = isentropic Mach number $=f(p/p_{t1})$
Ra = arithmetic average roughness
Re = Reynolds number $=u_1 c/\nu_1$
T = temperature
T_W = adiabatic wall temperature
Tu = turbulence level
c = profile chord length
p = pressure
s = blade spacing, pitch
U = velocity at edge of boundary layer
u = velocity
β = flow angle with respect to cascade front

$\Delta\beta$ = flow turning $= \beta_1 - \beta_2$
ν = kinematic viscosity
ρ = density
ω = total pressure loss coefficient $= (p_{t1} - p_{t2})/(p_{t1} - p_1)$
θ = boundary layer momentum thickness

Subscripts

1 = inlet plane
2 = exit plane
is = isentropic entity
t = total, stagnation value
t = transition

References

[1] Dong, Y., and Cumptsy, N., 1990, ''Compressor Blade Boundary Layers: Part 2—Measurements With Incident Wakes,'' ASME J. Turbomach., **112**, pp. 231–240.

[2] Teusch, R., Fottner, L., and Swoboda, M., 1999, ''Experimental Investigation of Wake-Induced Transition in a Linear Compressor Cascade With Controlled Diffusion Blading,'' 14th ISABE Conference, Florence, Sept., Paper No. 99-7057.

[3] Solomon, W. J., and Walker, G. J., 1995, ''Observation of Wake-Induced Transition on an Axial Compressor Blade,'' ASME Paper No. 95-GT-381.

[4] Halstead, D. E., Wisler, D. C., Okiishi, T. H., Walker, G. J., Hodson, H. P., and Shin, H. W., 1997, ''Boundary Layer Development in Axial Compressors and Turbines: Part 1–4,'' ASME J. Turbomach., **119**, pp. 114–127; 426–444; 225–237; 128–139.

[5] Pieper, S., Schulte, J., Hoynacki, A., and Gallus, H.E., 1996, ''Experimental Investigation of a Single Stage Axial Flow Compressor With Controlled Diffusion Airfoils,'' ASME Paper No. 96-GT- 81.

[6] Cumpsty, N. A., Dong, Y., and Li, Y. S., 1995, ''Compressor Blade Boundary Layers in the Presence of Wakes,'' ASME Paper No. 95- GT-443.

[7] Hourmouziadis, J., 1989, ''Aerodynamic Design of Low Pressure Turbines,'' AGARD Lecture Series No. 167.

[8] Köller, U., Mönig, R., Küsters, B., and Schreiber, H. A., 2000, ''Development of Advanced Compressor Airfoils for Heavy-Duty Gas Turbines, Part I: Design and Optimization,'' ASME J. Turbomach., **122**, pp. 397–405.

[9] Küsters, B., Schreiber, H. A., Köller, U., and Mönig, R., 1999, ''Development of Advanced Compressor Airfoils for Heavy Duty Gas Turbines, Part II: Experimental and Analytical Analysis,'' ASME J. Turbomach., **122**, pp. 406–414.

[10] Wisler, D. C., 1985, ''Loss Reduction in Axial-Flow Compressors Through Low Speed Model Testing,'' ASME J. Eng. Gas Turbines Power, **107**, pp. 354–363.

[11] Abu-Ghannam, B. J., and Shaw, R., 1980, ''Natural Transition of Boundary Layers—The Effect of Turbulence, Pressure Gradient and Flow History,'' J. Mech. Eng. Sci., **22**, No. 5, pp. 213–228.

[12] Gostelow, J. P., and Bluden, A. R., 1989, ''Investigation of Boundary Layer Transition in an Adverse Pressure Gradient,'' ASME J. Turbomach., **111**, pp. 366–375.

[13] Mayle, R. E., 1991, ''The 1991 GTI Scholar Lecture: The Role of Laminar–Turbulent Transition in Gas Turbine Engines,'' ASME J. Turbomach., **113**, pp. 509–537.

[14] Blair, M. F., 1982, ''Influence of Free-Stream Turbulence on Boundary Layer Transition in Favorable Pressure Gradients,'' ASME J. Eng. Power, **104**, pp. 743–750.

[15] Drela, M., and Youngren, H., 1991, ''Viscous/Inviscid Method for Preliminary Design of Transonic Cascades,'' AIAA Paper No. 91-2364.

[16] Drela, M., 1995, ''Implementation of Modified Abu-Ghannam Shaw Transition Criterion,'' MISES User's Guide, MIT, Computational Aerospace Science Lab., Cambridge, MA.

[17] Schreiber, H. A., Starken, H., and Steinert, W., 1993, ''Transonic and Supersonic Cascades,'' AGARDOgraph ''Advanced Methods for Cascade Testing,'' AGARD AG 328, pp. 35–59.

[18] Steinert, W., and Starken, H., 1996, ''Off-Design Transition and Separation Behavior of a CDA Cascade,'' ASME J. Turbomach., **118**, pp. 204–210.

[19] Bize, D., Lempereur, C., Mathe, J. M., Mignosi, A., Seraudie, A., and Serrot, G., 1998, ''Transition Analysis by Surface Temperature Mapping Using Liquid Crystals,'' Aerospace Sci. Tech., Paris, No. 7, pp. 439–449.

[20] Mick, W. J., 1987, ''Transition and Heat Transfer in Highly Accelerated Rough-Wall Boundary Layers,'' Ph.D. Thesis, Rensselaer Polytechnic Institute, Troy, NY.

[21] Schäffler, A., 1980, ''Experimental and Analytical Investigation of the Effect of Reynolds Number and Blade Surface Roughness on Multistage Axial Flow Compressors,'' ASME J. Eng. Power, **102**, pp. 5–12.

Multi-Blade Row Interactions in a Transonic Axial Compressor: Part I—Stator Particle Image Velocimetry (PIV) Investigation

A. J. Sanders[1]
J. Papalia
S. Fleeter

School of Mechanical Engineering,
Purdue University,
West Lafayette, IN 47907

Multi-blade row interactions in an advanced design 1&1/2 stage axial-flow compressor are experimentally investigated at both subsonic and transonic rotor operating conditions using particle image velocimetry (PIV). Transonic rotor operation had a significant impact on the downstream stator unsteady flow field due to phenomena associated with the intra-stator transport of the chopped rotor wake segments. In the stator reference frame, the rotor wakes have a slip velocity relative to the mean flow that causes the low-momentum wake fluid to migrate across the vane passage and accumulate on the stator pressure surface as the chopped wake segments are transported downstream. This results in the generation of counterrotating vortices on each side of the chopped wake segment that convect downstream with the mean flow and act as an additional source of unsteadiness to the vane pressure surface. These interaction phenomena are not evident in the PIV data at the part-speed compressor operating condition due to the much lower velocity deficit and hence slip velocity associated with the subsonic rotor wakes.
[DOI: 10.1115/1.1411973]

Introduction

To predict blade row interaction phenomena, design system unsteady aerodynamic analyses generally consider the response of an isolated blade row, with both linearized frequency domain and nonlinear time-accurate computational fluid dynamic (CFD) analyses utilized. Both approaches first require the specification of the unsteady aerodynamic forcing functions as a boundary condition, with viscous wakes generated by an upstream blade row the most common type of forcing function considered in these analyses. In the unsteady analysis, the wake profiles are specified using either the results of a steady CFD analysis or empirical correlations based on far field measurements taken behind low-speed cascades or isolated blade rows. This approach, however, is often found to be inadequate when predicting the forced response behavior of multistage turbomachinery, due in part to multi-blade row interaction effects not being accounted for in the analysis.

In multistage turbomachines, downstream blade rows periodically chop upstream-generated vane wakes, with the chopped wake segments reoriented as they are transported through the rotor passage. These chopped wake segments do not become reunited at the rotor exit due to the airfoil circulation, thereby causing attenuation of the wake segments by dispersion [1]. This inviscid wake transport process is often referred to as wake recovery, with the inviscid straining of the chopped wake segments by the downstream vane row potential flow field enhancing the rotor wake decay by a reversible process that reduces the viscous mixing losses. Van Zante et al. [2] developed a model to evaluate the relative contributions of viscous dissipation and inviscid stretching to the decay of rotor wakes as they are transported through a downstream stator passage, with the model predicting inviscid stretching to be the dominant wake decay mechanism. Poensgen and Gallus [3] investigated the decay of wakes generated by a rotor consisting of circular cylinders both with and without a downstream stator. The presence of the downstream stator was found to cause the rotor wakes to decay twice as fast as those produced by the rotor in isolation.

In the reference frame of the downstream stator, the wake fluid has a higher tangential velocity component than the free stream, Fig. 1. This slip velocity causes the low-momentum wake fluid to drift across the vane passage and collect on the airfoil pressure surface as the chopped wake segments are transported downstream. This results in a local broadening of the wake segment near the pressure surface and a thinning near the suction surface due to ''negative jet'' effects. Recirculating flow patterns are also generated as high-momentum free-stream fluid is drawn into the chopped wake segment near the suction surface to replace the low-momentum wake fluid that has drifted across the passage. As the low-momentum wake fluid accumulates on the airfoil pressure

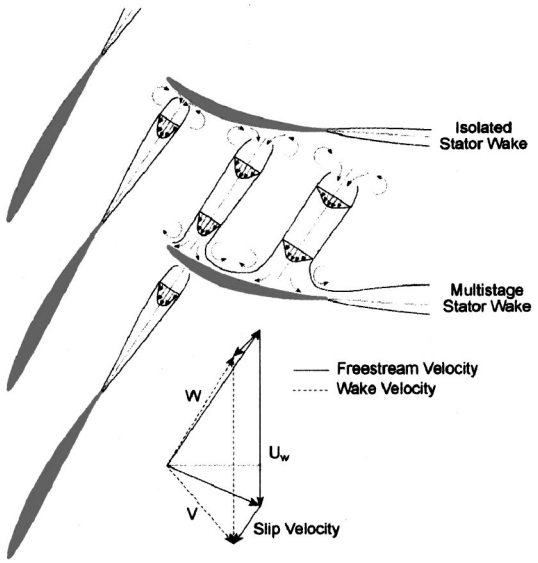

Fig. 1 Intra-stator transport of chopped rotor wake segments

[1]Currently at Honeywell Engines & Systems, Phoenix, AZ.

Contributed by the International Gas Turbine Institute and presented at the 46th International Gas Turbine and Aeroengine Congress and Exhibition, New Orleans, Louisiana, June 4–7, 2001. Manuscript received by the International Gas Turbine Institute February 2001. Paper No. 2001-GT-268. Review Chair: R. Natole.

surface, it will interact with the airfoil boundary layer and eventually end up appearing in the wakes of the blade row that performs the chopping.

Hodson [4] investigated the wake-generated unsteady flow field in a turbine rotor using a two-dimensional inviscid analysis. The chopped wake segments became bowed as they were ingested into the blade passage due to the convection velocity being much higher near midpassage than at the leading edge stagnation points. The chopped wake segments also behaved as ''negative jets'' as they were transported downstream, with the low-momentum wake fluid drawn across the passage from the pressure toward the suction surface of the blade. This wake migration resulted in a recirculating flow pattern and the generation of a large pair of vortices of opposite sign on each side of the chopped wake segment.

Valkov and Tan [5] used an incompressible two-dimensional Navier–Stokes analysis to investigate the unsteady flow field generated in a stator vane row due to its interaction with incoming rotor wakes. The unsteady flow over the vane pressure surface was substantially different in nature from that on the suction surface due to the wake chopping and transport process. Once the wakes entered the vane passage, the slip velocity in the rotor wakes caused the wake fluid to migrate toward the vane pressure surface where it piled up and evolved into two counterrotating vortices. For strong wakes with a rotor relative velocity deficit of 75 percent, these nonlinear self-advective wake migration effects were significant compared to the convective action of the free stream flow. When the incoming velocity deficit was reduced to 30 percent, the free-stream convective effects became dominant and the solution was characterized by more persistent wake segments and weaker vortices.

Circumferential nonuniformities in the stage exit total temperature profiles have also been attributed to the transport of the chopped rotor wake segments through downstream stator passages, with these nonuniformities sometimes as large as 10 percent of the temperature rise across the stage [6]. This is due to the chopped rotor wake segments collecting on the stator pressure surface as they are transported downstream, with the low-momentum rotor wake fluid tending to appear in the stator wake regions. Since the rotor wakes have a higher stagnation temperature than the free stream, this intra-stator transport process leads to a circumferential variation in the stator exit total temperature profile.

Particle image velocimetry (PIV) is a relatively new whole-field technique that provides quantitative measurement and visualization of a two-dimensional velocity field. In this technique, seed particles within the flow field are illuminated by a thin light sheet generated by a double-pulsed high-power laser, with images of the particles corresponding to the first and second laser pulse recorded. The distances traveled by the particles over this time interval are determined using correlation algorithms, with the velocity field calculated by dividing each distance by the known time between pulses. The result is an instantaneous measurement of the two-dimensional velocity field at a single instant in time, thereby providing quantitative visualization of flow field structures that would be difficult if not impossible to obtain using conventional point measurement techniques such as laser doppler velocimetry (LDV).

However, there have been relatively few PIV applications to turbomachinery, with most focusing on the steady blade-to-blade flow field. These include measurements in a two-dimensional turbine cascade [7], a transonic three-dimensional annular turbine nozzle [8], a low-speed compressor rotor [9], and the first-stage vanes of a low-speed turbine with and without leading edge showerhead film cooling [10]. Funes-Gallanzi et al. [11] have also made PIV measurements in the wake region behind an isolated transonic turbine nozzle and reported reasonable agreement with a steady three-dimensional viscous analysis.

Day-Treml and Lawless [12] investigated vane–blade interactions in a low-speed turbine, with PIV data acquired between the first-stage vane and blade row. Near the rotor leading edge, the flow underturning in the vane wake was dominated by overturning caused by the periodic passing of the rotor potential field. Ehrlich and Fleeter [13] used PIV to characterize the unsteady flow over an annular cascade airfoil driven to oscillate in a chordwise bending mode. High leading edge unsteady loading occurred at zero mean incidence as the stagnation point migrated from the upper to the lower surface of the airfoil over one oscillation cycle, with this unsteadiness enhanced by the periodic formation and collapse of a leading edge separation bubble.

Time-accurate multi-blade row CFD analyses are beginning to be utilized to analyze nonlinear blade row interactions in advanced turbomachine designs. These analyses account for blade row interaction effects and also eliminate the need to specify the forcing functions as boundary conditions since they are determined as part of the solution. However, the computational domain utilized for these simulations is usually reduced by scaling the geometry such that each airfoil row is represented at most by a few passages. This greatly reduces computer processing time and storage requirements, but alters the fundamental periodicity of rotor–stator interactions, i.e., the interblade phase angle, which is specified by the blade–vane count ratio. Additionally, the solutions converge very slowly and require vast computational resources. Fundamental blade row interaction data are thus needed to assess the validity of these time-accurate multi-blade row CFD analyses.

This two-part paper is directed toward addressing this need, while also providing an improved understanding of unsteady aerodynamic interactions in multi-blade row turbomachinery. This is accomplished by obtaining detailed benchmark rotor–stator unsteady aerodynamic blade row interaction data in an advanced design transonic 1&1/2 stage axial-flow research compressor at both design and part-speed operating conditions. These detailed data include measurements of the rotor wake generated unsteady aerodynamic forcing function to the downstream stator, the resultant stator vane steady and unsteady aerodynamic response, and PIV measurements of the time-variant stator midspan vane-to-vane flow field. This portion of the paper describes time-variant PIV measurements of the downstream stator flow field, with the rotor wake-generated forcing function and downstream stator steady and unsteady aerodynamic response data described in Part II.

Research Facility

The Purdue Transonic Research Compressor Facility features a 1&1/2 stage axial-flow geometry representative of that used in the front stages of advanced aircraft engine high-pressure compressor designs. The drive system consists of a 400-hp AC motor, a variable speed magnetic clutch, and an 8:1 ratio gearbox, the output of which drives the compressor rotor, Fig. 2. Atmospheric air is drawn into the test section through a converging bellmouth inlet with a 16:1 contraction ratio and exits the test section through discharge piping, which contains a butterfly throttle valve to regulate the flow rate.

The test section has a constant hub–tip ratio of 0.67 with a tip diameter of 0.3 m (12.0 in.) and features an inlet guide vane (IGV) row, a blisk with 19 rotor blades, and a downstream stator. The compressor design speed is 20,000 rpm, with a maximum pressure ratio of 1.38. The rotor blades consist of NACA 65 series profiles on circular arc meanlines with a 5.08 cm (2.0 in.) chord and a thickness distribution varying from 10 percent at the root to 6 percent at the tip. The IGV and stator vanes are an advanced controlled diffusion airfoil (CDA) design with a 4.45-cm (1.75-in.) chord and a constant 7 percent thickness. Both the IGV row and stator feature variable stagger angles, adjustable axial spacings, and can be independently configured with either 18 or 20 vanes. Additionally, the IGV row is indexable, i.e., the IGV ring can be clocked circumferentially relative to the downstream stator and stationary instrumentation probes.

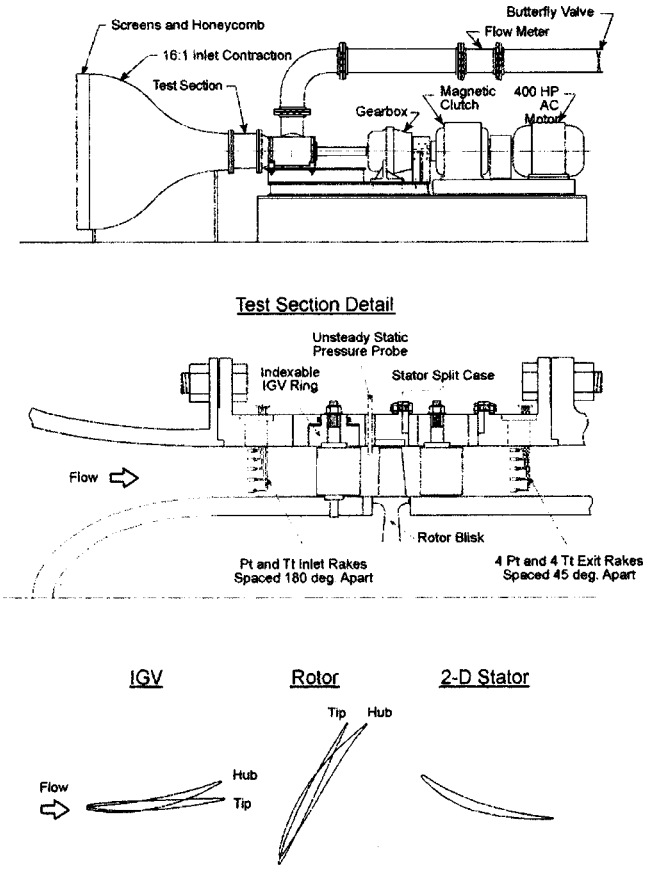

Fig. 2 Purdue transonic compressor research facility

Particle Image Velocimetry

Particle image velocimetry (PIV) is a whole-field measurement technique, providing quantitative flow visualization of a two-dimensional velocity field. The flow is seeded with tracer particles, with the two-dimensional blade-to-blade plane of interest illuminated by a laser sheet generated by a timed double pulse of a high-power laser. In the digital PIV technique, a CCD (charge coupled device) camera synchronized to the laser is used to record the images of the seed particles within the light sheet for both laser pulses. The camera images are then divided into rectangular interrogation regions and correlation algorithms used to determine an average displacement vector for each region. The velocity vectors are then determined by dividing each displacement vector by the specified time between pulses.

PIV System. The DANTEC PIV system utilized for these experiments consists of a 30-mJ NewWave Research Minilase III Nd:YAG laser, a high-resolution Kodak Megaplus ES 1.0 digital camera, and a dedicated personal computer (PC) controlled PIV 2100 Processor. The laser has twin oscillators operated in single Q-switch mode and are capable of delivering a 5–7 ns duration pulse with a wavelength of 532 nm (visible green light) at a repetition rate of 10 Hz. The two oscillators are necessary to provide a pair of equal energy laser pulses in the short time interval required to expose the images in a high-speed flow, with the time between pulses specified using software. The digital camera has a 1008×1018 CCD array operated in cross-correlation mode, with the images corresponding to the first and second pulse of the laser recorded separately. Both images are then transferred to the PIV 2100 Processor that provides near real-time vector processing of the images using Fast Fourier Transform (FFT) correlation techniques. This unit also synchronizes the camera and laser, and is capable of resolving the particle displacement to within 1/10 of a pixel through the use of sub-pixel interpolation schemes. PC controlled software is used to perform off-line validation and post-processing of the vector maps, with directional velocity information unambiguously determined since the initial and final particle positions are recorded as separate images.

Flow Seeding. Reliable PIV measurements require that the flow be seeded with tracer particles small enough to track the flow accurately and large enough to scatter sufficient light to be detected with the imaging system. These particles must be introduced in a manner that does not significantly disturb the flow field and at the same time provides a sufficient and uniform seeding density in the region of interest. Due to the high flow rate through the compressor, a Rosco 1600 Fog Machine is used to generate the seed particles. This is a thermal aerosol generator that produces a high volume of seed particles by discharging a heated and pressurized glycol-based mixture into the atmosphere where it immediately vaporizes and then condenses into a fine mist of monodisperse particles. A uniform seeding density in the test section is achieved by introducing these seed particles upstream of the bell-mouth inlet and allowing them to disperse into the ambient air prior to being drawn through the facility.

PIV Image Acquisition. To characterize the downstream stator unsteady flow field generated by the rotor–stator interactions, the instantaneous midspan vane-to-vane flow field is measured for several time instants over one rotor blade-passing period. A once-per-revolution pulse from a photo-optic sensor on the compressor shaft triggers the PIV 2100 Processor that then fires the lasers and records the camera CCD images. To record images at different points over one interaction cycle, the measured rotor speed is used to calculate the time delay to position the rotor at the desired angular location relative to the stationary vanes. This value is then programmed into a LaserStrobe 165 Phase Delay Generator, which can deliver an accurate time delay up to 999.9 μs in 0.1-μs increments.

Optical access for the PIV measurements is provided to a single stator passage using a removable window assembly, which features 2.54 cm (1.0 in.) constant-thickness Plexiglas contoured to the flow path O.D., Fig. 3. Note that the PIV data are acquired for the same passage at which the unsteady rotor wake generated forcing and vane unsteady aerodynamic response measurements were made, but these data are not simultaneous. The midspan vane-to-vane flow field is illuminated by a 1-mm-thick sheet introduced downstream of the stator through an optical probe, Fig. 4. The probe has a 7.94-mm O.D. and consists of a 45-deg high-energy Nd:YAG mirror and a +4.0-mm plano-cylindrical lens. Prior to entering the probe, the laser beam is passed through an iris and a 1000-mm plano-convex lens located on a breadboard

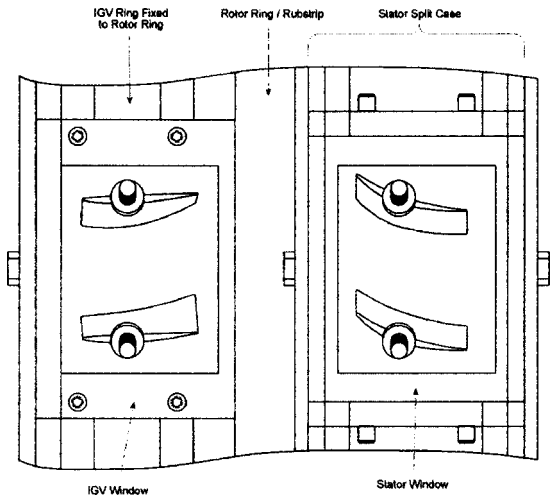

Fig. 3 Flow path optical access

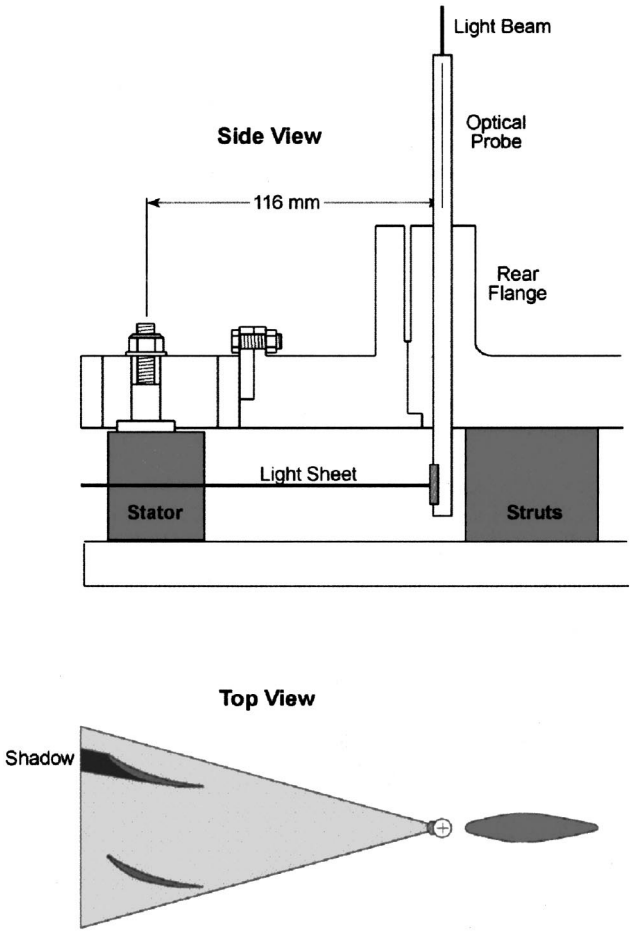

Fig. 4 Stator optical probe and light sheet optics

adjacent to the test section. To minimize disturbances produced by the finite size of the probe, it is positioned ahead of the support strut leading edge 2.06 stator chord lengths downstream of the stator trailing edge.

A 60-mm Nikon lens with an aperture setting of f/4.0 is used to image the flow through the entire vane passage onto the CCD array. This provides information about the global features of the downstream stator unsteady flow field generated by rotor–stator interactions, but the spatial resolution is inadequate to resolve small-scale flow structures. To examine the details of the downstream stator unsteady flow field generated by these interactions, a Nikon 105-mm lens is used to image only a small portion of the vane flow field onto the CCD array. The magnification factors for both lenses are determined by photographing a test grid with known spacing through the window assembly, with optical distortion caused by the curved window accounted for by using separate scale factors in the horizontal and vertical directions.

PIV Image Analysis. The images corresponding to the first and second laser pulses are divided into rectangular interrogation areas, with cross-correlation software used to determine an average particle displacement for each region. To obtain a high signal-to-noise ratio, the interrogation area must be small enough so that the flow velocity is homogeneous within each region and at the same time large enough to encompass a sufficiently large population of particle pairs. When imaging large areas with high gradients such as unsteady flow through turbomachinery blade passages, it may not be possible to satisfy both of these requirements simultaneously, and a compromise must be made when choosing the size of the interrogation area.

The FFT processing algorithm that computes the cross-correlations generates artificial cyclic background noise at the edges of each interrogation area, since this approach assumes that the sampled regions are periodic in space. This can result in the loss of particle pairs due to a low signal-to-noise ratio at the boundaries, with particles near the edges not used in the velocity calculation. However, this information is recovered by oversampling the images using overlapping interrogation regions. This process does not increase the fundamental spatial resolution, but generates additional vectors as suitable interpolations. For the present investigation 32×32 pixel interrogation areas with 50 percent overlap are used to process the image maps, which results in 3844 raw velocity vectors per image. The maximum uncertainty in these velocity measurements is estimated to be 2.5 percent.

Results

The downstream stator unsteady flow field generated by rotor–stator interactions is experimentally investigated along the nominal operating line at both the transonic design speed ($N_c = 20{,}000$ rpm) and part-speed condition in which the rotor flow is subsonic ($N_c = 15{,}000$ rpm), Fig. 5. For these experiments, the compressor test section is configured with moderate axial spacings, with the IGV–rotor and rotor–stator midspan axial spacings set at 41.4 and 39.0 percent stator chord, respectively. Both the IGV and stator have 18 vanes set at their design stagger angles (minimum loss incidence), with the IGV row fixed in the unclocked position, i.e., the stacking axes of the IGV and stator vanes coincide at the same circumferential position, Fig. 2. Note that the unsteady data presented in Parts I and II of this paper are acquired for the same reference stator passage, i.e., the rotor wake generated forcing function, stator vane unsteady aerodynamic response, and PIV data are for the same stator passage but are not simultaneous. Additionally, the vane-blade initial position for these data correspond to the rotor stacking axis being at the center of the reference passage at time $t=0$.

PIV Data Ensemble Averaging. The PIV data are ensemble-averaged in order to obtain clean periodic snapshots of the downstream stator flow field at several time instants over one interaction cycle. Figure 6 shows the effect of using different numbers of images to determine the ensemble-averaged axial Mach number contours for a single frozen rotor blade position at the transonic design speed. The instantaneous stator flow field for one ensemble contains a high degree of random unsteadiness, but with 30 ensembles a clean periodic snapshot of the flow field is obtained. Relatively few ensembles are required for the PIV data since the vector fields for each image are constructed using a ''spatial average'' of the velocity within each interrogation region, with processing of the image maps averaging out many of the small-scale structures associated with turbulent flow.

Note that there are some regions of the flow field where it was not possible to acquire valid data. Since the flow field is turbulent, there is a finite probability that some particles will travel out of the plane of the light sheet between successive images. This loss of particle pairs causes some interrogation regions to yield no

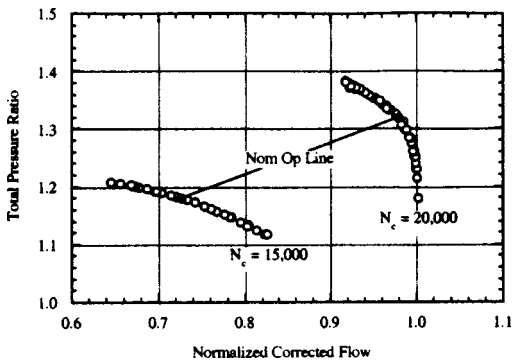

Fig. 5 Purdue transonic compressor performance map

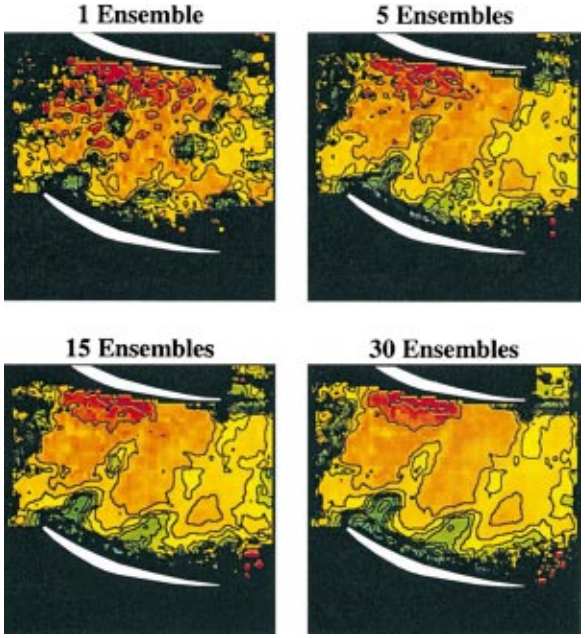

Fig. 6 Effect of ensemble-averaging the stator flow field at transonic rotor speed

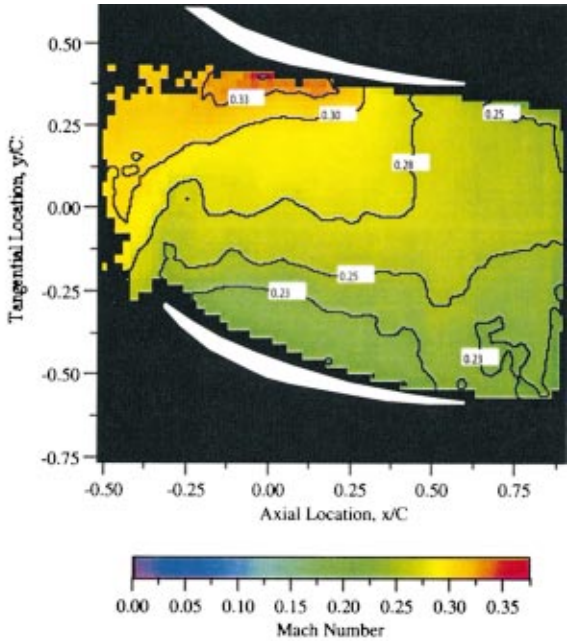

Fig. 7 Time-averaged stator flow field at subsonic rotor speed

valid data, with this loss of data occurring at random locations in each image. Additionally, there are other regions of the flow field where it was not possible to obtain valid data regardless of the number of ensembles used, i.e., near the vane surfaces and passage inlet. The lack of data in these regions is attributed to a combination of factors such as saturation of the raw image caused by shadows and reflections off the vane surfaces and secondary reflections off the rotating rotor blades back into the vane passage. Three-dimensional effects associated with the highly loaded rotor wakes and their transport through the vane passage may also contribute to the lack of data in certain regions of the flow field, particularly near the pressure surface of the vane, where the chopped wake segments collect on the airfoil surface. In general, the number of valid vectors used to compute the ensemble average flow field is less than the number of images acquired, with no valid data present in some regions of the flow. For the subsequent analysis, 30 images are used to calculate the ensemble-averaged velocity field for each rotor position, with at least ten valid vectors required to compute the mean for each interrogation area.

Stator Vane-to-Vane Flow Field. The time-variant downstream stator midspan vane-to-vane flow field is measured using PIV, with ensemble-averaged snapshots of the periodic unsteady flow field generated by rotor–stator interactions presented for ten equally spaced increments over one blade-passing period. The time-average of the unsteady flow field is also presented, with this vector field calculated by arithmetically averaging the ensemble-averaged flow field over one complete interaction cycle. Since it was not possible to obtain valid data at every point in the flow field, the time-average is calculated only for interrogation regions that had valid velocity vectors at all ten time instants.

The time-averaged stator midspan Mach number contours are shown in Figs. 7 and 8 for the subsonic and transonic compressor operating conditions, respectively. These time-averaged PIV data are in excellent agreement with the steady surface Mach number distributions shown in Fig. 9, with the surface Mach number calculated from the pneumatic pressure tap data described in Part II of this paper. Specifically, the steady surface Mach number distributions for the subsonic rotor speed indicate that the average inlet and exit Mach numbers are 0.30 and 0.25, respectively, with the pressure surface Mach number nearly constant at 0.23 and the suction surface Mach number peaking at 0.38 at 30 percent chord. At the transonic rotor speed, the average inlet and exit Mach numbers determined from the pneumatic surface pressure data are 0.39 and 0.34, with the pressure surface Mach number nearly constant at 0.30 and the suction surface Mach number peaking at 0.51 at 30 percent chord. These values are in excellent agreement with the time-averaged PIV data for both rotor speeds.

Two unsteady flow phenomena occur as the rotor wakes are chopped and transported through the downstream stator passages. First, the circulation around the stator vanes enhances the decay rate of the rotor wakes due to an inviscid straining of the wake fluid as the chopped wake segments are convected downstream, Fig. 10. For an incompressible inviscid two-dimensional flow,

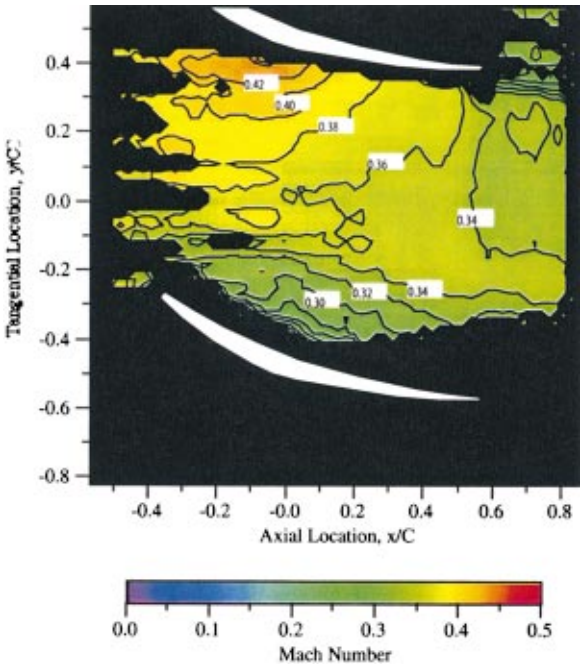

Fig. 8 Time-averaged stator flow field at transonic rotor speed

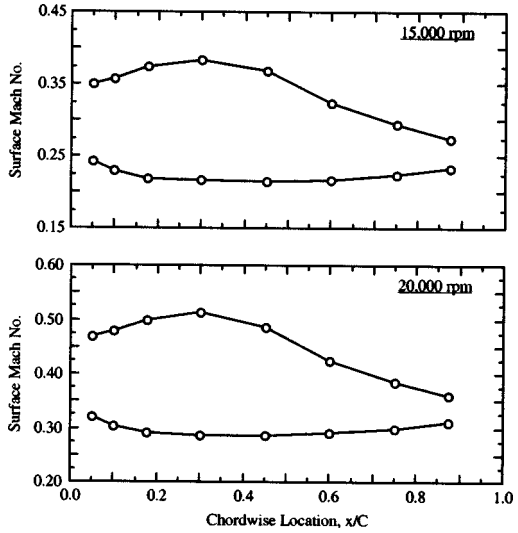

Fig. 9 Stator steady midspan surface Mach number distributions

Kelvin's theorem requires that the circulation associated with the incoming wake segment remain constant as it is transported through the vane passage. Thus, the length of the chopped wake segment increases and its width is reduced as it convects downstream to maintain the same vorticity. Since the velocity deficit is proportional to the width of the wake for a fluid with constant vorticity, the straining of the wake fluid by the vane row potential field causes the chopped wake segments to decay faster than they would behind an isolated blade row. This inviscid straining occurs in addition to viscous dissipation and is commonly referred to as wake recovery, which is a reversible process that reduces the viscous mixing losses.

Second, the low-momentum rotor wake fluid has a slip velocity relative to the free stream that causes it to drift across the vane passage and accumulate on the vane pressure surface as the chopped rotor wake segments are transported downstream, Fig. 1. This slip velocity causes the low-momentum rotor wake fluid to drift across the vane passage and collect on the airfoil pressure surface as the chopped wake segments are transported downstream. This results in a local broadening of the wake segment near the pressure surface and a thinning near the suction surface due to ''negative jet'' effects. Recirculating flow patterns are also generated as high-momentum free-stream fluid is drawn into the chopped wake segment near the suction surface to replace the low-momentum wake fluid that has drifted across the passage. As the low-momentum rotor wake fluid accumulates on the vane pressure surface, it will interact with the airfoil boundary layer and eventually end up appearing in the stator wake regions.

These unsteady phenomena are investigated by examining the downstream stator time-variant midspan vorticity and axial Mach

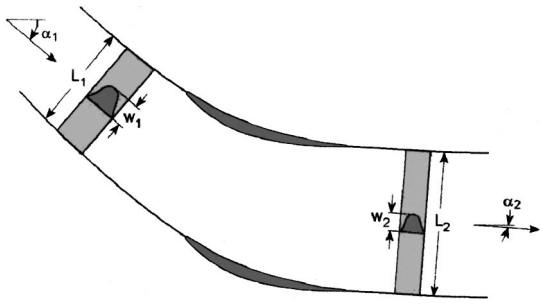

Fig. 10 Inviscid wake recovery process for a stator row

number contours at ten time instants over one blade-passing period. The time-variant vorticity field is shown in Figs. 11 and 12 for the subsonic and transonic rotor speeds, respectively. The vorticity is calculated from the ensemble-averaged velocity using central differencing and is normalized by the compressor inlet stagnation speed of sound and stator chord length, with the calculation performed only if there are valid velocity vectors present for all four neighboring interrogation areas. The shear flow in the rotor wake causes the vorticity to be negative on the suction side of the wake and positive on the pressure side. Thus, the chopped wake segments appear as alternating bands of positive and negative vorticity that extend across the vane passage and are convected downstream with the mean flow.

The reduced frequency is defined as the ratio of the time it takes a fluid particle to convect through the vane row to the time scale of the wake-generated unsteadiness. Thus, this parameter provides an indication of the number of chopped wake segments residing within the vane passage at any given instant in time. The reduced frequencies based on the mass-averaged midspan stator inlet velocity are 2.42 and 2.45 for the subsonic and transonic rotor speeds, respectively, indicating that it takes approximately 2.5 blade-passing periods for one chopped wake segment to be completely transported through the vane row.

For both rotor speeds, the rotor wake is in the process of being cut by the lower vane between $t/T=0.5$ and $t/T=0.8$. Notice that this wake was cut by the upper vane in the passage at an earlier time, with the blade-vane count ratio setting the spatial periodicity of the wake chopping and transport process. For the present geometry with 19 rotor blades and 18 stator vanes, the interblade phase angle is 380 deg. Thus, the rotor wake was cut by the upper vane 1.06 blade-passing periods earlier, with the resulting unsteady flow in the vane passage periodic at blade-pass frequency.

After being cut by the vane, the chopped wake segment acts a ''negative jet,'' with the slip velocity in the wake region causing low-momentum wake fluid to drift across the vane passage and collect on the pressure surface as it convects downstream. The effects of this are first visible at $t/T=0.8$ for both rotor speeds, with the chopped wake segment becoming noticeably broader along the pressure surface of the lower vane and thinner near the suction surface of the upper vane in the passage. Both viscous dissipation and the inviscid straining of the wake fluid by the vane row potential field cause it to decay as it is transported through the vane passage, with the vorticity of the wake segment thus reduced as the cycle progresses.

The subsonic rotor wakes decay very rapidly after they are chopped and ingested into the stator passage, Fig. 11. This decay is evident by examining the vorticity contours for the first chopped wake segment between $t/T=0.8$ and $t/T=0.2$, with the dispersion of the chopped wake segment very noticeable. The chopped wake segment continues to disperse as the cycle progresses, with both the wake width increasing and the vorticity decreasing considerably by the time it exits the stator passage 2.5 blade-passing periods after being initially cut. Note, however, that even though the subsonic rotor wakes decay considerably as they are chopped and transported through the stator, the chopped rotor wake segments are still clearly evident downstream of the stator trailing edge.

The chopped rotor wakes appear to disperse much more rapidly at the transonic rotor speed, and are not evident downstream of the stator trailing edge as they were for the subsonic compressor operating condition, Fig. 12. This result is surprising considering that the transonic rotor wakes are much larger than those generated by subsonic flow, with the transonic rotor wake velocity deficit 25.7 percent of the free-stream relative Mach number versus 15.2 percent at the subsonic rotor speed. Thus, it might be expected that the transonic rotor wakes would persist for longer distances downstream of the rotor. However, the reasons for the more rapid decay of the rotor wakes at the transonic rotor speed are due to unsteady flow effects. Specifically, the slip velocity in

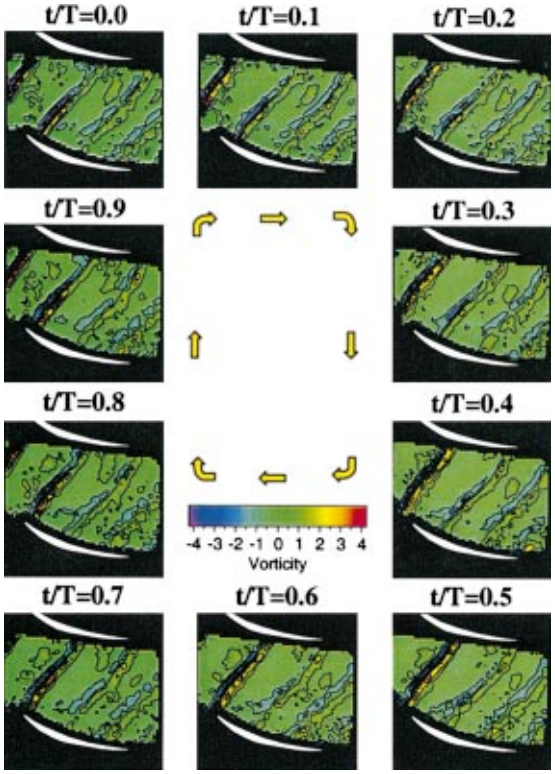

Fig. 11 Time-variant stator vorticity at subsonic rotor speed

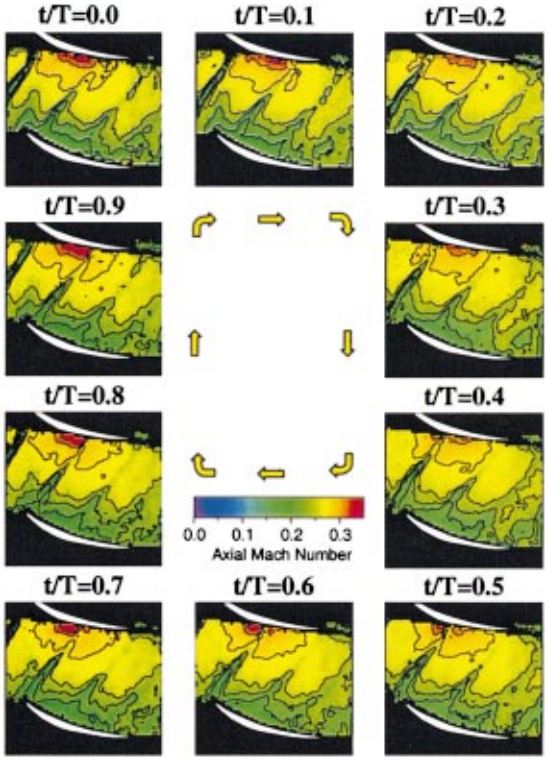

Fig. 13 Time-variant stator axial Mach number at subsonic rotor speed

the rotor wakes causes low-momentum fluid to drift across the stator passage as the chopped wake segments are transported downstream, with this rotor wake fluid accumulating on the vane pressure surface and thus appearing in the stator wake regions during the transport process. This unsteady intra-stator wake transport process is more significant at the transonic rotor speed due to the much deeper and broader rotor wakes generated by transonic compressor operation, with the differences between the subsonic and transonic rotor wakes described in Part II of this paper.

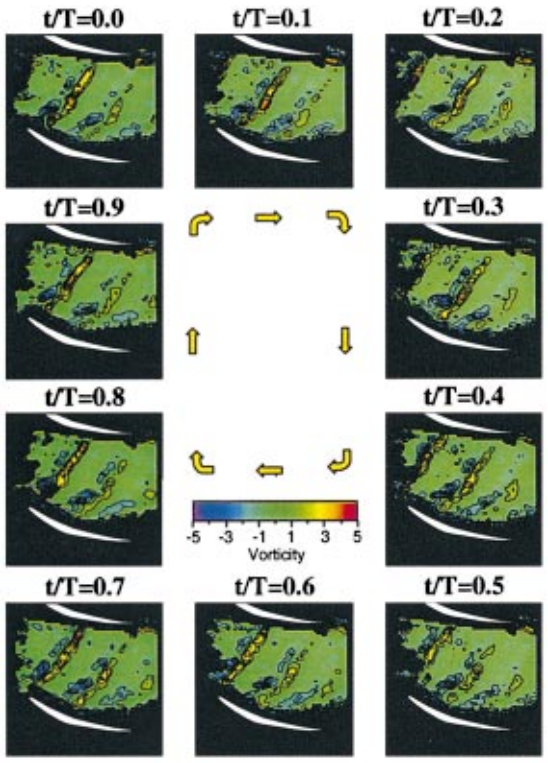

Fig. 12 Time-variant stator vorticity at transonic rotor speed

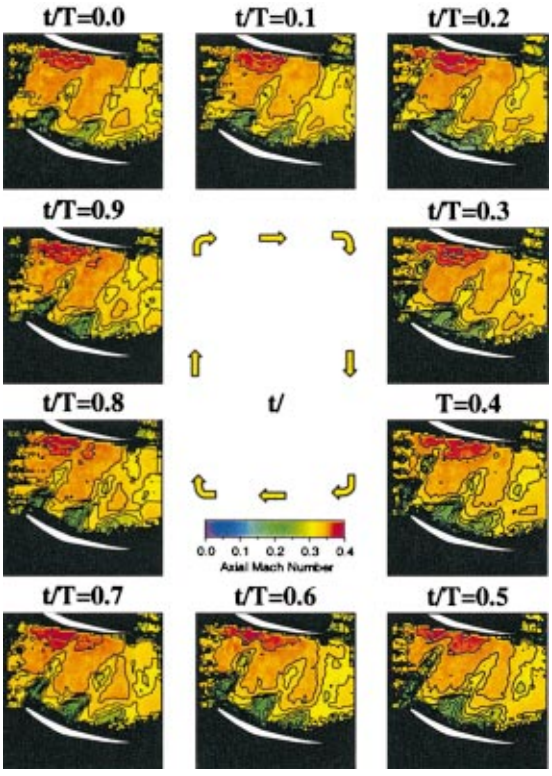

Fig. 14 Time-variant stator axial Mach number at transonic rotor speed

This intra-stator wake transport process is further investigated by examining the axial Mach number contours for the subsonic and transonic rotor speeds, Figs. 13 and 14, respectively. Notice that the low-velocity regions associated with the chopped wake segments do not extend across the entire passage as did the vorticity contours, with this evident in the data for both rotor speeds. This is due to the wake segments being cut by the upper vane 1.06 blade-passing periods earlier, with a significant portion of the low-momentum wake fluid drifting toward the pressure surface during this time. Also recall that the chopped wake segments act as "negative jets" as they are transported downstream. Thus, high-momentum free-stream fluid is drawn into the wake segments on the suction side of the passage to replace the low-momentum wake fluid that has drifted toward the pressure surface during this time interval. It is this transport process that causes the low-velocity regions to be concentrated only on the pressure side of the passage.

At the subsonic rotor speed, the low-velocity regions associated with the chopped wake segments are superimposed on the steady flow field, with the time-variant flow field outside of the wake regions very similar to the time-average flow field depicted in Fig. 7 at each time instant. Additionally, very little low-momentum rotor wake fluid accumulates on the stator pressure surface as the chopped wake segments are transported through the vane row. This is consistent with the surface pressure data presented in Part II of this paper, in which the convection of the chopped wake segments through the vane passage have a low-order effect on the vane response at the subsonic rotor operating condition. In fact, the stator response at this operating condition is mainly due to changes in the airfoil circulation distribution due to the incidence change associated with the passing of the rotor wakes.

This is not the case for the transonic rotor speed, in which the higher slip velocity in the rotor wakes causes a significant amount of low-momentum wake fluid to accumulate on the vane pressure surface as the chopped wake segments convect downstream, Fig. 14. Also notice that distinct low-velocity regions associated with the various chopped wake segments are only evident in the leading edge region at the beginning of the wake chopping cycle between $t/T=0.5$ and $t/T=0.1$. For times $t/T=0.2$ to $t/T=0.5$, the low-velocity regions of the two adjacent chopped wake segments have begun to merge and encompass a significant portion of the airfoil pressure surface. This is due to the chopped wake segments becoming broader as they convect further downstream, with more and more low-momentum wake fluid accumulating on the vane pressure surface as the cycle progresses. This is again consistent with the surface pressure data presented in Part II of this paper, with the intra-stator transport of the chopped rotor wake segments through the vane passage significantly impacting the character of the vane pressure surface response at the transonic rotor speed.

Time-Variant Stator Pressure Surface Flow Field. To examine the detailed unsteady flow field generated by the accumulation of low-momentum rotor wake fluid on the stator vane pressure surface at the transonic rotor speed, PIV images were also acquired focusing on the pressure surface leading edge flow field. The wake migration process is depicted in Fig. 15, which shows the unsteady velocity vectors superimposed on the time-variant axial Mach number contours for the transonic rotor operating condition. This unsteady velocity field was calculated by subtracting the time-averaged velocity and shows how the steady flow field is perturbed at each time instant during the wake chopping cycle.

The slip velocity is largest prior to the wake being cut by the vane ($t/T=0.4$). Once the wake has been cut, this slip velocity causes the low-momentum rotor wake fluid to accumulate on the airfoil pressure surface as the chopped wake segment is transported downstream. Notice that the wake slip velocity is reduced as the cycle progresses and the chopped wake segment is convected farther downstream. This is due to both viscous dissipation and wake recovery effects enhancing the rotor wake decay rate, as

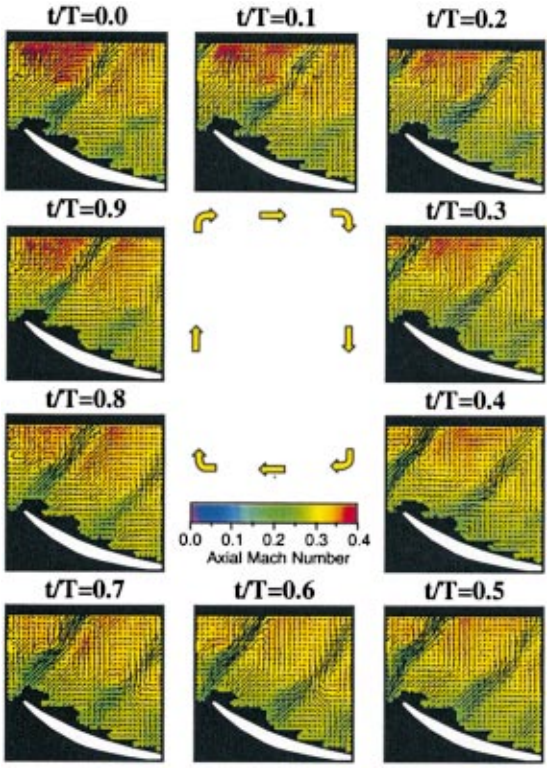

Fig. 15 Unsteady stator pressure surface velocity vectors at transonic rotor speed

can be seen by examining the length of the velocity vectors in the wake region as the cycle progresses onward from $t/T=0.5$.

As the wake fluid collects on the vane pressure surface, counterrotating vortices are generated near the airfoil that are evident throughout the entire cycle. These vortices are convected downstream along with the chopped wake segments and are an additional source of unsteady aerodynamic excitation to the stator vanes. Recirculating flow patterns are also established away from the vane surface on each side of the chopped wake segment as high-momentum free-stream fluid is drawn into the wake region to replace the low-momentum wake fluid that has migrated toward the airfoil pressure surface. Also, notice that these vortices actually appear to distort the chopped wake segment. This distortion, however, may be an artifact of a large radial velocity component in the convected wake regions that cannot be measured using conventional two-dimensional PIV techniques that only measure the axial and tangential velocity components. These three-dimensional effects may also be responsible for the lack of data near the vane pressure surface, with the radial velocity component at the impingement point on the airfoil surface probably significant.

Summary and Conclusions

The unsteady aerodynamic flow field of a downstream stator in an advanced design transonic 1&1/2 stage axial-flow compressor has been experimentally investigated at both subsonic and transonic compressor operating conditions. The blade row interaction data presented in Parts I and II of this paper were acquired at midspan and included measurements of the rotor wake generated forcing function, the resultant stator steady and unsteady aerodynamic response, and particle image velocimetry (PIV) measure-

ments of the time-variant stator midspan vane-to-vane flow field. This data provides a benchmark test case for unsteady multi-blade row CFD code validation.

Two unsteady flow phenomena occurred as the rotor wakes were chopped and transported through the downstream stator passages. First, the circulation around the stator vanes enhanced the decay rate of the rotor wakes due to an inviscid straining of the wake fluid as the chopped wake segments were transported through the vane row. This inviscid stretching, or wake recovery, occurred in addition to viscous dissipation and enhanced the rotor wake decay rate. Second, the chopped rotor wake segments acted as ''negative jets'' after being cut by the downstream vanes. This was due to the slip velocity in the wake region causing low-momentum wake fluid to drift across the stator passage and collect on the vane pressure surface as the chopped rotor wake segments were transported through the vane row.

The rotor wakes decayed very rapidly after they were chopped and ingested into the downstream stator passage, but were still evident downstream of the vane trailing edge for the subsonic rotor operating condition. This was not the case at the transonic rotor speed, in which the chopped rotor wakes dispersed much more rapidly and were no longer evident by the time they reached the stator exit. This increased decay rate was due to the much higher levels of unsteadiness at the transonic operating condition. In fact, even though the rotor wakes were much deeper at the transonic rotor speed, the higher slip velocity in the wake region caused more low-momentum fluid to drift across the stator passage and accumulate on the vane pressure surface as the chopped rotor wake segments were transported downstream.

As the low-momentum wake fluid collected on the vane pressure surface, counterrotating vortices were generated on each side of the chopped wake segment. These vortices were convected downstream by the mean flow and acted as an additional source of unsteadiness to the vane pressure surface. It should be noted that the presence of these vortices is not accounted for in linearized analyses that utilize the frozen gust assumption since they are generated by a nonlinear process. These interaction phenomena were not evident in the PIV data at the part-speed compressor operating conditions due to the subsonic rotor wakes having a much lower velocity deficit, and hence slip velocity, with the intra-stator wake transport process dominated by the convective action of the inviscid free-stream flow at the subsonic rotor speed.

These conclusions are consistent with the surface pressure data presented in Part II of this paper, in which the convection of the chopped wake segments through the vane passage had a low-order effect on the vane response at the subsonic rotor speed. In fact, the stator response at the subsonic rotor speed was mainly due to changes in the airfoil circulation distribution due to the incidence change associated with the passing of the rotor wakes. This was not the case at the transonic rotor speed, in which the intra-stator transport of the chopped rotor wake segments generated very high levels of unsteadiness on the vane pressure surface as the low-momentum rotor wake fluid accumulated on the vane surface during the transport process.

Finally, since the rotor wake fluid ultimately tends to appear in the stator wake regions, the characteristics of the wake-generated forcing function to a downstream rotor in a multistage compressor would be significantly impacted by this unsteady intra-stator wake transport process. Thus, these multi-blade row interaction effects must be accounted for to accurately predict the forced response characteristics of multistage turbomachinery.

Acknowledgments

This research was sponsored by the Air Force Office of Scientific Research (AFOSR) and Pratt & Whitney. This support is most gratefully acknowledged.

References

[1] Smith, L. H., Jr., 1966, ''Wake Dispersion in Turbomachines,'' ASME J. Basic Eng., **88**, pp. 688–690.
[2] Van Zante, D. E., Adamczyk, J. J., Strazisar, A. J., and Okiishi, T. H., 1997, ''Wake Recovery Performance Benefit in a High-Speed Axial Compressor,'' ASME Paper No. 97-GT-535.
[3] Poensgen, C., and Gallus, H. E., 1990, ''Three-Dimensional Wake Decay Inside of a Compressor Cascade and Its Influence on the Downstream Unsteady Flow Field Part I: Wake Decay Characteristics in the Flow Passage,'' ASME Paper No. 90-GT-21.
[4] Hodson, H. P., 1984, ''An Inviscid Blade-to-Blade Prediction of a Wake-Generated Unsteady Flow,'' ASME Paper No. 84-GT-43.
[5] Valkov, T., and Tan, C. S., 1993, ''Control of the Unsteady Flow in a Stator Blade Row Interacting With Upstream Moving Wakes,'' ASME Paper No. 93-GT-23.
[6] Kerrebrock, J. L., and Mikolajczak, A. A., 1970, ''Intra-Stator Transport of Rotor Wakes and Its Effect on Compressor Performance,'' ASME J. Eng. Power, **92**, pp. 359–368.
[7] Post, M. E., Goss, L. P., and Brainard, L. F., 1991, ''Two-Color Particle-Imaging Velocimetry in a Turbine Cascade,'' AIAA Paper No. 91-0274.
[8] Bryanston-Cross, P. J., Towers, C. E., Judge, T. R., Towers, D. P., Harasgama, S. P., and Hopwood, S. T., 1992, ''The Application of Particle Image Velocimetry (PIV) in a Short-Duration Transonic Annular Turbine Cascade,'' ASME J. Turbomach., **114**, pp. 504–509.
[9] Tisserant, D., and Breugelmans, F. A. E., 1997, ''Rotor Blade-to-Blade Measurements Using Particle Image Velocimetry,'' ASME J. Turbomach., **119**, pp. 176–181.
[10] Day, K. M., Lawless, P. B., and Fleeter, S., 1996, ''Particle Image Velocimetry Measurements in a Low-Speed Research Turbine,'' AIAA Paper No. 96-2569.
[11] Funes-Gallanzi, M., Bryanston-Cross, P. J., and Chana, K. S., 1994, ''Wake Region Measurements of a Highly Three-Dimensional Nozzle Guide Vane Tested at DRA Pyestock Using Particle Image Velocimetry,'' ASME Paper No. 94-GT-349.
[12] Day-Treml, K. M., and Lawless, P. B., 1998, ''Particle Image Velocimetry of Vane–Rotor Interaction in a Turbine Stage,'' AIAA Paper No. 98-3599.
[13] Ehrlich, D. A., and Fleeter, S., 1997, ''Particle Image Velocimetry Characterization of a Chordwise Bending Cascade Flowfield,'' AIAA Paper No. 97-3022.

U. Orth

H. Ebbing

MAN Turbomaschinen AG GHH BORSIG,
Oberhausen, Germany

H. Krain

A. Weber

B. Hoffmann

German Aerospace Center (DLR),
Cologne, Germany

Improved Compressor Exit Diffuser for an Industrial Gas Turbine

Cycle studies carried out for the medium pressure ratio gas turbine THM 1304 of 10 MW power output manufactured by MAN Turbomaschinen AG GHH BORSIG predicted that the overall efficiency of the multistage compressor, composed of a ten-stage axial and a single-stage centrifugal compressor, would improve by 0.8 percent if the efficiency of the back stage centrifugal unit could be raised by 4 percent. It was expected that this would result in a noticeable improvement of the thermal gas turbine efficiency. The paper describes the aerodynamic design process used for the stage optimization, applying today's advanced design tools for blade generation and three-dimensional aerodynamic calculation methods. Additionally, it describes the manufacturing procedure for the resulting three-dimensional blades and the experimental verification of the design approach.
[DOI: 10.1115/1.1413476]

Introduction

The THM 1304 industrial gas turbine is a two-shaft design in the 10-MW power class, suited for mechanical drive as well as generator drive applications (Bauermeister et al. [1]). The main features are a ten-stage axial compressor followed by a centrifugal compressor stage, two external combustion chambers, a two-stage high-pressure turbine and a two-stage low-pressure turbine to power the driven equipment (Fig. 1).

As part of an ongoing up-rating process aimed at increasing power and efficiency, the centrifugal compressor was studied in detail regarding potential for improving efficiency and pressure ratio. The study included a thermodynamic cycle analysis of the effect of centrifugal compressor improvement on power output and efficiency of the gas turbine, and flow analysis for the impeller, the radial vaned diffuser, and the axial deswirl vanes.

Using a thermodynamic cycle model of the THM 1304 gas turbine, the effects of centrifugal compressor improvement on the overall cycle were evaluated. The study yielded the result that a 4-percent improvement of the centrifugal stage efficiency would improve the overall compressor isentropic efficiency by 0.8 percent, resulting in a gas turbine heat rate reduction close to 1.5 percent.

Improved compressor efficiency leads to a reduction in the required power to drive the compressor for any given engine operating point. It therefore becomes necessary in a two-shaft engine to change the power split between the high-pressure and low-pressure turbines. This is achieved by modifying turbine nozzle flow areas by small changes in guide vane stagger angles. The power saved, due to the improved compressor, can be utilized in the low-pressure turbine to drive the equipment only if this matching is done.

Impeller Study

The rotor geometry was generated with a design system available at DLR (Krain and Hoffmann [2]) based on a Bezier spline concept, and thus offers many degrees of freedom. The meridional contours and blade shapes can be modified interactively and adjusted to prescribed conditions. The blade geometry, for example, is modified by a variation of blade angle and thickness distribution along hub and shroud contour. A precondition for the rotor design was that the main dimensions are kept constant to allow easy retrofit in an existing engine. A series of nine rotors was aerodynamically analyzed. Figure 2 shows the meridional contours of two of these rotors, denoted as rotors Ro0 and Ro5, that were generated during the optimization process. Both rotors have different blade backsweep and exit width at the impeller discharge, the original impeller having a greater backsweep. The examples demonstrate that the rotor geometry can be varied over a wide range. The blade surfaces are always generated by straight lines, which ensures that the rotor can be manufactured in a flank milling mode on a five-axis milling machine.

The three-dimensional impeller flow field study was carried out using an available three-dimensional steady-state calculation method that had been verified previously with a series of optical measurement results taken in different types of rotors (Krain and Hoffmann [3]). For the calculations, a program system developed by Hoffmann [4] was applied. The flow solver embedded is based on the unstructured code published by Dawes [5], which has been further developed for special radial turbomachinery requirements. It solves the basic flow equations with a four-step Runge-Kutta scheme; the k-ε turbulence model is used to close the system of equations.

A constant static pressure was prescribed at the exit of the diffuser to adjust the mass flow rate. At the inlet the boundary conditions were taken from the available result of a multistage hub-to-tip calculation performed for the ten-stage axial compressor ahead of the radial compressor stage. The imposed inlet flow conditions shown in Fig. 3 include both the throughflow calculation result and assumed inlet boundary layer profiles at hub and shroud.

Figure 4 shows the results of this study for rotors Ro0 and Ro5. The calculated efficiencies plotted for both rotors on mean meridional planes clearly show that rotor Ro0, the original one, shows better performance than the modified rotor Ro5. The study finally revealed that a slightly higher pressure ratio with almost equal efficiency could be obtained with rotors having less backsweep than the original one, but only if the main dimensions were modified. Significant improvement within the prescribed axial and radial limits was not obtained. Therefore, it was decided to keep the original rotor design, and to try to reach the envisaged overall efficiency improvement solely by an improved design of the diffuser system. The inlet flow conditions for the diffuser design were taken from the three-dimensional solution obtained for rotor Ro0.

Contributed by the International Gas Turbine Institute and presented at the 46th International Gas Turbine and Aeroengine Congress and Exhibition, New Orleans, Louisiana, June 4–7, 2001. Manuscript received by the International Gas Turbine Institute February 2001. Paper No. 2001-GT-323. Review Chair: R. Natole.

Fig. 1 THM 1304 Gas Turbine

Aerodynamic Diffuser System Design

Radial Diffuser Redesign. Although the pressure ratio of the centrifugal compressor stage is not very high, design constraints made it necessary to apply a vaned, instead of a vaneless diffuser. The whole diffuser system consisted of the vaned diffuser part, a 90-deg bend, and an axial deswirl cascade. The original vaned diffuser was a tandem design that generated a significant amount of turning.

An inverse diffuser design method available at DLR was used to generate the profiles. In this method, described by Krain and Hoffmann [2], a reasonable velocity profile along the diffuser blades is predicted via an inverse boundary layer calculation, using the boundary layer blockage from the three-dimensional impeller calculation and a prescribed skin friction distribution as inputs. This resulting velocity profile is then used as input for the following inverse blade design. The main diffuser dimensions like inlet and exit radii are prescribed. Other geometric parameters, as for example blade height, thickness distribution, blade number, and shape of the blade mean camberline, are used to find an optimized diffuser geometry. Figures 5 and 6 illustrate the result of such a design procedure. For the imposed skin friction distribution shown at the bottom of Fig. 5, the inverse boundary layer calculation delivers the pressure rise and deceleration shown on top of Fig. 5. Additionally, it delivers information about the boundary layer displacement thickness to be expected, as shown in the lower part of Fig. 5.

Figure 6 illustrates the difference in blade shape that resulted from the inverse blade design method for identical input, except blade number. Obviously, the resulting blade shape strongly depends on blade number, which is mainly due to the different blockage belonging to both designs. To achieve the same pressure recovery the diffuser with higher blade number (RD7) has to generate more turning than diffuser RD5.

The data shown in Figs. 5 and 6 can be used for initial judgement of the diffuser performance, but they give only little information about the influence of the rotor exit conditions on the diffuser flow that are known to influence the diffuser performance significantly, especially if a strongly distorted rotor exit velocity profile is present, as was found in this case (Fig. 4).

The three-dimensional steady-state calculation method developed by Vogel [6] was used for the aerodynamic studies. This method was validated extensively for axial compressor and turbine bladings before. The calculation domain covers the area between rotor exit up to the collector and includes the vaneless space ahead of the vaned diffuser part, the vaned diffuser part itself, the 90-deg bend, and the region of the axial deswirl cascade. At the beginning of the optimization process the area of the deswirl cascade was taken as a vaneless area, because it was assumed that a redesign of this cascade could be avoided. Total pressure, flow angle, and temperature distributions between hub

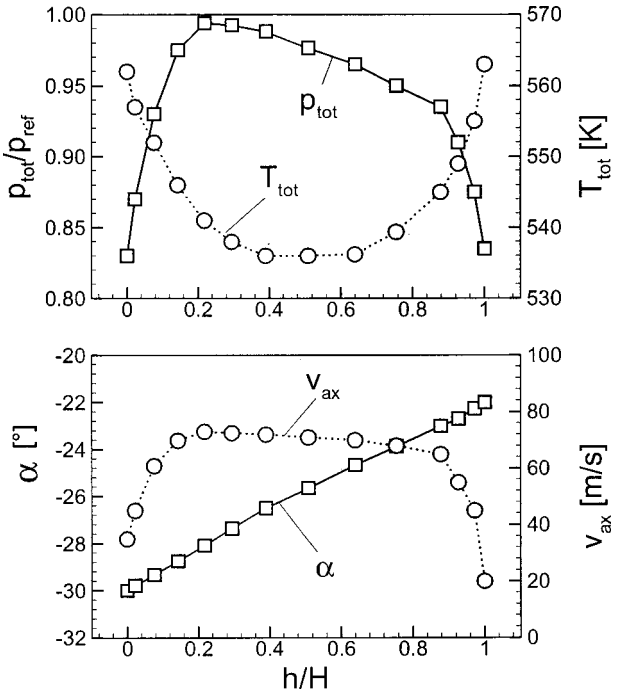

Fig. 3 Inlet boundary conditions for impeller calculations

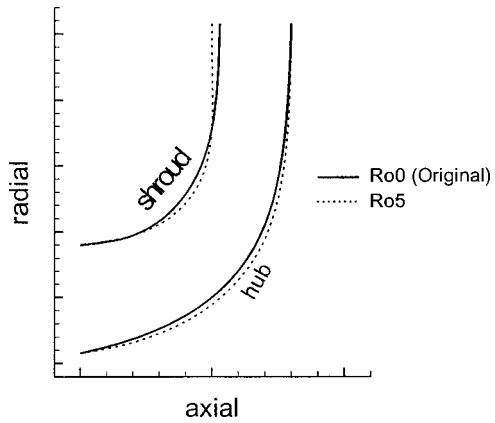

Fig. 2 Meridional contours of rotors Ro0 and Ro5

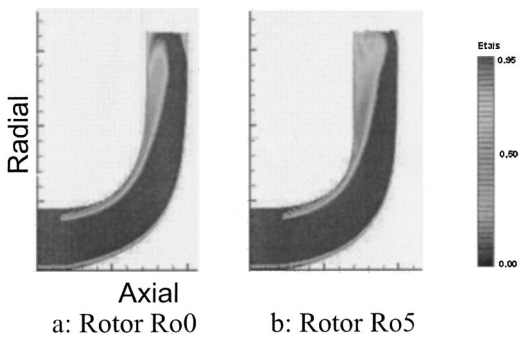

Fig. 4 Total/total isentropic efficiencies calculated for rotors Ro0 and Ro5

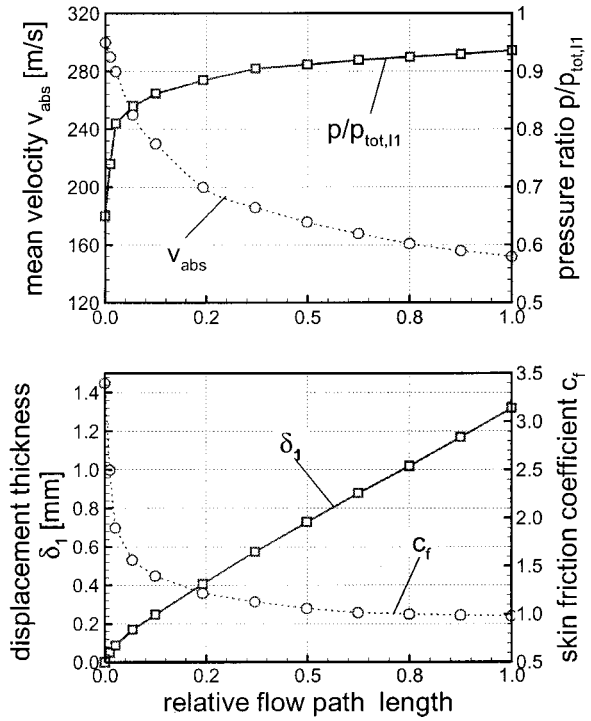

Fig. 5 Radial diffuser inverse boundary layer calculation

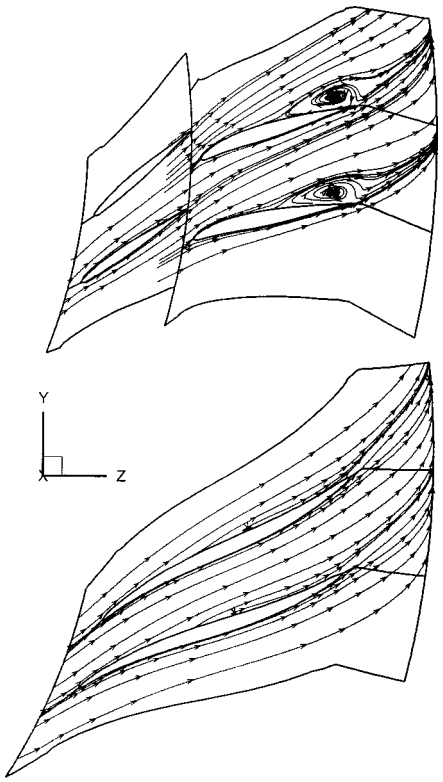

Fig. 7 Velocity vectors at 50 percent span Original (tandem blading, top) and final design (bottom)

and shroud were given as boundary conditions at the inlet of the calculation domain. At the exit, the static pressure was prescribed. The inlet conditions were taken from the three-dimensional flow field solutions available for the original rotor Ro0 (Fig. 4). For reference the flow field of the original diffuser RD0 was also analyzed. After an intensive pre-optimization with the described inverse diffuser design method, a detailed study of the following parameters was carried out with the help of the three-dimensional flow solver:

- Blade number
- Position of vaned diffuser inlet and exit radii
- Blade twist
- Maximum flow deceleration

Although the number of diffuser blades has a significant influence on the overall diffuser concept (Fig. 6), it was nonetheless retained as in the original diffuser. By this, rotor blade resonances were strictly avoided. Inlet and exit radii could only be varied in a small range. Therefore, mean stagger angle, blade twist, and acceptable deceleration were the remaining quantities of most interest.

Figure 7 shows a comparison of the flow fields calculated for the original tandem diffuser and for the final design. The flow traces are plotted for the midspan sections of both designs. Obviously, the original diffuser shows a significant separation at the pressure side of the rear blade, whereas the new diffuser avoids a separation like that which results in higher total exit pressure, but less static pressure rise and more exit swirl, as shown in Table 1. The higher pressure recovery of the new design results also from the higher static pressure at the impeller exit, which is due to the different rotor/stator matching. This result clearly indicated that an improvement of the overall diffuser system also necessitated a new design of the axial deswirl cascade. Otherwise, it would have been impossible to reach the required higher static exit pressure with almost no swirl.

Redesign of Axial Deswirl Blading. Based on the three-dimensional flow results of the radial diffuser, the inlet flow conditions of the axial deswirl blading were known. Figure 8 shows the spanwise inlet distributions of swirl angle α and tangential velocity after the 90-deg bend in comparison with the original design. In contrast to the original one, there remains a much higher swirl behind the new radial diffuser. Therefore, a significantly greater flow turning ranging from 34 deg at the hub to 58 deg at the shroud for the new axial blading is required. As a very

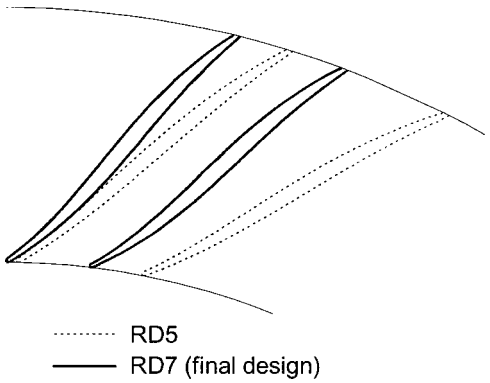

Fig. 6 Two different blade shapes for radial diffuser

Table 1 Mean radial diffuser system characteristics

Build	RD0	RD7
Exit swirl angle α_2	29.2°	45.5°
Static pressure ratio	1.215	1.195
Total pressure ratio p_{tot2}/p_{tot1}	0.92	0.95
Diffuser pressure recovery c_p	0.58	0.61

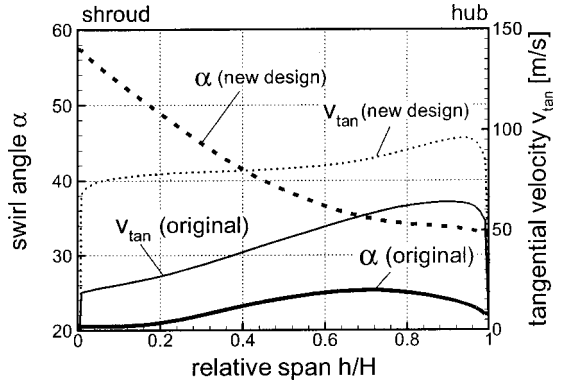

Fig. 8 Inlet distributions for original tandem arrangement and new radial blading at reference plane I_2 of Fig. 10. Three-dimensional result without axial blading.

first step in the design process, a two-dimensional analysis for the mean flow having 40 deg flow turning at an inlet Mach number of 0.20 in the axial part was performed using the MISES code (Drela [7]). The optimization goal was to create a cascade with no exit swirl; i.e., $\alpha_2=0$ deg. The result is a cascade with a pitch-to-chord ratio of 0.40 for the axial diffuser. The profile shape with boundary layer displacement and the isentropic profile Mach number distribution for a nominal design point with $\alpha_1=40$ deg as well as the performance map are shown in Fig. 9.

Due to the very low aspect ratio of the deswirler and due to manufacturing constraints, it was decided to use the same profile shape along the whole span. To account for three-dimensional flow phenomena, the blade sections were stacked accordingly.

As the final geometry of the radial part was already established, it was possible to include the whole diffuser system in the three-dimensional analysis during the design of the axial deswirler. In

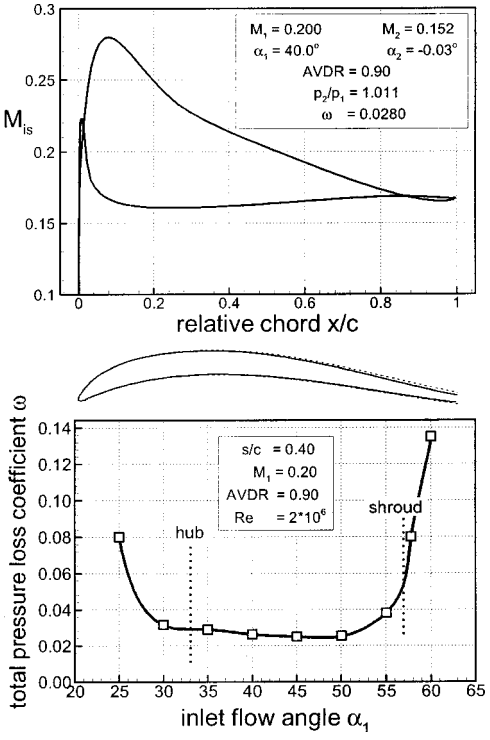

Fig. 9 Q3D-MISES optimization for $M_1=0.20$ and AVDR=0.90. Isentropic profile Mach number distribution for $\alpha_1=40$ deg and simulated total pressure losses.

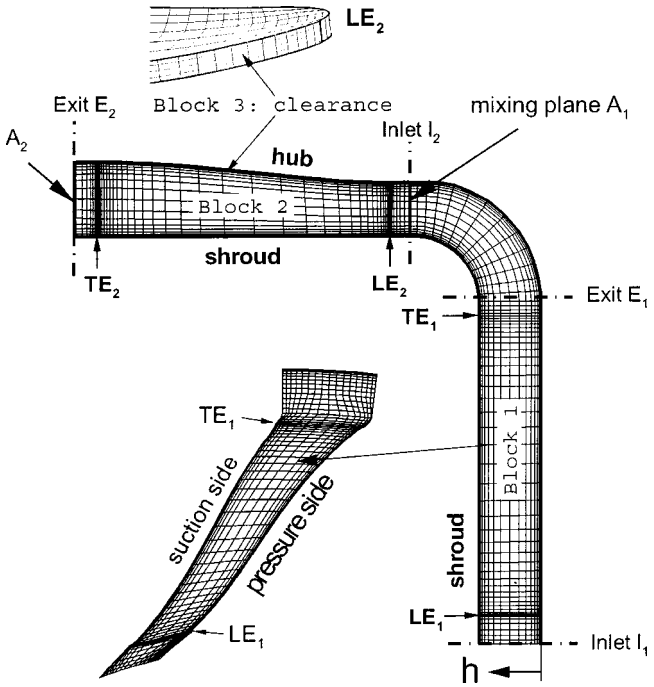

Fig. 10 S_{2m} grid topology (each second grid line skipped) and reference planes, S_1 grid inside of radial blading and modeling of clearance

general, there are different blade numbers in the radial and axial part. Therefore, a quasi multistage calculation was performed using a mixing plane behind the 90-deg bend as can be seen in Fig. 10. A small radial gap at the hub, required for mechanical design reasons, had to be taken into account and was also modeled in the three-dimensional analysis.

The design process of the axial blading consists of the following steps (Weber and Steinert [8]):

- Generation of flow path and profile geometry using fast interactive tools
- Generation of the three-dimensional multiblock structured grid (Eriksson [9])
- Three-dimensional Navier-Stokes analysis of the flow (Vogel [6,10])
- Circumferential averaging and determination of characteristic mean values

In the three-dimensional analysis, the same grid resolution as for the radial part alone was used. There are 33 nodes in the radial direction and 250,000 points overall. At the inlet plane I_1 spanwise distributions for total pressure, total temperature, and flow angle α according to the mean impeller exit conditions were imposed, whereas at the exit plane E_2 a radially constant pressure is imposed to adjust the mass flow. To have a criterion for the comparison, the original geometry consisting of a radial tandem diffuser and the linear axial blading was analyzed first.

During the whole design process, the flow path in the axial part as well as the shape of the 90-deg bend were optimized, but due to design constraints the outer contour (hub) was not changed. An intermediate flow path and the final geometry can be seen in Fig. 11. The final geometry is nearly the same as in the basic design; there are only minor differences in the inner bend part. The dominating flow phenomenon in the axial deswirler is a large passage vortex, as can be seen in Fig. 12 for both, original and final axial blading for an $x=$const plane at midchord. The driving forces for this vortex are

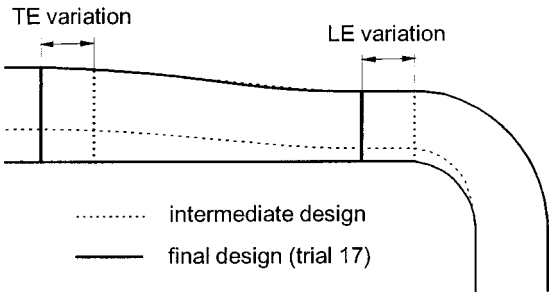

Fig. 11 Geometry variation: Flow path and positioning of axial blading

- The large pressure gradient from hub towards the shroud: $p_{hub} > p_{shroud}$
- The variation in tangential velocity in spanwise direction (Fig. 8)
- The hub clearance gap

The major design goals are to have a maximum static pressure recovery and no exit swirl, or at least to keep the exit swirl as low as possible. Additionally, the flow inside the blade passages should not be separated. To reach these goals, the shape of the flow path (Fig. 11), the profile shape, the blade number, the chord length, the axial position of the blading, and the profile stacking line had to be optimized (Weber and Nicke [11]). In addition, a more complex splitter blading was analyzed. Overall, 21 different three-dimensional geometries with two different profile shape concepts, one with a higher flow deflection in the leading edge part and another (Fig. 9) with a well-balanced deflection along the chord, were analyzed during the design process. The most important aspects derived from the optimization process are:

- The dominating passage vortex could neither be eliminated nor remarkably reduced unless an excessively high blade number was chosen. Therefore, a remaining exit swirl was present in all trials.
- The original flow path contour nearly met the requirements regarding maximum pressure recovery and design constraints.
- Using a linear cascade, i.e., applying radial stacking, results in an exit swirl angle which, over the whole span, is nearly 3 deg higher than for a twisted blade.
- An axial chord length and an axial positioning comparable to the basic design was found to be preferable.

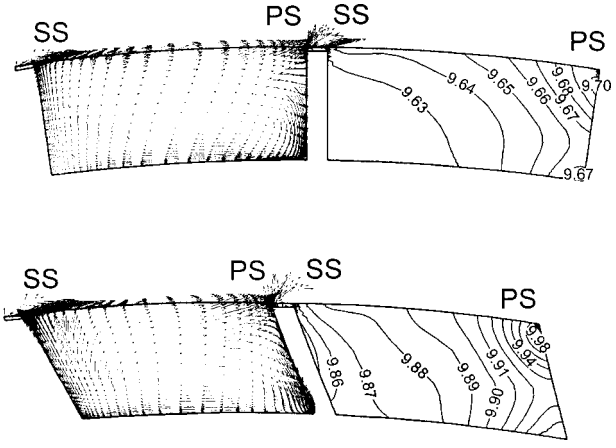

Fig. 12 Static pressure contours and velocity vectors inside of axial blade passage at 50 percent chord. Comparison original versus final design (bottom).

	radial part	axial part	area ratio A_1/A_2
Original	old	old	0.74
NRO	new	none	0.74
Mixed	new	old	0.74
trial 15	new	new	0.88
trial 17 (final design)	new	new	0.74
trial 19 (splitter)	new	new	0.88

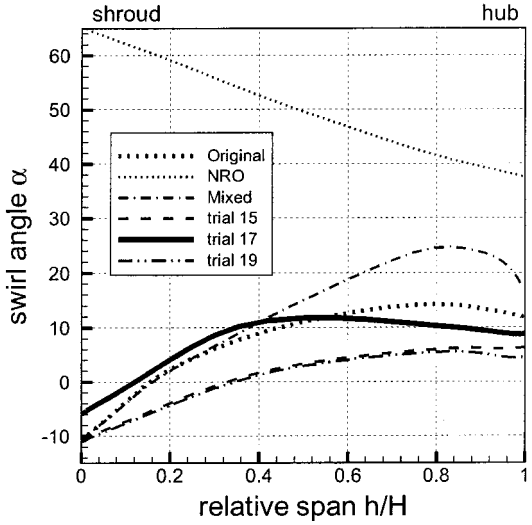

Fig. 13 Exit swirl angle distribution α in reference plane E_2 (NRO: axial part without blading)

- A splitter blading leads to high manufacturing costs and does not have a significant advantage compared to a single blading.

The exit swirl distributions for selected design steps in comparison with the original can be seen in Fig. 13. Additionally, the analytical result using the new radial design without deswirler is shown. As can be seen in Fig. 14, the pressure level inside of the axial blading is significantly higher than in the original deswirler. Figure 14 shows mean total pressure isobars in the whole diffuser flow path. Compared to the original design the final design shows a remarkable reduction in the extension of the high loss region near the shroud in the radial blading.

The development of circumferentially averaged distributions of swirl angle and total pressure in specific reference planes I_1 to E_2 (see Fig. 10) is shown in Fig. 15. As the shading for the swirl angle indicates, the split of the flow deflection into radial and axial

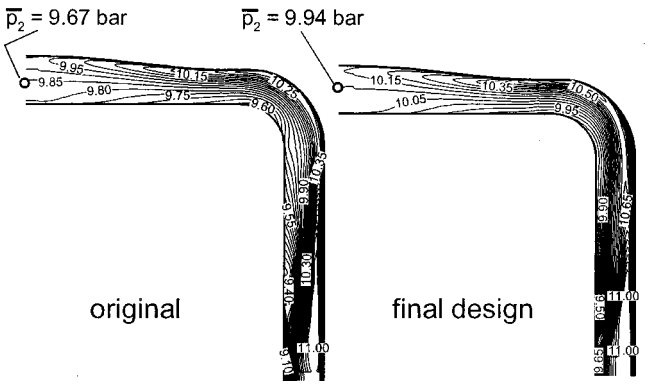

Fig. 14 Mean total pressure distribution in meridional plane (conservative averaging); (p_2: mean static pressure at exit plane)

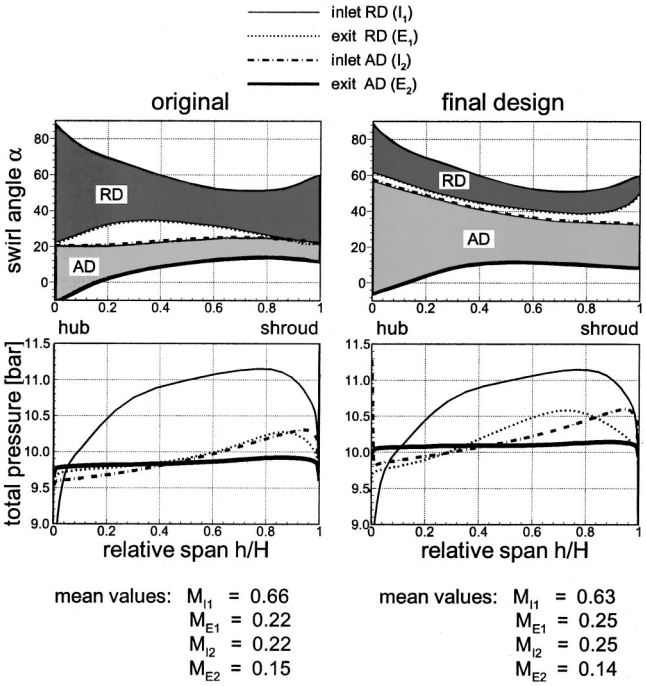

Fig. 15 Spanwise development of circumferentially averaged swirl angle and total pressure along complete diffuser flow path

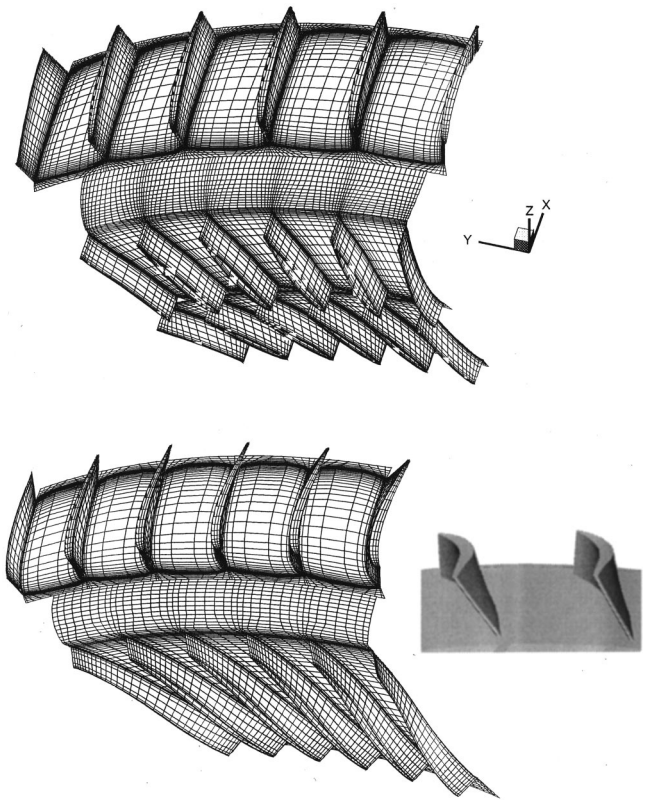

Fig. 16 Diffuser geometry: Comparison original (top) versus final design. Right: axial blading.

part remaining at the impeller exit is completely different for both designs. In the original design the main flow turning is done in the tandem radial diffuser, whereas in the final design the axial blading has to do the main deflection. The total pressure distributions at the exit plane E_2 show a significant total pressure rise for the new design. As explained before, the Mach number discrepancy at the diffuser inlet is due to the different rotor/stator matching.

Table 2 delivers the results of two new designs in comparison with the original. Diffuser mean values and the stage efficiency gain (including impeller) are listed. For the new diffuser designs the mean static exit pressure as well as the overall pressure level are significantly higher than the corresponding values of the original diffuser. Figure 16 illustrates the different three-dimensional designs of original and final diffuser.

Mechanical Design and Manufacturing

Requirements for New Diffuser. The main purpose of the radial diffuser vanes is to convert dynamic pressure into static pressure. At the same time, the vanes are also the connection and centering element between the stator vane carrier and the rear bearing housing. Another requirement for the diffuser redesign was to permit retrofit of existing engines at reasonable cost.

Hardware Design. Because of the new vane geometry, a number of modifications were necessary in the surrounding region also (Fig. 17). Whereas the existing diffuser has two vane rows, the new diffuser has one single row with a greater diffuser leading edge/rotor exit radius ratio. The outer ring of the diffuser could be simplified significantly because the second vane row was omitted. It now carries only the axial deswirl vanes. The rear bearing housing as well as the main case can be retained without any modifications.

Based on the coordinates generated by DLR for the new vane profiles, three-dimensional-CAD models were created for use in the manufacturing process of the diffuser and deswirl vanes.

Table 2 Mean diffuser system characteristics (radial+axial)

Build	AD0 (original)	AD21 (splitter)	AD17 (final design)
Mean exit swirl angle α	8.0°	1.8°	8.6°
Exit static pressure [bar]	9.67	9.82	9.94
Pressure ratio p_{tot2}/p_{tot1}	0.916	0.938	0.939
Efficiency gain $\eta_{is,tt,stage}$	0%	+5%	+5%

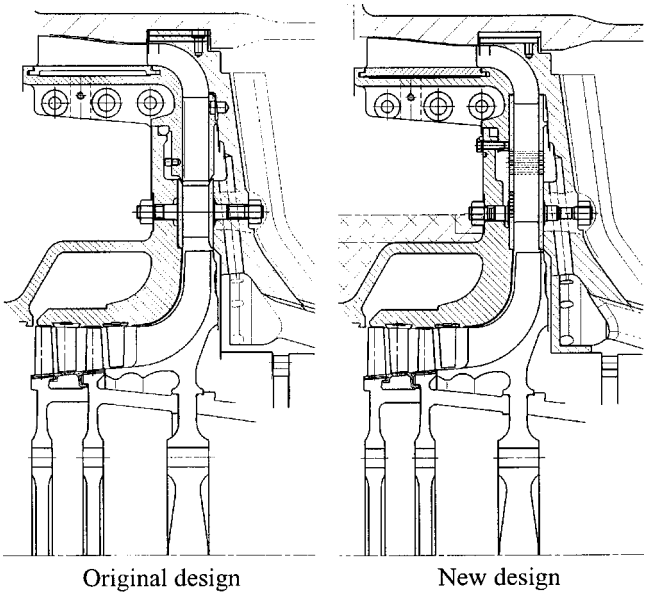

Fig. 17 Comparison of original and new diffuser region

Manufacturing drawings, including the required dimensional and shape tolerances, surface quality and control points, were derived from these models.

Casting, forging, or milling were considered as possible manufacturing processes. Milling out of a block turned out to be the most economical and, at the same time, the fastest method, since sophisticated foundry patterns or forging dies are not required. The three-dimensional-CAD models created earlier in the process were used again for NC-manufacturing and for final dimensional check of the vanes.

In addition to the aerodynamic benefits of the new diffuser, which led to improved overall efficiency, manufacturing costs could also be reduced due to a reduction of the number of parts. The new radial diffuser and axial deswirl vanes are now used in THM 1304 production engines.

Experimental Verification

Test Configuration and Instrumentation. In order to verify the analytical results and the mechanical design, tests were performed on a THM 1304 engine in the full-load gas turbine test cell of MAN Turbomaschinen AG GHH BORSIG.

The compressor was operated not only on its design working line (pressure versus flow), but also at increased pressure levels in order to gain additional information concerning compressor characteristics. Working lines at elevated pressures were achieved by installing a throttling device between the compressor discharge and the combustion chambers. Similar tests had earlier been performed on the engine with the original diffuser to allow a back-to-back comparison.

The engine was adequately equipped with instrumentation to permit evaluation of the efficiency of the overall compressor as well as of the centrifugal stage. This included multiple measurements of total pressure and temperature at the compressor exit, and total and static pressure as well as total temperature at the inlet to the radial stage. Additional pressure measurements, e.g., at the diffuser vane leading edge were also carried out for comparison with the three-dimensional flow calculations.

Results of Testing. Results of the gas turbine tests are summarized in Figs. 18 and 19. All results are normalized by the nominal values of the original design. The overall compressor pressure ratios and the corresponding efficiencies are plotted for three speed lines. Each diagram shows three lines at constant rotor speed (99, 100, 101 percent). Open symbols are for the configuration with the original radial diffuser, filled symbols are for the new diffuser. For each speed line, there are three pressure ratios, achieved by using the throttling device downstream of the compressor.

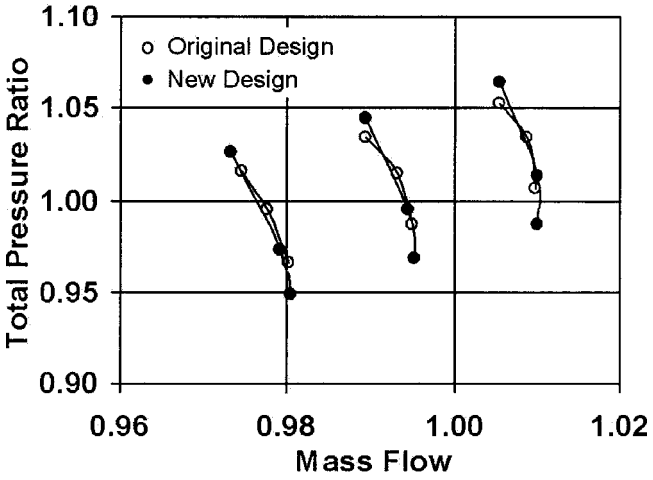

Fig. 18 Total compressor pressure ratio versus mass flow

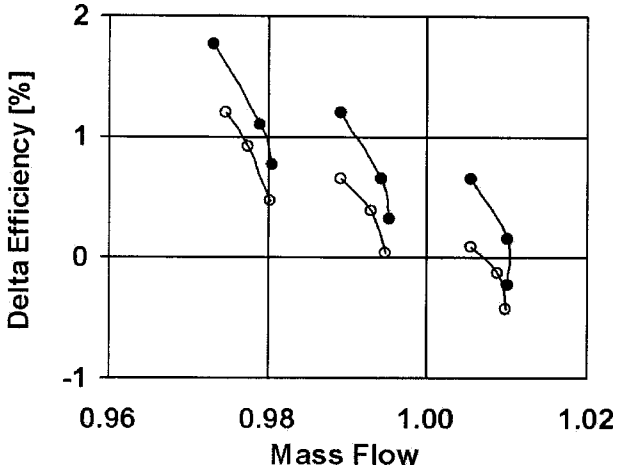

Fig. 19 Total compressor efficiency versus mass flow

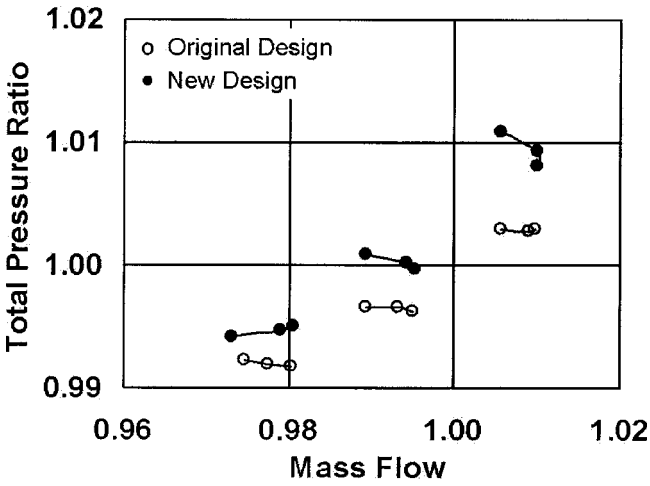

Fig. 20 Centrifugal stage pressure ratio versus mass flow

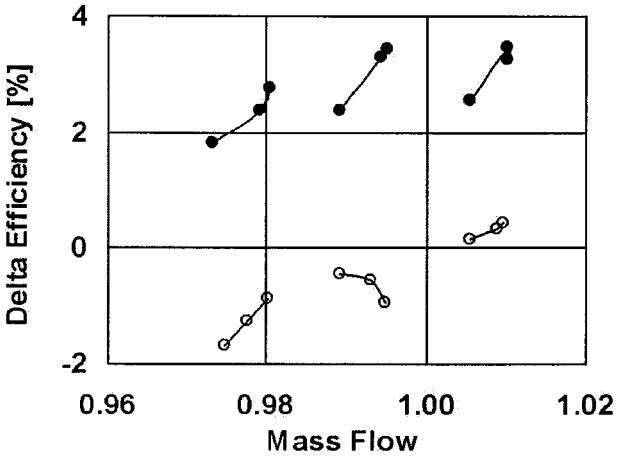

Fig. 21 Centrifugal stage efficiency versus mass flow

It is evident that the efficiency has improved noticeably (approximately 0.6 to 0.8 percent), whereas the pressure versus mass flow characteristic remains largely unchanged. Figures 20 and 21

show the corresponding measurement results for the centrifugal stage alone. Clearly, the envisaged efficiency improvement of around 4 percent has been achieved.

Also, pressure ratio has increased slightly, indicating that the centrifugal stage is producing a greater share of the total pressure rise compared to the original configuration.

Conclusions

The aerodynamic tools available at DLR were used for a study of the three-dimensional flow occurring in the backswept rotor, the vaned diffuser, and the deswirl cascade of a centrifugal compressor rear stage, which is part of a medium pressure ratio gas turbine. It was found that there was almost no potential for a further improvement of rotor efficiency within the given geometric constraints, but a rather high potential for better flow conditions in the diffusing system by redesigning the vaned diffuser and the deswirl blading. Therefore, these components were aerodynamically optimized with the help of available blade generators. A three-dimensional calculation method was applied to the overall diffusing system, consisting of a vaned diffuser, a 90-deg bend, and the deswirl cascade. The resulting diffuser and deswirl blades are fully three-dimensional, whereas the meridional flow path could be retained. Therefore, a replacement of the original blades is easily possible. Using modern design and production methods, it was possible to manufacture the complex three-dimensional blades within a short time and to test the gas turbine in the test cell of MAN Turbomaschinen AG GHH BORSIG, Oberhausen. The radial compressor part of the gas turbine was equipped with static pressure taps, total pressure and total temperature probes. Tests performed with this instrumentation confirmed that the efficiency rise aimed at was achieved.

Nomenclature

A = area
AVDR = axial velocity density ratio $=(\rho_2 u_2)/(\rho_1 u_1)$
c = chord length
c_p = diffuser pressure recovery $=(p_2-p_1)/(p_{\text{tot }1}-p_1)$
c_f = skin friction coefficient
h = local blade height (hub)$=0$
H = blade height $=h_{\text{tip}}-h_{\text{hub}}$
M = Mach number
p = pressure
Re = Reynolds number
s = mean meridional coordinate
T = temperature
Tu = turbulence intensity
v = velocity
α = swirl angle $=a\tan(v_{\text{tan}}/v_{\text{mer}})$
δ_1 = displacement thickness
ρ = density
w = ω total pressure loss coefficient $=(p_{\text{tot }1}-p_{\text{tot }2})/(p_{\text{tot }1}-p_1)$
η_{stt} = isentropic total-to-total efficiency

Subscripts

1 = inlet plane upstream of leading edge
2 = exit plane downstream of trailing edge
AD = axial deswirler/diffuser
abs = absolute
ax = axial
is = isentropic entity
LE = leading edge
mer = meridional
rad = radial
tan = tangential
tot = total
tt = total to total
RD = radial diffuser
TE = trailing edge

References

[1] Bauermeister, K. J., Schetter, B., and Mohr, K. D., 1993, "A 9.25 MW Industrial Gas Turbine With Extreme Low Dry NO_x and CO Emissions," ASME Paper No. 93-GT-307.
[2] Krain, H., and Hoffmann, B., 1996, "Flow in Radial Turbomachines," *Aerodynamics of Centrifugal Compressors With Transonic Flow*, VKI LS-1996-01, p. 59.
[3] Krain, H., and Hoffmann, B., 1998, "Flow in Radial Turmbines," "Aerodynamics of Centrifugal Compressor Impeller With Transonic Inlet Conditions," *Proc. 1998 ASME Fluids Engineering Division Summer Meeting*, June, Washington, DC.
[4] Hoffmann, W., 1990, "A Computer Program System for the Analysis of 3D-Steady Flows in Turbomachinery" [in German], DLR-FB90-18.
[5] Dawes, W. N., 1991, "The Simulation of Three-Dimensional Viscous Flow in Turbomachinery Geometries Using a Solution Adaptive Unstructured Mesh Methodology," ASME Paper No. 91-GT-124.
[6] Vogel, D. T., 1994, "Navier-Stokes Calculation of Turbine Flow and Heat Transfer for the Application to Film-Cooled Turbine Blades," AGARD-CP-510.
[7] Drela, M., 1989, "Newton Solution of Coupled Viscous Inviscid Multielement Flows," NASA Technical Memorandum 101557, Langley Research Center, Hampton, VA, USA.
[8] Weber, A., and Steinert, W., 1997, "Design, Optimization, and Analysis of a High-Turning Transonic Compressor Cascade," ASME Paper No. 97-GT-412.
[9] Eriksson, L. E., Orbekk, E., and Oye, I., 1990, "G3DMESH Manual and G3DEUL Run Manual," CFD Report 111, Trondheim, Norway.
[10] Vogel, D. T., 1999, "A Simulation Package for Turbomachinery Components," *Proc. First ONERA-DLR Aerospace Symposium*, Paris, France.
[11] Weber, A., and Nicke, E., 1997, "A Study of Sweep on the Performance of a Transonic Cascade With and Without Endwall Influence," *Proc. 13th International Symposium on Air Breathing Engines*, Vol. 2, Chattanooga, TN, pp. 877–888.

Franco Blanchini
University of Udine,
Dipartimento di Matematica e Informatica,
Udine, Italy

Pietro Giannattasio
University of Udine,
Dipartimento di Energetica e Macchine,
Udine, Italy

Diego Micheli
University of Trieste,
Dipartimento di Energetica,
Trieste, Italy

Piero Pinamonti
University of Udine,
Dipartimento di Energetica e Macchine,
Udine, Italy

Experimental Evaluation of a High-Gain Control for Compressor Surge Suppression

The present paper considers the suppression of surge instability in compression systems by means of active control strategies based on a high-gain approach. A proper sensor-actuator pair and a proportional controller are selected that, in theory, guarantee system stabilization in any operating condition for a sufficiently high value of the gain. Furthermore, an adaptive control strategy is introduced that allows the system automatically to detect a suitable value of the gain needed for stabilization, without requiring any knowledge of the compressor and plant characteristics. The control device is employed to suppress surge in an industrial compression system based on a four-stage centrifugal blower. An extensive experimental investigation has been performed in order to test the control effectiveness in various operating points on the stalled branch of the compressor characteristic and at different compressor speeds. On one hand, the experimental results confirm the good performance of the proposed control strategy; on the other, they show some inherent difficulties in stabilizing the system at high compressor speeds due to the measurement disturbances and to the limited operation speed of the actuator.
[DOI: 10.1115/1.1413475]

Introduction

Surge instability strongly limits the operating range and the performance of compression systems. As is known, surge occurs at low compressor flow rates, causing highly undesirable oscillations in the system. By means of a control system it is possible to attenuate or eliminate the phenomenon, allowing the plant to operate at naturally unstable points. In particular, the active control techniques are based on the use of a suitable sensor/actuator pair in a closed-loop control device. The control is effective if the actuation is capable of dissipating the unsteady energy surplus introduced in the system by the compressor when it operates in the stalled region.

In the last decade, much work has been devoted to the study of active suppression of compressor surge. A large part of the literature is based on the work of Greitzer [1] and Moore and Greitzer [2], who proposed dynamic models of the compressor instability that have been deeply exploited for the analysis and the design of control systems. Epstein et al. [3] first suggested that surge can be prevented by actively damping the small disturbances from which the instability originates while their amplitude is low. Experimental demonstrations of active stabilization of surge have been given by several investigators, e.g., Ffowcs Williams and Huang [4] and Pinsley et al. [5]. An extensive study was carried out by Simon et al. [6], who analyzed the performance of several sensor/actuator configurations, together with a proportional compensator, by means of a local stability analysis based on a linearized model.

After these pioneering works, the compressor surge control has attracted many researchers, as it appears from several recent contributions that suggest more sophisticated techniques to face the problem. A Lyapunov approach has been proposed by Behnken and Murray [7] and by Gravdal and Egeland [8]. A nonlinear approach based on backstepping has been suggested by Gravdal and Egeland [9] and by Banaszuk and Krener [10]. The problem of bifurcation control, based on the Moore–Greitzer model, is addressed by McCaughan [11], Abed et al. [12], and Kang et al. [13]. A feedback linearization method is presented by Badmus et al. [14]. Extensive surveys are provided by Gu et al. [15] and by Willems and de Jager [16].

The aim of the present work is to investigate the application of a high-gain-type control for the suppression of surge instability in an industrial size compression system. With ''high-gain control'' we mean an approach based on a proper selection of sensor, actuator and control law, which, at least in theory, guarantees system stabilization in any operating condition for a sufficiently high value of the gain. Furthermore, surge suppression is here intended as the capability of removing the system from a surge limit cycle, rather than the easier task of avoiding instability by damping the small disturbances that cause it. Consequently, any local stability analysis or linearized model of the controlled compression system is here avoided for purposes of control design and performance prediction. Indeed, the dynamics of a compression system under unstable operation is strongly nonlinear, and the assumption of small perturbations of the steady equilibrium point is far from being fulfilled, especially in the case of compressors that exhibit abrupt stall [17].

The compression system considered in the present work is based on a four-stage centrifugal compressor, which has been previously used by the authors for various experimental investigations in both stable and unstable operating conditions [18–20]. A nonlinear lumped-parameter model of the compression system was also worked out, which proved to be capable of correctly predicting the system dynamics at different compressor speeds and throttle valve settings [21]. Finally, this compression system was employed to investigate the effectiveness of an innovative device for the passive control of surge based on the use of an oscillating water column [22].

The present active control device includes a sensor of differential pressure between the plenum and the compressor outlet, a proportional controller, and an actuation valve at the plenum exit. The sensor/actuator pair has been selected on the basis of a theoretical analysis performed by Giannattasio [23], who critically revised the work of Simon et al. [6]. Furthermore, Blanchini and Giannattasio [24] demonstrated, by using a nonlinear approach, that such a control has the ''high-gain'' property, and they also discussed the limitations introduced by the occurrence of control saturation. All these results are synthetically reported in the

Contributed by the International Gas Turbine Institute and presented at the International Gas Turbine and Aeroengine Congress and Exhibition, New Orleans, Louisiana, June 4–7, 2001. Manuscript received by the IGTI, January 11, 2001; revised manuscript received July 25, 2001. Paper No. 2001-GT-570. Review Chair: R. A. Natole.

present paper, together with further considerations about the influence of measurement disturbances, unmodeled fast dynamics, and low-pass filter on the effectiveness of the proposed control system. In particular, a simple linear model is employed to show that, in practice, the gain value cannot be chosen arbitrarily large without the risk that the disturbances compromise the local stability. This latter argument suggested the idea of using an adaptive control strategy, which allows the controller to increase the gain automatically until the system is removed from surge, so avoiding the overtuning of the gain. Furthermore, the adaptive control has the remarkable property that it does not require any knowledge of the compressor and valve characteristics.

After introducing some theoretical arguments concerning the aforementioned topics, the present paper reports the results of an experimental analysis of the actively controlled compression system. Unsteady measurements of compressor and plenum pressures, mass flow rate, and actuator position have been performed in different naturally unstable operating conditions, by varying both steady flow rate and compressor speed. Tests have been carried out by using both the classic proportional control and the adaptive strategy. The experimental results provide a rather complete information about the effectiveness and the limits of the proposed control system.

System Description and Model

Figure 1 shows a sketch of a compression system with some of the sensors and actuators proposed in the literature for the control of surge instability. The basic system is formed of a compressor, a volume (plenum), and a throttle valve, while the control device consists of a sensor of a proper system output, a controller where the required control law is applied, and an actuator that introduces the feedback signal into the system. The control effectiveness strongly depends on the appropriate selection of the sensor/actuator pair, which has to be based on the knowledge of the compression system dynamics under unstable operation and on the specific technical features of the considered plant.

Model of the Basic Compression System. A simple and useful model of the basic compression system is the one proposed by Greitzer [1] and successfully employed by the authors for simulating the system dynamics in both uncontrolled and controlled conditions [17,21,22]. It is a nonlinear lumped-parameter model, which results in the following dimensionless equations:

$$\frac{d\varphi_c}{d\tau} = B(\psi_c - \psi_p) \tag{1}$$

$$\frac{d\varphi_t}{d\tau} = \frac{B}{G}(\psi_p - \psi_t) \tag{2}$$

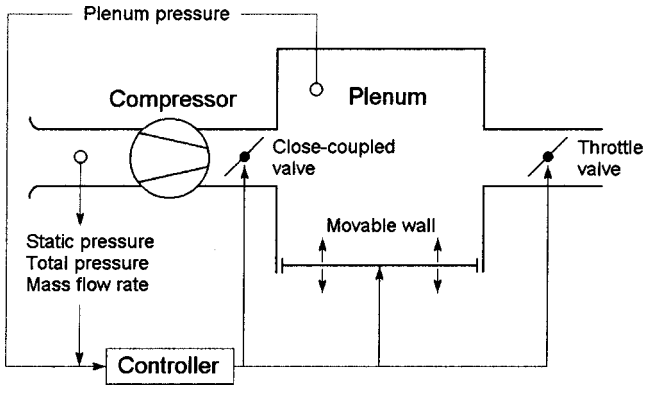

Fig. 1 Controlled compression system

$$\frac{d\psi_p}{d\tau} = \frac{1}{B}(\varphi_c - \varphi_l) \tag{3}$$

$$\frac{d\psi_c}{d\tau} = \frac{1}{\tau_c}[\psi_{cs}(\varphi_c) - \psi_c] \tag{4}$$

$$\psi_t = (A_c/A_t)^2 \varphi_t^2 \tag{5}$$

Equations (1) and (2) are the momentum conservation equations in the compressor and throttle pipes, respectively; Eq. (3) expresses mass conservation in the plenum; Eq. (4) is a first-order model of the compressor dynamics; Eq. (5) represents the steady characteristic of the throttle. Greitzer parameter B, which appears in Eqs. (1)–(3), is defined as $B = U/2\omega_H L_c = (U/2a_p)\sqrt{V_p/A_c L_c}$ and it can be interpreted as the ratio of pressure and inertial forces acting in the compressor pipe [1]. The value of this parameter strongly affects the system stability and the control effectiveness. The valve parameter G in Eq. (2) is defined as $G = L_t A_c / L_c A_t$ and exerts a minor influence on the system dynamics [1]. Term $\psi_{cs}(\varphi_c)$ in Eq. (4) refers to the steady-state compressor characteristic, while the time constant of the first-order compressor dynamics, τ_c, can be related to the time needed for the complete development of a stall cell [1,21].

Sensor-Actuator Selection and Model. The sensor/actuator pair considered in the present work has been selected from the twelve different options suggested by Simon et al. [6]. Those authors considered a standard proportional control and all the combinations of four sensors (compressor flow rate, plenum pressure, compressor face total and static pressure) and three actuators (close-coupled valve in the compressor delivery pipe, plenum bleed valve, movable plenum wall), see Fig. 1. On the basis of a linear stability analysis, Simon et al. came to the conclusion that the combination of a sensor of compressor mass flow rate with a close-coupled valve is far the best choice for a control device of maximum effectiveness. However, such a result was obtained for fixed values of some operating parameters (steady equilibrium positions of throttle valve and close-coupled valve) which, moreover, were not reported in the paper. On the contrary, the variation of the steady operating point of an actual compression system was duly considered by Giannattasio [23], who revised the comparative analysis of Simon et al. by using the same linear approach. The results of that study show that pair ''compressor mass flow sensor/close-coupled valve'' is clearly superior to the other ones only for comparatively small values of the close-coupled valve fraction open, which imply large pressure losses in the compressor delivery pipe. Moreover, it turns out that five of the twelve sensor/actuator pairs have to be discarded because of severe gain-independent stability constraints, which cannot be removed by the control. Finally, some other combinations require extremely large values of the gain for an effective system stabilization (compressor face total or static pressure/close-coupled valve) or involve technical complications (control of both speed and position of the movable plenum wall). In conclusion, the best compromise between control performance and technical requirements appears to be attained by the use of a sensor of total or static pressure at the compressor inlet and of an actuation valve at the plenum exit. These controls turn out to be high-gain ones, in the sense that both allow system stabilization to be attained in any operating condition of the compressor for a sufficiently high value of the gain. In theory, the solution with the static pressure sensor appears to be superior to the other one because it does not imply any gain-independent constraint to system stability, while the total pressure sensor is effective only when the static stability condition is satisfied (the slope of the compressor characteristic must be less than the slope of the valve characteristic in the steady equilibrium point) [6,23]. However, such a condition is commonly satisfied in most of the actual compression systems, while a much simpler implementation of the sensing device is allowed by the use of the compressor face total pressure as system output. In fact, a simple

application of the one-dimensional momentum equation shows that the compressor face total pressure, referred to as the ambient pressure, is proportional to the mass flow acceleration in the compressor duct, i.e.,

$$\psi_{01}=\frac{p_{01}-p_0}{1/2\rho_0 U^2}\propto -\frac{1}{B}\frac{d\varphi_c}{d\tau}=\psi_p-\psi_c$$

where the last equality descends from Eq. (1). This means that ψ_{01} is also proportional to the pressure difference between any two points of the compressor duct, so that a representative sensor signal can be drawn by simply using a differential pressure transducer between plenum and compressor outlet. For this reason, the following system output is defined and used in the present work:

$$y=\frac{p_p-p_c}{1/2\rho_0 U^2}=\frac{L_d}{L_c}(\psi_p-\psi_c) \tag{6}$$

where L_d/L_c is the ratio of the equivalent lengths of the compressor delivery pipe and the whole compressor duct. This ratio is introduced in order to reduce the pressure difference $\psi_p-\psi_c$, which is responsible for the flow acceleration in the whole compressor duct, to the pressure difference which causes the acceleration of the only mass contained in the duct portion between compressor outlet and plenum. With definition (6) of the system output, the present control law is written as

$$u_r=\left(\frac{A_t-A_{ts}}{A_{ts}}\right)_r=Ky \tag{7}$$

where K is the gain and the system input required by the controller, u_r, is defined as the dimensionless difference between the throttle flow area, A_t, and its steady equilibrium value, A_{ts}. In the present work, the valve at the plenum outlet is assumed to perform both functions of throttling device and actuator. These functions can be kept apart by simply introducing a bleed valve, as the actuator, in parallel with the throttle valve [6]. The two options are quite equivalent from a conceptual point of view, the best choice depending only on technical considerations.

To complete the model of the control device, a simple first-order model of the actuator dynamics is introduced in order to account for the time lag between the command output of the control law, u_r, and the response of the actuator, u

$$\frac{du}{d\tau}=\frac{1}{\tau_a}(u_r-u) \tag{8}$$

With the introduction of system input u, Eq. (5) can be rewritten as

$$\psi_t=(A_c/A_t)^2\varphi_t^2=(A_c/A_{ts})^2\left(\frac{\varphi_t}{1+u}\right)^2 \tag{9}$$

If ψ_t is eliminated from Eq. (2) by using Eq. (9) and Eqs. (6) and (7) are introduced in Eq. (8), the model of the controlled compression system results in five ordinary differential equations in the unknowns φ_c, φ_t, ψ_p, ψ_c and u. They can be solved numerically for given values of parameters B, G, τ_c, τ_a, L_d/L_c, and gain K, if the steady-state characteristics of the compressor, $\psi_{cs}(\varphi_c)$, and of the throttle valve, A_{ts}, are known. Numerical simulations performed by Giannattasio et al. [17] showed that the proposed control device is capable of suppressing surge within almost the whole unstable operating range of the compressor with reasonable values of the gain. Furthermore, they showed that the predictions of the nonlinear model can be substantially different from the ones of a linear stability analysis, especially in the case of compressors which exhibit abrupt stall.

Suppression of Surge Cycles

A considerable simplification of the model described in the previous section can be obtained by neglecting the flow inertia in the throttle duct ($G=0$) and the time-lags in the transient responses of compressor and actuator ($\tau_c=\tau_a=0$). Such approximations are well accepted in the literature since the simplified model has been shown to capture the fundamental dynamics of the compression system [1,6]. In this case, the system of equations reduces to

$$\frac{d\varphi_c}{d\tau}=-B[\psi_p-\psi_{cs}(\varphi_c)] \tag{10}$$

$$\frac{d\psi_p}{d\tau}=\frac{1}{B}[\varphi_c-(1+u)\varphi_{ts}(\psi_p)] \tag{11}$$

where $\varphi_{ts}(\psi_p)=A_{ts}/A_c\sqrt{\psi_p}$ is the steady characteristic of the throttle and $u=A_t/A_{ts}-1$ represents the control action. This system is associated with the output

$$y=\frac{L_d}{L_c}[\psi_p-\psi_{cs}(\varphi_c)] \tag{12}$$

For a more compact notation, denote by $\mathbf{x}(\tau)=(\varphi_c(\tau),\psi_p(\tau))^T$ the system state at time τ, and by $\mathbf{x}_s=(\varphi_s,\psi_s)^T$ the steady equilibrium state which is the solution of the equations

$$-B[\psi_p-\psi_{cs}(\varphi_c)]=0 \tag{13}$$

$$\frac{1}{B}[\varphi_c-\varphi_{ts}(\psi_p)]=0 \tag{14}$$

As mentioned in the introduction, the main goal of the present control strategy is to remove the system from surge limit cycles driving the state to the target equilibrium point, $\mathbf{x}_s$. When the system is under deep surge, linearization methods cannot be applied to the stabilization problem, since surge regime is characterized by a strongly nonlinear behavior [1,17]. Therefore, we consider the nonlinear stabilization approach adopted by Blanchini and Giannattasio [24]. Let us consider the proportional control

$$u(\tau)=Ky(\tau) \tag{15}$$

where K is a real constant. This simple control has been investigated by several authors (see, e.g., [4,6]) and it has the following property if applied to system (10)–(11) [24].

Proposition (High-Gain Stabilization). There exists $\overline{K}>0$ such that for each $K\geq\overline{K}$ and for any initial condition $\mathbf{x}(0)$ that belongs to (or which is inside) a limit cycle, the convergence condition, $\mathbf{x}(\tau)\to\mathbf{x}_s$ as $\tau\to\infty$, is guaranteed. This theoretical result, which is based on model (10)–(11), states that control (15) with a sufficiently large value of $K>0$ is a suitable stabilizing control for the present class of systems.

However, from a practical standpoint, the following considerations hold that partially invalidate this result:

(*i*) The control is subject to saturation constraints of the form $-1\leq u\leq M=A_{t,\max}/A_{ts}-1$, which means that the actual control action will be

$$u=\mathrm{sat}_{[-1,M]}(Ky)$$

where

$$\mathrm{sat}_{[\alpha,\beta]}(q)=\begin{cases}\alpha & \text{if } q<\alpha\\ q & \text{if } \alpha\leq q\leq\beta\\ \beta & \text{if } q>\beta\end{cases}$$

Having an overly large value of the gain is useless in the presence of such strict saturation constraints. This problem has been theoretically investigated by Blanchini and Giannattasio [24], who showed that, even for the simplified model (10)–(11), whenever the high-gain saturated controller fails, there will be no controller that removes the system from limit cycles.

(*ii*) The real system is affected by disturbances. In particular, the presence of sensor noise can compromise the control performance. To attenuate such a noise, the sensor signal must be processed by a low-pass filter, the cut-off frequency of which

must be suitably chosen. Sensor noise affects the control output, so producing actuator oscillations the amplitude of which increases with the value of the gain. High permanent oscillations are not desirable because they cause actuator mechanical and electrical stress.

(*iii*) The second-order system (10)–(11) does not consider part of the system dynamics such as the actuator dynamics, the compressor dynamics, and the filter dynamics. As previously mentioned, these dynamics can be reasonably neglected in the simulation of an open loop system. Unfortunately, it is known that a high gain feedback can excite such dynamics at the point that they may compromise stability.

The foregoing three points show that an overly high value of gain K may be not practically useful or even dangerous. To better explain this fact one can use a linearized model of the system.

Linear Analysis. Linear analysis is not sufficient on its own to assure global stability; that is, in the present case, to assure surge suppression. Nevertheless, it turns out to be very useful to point out some limitations. Indeed, the stabilization problem requires, as a necessary condition, that the considered equilibrium point is locally stable, because as the system approaches the equilibrium the linear model provides a faithful description of its behavior. System (10)–(12) admits the following linear approximate representation

$$\frac{d\delta\varphi_c}{d\tau} = -B(\delta\psi_p - m_c\delta\varphi_c) \tag{16}$$

$$\frac{d\delta\psi_p}{d\tau} = \frac{1}{B}\left(\delta\varphi_c - \frac{1}{m_t}\delta\psi_p - \varphi_s\delta u\right) \tag{17}$$

$$\delta y = \delta\psi_p - m_c\delta\varphi_c \tag{18}$$

where $m_c=(d\psi_{cs}/d\varphi_c)_s$ and $m_t=(d\psi_t/d\varphi_t)_s=2(A_c/A_{ts})^2\varphi_s$ denote the slopes of the compressor and valve characteristics, respectively, in the steady equilibrium point, and term L_d/L_c has been omitted in Eq. (18) since it can be thought to be included in the gain. The transfer function of the open loop system is

$$F(s) = \frac{-cs}{s^2+bs+a} \tag{19}$$

where $a=1-m_c/m_t$, $b=1/Bm_t-Bm_c$ and $c=\varphi_s/B$. The denominator of the closed-loop transfer function is

$$p(s,K) = s^2+(b+cK)s+a \tag{20}$$

which turns out to have roots with negative real part (linear stability condition) for a sufficiently large value of K, i.e., for

$$K > -b/c = \frac{B}{\varphi_s}\left(Bm_c - \frac{1}{Bm_t}\right) = B^2\frac{m_c}{\varphi_s} - \frac{1}{2\psi_s} \tag{21}$$

However, the situation is slightly different if fast dynamics or a low-pass filter are considered. For the simple exposition, let us consider the case in which only the filter is taken into account (its use is necessary in practice) and let us consider, for instance, a filter having the following transfer function:

$$F_{\text{filter}}(s) = \frac{1}{1+2(\xi/\omega_0)s+s^2/\omega_0^2} \tag{22}$$

where $\omega_0/2\pi$ is the cut-off frequency and $\xi<1$ is a positive parameter that depends on the particular filter. The closed-loop characteristic polynomial turns out to be

$$p_{\text{filter}}(s,K) = (s^2+bs+a)\left(1+2\frac{\xi}{\omega_0}s+\frac{s^2}{\omega_0^2}\right)+cKs \tag{23}$$

and, for any value of a, b, c, ξ, ω_0, there exists a limit value, $K_{\text{INST}}>0$, such that for $K\geqslant K_{\text{INST}}$ local stability is lost. This property can be proved by plotting the positive root locus or just using the parameterized Routh–Hurvitz table; the formal proof is skipped for brevity. Furthermore, even under condition $K<K_{\text{INST}}$ there may be some problems. Indeed, for high values of K, the closed-loop linearized system may have (stable) modes which are poorly damped. These modes are extremely sensitive to disturbances, so that their effect can result in permanent oscillations around the equilibrium point. In a nonlinear context, these oscillations may have a destabilizing effect and they can prevent the surge from being completely suppressed.

A Trade-Off Choice of *K*: The Adaptive Control. The previous considerations show that, practically speaking, K has to be chosen large, but not so much as to compromise local stability. This choice is hard to be made by computation due to the nonlinear nature of the system behavior during surge.

An efficient way to tune K is to do it adaptively. The basic idea behind this approach is that the controller automatically increases the gain until the system is removed from surge. This goal can be accomplished by using, instead of a constant K, a time-varying nondecreasing gain, $K(\tau)$, as long as system output y is outside a tolerance interval having an amplitude, ε, fixed by the user. Such a gain can be computed by the adaptive control law

$$\frac{dK(\tau)}{d\tau} = \mu\sigma(|y|) \tag{24}$$

where $\mu=\text{const}>0$ is an adaptation parameter and

$$\sigma(|y|) = \begin{cases} 0 & \text{if } |y|\leqslant\varepsilon \\ |y|-\varepsilon & \text{if } |y|>\varepsilon \end{cases}$$

represents the distance of output y from threshold interval $[-\varepsilon,\varepsilon]$. The convergence of this control law has been theoretically investigated and numerically validated by Blanchini and Giannattasio [24]. Note that, if convergence occurs and $y(\tau)$ enters interval $[-\varepsilon,\varepsilon]$, then condition $dK/d\tau=0$ holds and the adaptation stops; from that moment we have $K(\tau)=\text{const}=K_\infty$. A great advantage of this procedure is that it does not require any knowledge of the compressor and valve characteristics. Furthermore, by its nature, K is increased as far as it is necessary for stabilization, so that the practical problem of having a too high value of the gain can be solved.

In practice, the adaptive procedure can be used in two steps:

1) *Training session*: the adaptive control is applied and the limit value of the gain, K_∞, is detected.

2) *Working session*: the controller $u=Ky$ is applied with $K=\text{const}=K_\infty$.

Experimental Tests

In order to verify the effectiveness of the proposed control strategy, an industrial compression plant has been coupled to a properly designed control device and a comprehensive set of measurements has been performed.

Test Plant and Instrumentation. The compression system, shown in Fig. 2, is based on a low-pressure multistage centrifugal compressor driven by a DC motor through a speed increasing gear. The blower includes four impellers, with 16 backswept blades and 465 mm outer diameter, and vaned diffusers. The compressor inlet consists of a radial bellmouth duct with a 125 mm inner diameter ($A_c=122.7\,\text{cm}^2$), while the delivery pipe is connected to a cylindrical plenum of large volume ($V_p=3.1332\,\text{m}^3$). The equivalent length of the compressor ducting turns out to be $L_c=13.5\,\text{m}$, while the equivalent length of the compressor delivery pipe is $L_d=7\,\text{m}$.

The normal operation speed of the considered blower ranges from 2000 to 4000 rpm. The minimum value of the system stability parameter B, corresponding to the compressor speed of 2000 rpm, is 0.304, which turns out to be far higher than the critical value of the present compressor, $B_{\text{crit}}=0.06$ (see [12] for a rigorous definition of bifurcation parameter B_{crit}). This results in a

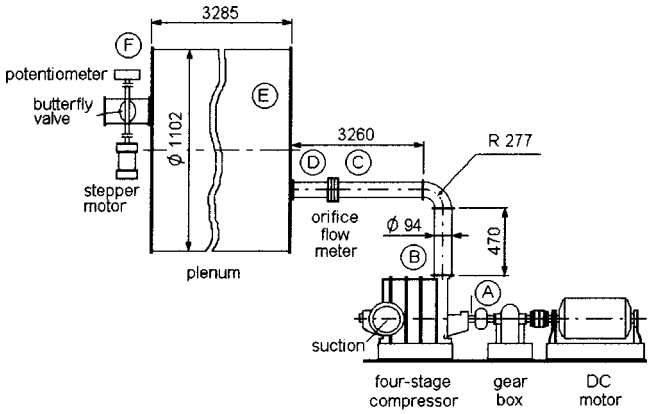

Fig. 2 Experimental compression plant

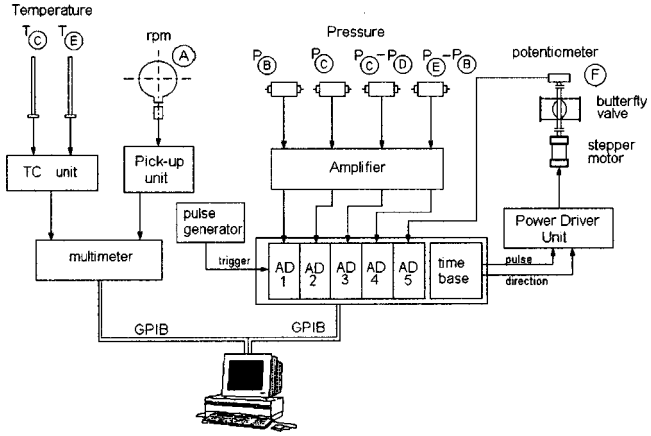

Fig. 3 Schematic of the instrumentation system

great system tendency to instability and accounts for the deep surge conditions observed by Arnulfi et al. [20] also at the lowest compressor speeds.

A butterfly valve at the plenum exit performs both functions of throttling device and actuator. The valve has a disk of 101 mm diameter, and its movable part, having a moment of inertia of 1.5 kg cm^2, is mounted on ball bearings. It is driven by a stepper motor with a rotor inertia of 0.56 kg cm^2, a maximum torque of 1 Nm, and a resolution of 200 steps/rev.

The instrumentation system is shown in Fig. 3, where the capital letters refer to the measurement point locations in Fig. 2. Pressures and temperatures are measured by means of inductive transducers and K-thermocouples, respectively, while a magnetic pickup is used for the compressor rotational speed. The mass flow rate is measured by means of an orifice flow meter mounted in the compressor delivery pipe. Although this instrument is normally used for steady flow measurements, it was considered acceptable in the present case because of the slow dynamics of surge (a few cycles per second). The throttle angular position is measured by means of a precision potentiometer. The stepper motor is driven by a Power Driver Unit, which allows a quarter of step resolution (0.45 deg) to be selected.

The acquisition of temperatures and rotational speed is performed only once at the beginning of each test, while the signals of pressure and valve angular position are acquired simultaneously at a sampling rate that must be high enough to represent surge dynamics correctly. This sampling rate is determined by an external trigger provided by a pulse generator.

Experimental Procedure. Previous experimental tests performed by Giannattasio et al. [17] had shown some difficulties in stabilizing the compression system due to software limitations and to the use of a stepper motor with an excessively large rotor inertia. These limitations have been largely reduced in the present work by using a more efficient computer-based system for data acquisition and control and by selecting a lighter and faster actuation device.

A new software has been developed with the aim of maximizing the control speed. A sampling rate of 30 Hz has been selected as a compromise between the need of a faithful reproduction of the surge dynamics and the requirement of a sufficiently large time interval between two subsequent acquisitions which allows the desired angular displacement of the actuator to be completed. The stepper motor has been driven at the frequency of 4000 Hz. Over this value the strong accelerations of the actuator during the control originate inertial torques that can exceed the motor torque. On the basis of the values of sampling rate and motor frequency, the code computes the maximum number of motor steps allowed in a sampling period. When the time needed for calculations and I/O operations is considered, the residual sampling period allows a maximum of about 110 motor steps (50 deg). If the controller requires a larger actuator displacement, the code limits the number of steps at its maximum value.

As mentioned above, the acquisition of the pressure and angular displacement signals occurs simultaneously on five separate channels. The system output signal, which is acquired as the differential pressure between plenum and compressor outlet, is first corrected by adding the pressure losses between the two measurement sections. These losses are estimated as a fraction of the differential pressure signal from the orifice flow meter (a fraction of 60 percent has been considered on the basis of preliminary calibration tests). After being acquired and corrected, the system output signal is filtered by means of a low-pass second-order Butterworth filter ($\xi = 1/\sqrt{2}$ in transfer function (22)) in order to reduce the measurement disturbances. Preliminary tests suggested an optimum value for the cut-off frequency between 4 and 6 Hz (the maximum frequency of the surge oscillations in the present compression system is close to 1 Hz). At this point, the proportional or adaptive control law is applied to the filtered data, so obtaining the valve flow area required by the control. This area value is turned into valve angular position and is compared with the actual butterfly angle computed from the potentiometer signal. The difference between these two angles is converted into number of pulses to the stepper motor, which are limited in case they exceed the maximum allowable value.

The present software for data acquisition and control allows the throttle valve to be moved to the desired steady position and the control device to be enabled or disabled when required, without interrupting the processes of data acquisition and recording.

Experimental Results. Tests have been carried out at the compressor speeds of 2000, 2500, 3000, and 3500 rpm and for nine different angular positions of the throttle valve (from 5 to 25 deg with a step of 2.5 deg) corresponding to operating points on the unstable branch of the compressor characteristic curves, see Fig. 4. In each of these test conditions, the two-stage procedure described previously (training session and working session) has been applied, by always starting the control after a fully developed surge had been obtained. At first, the adaptive control has been performed by assuming the value of $50/\omega_H$ for the dimensionless adaptation parameter, μ. However, a different choice of this parameter within a very large range does not change significantly either the limit gain, K_∞, or the stabilization time, as claimed in [24]. In the cases of successful adaptive stabilization, the system has been taken back to unstable operation and the control test has been repeated, by using the value of K_∞ obtained in the training session as the constant gain of a standard proportional control.

The suppression of surge has been obtained in all the test conditions, except the ones at the highest compressor speed, 3500

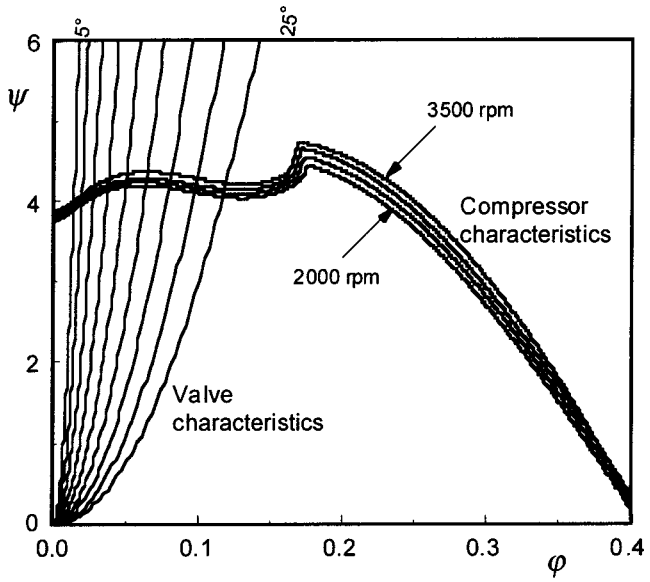

Fig. 4 Test points as intersections of valve and compressor characteristics

rpm. The summary of the present results is shown in Fig. 5, which reports the values of K_∞ obtained in the stabilized conditions. The limit gain turns out to increase strongly with compressor speed and throttle closing. These expected trends can be justified even by a linear stability analysis. In fact, Eq. (21) shows that, if $m_c > 0$, the gain grows with B^2, and hence with U^2, while it varies as the inverse of the steady equilibrium flow coefficient, φ_s.

Detailed representations of the adaptive control action are provided in Figs. 6(*a–d*), which show the time traces of flow coefficient, plenum pressure coefficient, filtered system output, and valve angle for the steady equilibrium condition corresponding to $\theta_s = 20$ deg and for all the considered compressor speeds. The time required for the system stabilization is observed to increase with the compressor speed, i.e., with B: at 2000 rpm 3 Helmholtz periods are sufficient while about 50 periods are required at 3000 rpm. The achievement of system stabilization is shown by the disappearance of the low-frequency surge oscillations in the signals of flow rate, plenum pressure, and system output. After the system stabilization has been reached, the flow rate appears to be almost constant, while the plenum pressure signal is affected by high-frequency oscillations, the amplitude of which increases with the compressor speed. These oscillations result from the fact that the plenum pressure has been obtained by summing up the signals of compressor delivery pressure (which is highly disturbed) and differential pressure between plenum and compressor outlet, rather than from direct measurements.

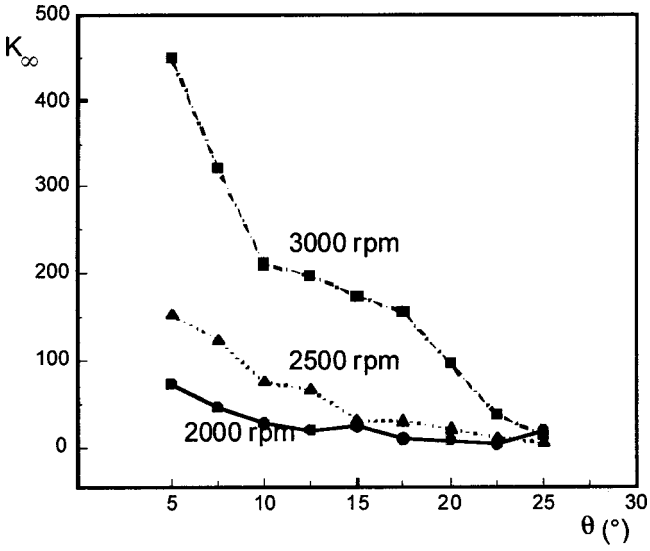

Fig. 5 Limit gain values of the adaptive control

The behavior of the adaptive control is quite evident in the plots of the valve angle. After the control has been started, the valve moves with oscillations of growing amplitude, due to the increasing gain, until the system stabilization is attained. However, high-frequency oscillations remain in the angle signal after the surge has been suppressed. They are due to residual disturbances in the filtered output signal, which are amplified by the gain, resulting in oscillations whose amplitude increases with the compressor speed.

The operating condition at 3500 rpm (Fig. 6(*d*)) shows the limits of the performance of the present control device. In fact, the actuator is not capable of performing the large displacements required by the controller (frequent saturated valve openings should occur in this operating condition), due to valve accelerations which exceed the stepper motor capability.

The harmful effects of disturbances and actuator speed limitations on system stabilization have been fully confirmed by numerical simulations of the controlled system dynamics. The model of Eqs. (1)–(8), together with adaptive control law (24), has been employed to test the operating condition of Fig. 6(*d*) numerically, by introducing either a limitation of the maximum angular velocity of the valve or a sinusoidal disturbance of system output y. The simulations have been performed with the following values of the parameters: $B=0.53$, $G=0.025$, $\tau_c=4$, $\tau_a=0.1$, $L_d/L_c=0.52$, $K(0)=0$, $\mu=8.4$, $\varepsilon=0.1$. The amplitude and the frequency of the disturbance have been set equal to 0.05 and 4 Hz, respectively, which correspond to the leading component of the measured residual noise in the filtered y signal. Under ideal conditions (absence of disturbances and actuator speed limitations) the simulation predicted a complete suppression of surge. On the contrary, when varying the maximum allowable actuator speed (without disturbances), system stabilization was observed only for values of $(d\theta/dt)_{\max}$ greater than about 1500 deg/s, which is close to the estimated limit performance of the actual control device. Furthermore, stability was never reached when the sinusoidal disturbance was added to the system output, not even in conditions of no actuator speed limitation.

The effects of the proportional control are shown in Figs. 7(*a–c*), which report the time traces of φ_c, ψ_p, y and θ, together with the corresponding system trajectories in plane (φ_c, ψ_p), in three different operating points ($\theta_s = 7.5$, 15, 22.5 deg) at the compressor speed of 2500 rpm. It is observed that, when using the limit gain values of the adaptive control, the proportional control turns out to be very effective since the system stabilization is obtained in a short time even in the more difficult case of very closed valve (the stabilization time varies from 1 Helmholtz period at 22.5 deg to 5 periods at 7.5 deg). The stabilization test has been completed by inhibiting the control after the surge cycles have been completely suppressed and by observing the consequent system behavior. As the cases in Figs. 7(*a–c*) are concerned, it is noticed that the system continues to be stable after the control has been removed at the steady valve angles of 15 and 22.5 deg, while at 7.5 deg it immediately returns to a surge condition. This behavior, which has been observed also at the other compressor speeds, can be explained by observing that for large values of θ_s the equilibrium point is a locally stable one (the slope of the compressor characteristic is negative or slightly positive), while the dynamic stability condition ($b>0$ in Eq. (19)) is not satisfied at valve angles less than about 10 deg.

For a clearer representation of the system trajectories in plane (φ_c, ψ_p), the data to be plotted have been properly filtered to eliminate the high-frequency disturbances and they have been lim-

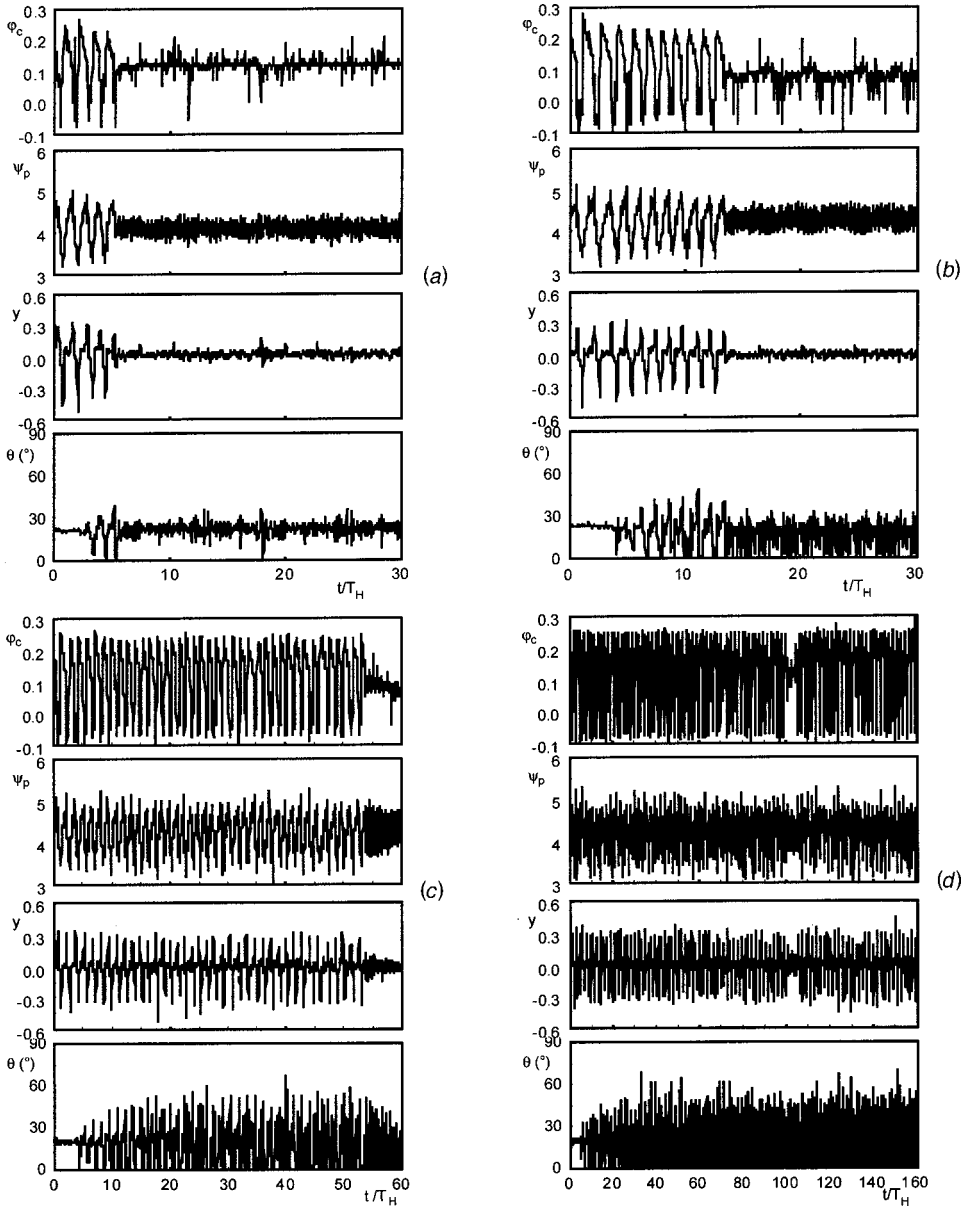

Fig. 6 Time traces of the system parameters during the adaptive control for $\theta_s = 20$ deg: (*a*) 2000 rpm; (*b*) 2500 rpm; (*c*) 3000 rpm; (*d*) 3500 rpm

ited to few oscillations before system stabilization. Furthermore, the (φ_c, ψ_p) plots in Figs. 7(*a–c*) report the compressor characteristic at 2500 rpm (dashed line) and the steady characteristic of the valve (dashed–dotted line). These plots show that the system proceeds from a deep surge cycle to a stable condition through a short transient evolution. It is also observed that for the larger values of valve steady angle, the system correctly converges to the equilibrium point (the intersection of the compressor and throttle characteristics), while for $\theta_s = 7.5$ deg the system moves to a flow coefficient value which is considerably larger than φ_s. This behavior has been observed in all the other operating conditions at very low values of θ_s and it can be explained by considering that, in these cases, the possible valve motion around the equilibrium position is not symmetric, being limited below by the saturation constraint of complete closing. Consequently, the valve oscillations, which are observed also in stabilized conditions due to the disturbances that affect the system output signal, occur around an average angular position that is larger than the desired one. Such a behavior resulted also from numerical simulations of the controlled system dynamics, when a sinusoidal disturbance was added to output signal *y*.

Conclusions

A high-gain approach for the active control of compressor surge has been introduced and validated by experiments. The differential pressure between plenum and compressor outlet has been selected as the sensor signal, while the actuation is performed by means of the throttle valve at the plenum exit. Besides a standard proportional control, an adaptive strategy has been introduced in order to perform a satisfactory tuning of the gain. A computer-based control system has been coupled to an industrial compression plant based on a four-stage centrifugal blower, and an extensive experimental investigation has been performed.

The experimental results show that the proposed control strategy is capable of suppressing surge in almost the whole unstable

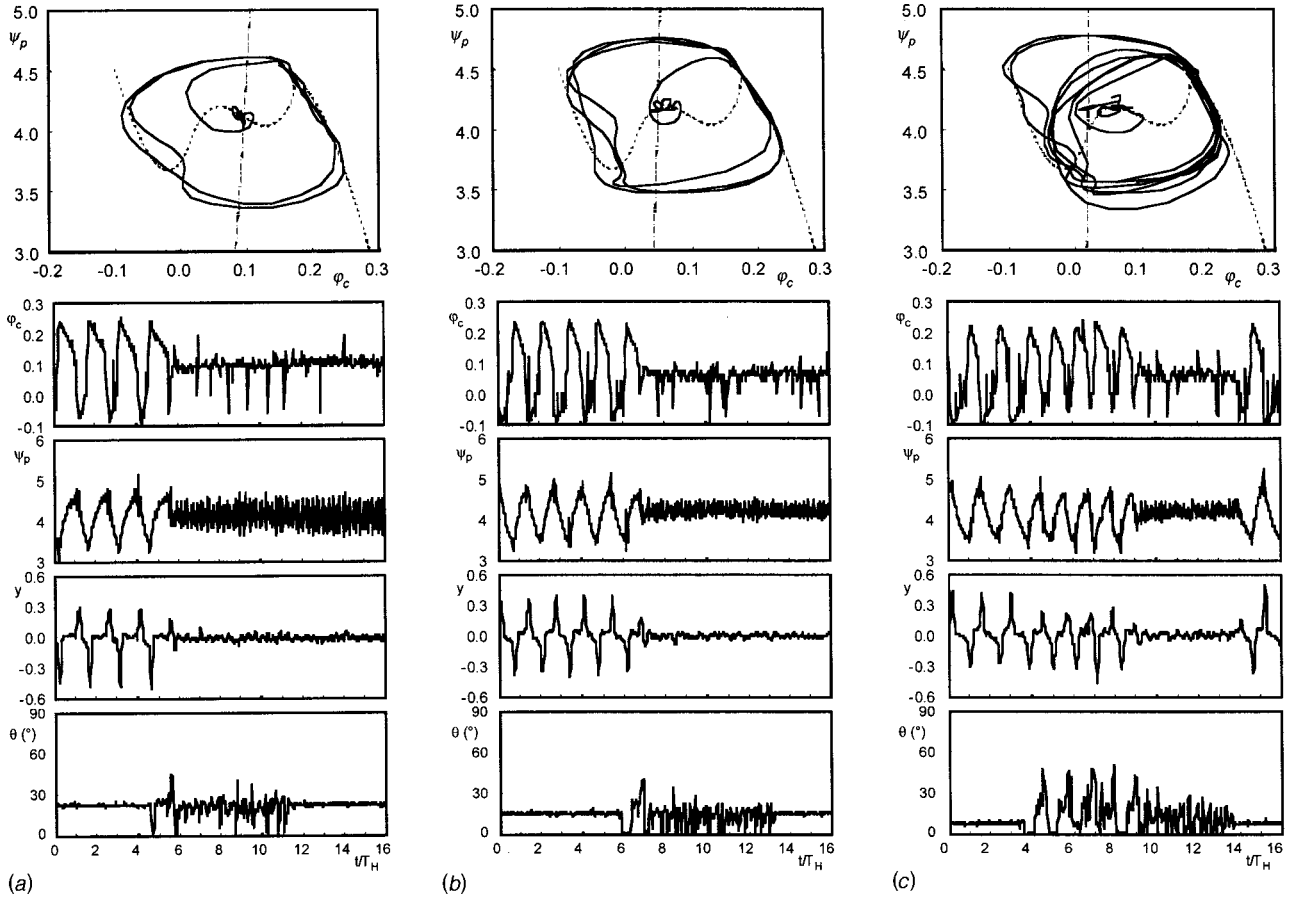

Fig. 7 System trajectories in plane (φ_c, ψ_p) and time histories produced by the proportional control at 2500 rpm: (*a*) $\theta_s = 22.5$ deg; (*b*) $\theta_s = 15$ deg; (*c*) $\theta_s = 7.5$ deg

branch of the compressor characteristic for rotational speeds up to 3000 rpm. Under these conditions, the standard proportional control turns out to be very effective if the limit gain values provided by the adaptive control are imposed. At the highest compressor speed (3500 rpm) the control strategy fails. This is not a conceptual limitation of the high-gain approach, which in theory assures system stabilization in any operating condition, but it mainly results from the limited actuation speed and from the interaction of high gain, sensor disturbances, and actuator saturation. In fact, as the compressor speed, and hence parameter *B*, is increased, the system requires higher gain values to be stabilized. On one hand, such high gains cause very fast actuator displacements to be required by the controller, so that the inertial resistance of the valve can exceed the motor torque. On the other hand, the unavoidable disturbances of the system output signal are strongly amplified by the high gain, so resulting in large valve oscillations and hence in frequent conditions of actuator saturation (complete valve closing). Saturation does not necessarily cause system instability on its own (the so called ''bang-bang'' controls, which are based on actuator saturation, have several technical applications), but it is clear that the saturation induced by disturbances has no correlation with the system dynamics to be controlled.

Another negative effect of amplified disturbances and valve saturation is observed in the stabilized conditions at small valve steady angles: the asymmetric valve oscillations around the equilibrium position determines an average flow rate which is significantly larger than the desired one.

In order to attenuate or possibly eliminate the limits of the proposed control strategy, further work is required, which should be focused on two main topics. On one hand, an actuator of higher performance should be selected, which is not an easy task due to the difficulty of increasing both motor torque and speed (a motor with a higher torque has usually a larger rotor inertia). On the other hand, the origin of the sensor disturbances should be carefully investigated (the low-frequency disturbances in the filtered signal might be due to secondary dynamics, which are excited by the high gain feedback), and different filtering techniques should possibly be considered. Although the solution of both problems appears to be a rather difficult task, the authors believe that further investigations are worth pursuing, since the proposed high-gain approach has the potential for very effective applications in the field of compressor surge control.

Acknowledgments

The present research has been supported by the Italian National Council of Research (CNR).

Nomenclature

A = area
B = Greitzer parameter
G = valve parameter
K = control gain
L = equivalent length
T_H = Helmholtz period
U = impeller tip speed
V = volume
a = speed of sound
$\dot{m}$ = mass flow rate
p = absolute pressure
s = Laplace transform variable

t = time
u = system input
y = system output
Δp_c = compressor pressure rise
$\delta(\cdot)$ = small perturbation
θ = valve angular position
ρ = density
τ = dimensionless time$=\omega_H t$
τ_a = actuator dynamics time constant
τ_c = compressor dynamics time constant
φ = flow coefficient$=\dot{m}/\rho_0 U A_c$
ψ = pressure coefficient$=2(p-p_0)/\rho_0 U^2$
ψ_c = compressor pressure coefficient$=2\Delta p_c/\rho_0 U^2$
ω_H = Helmholtz angular frequency$=a_p\sqrt{A_c/L_c V_p}$

Subscripts

0 = ambient
1 = compressor inlet
c = compressor
p = plenum
r = required by the controller
s = steady-state
t = throttle valve

References

[1] Greitzer, E. M., 1976, ''Surge and Rotating Stall in Axial Flow Compressors—Part I: Theoretical Compression System Model,'' ASME J. Eng. Power, **98**, pp. 190–198.

[2] Moore, F. K., and Greitzer, E. M., 1986, ''A Theory of Post-Stall Transients in Axial Compression Systems: Part I—Development of Equations,'' ASME J. Eng. Gas Turbines Power, **108**, pp. 68–76.

[3] Epstein, A. H., Ffowcs Williams, J. E., and Greitzer, E. M., 1989, ''Active Suppression of Aerodynamic Instabilities in Turbomachines,'' J. Propul. Power, **5**, No. 2, pp. 204–211.

[4] Ffowcs Williams, J. E., and Huang, X., 1989, ''Active Stabilization of Compressor Surge,'' J. Fluid Mech., **204**, pp. 245–262.

[5] Pinsley, L. E., Guenette, G. R., Epstein, A. H., and Greitzer, E. M., 1991, ''Active Stabilization of Centrifugal Compressor Surge,'' ASME J. Turbomach., **113**, pp. 723–732.

[6] Simon, J. S., Valavani, L., Epstein, A. H., and Greitzer, E. M., 1993, ''Evaluation of Approaches to Active Compressor Surge Stabilization,'' ASME J. Turbomach., **115**, pp. 57–67.

[7] Behnken, R. L., and Murray, R. M., 1997, ''Combined Air Injection Control of Rotating Stall and Bleed Valve Control of Surge,'' *Proc. 1997 American Control Conference*, Albuquerque, NM, pp. 987–991.

[8] Gravdal, J. T., and Egeland, O., 1999, ''Centrifugal Compressor Surge and Speed Control,'' IEEE Trans. Control Syst. Technol., **7**, No. 5, pp. 567–579.

[9] Gravdal, J. T., and Egeland, O., 1997, ''Compressor Surge Control Using a Close-Coupled Valve and Backstepping,'' *Proc. 1997 American Control Conference*, Albuquerque, NM, pp. 982–986.

[10] Banaszuk, A., and Krener, A. J., 1999, ''Design of Controllers for MG3 Compressor Models With General Characteristic Backstepping,'' Automatica, **35**, pp. 1343–1368.

[11] McCaughan, F. E., 1990, ''Bifurcation Analysis of Axial Flow Compressor Stability,'' SIAM (Soc. Ind. Appl. Math.) J. Appl. Math., **50**, pp. 1232–1253.

[12] Abed, E. H., Houpt, P. K., and Hosny, W. M., 1993, ''Bifurcation Analysis of Surge and Rotating Stall in Axial Flow Compressors,'' ASME J. Turbomach., **115**, pp. 817–824.

[13] Kang, W., Gu, G., Sparks, A., and Banda, S., 1997, ''Surge Control and Test Functions for Axial Flow Compressors,'' *Proc. 1997 American Control Conference*, Albuquerque, NM, pp. 3721–3725.

[14] Badmus, O. O., Chowdhury, S., and Nett, C. N., 1996, ''Nonlinear Control of Surge in Axial Compression Systems,'' Automatica, **32**, No. 1, pp. 59–70.

[15] Gu, G., Sparks, A., and Banda, S., 1999, ''On Overview of Rotating Stall and Surge Control for Axial Flow Compressors,'' IEEE Trans. Control Syst. Technol., **7**, No. 6, pp. 639–647.

[16] Willems, F., and de Jager, B., 1999, ''Modeling and Control of Compressor Flow Instabilities,'' IEEE Control Syst. Mag., **19**, No. 5, pp. 8–18.

[17] Giannattasio, P., Micheli, D., and Pinamonti, P., 2000, ''Active Control of Surge in Compressors Which Exhibit Abrupt Stall,'' *Proc. Active Control Symp. for Power Systems and Propulsion*, RTA/AVT, Braunschweig, Germany, paper MP-051-PSP-15.

[18] Arnulfi, G. L., Micheli, D., and Pinamonti, P., 1995, ''Velocity Measurements Downstream of the Impellers in a Multistage Centrifugal Blower,'' ASME J. Turbomach., **117**, pp. 593–601.

[19] Arnulfi, G. L., Micheli, D., and Pinamonti, P., 1996, ''Experimental Investigation on Rotating Stall in a Centrifugal Blower With Two and Four Stages and Vaneless Diffusers,'' ASME Paper No. 96-GT-171.

[20] Arnulfi, G. L., Giannattasio, P., Giusto, C., Massardo, A. F., Micheli, D., and Pinamonti, P., 1999, ''Multistage Centrifugal Compressor Surge Analysis: Part I—Experimental Investigation,'' ASME J. Turbomach., **121**, pp. 305–311.

[21] Arnulfi, G. L., Giannattasio, P., Giusto, C., Massardo, A. F., Micheli, D., and Pinamonti, P., 1999, ''Multistage Centrifugal Compressor Surge Analysis: Part II—Numerical Simulation and Dynamic Control Parameter Evaluation,'' ASME J. Turbomach., **121**, pp. 312–320.

[22] Arnulfi, G. L., Giannattasio, P., Micheli, D., and Pinamonti, P., 2001, ''An Innovative Device for Passive Control of Surge in Industrial Compression Systems,'' ASME J. Turbomach., **123**, pp. 473–483.

[23] Giannattasio, P., 1999, ''Analisi di stabilità di un sistema di compressione industriale con controllo attivo del pompaggio'' [in Italian], *Proc. 54th Congresso Nazionale ATI*, L'Aquila, Italy, pp. 1437–1451.

[24] Blanchini, F., and Giannattasio, P., 2000, ''Adaptive Control of Compressor Surge Instability,'' submitted for publication to Automatica.

Numerical Investigation of Tandem-Impeller Designs for a Gas Turbine Compressor

Douglas A. Roberts

Suresh C. Kacker

Pratt & Whitney Canada,
Mississauga, Ontario, Canada

The tandem-bladed impeller centrifugal compressor, which may offer potential aerodynamic benefits over conventional designs, is rarely employed in production gas turbine applications. Conventional impeller designs are often favored because of concerns for both significant performance losses and increased manufacturing costs associated with tandem configurations. In addition, much of the available literature concerning the characteristics of tandem-impellers is inconclusive, and at times contradictory. Because of the scarcity of tandem-impellers, rules for their design are nearly nonexistent. Also, the effects of inducer/exducer clocking upon tandem-impeller performance and exit flow characteristics are not fully understood. In the present study, a numerical investigation was performed to investigate the aerodynamic characteristics of a tandem-impeller design for the rear stage of a gas turbine compressor (target impeller $PR_{t-t} \approx 3.0$*). A parametric study of tandem-impeller inducer/exducer clocking was performed in order to explore its effect upon performance and exit flow quality. Because the tandem impeller was designed to be retrofittable for an existing conventional impeller, it was also compared to predictions for the baseline conventional design. Results of the study indicated that the tandem-impeller was less efficient than the conventional design for all clocking configurations studied. Tandem-impeller blade clocking was found to have a significant effect upon predicted pressure ratio, temperature ratio, efficiency, and slip factor; the maximum values for these parameters were predicted for the in-line tandem configuration. The minimum predicted tandem-impeller isentropic efficiency occurred at a clocking fraction of 50 percent, falling 3.8 points below that of the in-line case. Although the tandem-impeller performance was predicted to diminish as blade clocking was increased, significant improvements in the uniformity of impeller exit velocity profiles were observed. Profiles of both total pressure and swirl at impeller exit indicated that the tandem-impeller design may offer both improved diffuser recovery and stalling margin over the conventional design.* [DOI: 10.1115/1.1413472]

Keywords: Impeller, Numerical, Tandem, Compressor

Introduction

Tandem-blade impeller designs may be used in centrifugal compressors for a number of reasons. The most common reason for their application is to reduce the highly distorted jet/wake exit velocity profiles typically encountered in conventional impeller designs. In some cases, tandem-impeller designs may also provide structural benefits over conventional impeller designs. In spite of potential benefits, the tandem-impeller concept is often not considered for aircraft engine applications because of increased manufacturing costs, and concern for potentially large losses in aerodynamic performance.

A tandem-blade arrangement refers to pairs of blade rows in close axial proximity having some circumferential spacing, and can encompass both stationary (e.g., double-row stators) and rotating airfoils. For rotating tandem-blade arrangements such as in an impeller, it is assumed that no relative circumferential motion occurs between the blade pairs. Figure 1 shows a shaded three-dimensional representation of a tandem-bladed impeller. As shown, the upstream and downstream blades are referred to as ''inducer'' and ''exducer'' blades, respectively. Figure 2 shows a top view detailing the nomenclature for the blading configuration. The axial gap between airfoils is Δx_s, while the circumferential angle between inducer trailing edge and exducer leading edge is θ_s. In the present paper, the circumferential spacing shall be referred to as a fraction of blade pitch, where $\lambda_s = \theta_s / (360 \text{ deg}/N_{\text{blades}})$. Positive values of θ_s and λ_s refer to a positioning of the exducer L.E. relative to the inducer T.E. such that the exducer suction surface is closest to the pressure surface of the inducer, as shown in Fig. 2. All values of λ_s refer to inducer/exducer alignment at the shroud.

Because of the relatively small number of designs in existence, the aerodynamic merits of tandem-impellers are not well documented. From one perspective, the presence of a tandem gap, which reduces the effective loading area and forces premature diffusion in the inducer passage, should handicap the tandem design both in terms of achievable efficiency and pressure ratio as compared to a similar conventional impeller. From another perspective, however, the close proximity of the inducer and exducer airfoils could prevent the onset of downstream suction surface separation by re-energizing the blade-surface boundary layer much like a wing-flap configuration. Such a potential improvement in flow quality could reduce the distortion in impeller exit velocity profiles, consequently improving both diffuser recovery and range of operability.

Most of the available publications dealing with tandem-blade turbomachines have historically favored axial configurations over centrifugal devices. The relatively few publications that have investigated tandem-bladed centrifugal turbomachines have for the most part been inconclusive as to the impact on performance. When summarizing various tandem-impeller studies in their 1992 paper, Kadner and Hoffman [1] concluded that ''... there are very

Contributed by the International Gas Turbine Institute and presented at the 46th International Gas Turbine and Aeroengine Congress and Exhibition, New Orleans, Louisiana, June 4–7, 2001. Manuscript received by the International Gas Turbine Institute February 2001. Paper No. 2001-GT-324. Review Chair: R. Natole.

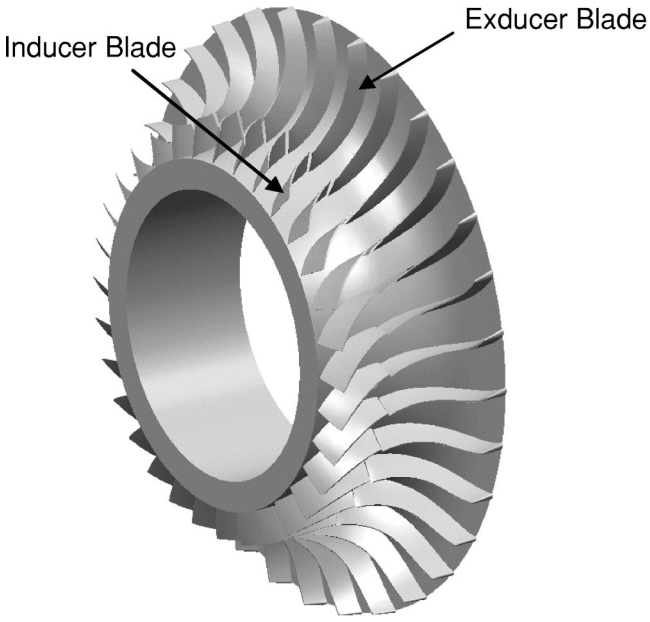

Fig. 1 Three-dimensional representation of tandem-impeller design (λ_s=5 percent configuration shown)

contradictory statements of the attainable improvements of such a blade arrangement so that no design rules are available.'' Despite these contradictions, a brief summary of several studies is presented herein.

Boyce and Nishida [2] explored a tandem-blade impeller design in an attempt to reduce a flow separation on the splitter blade of a corresponding conventional impeller design. A clocking fraction of λ_s=33 percent between the inducer and exducer blades was used. The authors found that the tandem arrangement both eliminated the separation and had a slight improvement on measured efficiency. It is unclear, however, as to whether the tandem arrangement would have delivered a superior efficiency if the baseline design had been properly designed without flow separation.

In a numerical study of a high head-coefficient pump impeller, Bache [3] compared a conventional baseline impeller to several tandem arrangements. The results of this study showed that significant gains in flow uniformity could be achieved by a tandem blade arrangement. In addition, the author showed that clocking, rather than the meridional split location, had the greatest impact on flow uniformity. No efficiency data were included in this work.

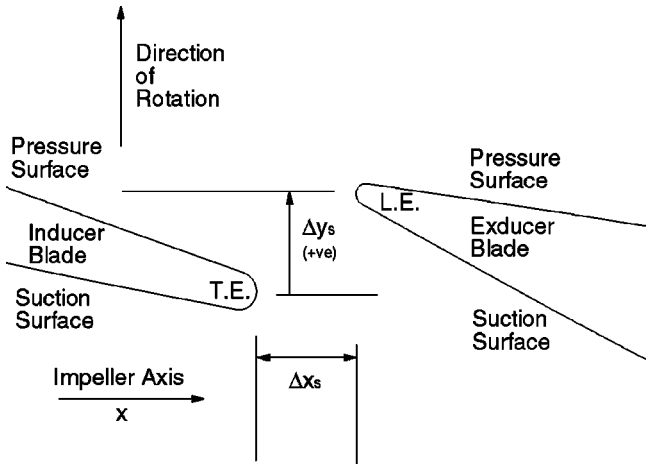

Fig. 2 Nomenclature for tandem-impeller clocking arrangement

A parametric computational fluid dynamic (CFD) study of a tandem blade turbopump was performed by Cheng et al. [4] in 1993. In this study, two versions of a tandem-impeller design having clocking fractions of 7.5 and 22.5 percent were compared to a baseline consortium impeller. Numerical results predicted that both tandem designs delivered lower efficiency and head than the baseline due to large flow distortions. A flow separation was found to occur on the suction side of the splitter blade in both tandem-impeller cases.

Two very thorough experimental tandem-impeller studies were performed by Kadner and Hoffman [1] and Kadner [5]. These papers are of particular interest because their centrifugal designs are the most similar to that of the present appear. In the first study, the authors studied a medium pressure ratio (PR=3.9) tandem-impeller having 14 inducer and 28 exducer blades, 32 deg of backsweep, and an axial gap of approximately 1.5 percent of tip radius. The design was tested in combination with a vaneless diffuser for five different relative circumferential inducer/exducer (or clocking) positions. Because of structural limitations, the design could only be tested up to 88 percent of its design speed. At this speed, the inducer/exducer positioning had a relatively small impact on performance, resulting in a maximum deviation in polytropic efficiency of approximately 0.5 percent and in total pressure ratio of 2 percent. The optimum positioning was found to be the in-line configuration and the poorest performance was observed when the exducer pressure surface was placed closest to the inducer suction surface. The authors also observed that the effect of blade positioning mostly impacted the pressure ratio of the inducer blade and the leading edge region of the exducer. A series of impeller exit velocity traverses using laser velocimetry (L2F) were also taken, and it was concluded that velocity profiles were not significantly affected by relative blade position.

In the follow-up study by Kadner [5], a similar impeller design was once again tested for various inducer/exducer clockings. In this case, however, a different impeller material was used so that the correct aerodynamic design speed could be achieved. In addition, the axial gap between the inducer and exducer blades was reduced to zero in an attempt to increase the sensitivity of the design to the relative circumferential positions. Findings indicated that the total-to-total pressure ratio was not significantly impacted by inducer/exducer clocking. It was found, however, that the stage surge margin could be improved by blade clocking. The maximum improvement in surge margin corresponded with the closest to, but not in-line, blading arrangement in which the exducer suction surface was closest to the inducer pressure surface at 27 percent of exducer pitch. Also, in contrast to the rotor total-to-total pressure ratio, the stage total-to-static pressure ratio was found to be significantly affected by blade positioning. The optimum surge margin position also resulted in the highest total-to-static pressure ratio. This was the only arrangement in which the stage total-to-static pressure ratio was found to exceed that of the in-line configuration; all other configurations were lower. The authors attributed the improvements in both stage pressure ratio and surge margin to a smaller wake zone and more balanced velocity field at the impeller exit, which improved diffuser performance. Measurements of exit meridional velocity profiles affirmed this argument, showing a significant reduction in jet/wake velocity differences for the optimal clocking configuration as compared to the in-line case. In addition, it was observed that the velocity profiles of the two exducer (i.e., main/splitter) channels were more balanced in the optimum case than for the in-line configuration.

The present study explores the aerodynamic characteristics of a retrofittable tandem-impeller design, intended to perform a similar duty as an existing conventional rear-stage impeller for a multistage aircraft gas turbine compressor. The intent of the study is to compare both the flowfield and performance characteristics of a

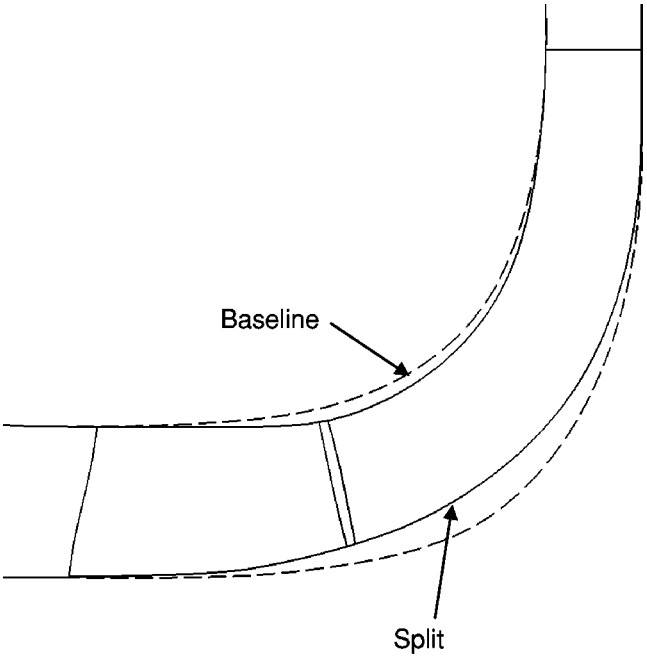

Fig. 3 Comparison of conventional and tandem-impeller meridional gas-path profiles

tandem-impeller with a conventional design of a similar duty, and to explore the impact of inducer/exducer blade clocking upon impeller performance and exit flow quality.

Description of Impeller Geometries

The conventional full-bladed impeller design is intended for an aircraft gas turbine application behind a multistage axial compressor. It is designed to function in combination with a downstream discrete-passage type diffuser, and to deliver a target impeller total-to-total pressure ratio of approximately 3.0. The design is fully subsonic at entry, and is designed for a mean upstream preswirl of 22 deg. This impeller consists of 28 main blades without splitters, and has 36 deg of trailing edge backsweep.

The tandem-impeller design was designed as a retrofit to the baseline design, which could be ''dropped in'' between the upstream axial compressor and downstream diffuser, maintaining common entry and exit gas-path corner points. The tandem design was required to deliver at least the same pressure ratio as the conventional design for the smallest possible efficiency penalty. The inducer blade was designed using axial airfoil methods while the exducer blade was designed using conventional impeller techniques. Initially, the first tandem-impeller design was a two-bladed copy of the conventional impeller, having clocked airfoils and an axial split-gap. It was found, however, that several design changes were necessary in order for the tandem-impeller to deliver a similar pressure ratio to the conventional with a minimal efficiency penalty. Several features of the final tandem-impeller design include modified blade camber distributions, a narrower gas-path in the ''knee'' region, 31 inducer and 31 exducer blades, and 24 deg of backsweep. In addition, the inducer/exducer blade axial gap, x_s, is 0.6 percent of impeller-tip radius. The design was optimized in such a way that it delivered a slightly higher pressure ratio than the conventional design for a clocking pitch fraction (λ_s) of 5 percent; the additional pressure ratio was incorporated into the design to improve matching with upstream components. This design is shown in Fig. 1. A comparison of the meridional gas-path profiles for both the conventional and tandem-impeller designs is shown in Fig. 3.

Numerical Modeling

All CFD calculations were performed using a finite-element, turbulent, compressible flow solver called NS3D [6]; the solver was jointly developed by Pratt & Whitney Canada and Concordia University. The primary flow variables are pressure, p, and mass flux, ρV, with a pressure dissipation term in the continuity equation. By introducing this dissipation term, the odd–even decoupling (or checkerboarding) effect is avoided, hence allowing equal-order interpolation to be used for velocities and pressures. Stabilization of the momentum equations is achieved by means of the Streamline Upwind Petrov Galerkin (SUPG) scheme [7].

The code presently supports hexahedral, tetrahedral, and prismatic element types. Equations are linearized using a Newton method, and are solved in a fully coupled manner using a highly parallelized preconditioned iterative solver [8].

Both $k-\varepsilon$ and $k-\omega$ turbulence models are supported by the code, but the $k-\omega$ model was used because it has been found to be more stable. Equations are integrated to the wall by means of a special logarithmic element [9] spanning the region from the wall to the first near-wall grid mode. The y^+ value of the first node is allowed to vary over a range from 30 to 300. By using this scheme, computational time is significantly reduced, as compared to traditional wall integration schemes, in which numerous linear elements are required to capture high near-wall gradients. In addition, superior accuracy is achieved as compared to conventional wall function approaches, with only a small increase in computational cost.

In this study, the NS3D code was used to analyze seven impeller configurations. The configurations consisted of the conventional impeller as well as the clocked tandem-impeller at 0, 5, 10, 25, 50, and 75 percent clocking fractions (λ_s). Finite element grids of the impeller flow domains were created using a method developed at PWC called ''ICAST.'' Prior to this method, an axial compressor grid-generation tool was used to generate impeller grids; this former technique, although generally sufficient for conventional geometries, lacked the capability to accommodate tandem-impeller designs. ICAST combines the three-dimensional CAD package CATIA with the commercial three-dimensional hexahedral grid-generation package ICEM-HEXA. Interactive routines programmed in CATIA are used in combination with HEXA to construct impeller grids for multiple topologies in a rapid, automated fashion. An additional benefit to this method is that the user is afforded much greater control over grid spacing, including the distribution of near-wall grid y^+ values, hence improving the quality of solutions.

All grids were of the structured hexahedral type, consisting of linear quadrilateral elements. The grids were extended upstream of the leading edge axially at the inlet and downstream of the trailing edge radially at the exit by a distance of 10 percent of the impeller tip radius. Three separate grid topologies were used to model the conventional impeller, the clocked tandem-impellers, and the in-line ($\lambda_s=0$) tandem-impeller. Grid sizes for each of these three topologies were allowed to vary in order to maintain similar near-wall grid spacings and bunchings in the flow domains. The grid sizes are summarized as follows: (*i*) conventional impeller: 120,096 elements ($i=140$, $j=33$, $k=28$), (*ii*) clocked tandem-impellers: 277,020 elements ($i=181$, $j=58$, $k=28$), and (*iii*) in-line tandem-impeller: 228,312 elements ($i=152$, $j=55$, $k=29$). A cut of a typical tandem-impeller mesh is shown in Fig. 4. For all impeller analyses, a constant tip clearance value of 1.6 percent of impeller exit blade height was modeled using six k-planes to grid the tip clearance region.

In all cases, the impeller flowfield was analyzed in isolation without a diffuser. For the analysis, a steady-state, compressible, three-dimensional, fully turbulent flow was assumed. The imposed upstream radial boundary condition profiles for total pressure, total temperature, swirl (α), and radial flow angle (ϕ) were taken from predicted exit profiles for the upstream axial compressor, and were identical for all runs. Inlet turbulence boundary conditions of

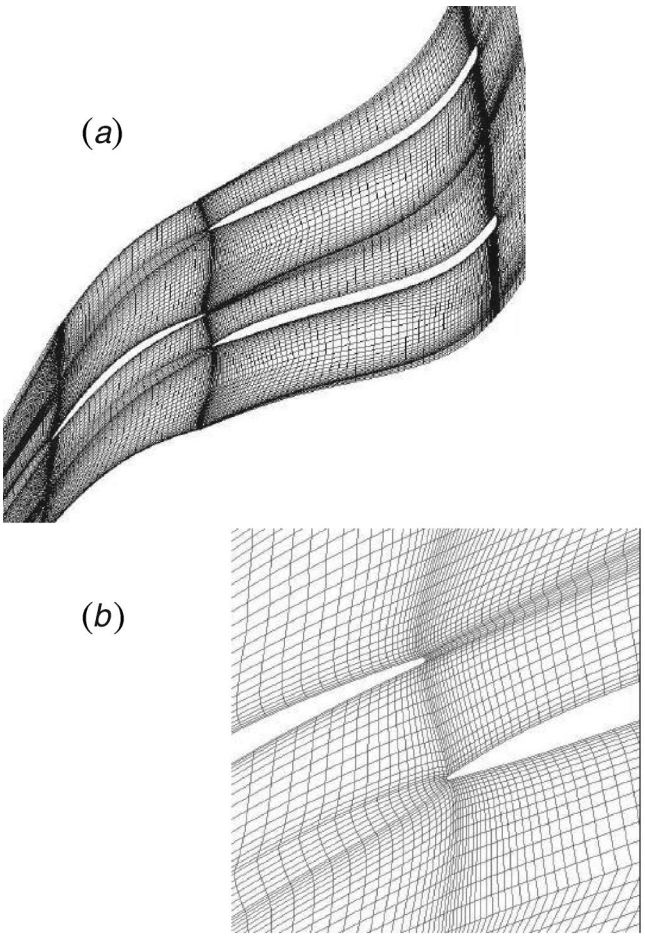

Fig. 4 Sample computational grid for tandem-impeller

$k=0.001$ and $\varepsilon=0.004$ were also imposed in all cases. For each case, a constant static pressure was imposed at the downstream exit boundary while the mass-averaged values of total temperature and pressure were held constant at the inlet. All cases were analyzed at the impeller design speed over a range of several flows by varying the exit static pressure imposed. All solutions were run to a sufficient convergence level such that the overall residual was of the order 10^{-4} and the exit mass flux was within less than 0.5 percent of the inlet value. Mass-averaged thermodynamic impeller performance calculations (i.e., PR, TR, and efficiency) were based upon inlet total temperature and pressure at 5 percent (of impeller tip radius) upstream of the leading edge, exit total temperature at the trailing edge, and total pressure at 5 percent downstream of the trailing edge. Total pressure was calculated downstream of the trailing edge to partially account for mixing which would normally occur downstream of the impeller.

Results and Discussion

The predicted impeller running-line total pressure ratio, total temperature ratio, and isentropic efficiency values have been plotted versus clocking fraction (λ_s) in Figs. 5(*a*)–(*c*). Running line values were calculated for a constant value of impeller exit corrected flow (W_{cor}), in an attempt to represent the engine matching points for the various designs. Note that the results have been normalized to the impeller design targets. From the large degree of variation in predicted performance, it is clear that the inducer/exducer clocking had a significant impact upon tandem impeller performance.

It is immediately apparent from the plots of Fig. 5 that the tandem-impeller running-line pressure-ratio, efficiency, and temperature ratio values were highest for the in-line (0 percent) case. All three parameters were observed to decrease continually as a function of clocking fraction, reaching minimum values at $\lambda_s=50$ percent. Increasing further to 75 percent clocking fraction, both temperature ratio and pressure ratio were found to increase, while efficiency was virtually unchanged. In general, the tandem-impeller design was found to be less efficient than the conventional impeller for all configurations, having a minimum efficiency penalty of 0.55 points at $\lambda_s=0$ percent and a maximum efficiency penalty of 3.8 points at $\lambda_s=50$ percent. In spite of its lower backsweep value, the tandem-impeller total pressure ratio was found to exceed that of the conventional design only for the 0 and 5 percent configurations, while the 10 percent design delivered a nearly identical level.

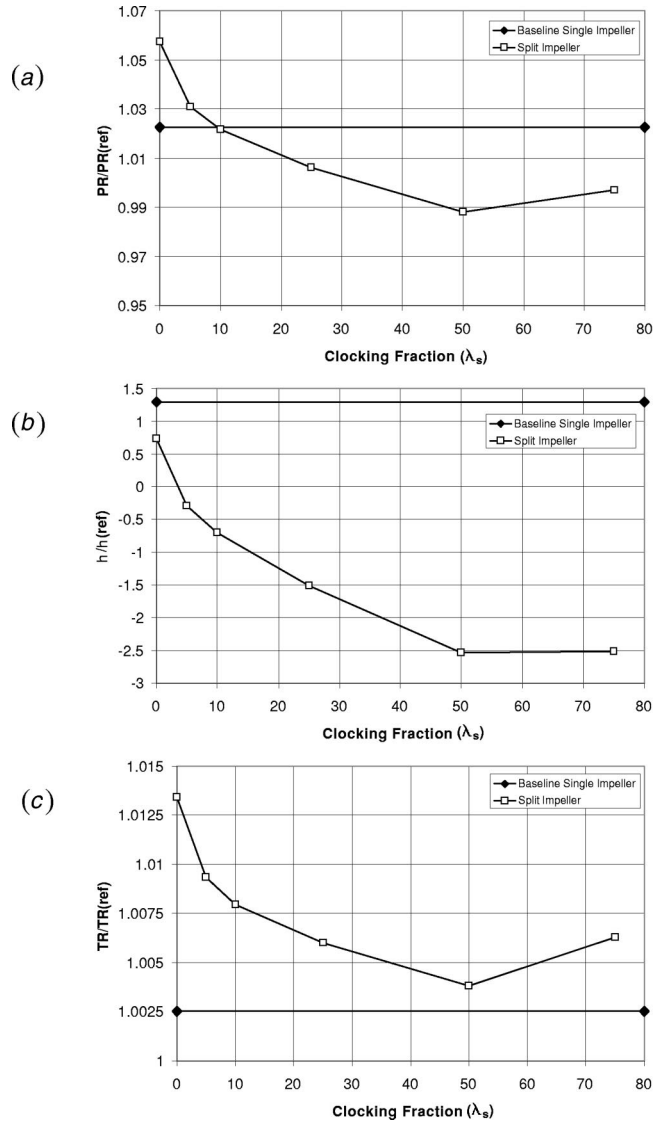

Fig. 5 Comparison of predicted impeller: (*a*) total-to-total pressure ratio, (*b*) isentropic efficiency, and (*c*) total temperature ratio at running line

Due to the backsweep difference, the predicted tandem-impeller temperature rise was, not surprisingly, higher than that of the conventional design. The dependence of tandem-impeller temperature rise upon clocking fraction, however, does suggest that trailing edge slip factor is dependent upon relative circumferential position. Understanding this variation of tandem-impeller slip factor as a function of inducer/exducer clocking is a highly important relationship for a compressor designer sizing impeller designs to

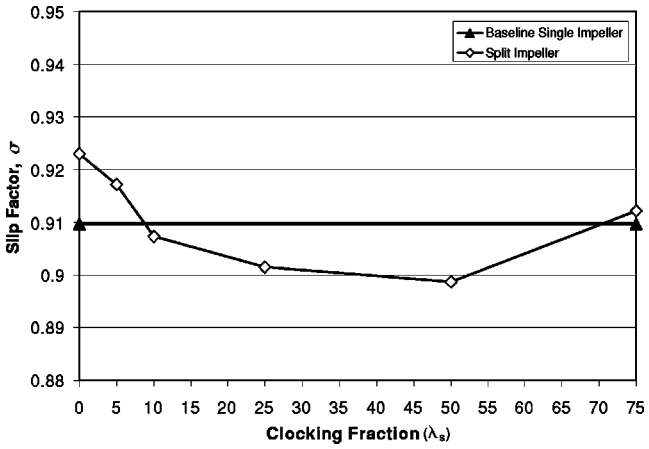

Fig. 6 Predicted impeller slip factor versus clocking fraction (λ_s)

meet a target pressure ratio. Figure 6 shows the predicted running line slip factor (σ) values as a function of tandem-impeller clocking fraction. The slip factor was found to vary from a maximum value of 0.923 at 0 percent clocking to a minimum of 0.898 at 50 percent; by comparison the predicted conventional impeller slip factor was 0.909. The observed increase in slip ($1-\sigma$) from 0 to 50 percent clocking is most likely the result of increased exducer blade-to-blade loading with increased clocking. Generally, for lower backsweep designs such as the tandem-impeller, it is expected that the amount of slip would be greater than for designs having higher backsweep due to increased aerodynamic loading at the back-end of the exducer. In the present study, however, this was only found to be true for the 10, 25, and 50 percent cases; for the 0, 5, and 75 percent cases, the velocity field due to the tandem arrangement resulted in less slip than for the conventional design. A general conclusion that can be drawn is that conventional impeller slip factor correlations may not necessarily apply to tandem-impeller designs because of the strong effect of inducer/exducer clocking.

Contour plots of the predicted running-line impeller flowfields for the conventional as well as three of the tandem-impeller ($\lambda_s = 0$, 5, and 50 percent) cases are shown in Figs. 7–10. For each of these cases, relative Mach contours are shown for cuts at 25, 50, 75, and 95 percent span in (*a*)–(*d*), at the trailing edge in (*e*), and a meridional velocity contour is shown at a location 3 percent downstream of the trailing edge in (*f*). The Mach contours near the hub at 25 percent span showed little difference between the various tandem-impeller configurations. For the conventional impeller at 25 percent span, a low-velocity region was observed near the knee of the impeller along the pressure side of the blade. Such a pronounced low-velocity region was not observed on the pressure side of the exducer for any of the tandem-impeller designs, likely because of the narrower gas-path of the tandem design.

The M_{rel} contours from 50 to 95 percent (*b*–*d*) span are more revealing in terms of differences in flow characteristics. Observation of the flow in the split-gap region shows that the suction surface near the leading edge of the exducer is affected by its relative circumferential position to the inducer. For the in-line tandem-impeller case ($\lambda_s = 0$ percent), acceleration about the exducer leading edge was negligible, while for the 50-percent clocked case, a strong acceleration was observed in this region. For the 5 percent clocked case, more modest exducer leading edge suction surface acceleration was observed, which, because of the small circumferential gap between airfoils, was found to create a "jet" of high-momentum flow along the exducer suction surface. Changes in the degree of acceleration about the exducer leading edge are due to variations in incidence, resulting from circumferential variations in inducer T.E. deviation. In addition, inducer

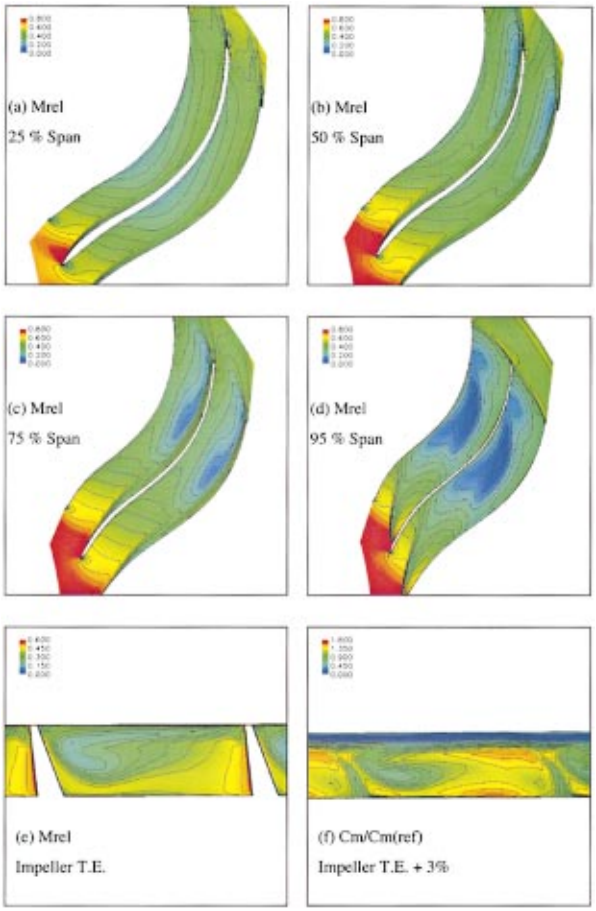

Fig. 7 Conventional impeller: (*a*–*d*) M_{rel} contours at 25, 50, 75, and 95 percent span; (*e*) M_{rel} contour at impeller trailing edge; (*f*) meridional (Cm) velocity contour at trailing edge + 3 percent

trailing edge deviation is very likely affected by airfoil clocking. The observed reduction in slip factor from $\lambda_s = 0$ to 50 percent discussed above is consistent with the increased exducer incidence and hence higher exducer loading.

Flow in the downstream portion of the exducer (past the gas-path bend to radial) was characterized by varying degrees of low-momentum flow and separation for the different tandem configurations. In the conventional full-blade design (Fig. 7(*d*)), a separation was observed near the shroud, occupying approximately 2/3 of the blade-to-blade passage closest to the pressure surface at 95 percent span. In the case of the tandem-impeller, both the shape and the extent of the separation zone were found to vary due to the clocking arrangement. At 75 percent span (Figs. 8–10(*c*)), the separation zone was found to move closer to the exducer suction surface, and to increase in size as the clocking fraction was increased. The tandem-impeller separation patterns observed at 95 percent span (Figs. 8–10(*d*)) were more complex than those at 75 percent, showing the effects of both clocking and the tip-clearance vortex on the separated flow distributions. The chordwise extent of the 95-percent span separated region appears to have increased as blade clocking was increased, but the shape of the low-momentum distributions has changed the appearance of the flow for each case. Comparing the tandem-impeller designs to the conventional impeller, the chordwise extent of separation in the tandem-impeller designs appears to be less extensive at 95 percent and more extensive at 75 percent. An additional observation is that, in the conventional design, the separated flow has reattached by the impeller trailing edge. In the tandem-impeller designs, however, various degrees of separation were observed at the trailing edge with reattachment occurring slightly downstream.

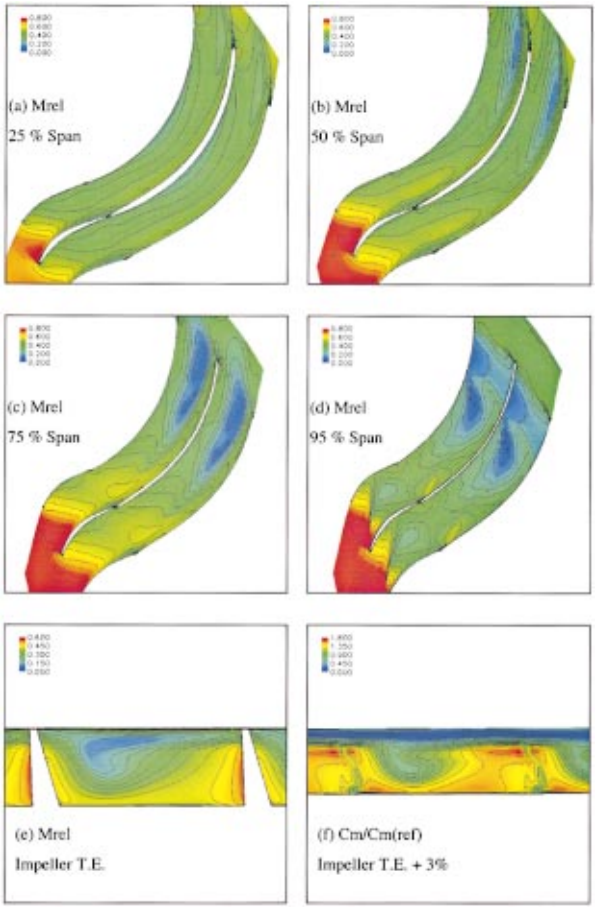

Fig. 8 Tandem-impeller ($\lambda_s = 0$ percent): (*a–d*) M_{rel} contours at 25, 50, 75, and 95 percent span; (*e*) M_{rel} contour at impeller trailing edge; (*f*) meridional (Cm) velocity contour at trailing edge + 3 percent

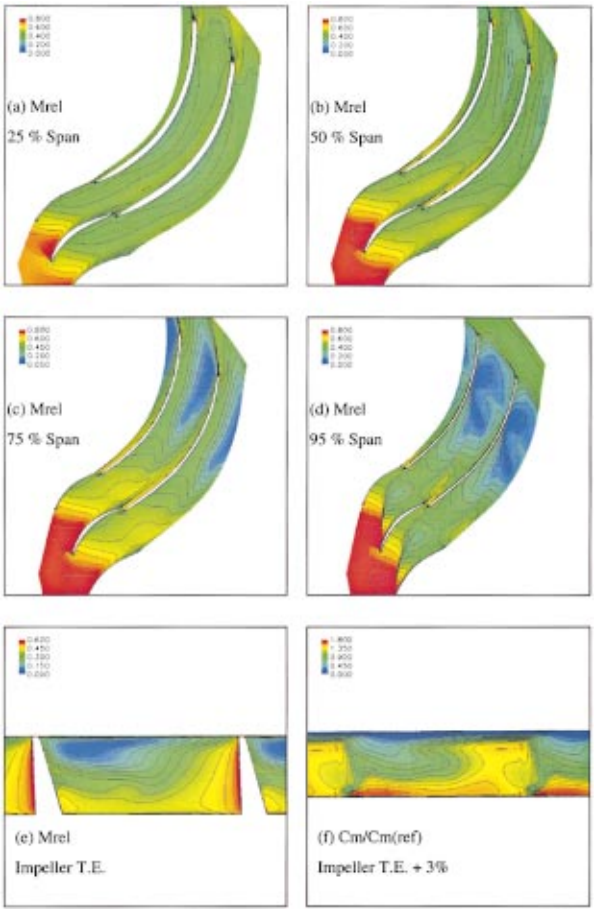

Fig. 9 Tandem-impeller ($\lambda_s = 5$ percent): (*a*)–(*d*) M_{rel} contours at 25, 50, 75, and 95 percent span; (*e*) M_{rel} contour at impeller trailing edge; (*f*) meridional (Cm) velocity contour at trailing edge + 3 percent

The flow was likely to reattach farther upstream in the conventional design due to the less aggressive diffusion caused by the higher backsweep angle.

Plots of impeller exit flow predictions are shown in Figs. 7–10(*e*),(*f*). Both relative Mach contours (*e*) at the trailing edge, and meridional velocity contours (*f*) at 3 percent downstream of the trailing edge, are shown. In each of the impeller cases, it was found that a low relative velocity region, or wake, developed near the suction surface/shroud zone at the trailing edge; this jet/wake phenomenon is typical in many impeller designs. This wake was found to be more pronounced in the tandem-impeller cases than for the conventional design, due to the different backsweep values. In the tandem-impeller cases, both the size and strength of these wakes were found to increase as a function of increased clocking from 0 to 50 percent. In addition, this wake was found to migrate toward both the shroud and the suction surface of the exducer as the relative blade clocking was increased up to 50 percent. The increased exducer blade-to-blade loading with increased clocking is a likely explanation for both the increased extent of the wake size, and the secondary effect of the wake migration.

The downstream meridional velocity contours of Figs. 7–10(*f*) show the impeller exit flow in the absolute sense following some mixing; these plots are representative of the flowfield, which would be seen at entry to the downstream diffuser. The TE+3 percent meridional velocity contours indicate that the shroud/suction surface relative velocity wake seen at the trailing edge has mixed out somewhat (from plots (*e*) to (*f*)). What is more noteworthy is that at the TE + 3 percent location for both the conventional and in-line tandem-impeller, the lowest absolute region was observed along the shroud over the entire passage. This region of low momentum across the shroud was found to diminish as the clocking fraction was increased. For the 50-percent clocked configuration, a much less diminished shroud velocity profile was observed as compared to the 0 percent case; however, the low velocity region in the shroud/suction surface corner at the trailing edge, which had mixed out for the other configurations, could still be observed at the TE + 3 percent location for the $\lambda_s = 50$ percent case.

The amount of distortion in the absolute velocity field exiting the impeller is known to be important in terms of its impact both upon the downstream diffuser recovery and compressor surge margin. Although the diffuser is not modeled in the present study, the trends in the impact of various impeller designs upon diffuser performance can be postulated. It is known that the level of aerodynamic blockage at the impeller throat has a strong impact upon diffuser static pressure recovery. Hence, impeller designs having lesser distortions in their absolute exit velocity profiles should result in improved diffuser performance. In order to compare the various configurations quantitatively, a velocity distortion parameter, *r*, was defined. This parameter expresses the degree of variation in radial velocity about the mean value at the TE + 3 percent location. Figure 11 expresses running-line impeller exit velocity nonuniformity parameters versus clocking fraction. The in-line tandem-impeller case was found to have the highest degree of velocity distortion ($r = 0.56$) as compared to $r = 0.48$ for the con-

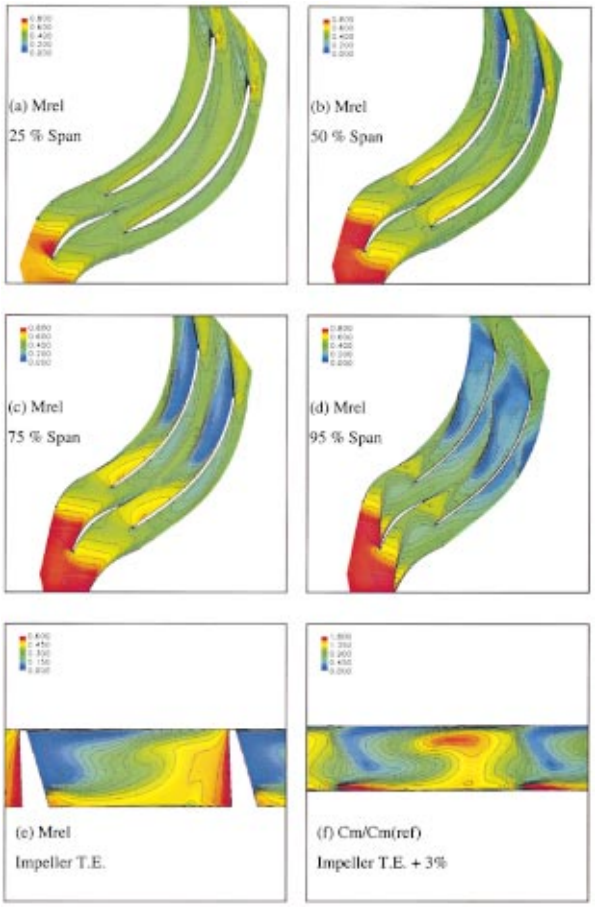

Fig. 10 Tandem-impeller (λ_s=50 percent): (*a–d*) M_{rel} contours at 25, 50, 75, and 95 percent span; (*e*) M_{rel} contour at impeller trailing edge; (*f*) meridional (Cm) velocity contour at trailing edge + 3 percent

ventional impeller. All other tandem-impeller configurations, however, were found to have significantly lower values of radial velocity distortion than the full-blade design.

The 5-percent clocked case was found to have a nonuniformity parameter value of 0.42, while the 25 percent clocked case had the lowest value of r=0.38. The degree of exit velocity nonuniformity was found to increase from this minimum for clocking values beyond λ_s=25 percent.

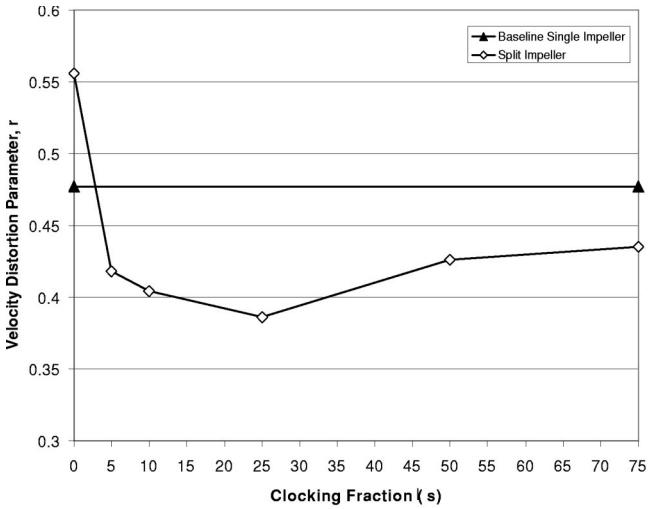

Fig. 11 Radial velocity distortion parameter (*r*) at trailing edge + 3 percent versus clocking fraction (λ_s)

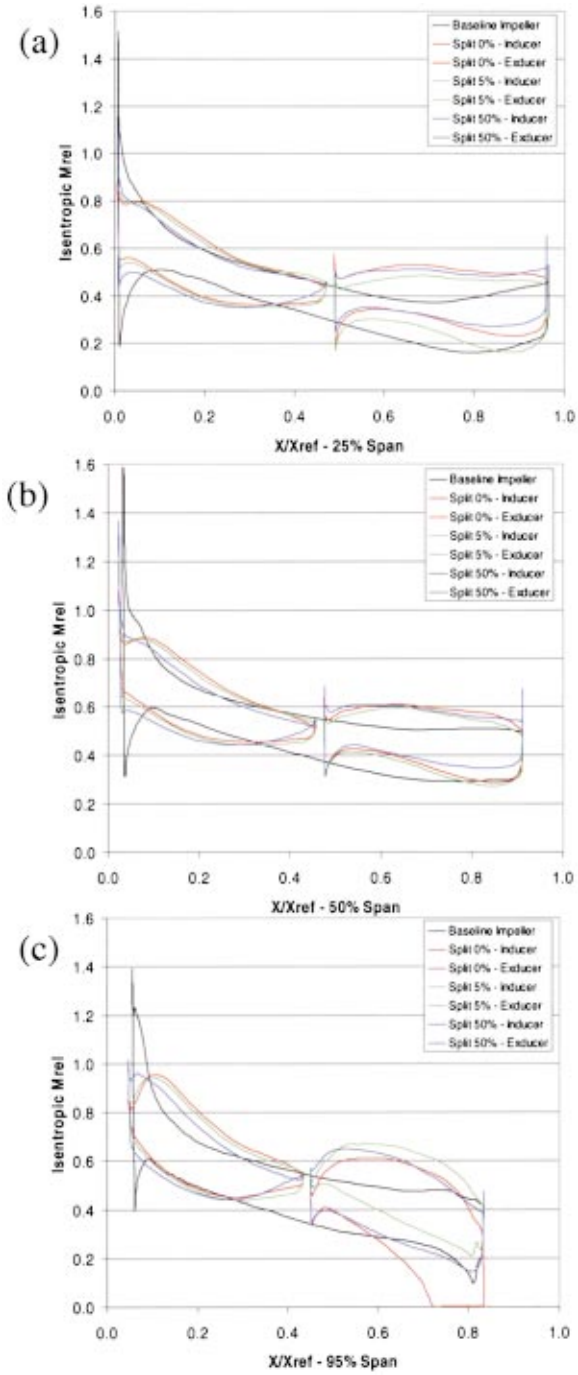

Fig. 12 Impeller blade surface loading (isentropic relative Mach number) distributions at (*a*) 25, (*b*) 50, and (*c*) 95 percent span

The reduction in velocity nonuniformity from 5 to 25 percent clocking is most likely due to the improvements in shroud velocity deficit levels; for the 50 and 75-percent cases, however, the impeller trailing edge wake zone became so predominant that the velocity distortion was increased in spite of the improved shroud velocity profiles.

Impeller running line ''loading'' diagrams, or blade surface isentropic relative Mach number plots comparing the conventional, 0, 5, and 50 percent tandem-impeller cases are shown in

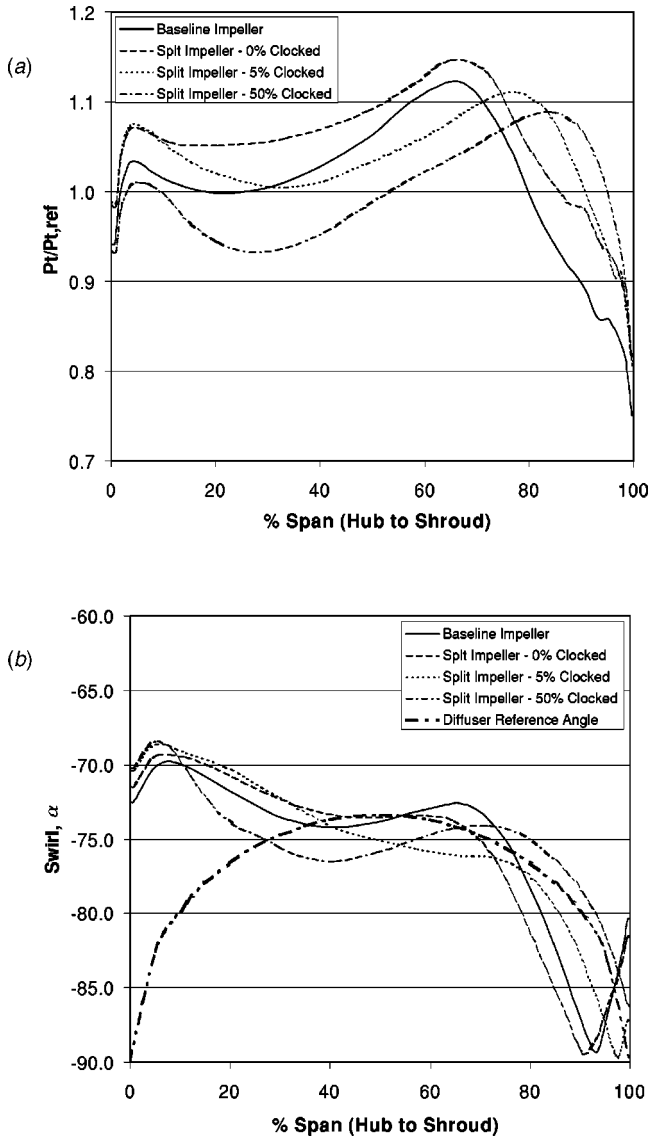

Fig. 13 Hub-to-shroud profiles of pitch-averaged (*a*) total pressure, and (*b*) swirl (α) at trailing edge + 3 percent

Figs. 12(*a*)–(*c*). These plots express the airfoil surface pressure distributions in terms of an equivalent Mach number, and help to show the distributions of aerodynamic loading for the various designs. Comparing the conventional impeller loading distributions to those of the 0-percent tandem-impeller case clearly illustrates that the tandem-impeller blade-to-blade loadings were much more aggressive and had to be redistributed in order to compensate for the lack of available loading area in the split-gap region. A subtle point, which is not fully understood, is the much larger local acceleration about the leading edge of the conventional impeller. Because the inducer blade was designed using different methods, a possible explanation lies in the more elliptic inducer leading edge shape. Another observation that is immediately noticeable is that the surface isentropic relative Mach number levels became somewhat smaller as the clocking fraction was increased. Because the designs were compared at a constant value of exit corrected flow, this phenomenon was simply the result of reduced inlet corrected flow due to reduced pressure ratio as a function of clocking.

A more detailed comparison of the loading diagrams for the various tandem-impeller configurations reveals some subtle effects of airfoil clocking. In the $\lambda_s = 5$ percent case, it was found that the inducer trailing edge blade-to-blade loading was higher than for the in-line case. This increased loading likely results from a combination of reduced trailing edge deviation and boundary layer thickness due to an airfoil flap type of interaction. In the $\lambda_s = 5$ percent case, the near, but offset location of the exducer suction surface draws flow toward it, both energizing the boundary layer and helping the suction surface flow to continue turning approaching the trailing edge. Although the in-line configuration also assisted in preventing boundary layer growth, the position of the exducer suction surface did not result in a circumferential suction component on the trailing edge flow, and hence, had a lesser impact upon deviation. As a result of the reduced inducer deviation in the $\lambda_s = 5$ percent case, incidence at the exducer leading edge was found to be less than that of the in-line case.

Loading diagrams for the $\lambda_s = 50$ percent tandem-impeller case show an observed loss in inducer blade-to-blade loading from 70 to 100 percent chord as compared to the 5 percent case. Because the exducer suction surface was no longer in close proximity for this case, the inducer suction surface boundary layer was able to thicken near the T.E., resulting in a loss of aerodynamic loading. In addition, the exducer leading edge incidence was observed to be greater for the 50-percent case than for the in-line and 5-percent clocked cases. The increased incidence indicates that either the exducer circumferential position is in a region of increased inducer trailing edge deviation, or the increased inducer boundary layer thickness has increased inducer deviation. The net effect of this arrangement was higher loading in the front portion of the exducer, while loading near the rear of the exducer was diminished due to the larger wake zone discussed above.

The running line impeller exit flow is characterized in terms of pitch-averaged exit total pressure and air-angle (α) profiles at the TE + 3 percent location in Figs. 13(*a*),(*b*). The hub-to-shroud total pressure profiles for both the conventional impeller and the in-line tandem-impeller cases indicated similarly shaped profiles, both having a strong shroud total pressure deficit from approximately 65 to 100 percent span. The 5 and 50-percent tandem-impeller cases were observed to have more pronounced ''dips'' in the total pressure profiles at approximately 35–40 percent span, but also showed significantly improved tip total pressure profiles. The observed locations for the onset of the tip total pressure deficits were at approximately 77 and 85 percent span for the 5 and 50-percent clocked cases, respectively. The profiles reflect significantly stronger shroud boundary layer profiles as the inducer/exducer clocking fraction is increased.

The effects of tandem-impeller clocking upon the exit swirl (α) distributions are illustrated in Fig. 13(*b*). A curve showing the downstream diffuser reference angle distribution is also shown in order to compare the effects upon incidence in the vaneless space region, most importantly near the shroud. Near the shroud region, incidence was found to be more positive for the in-line tandem-impeller case than for the conventional case, which would tend the design more toward stalling. For the 5-percent case, however, incidence in the shroud region was significantly reduced. In the case of the 50-percent clocked design, tip swirl was reduced to the point that the shroud region incidence was negative. Overall, the 5-percent clocked case was thought to have the most preferable impeller exit total pressure and swirl distributions of those shown in Fig. 13. Both the improved shroud boundary layer profile and the reduced diffuser shroud incidence are very likely beneficial to reducing diffuser throat blockage, delaying the onset of separation in the diffuser, and hence, providing both additional diffuser recovery and surge margin.

Conclusion

A computational study of a retrofittable rear-stage, medium pressure ratio tandem-bladed impeller was performed for various inducer/exducer clocking configurations. The various tandem-impeller configurations were also compared against a conventional impeller design for the same intended application. The key conclusions of this investigation are summarized as follows:

• Results of the study showed that inducer/exducer relative circumferential position, or, clocking, had a significant impact on tandem-impeller performance.

• Values of impeller pressure ratio, temperature ratio, and isentropic efficiency were found to be greatest for the in-line tandem-impeller case and lowest for a clocking fraction of 50 percent of airfoil pitch.

• The maximum variation in predicted running-line impeller efficiency for various tandem-impeller configurations was approximately 3.8 points.

• When compared to the conventional impeller design, the tandem-impeller was found to be less efficient for all clocking configurations.

• A significant degree of variation in impeller trailing edge slip factor was also observed as a function of clocking; this was likely the result of variation in both exducer blockage and loading.

• Observation of the impeller trailing edge relative velocity fields showed a shroud/suction surface wake zone which increased in size with increased clocking fraction. In spite of the growing trailing edge wake, radial velocity contours downstream of the impeller showed a reduced shroud velocity deficit as clocking increased.

• A statistical expression for the nonuniformity of the downstream radial velocity profiles quantitatively showed that distortions in the impeller exit absolute velocity field could be significantly reduced by an appropriately clocked tandem-impeller arrangement versus a conventional design.

• Hub-to-shroud profiles of impeller downstream total pressure and swirl indicated that a tandem-impeller configuration could significantly energize the shroud boundary layer and, in addition, improve the diffuser vaneless space incidence matching.

Recommendations

Although improvements to the impeller exit flow profiles as a result of the tandem arrangement are speculated to improve the diffuser recovery and stall margin, these benefits are presently unsubstantiated. In addition, there is a likely tradeoff between the benefits of improved impeller exit flow quality with increased clocking and the predicted drop-off in impeller efficiency. It is recommended that future work be performed that explores the effects of the tandem-impeller clocking arrangement on the overall centrifugal stage performance. One recommendation is to perform an unsteady CFD analysis of the entire centrifugal stage. The second recommendation is to test various tandem configurations in an experimental facility. Such tests should provide validation for the work presented in this paper.

Nomenclature

C = velocity, absolute frame of reference

i,j,k = topological grid dimensions, i = streamwise, j = circumferential, k = spanwise

k = turbulent kinetic energy

M = Mach number

P = pressure

PR = total pressure ratio

TR = total temperature ratio

V = velocity, relative frame of reference

r = velocity nonuniformity parameter

$$r = \frac{\sqrt{\int (C_r - \overline{C}_r)^2 dA}}{\int C_r dA}$$

W = absolute mass flow

W_{cor} = corrected flow $W_{\text{cor}} = \dfrac{W\sqrt{T_t}}{P_t}$

Δx_s = tandem blade axial split gap

α = absolute swirl angle relative to meridional plane

ε = turbulent dissipation

ϕ = radial flow angle on meridional plane

ρ = density

σ = impeller slip factor $\sigma = \dfrac{C_{u,\text{actual}}}{C_{u,\text{ideal}}}$

θ_s = tandem blade relative ''clocking'' angle

λ_s = tandem blade inducer/exducer relative clocking angle as fraction of blade pitch (positive quantities below 50 percent refer to orientation in which exducer suction surface is closest to inducer pressure-surface)

η = isentropic efficiency

ω = turbulent dissipation normalized by turbulent kinetic energy

Subscripts

1 = impeller inlet quantity

actual = actual velocity component

ideal = ideal velocity component (assuming no trailing edge deviation)

m = meridional velocity component

r = radial velocity component

ref = reference quantity from design targets

rel = relative quantity (rotating frame of reference)

s = tandem-impeller split-gap quantity

t = total quantity

t-t = total-to-total ratio

u = tangential velocity component

Acknowledgments

The authors wish to thank both Anthony Brown and Art Hammerschmidt for their invaluable assistance with coding of the grid-generation and post-processing routines used in this work. Additional thanks go to Martin Peeters for his help with the NS3D code. Finally, the authors wish to express their gratitude to Pratt & Whitney Canada for granting permission to publish this work.

References

[1] Josuhn-Kadner, B., and Hoffman, B., 1992, ''Investigations on a Radial Compressor Tandem-Rotor Stage With Adjustable Geometry,'' ASME Paper No. 92-GT-218.

[2] Boyce, M. P., and Nishida, A., 1977, ''Investigation of Flow in Centrifugal Impeller With Tandem Inducer,'' Tokyo Joint Gas Turbine Congress, Paper No. 43.

[3] Bache, G., 1992, ''Impeller Tandem Blade Study With Grid Embedding for Logical Grid Refinement,'' *Tenth Workshop for Computational Fluid Dynamic Applications in Rocket Propulsion*, NASA Conference Publication 3163, Part 1.

[4] Cheng, G. C., Chen, Y. S., Garcia, R., and Williams, R. W., 1993, ''CFD Parametric Study of Consortium Impeller,'' *Eleventh Workshop for Computational Fluid Dynamic Application in Rocket Propulsion*, NASA Conference Publication 3221, Part 1.

[5] Josuhn-Kadner, B., 1994, ''Flow Field and Performance of a Centrifugal Compressor Rotor With Tandem Blades of Adjustable Geometry,'' ASME Paper No. 94-GT-13.

[6] Peeters, M. E., Habashi, W. G., Nguyen, B. Q., and Kotiuga, P. L., 1992, ''Finite Element Solutions of the Navier–Stokes Equations for Compressible Internal Flows,'' J. Propul. Power, **8**, No. 1, pp. 192–198.

[7] Hughes, T. J. R., 1987, ''Recent Progress in the Development and Understanding of SUPG Methods With Special Reference to the Compressible Euler and Navier–Stokes Equations,'' Int. J. Numer. Methods Fluids, **7**, pp. 1261–1275.

[8] Robichaud, M., Habashi, W., Peeters, M., Dutto, L., and Fortin, M., 1995, ''Parallel Finite Element Computation of 3D Compressible Turbomachinery Flows on Workstation Clusters,'' in *Solution Techniques for Large-Scale CFD Problems*, W. G. Habashi, ed., pp. 41–56.

[9] Haroutunian, V., and Engelman, M. S., 1991, ''On Modeling Wall-Bound Turbulent Flow Using Specialized Near-Wall Finite Elements and the Standard $k-\varepsilon$ Turbulence,'' in: *Advances in Numerical Simulation of Turbulent Flows*, ASME FED-Vol. 117, p. 97.

Frank Haselbach
Heinz-Peter Schiffer
Manfred Horsman
Stefan Dressen

Rolls-Royce Deutschland,
D-15827 Dahlewitz, Germany

Neil Harvey
Simon Read

Turbine Systems,
Rolls-Royce plc,
Derby, United Kingdom

The Application of Ultra High Lift Blading in the BR715 LP Turbine

The original LP turbine of the BR715 engine featured "High Lift" blading, which achieved a 20-percent reduction in aerofoil numbers compared to blading with conventional levels of lift, reported in Cobley et al. (1997). This paper describes the design and test of a re-bladed LP turbine with new "Ultra High Lift" aerofoils, achieving a further reduction of approximately 11 percent in aerofoil count and significant reductions in turbine weight. The design is based on the successful cascade experiments of Howell et al. (2000) and Brunner et al. (2000). Unsteady wake-boundary layer interaction on these low-Reynolds-number aerofoils is of particular importance in their successful application. Test results show the LP turbine performance to be in line with expectation. Measured aerofoil pressure distributions are presented and compared with the design intent. Changes in the turbine characteristics relative to the original design are interpreted by making reference to the detailed differences in the two aerofoil design styles.
[DOI: 10.1115/1.1415737]

Introduction

The BR715 21 klb. thrust engine powers the new B717-200 regional aircraft and is the latest in the BR700 engine series for Gulfstream and Canadair executive jets. As part of achieving the BR715 program, an advanced technology LP turbine (Fig. 1) was designed by RR based on technology derived from the BR700 and RR Trent engine programs and research work of Universities in Germany and the UK. This design and its successful test, which achieved a turbine efficiency more than 1 percent above bid and a blade count reduction, are reported in Cobley et al. [1] and Harvey et al. [2].

In modern high-bypass-ratio engines, the weight of the LP turbine can be one third of total engine weight. Maintaining the same levels of stage work in small engines as in larger ones results in excessively heavy LP turbines with too many stages. Thus stage pressure ratios and Mach number (M) levels are higher for the BR700 series of engines compared to the Trent. Given the importance of weight in such machines, work has continued on reducing aerofoil count even further while trying to mitigate any loss of performance. The latter arises because there is a strong trade-off between LP turbine efficiency and engine fuel burn.

Since the aspect ratios of the LP Turbine blading for the BR715 are between 4 and 5, the losses are largely two-dimensional in origin. Thus successfully achieving reduced aerofoil count is largely an exercise of optimizing the two-dimensional aerodynamics. A considerable amount of research work has been carried out in the past, to support this optimization process (described in the next section). This research effort finally resulted in a new ''ultra high lift'' aerofoil design with lift coefficients being approximately 11 percent higher than those of the original BR715; see Fig. 2.

Cascade Research

The first comprehensive statement on high lift, low-Reynolds-number blading was made by Hourmouziadis [3]. Extensive research undertaken subsequently such as that by Hodson et al. [4,5], Banieghbal et al. [6], and Curtis et al. [7] showed that for such blading consideration of the unsteady effects in the engine (in particular wake interaction with downstream blade rows) is indispensable. Further fundamental investigations into the effects of moving bars and their wakes on the performance of LP turbine blades was performed by Schulte and Hodson [8–10]. They argued that the becalmed regions behind (wake-generated) turbulent spots, which propagate downstream on the aerofoil suction surface, are capable of withstanding strong adverse pressure gradients without separation. Their conclusion was that this effect is responsible for the loss reduction seen on such blades in unsteady inflow conditions. Halstead et al. [11] also investigated wake/blade interference and concluded that the location of spots coincided with regions of raised free-stream turbulence due to the wakes from the upstream blade rows. A complete overview on the topic of wake-blade interaction is given by Hodson [12,13]. The overall conclusion from all this research is that the key to achieving good aerodynamic performance is the control of boundary layer separation and transition on these aerofoil surfaces in the unsteady environment.

To support the work described in this paper, complementary research in high-speed and low-speed cascades (both with simulated wakes) was conducted by Rolls-Royce Deutschland in Germany and Rolls-Royce plc in the UK. The experiments focused on the optimization of the two-dimensional aerodynamics of aerofoils that had lift coefficients that were approximately 15 percent higher than those of high lift blading.

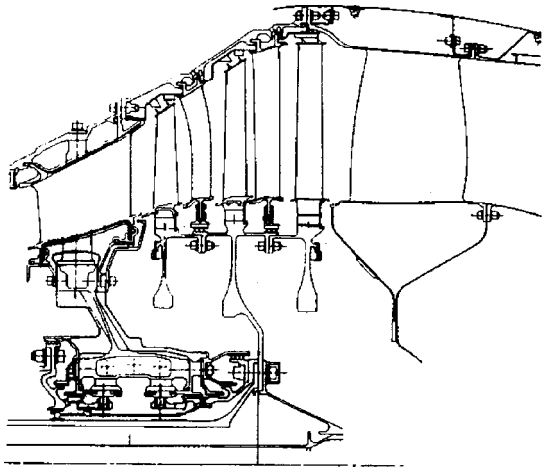

Fig. 1 BR715 GA

Contributed by the International Gas Turbine Institute and presented at the 46th International Gas Turbine and Aeroengine Congress and Exhibition, New Orleans, Louisiana, June 4–7, 2001. Manuscript received by the International Gas Turbine Institute February 2001. Paper No. 2001-GT-436. Review Chair: R. Natole.

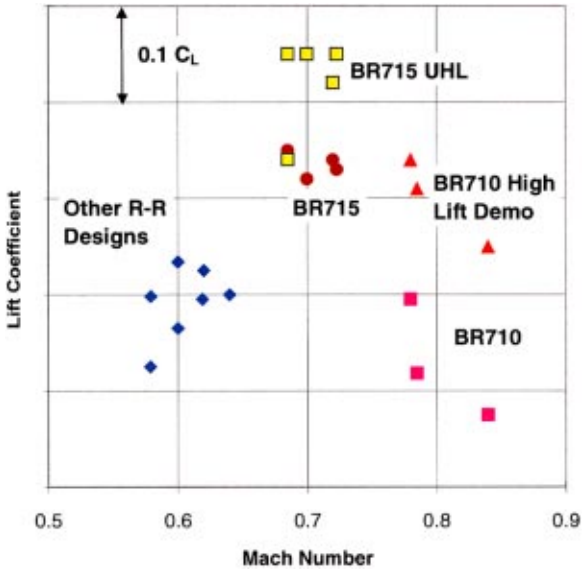

Fig. 2 Lift coefficients versus Mach number of several LP Turbines

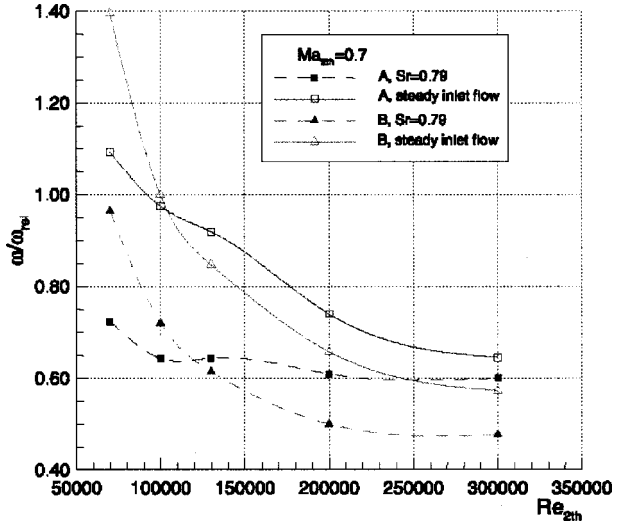

Fig. 4 Nondimensional total pressure losses [14]

High-Speed Cascade. High-speed cascade tests have been carried out at the University of German Armed Forces Munich (Brunner et al. [14]). Figure 3 shows this facility, which enables aerofoils to be tested at engine representative Mach numbers as well as Reynolds numbers and at nondimensional wake passing frequencies slightly below engine values.

In the following, the results from the Munich Test facility will be discussed. The results of the wake-traverses of turbine cascade A (high lift) and B (ultra high lift) at steady and unsteady inlet flow conditions are shown in Fig. 4 at an exit Mach number of 0.7. Profile B (UHL) had a 15-percent higher lift coefficient than Profile A (HL). The figure draws out discrepancies between cascade A and B concerning total pressure losses at various outlet Reynolds numbers (Re_{2th}=70,000 to 300,000) at steady and unsteady (Sr=0.79) inlet flow conditions.

To start with, the steady inlet flow conditions will be considered, where a strong Reynolds dependency is visible. With decreasing outlet Reynolds number the total pressure losses of both cascades are increased. Turbine cascade B (UHL) showing smaller total pressure losses at outlet Reynolds-numbers higher than Re_{2th}=105,000, exhibits a very sharp loss increase at an outlet Reynolds number of Re_{2th}=70,000. The latter is because a strong separation in the trailing edge region of the suction side occurs, whereas cascade A (high lift design) still shows a reattaching laminar separation bubble. From a design point of view it is important to notice that the total pressure losses of both design styles, high lift and ultra high lift, are almost equal at design point conditions of both cascades (Re_{2th}=100,000).

For unsteady inflow, i.e., with presence of wakes, a loss reduction over the entire Reynolds number range of both cascades is obvious. The Reynolds dependency of the loss is mitigated but still visible in the results. Furthermore, it can be seen that the intersection point of the total pressure loss distributions of both cascades moves to a higher outlet Reynolds number of about Re_{2th}=120,000 for unsteady flow. Despite the sharp loss increase of the cascade B (UHL), which is still visible for unsteady inflow, the total pressure loss for both cascades are clearly below the appropriate steady flow losses over the entire outlet Reynolds number range.

Low-Speed Cascade. In the low-speed cascade test facility at the Whittle Laboratory, engine representative Reynolds numbers and wake passing frequencies are achieved, but not of course Mach numbers. Despite this latter limitation, this style of testing has allowed a novel set of parametric investigations to be undertaken (Howell [15], Howell et al. [16], and Hodson [13]). The moving bar linear cascade facility of Cambridge is shown in Fig. 5.

The basic trends of the low-speed test results obtained at the University of Cambridge are similar to the ones discovered in the previously mentioned cascade experiments. Figure 6 shows the results of the Cambridge work where two UHL profiles U1 and U2 were investigated, providing 15 percent higher lift with respect to a high lift profile *H*. The profiles were designed based on similar design goals as the high-speed ones, although not directly scaled from the latter. Again, significant Re-dependency even with bar passing is to be seen from the variation of the total pressure loss for both profiles investigated. The relative total pressure

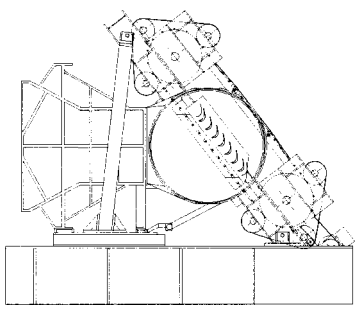

Fig. 3 Munich bar passing cascade [14]

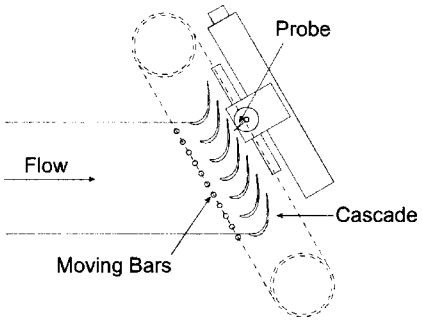

Fig. 5 Cambridge bar passing cascade [16]

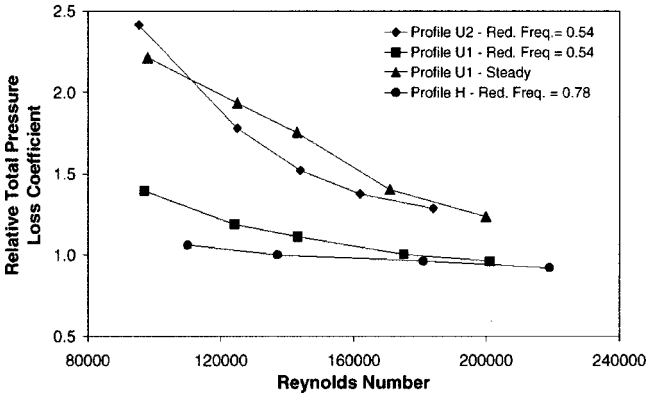

Fig. 6 Nondimensional total pressure loss versus Reynolds number for datum and UHL profiles (U1, U2) [16]

losses are given for a number of reduced frequencies. All total pressure loss values are made nondimensional by the loss of the datum profile (*H*), which was measured at a Reynolds number of 130,000 and a reduced frequency of 0.78. The losses generated by profile U2 are considerably higher than those of the other profiles, even when wakes are present. To illustrate this, the losses produced for steady-state inflow conditions were seven times higher than the losses of the datum profile for unsteady inflow conditions. This is due to the elevated level of deceleration caused by the suppressed trailing edge velocity of profile U2. Profile U1 produces losses that are also very high for steady inflow conditions. However, when wakes are present, the losses achieve a level that is more comparable to that of the datum profile. It has to be pointed out that both profiles U1 and U2 have 15 percent more lift than profile *H*. With increasing Reynolds numbers, the performance of the ultra high lift profiles improves significantly, because the separation bubble losses are being reduced. At Re $=170{,}000$, the losses are roughly the same as for the datum profile. Generally speaking, the results of this low-speed test are less promising results than the Munich high-speed tests. The loss increase because of change from HL to UHL in high speed is roughly 11 percent (Re$=100{,}000$), while the loss increase in the low-speed test at design conditions is about 20 percent for the U2 profile and almost 75 percent for the U2 profile. Here, it is indicated that some loss of performance occurs even with best of the UHL profiles (the U1 profile).

Aerodynamic Redesign

Before the results of this cascade research could be applied to an engine design with confidence, further validation, in the form of a high-speed cold flow turbine rig test, was required. The BR715 LP turbine was chosen for this task, since a rig test of its engine parts had previously been used to validate the original high lift concept. The first stage of the LP turbine had been optimized mechanically for the engine, and this meant that for practical purposes the validation of the UHL technology could be demonstrated only in a redesign of the blading of stages 2 and 3.

The two-dimensional aerodynamic design was based on the previous cascade research. The evolution of blade surface pressure distribution, going from conventional via high lift to the ultra high lift loading style, is depicted in Fig. 7. It can be seen that a considerable amount of load was put to the front part of the aerofoil suction side and rear part of the pressure side, while maintaining the amount of aft loading known to be favorable for the high lift profiles.

The new design style resulted in a reduction in the aerofoil count of approximately 11 percent in stages 2 and 3, because not all of the UHL benefits (i.e., the 15 percent increase) could be transferred to the engine application because of multistage consid-

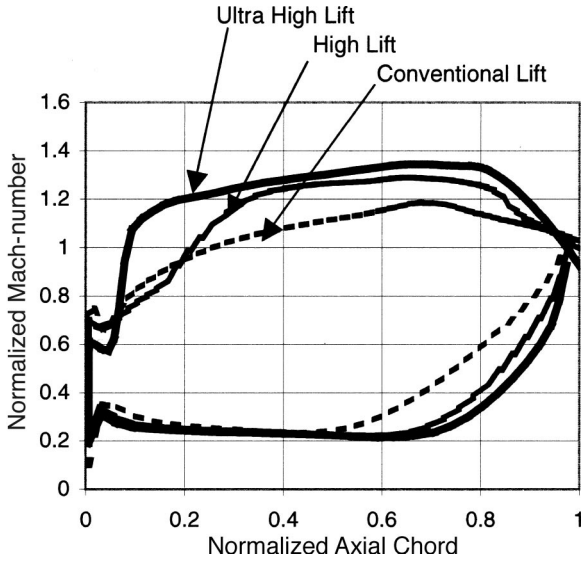

Fig. 7 Comparison of conventional, high lift, and UHL Mach number distributions (normalized)

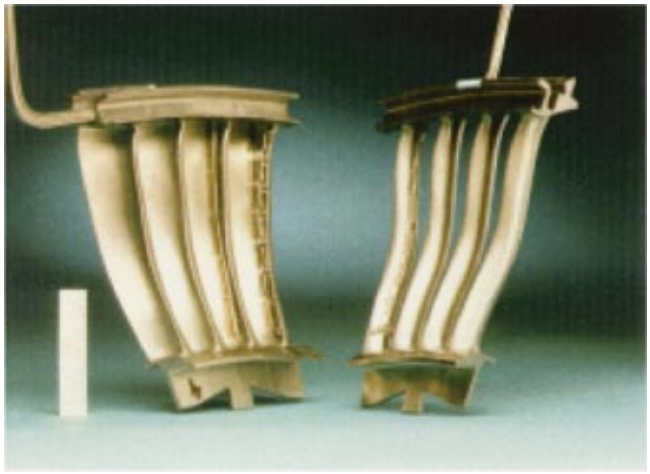

Fig. 8 Photograph of a segment of NGV2

erations. In addition the aerofoils were made thinner to enable even greater weight reductions. The net volumetric reduction of the blading was 20 percent on average. Thinner blading, of course, gives rise to the concern that this might incur increased secondary flows; see Brear [17]. To mitigate this risk, some of the blading was thickened on the pressure surface near the end walls, see Duden et al. [18].

Generally the vortex design was similar to that of the original BR715, with some local adjustments to incorporate the UHL profiles into the existing annulus. The three-dimensional design, tangential lean, and axial sweep is very similar to the BR715, following the design criteria and philosophy described in Scrivener et al. [19]. Figure 8 depicts some of the three-dimensional features incorporated into the design, such as orthogonal design, tangential leans, and axial sweeps.

Cold Flow Rig Test Validation

For this validation of the UHL blading, the turbine rig test incorporated extensive instrumentation; see Fig. 9. Beside static pressure tappings at outer and inner annulus, and vane platforms, the instrumentation included L/E pressure and temperature measuring devices on all nozzle guide vane blade rows and the outlet

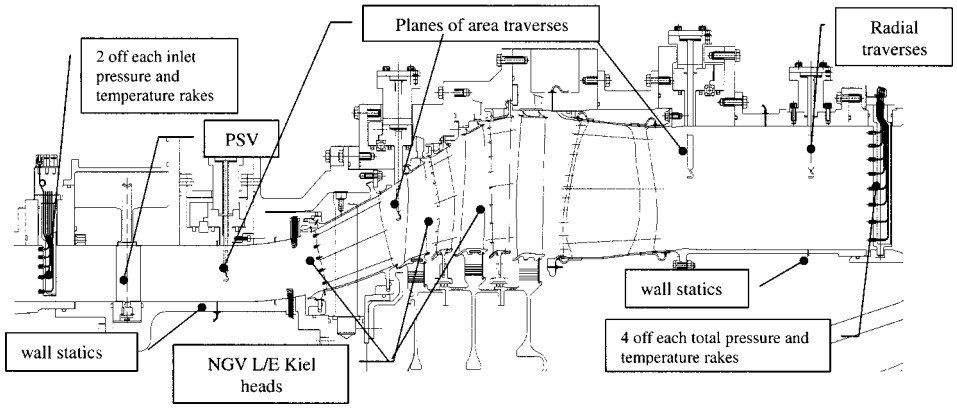

Fig. 9 Schematic sketch of the rig test setup

guide vanes (OGV) and pressure and temperature rakes at the intake section of the LPT Rig and behind the OGV. Yaw probes were installed in the parallel duct (Intake), behind NGV 1, OGV and exit duct to allow for radial and area traverses (pressure, flow angle). A telemetry system allowed the measurement of the static pressure distribution on the Rotor 1 aerofoil. Two vanes of stage 2 and one vane of stage 3 were equipped with surface hot-film arrays, the results of which are reported in Howell et al. [20]. The turbine torque was measured with a torquemeter placed between the drive shaft and water bake.

The test was carried out at the Institut für Luftfahrtantriebe of the University of Stuttgart. The test program included Reynolds number variation for hot-film measurements and the measurement of an altitude characteristic line. Performance working lines were measured for 140, 120, 100, 90, 80, and 60 percent N/Nd. Detailed area flow-field measurements were carried out at design speed with nominal and ± 15 deg pre-swirl vane (PSV) setting. The test setup and the facility enabled a high measurement accuracy, capable of resolving small changes in overall turbine efficiency to a very high degree (better than 0.4 percent).

Results

Overall Performance. The overall performance of the LP Turbine was measured to a very high degree of accuracy. Even more important, a true back-to-back comparison is provided because exactly the same test setup was used as for the high lift investigations reported by Harvey [2]. This enabled a straightforward comparison of the high lift and the UHL LP Turbine with regard to turbine performance.

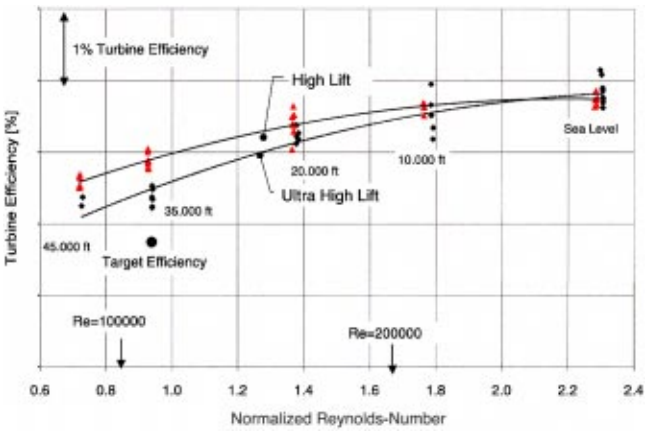

Fig. 10 Turbine efficiency versus normalized Reynolds number for HL and UHL blading

Figure 10 shows the variation of measured LPT efficiency at engine design work and design speed against average blade row Reynolds number (i.e., with altitude). At design point (35,000 ft) this discrepancy is approximately -0.5 percent in turbine efficiency between the original High Lift design and the new UHL design. From the figure, it can be seen that at sea level condition, the UHL efficiency is within the efficiency level of the high lift LPT currently in the production engines. However, for decreasing Reynolds numbers, the drop of efficiency is worse for UHL compared to the original design.

This is in line with the findings of the cascade research work mentioned in the previous section, where a stronger Reynolds number dependency was discovered for the UHL profiles compared to the high lift profiles. Nonetheless, the net drop in efficiency from take-off to 35,000 ft cruise is about -1.5 percent. This is still favorable when compared to values of -2 percent quoted by Ashpis [21] for other, large aero gas turbines. The original target efficiency of the BR715 high lift LPT is included for comparison and shows that the UHL has achieved an aerodynamic efficiency which is still about $+0.5$ percent above this target value.

Two-Dimensional Aerodynamics. Considerable data have been taken from the aerofoil pressure tappings at a number of conditions. Only some of the data, taken at the design condition, are presented here. This has been compared with CFD calculations; see Figs. 11 and 12. The CFD code utilized for this investigation is a full Navier-Stokes code (steady, three-dimensional), using structured grids and an explicit time marching technique with second-order accuracy. From the comparison of CFD results and experimental data, the following can be noted:

1 The basic two-dimensional aerodynamics is well captured by the CFD prediction (used in design process and re-run for exact rig conditions tested).

2 The pressure distributions of the aerofoil sections appear slightly more front loaded than originally intended.

3 Apart from this, the measured midheight pressure distributions are largely as designed. The effects of pressure side separation bubbles are visible in Figs. 11(*b*) and 12, but their blockage is small and so they do not alter the pressure distribution on the suction side.

4 On the suction surface, there is no visible evidence in the time-averaged pressure distributions of the presence of the back surface separation bubble. It seems to have been completely suppressed by wake passing. This is in line with the findings of Harvey et al. [2].

5 The CFD prediction seems to under estimate the off-loading at hub section of NGV2 caused by the secondary flows (compare Fig. 11(*a*)).

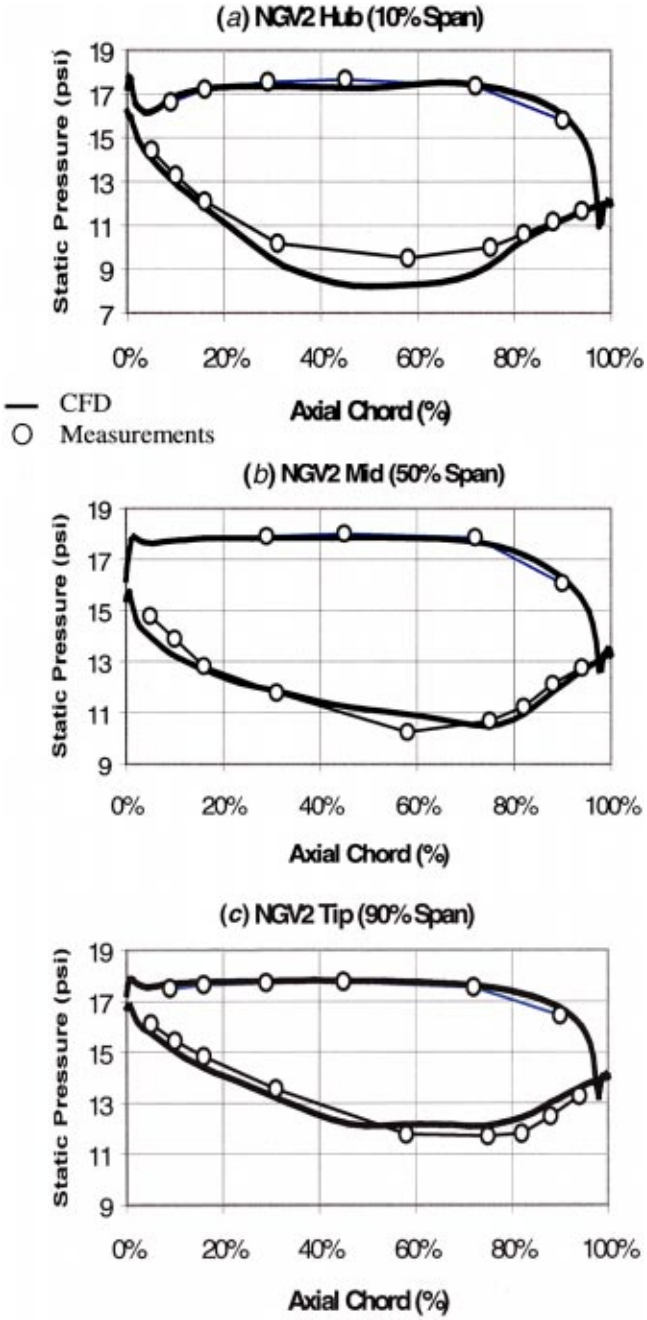

Fig. 11 Static pressure readings from surface tapping versus 3D-CFD results: (*a*) NGV2 10 percent height, (*b*) 50 percent height, and (*c*) 90 percent height

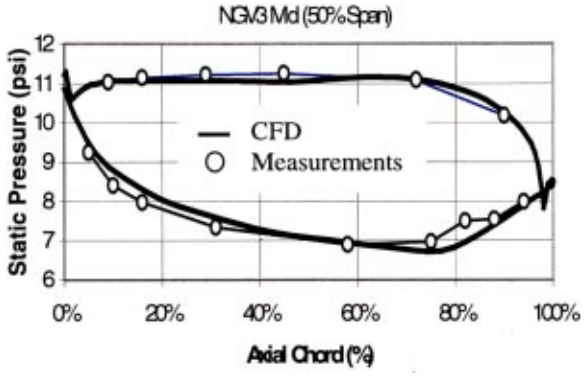

Fig. 12 Static pressure readings from surface tapping versus 3D-CFD results: NGV3 50 percent height

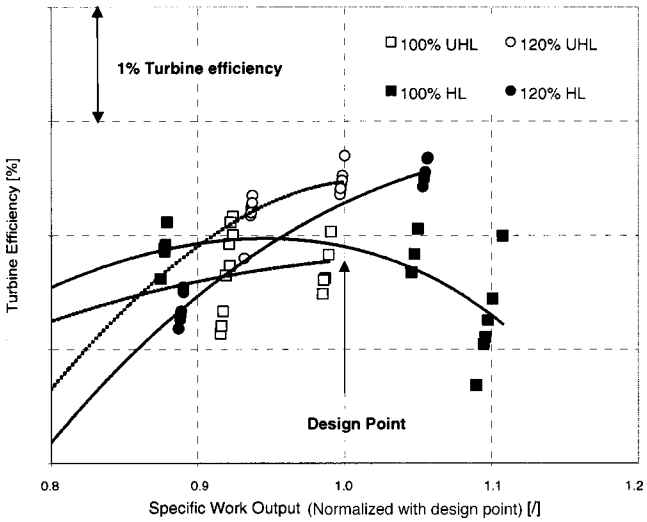

Fig. 13 Off-design performance of high lift versus ultra high lift LPT (100 and 120 percent *N*/*Nd*)

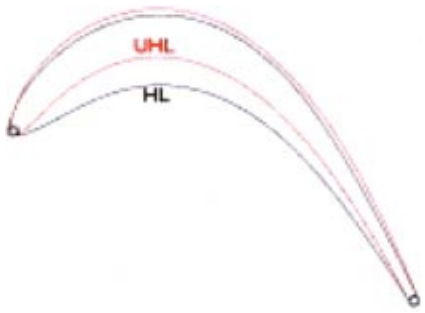

Fig. 14 Midheight sections of HL and UHL designs

Off-Design Behavior. Figure 13 compares the characteristics of the BR715 HL and UHL LP turbines at 100 and 120-percent design speeds. It shows the variation of the measured LPT efficiency against specific work for each of these ''speed lines,'' at the sea level condition. Significant performance improvement at overspeed for both designs is visible from Fig. 13. This is in fact not surprising as higher speed (for given work) reduces stage loading. [Eventually the speed is high enough to give negative incidence onto the blading sufficient to causes large pressure side separation which cause the performance to deteriorate again.] The surprising result is that the UHL overspeed seems to gain even more efficiency than HL. There are two possible explanations:

1 The UHL Turbine has achieved a significant change in the balance of losses between two-dimensional and three-dimensional, at the design point. The two-dimensional behavior may be more like Brunner's cascade result, i.e., not largely increased, but the three-dimensional loss has been, not surprisingly, given the higher lift coefficients. Thus, as the blading goes to negative incidence and the stage loading decreases, the three-dimensional loss is reduced more in the UHL design than in the HL one.

2 The UHL blading runs with lower wake passing frequencies (11 percent down simply because the blade count is reduced by that amount). The cascade tests at Munich (Brunner [14]), indicated a significant effect of the wake passing frequency on loss. It

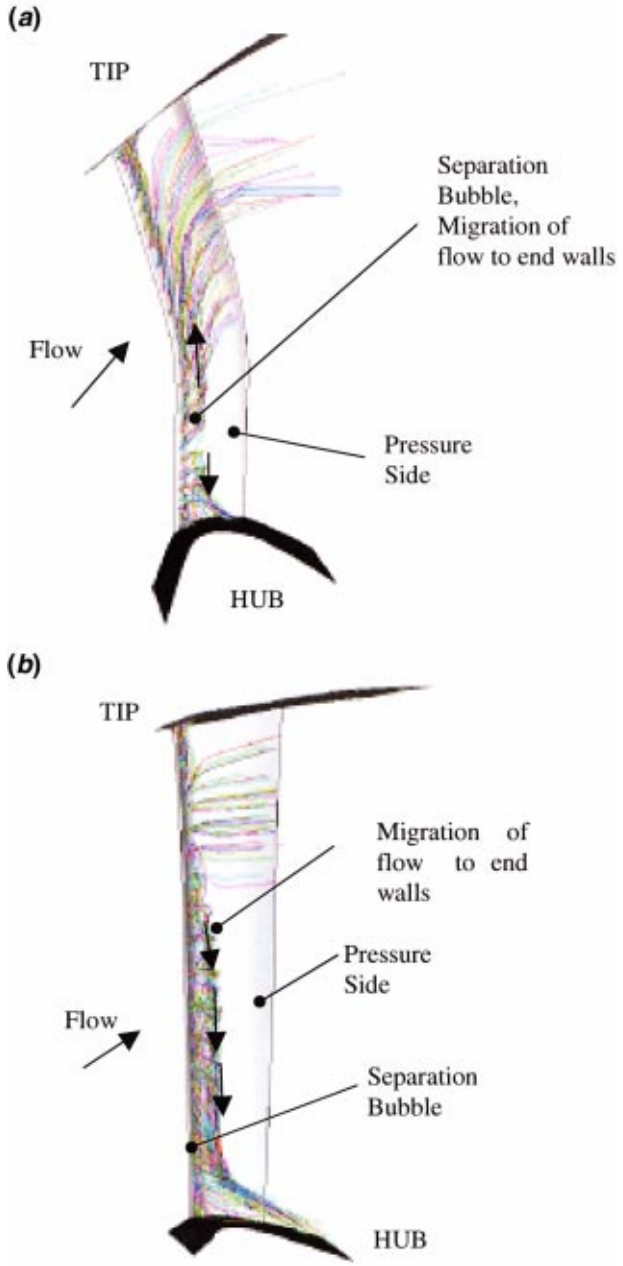

Fig. 15 Visualization of the pressure side flow of: (*a*) NGV2 and (*b*) NGV3 of the BR715 UHL Rig based on 3D-CFD solutions

may be that the UHL blading is below the optimum passing frequencies (for minimum loss) and that at 120 percent speed it is closer to optimum. Thus, it improves more than the HL design.

Performance: Three-Dimensional Behavior. As stated previously, the UHL blading has achieved significant weight savings beyond those simply from reduced blade count, by thinning the aerofoils. Figure 14 compares the NGV2 mid height sections of the datum (high lift) and UHL designs illustrating this. Recent research (Brear [17,22,23]) has shown that pressure side separation bubbles contribute to additional losses, both two-dimensional and three-dimensional. These thin UHL profiles are more prone to such pressure side separations, and this will have contributed to the loss of performance of the UHL turbine relative to the high lift datum.

More work is needed to quantify these effects, but the qualitative ones are shown in Fig. 15(*a*,*b*). This shows a visualization of the pressure side flow of the NGV2 and NGV3, respectively, as calculated by CFD obtained by tracking particle paths initiated on the early pressure side. As can be seen, the flow in the separation bubble experiences significant radial migration which is indicative of increased loss.

Conclusions

A new UHL LP Turbine blading design philosophy has been developed from an extensive research program and applied to a redesign of the BR715 LPT.

Low and high-speed cascade tests showed that a UHL design with minimum loss increase is possible. However, some of the designs tested showed very poor performance, which implies that the risk of getting it wrong is there.

With the full-scale LP Turbine rig test comparable LPT efficiencies were found for the sea level condition. However, lower LPT efficiencies were discovered at the design point of the turbine (0.5 percent at cruise) than for the datum, high lift design.

This performance is still better than the original target of the BR715. In addition the performance fall-off with altitude is still good by industry standards.

Important data have been obtained giving the LP turbine better informed cost/weight/performance trade-offs.

Further work is needed to identify the sources of the increased loss in the UHL design at low Reynolds number. In particular the loss split between two-dimensional and three-dimensional elements needs to be quantified. However, analysis so far indicates that in the future more emphasis should be placed on reducing secondary losses in LP turbines (even with their high aspect ratio blading) and on some means of substituting for the ''lost'' wake interaction (due to the lower wake passing frequencies of the UHL blading).

Acknowledgments

Some of the work of this project has been supported and funded by the German Federal Ministry of Economy and Technology as part of the AG Turbo framework (Project 1.431, Founding No. 0327 040L) and Rolls-Royce Deutschland jointly together with Rolls-Royce plc and DTI (UK), which also put work and funding into the project. The permission for publication is gratefully acknowledged.

Nomenclature

C_{ax} = axial velocity, m/s
f = frequency, Hz
h = aerofoil height, m
l = chord length, m
N = shaft speed, 1/min
p, pt = static pressure, total (stagnation) pressure, psi
t = pitch, time, m, s
Tt = total (stagnation) temperature, K
Tu = turbulence intensity, percent
w = velocity, m/s
x = coordinate along axial chord length, m
y = coordinate normal to blade surface, m
β = circumferential (pitchwise) flow angle, deg
δ = boundary layer thickness, m
ρ = density, kg/m^3
ω = loss coefficient=$(pt_1-pt_2)/(pt_1-p_2)$

Subscripts and Superscripts

1,2 = inlet and outlet flow conditions
2_{th} = downstream conditions for isentropic flow
ax = axial
b = bar
c = cascade
d = design

is = isentropic
t = total

Abbreviations

BL = boundary layer
HL = high lift
M = Mach number
Re = Reynolds number
Sr = Strouhal number$=f^{*}l/C_{ax}$
UHL = ultra high lift

References

[1] Cobley, K., Coleman, N., Siden, G., and Arndt, N., 1997, ''Design of New Three Stage Low Pressure Turbine for the BMW Rolls-Royce BR715 Engine,'' ASME Paper No. 97-GT-419.

[2] Harvey, N. W., Cox, J. C., Schulte, V., Howell, R., and Hodson, H. P., 1999, ''The Role of Research in the Aerodynamic Design of an Advanced Low-Pressure Turbine,'' Proc. Inst. Mech. Eng., Part C: J. Mech. Eng. Sci., **213**, Part A.

[3] Hourmouziadis, J., 1989, ''Aerodynamic Design of Low Pressure Turbines,'' AGARD Lecture Series, 167.

[4] Hodson, H. P., Huntsman, I., and Steele, A., 1994, ''An Investigation of Boundary Layer Development in a Multistage LP Turbine,'' ASME J. Turbomach., **116**, pp. 375–383.

[5] Hodson, H. P., Banieghbal, M. R., and Dailey, G. M., 1994, ''The Analysis and Prediction of the Effects of Bladerow Interactions in Axial Flow Turbines,'' IMechE Conf. Turbomachinery, Oct.

[6] Banieghbal, M. R., Curtis, E. M., Denton, J. D., Hodson, H. P., Huntsman, I., Schulte, V., Harvey, N. W., and Steele, A. B., 1995, ''Wake Passing in LP Turbine Blades,'' AGARD CP-571.

[7] Curtis, E. M., Hodson, H. P., Banieghbal, M. R., Denton, J. D., Howell, R. J., and Harvey, N. W., 1997, ''Development of Blade Profiles for LP Turbine Applications,'' ASME J. Turbomach., **119**, pp. 531–538.

[8] Schulte, V., and Hodson, H. P., 1994, ''Wake Separation Bubble Interaction in Low Pressure Turbines,'' Paper No. AIAA-94-2931.

[9] Schulte, V., and Hodson, H. P., 1998, ''Unsteady Wake-Induced Boundary Layer Transition in High Lift LP Turbines,'' ASME J. Turbomach., **120**, pp. 28–35.

[10] Schulte, V., and Hodson, H. P., 1998, ''Prediction of the Becalmed Region for LP Turbine Profile Design,'' ASME J. Turbomach., **120**, pp. 839–846.

[11] Halstead, D. E., Wisler, D. C., Okiishi, T. H., Walker, G. J., Hodson, H. P., and Shin, H. W., 1997, ''Boundary Layer Development in Axial Compressors and Turbines. Parts 1–4,'' ASME J. Turbomach., **119**, pp. 114–126.

[12] Hodson, H. P., 1998, ''Blade Row Interactions in Low Pressure Turbines,'' VKI Lecture Series 1998-02, ''Blade Row Interference Effects in Axial Flow Turbomachinery Stages.''

[13] Hodson, H. P., and Howell, R. J., 2000, ''Unsteady Flow: Its Role in the Low Pressure Turbine,'' Minnowbrook III, Workshop on Boundary Layer Transition in Turbomachines, Syracuse University.

[14] Brunner, S., Fottner, L., and Schiffer, H.-P., 2000, ''Comparison of Two Highly Loaded Low Pressure Turbine Cascades under the Influence of Wake-Induced Transition,'' ASME Paper No. 2000-GT-268.

[15] Howell, R. J., 1999, ''Wake Separation Bubble Interaction on Low Reynolds Number Turbomachinery,'' PhD Thesis, Cambridge University.

[16] Howell, R. J., Ramesh, O. N., Hodson, H. P., Harvey, N. W., and Schulte, V., 2001, ''High Lift and Aft Loaded Profiles for Low Pressure Turbines,'' ASME J. Turbomach., **123**, pp. 181–188.

[17] Brear, M., 2000, ''Pressure Surface Separations in Low Pressure Turbines,'' PhD Thesis, Cambridge.

[18] Duden, A., Raab, I., and Fottner, L., 1999, ''Controlling the Secondary Flow in a Turbine Cascade by Three-Dimensional Airfoil Design and End Wall Contouring,'' ASME J. Turbomach., **121**, pp. 191–200.

[19] Scrivener, C. T. J., Connolly, C. F., Cox, J. C., and Dailey, G. M., 1991, ''Use of CFD in the Design of a Modern Multistage Aero Engine LP Turbine Design,'' [AUTHOR PLEASE UPDATE].

[20] Howell, R. J., Hodson, H. P., Schulte, V., Schiffer, H.-P., Haselbach, F., and Harvey, N. W., 2002, ''Boundary Layer Development in the BR710 and BR715 LP Turbines—The Implementation of High Lift and Ultra High Lift Concepts,'' ASME J. Turbomach., in press.

[21] Ashpis, D., 1997, ''Low Pressure Turbine Flow Physics Program,'' Minnowbrook II, Workshop on Boundary Layer Transition in Turbomachines, Syracuse University.

[22] Brear, M. J., Hodson, H. P., Gonzalez, P., and Harvey, N. W., 2002, ''Pressure Surface Separations in Low Pressure Turbines: Part 1—Midspan Behavior,'' ASME J. Turbomach., in press.

[23] Brear, M. J., Hodson, H. P., and Harvey, N. W., 2002, ''Pressure Surface Separations in Low Pressure Turbines—Part 2: Interactions With Secondary Flow,'' ASME J. Turbomach., in press.

Clocking Effects in a 1.5 Stage Axial Turbine—Steady and Unsteady Experimental Investigations Supported by Numerical Simulations

U. Reinmöller

B. Stephan

S. Schmidt

R. Niehuis

Institut für Strahlantriebe und
Turboarbeitsmaschinen,
RWTH Aachen, University of Technology,
D-52062 Aachen, Germany

The interaction between rotor and stator airfoils in a multistage turbomachine causes an inherently unsteady flow field. In addition, different relative circumferential positions of several stator rows and rotor rows, respectively, have an influence on the flow behavior in terms of loss generation, energy transport and secondary flow. The objective of the presented study is to investigate the effects of stator airfoil clocking on the performance of a 1-1/2 stage axial cold air turbine. The investigated axial turbine consists of two identical stators. The low aspect ratio of the blades and their prismatic design leads to a three-dimensional outlet flow with a high degree of secondary flow phenomena. Nevertheless, the small axial gaps between the blade rows are responsible for strong potential flow interaction with the radial wake regions in the measurement planes. Consequently, parts of the wakes of the first stator are clearly detected in the rotor outlet flow. To give an overview of the time-averaged flow field, measurements with pneumatic probes are conducted behind each blade row at ten different clocking-positions of the second stator. Further, an optimized clocking position was found due to a minimum in pressure loss behind the second stator. The unsteady measurements are carried out with hot-wire probes for three selected stator-stator positions. Animations of selected flow properties show the influence of different circumferential positions of the second stator on the unsteady flow behavior and secondary flow field. In addition and compared with experimental results three-dimensional unsteady viscous flow computations are performed.
[DOI: 10.1115/1.1425811]

Introduction

Rotor-stator interaction in turbomachines causes inherently unsteady effects based on the interaction of adjacent blade rows. The potential flow and wake interaction are the main responsible time-dependent phenomena with a three-dimensional-character. In addition, vortex shedding, shock/boundary layer interaction, and flutter have to be considered. Many researchers investigated in these different kinds of flow behavior by measurements and numerical simulations in axial compressor and turbine stages to determine and to understand the loss mechanisms (e.g., Sharma [1], Hodson [2], Halstead [3]).

The most complex step of flow simulation in turbomachines is the prediction of the real flow in stages and multistage machines. To improve the flow prediction in multistage turbomachines, the influence of unsteady effects on loss production due to rotor-stator interaction, blade flutter, and turbulence level have to be considered. During the last years several methods were proposed for the calculation of the unsteady three-dimensional viscous flow in multistage turbomachines. One approach is to use a ratio of small integers as an approximation to the pitch ratio and perform simulations with multiple blade passages (e.g., Rai and Madavan [4], Dawes [5], Arnone and Pacciani [6]). Another approach was developed by Giles [7] who handles the problem of periodic boundary treatment for any pitch ratio by performing time transformations and using different time steps for the stator and rotor domains (see also Jung [8]). The method, which is used for the numerical simulations presented in this paper, is based on the idea of Erdos [9], who proposed to store the solution at the periodic boundaries at every time step during a blade passage period and to use them as boundary conditions for the succeeding period.

In terms of turbomachinery, clocking or indexing describes different circumferential positions of consecutive stator/rotor blade rows. In the last years, numerous experimental and numerical studies have shown that airfoil-clocking is another tool to increase the efficiency of compressor and turbine stages in a moderate way. It is well known that in all these research activities the maximum in efficiency occurs when the wake of the first stator vanes impinges on the leading edge of the downstream stator. In contrast to that, the lowest efficiency could be found when the first stator wake segments reaches the mid-region of the second stator blade passage.

Huber [10] measured an increase in efficiency of about 0.8 percent in a two-stage turbine for an optimized circumferential position of the second stator blade row. The numerical simulation by Griffin [11] predicted at mid-span for the same turbine the measured maximum efficiency clocking positions correctly. Eulitz [12] made numerical clocking investigations in a 1 1/2-stage low pressure turbine which lead to the same results. Time accurate numerical studies by Dorney [13] in a 1 1/2-stage high pressure turbine observe the maximum efficiency when the first stage stator wake is aligned with the leading edge of the second stator. In this case, the maximum in unsteady surface pressure fluctuations appear on the second stator. Cizmas [14,15] show in a numerical study of a three-stage turbine that not only stator clocking but, in addition with rotor clocking, a twice increase in efficiency is pre-

Contributed by the International Gas Turbine Institute and presented at the 46th International Gas Turbine and Aeroengine Congress and Exhibition, New Orleans, Louisiana, June 4–7, 2001. Manuscript received by the International Gas Turbine Institute February 2001. Paper No. 2001-GT-304. Review Chair: R. Natole.

dicted. Another time-accurate numerical study for this turbine shows an increase in the amplitude of unsteady pressure when the efficiency increases by second stator clocking.

In contrast to the experimental work of Walraevens [16,17] and computational work of Volmar [18], the presented work focuses on the flow in a 1 1/2-stage axial turbine in which the second stator was clocked over several circumferential positions. Extensive measurements are performed using steady and unsteady measurement techniques behind the rotor and second stator. In addition with experimental investigations, three-dimensional unsteady viscous flow computations are performed which confirm the major effects of clocking.

Experimental Setup and Instrumentation

Experimental data behind the first stator, the rotor, and the second stator were acquired in a 1 1/2-stage axial turbine shown in Fig. 1. A ''Traupel profile'' is used for both stators (Utz [19]). Profile geometry, number of blades, and stagger angle are identical for the first and second stator. For the rotor blades a modified VKI-profile is used. An outlet guide vane takes out the swirl provided by the second stator. Each stator and the rotor consist of untwisted blades. The stator vanes are stacked at the trailing edge, the rotor blades are stacked at the center line of gravity. For turbine geometry and design data see Table 1.

The results presented in this paper have been acquired at the design point of the turbine, at a rotational speed of 3500 rpm, and a massflow rate of 7.2 kg/s. The shaft speed variation was less than 0.2 percent. The turbine inlet conditions were maintained at $T_{t0}=308\,\mathrm{K}\pm0.5\,\mathrm{K}$ and $p_{t0}=155{,}000\,\mathrm{Pa}$. The inlet total pressure varies slightly due to the running in an open loop.

Steady flow field properties behind both stators and the rotor were measured with pneumatic five-hole-probes with NTC-temperature-sensors 8 mm behind the blade rows. Both unsteady and steady flow properties were gained at equal positions in the turbine. The unsteady flow measurements were conducted with triple-hot-wire-probes. The used hot-wire data acquisition and reduction is briefly described in Stephan [20].

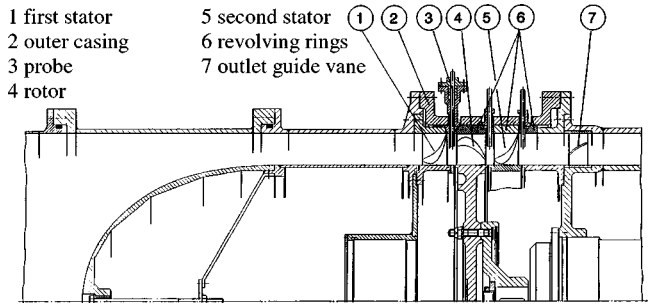

Fig. 1 Turbine test facility

Table 1 Turbine geometry and design data

	First and second stator (Traupel)	Rotor (VKI)
Tip diameter	600 mm	600 mm
Hub diameter	490 mm	490 mm
Passage height	55 mm	55 mm
Rotational speed	···	3500 rpm
Radial gap	···	0.4 mm
Aspect ratio h/s	0.887	0.917
Blade number	36	41
Pitch (mid-span) t	47.6 mm (10 deg)	41.8 mm (8.78 deg)
Flow angle α	20 deg	90 deg
Relative flow angle β	49.3 deg	151.2 deg

Numerical Scheme and Computational Grids

Time-marching numerical methods for solutions of the Euler and the Navier-Stokes equations have been highly developed and have gained remarkable popularity in solving steady flow problems (e.g., Denton [21], Dawes [22]). A basic and obvious requirement for a time-marching method to be used for unsteady flows is that the numerical scheme should be time-accurate and should allow numerical time steps up to a physically motivated magnitude. Due to the long physical periods of rotor-stator interaction phenomena and the limitations of explicit schemes concerning the possible magnitude of the numerical time step, an implicit scheme for the numerical simulation is recommended.

The presented numerical method is based on the recent work of Brouillet [23] and uses a second order time-accurate implicit discretization scheme. It is based on the Fauvre-averaged Navier-Stokes equations along with a Low-Reynolds-Number k-ε turbulence model by Chien [24]. The procedure consists of a cell-centered finite-volume scheme and uses a higher order upwind biased approximation of the inviscid fluxes with an approximate Riemann solver. The viscous fluxes are discretized according to the scheme developed by Chakravarthy [25]. For a detailed description of the numerical algorithm see Volmar [18,26] and Brouillet [23].

The implicit algorithm solves for the conserved quantities Q assuming the flux balance (augmented by source terms) F to be known at the new time level $n+1$:

$$\frac{Q^{n+1}-Q^n}{\Delta t}+F(Q^{n+1})=G(Q^{n+1})=0 \tag{1}$$

The corresponding non-linear system of equations with unknown Q^{n+1} are solved by several Newton iterations p:

$$\frac{dG}{dQ}(Q^{n+1^{(p)}})\cdot(Q^{n+1^{(p+1)}}-Q^{n+1^{(p)}})=-G(Q^{n+1^{(p)}}) \tag{2}$$

Each Newton iteration is solved by a block Gauss-Seidel iterative algorithm involving LU inversions of the local 7×7 blocks. As mentioned above, second order time accuracy is achieved by using a three point formulation:

$$\frac{3}{2}\frac{Q^{n+1}-Q^n}{\Delta t}-\frac{1}{2}\frac{Q^n-Q^{n-1}}{\Delta t} \tag{3}$$

The multistage simulations have been performed by using phase-shifted periodic boundary conditions for the single blade channel calculations. Therefore a flow variable at the upper and lower periodic boundary have to satisfy the phase-shifted periodic condition:

$$Q(x,\varphi,t)=Q(x,\varphi-\Delta\varphi_{\text{pitch }b},t-\Delta T) \tag{4}$$

$$Q(x,\varphi,t)=Q(x,\varphi+\Delta\varphi_{\text{pitch }b},t+\Delta T-T_b) \tag{5}$$

where ΔT is defined by the time a blade needs to assume at time $t+\Delta T$ the same state as its circumferential neighbor at time t and T_b represents the blade passing time period of a blade row referred to its neighboring blade row.

At the sliding blade row interface between the adjacent blade rows relative motion is taken into account by using a partial surface concept. This implies that at each time step the sets of contacting cells are determined and that the partial cell faces and fluxes are computed and assembled to yield a fully conservative flux balance for each cell located at the sliding interface.

The computational grids for the numerical simulations were generated with an elliptic grid generator. For each blade row, an O-type grid is used to discretize the flow field of the rotor-stator configuration. Inside the rotor tip clearance region, an embedded O-type grid with a singular center line is placed into the primary grid. Table 2 shows the number of grid nodes in each blade row.

Table 2 Grid characteristics

Row	Grid	$i \times j \times k$	Number of nodes
1	First stator	145×37×40	214,600
2	Rotor	165×37×40	244,200
2	Clearance	165×19×10	31,350
3	Second stator	155×37×40	229,400

Clocking Test Series

The second stator is clocked in steps of 1 deg in a range of one stator pitch (Fig. 2) to receive steady data for 10 different stator-stator positions. Three discrete stator-stator positions (4 deg, 7 deg and 9 deg) were selected to carry out measurements of the unsteady flow field whereas five clocking positions (0 deg, 1 deg, 3 deg, 5 deg and 7 deg) are computed in unsteady stage simulations.

In the following text, the circumferential shift of the two stators is denoted as ''clocking angle''. With the expression a ''clocking angle of 3 deg'' the stator-stator position as shown in Fig. 2 can be determined. Relative to the trailing edge of a stator blade the probes were positioned at 25 different circumferential positions and 25 radial positions (between 0.07 and 0.93 relative span). The measurement planes covered the whole passage between adjacent blades.

As it was described above, all flow field measurements were carried out at fixed places relative to the first stator, while the second stator was clocked. Behind the rotor, the strong upstream potential disturbances from the downstream second stator are shifted in circumferential direction relative to the measurement plane. In consequence, the assumed weak influence of the upstream first stator is very difficult to observe.

In order to analyze the results received from different stator-stator positions, a kind of a filter post-processing has to be conducted for the pneumatic and time-averaged data: The measured data were shifted according to the clocked second stator in the sense that the position of the second stator trailing edge is identical for all second stator positions. For this algorithm the reference clocking position is 9 deg. Applying this filter, the effects generated in the second stator appear at the same position, but flow phenomena which have their origin in the first stator change their circumferential position in the contour plots and radial averaged plots. Figure 3 demonstrates this behavior clearly. The dimensionless static pressure is shown behind the rotor as radial averaged values for five selected clocking positions. The circumferential averaged data are not affected from this shifting routine. The right plot shows the unshifted values, the left plot the shifted ones. The number symbols refer to the adjusted clocking angle.

The formation of the pressure field in front of the second stator

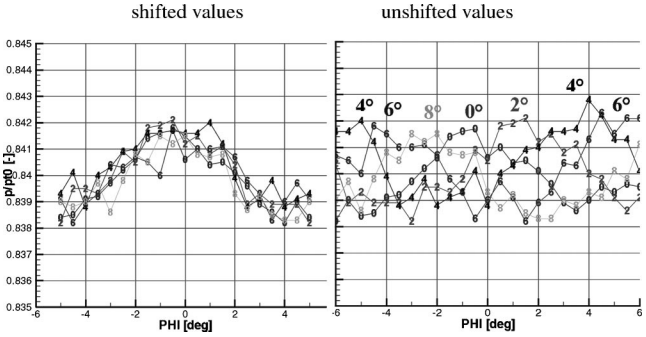

Fig. 3 Measured radially averaged dimensionless static pressure behind the rotor for five stator-stator positions

can be clearly observed in the shifted radially averaged values. An obvious ''moving'' influence of the first stator cannot be detected in the presentation of this parameter.

In contrast to Fig. 3 the graphs of Mach-number (Fig. 4) show a common minimum in the unshifted radially averaged distribution for all investigated clocking angles in the range between 0 deg$<\varphi<$3 deg. This minimum moves with different extent in the shifted values from right to left and corresponds to the first stator wake.

Total pressure loss is defined as:

$$\zeta_i(r,\varphi) = \frac{\bar{\bar{p}}_{ti-1}(r) - p_{ti}(r,\varphi)}{\bar{\bar{p}}_{ti} - \bar{\bar{p}}_i} \tag{6}$$

where p_{ti-1} marks the averaged value of the three highest values of the i-plane at each radius (Hi3-method, Roberts [27], 1988). The thermodynamic efficiency and entropy production are calculated from the circumferentially averaged pressure and temperature measurements as follows:

$$\overline{\eta}_i(r) = \frac{1.0 - \dfrac{\overline{T}_{t3}(r)}{\bar{\bar{T}}_{t0}}}{1.0 - \left(\dfrac{\overline{p}_{t3}(r)}{\bar{\bar{p}}_{t0}}\right)^{\gamma-1/\gamma}} \tag{7}$$

All graphs presented in this paper are views in the upstream direction. The definition used for the measured secondary flow vector is given by Stephan [20]. Unsteady results are presented by showing secondary flow fields and selected flow quantities at different rotor positions relative to the first stator. Vector plots of the rotor exit flow and the second stator exit flow are shown at four different stator-rotor positions. Each data set is numbered with an index which can be seen in the figures as ''TimeIndex'' (TI). Table 3 shows the reference between ''TimeIndex'' and rotor position.

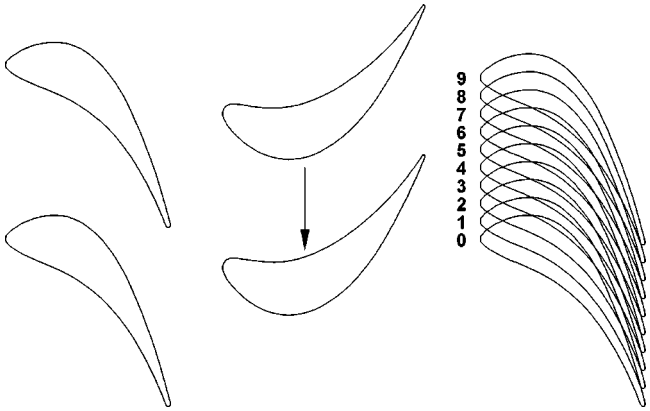

Fig. 2 Investigated clocking positions

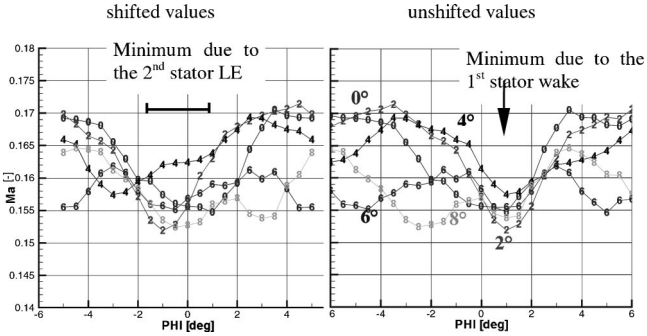

Fig. 4 Measured radially averaged Mach-number behind the rotor for five stator-stator positions

Table 3 Reference of "TimeIndex" and rotor movement

TI	Movement*	TI	Movement*
1	0.0%	33	50.0%
17	25.0%	49	75.0%

*Rotor movement in percent of rotor pitch starting at a point of reference

Animations were made additionally to the graphs from the scalar and vector flow properties due to a better analysis of the time-dependent flow behavior and transportation processes.

Experimental and Numerical Results

Turbine inlet flow, rotor inlet flow, and first stator outlet flow are not discussed in this publication. This information can be found at Walraevens [28], Reinmöller [29] and Stephan [20], who also discussed flow phenomena in relation to other topics. But the strong upstream influence of the moving rotor, as it was calculated by Volmar [18] and measured by Walraevens [28], should be kept in mind during the discussion of results gained behind the rotor below.

Flow behind the rotor. Selected flow properties, obtained from pneumatic measurements, are presented as circumferentially or radially averaged values or as contour-plots.

In Fig. 5, shifted distributions of the local Mach-number are presented in contour-plots for all ten investigated stator clocking positions. The flow field exhibits remarkable differences in the level of Mach-number. The wake of the first stator can be detected as a bowed ribbon of low values (dotted lines) from hub to casing ($Ma<0.15$), except for the region at 80 percent h/H. It moves from right to left with increasing clocking angle. As it was shown in Fig. 3, for shifted values behind the rotor, the upstream pressure influence of the downstream second stator appears at a constant circumferential position between 2 deg and 0 deg.

Consequently, the cutted wake of the first stator interacts mainly with this pressure field for clocking angles 0 deg, 1 deg, and 2 deg, where higher circumferential gradients of Mach-number can be detected. At clocking angles of 5 deg and 6 deg, the plots show a more homogeneous Mach-number distribution, where the first stator wake segments reach the mid-region of the second stator blade passage. The printed vectors in Fig. 5 exhibit the time averaged secondary flow field, calculated from data of the measurements with pneumatic five hole-probes. Nevertheless, in the lower part below mid-span, the influence of the passing rotor passage vortex can be clearly identified in the absolute frame of reference. In the pneumatic time-averaged data this vortex appears as a circumferentially stretched section at constant radii.

The local values of shifted total pressure behind the rotor are plotted in Fig. 6. The appearance of the first stator wake is distinguishable at the pressure drop in the same marked region as in Fig. 5. The local maximum in total pressure occurs in the middle of the measurement plane when the wake structure of the first stator moves out of the influence zone of the static pressure field of the downstream stator to rotor movement. The contour-plots for clocking angles 2 deg through 5 deg show this behavior.

Another phenomenon resulting from the first stator wake can be seen in Figs. 5 and 6 on the left hand side of the marked region near to the hub. The Mach-number and the dimensionless total pressure increase and in the secondary flow field, the low rotor passage vortex outlet zone is disturbed. An explanation for this deviation can be given with the analysis of unsteady data in this measurement plane.

Both experimental data and numerical simulations show that the clear and distinct wake, detectable behind the first stator, changes its shape during its passage through the rotor. Figure 7 gives a view on the wake transport at three different radial positions at the same time-step in entropy-distributions. The red contours correspond to high entropy values, the blue contours represent low values. While the first stator wake enters the rotor passage, it is accelerated in axial direction in the mid-pitch region between neighboring blades. Further downstream in the first stator wake, low energy material is transported from the pressure to the suction side in the rotor passage, so that the highest entropy values arise close to the suction side near the rotor blade surface. On the pressure side of the rotor blade the wake structure decreases in entropy intensity due to transient effects. Passing the rotor, the wake forms a bowed contour, which adapts at the cutted ends to the profile boundary layer and further downstream to the rotor wake. The pressure gradient in circumferential direction and the "negative jet" (Meyer [30]) mechanism are the main sources for this behavior. A detailed view of the contours reveals that the wake changes its structure with the radius. At the rotor inlet near the hub and casing the wake width increases due to the endwall

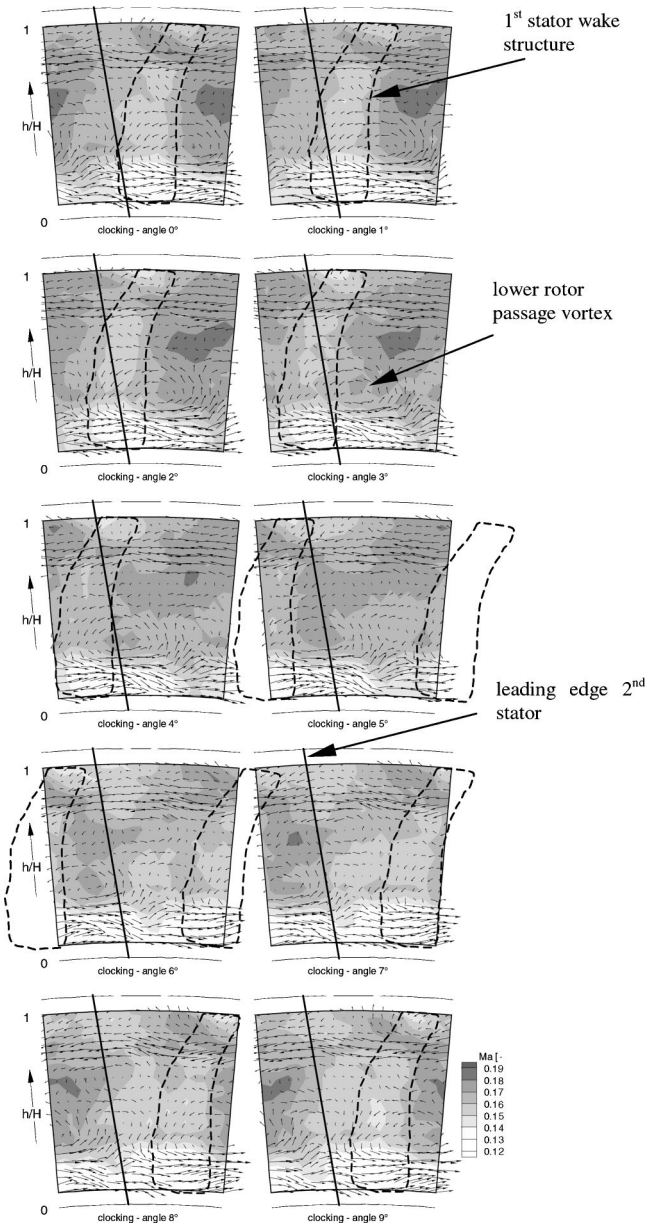

Fig. 5 Mach-number-distribution behind the rotor for ten clocking positions with secondary flow field, pneumatic measurements, shifted values

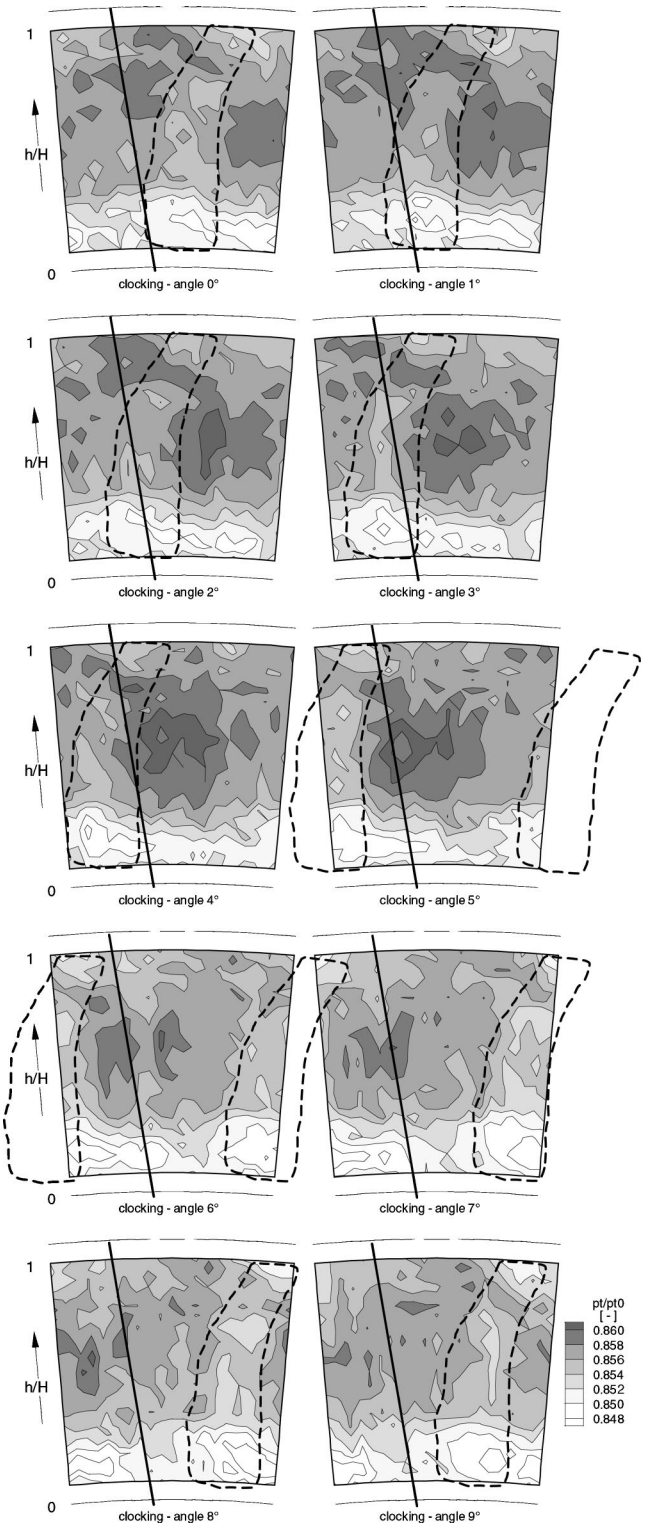

Fig. 6 p_t/p_{t0}-distribution behind the rotor for ten clocking positions, pneumatic measurements, shifted values

losses of the first stator. Subsequently, at the rotor outlet the wake structure exhibits higher entropy values. Altogether, there are three first stator wakes inside the rotor passage.

Due to the fact that this test rig is equipped with a low aspect ratio blading, secondary flow can be detected in a wide range from casing and hub, respectively, near to mid-span in all measurement

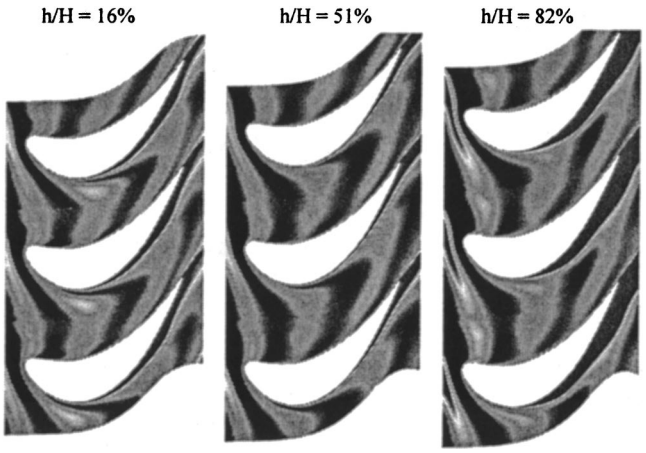

Fig. 7 Predicted entropy-contours, at 16 percent, 51 percent and 82 percent h/H, 0 deg clocking angle

planes. Near the hub and casing, the structure of the wake differs significantly from the ''pure'' wake formation at mid-span.

The unsteady turbulence level behind the rotor is dominated by the rotor wake, where the measured turbulence intensity is shown at mid-span versus time in Fig. 8. The 256 time indices are rep-

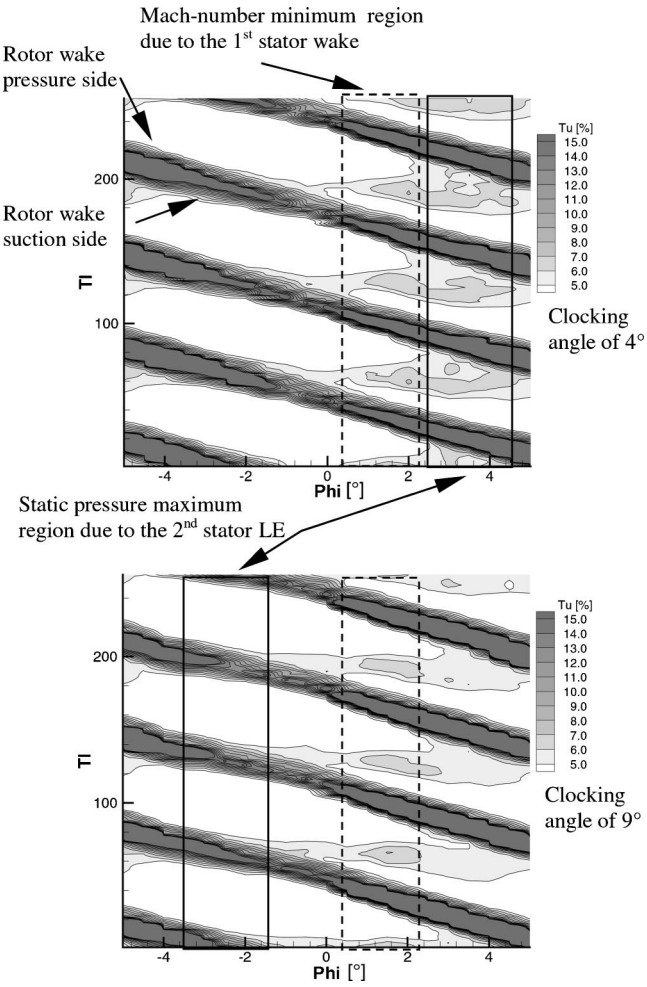

Fig. 8 Measured turbulence intensity versus time (four periods) at mid-span, clocking angle 4 deg and 9 deg, behind rotor, unshifted values

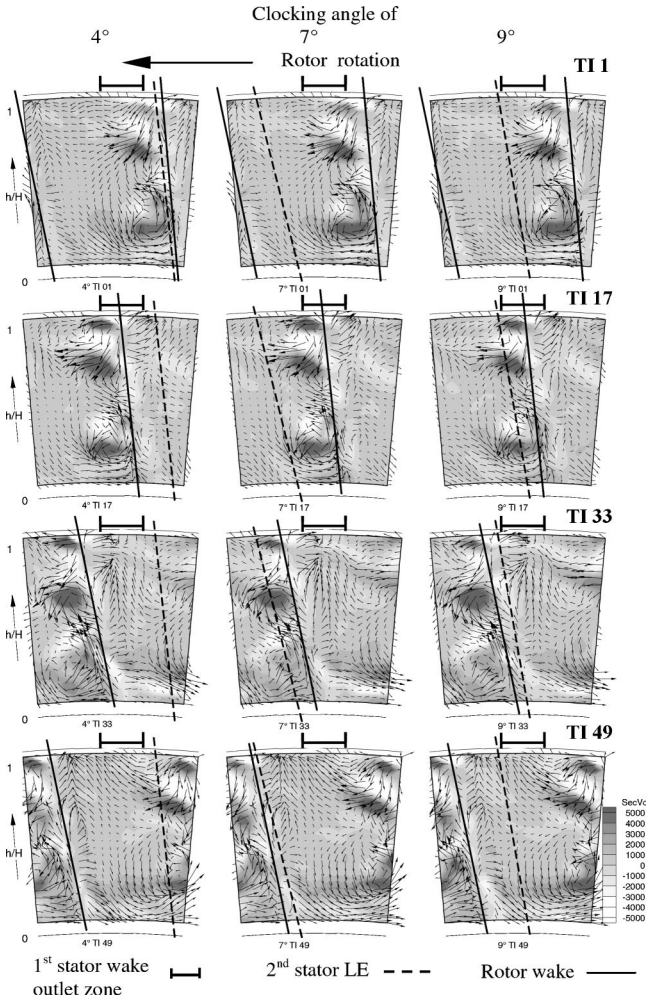

Fig. 9 Secondary vorticity with secondary flow field calculated from time-accurate measurements, three clocking angles, four rotor-stator positions, unshifted values

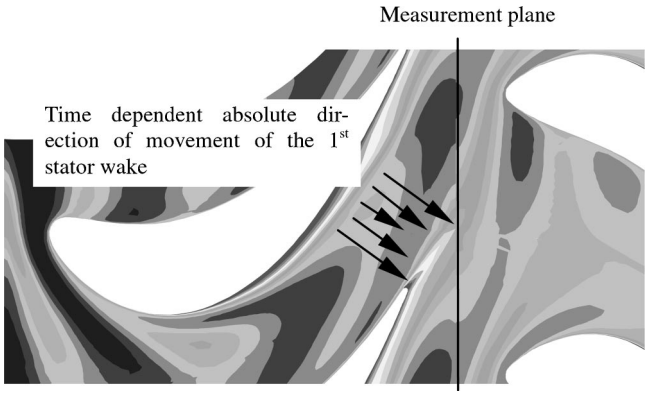

Fig. 10 Predicted entropy contours at hub region (16 percent h/H) at a discrete time step, CFD simulation, clocking angle of 0 deg

resenting four rotor periods measured for a clocking angle of 4 deg and 9 deg. Ribbons of high turbulence level represent the passing rotor wake. These regions are not of uniform strength; they change their width with dependency on the circumferential position of the wake. In the two plots, the minimum in Mach-number caused by the first stator wake (see Fig. 4) and the maximum in static pressure due to the leading edge of the second stator (see Fig. 3) are marked.

Between two passing rotor wakes the cut first stator wake can be detected as a region of higher turbulence up to 8 percent in both contour-plots with slightly increased values for the 9 deg clocking position. This zone is located between -2 deg and 5 deg in the circumferential direction and depends not on the clocking angle. In addition to that, an expanded region of higher turbulence due to the first stator wake appears on the suction side of the rotor wake. This phenomenon corresponds to the predicted relative maximum (green color) in the entropy distribution inside the rotor passage in Fig. 7 near mid-span.

Figure 9 shows vector-plots of the unsteady secondary flow field behind the rotor at four discrete stator-rotor-stator positions for three clocking angles, combined with the parameter secondary vorticity. The wake of the rotor is leaned in the circumferential direction to the suction side of the rotor blade. For a better orientation, the detected rotor trailing edge and the location of the leading edge of the second stator are labeled. Furthermore, the fixed zone is marked where the first stator wake periodic appears.

Additionally, both parameters give an impression of the intensity of the vortex systems in the same manner. It can be stated that the dominating structure is generated by the secondary flow field of the rotor, especially the strong hub passage vortex which appears in an extent zone on the suction side of the rotor blade. Vortex systems originating from the upstream stator are difficult to detect. Only a detailed view from the animation* of this unsteady data enables the passage vortex to be observed near the hub. It can be detected on the right hand side of the first stator outlet zone at certain rotor-stator positions (i.e. TI 33).

This behavior can be explained with the bowed wake structure inside the rotor passage which includes the vortical systems of the first stator. As Walraevens [28] mentioned, these systems are attached to the suction side of the first stator wake when passing the rotor passage. They reach the measurement plane first. CFD simulations confirm this behavior, e.g., see Fig. 10, where the red color represent high entropy levels and blue color low entropy levels. As one can see in Fig. 9, the vortices coupled with the rotor movement are of the same shape and differ only slightly for the varied clocking angles; i.e., it seems that the position of the second stator leading edge does not influence the detected vortex structures. Focusing on TI 33, a disturbance zone appears at the same time the structure of the rotor hub passage vortex loses its shape and intensity. The vortex is split in two in the same direction as the rotating vortices. At this rotor-stator, the wake of the moving rotor is located near the hub in the outlet zone of the first stator.

Flow behind the second stator. Inside the passage of the second stator, no measured data referring to stator indexing are available. Flow phenomena like wake transport, etc., can be detected by the analysis of numerical simulations.

Behind the second stator the measured radially averaged Mach-number (Fig. 11) shows a nearly uniform shape for all clocking angles. The stator wake is situated at a circumferential position of -3 deg in the shifted data referring to the reference clocking angle of 9 deg.

Only at the suction side ($\varphi=-2$ deg) can a saddle be detected, but differences in relation to clocking effects are not visible. In the unshifted values, the influence of the relative movement of the second stator at the measurement plane is obviously the main characteristic.

The results of the radially time-averaged secondary vorticity are shown in Fig. 12. They exhibit large differences for the data at clocking angle of 4 deg to the others. For all clocking angles, the vortical systems are located nearly at the same passage height and

*Remark: The authors used animations of various parameters for the unsteady flow analysis, but it is very difficult to give an active impression of unsteady flow phenomena with the help of print media.

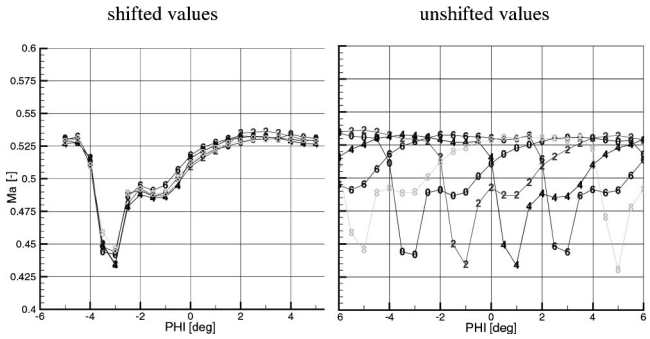

Fig. 11 Radially averaged Mach-number behind the second stator, five clocking angles, pneumatic measurements, shifted and unshifted values

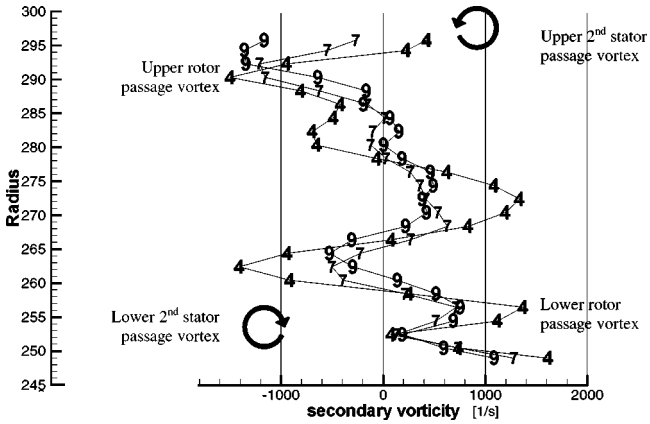

Fig. 12 Measured radially time-averaged secondary vorticity behind second stator, three clocking angles (4 deg, 7 deg, 9 deg)

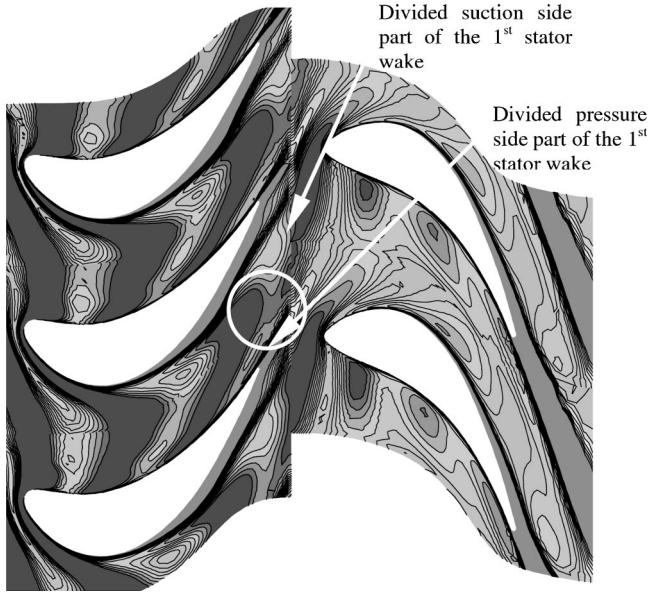

Fig. 13 Predicted entropy contours at mid-span for a distinct stator-rotor position, 0 deg clocking angle

the strongest systems appear for 4 deg clocking angle at mid-span and below. It is believed that in this case the vortex systems of the first stator—including its wake structure—reach the second stator passage with a decrease in interaction with the leading edge of the second stator or, more exactly, with its static pressure field.

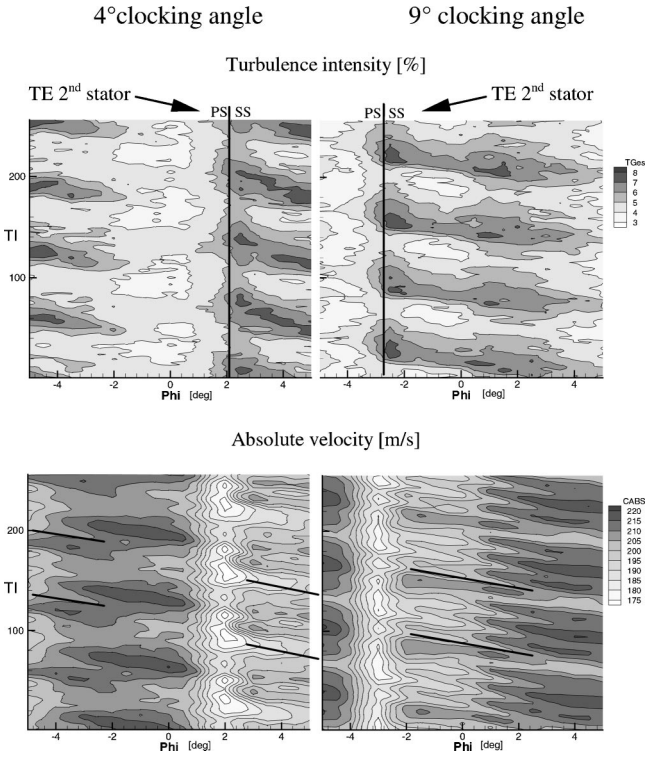

Fig. 14 Turbulence intensity and abs. velocity (4 periods) versus time at clocking angles 4 deg and 9 deg behind the second stator, unshifted values, mid-span

CFD simulations (Fig. 13) show that this upstream influence is detected for a clocking angle of 0 deg within the last third of the rotor passage. The interaction ends in a cutted first stator wake where one part is still located on the suction side of the rotor blade while the other part is appended to the pressure side of the adjacent blade. Both parts are then attached to the rotor wakes.

In Fig. 14, the measured time-accurate turbulence level and absolute velocity are presented at mid-span as contour-plots versus time. Near the suction side of the second stator trailing edge, the turbulence level increases for both adjusted clocking angles due to the interaction of the rotor wake with the second stator suction side boundary layer. As stated for the time dependent contour-plots of the secondary flow field, a higher turbulence level from the suction side up to half pitch in the circumferential direction to the pressure side corresponds to strong vortex systems. These regions of high turbulence are independent of the clocking angle; only the turbulence levels of the right contour-plot (clock-

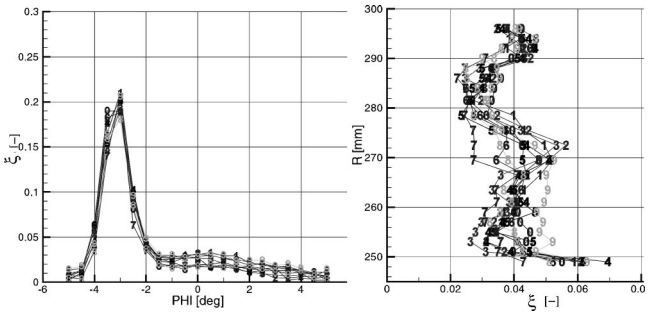

Fig. 15 Total pressure loss of the second stator at five clocking angles, radially and circumferentially averaged, shifted values

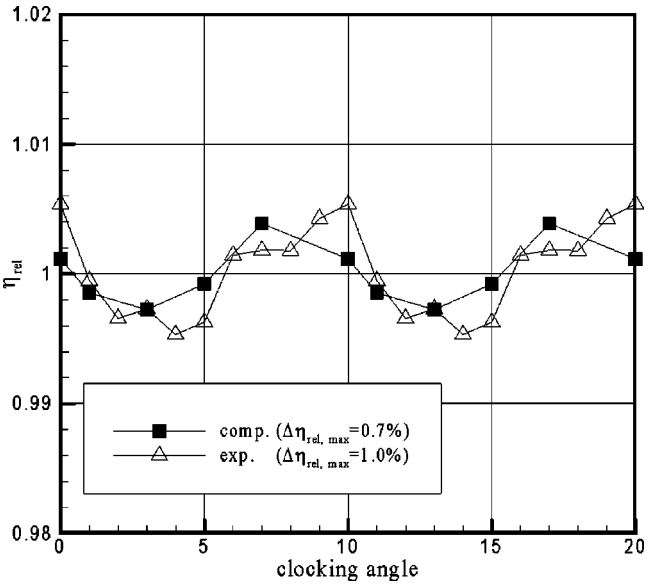

Fig. 16 Relative efficiency versus clocking angle, comparison with numerical results, mid-span

ing angle of 9 deg) exhibit a slight drop. The marked minima in the velocity contours for both cases follow the regions of high turbulence.

Total pressure loss (Eq. 6) is an applicable parameter to describe the effects due to the stator indexing. The radially and circumferentially mass-averaged shifted values are given in Fig. 15. Naturally, the wake is characterized by strong losses. The radially averaged shifted values are nearly identical in the wake region, whereas in the center of the measurement plane slight differences can be detected. The plot with circumferentially averaged values reveal three maximums in the radial distribution of the data. At the casing, the main pressure loss occurs due to the interaction of the rotor upper passage vortex with the upper second stator passage vortex. At mid-span losses for the clocking angles 9 deg to 4 deg are enlarged. Near hub (h/H=20 percent), the clocking angles 8 deg, 9 deg, and 0 deg distinguish from the remaining with an increase of loss. A possible interpretation is a different interaction between effects of the first stator wake, this includes vortical systems, and the inlet region of the second stator.

The thermodynamic total-to-total efficiency was calculated from Eq. 7. Due to the fact that the precision of the temperature measurements strongly influences the calculated efficiency level, only the variations of η_{rel} (Eq. 8) for all clocking angles are compared at mid-span with numerical results (Fig. 16).

$$\eta_{\mathrm{rel}}=\frac{\overline{\eta_i}}{\overline{\eta_i^*}}, \qquad \overline{\eta_i^*}=\frac{1}{n}\sum_{i=1}^{n}\overline{\eta_i} \tag{8}$$

The qualitative variation of the relative efficiency versus the clocking angle is very similar to that observed in the unsteady stage simulations. In both distributions, the maximum can be found between clocking angle 7 deg and 0 deg and the minimum between clocking angle 2 deg and 5 deg. The maximum variation of efficiency can be observed for the measurements of about $\Delta\eta_{\mathrm{rel,max}}=1.0$ percent and for the numerical simulations of about $\Delta\eta_{\mathrm{rel,max}}=0.7$ percent.

Conclusions

Steady and unsteady flow field measurements are performed behind each blade row for ten circumferential positions of the second stator in a 1 1/2-stage axial turbine. A method is presented to distinguish the second stator upstream influence from the flow field in the measurement plane behind the rotor and to identify the downstream influence of the first stator. In addition, time-accurate numerical simulations of five selected stator-stator positions are made, which give a closer look to the flow physics inside the rotor and second stator passage due to stator indexing.

Behind the rotor, the influence of the first stator wake is detected by the locally shifted parameters total pressure and Mach-number. It is shown that the wake radially varies in the circumferential direction. The influence of the theoretical potential upstream effect is clearly observed in the static pressure distributions of the different clocking angles. The numerical study reveals that this effect leads to a strong influence of the first stator wake inside the rear end of the rotor passage in the hub region. The impact of the first stator wake on the potential field of the second stator is shifted due to clocking in circumferential direction. This leads to a redistribution of turbulence intensity and absolute velocity behind the second stator. Furthermore, in the outlet of the second stator, strong changes in the secondary vorticity due to stator clocking exist.

Measurements show an optimized clocking position at 0 deg clocking angle due to the calculated integral total to total efficiency. This corresponds to measurements behind the rotor where the bowed first stator wake region at 0 deg clocking is nearly in line with the influence of the leading edge of the second stator. The comparison between the numerical and the experimental results exhibits a similar ''optimized'' second stator clocking position. In the same way, the position of minimum efficiency is observed when the bowed region is located between the neighboring second stator blades.

Further details of numerical simulations should explain the interaction mechanisms between the upstream first stator wake and the clocked second stator.

Nomenclature

c = velocity in the absolute frame of reference
F = vector of flux balance
G = vector of source terms
h, H = span
i = measuring plane
k = turbulent kinetic energy
Ma = Mach-number
n = time index
p = pressure
Q = vector of conserved quantities
r = radial direction
s = chord length, Newton iteration
T = temperature, time
t = pitch, time
u = circumferential velocity
w = velocity in the relative frame of reference
x = axial direction
α = pitchwise flow angle (abs. frame)
β = pitchwise flow angle (rel. frame)
γ = spanwise flow angle, ratio of specific heats (c_p/c_v)
ε = turbulent dissipation rate
ζ = loss coefficient
η = efficiency
λ = stagger angle
φ = circumferential direction
ω = vorticity

Subscripts

b = blade
i,j,k = grid indices
rel = relative
t = total
0 = first stator inlet
2 = rotor exit, second stator inlet
3 = second stator exit

Superscripts

n = time level
p = Newton iteration
$-$ = radially or circumferentially averaged
$=$ = integral average

Abbreviations

CFD = Computer Fluid Dynamics
LE = Leading Edge
NS = Navier-Stokes
NTC = Negative Temperature Coefficient
PS = Pressure Side
SS = Suction Side
TE = Trailing Edge
TI = TimeIndex
VKI = Von Karman Institute

References

[1] Sharma, O. P., Ni, R. H., and Tanrikut, S., 1994, ''Unsteady Flows in Turbines—Impact on Design Procedure,'' AGARD Lecture Series 195.
[2] Hodson, H. P., 1998, ''Blade Row Interference Effects in Axial Turbomachinery Stages,'' VKI Lecture Series 1998-02.
[3] Halstead, D. E., Wisler, D. C., Okiishi, T. H., Walker, G. J., Hodson, H. P., and Shin, H.-W., 1997, ''Boundary Layer Development in Axial Compressors and Turbines—Part 1 of 4: Composite Picture'' and Part 3 of 4 ''LP Turbines,'' ASME J. Turbomach., **119**, pp. 114–127.
[4] Rai, M. M., and Madavan, N. K., 1988, ''Multi-Airfoil Navier-Stokes Simulations of Turbine Rotor-Stator Interaction,'' NASA Ames Research Center, Reno-Meeting.
[5] Dawes, W. N., 1994, ''A Numerical Study of the Interaction of a Transonic Compressor Rotor Overtip Leakage Vortex with the Following Stator Blade Row,'' ASME Paper No. 94-GT-156.
[6] Arnone, A., and Pacciani, R., 1995, ''Rotor-Stator Interaction Analysis Using the Navier-Stokes Equations and a Multigrid Method,'' ASME Paper No. 95-GT-117.
[7] Giles, M. B., 1991, ''UNSFLO: A Numerical Method for the Calculating of Unsteady Flow in Turbomachinery,'' GTL Report No. 205, MIT Gas Turbine Laboratory.
[8] Jung, A., Mayer, J. F., and Stetter, H., 1996, ''Simulation of 3D-Unsteady Stator/Rotor Interaction in Turbomachinery Stages of Arbitrary Pitch Ratio,'' ASME Paper No. 96-GT-69.
[9] Erdos, J. I., Alzner, E., and McNally, W., 1977, ''Numerical Solution of Periodic Transonic Flow Through a Fan Stage,'' AIAA J., **15**, No. 11, pp. 1559–1568.
[10] Huber, F. W., Johnson, P. D., Sharma, O. P., Staubach, J. B., and Gaddis, S. W., 1995, ''Performance Improvement Through Indexing Turbine Airfoils Part 1—Experimental Investigation,'' ASME Paper No. 95-GT-27.
[11] Griffin, L. W., Huber, F. W., and Sharma, O. P., 1996, ''Performance Improvement Through Indexing of Turbine Airfoils: Part 2—Numerical Simulation,'' ASME J. Turbomach., **118**, pp. 636–642.
[12] Eulitz, F., Engel, K., and Gebing, H., 1996, ''Numerical Investigation of the Clocking Effects in a Multistage Turbine,'' ASME Paper No. 96-GT-26, Birmingham, UK.
[13] Dorney, D. J., and Sharma, O. P., 1998, ''Turbine Performance Increases Through Airfoil Clocking,'' International Journal of Turbo and Jet Engines, **15**, 119–127.
[14] Cizmas, P., and Dorney, D. J., 1998, ''Parallel Computing of Turbine Blade Clocking,'' AIAA Paper No. 98-3598, Cleveland, OH.
[15] Cizmas, P., and Dorney, D. J., 1999, ''The Influence of Clocking of Unsteady Forces of Compressor and Turbine Blades,'' ISABE Paper No. 99-72, Florence, Italy.
[16] Walraevens, R. E., and Gallus, H. E., 1995, ''Experimental Investigation of Three-Dimensional Unsteady Flow Downstream the Rotor in a 1-1/2 Stage Turbine,'' 95-Yokohama-IGTC-10.
[17] Walraevens, R. E., and Gallus, H. E., 1995, ''Stator-Rotor-Stator Interaction in an Axial Flow Turbine and its Influence on Loss Mechanisms,'' AGARD CP 571.
[18] Volmar, T. W., Brouillet, B., Gallus, H. E., and Benetschik, H., 1998, ''Time Accurate 3D Navier-Stokes Analysis of a 1 1/2-Stage Axial Turbine,'' AIAA Paper No. 98-3247.
[19] Utz, C., 1972, ''Experimentelle Untersuchung der Strömungsverluste in einer mehrstufigen Axialturbine,'' Thesis No. 4894, ETH Zürich, Switzerland.
[20] Stephan, B., Gallus, H. E., and Niehuis, R., 2000, ''Experimental Investigations of Tip Clearance Flow and its Influence on Secondary Flows in a 1 1/2-Stage Axial Turbine,'' ASME Paper No. 2000-GT-613, Munich, Germany.
[21] Denton, J. D., 1983, ''An Improved Time Marching Method for Turbomachinery Flow Calculation,'' ASME J. Eng. Power, **105**, pp. 514–524.
[22] Dawes, W. N., 1988, ''Development of a 3D Navier-Stokes Solver for Application to All Types of Turbomachinery,'' ASME Paper No. 88-GT-70.
[23] Brouillet, B., Benetschik, H., Volmar, T. W., Gallus, H. E., and Niehuis, R., 1999, ''3D Navier-Stokes Simulation of a Transonic Flutter Cascade near Stall Conditions,'' *Int. Gas Turbine Conf.*, Kobe, Japan.
[24] Chien, K.-Y., 1982, ''Predictions of Channel and Boundary-Layer Flows with a Low-Reynolds-Number Turbulence Model,'' AIAA J., **20**, No. 1, pp. 33–38.
[25] Chakravarthy, S., 1988, ''High Resolution Upwind Formulations for the Navier-Stokes Equations,'' VKI Lecture Series 1988-05.
[26] Volmar, T. W., 1999, ''Zeitgenaue dreidimensionale Simulation der Rotor-Stator-Interaktion in Turbomaschinen durch numerische Lösung der Navier-Stokes Gleichungen,'' Thesis, RWTH Aachen, Germany.
[27] Roberts, W. B., Serovy, G. K., and Sandercock, D. M., 1988, ''Design Point Variation of 3-D Loss and Deviation for Axial Compressor Middle Stages,'' ASME Paper 89-GT-6.
[28] Walraevens, R. E., 2000, ''Experimentelle Analyze dreidimensionaler instationärer Strömungseffekte in einer 1 1/2—stufigen Turbine,'' Thesis Research-Rep. VDI Series 7 No. 385, RWTH Aachen, Germany.
[29] Reinmöller, U., and Gallus, H. E., 1999, ''An Experimental Investigation of the Flow in an 1 1/2-Stage Axial Turbine with Regard to a High Level of Cooling Air Injection,'' ASME Paper No. 99-GT-41, Indianapolis.
[30] Meyer, R. N., 1958, ''The Effect of Wakes on the Transient Pressure and Velocity Distribution in Turbomachines,'' ASME J. Basic Eng., **80**, pp. 1544–1552.

Andrea Arnone

Michele Marconcini

Roberto Pacciani

"Sergio Stecco" Department of Energy Engineering, University of Florence, 50139 Firenze, Italy

Claudia Schipani

Ennio Spano

Fiat Avio S.p.A.—Direzione Tecnica, 10127 Torino, Italy

Numerical Investigation of Airfoil Clocking in a Three-Stage Low-Pressure Turbine

A quasi-three-dimensional, blade-to-blade, time-accurate, viscous solver was used for a three-stage LP turbine study. Due to the low Reynolds number, transitional computations were performed. Unsteady analyses were then carried out by varying the circumferential relative position of consecutive vanes and blade rows to study the effects of clocking on the turbine's performance. A clocking strategy developed in order to limit the number of configurations to be analyzed is discussed. The optimum analytically-determined clocking position is illustrated for two different operating conditions, referred to as cruise and takeoff. The effects of clocking on wake interaction mechanisms and unsteady blade loadings is presented and discussed. For low Reynolds number turbine flows, the importance of taking transition into account in clocking analysis is demonstrated by a comparison with a fully turbulent approach. [DOI: 10.1115/1.1425810]

Introduction

The presence of unstationary flows in axial turbines is primarily due to relative motion between stator and rotor rows. This relative motion generates viscous and potential interactions between rows. When considering more than one stage, the convection of wakes for several blade chords downstream is responsible for complex wake and blade interactions. Interactions between nonadjacent blade rows become significant and wake interaction, in particular, is a great contributor to unsteadiness on the blades.

Recently, great attention has been paid to airfoil *indexing* or *clocking* in multistage turbomachinery. Such a technique operates on the relative circumferential positions of fixed and rotating blade rows in consecutive stages, and aims at performance improvement. In particular, both experimental (i.e., Sharma et al. [1], Huber et al. [2]) and numerical (i.e., Dorney and Sharma [3], Eulitz et al. [4], Griffin et al. [5], Cizmas and Dorney [6], Dorney et al. [7]) investigations have shown how the time-averaged turbomachine efficiency varies periodically with stator and rotor clocking positions.

The axial and circumferential relative position of the rows, together with the blade count ratio between consecutive fixed and rotating rows, impact on the flow field unsteadiness induced by the wake interactions, and consequently on the performance. The amplitude of efficiency variation depends primarily on the blade count ratio of consecutive stator and rotor rows. It has been demonstrated that larger efficiency benefits can be achieved if this ratio is near 1:1, while practically no effect can be detected if it is far from unity.

For compressors, the effects of airfoil clocking have been predicted by Gundy-Burlet and Dorney [8,9]. The numerical results for a 2.5-stage compressor showed efficiency variations between 0.5 percent and 0.8 percent as a function of stator clocking position. Dorney et al. [7] have shown that wake effects related to clocking contain a steady component and an unsteady one which both impact on the losses.

The experimental results reported by Huber et al. [2] for a two-stage HP turbine showed a 0.8-percent efficiency variation due to clocking of the second stage stator. A two-dimensional numerical analysis at midspan performed by Griffin et al. [5] for the same turbine, correctly predicted the optimum clocking positions but the estimated efficiency variation was only 0.5 percent. Cizmas and Dorney [6] investigated the effects of *full clocking* (i.e., simultaneously clocking stator and rotor rows) in a three-stage steam turbine. They found that the clocking of the second stage gives larger efficiency variations than the clocking of the third stage and that the benefit of rotor row clocking was approximatively twice that of stator clocking.

The unsteady transitional behavior of blade boundary layers is known to have an important impact on multistage low-pressure turbine performance. Modern trends in turbomachinery design look at blade load increase as a promising solution for component reduction. Several authors (cf. Curtis et al. [10], Cobley et al. [11]) have shown how *high-lift* airfoils can be operated with acceptable losses by taking advantage of wake-induced transition effects in LPT low Reynolds number flows (Banieghbal et al. [12], Halstead et al. [13], Schulte and Hodson [14]). The next generation of LP turbine stages will probably rely on such a concept to reduce the number of blades. In such a scenario, the clocking analysis of a multistage low pressure turbine requires transitional computations. To this end a simple transition model was included in the numerical procedure. Two different flow conditions, one corresponding to *cruise* and the other to *takeoff* operation of the turbine, were analyzed. The Reynolds number was low for both of the two studied cases and transitional calculations were compared to fully turbulent ones to check for the impact of transition modeling on clocking effects.

When dealing with clocking optimization analysis with more than two stages, the first issue to address is how to limit the number of configurations to investigate. Five different locations of airfoils over one pitch are considered sufficiently accurate in order to appreciate clocking effects [1,6]. With three stages, the total number of possible configurations to be investigated is given by $25\times25=625$. In such a circumstance, design of experiment (DOE) techniques can help to reduce the number of cases to run. However, the periodic type with multiple peaks in the response surface methodology (RSM) made the DOE approach not straightforward to apply. For these reasons, an indexing strategy was defined which allows one to analyze fewer configurations to find the optimum tangential blade positions in terms of turbine efficiency.

Computational Procedure

The time-accurate release of the TRAF code (Arnone et al. [15]) was used in the present work. The unsteady, quasi-three-dimensional Reynolds Averaged Navier-Stokes equations are writ-

Contributed by the International Gas Turbine Institute and presented at the 46th International Gas Turbine and Aeroengine Congress and Exhibition, New Orleans, Louisiana, June 4–7, 2001. Manuscript received by the International Gas Turbine Institute February 2001. Paper No. 2001-GT-303. Review Chair: R. Natole.

ten in conservative form in a curvilinear, body-fitted coordinate system and solved for density, absolute momentum components in the axial and tangential directions, and total energy.

Numerical Scheme. The space discretization is based on a cell centered finite volume scheme. The artificial dissipation model used in this paper is basically the one originally introduced by Jameson, Schmidt, and Turkel [16]. In order to minimize the amount of artificial diffusion inside the shear layers, the eigenvalue scaling of Martinelli and Jameson [17] and Swanson and Turkel [18] was implemented to weigh these terms (cf. Arnone and Swanson [19]). The system of governing equations is advanced in time using an explicit four-stage Runge-Kutta scheme [19].

Residual smoothing, local time-stepping, and multigrid are employed to speed up convergence to the steady-state solution. The time step is locally computed on the basis of the maximum allowable Courant number, typically 5.0, and accounts for both convective and diffusive limitations [19].

A dual time stepping method (Jameson [20], Arnone and Pacciani [21]) is used to perform time accurate calculations. By introducing the dual time stepping concept, the solution is advanced in nonphysical time, and acceleration strategies, like local time stepping, implicit residual smoothing, and multigridding are used to speed up the residual to zero to satisfy the time-accurate equations.

Inflow and outflow boundaries are treated via a one-dimensional characteristic scheme. Inlet flow angle, total pressure and temperature are imposed at the inlet. At the outlet static pressure is assigned.

The described method has recently been used by the authors to compute natural unsteady phenomena (i.e., shock buffeting, wake shedding [21]) and rotor:stator interaction in turbine and compressor stages and it has indicated substantial reduction in the computational effort with respect to classical explicit schemes (Arnone et al. [22]).

Transition and Turbulence Model. A two-layer algebraic model based on the mixing length concept (Arnone and Pacciani [23]) was used for turbulence closure.

In transitional flows, an effective viscosity is defined as

$$\mu_{eff} = \mu_l + \gamma \cdot \mu_t \tag{1}$$

where μ_l and μ_t are the molecular and turbulent contributions and γ is the intermittency function. According to Abu Ghannam and Shaw [24], the location of transition onset is determined by the following condition:

$$\mathrm{Re}_\vartheta = \mathrm{Re}_{\vartheta,\mathrm{start}} \tag{2}$$

where Re_ϑ is the Reynolds number based on the momentum thickness. Its value at the start of transition $\mathrm{Re}_{\vartheta,start}$ is a function of the turbulence intensity Tu, and the Thwaites' pressure gradient parameter λ_ϑ.

In this study, a local formulation of the turbulence intensity (Zerkle and Lonsbury [25])

$$\mathrm{Tu} = \mathrm{Tu}_1 \cdot \frac{u_1}{u_e} \tag{3}$$

is used. Transition is allowed to begin if $\mathrm{Re}_\vartheta \geqslant \mathrm{Re}_{\vartheta,\mathrm{start}}$ and the acceleration factor:

$$K_t = \frac{\nu}{u_e^2} \cdot \frac{du_e}{ds} = \frac{\lambda_\theta}{\mathrm{Re}_\theta^2} \tag{4}$$

is less than the limit value of $3 \cdot 10^{-6}$. The latter condition is also used to force relaminarization in the turbulent part of the flow. If laminar separation occurs, transition is assumed to start at the separation onset location.

Downstream of the onset of transition the expression proposed by Mayle [26]

$$\gamma(s) = 1 - \exp[-\hat{n}\sigma(\mathrm{Re}(s) - \mathrm{Re}(s)_{\mathrm{start}})^2] \tag{5}$$

is used for the distribution of intermittency, where $\hat{n}\sigma$ is the nondimensional spot production rate, Re(s) is the local Reynolds number, and the subscript *start* indicates the onset of transition. The spot production rate is computed using the correlation proposed, for zero pressure gradient, by Mayle [26]. As far as the intermittency distribution is concerned, when laminar separation occurs, a pointwise transition is assumed at the separation onset location. More details on the transition model implementation can be found in Arnone et al. [27].

The Three-Stage Turbine

The turbine being studied features typical aspects of the current design practices of aircraft engine LP blades (Fig. 1), with shrouded rotors and relatively high aspect ratios. Detailed geometrical data are protected by Fiat Avio and can not be made available. For such configurations, the effects of secondary flows have been found to influence quite a small fraction of the span and, away from the endwalls, the flow can be considered almost two-dimensional for a large portion of the blade height.

Since the chord-based Reynolds number is of the order of a few hundred thousand for *cruise* operating point and increases by a factor of 3–4 during *takeoff*, the transitional behavior of the blade surface boundary layers was expected to be a major feature of the flowfield. The inlet freestream turbulence level for the transition model was set at 6 percent for both the operating conditions.

The midspan section of the turbine was then selected for the analysis and the streamtube thickness and radius distributions were established on the basis of steady, three-dimensional, viscous, multirow calculations (e.g., Arnone and Benvenuti [28]).

H-type grids (177×73, Fig. 2) were chosen for the analysis. With an H-type structure it is relatively easy to control the uniformity and density of the grid before the blade passage to prevent an excessive smearing of the incoming wakes. In order to reduce the

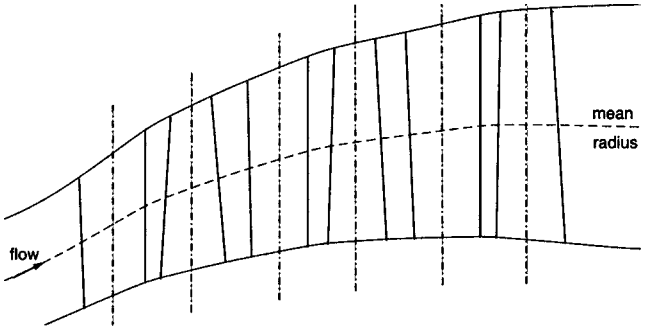

Fig. 1 LP turbine meridional section

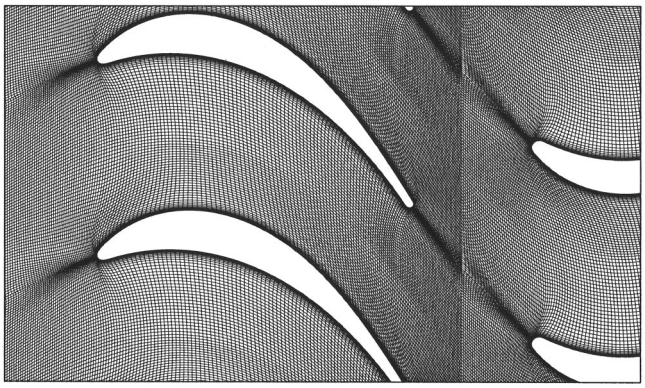

Fig. 2 H-type grid for the midspan section

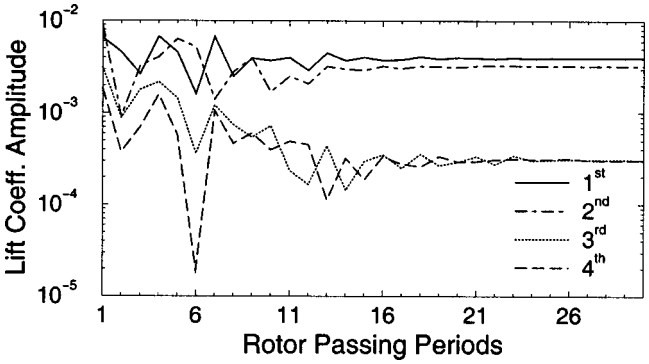

Fig. 3 Evolution of the nondimensional lift coefficient amplitude harmonics

mesh skewness, the grids are of the non-periodic type (i.e., Arnone et al. [15]). Based on past experiences on grid dependence in rotor-stator interaction analyses (Arnone and Pacciani [21]), the selected grid size was considered to be adequate for the purposes of this study.

The vane/blade count ratios were equal for all the stages and very close to one. In order to end up with reasonable memory and computer time requirements, approximate stage configurations, including one vane and one rotor, were considered. In particular, the rotor pitches were slightly modified to match an exact 1:1 vane/blade count ratio. Actually, the pitch alteration of rotor blade rows was of the order of 0.2 percent and, based on experience [21], it was considered negligible.

The nondimensional blade lift coefficient based on pressure distribution was used to monitor unsteadiness. Starting from an initial steady-state solution, up to 20 rotor passing periods were needed to obtain a periodic solution. Figure 3 shows the evolution of the nondimensional lift coefficient amplitude for the first four Fourier harmonics over 30 periods.

Indexing Strategy

It has been observed in all the performed computations that the indexing of a stage has little influence on the optimum clocking positions and efficiency values of the upstream stages. Such a circumstance seems consistent with the weak potential interactions expected for the turbine under investigation. In fact, Mach numbers in the LPT are relatively low (of the order of 0.3–0.4) and the axial gap between consecutive blade rows is relatively large. On the contrary, the entropy contours of Fig. 4 show significant wake interactions between coupled blade rows. In light of such considerations, the row indexing was carried out stage by stage starting from a full clocking of the 4th stage. In this phase, the circumferential position of the 4th-stage airfoils was varied while keeping all the other rows in their reference positions (see Fig. 5).

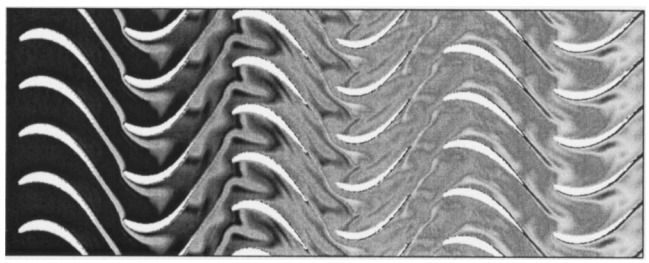

Fig. 4 Instantaneous entropy contours

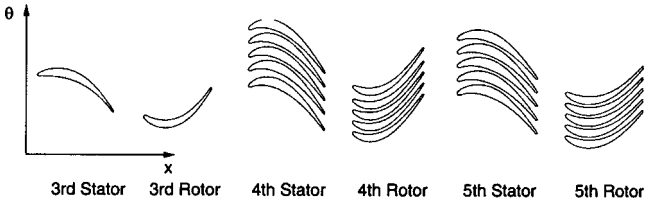

Fig. 5 Turbine geometry and clocking positions of 4th and 5th-stage blade rows

Once determined, the optimum positions for the 4th vane and blade are kept fixed and the 5th stage is then indexed. In such way, only 49 of the 625 initial different configurations have to be taken into account.

Clocking Analysis at Cruise Conditions

Efficiency Variations. In this investigation the total-to-total efficiency is defined as

$$\eta = \frac{1 - \frac{T_{t2}}{T_{t1}}}{1 - \left(\frac{p_{t2}}{p_{t1}}\right)^{\gamma - 1/\gamma}} \tag{6}$$

The average efficiency is calculated using the mass-average of the time-averaged total pressure and total temperature. Clocking effects are evidenced by turbine efficiency variation with respect to the average value $\Delta\eta = \eta - \eta_{av}$.

The effect of 4th-stage clocking on turbine efficiency is shown in Fig. 6 as a function of stator and rotor tangential positions. It is worthwhile to notice that the efficiency benefits coming from clocking the blades are quantitatively similar to those resulting from clocking the vanes. Such a circumstance indicates how a *full clocking* strategy is needed to obtain the maximum benefit from indexing effects. As far as the 5th stage is concerned, efficiency gains are still comparable for stator and rotor clocking (Fig. 7). It should be observed that while the efficiency variation due to 5th-stage clocking is comparable with that obtained from the 4th stage, care should be taken in evaluating the relative benefits on the maximum turbine efficiency value. For the case in consideration, the total turbine efficiency variation after the 4th stage indexing is given by

$$\eta_{t,\max,4\text{th}} - \eta_{t,\min,4\text{th}} = 0.50 \text{ percent}$$

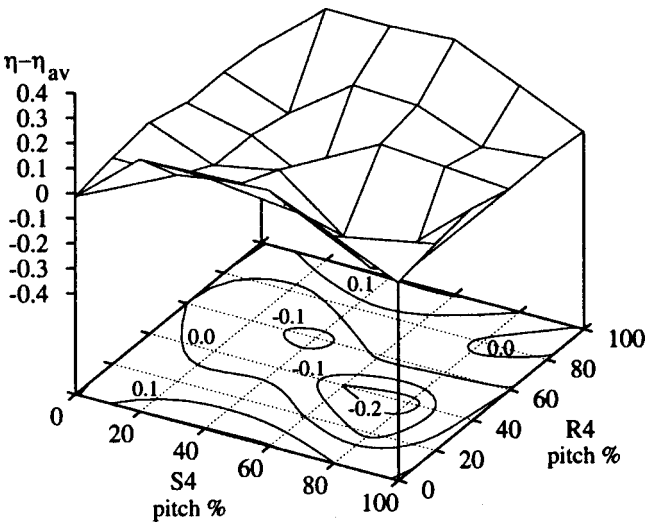

Fig. 6 Efficiency variations due to clocking stage 4

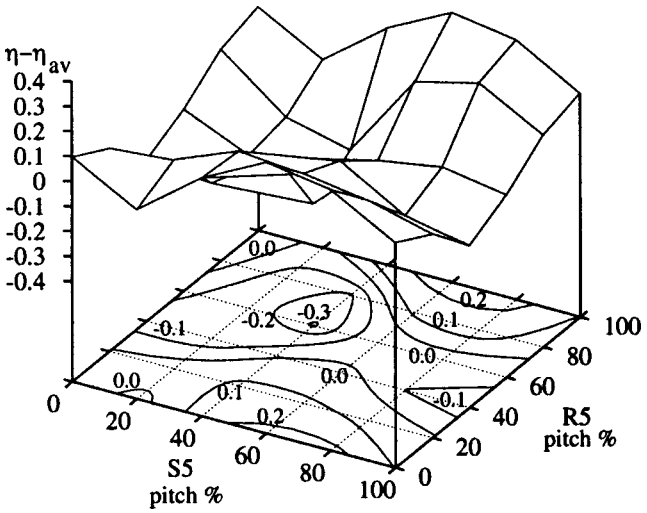

Fig. 7 Efficiency variations due to clocking stage 5

and the same difference, referred to the 5th one, is even higher

$$\eta_{t,\max,5\text{th}} - \eta_{t,\min,5\text{th}} = 0.60 \text{ percent}$$

On the other hand, it should be noticed that the difference between maximum efficiencies after the successive clocking of the two stages yields a value of

$$\eta_{t,\max,5\text{th}} - \eta_{t,\max,4\text{th}} = 0.18 \text{ percent}$$

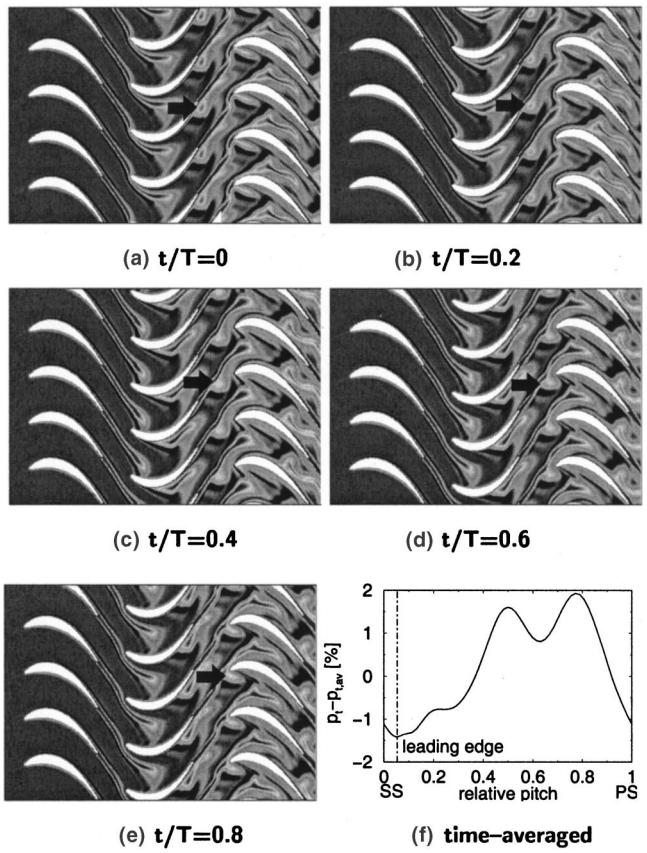

Fig. 8 Instantaneous entropy contours during one period ($\eta_{\min}$), and time-averaged total pressure pitchwise distribution in front of the 4th stator

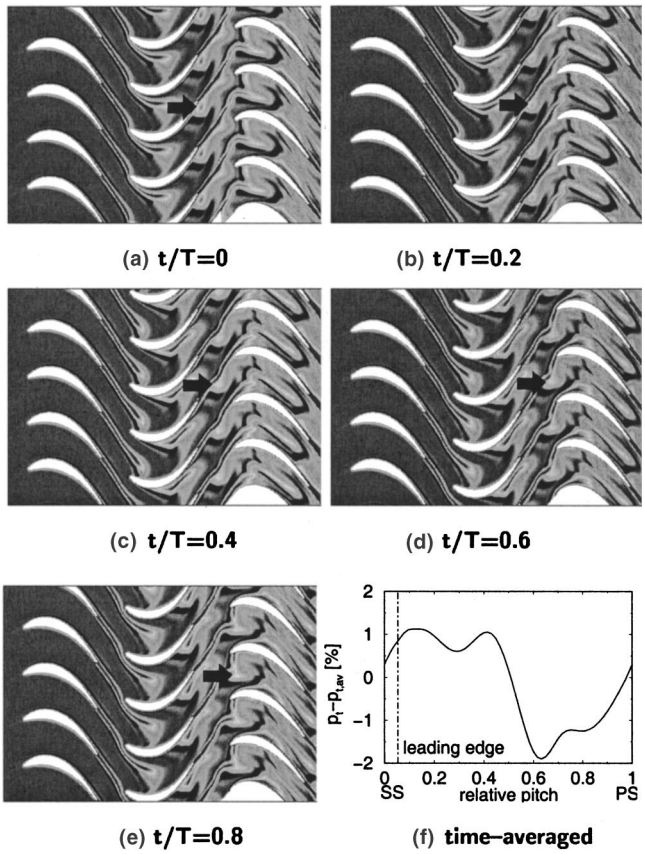

Fig. 9 Instantaneous entropy contours during one period ($\eta_{\min}$), and time-averaged total pressure pitchwise distribution in front of the 4th stator

This shows how the performance improvement coming from the 5th stage indexing, while still appreciable, is actually more than halved with respect to the previous stage contribution. Such an observation suggests a criterion to evaluate benefits from the indexing of successive airfoil rows in a multistage turbomachine. After having clocked a generic stage, a key parameter to assess the effective machine efficiency gain coming from successive stage indexing is given by the difference between maximum efficiencies relative to the two sequential clocking operations.

The lower contribution produced by the indexing of the 5th stage is consistent with the indexing strategy we adopted. While clocking the 4th stage, the 5th-stage bladings were kept fixed in their reference position. As a consequence, the 4th stage was clocked both with respect to the 3rd and the 5th stages at the same time, thus producing a more significant impact. Before choosing the indexing strategy, tests were performed maintaining the relative tangential positions between the 4th and 5th-stage blades while clocking the 4th stage. In this case, the contribution given by each stage clocking operation was of the same order of magnitude. However, the total gain in turbine efficiency, as well as the optimum blade positions predicted by the two strategies, was roughly the same.

The total predicted efficiency variation for the turbine is given by

$$\eta_{t,\max} - \eta_{t,\min} = 0.68 \text{ percent}$$

and it should be pointed out that such an estimate is actually safe. The clocking strategy described was used to find the maximum efficiency position and the minimum one was determined as the worst among the 49 analyzed configurations, without a systematic search. An absolute efficiency minimum prediction would require the application of the clocking strategy by starting from the 4th

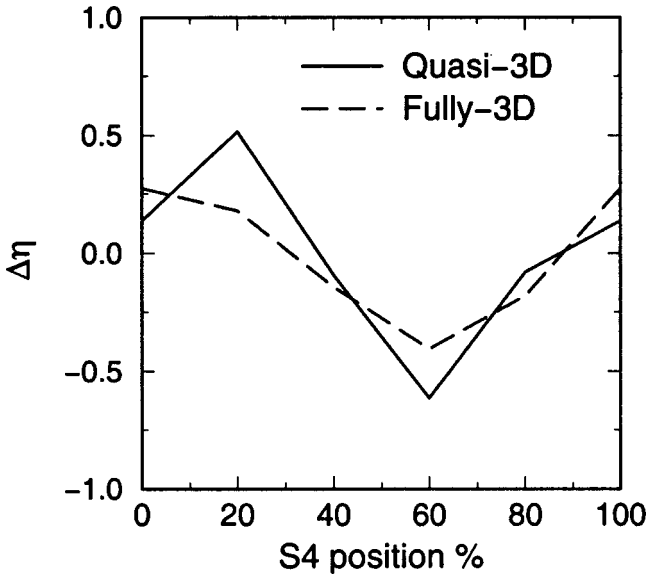

Fig. 10 Efficiency variation obtained with a quasi-three-dimensional and with a fully three-dimensional unsteady viscous analysis

minimum turbine efficiency configuration. As a consequence, the computed minimum efficiency is probably overestimated.

Effects on Wake Trajectories. Clocking effects seem to be directly linked to wake trajectories. Numerical results obtained by many authors with different numerical methods and turbulence models suggest that the maximum efficiencies can be achieved when the wake generated by a stator/rotor blade impinges on the leading edge of the next stator/rotor blade. Lower performance would correspond to a wake trajectory crossing the next stator/rotor vane [2–6].

The wake from a stator blade is convected downstream, and it is chopped into discrete spots by the leading edge of the rotating blades, and then approaches the next stator row. Such mechanism is well evidenced by the entropy contours of Figs. 8 and 9, which refer to the maximum and minimum efficiency configurations respectively.

The stator wake path is visible in the first 1.5 stage reported in Figs. 8 and 9 for the maximum and minimum efficiency configurations, respectively. The instantaneous entropy contours show how each stator wake segment, while convected through the rotor vane, is distorted and stretched as a consequence of the velocity gradient between pressure and suction side. The stator wake segment (shown by black arrows in Figs. 8 and 9) impinges the blade leading edge for the maximum efficiency configuration and is convected along the mid-vane path in the minimum one. The same situation has been observed in the rotor/rotor wake interaction and it appears very similar to the ones described by the other researchers.

It is worthwhile to notice that entropy contours can be very helpful when targeting wake paths between consecutive blade rows but the information they provide can be considered only qualitative. In the time-averaged flow field, stator wakes path appear as continuous low energy stripes, and their tangential location, compared to the successive stator leading edge, varies as a function of the circumferential position. Thus, to gain more quantitative indications on wake trajectories, one can, for example, compare traverses taken at different axial positions in the interblade gap. Figures 8(*f*) and 9(*f*) report total pressure variation traverses in front of the 4th stator for the maximum and minimum efficiency configurations. The wake energy defect and its different tangential position in the two cases is clearly evidenced. The minimum peak in total pressure is located just on the stator leading edge in the maximum efficiency configuration and about midpitch in the minimum efficiency one.

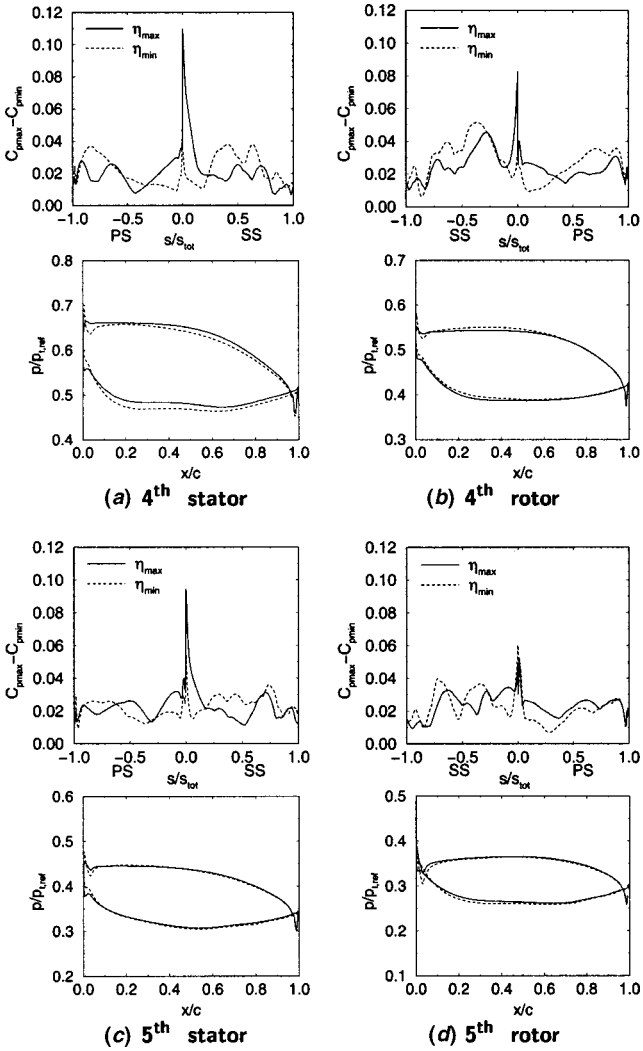

Fig. 11 Unsteady pressure coefficient distributions and time-averaged load

Assuming that performance improvements by clocking are due to the stator/rotor wake tangential position with respect to the successive stator/rotor blade, in three dimensions, this position can vary along the blade height due to blade twist and nonradial stacking, giving different contributions. Three-dimensional effects are then expected to be important (Huber et al. [2]).

Figure 10 compares the predicted efficiency variation obtained with the quasi-three-dimensional and with a fully three-dimensional unsteady viscous analysis. Maximum and minimum efficiency positions agree quite well, while the amplitude appears to be slightly overestimated by the quasi-three-dimensional approach. Such considerations can be valid for stages characterized by a relative high blade aspect ratio, while for low values of this parameter the fully three-dimensional flow field should be considered.

More multistage configurations should be analyzed before a general conclusion about the link between clocking effects and wake trajectories can be drawn.

Effects on Blade Loading. The unsteady pressure amplitude distribution was used to compare the unsteadiness levels on the blades in different configurations. The unsteady pressure coefficient is defined by

$$C_{p,\max} - C_{p,\min} = \frac{p_{\max} - p_{\min}}{p_{t,\text{ref}}} \tag{7}$$

where $p_{\min}$ and $p_{\max}$ are the minimum and maximum values of the instantaneous pressure registered during four periods.

Unsteady pressure coefficient and time-averaged pressure distributions on the 4th and 5th-stage bladings are shown in Fig. 11 for the maximum and minimum efficiency configurations respectively. As can be noticed, the maximum efficiency configuration is characterized by higher unsteady pressure coefficient values in the leading edge region.

High levels of unsteadiness in this region could be related to the stator wake segment impinging on the blade leading edge in maximum efficiency configurations, as discussed in the previous subsection. As far as the blade loading distribution is concerned, it can be noticed that, in all bladings but the 4th rotor, the maximum efficiency configuration shows higher surface pressure levels on both suction and pressure sides, as compared to the minimum efficiency one. Both circumstances, the one concerning the unsteady pressure coefficients and the one concerning the loading distributions, have also been noticed by other authors (i.e., Dorney and Sharma [3], Griffin et al. [5]). Assuming similar distributions of dissipation coefficients (Denton [29]) in the blade boundary layer for the two configurations, lower viscous losses are consistent with higher surface pressure levels. Total pressure losses would in fact be proportional to the cube of the boundary layer edge velocity, and would be lower in this case. This fact is consistent with the turbine efficiency variations and it is suspected to be related to the clocking effects.

Reynolds Number Effects

The clocking analysis was repeated for a higher Reynolds number, corresponding to *takeoff* conditions. Turbine efficiency variation maps, for the *cruise* and *takeoff* conditions, are compared in Fig. 12. The proposed clocking strategy, applied to the 4th and 5th stages, provided the same maximum and minimum turbine efficiency configurations detected for the *cruise* condition. Differences arise in the total efficiency variation which turned out to be lower for the higher Reynolds number condition. An explanation for that can be found in the wake-induced transitional patterns associated with the clocked wake segments (Halstead et al. [30]).

Time-distance diagrams of intermittency and nondimensional wall shear stress reported in Fig. 13 demonstrate how the simple model described above allows to predict a time-varying transitional pattern, with purely laminar regions embedded between intermittent stripes. In such diagrams, which refer to a generic position of the 4th stator (Arnone et al. [27]), a transitional stripe, induced by the upstream stator, is visible between two successive rotor wake paths.

At a low Reynolds number, when the blade boundary layer is laminar over most of the suction surface, the changes in wake-induced transitional paths due to clocking may have a major impact. To gain more insight into this phenomenon, one should investigate the Reynolds number effect on clocked wake-blade interaction.

Clocking With Fully Turbulent Flow

Efficiency variations are related to wake-blade interaction, and unsteady transition is expected to impact on both optimum clocking position and efficiency level. It was then decided to assess the influence of transition simulation on the results of clocking optimization. To this end, the whole analysis was repeated for the *cruise* condition with the transition model toggled off, thus assuming fully turbulent flow from the blade leading edges.

Comparisons between transitional and fully turbulent computations are shown in Table 1. It can be noticed that significant discrepancies exist between the two predictions both for the maximum and the minimum efficiency configurations. On the other hand, with different Reynolds numbers, and consequently differ-

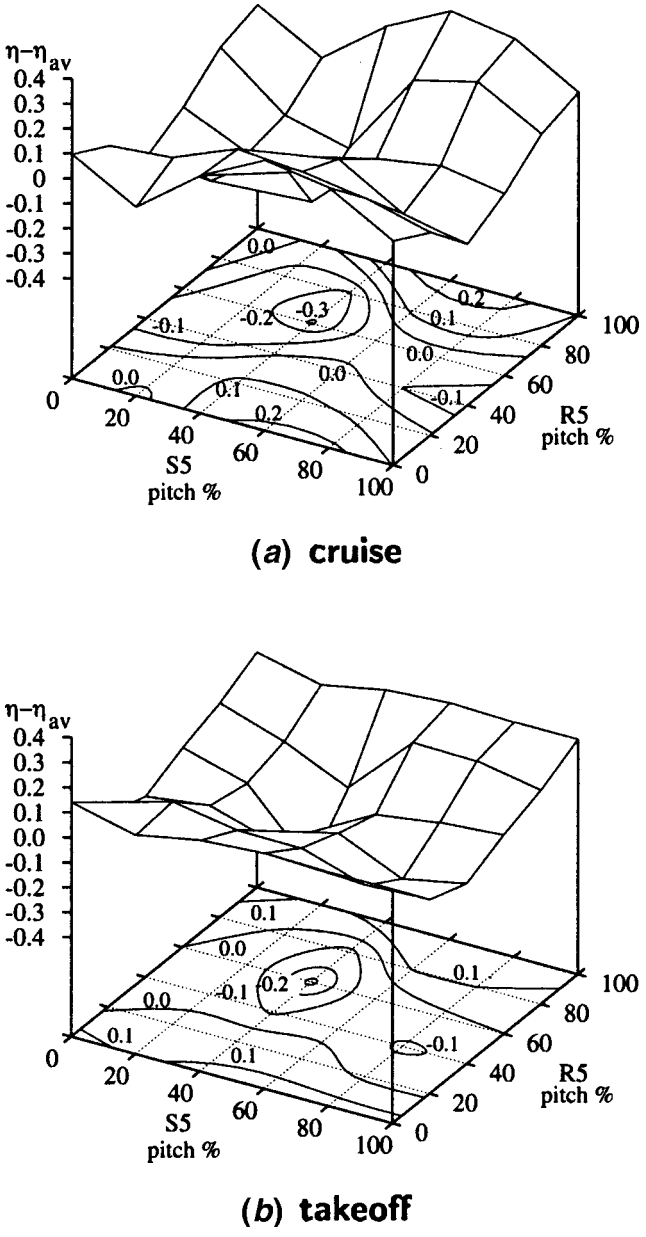

Fig. 12 Turbine efficiency variations after 5th-stage clocking

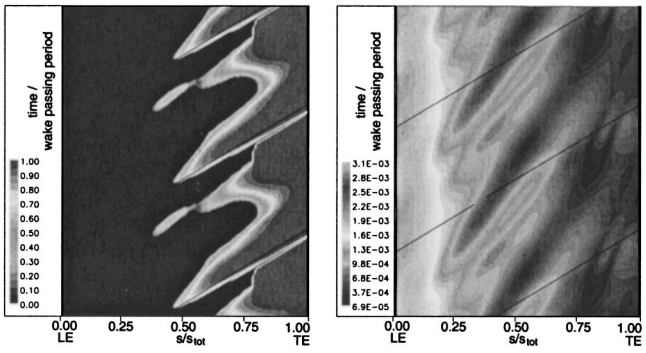

Fig. 13 Distance-time diagrams of intermittency (left) and nondimensional wall shear stress (right) for the 4th stator

Table 1 Predicted clocking positions

	$\Delta\vartheta_{S4}$	$\Delta\vartheta_{R4}$	$\Delta\vartheta_{S5}$	$\Delta\vartheta_{R5}$
$\eta_{t,max}$	20%	0%	60%	0%
$\eta_{t,min}$	80%	40%	0%	0%

(*a*) transitional flow

	$\Delta\vartheta_{S4}$	$\Delta\vartheta_{R4}$	$\Delta\vartheta_{S5}$	$\Delta\vartheta_{R5}$
$\eta_{t,max}$	0%	40%	40%	40%
$\eta_{t,min}$	40%	60%	0%	0%

(*b*) fully turbulent flow

ent unsteady transition patterns, the clocking optimization gave the same results in terms of the shape of efficiency variation maps. It can be concluded that transition plays a key role in clocking optimization for low Reynolds number flows. The assumption of fully turbulent flow leads to the prediction of optimum configuration which may be different from the one determined by a more physically realistic transitional flow.

Conclusions

A quasi-three-dimensional unsteady Navier-Stokes analysis was used to investigate the flow physics associated with *full clocking* in a three stage LP turbine. A clocking strategy was defined in order to reduce the number of configurations to analyze. Various aspects of the unsteady flow interactions associated with clocking effects have been studied. Such aspects concerned efficiency variations, wake interaction patterns, and flow unsteadiness.

The maximum efficiency variation was determined for the *cruise* condition and was estimated to be 0.7 percent, such a result is consistent with previous investigations for low pressure turbines. Computations for a higher Reynolds number corresponding to *takeoff* condition predict essentially the same efficiency map but with reduced total variations.

Maximum and minimum efficiency conditions correspond to specific wake interaction patterns. For both stators and rotors, maximum efficiency is observed when clocked wake segments impinge the blade leading edge. Vice versa, the lowest efficiency is associated with clocked wake segments following a mid-vane path. The wake interaction effects described seem to enhance leading edge flow unsteadiness when the blades are clocked to the best efficiency positions. Such configurations also correspond to the maximum level of blade surface pressure.

The comparisons with fully turbulent calculations have shown that the transitional nature of the flow has a crucial influence on clocking effects and must be taken into account.

Acknowledgments

The authors would like to express their gratitude to Prof. Ennio Carnevale for his support on this work. The authors are also indebted to the Technical Division of Fiat Avio and in particular to Drs. Emilio Ferrari, Gabriele Cartocci, and Stefania Migaldi for the numerous and useful discussions.

Nomenclature

C_p = unsteady pressure coefficient
K = boundary layer acceleration parameter
n = turbulent spot production rate
p = pressure
PS = pressure surface
Re = Reynolds number
s = curvilinear abscissa along the blade surface
SS = suction surface
T = temperature
Tu = turbulence intensity
u = velocity
η = total-to-total efficiency
γ = intermittency function, specific heat ratio
λ_ϑ = pressure gradient parameter
μ = dynamic viscosity
ν = kinematic viscosity
σ = turbulent spot propagation rate
ϑ = boundary layer momentum thickness, tangential angle

Subscripts

1 = inlet
2 = outlet
av = averaged
e = boundary layer edge
max = maximum value
min = minimum value
ref = reference value
start = transition onset
t = turbulent, total value, turbine

References

[1] Sharma, O. P., Ni, R. H., and Tanrikut, S., 1994, ''Unsteady Flow in Turbines—Impact on Design Procedure,'' AGARD Lecture Series 195, Turbomachinery Design Using CFD.
[2] Huber, F. W., Johnson, P. D., Sharma, O. P., Staubach, J. B., and Gaddis, S. W., 1996, ''Performance Improvement Through Indexing of Turbine Airfoils: Part I—Experimental Investigation,'' ASME J. Turbomach., **118**, pp. 630–635.
[3] Dorney, D. J., and Sharma, O. P., 1996, ''A Study of Turbine Performance Increases Through Airfoil Clocking,'' AIAA Paper No. 96-2816.
[4] Eulitz, F., Engel, K., and Gebing, H., 1996, ''Numerical Investigation of the Clocking Effects in a Multistage Turbine,'' ASME Paper No. 96-GT-26.
[5] Griffin, L. W., Huber, F. W., and Sharma, O. P., 1996, ''Performance Improvement Through Indexing of Turbine Airfoils: Part II—Numerical Simulation,'' ASME J. Turbomach., **118**, pp. 636–642.
[6] Cizmas, P., and Dorney, D., 1998, ''Parallel Computation of Turbine Blade Clocking,'' AIAA Paper No. 98-3598.
[7] Dorney, D. J., Sharma, O. P., and Gundy-Burlet, K. L., 1998, ''Physics of Airfoil Clocking in a High-Speed Axial Compressor,'' ASME Paper No. 98-GT-082.
[8] Gundy-Burlet, K. L., and Dorney, D. J., 1997, ''Investigation of Airfoil Clocking and Inter-Blade-Row Gaps in Axial Compressors,'' AIAA Paper No. 97-3008.
[9] Gundy-Burlet, K. L., and Dorney, D. J., 1997, ''Physics of Airfoil Clocking in Axial Compressors,'' ASME Paper No. 97-GT-444.
[10] Curtis, E. M., Hodson, H. P., Banieghbal, M. R., Denton, J. D., Howell, R. J., and Harvey, N. W., 1996, ''Development of Blade Profiles for Low Pressure Turbine Applications,'' ASME Paper No. 96-GT-358.
[11] Cobley, K., Coleman, N., Siden, G., and Arndt, N., 1997, ''Design of Three Stage Low Pressure Turbine for the BMW Rolls-Royce BR715 Turbofan Engine,'' ASME Paper No. 97-GT-419.
[12] Banieghbal, M. R., Curtis, E. M., Denton, J. D., Hodson, H. P., Huntsman, I., Schulte, V., Harvey, N. W., and Steele, A. B., 1995, ''Wake Passing in LP Turbine Blades,'' Tech. Rep., AGARD Conf., Derby, UK.
[13] Halstead, D. E., Wisler, D. C., Okiishi, T. H., Walker, G. J., Hodson, H. P., and Shin, H. W., 1997, ''Boundary Layer Development in Axial Compressors and Turbines: Part 3 of 4—LP Turbines,'' ASME J. Turbomach., **119**, pp. 225–237.
[14] Schulte, V., and Hodson, H. P., 1998, ''Unsteady Wake-Induced Boundary Layer Transition in High Lift HP Turbines,'' ASME J. Turbomach., **120**, pp. 28–35.
[15] Arnone, A., Liou, M. S., and Povinelli, L. A., 1992, ''Navier-Stokes Solution of Transonic Cascade Flow Using Non-Periodic C-Type Grids,'' J. Propul. Power, **8**, No. 2, pp. 410–417.
[16] Jameson, A., Schmidt, W., and Turkel, E., 1981, ''Numerical Solutions of the Euler Equations by Finite Volume Methods Using Runge-Kutta Time-Stepping Schemes,'' AIAA Paper No. 81-1259.
[17] Martinelli, L., and Jameson, A., 1988, ''Validation of a Multigrid Method for Reynolds Averaged Equations,'' AIAA Paper No. 88-0414.
[18] Swanson, R. C., and Turkel, E., 1987, ''Artificial Dissipation and Central Difference Schemes for the Euler and Navier-Stokes Equations,'' AIAA Paper No. 87-1107-CP.
[19] Arnone, A., and Swanson, R. C., 1993, ''A Navier-Stokes Solver for Turbo-

machinery Applications,'' ASME J. Turbomach., **115**, No. 2, pp. 305–313.
[20] Jameson, A., 1991, ''Time Dependent Calculations Using Multigrid with Applications to Unsteady Flows Past Airfoils and Wings,'' AIAA Paper No. 91-1569.
[21] Arnone, A., and Pacciani, R., 1996, ''Rotor-Stator Interaction Analysis Using the Navier-Stokes Equations and a Multigrid Method,'' ASME J. Turbomach., **118**, No. 4, pp. 679–689.
[22] Arnone, A., Pacciani, R., and Sestini, S., 1995, ''Multigrid Computations of Unsteady Rotor-Stator Interaction Using the Navier-Stokes Equations,'' ASME J. Fluids Eng., **117**, pp. 647–652.
[23] Arnone, A., and Pacciani, R., 1998, ''IGV-Rotor Interaction Analysis in a Transonic Compressor Using the Navier-Stokes Equations,'' ASME J. Turbomach., **120**, No. 1, pp. 143–155.
[24] Abu Ghannam, B. J., and Shaw, R., 1980, ''Natural Transition of Boundary Layers—The Effect of Turbulence, Pressure Gradient and Flow History,'' J. Mech. Eng. Sci., **22**, No. 5, pp. 213–228.
[25] Zerkle, R. D., and Lonsbury, R. J., 1987, ''The Influence of Freestream Turbulence and Pressure Gradient on Heat Transfer to Gas Turbine Airfoils,'' AIAA Paper No. 87-1917.
[26] Mayle, R. E., 1991, ''The Role of Laminar-Turbulent Transition in Gas Turbine Engines,'' ASME J. Turbomach., **113**, pp. 509–537.
[27] Arnone, A., Marconcini, M., Pacciani, R., and Spano, E., 1999, ''Numerical Prediction of Wake-Induced Transition in a Low Pressure Turbine,'' ISABE Paper No. 99-058.
[28] Arnone, A., and Benvenuti, E., 1994, ''Three-Dimensional Navier-Stokes Analysis of a Two-Stage Gas Turbine,'' ASME Paper No. 94-GT-88.
[29] Denton, J. D., 1993, ''The 1993 IGTI Scholar Lecture—Loss Mechanisms in Turbomachines,'' ASME J. Turbomach., **115**, No. 4, pp. 621–656.
[30] Halstead, D. E., Wisler, D. C., Okiishi, T. H., Walker, G. J., Hodson, H. P., and Shin, H. W., 1997, ''Boundary Layer Development in Axial Compressors and Turbines: Part 1 of 4—Composite Picture,'' ASME J. Turbomach., **119**, pp. 114–127.

Wake–Wake Interaction and Its Potential for Clocking in a Transonic High-Pressure Turbine

Frank Hummel
Institute of Propulsion Technology,
German Aerospace Center (DLR),
Göttingen, Germany

Two-dimensional unsteady Navier–Stokes calculations of a transonic single-stage high-pressure turbine were carried out with emphasis on the flow field behind the rotor. Detailed validation of the numerical procedure with experimental data showed excellent agreement in both time-averaged and time-resolved flow quantities. The numerical timestep as well as the grid resolution allowed the prediction of the Kármán vortex streets of both stator and rotor. Therefore, the influence of the vorticity shed from the stator on the vortex street of the rotor is detectable. It was found that certain vortices in the rotor wake are enhanced while others are diminished by passing stator wake segments. A schematic of this process is presented. In the relative frame of reference, the rotor is operating in a transonic flow field with shocks at the suction side trailing edge. These shocks interact with both rotor and stator wakes. It was found that a shock modulation occurs in time and space due to the stator wake passing. In the absolute frame of reference behind the rotor, a 50-percent variation in shock strength is observed according to the circumferential or clocking position. Furthermore, a substantial weakening of the rotor suction side trailing edge shock in flow direction is detected in an unsteady flow simulation when compared to a steady-state calculation, which is caused by convection of upstream stator wake segments. The physics of the aforementioned unsteady phenomena as well as their influence on design are discussed. [DOI: 10.1115/1.1415036]

1 Introduction

The aerodynamic design of modern aircraft engines has reached a state where most manufacturers will not fund major research projects for improving aircraft efficiency, according to Wisler [1]. However, reducing the number of blades or even stages while keeping the efficiency at a constant high level is still an issue for new engine design.

Modern high-pressure turbines (HPT) operate in a transonic flow regime. In aircraft engines they are made up of either one or two stages. The two-stage configuration is longer and heavier, but has a higher efficiency and operates in high-subsonic to low-transonic flow environment. The one-stage configuration is smaller and lighter, but the flow regime is transonic with distinct trailing edge shocks on all blades. Further details about advantages and disadvantages of both variants of HPTs are discussed by Ahmad and Mirzamoghadam [2].

Although Tiedemann and Kost [3] state that from a boundary layer point of view, an increased blade load seems possible without a major disadvantage in efficiency, there is little published work on interaction of shocks from a high-pressure turbine rotor with an adjacent second stator. This second stator can be either of the high-pressure turbine itself, or the inlet guide vane (LPT vane) of the following low-pressure turbine. The rotating shocks can cause periodic flow separations [4] and induce unsteady blade loadings to be accounted for in forced response analysis.

Jennions and Adamczyk [5] describe an experimental investigation where the difference in efficiency between an isolated LPT vane and the same vane behind a transonic HPT rotor can be as much as 5.6 percent. The authors blame the unsteady shock system behind the HPT rotor for the higher losses. In order to reduce the loss increase due to the shocks, Jennions and Adamczyk used a modified rotor blade, which shows minimum circumferential pressure variations in the wake. The overall efficiency gain of the modified HPT and the LPT vane was +0.6 percent compared with the original configuration.

Within a current research project at DLR—Göttingen, the influence of a single-stage highly loaded ($\Pi > 4{:}0$) transonic HPT on an LPT vane is investigated numerically and experimentally. In order to analyze in detail the unsteady flow field behind such a turbine, two-dimensional Navier–Stokes simulations of a similar transonic HPT at midspan were carried out. The stage used by Tiedemann and Kost [3] for a rotor boundary layer investigation was chosen for this analysis because of the excellent database existing at DLR.

2 Turbine Stage

2.1 Geometry. The investigated turbine stage was tested at the "Windtunnel for Rotating Cascades (RGG)" at DLR—Göttingen. The RGG is a continuously running, closed-circuit windtunnel. Further details of the facility are given by Tiedemann and Kost [3]. The stage was designed by Alfa Romeo Avio within a European turbine project. It is a state-of-the-art, full-size aeroengine HPT. Characteristic geometric information is supplied in Table 1. Figure 1 shows the stage at midspan and the positions of Kulite fast-response pressure transducers on the rotor blades, which will be used for validation purposes in this investigation. The trigger position is marked by a line that represents the relative position of the rotor at time $t=0$.

The vanes are equipped with a pressure side coolant ejection slot. Two different axial gaps ($\Delta x/c_{ax,s}=0.38$ and 0.49) between stator and rotor were investigated. The tip clearance of the rotor blades is assumed to be negligible due to an abrasion casing liner. Therefore, secondary flow is unlikely to influence the midspan section analyzed here and a two-dimensional numerical approach will give a good representation of the midspan flow field.

In addition to the Kulite fast pressure transducers, the rotor boundary layer was investigated by Tiedemann and Kost [3] using hot-film gages and the unsteady rotor flow field was measured by Kost et al. [6] using a Laser-2-Focus (L2F)-velocimeter.

Contributed by the International Gas Turbine Institute and presented at the 46th International Gas Turbine and Aeroengine Congress and Exhibition, New Orleans, Louisiana, June 4–7, 2001. Manuscript received by the International Gas Turbine Institute February 2001. Paper No. 2001-GT-302. Review Chair: R. Natole.

Table 1 Geometric parameters of the turbine blade rows

	Stator	Rotor
axial chord c_{ax}	29.86 mm	27.45 mm
tip radius	274.00 mm	274.00 mm
hub radius (inlet)	238.84 mm	238.00 mm
hub radius (exit)	238.84 mm	235.31 mm
aspect ratio (inlet)	0.71	1.07
stagger angle	51.90 °	32.71 °
number of blades	43	64
trailing edge diameter d	1.18 mm	0.9 mm

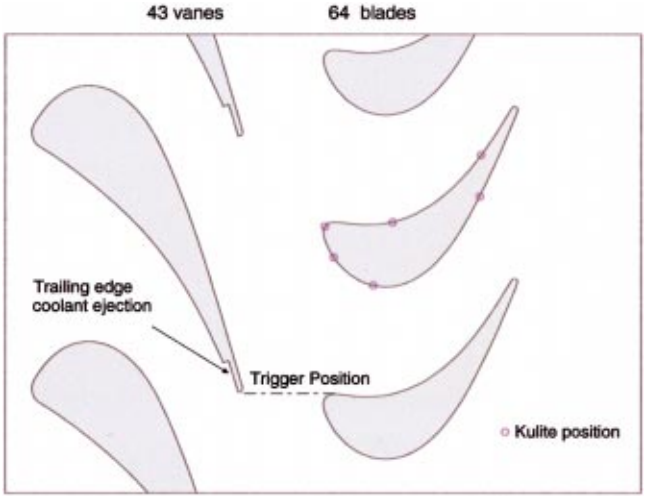

Fig. 1 Stage configuration at midspan (axial gap 0.38 $c_{ax,s}$) with trigger position indicated

2.2 Test Parameters. The operating parameters of the stage are given in Table 2. The error margins of the pressures are in the order of 0.1 percent of the measured value, temperatures are determined within ± 0.3 K, the rotor speed is accurate to within ± 1 rpm. The Mach number value in Table 2 was determined by averaging L2F measurements. The Reynolds number Re_{v2} is based on stator exit conditions and stator chord, while Re_{w3} is based on rotor exit conditions in the relative frame of reference and rotor chord.

Tests were conducted with a design coolant ejection of 3 percent of the main mass flow at the stator trailing edge and without coolant ejection. No noticeable changes in the unsteady rotor flow field or the unsteady boundary layer behavior were observed between the different tests (see Tiedemann and Kost [3] for details).

Table 2 Operating parameters of the turbine stage

inlet total temperature T_1^0 [K]	311.2
inlet total pressure p_1^0 [kPa]	131.7
relative rotor exit Mach number Ma_{w3}	0.940
absolute stator exit Reynolds number Re_{v2}	$0.866 \cdot 10^6$
relative rotor exit Reynolds number Re_{w3}	$0.396 \cdot 10^6$
absolute stator inlet angle α_1	0.0°
relative rotor exit angle β_3	−56.5°
rotor speed N [1 / min]	7894
rotor exit total temperature T_{v3}^0 [K]	243.0
rotor exit total pressure p_{v3}^0/p_1^0	0.380
rotor exit static pressure p_{v3}/p_1^0	0.316
reduced frequency Ω	1.23

The reduced frequency for the rotor flow field, affected by the stator wakes, is defined as

$$\Omega = \frac{f_s c_{ax,r}}{\overline{u}} \tag{1}$$

where f_s is the stator wake passing frequency in the relative frame of reference and $\overline{u}$ is the mean axial velocity in the rotor, which represents the convective velocity of the stator wakes. The two time scales, stator pitch t_s and rotor pitch t_r, will be used when presenting time-dependent data. They are defined as

$$t_r = \frac{60}{64N}, \quad t_s = \frac{60}{43N} \tag{2}$$

3 Numerical Method

For the numerical computations, the parallelized multi-block Navier–Stokes Code "TRACE—U" of the DLR Institute for Propulsion Technology was used. The program is based on the two-dimensional Reynolds-averaged Navier–Stokes equations for a compressible ideal gas. A source term is added to account for varying stream-tube thickness. Turbulence is treated by an eddy-viscosity transport model according to Spalart and Allmaras, which has been split up by Eulitz et al. [7] into a two-layer formulation. The transition point is specified separately on the pressure and the suction side by the user. The discretization is of second order, both in time and space. Time integration is done by a four-stage Runge–Kutta scheme. Further details about the numerical model are presented by Eulitz et al. [8] and Eulitz and Engel [9]. Nonreflecting boundary conditions are employed at inlet and outlet boundaries according to Acton and Cargill [10] as well as the time-accurate coupling of moving and nonmoving grid interfaces by the sheared-cell technique according to Giles [11].

The vane/blade number ratio of 43/64 is close to 2/3; therefore, the pitches of the blade rows can be adjusted to match the ratio of 2/3. For the calculations presented, the rotor geometry was adjusted, because under design conditions the vane was supposed to be choked, and therefore the mass flow through the stage is less sensitive to the rotor pitch.

Within the computational domain, two vanes and three blades are represented by a total of 100,000 mesh points. The vane surface contains 241 points, the blade surface 316. The grid topology is of HOH-type, the value of y^+ for the first grid line above the wall is 1.0–2.0 for the vanes and 0.5–1.0 for the blades. Stator blades with full trailing edges were chosen for the computation. Note that the cascade measurements of Kapteijn et al. [12] demonstrated that there is no significant difference between the full trailing edge stator without coolant ejection and the stator with a coolant slot on the pressure side with coolant ejection. Furthermore, Tiedemann [3] showed that the stator trailing edge cooling had no significant effect on transition and pressure distribution on the rotor blade.

The trailing edges of the vanes and blades are resolved by 50 mesh points. For both axial gaps between stator and rotor ($\Delta x/c_{ax,s} = 0.38$ and 0.49) an identical mesh structure was used. The resulting grid is show in Fig. 2.

At the inlet boundary total pressure, total temperature and flow angle and at the exit boundary the static pressure is prescribed according to Table 2. The inlet turbulence is fixed by a free-stream value for the eddy-viscosity of $\mu_t/\mu_l = 1 \times 10^{-4}$. Transition points for the pressure sides of both vane and blade were set at the trailing edges. The transition point for the vane suction side was set at peak suction. On the blade suction side, the transition point was set at the end of a shock-boundary interaction zone according to hot-film data of Tiedemann and Kost [3], i.e., $x/c_{ax,r} = 0.76$. The stream tube thickness was evaluated according to mass flow rates computed from the L2F data. The unsteady flow field was recorded 128 times in one period. One simulation period is the time one rotor blade needs to pass two stator vanes. The sampling

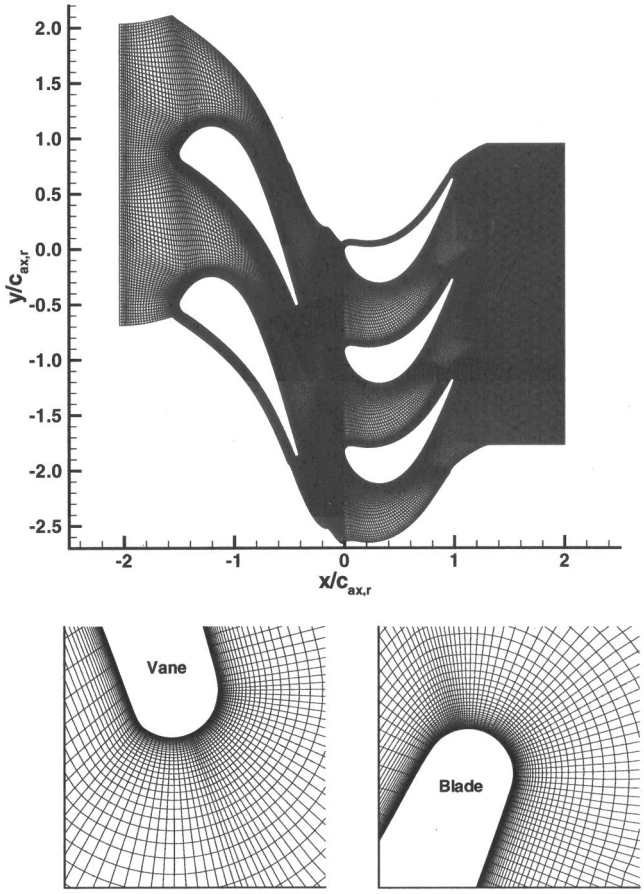

Fig. 2 Computational grid, entire domain, and details of vane and blade trailing edges

frequency for the simulation is 363.57 kHz. The unsteady stage simulation was run for 12 simulation periods before recording the unsteady flow field.

4 Validation of the Numerical Method

Figure 3 shows the comparison between time-averaged surface isentropic Mach numbers from computation and experiment. The experimental data are obtained by extrapolating L2F measurements onto the blade surface. Details about the measurements and the extrapolation are discussed by Kost et al. [6]. The experimental data shown were taken with the stator trailing edge cooling slot ejecting a $c_m = 3$ percent mass flow. Because all L2F data were measured for the small axial gap of $\Delta x/c_{ax,s} = 0.38$, the results from the calculation shown in Fig. 3 are also from the small gap simulation.

The good overall agreement of simulation and experiment in the rotor blade Mach number distribution underlines the small influence of the stator trailing edge cooling, omitted in the simulation, on the operating point of the rotor. The slightly lower Mach numbers in the simulation at $x/c_{ax,r} = 0.1$ on the suction side indicate a small discrepancy in the incidence angle.

Figure 4 shows the comparison between the measured and calculated pressure fluctuations at the six measurement positions on the rotor surface, which are marked in Fig. 1 as Kulite positions. The experimental data was ensemble-averaged; details about the data processing are given by Tiedemann and Kost [13]. Since the experimental pressure fluctuations were recorded for the large axial gap configuration ($\Delta x/c_{ax,s} = 0.49$) only, the pressure fluctuations from the simulation in Fig. 4 are also for the large gap case.

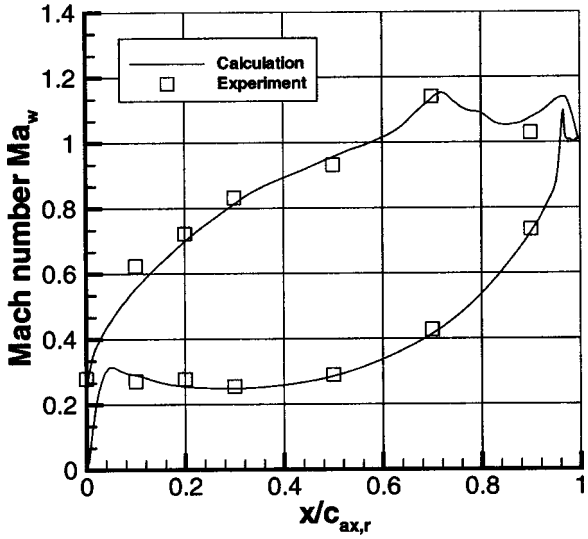

Fig. 3 Comparison of the time-averaged rotor blade isentropic surface Mach numbers from computation with values from the L2F measurements (obtained by extrapolating to the blade surface)

The agreement between the pressure fluctuations in experiment and simulation regarding amplitude and phase is good at all six measurement positions. Within the calculated pressure fluctuations, two distinct superposed frequency bands are observed; the lower one is connected to the stator wake passing, the higher one is caused by the stator vortex street. The experimental data do not

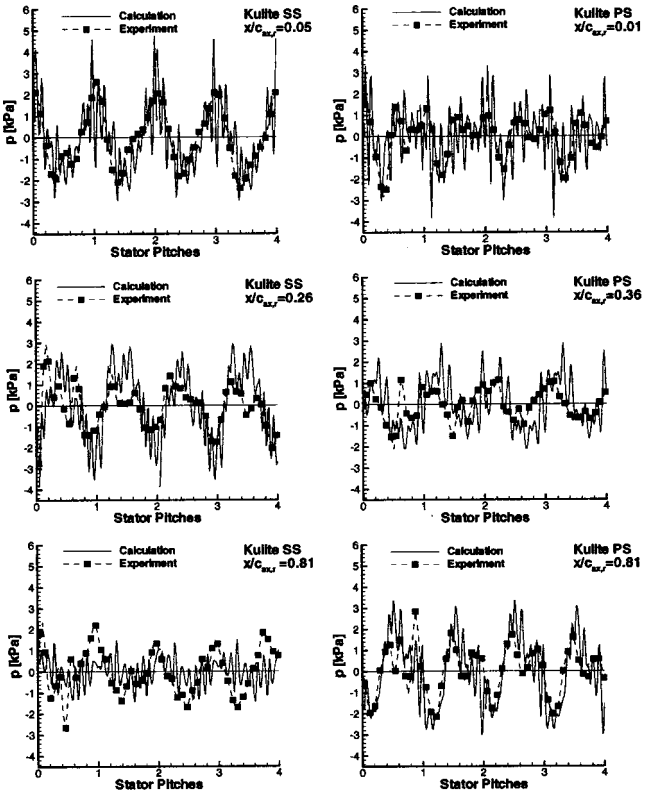

Fig. 4 Measured and calculated pressure fluctuations at the rotor blade surfaces (gap $0.49c_{ax,s}$; SS=suction side, PS =pressure side)

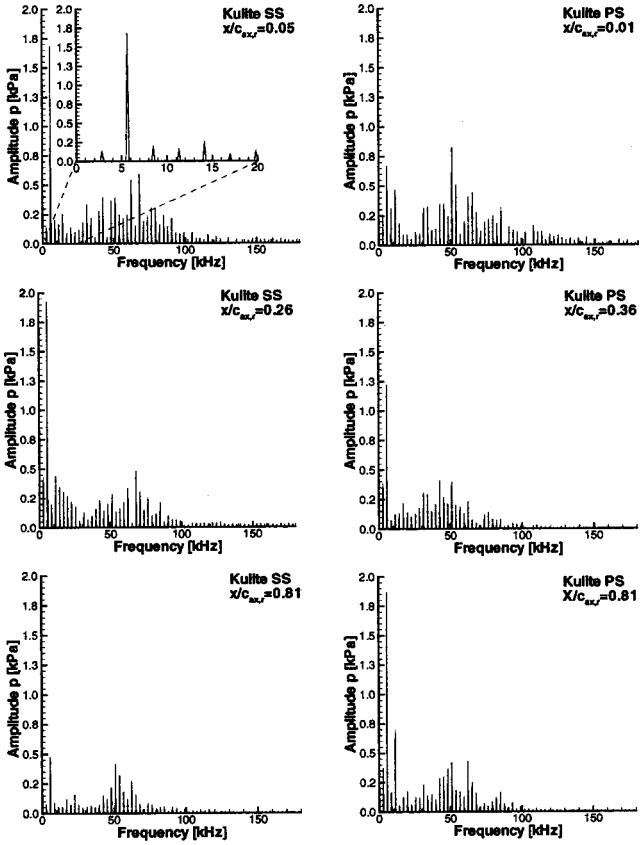

Fig. 5 Calculated frequency spectra of pressure fluctuations at the rotor blade surfaces (SS=suction side, PS=pressure side)

show the higher frequency band because the cut-off frequency of the data processing of 45 kHz was too low for resolving the higher frequency band.

A comparison of the calculations presented here with the time-dependent flow field in the rotor passage measured with the L2F velocimeter gives a similarly good agreement as discussed by Kost et al. [6].

5 Results and Discussion

5.1 Stator Vortex Street. As indicated by the pressure fluctuations on the rotor blade, the stator vortex street is strongly influencing the rotor inlet flow field. Figure 5 shows the Fourier decomposition of the pressure fluctuations on the rotor blades in terms of amplitude frequency spectra. For all six positions, the vane passing frequency of 5.66 kHz and its first and second harmonic are recognizable at the bottom end of the frequencies shown. A second area of amplitude peaks lies around 50–75 kHz for all six positions and is related to the stator vortex street. The vortex street causes a broad spectrum and not a distinct frequency, which is in good agreement to the observations of Sondak and Dorney [14]. The reason for this effect is the modulation of the time-periodic flow separation at the stator trailing edge by the unsteady pressure field of the blades rotating behind the stator. Therefore, the stator vortex street will adopt higher harmonics of the blade passing frequency. Sondak and Dorney [14] found that the stator vortex street in their stage simulation had an amplitude peak between the sixth and ninth harmonic of the blade passing frequency. All six positions in Fig. 5 show amplitude peaks in the frequency band between 50–75 kHz, which corresponds to the sixth through ninth harmonic of the blade passing frequency (8.4 kHz) for this case; so again, there is good agreement with Sondak and Dorney's stage simulations.

With a circumferentially averaged stator exit velocity of $U=280$ m/s computed from the simulated flow field and the trailing edge diameter from Table 1, the Strouhal number

$$\mathrm{Sr}=\frac{fd}{U} \tag{3}$$

for a frequency band of $f=50-75$ kHz lies between Sr=0.2 and 0.3. Heinemann and Bütefisch [15] found exactly the same spectrum for isolated turbine cascades in an experimental study.

A vortex street causes not only pressure fluctuation, but also total temperature distortions in the wake of a blunt body, discovered by Eckert and Weise [16]. The connection between pressure fluctuations and total temperature distortions becomes apparent when looking at the well-known first law of thermodynamics for an adiabatic flow of a perfect gas [17]

$$\frac{Dh^0}{Dt}=Cp\frac{DT^0}{Dt}=\frac{1}{\rho}\frac{\partial p}{\partial t} \tag{4}$$

Kurosaka et al. [18] describe that the pressure fluctuations, of a vortex street lead to a total temperature distribution, where on the outside part of a vortex street toward the main flow, the total temperature is higher than in the main flow, and on the inside of the vortex street toward the centerline of the wake, the total temperature is lower than in the main flow.

Figure 6 shows the calculated vorticity and total temperature distribution behind the vane at an instant in time. The vorticity is defined as

$$\omega=\frac{\partial v}{\partial x}-\frac{\partial u}{\partial y} \tag{5}$$

The vorticity is negative shed from the vane suction side, and positive from the pressure side. The vorticity distribution shows that the suction side boundary layer is about twice as thick at the trailing edge as the pressure side boundary layer. However, the vortices shed from the pressure side are much stronger than from the suction side due to the steeper velocity gradients normal to the wall at the pressure side trailing edge.

In Fig. 6, the center of one vortex in the pressure side branch of the vortex street is marked in the vorticity distribution as well as in the total temperature distribution. The total temperature distribution shows the distinct increased total temperature on the outside and the decreased total temperature on the inside portion of the marked vortex compared to the total temperature of the main flow. The increase in total temperature on the outside portion of the vortices at the marked vortex position is $\Delta T^0=+14$ K, the decrease on the inside portion of the vortices is $\Delta T^0=-9$ K from the main flow value of $T^0=311$ K. Carscallen et al. [19] found experimentally for a vane cascade with an exit Mach number of Ma=0.95 T^0 an increase of $\Delta T^0=+8$ K and a decrease of $\Delta T^0=-16$ K at 5.76 times the trailing edge diameter behind the vane trailing edge. The marked vortex in Fig. 6 is geometrically approximately at that position. Despite a small discrepancy in positive and negative amplitude, there is good agreement in the total temperature fluctuation with Carscallen's [19] work.

5.2 Rotor Vortex Street and Wake–Wake Interactions. The vorticity and total temperature distribution in the relative frame of reference within and behind the rotor are shown in Figs. 7 and 8. The time-dependent flow field behind the rotor is much more complex than behind the stator because of the time-periodic stator wake passing. The stator wakes are chopped by the rotor leading edge and convected through the rotor; details of this process are given by Hodson and Dawes [20].

The rotor vortex street differs from the stator vortex street close to the blade trailing edge. The vorticity shed by the rotor departs from the blade trailing edge in a smooth way until the wake in-

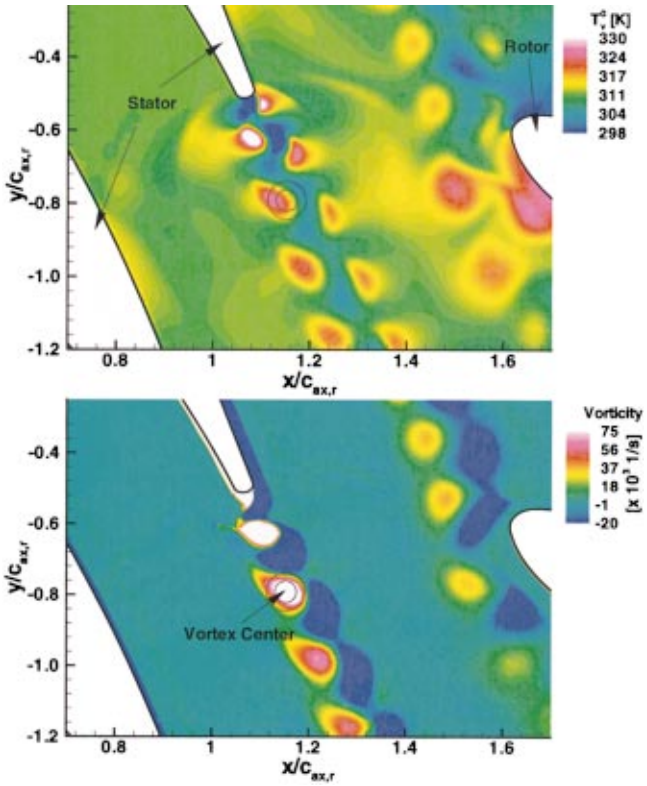

Fig. 6 Total temperature and vorticity distribution behind the stator, absolute frame of reference

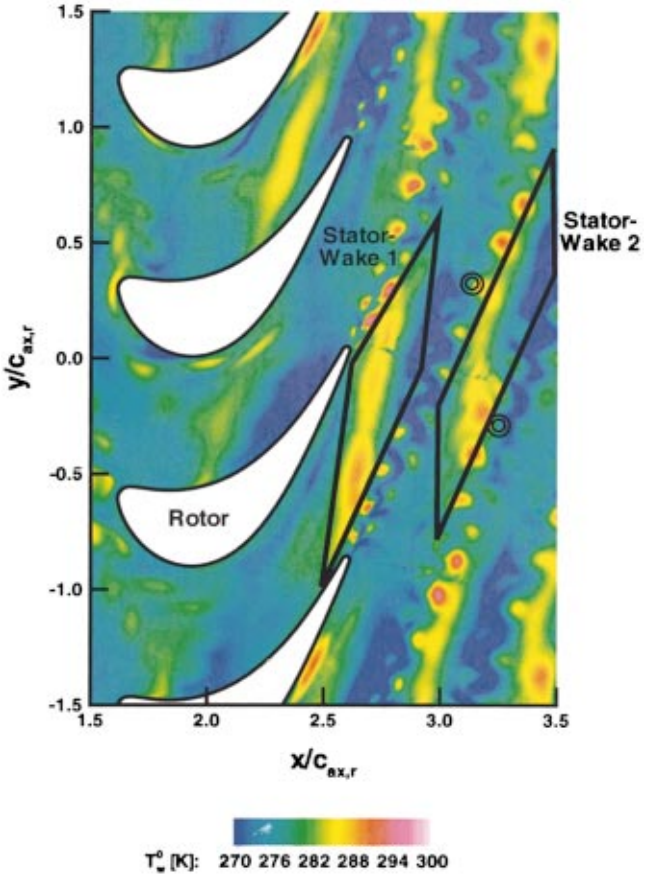

Fig. 8 Total temperature distribution behind the rotor, relative frame of reference

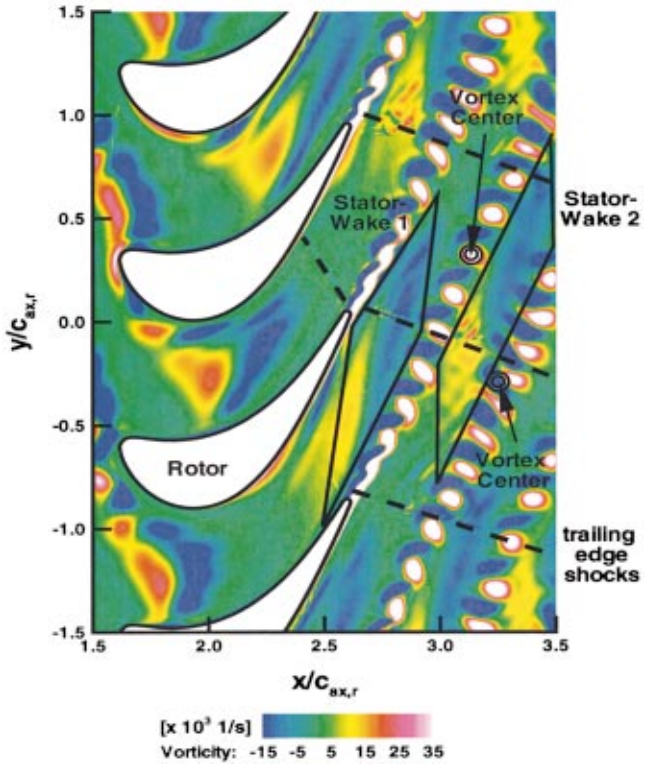

Fig. 7 Vorticity distribution behind the rotor, relative frame of reference

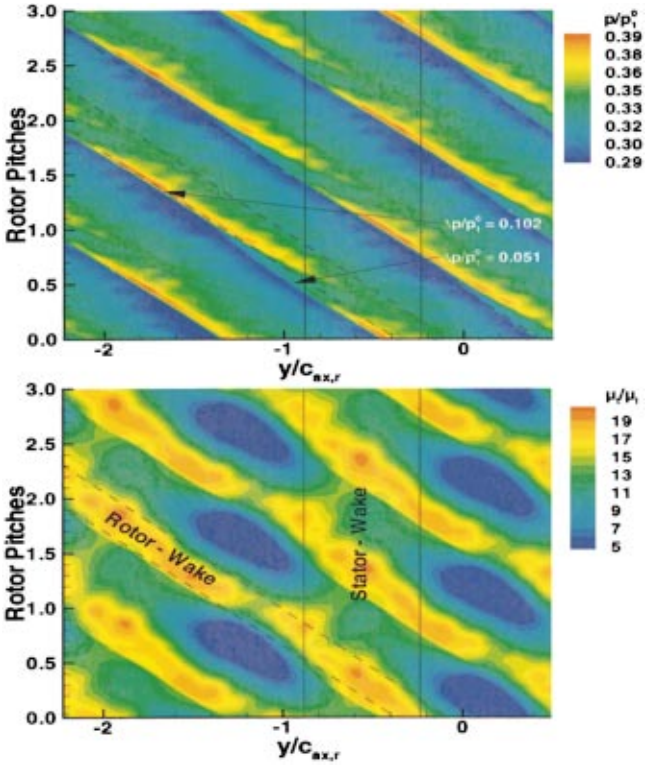

Fig. 9 Space–time diagram of normalized static pressure and eddy viscosity at $\Delta x/c_{ax,s}=0.4$ behind the rotor trailing edge

terferes with the rotor trailing edge shocks, which act as an instability on the wake causing the evolution of the vortex street. The reason for this difference in the structure of the vortex street is the supersonic flow regime at the rotor trailing edge compared to the high subsonic flow field at the stator trailing edge. Nash [21] gives experimental evidence of this structural change in the development of a vortex street by a series of Schlieren pictures of a blunt body for exit Mach numbers ranging from Ma=0.925 to 1.05.

Two stator wake segments are marked in Fig. 7 and can be identified by coupled fields of counterrotating vorticity. Outside the blade boundary layers these stator wake segments are convected through the rotor passage at the local free-stream velocity.

Von Kármán [22] found that the convective speed of the vortex centers in an incompressible and frictionless flow is given by

$$u_s = U - fl \tag{6}$$

where U is the free-stream velocity, f the frequency of the vortex shedding, and l is the distance between two vortices in the same vortex street branch (shed from the suction or pressure side of the trailing edge). Disregarding compressibility effects, Eq. (6) shows that the vortices depart from the blade trailing edge with a smaller convective velocity than the main stream, which convects the stator wake segments. Therefore, the stator wake segments shown in Fig. 7 move past the vortices of the rotor vortex streets with an approximate relative velocity of $fl=135$ m/s ($f\approx 75$ kHz, $l\approx 2\times d_r$) according to Eq. (6).

While passing the vortices within the rotor vortex street, the vorticity of the stator wake segment modulates the vortices in a way that some are enhanced while others are diminished. In order to gain further understanding of this process, Fig. 8 shows the total temperature distribution in the relative frame of reference. In the near field close to the rotor trailing edge, the energy separation according to Eq. (4) is observable. As shown for the stator vortex street, one would expect a decrease in vorticity and total temperature extrema due to wake mixing and dissipation with increasing distance from the rotor trailing edge. The total temperature distribution in Fig. 8 shows a different behavior in the vicinity of the stator wake segment titled ''Stator-Wake 2.'' On the edge of that stator wake segment, two vortices in different blade wakes are marked according to the vorticity distribution. The total temperature distribution shows that the vortices marked have higher total temperature peaks than vortices within the same vortex street which are closer to the blade trailing edges. These vortices can only be enhanced by the passing stator wake segments.

Figure 10 shows a schematic explanation of the wake–wake interaction process by suggesting a superposition of unsteady velocity components caused by both stator and rotor wakes. In terms of unsteady velocity, the stator wake segment causes the well-known negative jet structure [20] with counterrotating vortexlike

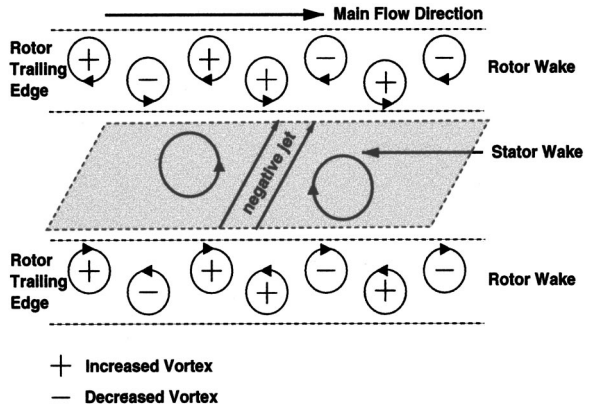

Fig. 10 Schematic of wake–wake interaction behind the rotor, relative frame of reference

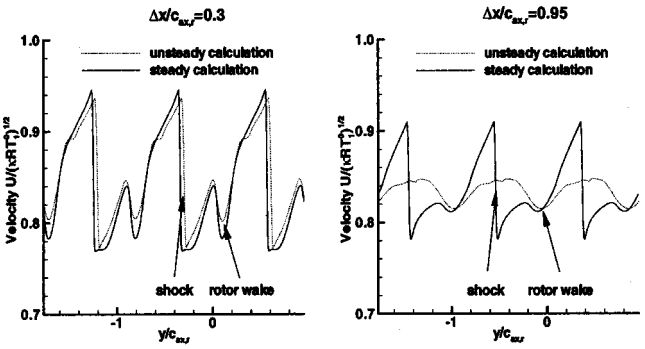

Fig. 11 Comparison of rotor wake decay for steady and time-averaged unsteady simulation at two axial positions behind the rotor trailing edge ($U=\sqrt{u^2+v^2}$, in relative frame of reference)

structures on each side of the jet center. The blade vortex streets are represented by lanes of vortices with alternating sense of rotation. Vortices that gain in strength are marked by a ''+,'' the ones that reduce in strength by a ''−.'' The vortices that meet in the contact area between the vortex and the negative jet (or the vortexlike unsteady velocity structure connected with it) are enhanced if their unsteady velocity vectors along the contact area are in the same direction. If both vectors are in the opposite direction, then the von Kármán vortex is diminished in strength. This modulation by increasing and decreasing certain vortices will certainly lead to a destabilization of the vortex street and an increased mixing of the rotor wakes.

The rotor wake decay is shown in Fig. 11 by looking at the velocity profiles in the relative frame of reference at two different axial positions behind the rotor. At both positions, the velocity profiles for a steady-state and the time-averaged velocity from an unsteady calculation are compared in order to analyze the influence of time-periodic stator wake passing on the rotor wakes. The shock and wake positions are marked for both axial positions.

At the axial position $\Delta x/c_{ax,r}=0.3$ behind the rotor trailing edge, there is little discrepancy between steady and unsteady calculation observable; therefore, close to the rotor trailing edge the influence of the passing stator wakes on the rotor wakes is small. The depth of the rotor wake in the unsteady calculation is smaller than in the steady calculation, indicating that the wake mixing is stronger in the stator wake-affected unsteady calculation. At the axial position $\Delta x/c_{ax,r}=0.95$, behind the rotor trailing edge, there is a large difference in the velocity profiles of steady and unsteady calculation observed. The difference is based on the rotor trailing edge shock, which seems to have disappeared in the time-averaged unsteady calculation. The rotor wakes have similar depths in steady and time-averaged unsteady calculation, but they are broader in the unsteady results, indicating a stronger wake mixing due to the unsteady stator wake passing.

Despite the slightly increased wake decay in the unsteady simulation, the dominant impact of the stator wake passing seems to be on the rotor trailing edge shocks, which will be analyzed in the next section.

5.3 Rotor Trailing Edge Shocks. Figure 9 shows space-time diagrams of the eddy viscosity and the static pressure at an axial position of $\Delta x/c_{ax,r}=0.4$ behind the rotor trailing edge in the absolute frame of reference. The $y/c_{ax,r}$ axis corresponds to the circumferential direction. The time is given in rotor pitches according to Eq. (2).

The axial distance of $\Delta x=c_{ax,r}=0.4$ from the rotor trailing edge chosen for this analysis is typical of axial gaps in high-pressure turbines. Within the eddy-viscosity distribution, a rotor wake and a stator wake were marked according to their comparatively higher values of eddy viscosity. The rotor wakes move in time toward the $y/c_{ax,r}$ direction because the rotor is rotating in

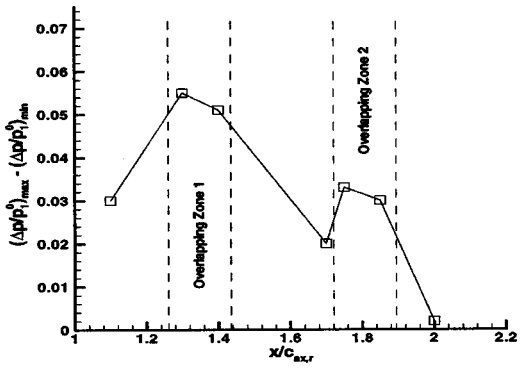

Fig. 12 Clocking potential for reduction of shock strength behind the rotor

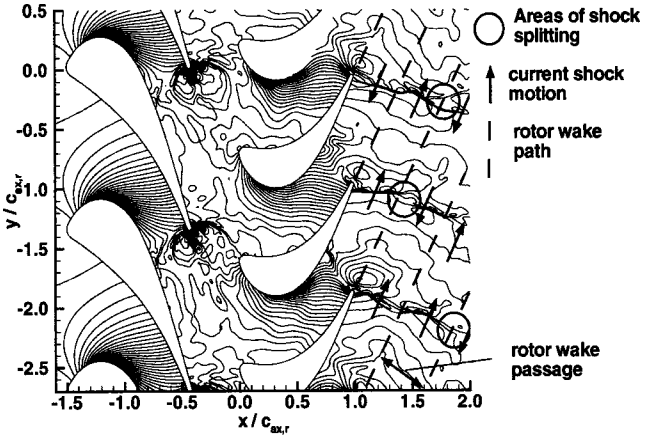

Fig. 13 Static pressure field at an instant in time, showing the unsteadiness of the rotor trailing edge shocks

that direction. The stator wakes exit the rotor in the absolute frame of reference at all times at the same circumferential position.

The space–time diagram of the static pressure in Fig. 9 shows the rotor suction side trailing edge shocks as lines of high pressure parallel to the rotor wake paths. Rotor wake and shock paths are parallel because both rotate with the same speed in the absolute frame of reference. For the axial distance shown, the rotor trailing edge shocks and the suction side edge of the rotor wakes coincide. While the shocks are rotating in the absolute frame of reference, a modulation in shock strength according to the circumferential position is observed. The modulation in the space–time diagram is parallel to the stator wake path, so it can be assumed that the stator wakes cause the circumferential variation in shock strength.

The difference between maximum static pressure after and minimum static pressure ahead of the shock ($\Delta p/p_1^0$, p_1^0; see Table 2) was chosen as an indicator for the shock strength a second stator behind the HPT rotor might encounter. A variation in shock strength from $\Delta p/p_1^0 = 0.051-0.102$ or 50 percent occurs at the axial position of $\Delta x/c_{ax,r} = 0.4$ behind the rotor trailing edge. The positions of the extrema are marked in Fig. 9.

Therefore, it seems possible to reduce the impact of the rotor trailing edge shocks of a highly loaded HPT on a second stator by clocking the second stator. From a designer's point of view it is especially interesting how the potential of the shock strength reduction varies with axial distance. The clocking-potential in terms of shock reduction will be discussed by looking at the difference between maximum and minimum shock strength $((\Delta p/p_1^0)_{\max} - (\Delta p/p_1^0)_{\min})$ in circumferential direction at a fixed axial position.

Figure 12 shows the potential for a reduction of shock strength by clocking as a function of the axial position behind the rotor. The rotor trailing edge is located at $x/c_{ax,r} = 1.0$.

Two relative maxima of the shock strength clocking potential occur at $x/c_{ax,r} = 1.35$ and 1.8. Both axial positions connected to these maxima are characterized by an interaction of the rotor trailing edge shocks, the rotor wakes of the next or a third blade (overlapping zone 2) in the circumferential direction, and the stator wake segments. The reason for this weakening of the rotor trailing edge shocks at the mentioned axial locations for certain circumferential positions is a splitting of the shocks due to stator wake-induced shock motions in the relative frame of reference.

Figure 13 shows the static pressure field of the calculated HPT stage at an instant in time. The wake paths of the blades are indicated by dashed lines. The blade wakes split the relative flow field behind the rotor into several passages. Within each rotor wake passage, stator wake segments are convected through the rotor modulating the flow field and forcing the rotor trailing edge shocks forward and backward while passing. The current direction of that shock motion is indicated in Fig. 13 for all three shocks depicted and all three rotor wake passages that lie within the computational domain. Due to phase differences in the modulation process between the single rotor wake passages, each rotor trailing edge shock is modulated in three different phases on its way from the blade trailing edge to the outflow boundary of the computational domain. This leads to a shearing or splitting of the shocks at the boundary lines of the rotor wake passages, which are given by the rotor blade wakes. The splitting of the shocks within the rotor wakes induced by the stator wake segments causes a significant reduction in shock strength observed at those circumferential positions where the stator wake segments pass periodically.

At the outflow boundary of the computational domain, the shock modulation has reached an amplitude where it is no longer detectable in a time-averaged velocity profile of an unsteady calculation, as shown in Fig. 11 at the axial position $\Delta x/c_{ax,r} = 0.95$. The steady-state calculation in that figure does not account for time-periodic stator-wake effects, and therefore the shock is still clearly detectable in the velocity profiles.

To reduce the impact of the rotor trailing edge shocks on a downstream stator for future highly loaded HPT/LPT designs, the stator/stator blade count ratio should be suitable for clocking applications. If the second stator is placed with its leading edge at that axial position where rotor wake and rotor trailing edge shock interact, it should be possible to reduce the strength of the rotor shocks by as much as 50 percent by selecting an ideal clocking position.

Future work will be concentrated on the influence of a second vane on the effects mentioned here as well as the three-dimensional influences of a highly loaded HPT rotor on an LPT vane.

6 Conclusions

The two-dimensional unsteady flow field behind a transonic single HPT stage at midspan has been numerically investigated. The simulation showed excellent agreement to experimental data for time-averaged and time-dependent flow quantities. The vortex streets of both stator and rotor were resolved in the calculated flow field. A significant influence of the vorticity shed by the stator on the vortices within the rotor wake is described and analyzed. A modulation of the rotor trailing edge shock system is observed in the absolute frame of reference. A maximum reduction in shock strength of 50 percent was found by varying the axial distance and the circumferential position behind the rotor in the absolute frame of reference. A guideline for positioning a second stator behind the transonic HPT rotor to minimize the shock strength is provided.

Acknowledgments

Part of this work has been sponsored through a scholarship by MTU Mororen- und Turbinen-Union München GmbH. The author gratefully acknowledges the financial support by MTU. Thanks also to F. Kost and M. Tiedemann of DLR Göttingen for providing the experimental data. Frank Eulitz and Dirk Nürnberger from DLR Cologne supplied me with the Navier–Stokes code. Special thanks to them too. Also, thanks to Paul Petrie-Repar of DLR Göttingen who added a native speaker's touch to my poor English and gave helpful comments.

Nomenclature

c = chord
d = diameter
h = enthalpy
N = rotor speed
p = pressure
t = time
u = streamwise velocity
U = velocity
r = radius
c_m = coolant mass flow ratio
f = frequency
l = distance
Ma = Mach no.
R = gas constant
T = temperature
u_s = convective velocity
v = transverse velocity
Sh = Strouhal no.
x = axial coordinate
α = angle (absolute frame)
κ = specific heat ratio
Π = total-to-total pressure ratio
ω = vorticity
y = circumferential coordinate
β = angle (relative frame)
μ = dynamic viscosity
ρ = density
Ω = reduced frequency

Subscripts

s = stator
ax = axial
t = turbulent
v = absolute frame of reference
1,2,3 = stator inlet, stator exit/rotor inlet, rotor exit
r = rotor
l = laminar
w = relative frame

Subscripts

$'$ = unsteady part
$\overline{}$ = time-averaged or mean value
0 = total condition

References

[1] Wisler, D. C., 1998, "The Technical and Economic Relevance of Understanding Blade Row Interaction Effects in Turbomachinery," Von Kármán Institute for Fluid Dynamics, Lecture Series 1998-02 on *Blade Row Interference Effects in Axial Turbomachinery Stages*.

[2] Ahmad, F., and Mirzamoghadam, A. V., 1999, "Single vs. Two-Stage High-Pressure Turbine Design of Modern Aero Engines," ASME Paper No. 99-GT-1.

[3] Tiedemann, M., and Kost, F., 1999, "Unsteady Boundary Layer Transition on a High Pressure Turbine Rotor Blade," ASME Paper No. 99-GT-194.

[4] Doorly, D. J., and Oldfield, M. L. G., 1985, "Simulation of the Effects of Shock Wave Passing on a Turbine Rotor Blade," ASME J. Eng. Gas Turbines Power, **107**, pp. 998–1006.

[5] Jennions, I. K., and Adamczyk, J. J., 1997, "Evaluation of the Interaction Losses in a Transonic Turbine HP Rotor/LP Vane Configuration," ASME J. Turbomach., **119**, pp. 68–76.

[6] Kost, F., Hummel, F., and Tiedemann, M., 2000, "Investigation of the Unsteady Rotor Flow Field in a Single HP Turbine Stage," ASME Paper No. 2000-GT-432.

[7] Eulitz, F., Engel, K., and Gebing, H., 1986, "Application of a One-Equation Eddy-Viscosity Model to Unsteady Turbomachinery Flow," *Engineering Turbulence Modelling and Experiments 3*, W. Rodi and G. Bergeles, eds., Elsevier Science B.V.

[8] Eulitz, F., Engel, K., and Gebing, H., 1996, "Numerical Investigation of the Clocking Effects in a Multistage Turbine," ASME Paper No. 96-GT-26.

[9] Eulitz, F., and Engel, K., 1998, "Numerical Investigation of Wake Interaction in a Low Pressure Turbine," ASME Paper No. 98-GT-563.

[10] Acton, E., and Cargill, M., 1988, "Non-Reflecting Boundary Conditions for Computations of Unsteady Turbomachinery Flow," *Proc. 4th Int. Symp. on Unsteady Aerodynamics and Aeroelasticity of Turbomachines and Propellers*, pp. 211–228.

[11] Giles, M. B., 1988, "Non-Reflecting Boundary Conditions for the Euler Equations," Technical Report CFDL-TR-88-1.

[12] Kapteijn, C., Amecke, J., and Michelassi, V., 1996, "Aerodynamic Performance of a Transonic Turbine Guide Vane with Trailing Edge Coolant Ejection: Part I—Experimental Approach," ASME J. Turbomach., **118**, pp. 519–528.

[13] Tiedemann, M., and Kost, F., 2001, "Some Aspects of Wake–Wake Interactions Regarding Turbine Stator Clocking," ASME J. Turbomach., **123**, pp. 526–533.

[14] Sondak, D. L., and Dorney, D. J., 1999, "Simulation of Vortex Shedding in a Turbine Stage," ASME J. Turbomach., **121**, pp. 428–435.

[15] Heinemann, H.-J., and Bütefisch, K. A., 1977, "Determination of the Vortex Shedding Frequency of Cascades With Different Trailing Edge Thicknesses," AGARD–CP-227.

[16] Eckert, E., and Weise, W., 1942, "Messungen der Temperaturverteilung auf der Oberfläche schnell angeströmter unbeheizter Zylinder," Forschg. Ing.-Wes., **13**, No. 6.

[17] Liepmann, H. W., and Roshko, A., 1957, *Elements of Gasdynamics*, Galcit Aeronautical Series, Wiley, New York.

[18] Kurosaka, M., Gertz, J. B., Graham, L. E., Goodman, J. R., Sundaram, P., Riner, W. C., and Hankey, W. L., 1987, "Energy Separation in a Vortex Street," J. Fluid Mech., **178**, pp. 1–29.

[19] Carscallen, W. E., Currie, T. C., Hogg, S. I., and Gostelow, J. P., 1999, "Measurement and Computation of Energy Separation in a Vortical Wake Flow of a Turbine Nozzle Cascade," ASME J. Turbomach., **121**, pp. 703–708.

[20] Hodson, H. P., and Dawes, W. N., 1998, "On the Interpretation of Measured Profile Losses in Unsteady Wake–Turbine Blade Interaction Studies," ASME J. Turbomach., **120**, pp. 276–284.

[21] Nash, J. F., 1962, "A Review of Research on Two-Dimensional Base-Flow," Reports and Memoranda of the Aeronautical Research Council, No. 3323, London.

[22] von Kármán, T., 1911, "Über den Mechanismus des Widerstandes, den ein bewegter Körper in einer Flüssigkeit erfährt," *Nachrichten der K. Gesellschaft der Wissenschaften zu Göttingen. Mathematischphysikalische Klasse*, Göttingen, pp. 324–338.

The Fluid Dynamics of LPT Blade Separation Control Using Pulsed Jets

Jeffrey P. Bons
Air Force Institute of Technology,
Wright-Patterson AFB, OH 45433

Rolf Sondergaard

Richard B. Rivir

Air Force Research Laboratory,
Wright-Patterson AFB, OH 45433

The effects of pulsed vortex generator jets on a naturally separating low-pressure turbine boundary layer have been investigated experimentally. Blade Reynolds numbers in the linear turbine cascade match those for high-altitude aircraft engines and industrial turbine engines with elevated turbine inlet temperatures. The vortex generator jets (30 deg pitch and 90 deg skew angle) are pulsed over a wide range of frequency at constant amplitude and selected duty cycles. The resulting wake loss coefficient versus pulsing frequency data add to previously presented work by the authors documenting the loss dependency on amplitude and duty cycle. As in the previous studies, vortex generator jets are shown to be highly effective in controlling laminar boundary layer separation. This is found to be true at dimensionless forcing frequencies (F^+) well below unity and with low (10 percent) duty cycles. This unexpected low-frequency effectiveness is due to the relatively long relaxation time of the boundary layer as it resumes its separated state. Extensive phase-locked velocity measurements taken in the blade wake at an F^+ of 0.01 with 50 percent duty cycle (a condition at which the flow is essentially quasi-steady) document the ejection of bound vorticity associated with a low-momentum fluid packet at the beginning of each jet pulse. Once this initial fluid event has swept down the suction surface of the blade, a reduced wake signature indicates the presence of an attached boundary layer until just after the jet termination. The boundary layer subsequently relaxes back to its naturally separated state. This relaxation occurs on a timescale which is five to six times longer than the original attachment due to the starting vortex. Phase-locked boundary layer measurements taken at various stations along the blade chord illustrate this slow relaxation phenomenon. This behavior suggests that some economy of jet flow may be possible by optimizing the pulse duty cycle and frequency for a particular application. At higher pulsing frequencies, for which the flow is fully dynamic, the boundary layer is dominated by periodic shedding and separation bubble migration, never recovering its fully separated (uncontrolled) state. [DOI: 10.1115/1.1425392]

Introduction

During high-altitude cruise, the operating Reynolds number (based on axial chord and inlet velocity) for the low-pressure turbine (LPT) in an aircraft gas turbine engine can drop below 25,000. This low Reynolds number condition is particularly acute in the class of small gas turbine engines typically used or planned for use in many high-altitude air vehicles. At these low Reynolds numbers, the boundary layers on the LPT blades are largely laminar, even in the presence of freestream turbulence, making them susceptible to flow separation near the aft portion of the blade suction surface, with associated loss increase and performance drop. Numerous industry reports have documented increased separation and secondary flow losses when operating at turbine inlet Reynolds numbers below 100,000 (Sharma et al. [1], and Matsunuma et al. [2,3]). Though the exact Reynolds number at which separation related losses become significant is machine specific, the increased loss inevitably translates to a significant decrease in turbine efficiency at these operating conditions (measured values have been as much as a six-point loss in component efficiency for the AE3007H [Helton [4]], a small high-altitude engine). Altering the blade shape to avoid this low Reynolds number separation problem is not desirable since such a modification is likely to impair the engine operation at higher (design) Reynolds numbers. As such, flow control techniques which can be practically implemented on a separating turbine blade are of current interest.

Boundary layer separation control in diffusing flows under pressure conditions similar to the aft portion of a turbine blade has been studied in the laboratory for many years. Lin et al. [5] presented results from a number of passive and active strategies employed with varying degrees of success to a turbulent boundary layer flowing over a backward-facing, curved ramp. Of the two classes, active techniques have the advantage that they can be shut off when not required for flow control. This is especially desirable for a turbine blade application, since any passive technique which is effective at low Reynolds number may increase the blade's drag penalty and surface thermal loading at higher (nonseparating) Reynolds numbers. Of the active strategies studied by Lin et al., only vortex generator jets (VGJs) had a significant effect on reducing diffuser separation.

VGJs are typically configured with a low pitch angle (30–45 deg) and aggressive skew angle (45–90 deg) to the near wall flow direction (see detail in Fig. 2 for the VGJ configuration in this study). Here, pitch angle is defined as the angle the jet makes with the local surface and skew angle is defined as the angle of the projection of the jet on the surface relative to the local freestream direction. In this skew configuration, the VGJ creates a horseshoe vortex pair with one very strong leg accompanied by a weak leg of opposite sign. The result is a single, dominant, slowly decaying streamwise vortex downstream rather than the two relatively weak counter-rotating horseshoe vortices generated by a jet with 0 deg skew or a symmetric, passive, boundary layer obstruction. It has been shown both experimentally (Compton and Johnston [6]) and

Contributed by the International Gas Turbine Institute and presented at the 46th International Gas Turbine and Aeroengine Congress and Exhibition, New Orleans, Louisiana, June 4–7, 2001. Manuscript received by the International Gas Turbine Institute February 2001. Paper No. 2001-GT-190. Review Chair: R. Natole.

computationally (Henry and Pearcey [7]) that this single-sign vortex energizes the separating boundary layer by effectively bringing high-momentum freestream fluid down near the wall.

Nonsteady pulsing has been combined with jet injection to inhibit separation of wall-bounded flows in a number of applications. Chang et al. [8] employed pulsed, normal (90 deg pitch, 0 deg skew) slot injection to inhibit laminar separation over an airfoil at high angle of attack. In the post-stall airfoil, forcing was most effective when applied at 1 percent chord and at dimensionless forcing frequencies ($F^+ = fc/U_\infty$) from 2 to 8. More recent applications of pulsed, normal jet injection include the use of synthetic (zero net mass flux) jets to promote flow reattachment over a thick airfoil (Amitay et al. [9]) and the application of pulsed upper surface blowing to control dynamic stall on a simulated helicopter rotor (Weaver et al. [10]). In the computational arena, Wu et al. [11] have documented the roll-up of the pulsed jets into large vortices which entrain higher momentum mainstream fluid down near the wall. Pulsed, streamwise (0 deg pitch. 0 deg skew) jet injection (from a backward facing slot or step) has also been successfully employed by Seifert et al. [12] and Kwong and Dowling [13].

In addition to the normal and streamwise pulsed jet injection experiments mentioned above, three studies have investigated the combination of unsteady forcing with skewed (VGJ) injection. McManus et al. [14] and Raghunathan et al. [15] have both employed pulsed VGJs to effectively control separation in two-dimensional diffusers. The authors have also previously reported their successful application of pulsed VGJs to LPT blade separation control (Bons et al. [16]). It was the encouraging results of this study which lead to the current work. This report documents the fluid dynamics associated with the implementation of pulsed VGJs on the suction surface of a prototypical LPT blade profile. The effects of jet pulsing frequency are addressed in detail.

Experimental Facility

The linear turbine cascade facility used for this study is described in detail in Sondergaard et al. [17] and Bons et al. [16], so only a brief description will be provided here. The open-loop, induction wind tunnel which houses the cascade draws air through the bell-mouth inlet equipped with flow straighteners and into the 0.85 m tall×1.22 m wide test section at up to 80 m/s (Fig. 1). Flow velocity uniformity across Blades 3–7 is within ±2 percent at a Reynolds number of 25,000, with an inlet turbulence level of less than 1 percent. The linear cascade consists of eight 0.88 m span by 0.18 m axial chord (C_x) blades fabricated from molded polyurethane resin. The two-dimensional blade shape studied is the Pratt & Whitney ''PakB'' research design, which is a Mach number scaled version of a typical highly loaded LPT blade design. The cascade has a solidity (axial chord to blade spacing) of 1.13, an inlet flow angle of 55 deg (measured from the plane of the cascade), and a design exit angle of 30 deg.

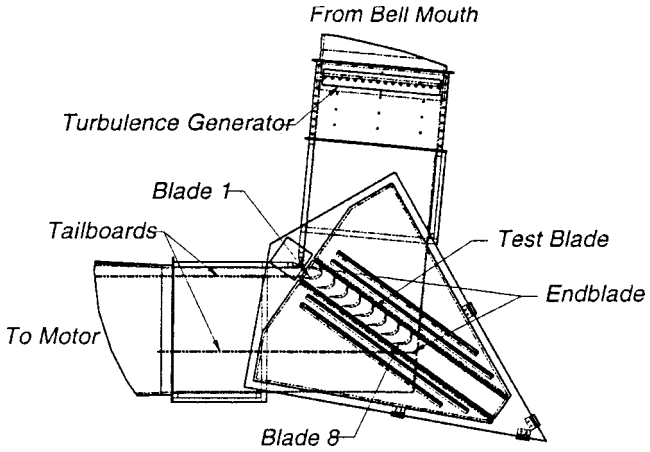

Fig. 1 Low-speed linear cascade test facility

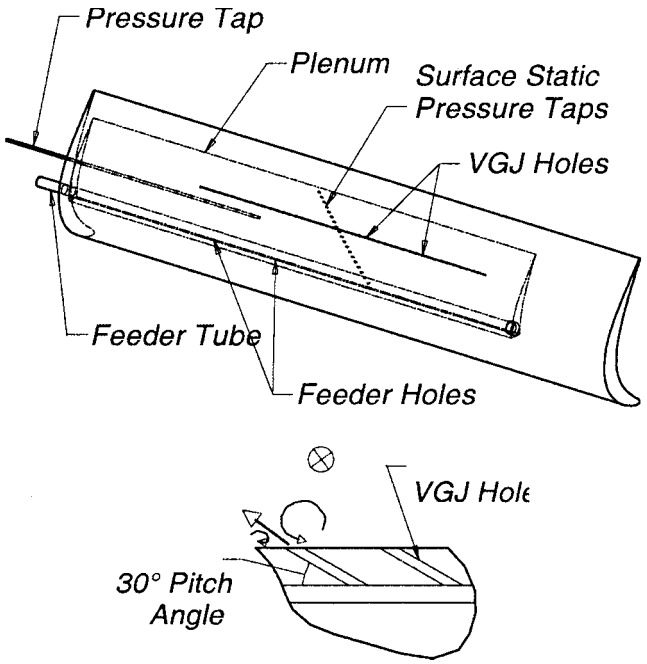

Fig. 2 Pulsed VGJ blade geometry, inset showing VGJ configuration (freestream into page)

For this study, all eight blades in the cascade were manufactured with a hollow cavity running their full span and covering the region from 40 percent to 90 percent axial chord (Fig. 2). Fittings at the lower end of each blade allow for pressurized feed air for the VGJs and cavity static pressure measurement. A valve located upstream of the feed port allows control of the mass flow rate into the blade cavity. A high-speed solenoid valve is located just downstream of this control valve. The solenoid is controlled by a General Valve Inc. Iota One pulse driver which has a frequency range from 0.1 Hz to 250 Hz with a minimum ''open'' pulse duration of less than 1 ms. Air exhausts from this valve into a manifold and then into the eight copper feed tubes running the span of each blade inside the cavities. Holes spaced every 2.54 cm along the copper tubes produce an even distribution of airflow to the VGJs. The 1-mm-dia (d) cylindrical VGJ holes have a 30-deg pitch angle and a 90-deg skew angle. They are spaced every 10d along the center 0.46 m of each blade span. For this study, rows of VGJ holes at 63 percent C_x were used. In preliminary testing of the full cascade, it was noted that pulsing on the full set of eight blades yielded comparable results to operating with just the three center blades (when taking measurements over the centermost blade). Thus, to allow a greater range of blowing ratio, only the three center blades were controlled for all the data reported in this study. When not in use, the holes were covered with 50 μm thick tape to eliminate any effect of the holes on boundary layer transition.

To determine the mean jet blowing ratio, the average static pressure of each blade cavity was monitored during tunnel operation. This pressure was then correlated to the average jet exit velocity, which had been measured at the hole exit plane with a sub-miniature hot-film probe prior to blade installation in the cascade. This measurement was made outside the cascade tunnel with the jets injecting into stagnant air. The mean jet blowing ratio (B) was computed as the ratio of the average jet exit velocity to the local freestream velocity as calculated from the local pressure coefficient ($\rho_{\text{jet}}/\rho_{\text{local}} \cong 1$). While making the jet exit velocity

measurements, it was noted that with multiple blades fed from the same high speed solenoid valve, jet exit velocity profiles began to resemble more of a sinusoid rather than the typical square wave at frequencies above 50 Hz ($F^+=1.6$).

The dimensionless forcing frequency, F^+, is used in this report to relate the current work to the external airfoil flow control studies published in the open literature. Rather than employ the common definition based on airfoil chord and freestream velocity, however, the F^+ here uses the surface distance from the injection site to the trailing edge and a local mid-passage velocity. The shortened distance ($0.72C_x$) was deemed more relevant in the current application since it represents the approximate lengthscale of the separation zone where eddies or unsteady waves would be present. This formulation is consistent with the slotted flap blowing work of Seifert et al. [12] where the relevant distance was the quarter-chord aft flap. Weaver et al. [10] also employed an F^+ lengthscale less than the blade chord in their helicopter rotor dynamic stall control study. The augmented velocity scale ($1.75U_{\text{in}}$) accounts for the substantial fluid acceleration that takes place through the PakB turbine cascade. Whether the boundary layer is attached or separated, the mid-passage velocity at the VGJ injection site is just under twice the cascade inlet velocity. Since this location is near the passage throat, there is then a modest diffusion ($\sim$10 percent) to the blade trailing edge. By employing a velocity scale equal to the average value over the separated zone, F^+ more accurately represents the ratio of the VGJ forcing frequency to the frequency at which fluid events will be convected down the blade surface by the freestream flow.

Another parameter in common use in the jet-boundary layer control arena is the momentum coefficient, c_μ, defined as the ratio of injected momentum to the freestream dynamic pressure. This parameter had its genesis in the application of two-dimensional slot blowing on external airfoils and can be written as follows:

$$c_\mu=\frac{(\text{slotwidth})\rho_{\text{jet}}U_{\text{jet}}^2}{(\text{chord})\dfrac{1}{2}\rho_\infty U_\infty^2} \tag{1}$$

The blowing parameter, used in this and previous reports on LPT separation control, has its origins in turbine film cooling and can be related to c_μ in a straightforward manner ($c_\mu \propto B^2$ at constant density). To be consistent with the reduced frequency formulation above, B employs a local channel velocity ($\sim 2U_{\text{in}}$) rather than the cascade inlet velocity. One additional adaptation is required for the comparison of the c_μ calculated in this work with those in the open literature. This regards the area difference between a two-dimensional slot (which extends across the entire airfoil span) and three-dimensional-discrete hole injection (VGJ). To generate an ''equivalent'' slot area for the circular VGJ holes at a pitch of 10, one can proceed as follows:

$$\begin{aligned}\frac{\text{slotwidth}}{\text{chord}}&=\frac{(\text{slotwidth})(\text{slotspan})}{(\text{chord})(\text{airfoilspan})}\\ &\cong\frac{\text{``equivalent}\cdot\text{slot}\cdot\text{area''}}{(0.72C_x)*\text{bladespan}}\\ &=\frac{\pi\left(\dfrac{d}{2}\right)^2\dfrac{\text{bladespan}}{(\text{holepitch})d}}{(0.72C_x)(\text{bladespan})}=6.06\times10^{-4}\end{aligned} \tag{2}$$

Thus with equal jet and freestream densities, $c_\mu\cong 0.00121B_{2\max}$.

Bulk flow instrumentation consisted of flow thermocouples for inlet temperature measurement and an upstream pitot-static reference probe. To calculate the blade wake loss coefficient a Kiel probe was used to measure the total pressure 0.64 C_x downstream of the trailing edge (see Fig. 10). A Dantec 3-axis traverse located atop the wind tunnel was used to traverse the blade wakes with the probe at midspan. Uncertainties in the pressure measurement translated to an uncertainty of ± 8 percent in the loss coefficient (at Re=25,000). A small National Aperture micro-traverse system, mounted inside the test section (but outside the outer tailboard), was used to make boundary layer profile measurements at several chordwise locations on the center blade (Blade 5). A standard single hot-wire probe was mounted on the micro-traverse to measure mean and fluctuating velocity components. When compared to a co-located pitot-static probe velocity measurement, the velocity error in the hot-wire and sub-miniature hot-film probes was within ± 2 percent at flow rates of interest. Phase-locked wake and boundary layer velocity data were acquired using a timing pulse from the Iota One pulse driver to trigger the acquisition process. Phase-average data presented in this report consisted of ensembles of between 30 (at low frequencies) and 200 (at high frequencies) cycles.

Results and Discussion

Previous Work. The low Reynolds number separation characteristics of the PakB blade profile have been documented in previous studies (Bons et al. [18], and Sondergaard et al. [17]). Figure 3 shows the γ_{int} versus Re data for this cascade at two freestream turbulence levels. Also shown is a Navier-Stokes CFD calculation using the two-dimensional Vane Blade Interaction (VBI) code developed by Allison Engine Company under contract to the US Air Force. VBI is an unsteady Reynolds Averaged Navier-Stokes code employing the algebraic Baldwin-Lomax boundary layer turbulence model, which assumes zero freestream turbulence. Data in this report were taken at Re$\cong$25,000 with low turbulence, where the heavy separation losses are prominent in the data (but not in the VBI prediction). At this Reynolds number, boundary layer data indicate that laminar separation occurs on the blade suction surface between 68 percent and 73 percent C_x.

Two previous control studies conducted by the authors in the same facility acted as the point of departure for the current study. Specifically, Sondergaard et al. [17] reported the effectiveness of steady blowing at various locations and blowing rates (B) for both 1 percent and 4 percent freestream turbulence. The steady data in Fig. 4 is taken from this work and shows a broad range of steady control effectiveness with a minimum B between 1 and 1.5 (in this and subsequent figures, γ_{int} is normalized by γ_{int0}, the value obtained without any control). This minimum B was found to be a weak function of injection location from 45 percent to 75 percent C_x. Over the range of B indicated in the figure, wake reduction is relatively flat at 60 percent from the minimum B value up to the maximum value tested ($B=4$). As a point of reference, a B value

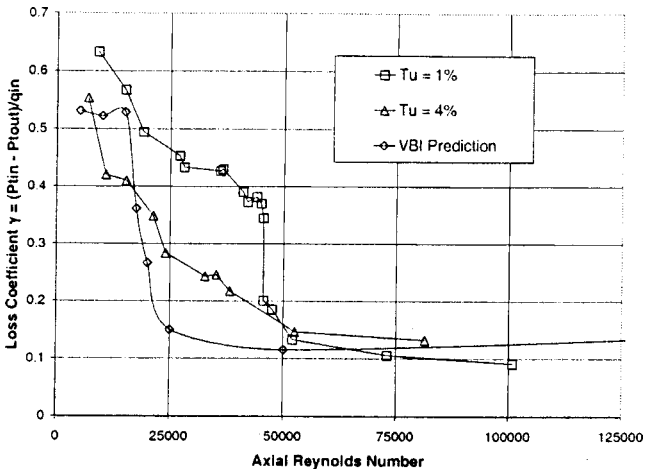

Fig. 3 Loss coefficient γ_{int} versus inlet Reynolds number; Tu_{in}=1 percent, Tu_{in}=4 percent, and VBI prediction

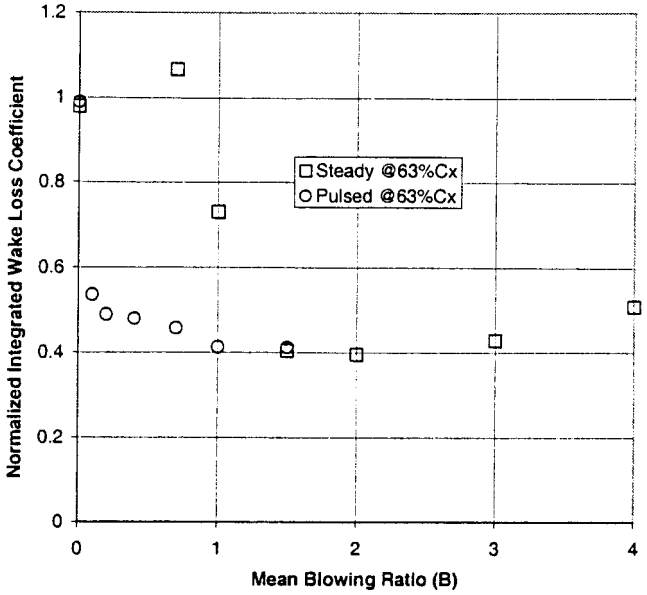

Fig. 4 Integrated wake loss coefficient (γ_{int}) profiles normalized by loss coefficient for $B=0$ versus mean blowing ratio (B); data for pulsed blowing at 10 Hz ($F^+=0.31$) and 50 percent duty cycle versus steady blowing at Re=25k and 63 percent C_x

of 2 at a VGJ hole pitch of 10 represents an application of 0.2 percent of the cascade throughflow. The corresponding value of c_μ is 0.0048. As another point of reference, typical film cooling holes are designed to operate at approximately $B=2$.

The second study, using pulsed VGJs, was reported in Bons et al. [16]. The principle finding of this study is also illustrated in Fig. 4 alongside the steady VGJ results. The pulsed data is for 10 Hz square wave modulation (no suction stroke) with a 50-percent duty cycle. This forcing frequency corresponds to an F^+ of order unity (0.31) and is 1/10 of the shear layer instability (measured at 100 Hz in the separating boundary layer). The blade shedding frequency (which is generally some fraction of the shear layer instability frequency) was found to be an effective forcing frequency in the computational study of Wu et al. [11], while others (Seifert et al. [12,19]) have found success near the blade reduced frequency (U_∞/c). For the pulsed data in Fig. 4, the average B over the cycle is used for comparison with the steady data. With pulsing, the minimum B required for effective control is reduced

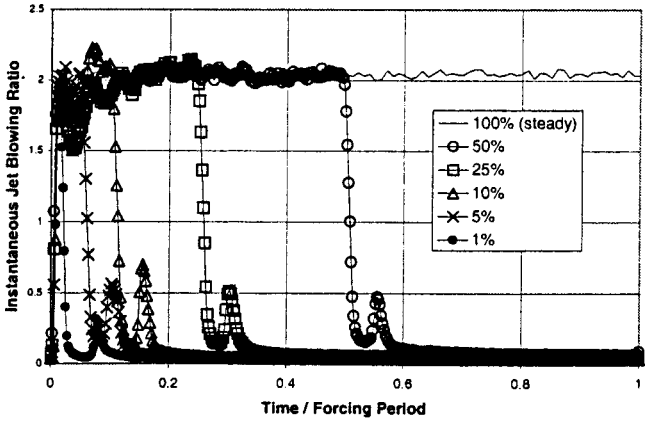

Fig. 5 Instantaneous jet exit blowing ratios for various duty cycles all at 10 Hz ($F^+=0.31$); data taken with subminiature hotfilm probe in VGJ exit at 63 percent C_x; Re=25k

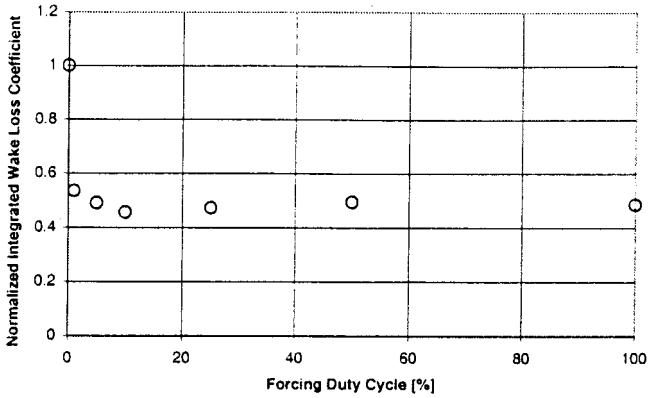

Fig. 6 Normalized integrated wake loss coefficient ($\gamma_{int}/\gamma_{int0}$) versus pulsing duty cycle for constant maximum blowing ratio (B_{2max} see Fig. 5); data for pulsed blowing at 10 Hz ($F^+=0.31$); Re=25k

to ~0.2. This represents nearly an order of magnitude reduction in required massflow for comparable separation control, a result seen by McManus et al. [14] in two-dimensional diffusers. Since in a potential turbine application of this control strategy, VGJ air will come from the compressor at a loss to the engine cycle, reducing the required massflow by nearly an order of magnitude is significant.

The remarkable success of pulsed versus steady VGJ control leads to questions regarding the physical mechanism(s) which are responsible for the bulk effect of separation control. In their report, Bons et al. postulated that the starting (and perhaps ending) vortex of the pulsed jet must be the mechanism responsible for altering the boundary layer. This was based in part on the work of Johari and McManus [20] which showed that the starting vortex associated with skewed jet injection generates much stronger streamwise vorticity than steady blowing at the same jet injection velocity. It is this streamwise vorticity in turn that is thought to be responsible for entraining the high momentum freestream fluid down near the blade surface to effectively energize the separating boundary layer. To test this hypothesis, Bons et al. varied the pulse duty cycle at constant frequency (10 Hz) and maximum jet exit velocity (B_{2max}), thus reducing the exit pulse to a narrow spike (Fig. 5). The result (Fig. 6) clearly showed that control was effective down to 1 percent of the massflow required for steady control at the same B_{max} (or 0.002 percent of the cascade throughflow). In determining the corresponding c_μ values for the data in Fig. 6, the reduced net momentum over the shortened duty cycle could be accounted for by multiplying c_μ by the duty cycle, $c_\mu \cong 0.00121 B_{2max}$(duty cycle/100). This would give a range of $4.8\times10^{-5}<c_\mu<4.8\times10^{-3}$ for duty cycles of 1 to 100 percent, respectively. As anticipated, the 1 percent duty cycle is equivalent to an extremely low c_μ.

New Results. These encouraging results at low duty cycle lead the authors to consider the following question. ''If a narrow spike (1 percent duty cycle) of injected fluid can control the bulk separation of a turbine airfoil, how often do these impulses need to occur for successful control?'' Or, in other words, what is the maximum allowable time between pulses that will still provide time-averaged wake reduction? As a first step in answering this, wake loss data was taken at constant duty cycle and average B while decreasing the forcing frequency. This essentially increases the time between pulse events while maintaining constant mass flow over the forcing cycle. Figure 7 provides this data for two duty cycles, 10 percent with average $B=0.2$ ($c_\mu=4.8\times10^{-4}$) and 50 percent with average $B=0.75$ ($c_\mu=1.4\times10^{-3}$) from $F^+=0.012$ to 7.71.

The data in Fig. 7 show a relatively flat effectiveness from $F^+=7.7$ down to a value of 0.1 (note the log frequency scale).

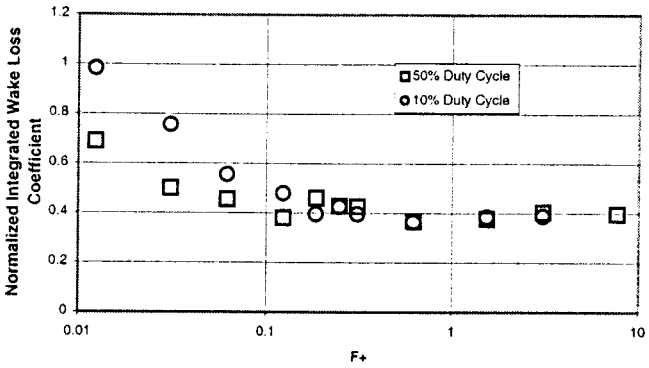

Fig. 7 Normalized integrated wake loss coefficient ($\gamma_{int}/\gamma_{int0}$) versus dimensionless forcing frequency (F^+) for two duty cycles and at constant mean blowing ratio ($B=0.2$ for 10 percent duty cycle and $B=0.75$ for 50 percent duty cycle); Re=25k

Variations in $\gamma_{int}/\gamma_{int0}$ over this range of F^+ are within the measurement uncertainty. This broad (nearly two orders of magnitude) effectiveness range and low minimum F^+ contrast with pulsed control results for external airfoils. Though the majority of references report lift coefficient rather than wake parameters, some data is available for comparison. Chang et al. [8] used leading edge blowing over an F^+ range of 1 to 20 and observed c_d reductions of roughly 35 percent over the range $1<F^+<10$. These reductions diminished slightly above in F^+ of 10. Amitay et al. [9] provided mean wake data for two cases ($F^+=0.95$ and 10) which can be integrated to produce a representation of the wake momentum deficit, $\theta_{def}=\int 1-(u/U)^2 dy$. Their data show a drop of approximately 8 percent and 23 percent in θ_{def} compared to the uncontrolled case for the two dimensionless forcing frequencies, respectively. Both of these studies concentrated on the regime of $F^+\geqslant 1$ based on indications that dimensionless forcing frequencies significantly less than one would not provide successful control. This is consistent with Seifert et al.'s conclusion [19] that pulsed blowing is most effective when there are one or two pulse disturbances on the airfoil surface at any given time. Seifert et al. [12] focused on a narrow range of F^+ (0.3 to 2) and observed a maximum beneficial effect in lift coefficient near $F^+=0.75$. Pressure drag reductions in this frequency range varied from 5 percent to 70 percent.

Compared to these references, the PakB cascade pulsed VGJ control application shows a much broader range of utility (F^+), with nearly double the wake (c_d) reduction at comparable levels of c_μ (the Chang et al. study used c_μ ranges of 1×10^{-4} to 1×10^{-3} and Amitay et al. reported $c_\mu=2.3\times10^{-3}$ while Seifert et al. employed a fluctuating $c_\mu=0.008$ to 0.016 on top of a steady c_μ ranging from 0 to 0.1 for their aft flap study).

As is evident from Fig. 7, at dimensionless forcing frequencies below the 0.1 cut-off, the 10-percent and 50-percent duty cycle data diverge. This suggests that the reduced control effectiveness at low F^+ may be related to physical timescales of the flowfield rather than simply the forcing dynamics. Following this line of reasoning, phase-locked velocity data were taken in the blade wake at $0.64C_x$ downstream of the trailing edge using a single hotwire. Figures 8(*a–d*) show phase-averaged color raster plots of wake velocity distributions for $F^+=0.012$, 0.031, 0.12, and 0.31 all at 50 percent duty cycle. The plot to the left of each y-t raster plot shows the wake average momentum deficit, θ_{def}, as a function of time as well as the VGJ jet time history. This phase-locked jet history was taken at the VGJ hole exit using a sub-miniature hot-film probe prior to blade installation in the cascade. A convective offset time of 0.065 s (equal to the distance from the VGJ holes to the wake measurement position divided by the average channel velocity) has been added to the hole exit velocity time history so that the reader can readily associate fluid events in the wake to the starting and stopping of the jet pulse. The jet exit velocity is normalized by its maximum value to permit plotting on the same scale with θ_{def}. The plots also show threshold lines corresponding to the uncontrolled θ_{def0} and the θ_{def} for steady ($B=2$) control (2.1 and 0.8 cm respectively). Both blade wakes 5 and 6 are shown in the raster plots, though the θ_{def} integration was performed over wake 5 only.

Beginning with the lowest F^+ plot (Fig. 8(*a*) with a cycle period of 2.5 s), the jet "on" cycle initiation immediately triggers a large oscillation in the wake deficit. In the first 0.11 sec after jet initiation, the unsteady deficit varies from over two times the uncontrolled wake level down to negative wake values. This is followed by a gradual (0.12 s) decrease in wake size to the controlled wake value. Then, for the duration of the "on" cycle, the wake remains narrow and shifted to the left (toward the blade pressure side).

When the pulse terminates, there ensues a high frequency (~33 Hz) damped oscillation with a mean θ_{def} which is actually further reduced from that of the "on" cycle. Not until approximately 0.45 s after the pulse termination does the wake gradually (over 0.14 s) resume its uncontrolled (separated) level. Due to this lagged relaxation of the boundary layer, the wake deficit spends only one third of the full cycle at the uncontrolled level. This added benefit of pulsed control (1.7 s of separation control for only 1.25 s of jet application=32 percent bonus) is one of nature's coveted synergies and will be explored in more detail below. The identical sequence of events is repeated in Fig. 8(*b*), however since F^+ has increased by a factor of 2.5, the next pulse arrives before the wake has time to relax back to its uncontrolled state. Due to the long relaxation time, the wake never exhibits quasi-steady, uncontrolled behavior. The next highest F^+ plot (8(*c*)) is at the threshold where wake loss reduction became independent of reduced frequency in Fig. 7. In this case, the initial "kick" or startup transient is buried in the 33-Hz termination oscillation. The gradual drop in momentum deficit following the startup transient never reaches the steady state value. In the final plot (8(*d*)), the startup transient comprises the entire cycle, though now at a considerably reduced amplitude. In essence, the flow in this case is constantly in an unsteady regime between the controlled and uncontrolled states, never settling at either condition. At reduced frequencies above 0.62 (not shown), the wake raster plots look essentially uniform over the pulsing cycle with only a slight perturbation corresponding to the pulse initiation. (It should be noted that it is in this same high F^+ regime that the jet exit pulses take on a more sinusoidal character rather than the square wave noted in the Fig. 8 and Fig. 5 plots.)

The benefit from inherent time lags in the boundary layer response becomes even more pronounced at lower duty cycles. Figure 9 shows two raster plots ($F^+=0.012$ and 0.031) with 4-percent and 10-percent duty cycle, respectively. In both these cases the pulse is terminated well before the controlled wake loss level is reached. Yet in the lower frequency case, the wake remains at or near the controlled level for 0.36 s or 360 percent longer than the VGJ pulse length (0.1 s). Recalling the data in Fig. 6, which showed effectiveness down to 1 percent duty cycle, one might conclude that this benefit will continue to increase exponentially with decreasing pulse duration. It seems that as long as there is a starting (jet "off" to jet "on") transition to trigger the ejection of bound vorticity, the boundary layer will respond in a timescale unrelated to the length of the ensuing jet pulse. A potentially related phenomenon was discovered by Gharib et al. [21] regarding the vortex ring formation from a jet injected into an otherwise stagnant fluid. In their controlled water tank experiment, they found that any additional injected jet fluid beyond a threshold formation length resulted in no net increase to the resulting vortex ring circulation. If such a minimum "formation number" exists for the generation of streamwise vortices via skewed jet injection in this cascade facility, it is probably below the physical limits of

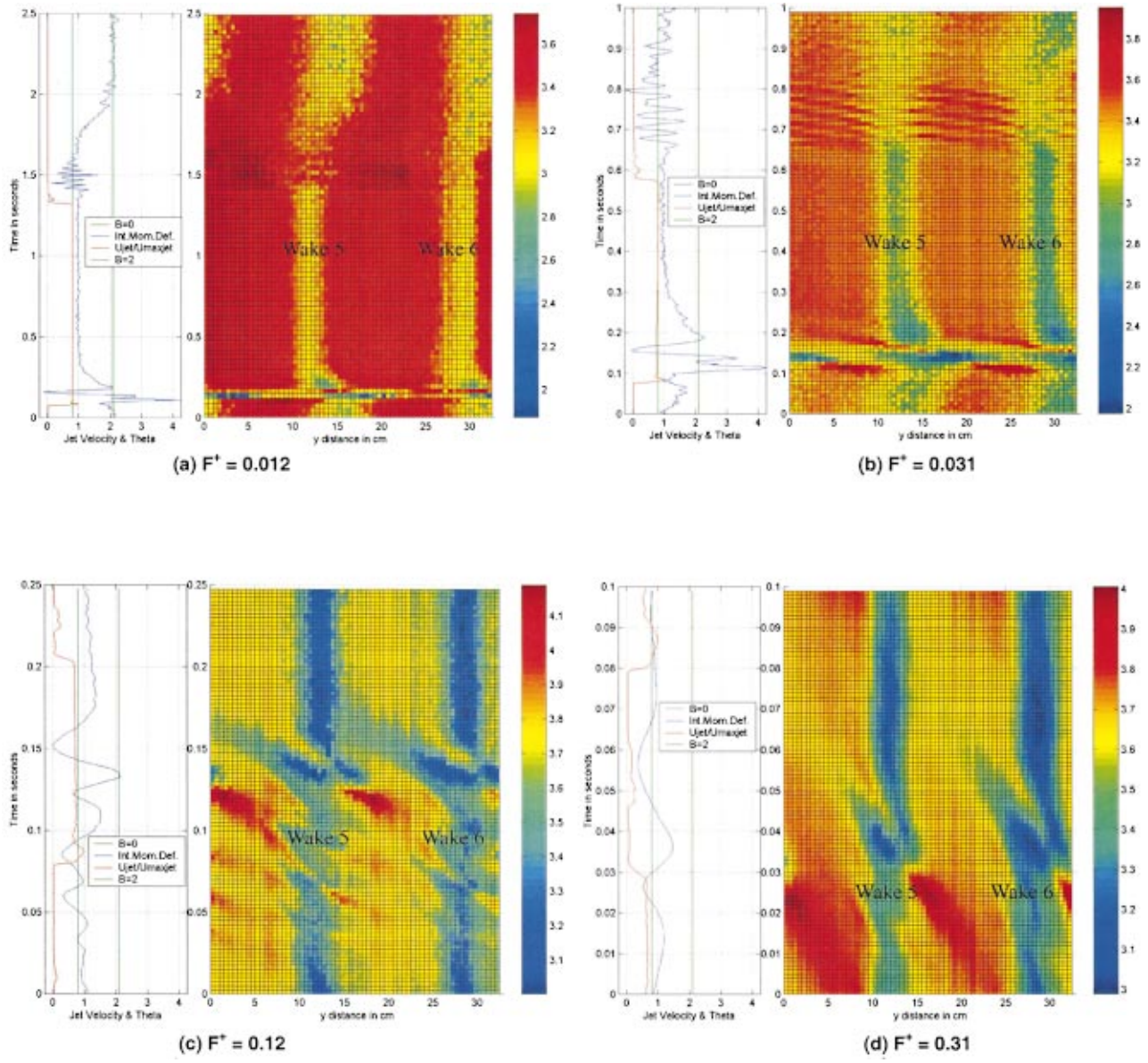

Fig. 8 Each figure includes a streamwise velocity (m/s) raster plot (*y* versus *t*) of wakes 5 and 6 over one VGJ pulse period (on the right) and a time history of jet exit velocity (with added time offset) and θ_{def} (on the left); green lines indicate $B=0$ and $B=2$ limits; data for $F^+=0.012$ (*a*), 0.031 (*b*), $F^+=0.12$ (*c*), and 0.31 (*d*), 50 percent duty cycle, and mean $B=0.75$

the current test apparatus. It can also be concluded from these data that the critical segment of the pulse is the starting transition versus the ending. In all the examples noted, this initial ''kick'' dominates the dynamic response of the blade, causing the wake to shrink dramatically, recovering only after the physical time constants have elapsed.

The data in Fig. 8 bear striking resemblance to the wake transient histories reported in Amitay et al. [9] for the initiation and termination of high frequency pulsed control ($F^+=10$). The initial large transient oscillation (''kick'') at startup and the beneficial reduction in wake deficit at termination (with subsequent gradual relaxation) are all noted by Amitay et al. and are nearly identical to the behavior outlined in the foregoing. Using two-component velocity measurements in the wake, Amitay et al. were able to identify the shedding of vortex pairs of alternating sign as the airfoil adjusted to the higher lift (attached flow) condition at control initiation. It is this same shedding of vorticity that appears as the initial ''kick'' of the wake in Figs. 8(*a–c*). One significant difference between the blade wake data in Fig. 8 and the Amitay et al. data is that Fig. 8 represents the transients associated with a single on-off cycle of the continuous pulsed control, while the similar transients observed by Amitay et al. were associated with the onset and cessation of a multi-period high frequency sinusoidal flow control. When they dropped the reduced frequency of control from $F^+=10$ to 0.95, the wake exhibited large oscillations at the forcing frequency, and they did not profit from the long transient relaxation times. These low F^+ oscillations were associated with ''a time-periodic shedding of a train of vortices that corresponded to (peak to peak) lift coefficient fluctuations of up to 45 percent of the mean lift''. As cited earlier, this same drop in F^+ resulted in a decreased time-averaged wake reduction from $\theta_{def}/\theta_{def0}=77$ percent at $F^+=10$ to roughly 92 percent at $F^+=0.95$. This is clearly not a desirable condition and represents a significant difference between the two sets of results. At the same F^+ of 1, the turbine cascade wakes exhibit only minimal oscillations associated with each starting transient and the wake loss reduction is virtually independent of reduced frequency (and re-

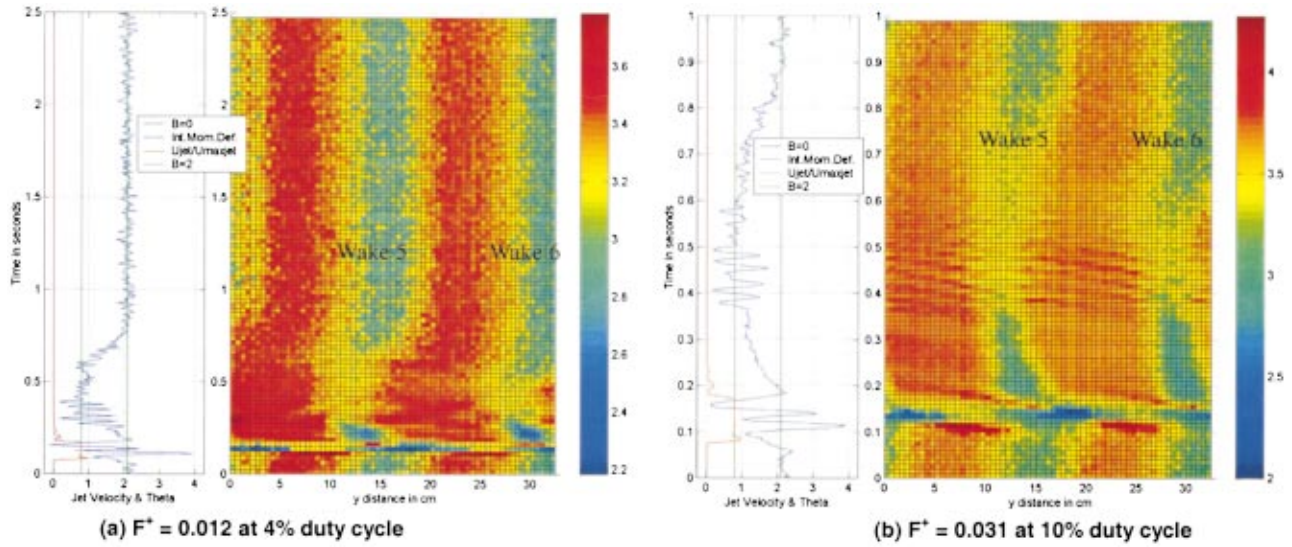

Fig. 9 Each figure includes a streamwise velocity (m/s) raster plot (*y* versus *t*) of wakes 5 and 6 over one VGJ pulse period (on the right) and a time history of jet exit velocity (with added time offset) and θ_{def} (on the left); green lines indicate $B=0$ & 2 limits; data for (*a*) $F^+=0.012$, 4 percent duty cycle, and mean $B=0.05$ and (*b*) $F^+=0.031$, 10 percent duty cycle, and mean $B=0.2$

mains so down to $F^+=0.1$). For some reason, the turbine cascade does not require the "one to two events on the airfoil" that external airfoil stall experiments require. Moreover, the blade shedding frequency does not appear to be a dominant factor in the forcing frequency optimization. This is likely due to the influence of adjacent blades in the cascade, which provide a stabilizing influence on the boundary layer which is not present in single airfoil or diffuser configurations. Previous experiments by the authors have shown that the application of control on one blade in the cascade can significantly alter the lift distribution on adjacent blades. As such, the simultaneous control of Blades 4 and 6 may have a beneficial, synergistic effect on Blade 5, damping out large-scale flow oscillations and preventing massive suction surface separation at low dimensionless forcing frequencies.

As instructive as they are, these figures only document the bulk or net effects of forcing on the blade wake performance. In order

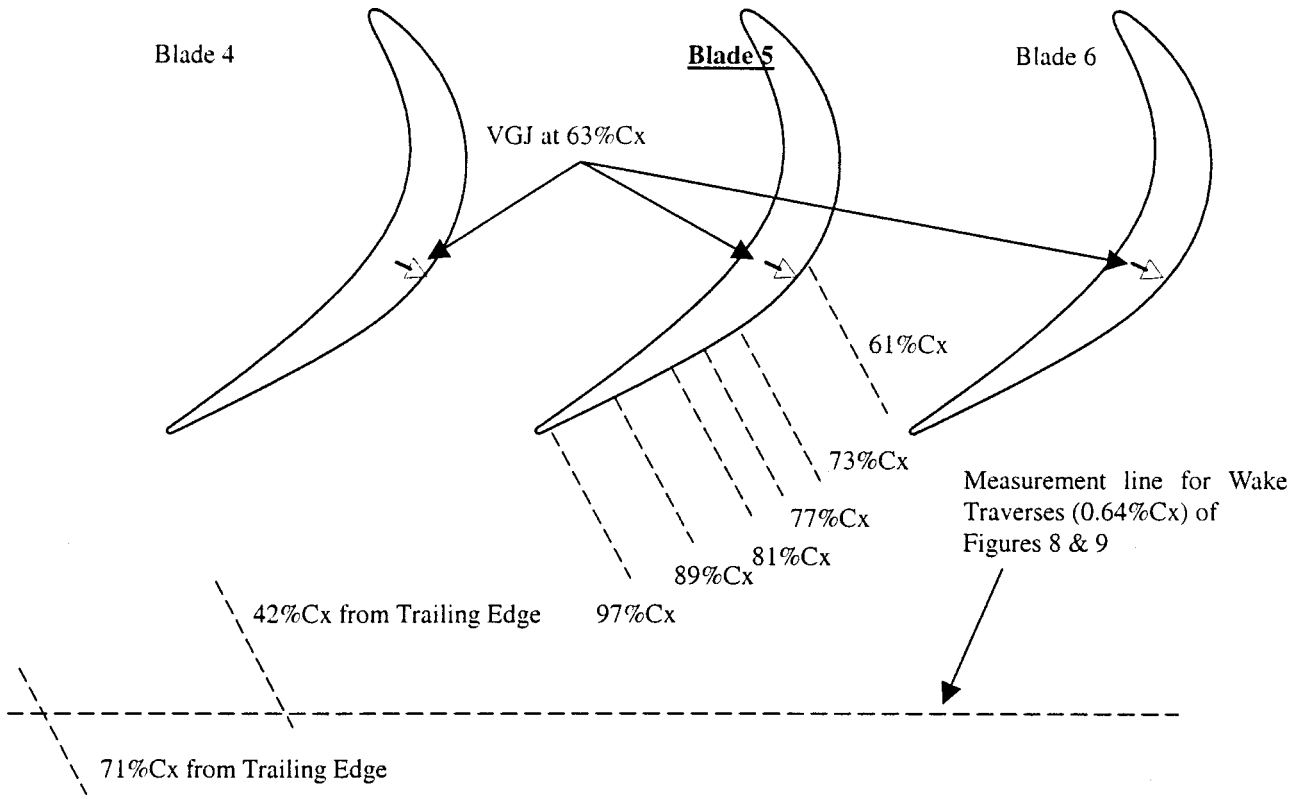

Fig. 10 Boundary layer measurement stations on Blade 5

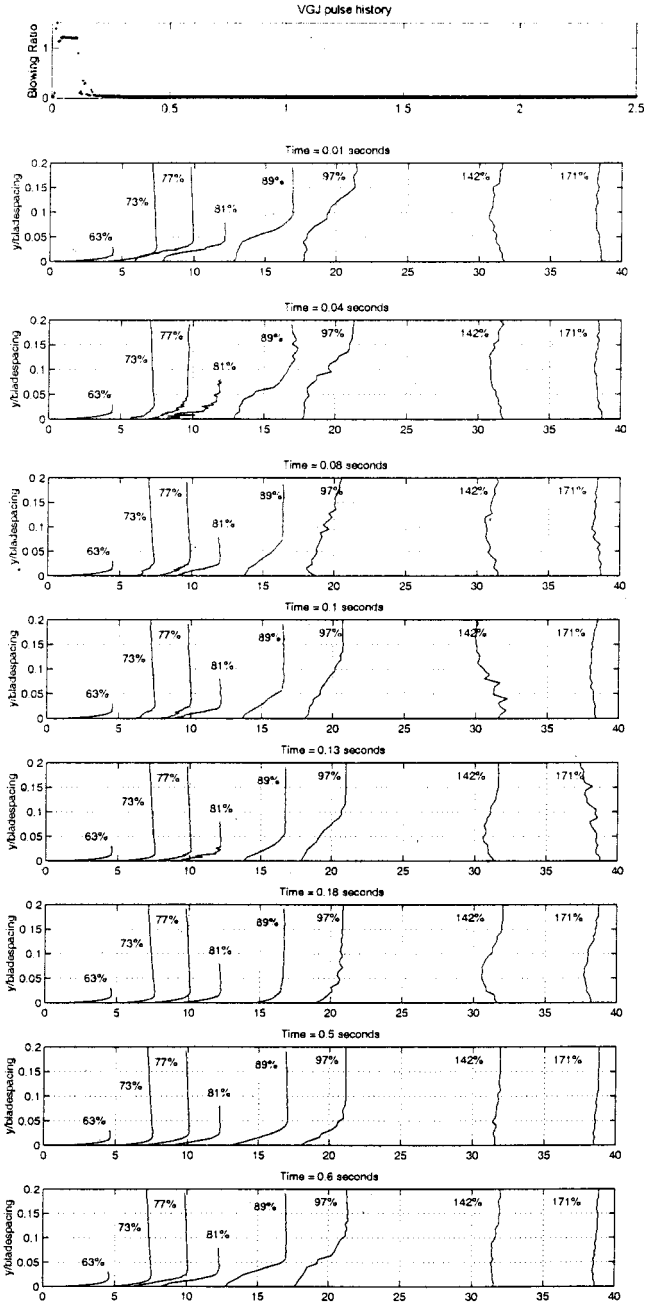

Fig. 11 Snapshots of flow over blade suction surface for $F^+ = 0.012$ and 4 percent duty cycle (mean $B = 0.05$); boundary layer profile positions indicated in Fig. 10; jet exit time history shown at top

to gain insight into the physical mechanisms which determine the time constants and oscillations associated with the pulse transitions, detailed boundary layer measurements are required. To this end, phase-locked single component velocity measurements were taken at successive stations along the blade suction surface from 61 percent C_x to beyond the trailing edge. Figure 10 illustrates the measurement stations relative to the VGJ location on Blade 5. As shown in the figure, the final downstream profile actually intersects the wake measurement station at $0.64C_x$ downstream of the trailing edge. All measurement lines are parallel and at the same spanwise location. Figure 11 shows a composite picture of all the boundary layer traces at eight distinct phases of the pulse cycle. The individual boundary layer profiles at each phase are staggered in the streamwise direction to represent their relative position in the cascade flowfield. The jet pulse time history is provided at the top of the figure for reference. The data in Fig. 11 is for $F^+ = 0.012$, mean $B = 0.05$ ($c_\mu = 7.6 \times 10^{-5}$), and 4 percent duty cycle.

The first frame ($t = 0.01$) is just prior to the pulse initiation. The 61-percent and 73-percent profiles appear attached, while all succeeding profiles on the blade are separated. The two profiles furthest downstream exhibit the broad separated wake deficit typical for this Reynolds number. The next frame is taken immediately following the jet injection ($t = 0.04$ s). The profile at 73 percent is attached, while at 77 percent and 81 percent the flow is unstable. The shed vorticity has just passed the 81 percent station and is sitting in the 89 percent boundary layer trace. By $t = 0.08$ s the profiles at 81 percent and 89 percent are beginning to reattach. The 73-percent and 77-percent profiles show a discontinuity in their attached profiles which is the actual location of the VGJ jet wake (there is elevated turbulence at these locations indicating increased mixing). The initial shed vortex is now off the blade and is convecting downstream, having swept the blade virtually clean of separated flow. By $t = 0.13$ s, the ejected vortex shows up as the ''kick'' in the last wake profile while the flow over the blade is already moving toward controlled status. The pulse has terminated at this point, but the boundary layer traces barely acknowledge this fact. At $t = 0.18$ s, the flow over the blade is fully attached. The wake is smaller and more localized. The last boundary layer trace (97 percent) continues to exhibit random fluctuations corresponding to separation migration and periodic shedding between 0.18 s and 0.5 s. Beyond 0.5 s, gradual relaxation proceeds until $t = 0.6$ s where the separation bubble has again engulfed the profile at 81 percent and 89 percent and has just reached 77 percent. After $t = 0.72$ s, the profiles have all resumed their $t = 0.0$ (fully separated) character.

This sequence of snapshots clearly documents the salient flow features highlighted previously in Figs. 8 and 9. The pulse initiation triggers the formation of a large vortex, which convects down the suction surface pulling with it the largely stagnant, separated fluid there. Attached flow is then established and remains in place for over three times the duration of the VGJ pulse. Instability growth at the blade trailing edge then gradually claims more and more real estate until the original separated blade condition is reestablished.

Conclusions

The fluid dynamics associated with the implementation of pulsed VGJs on the suction surface of a prototypical LPT blade profile have been documented in detail using phase-locked wake and boundary layer velocity measurements. The experiments were performed in a low-speed linear cascade using a typical high performance blade shape with documented separation limitations at low Reynolds numbers. Pulsed injection was employed over a wide range of dimensionless forcing frequencies from 0.012 to 7.7, at constant mean blowing ratio and at two duty cycles (10 percent and 50 percent). The following conclusions are submitted based on the data presented:

Pulsed VGJs dramatically reduce suction surface boundary layer separation at low Reynolds numbers. Reductions in wake losses of up to 60 percent were measured. The bulk effect on separation is insensitive to frequency over the range of $0.1 < F^+ < 7.7$.

The sequence of events affecting the success of control include an initial transient as vorticity is shed due to the increased blade circulation followed by the ''on'' (or controlled wake) cycle and a final relaxation period. The relaxation period is related to a physical time scale of the flowfield and acts as an effective multiplier of the beneficial jet influence. Because this relaxation time is essentially a constant of the flow, reducing the pulse duty cycle can greatly increase the ''free'' benefits of pulsed control. This behav-

ior indicates that some economy of jet flow is possible by optimizing the pulse duty cycle and frequency for a particular application.

Finally, phase-locked boundary layer data clearly show that it is the starting transient of the VGJ pulse that initiates the vortex shedding and thus determines the response of the blade.

These results lead the authors to conclude that the application of pulsed VGJs for low Reynolds number separation control on LPT blades shows great promise.

Acknowledgments

The authors are indebted to the Air Force Institute of Technology Machine Shop personnel (Russ Hastings, Jan LeValley, and Condie Inman) for the fine craftsmanship they demonstrated in the construction of the modified wind tunnel. Also, this work would not have been possible without the superior technical expertise of AFRL technician Bill Nilson. The assistance of Heribert Kreuter is also acknowledged. This work was performed under sponsorship from the Air Force Office of Scientific Research, with Dr. Tom Beutner as contract monitor. The views expressed in this article are those of the authors and do not reflect the official policy or position of the United States Air Force, Department of Defense, or U.S. Government.

Nomenclature

B = jet blowing ratio $=(\rho u)_{\text{jet}}/(\rho u)_{\text{local}}$
C_x = blade axial chord (0.18 m)
F^+ = dimensionless forcing frequency $(0.41 C_x f/U_{\text{in}})$
Re = inlet Reynolds number $=\rho_{\text{in}} u_{\text{in}} C_x/\mu$
c = airfoil true chord [m]
c_d = airfoil drag coefficient
c_μ = jet momentum coefficient $c_\mu \equiv 0.00121 B_{2\max}$ (duty cycle/100)
d = jet hole diameter (1 mm)
f = forcing frequency [Hz]
p = pressure [Pa]
t = time [s]
U or u = streamwise mean velocity [m/s]
y = blade normal or cross wake direction [m]
μ = dynamic viscosity [kg/m s]
γ = wake loss coefficient $=(p_{T,\text{in}}-p_{T,\text{ex}})/(p_{T,\text{in}}-p_{S,\text{in}})$
γ_{int} = integrated wake loss coefficient [cm]
γ_{int0} = integrated wake loss coefficient without control $(B=0)$ [cm]
θ_{def} = integrated wake momentum deficit $(\theta_{\text{def}}=\int 1-(u/U_{\text{local}})^2 dy)$ [cm]
θ_{def0} = integrated wake momentum deficit without control $(B=0)$ [cm]
ρ = density [kg/m^3]

Subscripts

ex = cascade exit conditions
in = cascade inlet conditions
jet = vortex generator jet conditions
local = local blade conditions
max = maximum over cycle
S = static or ambient conditions
T = stagnation or total conditions
∞ = freestream conditions

References

[1] Sharma, O., 1998, "Impact of Reynolds Number on LP Turbine Performance," *Proc. of 1997 Minnowbrook II Workshop on Boundary Layer Transition in Turbomachines*, NASA/CP-1998-206958.
[2] Matsunuma, T., Abe, H., Tsutsui, Y., and Murata, K., 1998, "Characteristics of an Annular Turbine Cascade at Low Reynolds Numbers," presented at IGTI 1998 in Stockholm, Sweden, June 1998. Paper No. 98-GT-518.
[3] Matsunuma, T., Abe, H., and Tsutsui, Y., 1999, "Influence of Turbulence Intensity on Annular Turbine Stator Aerodynamics at Low Reynolds Numbers," presented at IGTI 1999 in Indianapolis, Indiana, June 1999, Paper No. 99-GT-151.
[4] Helton, D., 1997, private communication.
[5] Lin, J. C., Howard, F. G., Bushnell, D. M., and Selby, G. V., 1990, "Investigation of Several Passive and Active Methods of Turbulent Flow Separation Control," AIAA Paper No. 90-1598.
[6] Compton, D. A., and Johnston, J. P., 1992, "Streamwise Vortex Production by Pitched and Skewed Jets in a Turbulent Boundary Layer," AIAA J., **30**, No. 3.
[7] Henry, F. S., and Pearcey, H. H., 1994, "Numerical Model of Boundary-Layer Control Using Air-Jet Generated Vortices," AIAA J., **32**, No. 12.
[8] Chang, R., Hsiao, F. B., and Shyu, R. N., 1992, "Forcing Level Effects of Internal Acoustic Excitation on the Improvement of Airfoil Performance," J. Aircr., **29**, No. 5, pp. 823–829.
[9] Amitay, M., Kibens, V., Parekh, D., and Glezer, A., 1999, "The Dynamics of Flow Reattachment over a Thick Airfoil Controlled by Synthetic Jet Actuators," AIAA Paper No. 99-1001.
[10] Weaver, D., McAlister, K., and Tso, J., 1998, "Suppression of Dynamic Stall by Steady and Pulsed Upper-Surface Blowing," AIAA Paper No. 98-2413.
[11] Wu, J., Lu, X., Denny, A., Fan, M., and Wu, J., 1998, "Post-stall flow control on an airfoil by local unsteady forcing," J. Fluid Mech., **371**, pp. 21–58.
[12] Seifert, A., Bachar, T., Koss, D., Shepshelovich, M., and Wygnanski, I., 1993, "Oscillatory Blowing: A Tool to Delay Boundary-Layer Separation," AIAA J., **31**, No. 11, pp. 2052–2060.
[13] Kwong, A., and Dowling, A., 1994, "Active Boundary-Layer Control in Diffusers," AIAA J., **32**, No. 12.
[14] McManus, K., Legner, H., and Davis, S., 1994, "Pulsed Vortex Generator Jets for Active Control of Flow Separation," AIAA Paper No. 94-2218.
[15] Raghunathan, S., Watterson, J., Cooper, R., and Lee, S., 1999, "Short Wide Angle Diffuser with Pulse Jet Control," AIAA paper No. 99-0280.
[16] Bons, J., Sondergaard, R., and Rivir, R., 2000, "Turbine Separation Control Using Pulsed Vortex Generator Jets," ASME J. Turbomach., **123**, pp. 198–206.
[17] Sondergaard, R., Bons, J., and Rivir, R., 2000, "Control of Low-Pressure Turbine Separation Using Vortex Generator Jets," accepted for publication in AIAA Power and Propulsion.
[18] Bons, J., Sondergaard, R., and Rivir, R., 1999, "Control of Low-Pressure Turbine Separation Using Vortex Generator Jets," AIAA Paper No. 99-0367.
[19] Seifert, A., Daraby, A., Nishri, B., and Wygnanski, I., 1993, "The Effects of Forced Oscillations on the Performance of Airfoils," AIAA Paper No. 93-3264. *AIAA Shear Flow Conf.* Orlando, FL, July 6–9.
[20] Johari, H., and McManus, K., 1997, "Visualization of Pulsed Vortex Generator Jets for Active Control of Boundary Layer Separation," AIAA paper No. 97-2021.
[21] Gharib, M., Rambod, E., and Shariff, K., 1998, "A Universal Time Scale for Vortex Ring Formation," J. Fluid Mech., **360**, pp. 121–140.

Improved Prediction of Turbomachinery Flows Using Near-Wall Reynolds-Stress Model

G. A. Gerolymos
J. Neubauer
V. C. Sharma
I. Vallet

Université Pierre-et-Marie-Curie,
91405 Orsay, Paris, France

In this paper an assessment of the improvement in the prediction of complex turbomachinery flows using a new near-wall Reynolds-stress model is attempted. The turbulence closure used is a near-wall low-turbulence-Reynolds-number Reynolds-stress model, that is independent of the distance-from-the-wall and of the normal-to-the-wall direction. The model takes into account the Coriolis redistribution effect on the Reynolds-stresses. The five mean flow equations and the seven turbulence model equations are solved using an implicit coupled $O(\Delta x^3)$ upwind-biased solver. Results are compared with experimental data for three turbomachinery configurations: the NTUA high subsonic annular cascade, the NASA_37 rotor, and the RWTH 1 1/2 stage turbine. A detailed analysis of the flowfield is given. It is seen that the new model that takes into account the Reynolds-stress anisotropy substantially improves the agreement with experimental data, particularly for flows with large separation, while being only 30 percent more expensive than the $k-\varepsilon$ model (thanks to an efficient implicit implementation). It is believed that further work on advanced turbulence models will substantially enhance the predictive capability of complex turbulent flows in turbomachinery. [DOI: 10.1115/1.1426083]

Introduction

Computational Fluid Dynamics (CFD) coupled to turbomachinery specific steady [1–3] and unsteady [4–6] models, and supported by carefully planed experiments [7–9], has greatly enhanced our understanding of the complex flow phenomena encountered in multistage turbomachinery [10,11]. There are three major research areas where progress is necessary for improving the predictive capability of computational methodologies:

1. Correct modeling of steady and unsteady multistage effects [11,12]
2. Inclusion of technological details [13–15], which is mainly a multiblock structured or unstructured grid management issue
3. Turbulence and transition modeling [16–18]

An examination of computational methodologies for steady and unsteady turbomachinery flows (Table 1) indicates that the Boussinesq hypothesis of tensorial proportionality between the Reynolds-stresses and the mean flow rate-of-deformation tensor [16] is almost invariably used, the more advanced models solving two transport equations (an equation for the turbulence kinetic energy and an appropriate scale-determining equation). Although two-equation models give better results than mixing-length models (and are independent of grid topology), they do not take into account the anisotropy of the Reynolds-stress tensor. More importantly they ignore the misalignment of the Reynolds-stress tensor and the mean flow rate-of-deformation tensor, which can be important in complex three-dimensional separated flows. Numerous variants of two-equation models exist, but globally results are very similar between variants. In order to improve upon the two-equation family, it seems necessary to use models that handle properly the Reynolds-stress tensor anisotropy. To the authors knowledge such models have not yet been evaluated for three-dimensional turbomachinery applications.

Contributed by the International Gas Turbine Institute and presented at the 46th International Gas Turbine and Aeroengine Congress and Exhibition, New Orleans, Louisiana, June 4–7, 2001. Manuscript received by the International Gas Turbine Institute February 2001. Paper No. 2001-GT-196. Review Chair: R. Natole.

The Reynolds-stress models (RSM) are seven-equation closures, solving six transport equations for the six components of the symmetric Reynolds-stress tensor, and one scale-determining equation [65–67]. An additional interest of these models for turbomachinery applications is that the transport equations for the Reynolds-stresses contain exact Coriolis redistribution terms, and as a consequence take naturally into account the effect of rotation on turbulence. Recently, a Reynolds-stress closure for compressible separated flows, that is independent of the distance-from-the-wall and of the normal-to-the-wall direction, and that includes near-wall terms allowing integration to the wall, has been developed [68] and validated for a number of configurations [70,71]. This closure has also been extended to rotating flows [69].

The purpose of the present work is to examine the predictive capability of this RSM closure for turbomachinery configurations, and to assess potential improvements compared to two-equation closures. Results are presented for three turbomachinery configurations:

1. The NTUA subsonic ($\breve{M}<0.7$) annular cascade [72–74], a stator with thin rotor-like profiles, subjected to inflow with important radial gradients and exhibiting a large separation at the hub, that computations using the Launder-Sharma $k-\varepsilon$ closure fail to predict.
2. The NASA_37 rotor a well-known turbomachinery test-case [75–78], for which mixing-length and two-equation closures fail to correctly predict the nominal-speed operating line.
3. The RWTH 1 1/2 stage turbine [79,80], for which results using the Launder-Sharma $k-\varepsilon$ closure show very good agreement with measurements.

Turbulence Model

The mean flow equations and the turbulence closure used in the present work are described in detail by Gerolymos and Vallet [68,69], and are summarized in the following for completeness. The transport equations for the mean-flow (Eqs. (1)–(3)), and the Reynolds-stresses (Eq. 4), are written in a Cartesian reference-frame rotating with constant (time-independent) rotational velocity $\vec{\Omega}=\Omega_i\vec{e}_i$

Table 1 Turbulence models used in three-dimensional turbomachinery CFD

authors	date	closure	model	space	time
Hah [19]	1986	2-eq	ARSM [20]	$O(\Delta x^2)$ upwind	implicit PB
Dawes [2,21,22]	1987	0-eq	ML [23]	$O(\Delta x^2)$ centered	implicit
Hah [24–26]	1988	2-eq	$k-\varepsilon$ [27]	$O(\Delta x^2)$ upwind	implicit PB
Adamczyk et al. [28–30]	1990	0-eq	ML [23]	$O(\Delta x^2)$ centered	RK+IRS
Chima [31,32]	1990	0-eq	ML [23]	$O(\Delta x^2)$ centered	RK+IRS
Lakshminarayana et al. [33–35]	1992	2-eq	$k-\varepsilon$ [27]	$O(\Delta x^2)$ centered	RK
Denton [3]	1992	0-eq	ML [3]	$O(\Delta x^2)$ centered	explicit+MLTGRD
Dawes [36,37]	1992	2-eq	$k-\varepsilon$ [38]	$O(\Delta x^2)$ centered†	RK+IRS
Hirsch et al. [39,40]	1993	0-eq	ML [23]	$O(\Delta x^2)$ centered	RK+IRS
Arnone [41–43]	1993	0-eq	ML [23]	$O(\Delta x^2)$ centered	RK+IRS+MLTGRD
Turner and Jennions [44,45]	1993	2-eq	$k-\varepsilon$ WF [46]	$O(\Delta x^2)$ centered	RK
Vogel et al. [47,48]	1997	2-eq	$k-\omega_T$ [49]	$O(\Delta x^2)$ centered	RK
Ameri et al. [50,51]	1998	2-eq	$k-\omega_T$ [49]	$O(\Delta x^2)$ centered	RK+IRS+MLTGRD
Furukawa et al. [52]	1998	0-eq	ML [23]	$O(\Delta x^3)$ upwind	implicit
Rhie et al. [53,54]	1998	2-eq	$k-\varepsilon$ WF [46]	$O(\Delta x^2)$ centered	implicit PB
Gerolymos and Vallet [55–57]	1998	2-eq	$k-\varepsilon$ [58]	$O(\Delta x^3)$ upwind	implicit
Arima et al. [59]	1999	2-eq	$k-\varepsilon$ [27]	$O(\Delta x^3)$ TVD	implicit
Fritsch et al. [60,61]	1999	2-eq	$k-\varepsilon$ WF [46]	$O(\Delta x^2)$ centered	RK+IRS
Sayma et al. [63]	2000	1-eq	1-eq [64]	$O(\Delta x^2)$ centered†	implicit
present	2000	7-eq	RSM [68,69]	$O(\Delta x^3)$ upwind	implicit

WF=wall-functions; IRS=implicit residual smoothing; PB=pressure-based; RK=Runge-Kutta; MLTGRD=multigrid; ML=mixing-length; ARSM=algebraic Reynolds-stress model; RSM=Reynolds-stress model; †unstructured

$$\frac{\partial \overline{\rho}}{\partial t}+\frac{\partial \overline{\rho}\widetilde{W}_l}{\partial x_l}=0 \tag{1}$$

$$\frac{\partial \overline{\rho}\widetilde{W}_i}{\partial t}+\frac{\partial}{\partial x_l}[\overline{\rho}\widetilde{W}_i\widetilde{W}_l+\overline{p}\,\delta_{il}]+2\overline{\rho}\varepsilon_{ijl}\Omega_j\widetilde{W}_l+\overline{\rho}\frac{\partial}{\partial x_i}[-\tfrac{1}{2}\Omega^2R^2]-\frac{\partial}{\partial x_l}[\overline{\tau}_{il}-\overline{\rho}\widetilde{w_i''w_l''}]=0 \tag{2}$$

$$\begin{aligned}&\frac{\partial}{\partial t}\left[\overline{\rho}\left(\breve{h}_{t_w}-\frac{1}{2}\Omega^2R^2\right)-\overline{p}\right]+\frac{\partial}{\partial x_l}\left[\overline{\rho}\widetilde{W}_l\left(\breve{h}_{t_w}-\frac{1}{2}\Omega^2R^2\right)\right]\\&\quad-\frac{\partial}{\partial x_l}[\widetilde{W}_i(\overline{\tau}_{il}-\overline{\rho}\widetilde{w_i''w_l''})-(\overline{q}_l+\overline{\rho}\widetilde{h''w_l''})]\\&\quad=\underbrace{-\left(P_k-\overline{\rho}\varepsilon+\overline{p'\frac{\partial w_l''}{\partial x_l}}\right)+\frac{\partial}{\partial x_l}[\overline{pw_l''}]+(-\overline{p}\,\delta_{il}+\overline{\tau}_{il})\frac{\partial \overline{w_i''}}{\partial x_l}}_{S_{\breve{h}_t}}\end{aligned} \tag{3}$$

$$\begin{aligned}&\underbrace{\frac{\partial \overline{\rho}\widetilde{w_i''w_j''}}{\partial t}+\frac{\partial}{\partial x_l}(\overline{\rho}\widetilde{w_i''w_j''}\widetilde{W}_l)}_{\text{convection } C_{ij}}=\underbrace{\frac{\partial}{\partial x_l}(-\overline{\rho}\widetilde{w_i''w_j''w_l''}-\overline{p'w_j''}\delta_{il}-\overline{p'w_i''}\delta_{jl}+\overline{w_i''\tau'_{jl}+w_j''\tau'_{il}})}_{\text{diffusion } d_{ij}}+\underbrace{\overline{p'\left(\frac{\partial w_i''}{\partial x_j}+\frac{\partial w_j''}{\partial x_i}-\frac{2}{3}\frac{\partial w_k''}{\partial x_k}\delta_{ij}\right)}}_{\text{redistribution } \phi_{ij}}\\&\quad+\underbrace{(-2\overline{\rho}\epsilon_{ilm}\Omega_l\widetilde{w_j''w_m''}-2\overline{\rho}\epsilon_{jlm}\Omega_l\widetilde{w_i''w_m''})}_{\text{Coriolis redistribution } G_{ij}}+\underbrace{\left(-\overline{\rho}\widetilde{w_i''w_l''}\frac{\partial \widetilde{W}_j}{\partial x_l}-\overline{\rho}\widetilde{w_j''w_l''}\frac{\partial \widetilde{W}_i}{\partial x_l}\right)}_{\text{production } P_{ij}}-\underbrace{\left(\overline{\tau'_{jl}\frac{\partial w_i''}{\partial x_l}+\tau'_{il}\frac{\partial w_j''}{\partial x_l}}\right)}_{\text{dissipation } \overline{\rho}\varepsilon_{ij}}\\&\quad+\underbrace{\frac{2}{3}\overline{p'\frac{\partial w_k''}{\partial x_k}}\delta_{ij}}_{\text{pressure-dilatation}}+\underbrace{\left(-\overline{w_i''}\frac{\partial \overline{p}}{\partial x_j}-\overline{w_j''}\frac{\partial \overline{p}}{\partial x_i}+\overline{w_i''}\frac{\partial \overline{\tau}_{jl}}{\partial x_l}+\overline{w_j''}\frac{\partial \overline{\tau}_{il}}{\partial x_l}\right)}_{\text{density fluctuation effects } K_{ij}}\end{aligned} \tag{4}$$

where t is the time, x_l the cartesian space coordinates in the relative frame-of-reference, ε_{ijk} the third-order antisymmetric tensor [81], δ_{ij} the Kronecker symbol [81], R the radius (distance from the axis of rotation: $R^2=[x_i-|\Omega|^{-2}x_j\Omega_j\Omega_i][x_i-|\Omega|^{-2}x_j\Omega_j\Omega_i]$), W_i the relative velocity components, $V_i=W_i+\varepsilon_{ijk}\Omega_jx_k$ the absolute velocity components, ρ the density, p the pressure, τ_{ij} the viscous stresses, $\widetilde{(\cdot)}$ Favre-averaging, $\overline{(\cdot)}$ nonweighted-averaging, $(\cdot'')$ Favre-fluctuations, $(\cdot')$ nonweighted-fluctuations, $\breve{h}_{t_w}=\widetilde{h}+1/2\widetilde{W}_i\widetilde{W}_i$ the total enthalpy of the relative mean flow (which is different from the Favre-averaged total en-

Table 2 Anisotropy tensor invariants and model functions for the pressure-strain closure (Eq. 8)

$$a_{ij}=\frac{\widetilde{w_i''w_j''}}{k}-\frac{2}{3}\delta_{ij};\quad A_1=a_{ii}=0;\quad A_2=a_{ik}a_{ki};\quad A_3=a_{ik}a_{kj}a_{ji};\quad A=\left[1-\frac{9}{8}(A_2-A_3)\right]$$

$$C_1=1+2.58AA_2^{1/4}[1-e^{-(\mathrm{Re}_T/150)^2}]$$

$$C_2=\min[1,0.75+1.3\max[0,A-0.55]]A^{[\max(0.25,0.5-1.3\max[0,A-0.55])]}\left[1-\max\left(0,1-\frac{\mathrm{Re}_T}{50}\right)\right]$$

$$\vec{e}_n=n_i\vec{e}_i=\frac{\mathrm{grad}\,l_n}{\|\mathrm{grad}\,l_n\|};\quad l_n=\frac{l_T[1-e^{-\mathrm{Re}_T/30}]}{1+2\sqrt{A_2}+2A^{16}};\quad l_T=\frac{k^{3/2}}{\epsilon},$$

$$C_1^w=0.83\left[1-\frac{2}{3}(C_1-1)\right]\|\mathrm{grad}\,l_1^w\|;\quad l_1^w=\frac{l_T[1-e^{-\mathrm{Re}_T/30}]}{1+2A_2^{0.8}}$$

$$C_2^w=\max\left[\frac{2}{3}-\frac{1}{6C_2},0\right]\|\mathrm{grad}\,l_2^w\|;\quad l_2^w=\frac{l_T[1-e^{-\mathrm{Re}_T/30}]}{1+1.8A_2^{\max(0.6,A)}}$$

thalpy $\tilde{h}_{t_w}=\tilde{h}+1/2\,\tilde{W}_i\tilde{W}_i+k=\breve{h}_{t_w}+k$), h the specific enthalpy, $k=1/2\overline{w_i''w_i''}$ the turbulence-kinetic-energy, w_i'' the frame-independent velocity fluctuations, $P_k=1/2P_{ll}$ the turbulence kinetic energy production (equal to the trace of the Reynolds-stresses production tensor P_{ij}), and ε the dissipation-rate of the turbulence kinetic energy (equal to the trace of the Reynolds-stresses dissipation-rate tensor ε_{ij}). The symbol $(\breve{})$ is used to denote a function of average quantities that is neither a Favre-average nor a nonweighted average. The foregoing equations are exact Favre-Reynolds-averaged unclosed equations.

Convection C_{ij}, Coriolis redistribution G_{ij}, and production P_{ij} are exact terms. In the present model [68,69] direct compressibility effects K_{ij}, pressure-dilatation correlation, and pressure-diffusion are neglected. The triple correlations are modeled following Hanjalić and Launder [82]. The major improvements in the present model concern the pressure-strain redistribution terms. The pressure-strain redistribution terms augmented by the dissipation tensor anisotropy [83] are split into the slow and rapid parts and the corresponding echo-terms. The slow part ϕ_{ij1} is modelled by a simple quasi-linear return-to-isotropy model whose coefficient has been optimized by Launder and Shima [83] so as to account also for the anisotropic part of the dissipation tensor $\varepsilon_{ij}-2/3\delta_{ij}\varepsilon$. The closure for the rapid terms uses an isotropization-of-absolute-flow-production model [84–86]. The echo terms are computed in the usual way [87], but the unit pseudonormal direction $\vec{e}_n=n_i\vec{e}_i$ is approximated by the gradient of a function of the turbulence length scale l_T, of the anisotropy tensor invariants, and of the Lumley flatness parameter A [88], thus making the model independent of wall topology [89]. The effect of the distance-from-the-wall is included in the functions C_1^w and C_2^w. The final model is

$$K_{ij}\cong 0;\quad \overline{p'\frac{\partial w_l''}{\partial x_l}}\cong 0;\quad \overline{pw_l''}\cong 0;\quad \overline{w_i''}\cong 0;\quad S_{\breve{h}_t}\cong-(P_k-\rho\varepsilon) \tag{5}$$

$$d_{ij}\cong\frac{\partial}{\partial x_k}\left[-\overline{\rho}\widetilde{w_i''w_j''w_k''}+\breve{\mu}\frac{\partial\widetilde{w_i''w_j''}}{\partial x_k}\right] \tag{6}$$

$$\widetilde{w_i''w_j''w_k''}\cong-C_s\frac{k}{\varepsilon}\left[\widetilde{w_i''w_l''}\frac{\partial\widetilde{w_j''w_k''}}{\partial x_l}+\widetilde{w_j''w_l''}\frac{\partial\widetilde{w_k''w_i''}}{\partial x_l}+\widetilde{w_k''w_l''}\frac{\partial\widetilde{w_i''w_j''}}{\partial x_l}\right];\quad C_s=0.11 \tag{7}$$

$$\begin{aligned}\phi_{ij}-\overline{\rho}\overline{\varepsilon}_{ij}&=[\phi_{ij}-\overline{\rho}(\varepsilon_{ij}-\tfrac{2}{3}\delta_{ij}\varepsilon)]\\&=\phi_{ij1}+\phi_{ij2}+\phi_{ij1}^w+\phi_{ij2}^w-\tfrac{2}{3}\delta_{ij}\varepsilon\\&\cong-C_1\overline{\rho}\varepsilon a_{ij}-C_2(P_{ij}+\tfrac{1}{2}G_{ij}-\tfrac{1}{3}\delta_{ij}P_{ll})\\&\quad+C_1^w\frac{\varepsilon}{k}[\overline{\rho}\widetilde{w_k''w_m''}n_kn_m\delta_{ij}-\tfrac{3}{2}\overline{\rho}\widetilde{w_k''w_i''}n_kn_j\\&\quad-\tfrac{3}{2}\overline{\rho}\widetilde{w_k''w_j''}n_kn_i]+C_2^w[\phi_{km2}n_kn_m\delta_{ij}-\tfrac{3}{2}\phi_{ik2}n_kn_j\\&\quad-\tfrac{3}{2}\phi_{jk2}n_kn_i]-\tfrac{2}{3}\delta_{ij}\varepsilon\end{aligned} \tag{8}$$

The model coefficients (C_1,C_2,C_1^w,C_2^w) are functions of the anisotropy tensor (A_2,A_3,A) and of the turbulence-Reynolds-number Re_T (Table 2). The pseudonormal direction $\vec{n}$ appearing in the echo terms is given by the direction of the gradient of a function of turbulence length-scale l_T and of the anisotropy tensor invariants (Table 2).

The dissipation-rate of the turbulence-kinetic-energy ε is estimated by solving a transport equation for the modified-dissipation-rate [93] $\varepsilon^*=\varepsilon-2\breve{\nu}(\mathrm{grad}\,\sqrt{k})^2$ ($\breve{\nu}$ the kinematic viscosity). The wall boundary-condition is $\varepsilon_w^*=0$, offering enhanced numerical stability.

The modelled Launder-Sharma [58] equation, with a tensorial diffusion coefficient [90] is used

$$\begin{aligned}&\frac{\partial\overline{\rho}\overline{\varepsilon}^*}{\partial t}+\frac{\partial}{\partial x_l}(\tilde{W}_l\overline{\rho}\overline{\varepsilon}^*)-\frac{\partial}{\partial x_l}\left[\left(\breve{\mu}\delta_{kl}+C_\varepsilon\frac{k}{\varepsilon^*}\overline{\rho}\widetilde{w_k''w_l''}\right)\frac{\partial\varepsilon^*}{\partial x_k}\right]\\&\quad=C_{\varepsilon1}P_k\frac{\varepsilon^*}{k}-C_{\varepsilon2}\overline{\rho}\frac{\varepsilon^{*2}}{k}+\frac{2\breve{\mu}\mu_T}{\overline{\rho}}(\nabla^2\tilde{W})^2\end{aligned} \tag{9}$$

$$C_\varepsilon=0.18;\quad C_{\varepsilon1}=1.44;\quad C_{\varepsilon2}=1.92(1-0.3e^{-\mathrm{Re}_T^{*2}}) \tag{10}$$

The turbulent heat-flux $\overline{\rho}\widetilde{h''w_i''}$ is closed by a simple gradient model [68]

$$\begin{aligned}&\overline{\rho}\widetilde{h''w_i''}=-\frac{\mu_Tc_p}{\mathrm{Pr}_T}\frac{\partial\tilde{T}}{\partial x_i};\quad c_p=\frac{\gamma}{\gamma-1}R_g;\quad \mu_T=C_\mu\breve{\mu}\,\mathrm{Re}_T^*\\&C_\mu=0.09e^{-3.4/(1+0.02\,\mathrm{Re}_T^*)^2};\quad \mathrm{Re}_T^*=\frac{\overline{\rho}k^2}{\breve{\mu}\varepsilon^*}\end{aligned} \tag{11}$$

where c_p is the heat capacity at constant pressure, Pr_T the turbulent Prandtl number (in the present work $\mathrm{Pr}_T=0.9$ to obtain the correct recovery temperature for turbulent flow over an adiabatic wall), and Re_T^* the turbulence Reynolds number based on the modified dissipation [93] $\varepsilon^*=\varepsilon-2\breve{\nu}(\mathrm{grad}\,\sqrt{k})^2$ (ε being turbulence-kinetic energy dissipation, and $\breve{\nu}$ the kinematic viscos-

ity). The thermodynamics of the working gas and the mean viscous stresses and heat-flux are approximated by standard closure assumptions [68,90,91]

$$\bar{p}=\bar{\rho}R_g\tilde{T}=\bar{\rho}\frac{\gamma-1}{\gamma}\tilde{h};\quad \breve{\mu}=\mu(\tilde{T})=\mu_{273}\frac{\tilde{T}^{3/2}}{273.15^{3/2}}\frac{T_S+273.15}{T_S+\tilde{T}}$$

$$\breve{\kappa}=\kappa(\tilde{T})=\kappa_{273}\frac{\mu(\tilde{T})}{\mu_{273}}[1+A_\kappa(\tilde{T}-273.15)] \tag{12}$$

$$\bar{\tau}_{ij}\cong\breve{\mu}\left(\frac{\partial\tilde{W}_i}{\partial x_j}+\frac{\partial\tilde{W}_j}{\partial x_i}-\frac{2}{3}\frac{\partial\tilde{W}_l}{\partial x_l}\delta_{ij}\right);\quad \bar{q}_i\cong-\breve{\kappa}\frac{\partial\tilde{T}}{\partial x_i} \tag{13}$$

where γ is the isentropic exponent, R_g the gas-constant, μ the dynamic viscosity, and κ the heat conductivity. For air $R_g=287.04\,\mathrm{m^2\,s^{-2}\,K^{-1}}$, $\gamma=1.4$, $\mu_{273}=17.11\times10^{-6}\,\mathrm{Pa\,s}$, $\kappa_{273}=0.0242\,\mathrm{W\,m^{-1}\,K^{-1}}$, $T_S=110.4\,\mathrm{K}$, and $A_\kappa=0.00023\,\mathrm{K^{-1}}$.

Numerics and Inflow Conditions

The computational method used is based on the solver developed by Gerolymos and Vallet [90,91]. Turbomachinery computations use multiblock structured grids [55–57] which are generated biharmonically [92]. The mean-flow and turbulence-transport equations are written in the (x,y,z) Cartesian rotating (relative) coordinates system, and are discretized in space, on a structured multiblock grid, using a third-order upwind-biased MUSCL scheme with Van Leer flux-vector-splitting and Van Albada limiters, and the resulting semi-discrete scheme is integrated in time using a first-order implicit procedure [55,90,91]. The mean-flow and turbulence-transport equations are integrated simultaneously. Source-terms (centrifugal, Coriolis, and RSM) are treated explicitly. The local-time-step is based on a combined convective (Courant) and viscous (von Neumann) criterion. The boundary conditions which are applied both explicitly and implicitly, using a phantom-nodes-technique at grid interfaces, are described in detail by Gerolymos et al. [55].

Inflow profiles of total-pressure, total-temperature and Reynolds-stresses are obtained by fitting, near the hub and the casing, analytic boundary-layer profiles of velocity, temperature and turbulence variables, in a manner similar to Gerolymos [99]. The velocity and temperature profiles are based on a van Driest [94] transformation of the Spalding profile [95], augmented by a Coles wake function [96]. Turbulence kinetic energy and dissipation-rate are obtained by a local equilibrium hypothesis $P_k=\bar{\rho}\bar{\varepsilon}^*$ (where the eddy viscosity is obtained using the Spalding profile [95] in the inner part, and Clauser's eddy-viscosity [97] in the outer part of the boundary-layers). The Reynolds-stresses are obtained using constant flat-plate boundary-layer structure values [98]. The basic initialization procedure is two-dimensional. It is applied in a frame-of-reference where the wall is fixed, and with a coordinate-system aligned to the external flow-velocity. A full description of the procedure for three-dimensional internal flows containing solid corners is given by Vallet [100], and has been applied to turbomachinery by Tsanga [101].

Comparison With Measurements

Configurations Studied. The proposed Reynolds-stress closure has been assessed through comparison with measurements and with computational results using the Launder-Sharma $k-\varepsilon$ closure [58], for three turbomachinery configurations (Table 3). For the three cases a careful study of grid-convergence of computational results was undertaken (Table 4). The nondimensional distance from the wall of the first grid point nearest to it $n_w^+=\Delta n_w u_\tau\breve{\nu}_w^{-1}$ (where u_τ is the friction velocity, Δn_w the distance from the wall, and $\breve{\nu}_w$ the kinematic viscosity at the wall) is an important parameter, which, for transonic flows with boundary-layer separation, should not exceed 3/4 [90].

Table 3 Configurations studied

	NTUA_1	NASA_37	RWTH_1
R_{HUB} (m)	0.244	0.175–0.194	0.245
R_{CASING} (m)	0.324	0.237–0.258	0.3
χ (m)	0.1	~0.056	~0.06
Re_χ	$\sim10^6$	$1.33-2.10\times10^6$	$0.20-0.45\times10^6$
N_B	19	36	36–41–36
RPM	0	17188.7	3500
$\dot{m}$ (kg s^{-1})	13.2	19.2–20.9	8.2
π_{T-T}	0.988	1.95–2.15	1/1.2
p_{t_i} (Pa)	97000	101325	169500
T_{t_i} (K)	288.15	288.15	305.75
T_{u_i}	4 percent	3 percent	3 percent
$\delta_{i_{\mathrm{HUB}}}$ (m)	0.014	0.005	0.0025
$\Pi_{i_{\mathrm{HUB}}}$	0.8	0	0
$\delta_{i_{\mathrm{CASING}}}$ (m)	0.0025	0.005	0.005
$\Pi_{i_{\mathrm{CASING}}}$	0	0	0

R_{HUB}=flowpath radius at the hub; R_{CASING}=flowpath radius at the casing; χ=chord; Re_χ=Reynolds-number based on inflow relative velocity, blade-chord, and viscosity at inflow conditions; RPM=revolutions per minute; N_B=number of blades; $\dot{m}$=massflow; π_{T-T}=total-to-total pressure-ratio; p_{t_i}=inflow total-pressure; T_{t_i}=inflow total-temperature; T_{u_i}=turbulence intensity at inflow; $\delta_{i_{\mathrm{HUB}}}$=boundary-layer thickness at inflow on the hub; $\Pi_{i_{\mathrm{HUB}}}$=Coles parameter at inflow on the hub; $\delta_{i_{\mathrm{CASING}}}$=boundary-layer thickness at inflow on the casing; $\Pi_{i_{\mathrm{CASING}}}$=Coles parameter at inflow on the casing

Annular Subsonic Cascade. The experimental set up is an annular compressor cascade studied at the Laboratory of Thermal Turbomachines of the National Technical University of Athens by Doukelis et al. [72–74]. The measurements were taken at inlet Mach numbers of ~0.6. Although the experiment was initially intended to investigate the effects of clearance between the blade-tip and the hub, the reference case with clearance $\delta_{HC}=0$ is a very interesting test-case, because of the experimentally observed large hub-corner-stall.

Preliminary $k-\varepsilon$ computations failed to predict the large separation region, and as a consequence gave very poor agreement with measured outflow angles. The incoming flow is quite complex, because the swirl necessary to obtain the desired inlet flow-angle was experimentally obtained by using a scroll (and not stator vanes). As a consequence inflow profiles of total-pressure p_{t_M} and flow-angle α_M contain important radial variations (Fig. 1). The turbulence intensity at inflow was experimentally estimated at the high values of 3–4 percent. The value $T_{u_i}=4$ percent was applied as inflow condition in the computations (Table 3).

Comparison of computed and measured pitchwise-averaged quantities at inflow and outflow planes (Fig. 1) shows substantial differences between the present RSM and the Launder-Sharma $k-\varepsilon$ [58] predictions. These computations were run using grid_D of 2.3×10^6 points (Table 4). This is a rather fine grid with $n_w^+<3/4$ everywhere. At the inflow plane (situated 0.2 axial chords χ_x downstream of the computational inflow plane where the inflow profiles are applied) it is seen that both models accurately simulate the radial distributions of α_M and p_{t_M}. They show, however, a difference in the turbulence profiles near the hub, due to a different development from computational inflow downstream, the RSM computations predicting a lower level of turbulence near the hub (unfortunately no detailed measurements of k_M were available). At the outflow the RSM computations correctly predict the experimentally measured high swirl near the hub. This swirl is associated with a large hub-corner-stall, on the suction-side of the blades (Fig. 2). The Mach-number plots show the large separation predicted by the RSM computations on the suction-side (Fig. 2). The flow has to go around the separation bubble, and this results in high outflow swirl at the hub (corresponding to substantial underturning at the hub), in accordance with measurements (Fig. 1). The $k-\varepsilon$ computations substantially underestimate the separation region (Fig. 2), and as a consequence predict lower than measured swirl at the exit of the cascade (Fig. 1). These differences between

Table 4 Computational grid summary

	UH	O	DH	TC	OZ	points†	$n^+_{w_B}$	$n^+_{w_{FP}}$
NTUA_1								
grid_B	17×47× 69	201×49× 69	51×51× 69	⋯	⋯	914 181	<0.7	<0.7
grid_D	17×47×141	201×53×141	91×51×141	⋯	⋯	2 269 113	<0.7	<0.7
grid_E	17×47×141	201×81×141	91×51×141	⋯	⋯	3 062 661	<0.7	<0.7
NASA_37								
grid_B	49×41× 65	201×45× 65	81×61× 65	201×11×21	201×21×31	1 149 421	<0.3	<1.5
grid_C	49×41×101	201×53×101	81×61×101	201×17×31	201×21×41	1 955 587	<0.3	<1.0
grid_D	49×41×161	201×53×161	81×61×165	201×17×41	201×21×61	3 067 042	<0.3	<0.5
RWTH_1								
grid_A	31×25× 51	181×31× 51	41×31× 51	181×21×21	181×21×31	1 010 772	<10.	<5.0
grid_B	31×31× 65	201×49× 65	41×41× 65	201×21×21	201×21×31	2 265 346	<1.0	<1.5
grid_C	31×31× 81	201×49× 81	41×41× 81	201×31×31	201×26×46	2 957 250	<1.0	<1.0
grid_D	31×31×121	201×49×121	41×41×121	201×31×41	201×26×61	4 359 380	<1.0	<0.7

UH=upstream-H-grid (axial×tangential×radial); O=blades-O-grid (around the blade×away from blade×radial); DH=downstream-H-grid (axial×tangential×radial); TC =tip-clearance-O-grid (around the blade×away from blade×radial); OZ=O-zoom-grid (around the blade×away from blade×radial); †without O-grid points overlapped by the OZ-grid; $n^+_{w_B}=n^+_w$ on the blades; $n^+_{w_{FP}}=n^+_w$ on the flowpath

the two models are also seen in the plots of turbulence-kinetic-energy k (Fig. 2), where one can also observe the larger wakes predicted by the RSM computations. Comparison of computed and measured total-pressure p_{t_M} distributions at cascade exit (Fig. 1) indicates good agreement. The RSM computations slightly overestimate losses near the hub. This, together with the slightly higher than measured values of α_M, suggest that the present model slightly overestimates the separated flow region, a problem attributed rather to delayed reattachment than to extensive separation. It is indeed believed that the predicted separation is not too thick, but that it does not end as abruptly as it should.

In order to assert grid independence of the results, computations were run using different grids (Table 4). Grid_B of $\sim 10^6$ points has 69 radial surfaces, and satisfactory n^+_w (<0.7), both on the flowpath walls and on the blades. Grid refinement strategy maintained the size of the first grid-cell away from the walls, by using more points with a lower stretching near the walls (geometric stretching was invariably used [92]). Grid_D of $\sim 2.3\times 10^6$ points has 141 radial stations, and slightly more blade-to-blade points (Table 4). Grid_E of $\sim 3\times 10^6$ points has the same radial resolution as grid_D, but a finer blade-to-blade grid (81 points from the blade surface to mid-passage, corresponding to 161 points from one blade to its neighbor), in order to examine the influence of blade-to-blade refinement (Table 4).

It should be noted that both the radial refinement (grid_B to

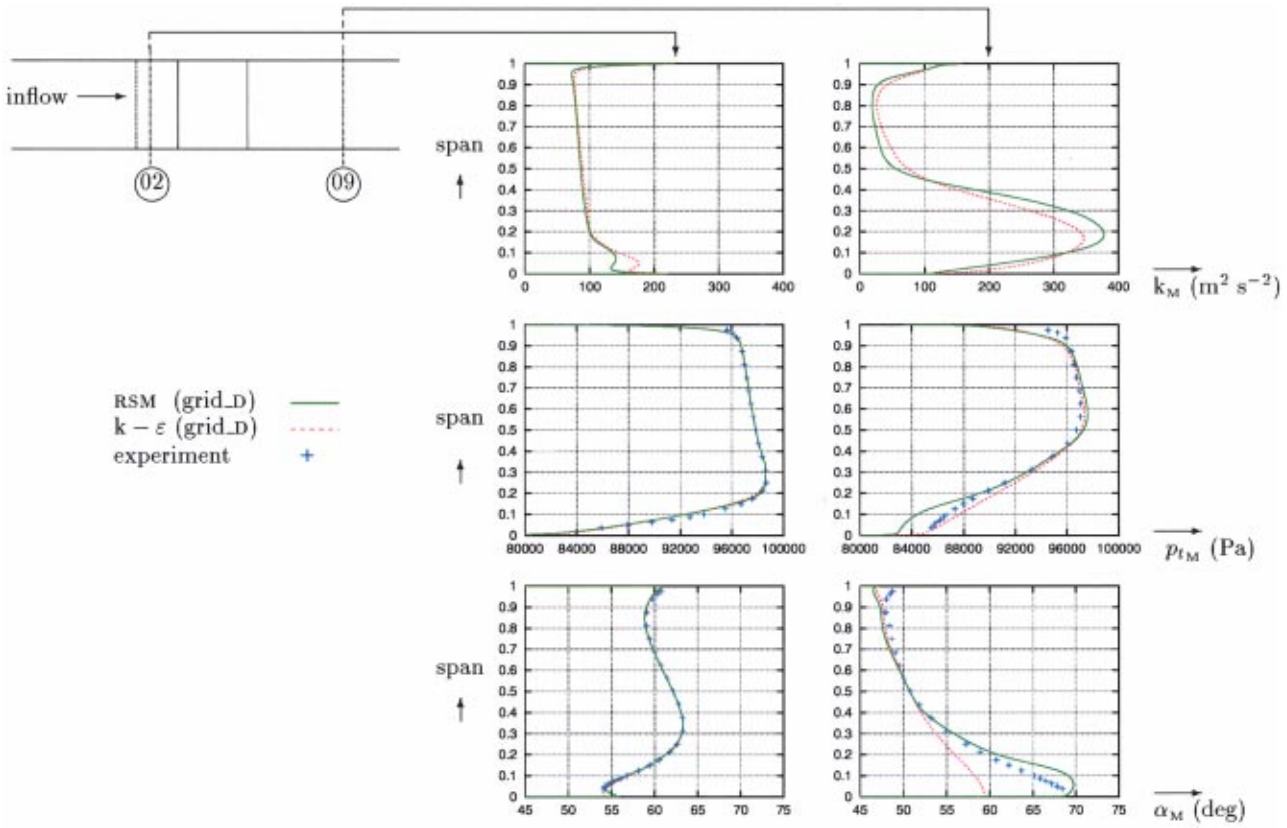

Fig. 1 Comparison of measured and computed (using the present RSM and the Launder-Sharma $k-\varepsilon$ [58]) pitchwise-averaged flow-angle α_M, total-pressure p_{t_M}, and turbulence-kinetic-energy k_M for the NTUA_1 annular cascade ($\dot{m}$ =13.2 kg s^{-1}; T_u=4 percent; grid_D)

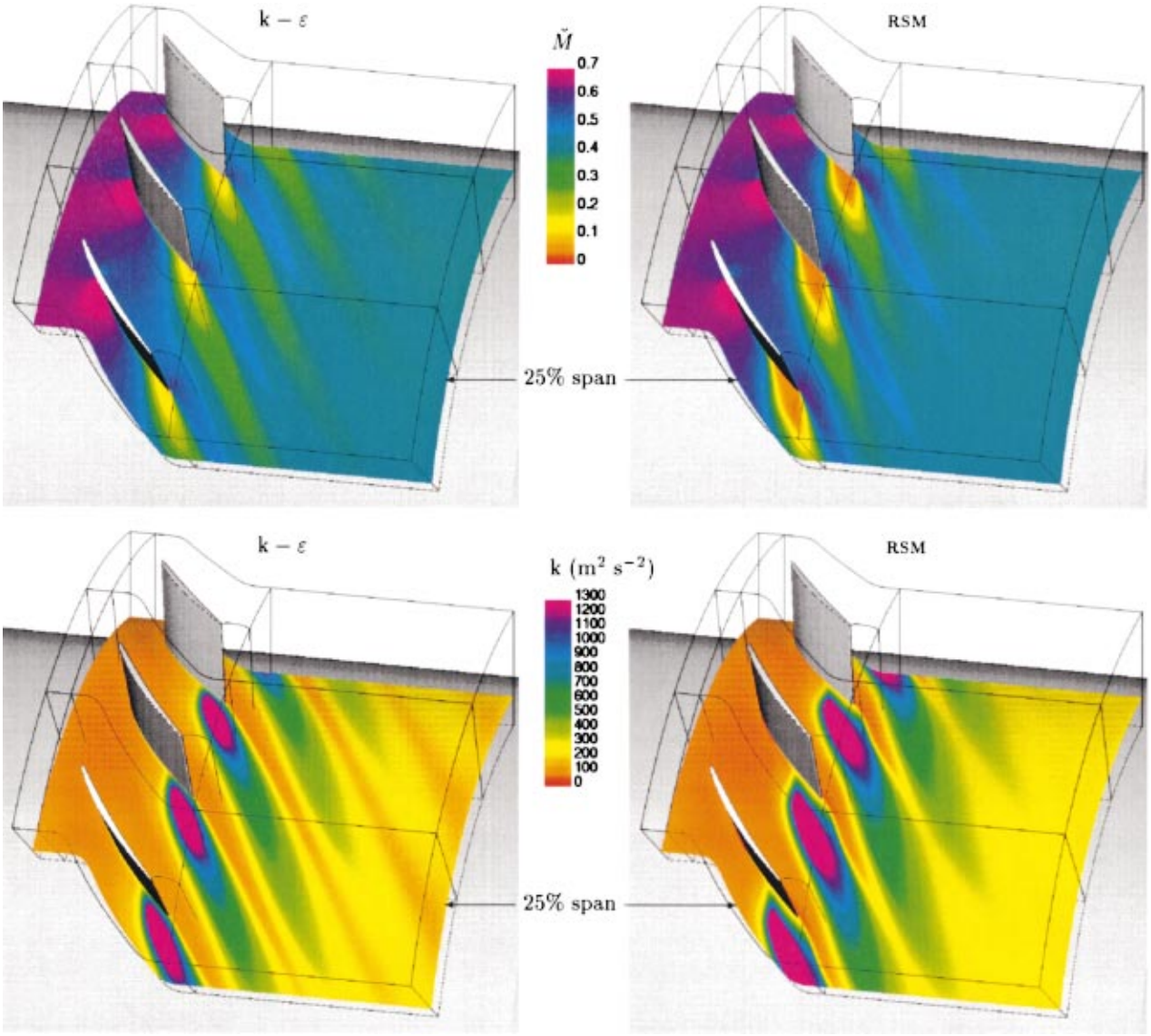

Fig. 2 Comparison of Mach-number $\breve{M}$ and turbulence-kinetic-energy k computed (using the present RSM and the Launder-Sharma $k-\varepsilon$ [58]), at 25 percent span ($\dot{m}=13.2$ kg s^{-1}; $T_u=4$ percent; grid_D)

grid_D) and the blade-to-blade refinement (grid_D to grid_E) are substantial (factor 2). Both the $k-\varepsilon$ and the RSM computations (Fig. 3) indicate that doubling the number of points radially enhances the prediction of the separation region (2.5 deg in α_M for the $k-\varepsilon$, and 4.5 deg in α_M for the RSM). The blade-to-blade refinement (grid_E) was investigated for both closures (Fig. 3), and results are identical with the results of grid_D. It is believed that grid_D is adequate, although computations with an even finer grid (radially) would be needed to demonstrate this assertion. It should be noted that even the coarse grid_B RSM computations are better than the fine grid_D $k-\varepsilon$ (Fig. 3), underlining the substantial improvement in flow angle prediction by the RSM closure. This improvement is associated with a better prediction of the separated flow structure.

Transonic Compressor Rotor. The NASA_37 transonic rotor [75–78] is a well known turbomachinery test-case. Experimental data for the NASA_37 transonic rotor were obtained at various measurement planes, using both LDV (LASER Doppler Velocimetry) and classical rake measurements of p_{t_M} and T_{t_M} (the averaging procedure $(\cdot)_M$ is described in Davis et al. [76]). This rotor has 36 blades, nominal speed 17,188.7 RPM, and maximum massflow at nominal speed $\dot{m}_{CH}=20.93\pm0.14$ kg s^{-1}. The nominal tip-clearance-gap is 0.356 mm [75]. The measurements uncertainties were reported by Suder [78]: massflow $\dot{m}\pm0.3$ kg s^{-1}; absolute flow angle $\alpha_M\pm1.0$ deg; total pressure $p_{t_M}\pm100$ Pa; total temperature $T_{t_M}\pm0.6$ K.

Computations by numerous authors [13,26,32,56,59,77,102,103] using a wide variety of turbulence models and numerical methods, highlight the predictive CFD state-of-the-art for this configuration. A careful examination of the computations indicates that, in the limit of grid-converged results, both zero-equation and two-equation models overestimate the total-to-total pressure ratio π_{T-T} as a function of massflow $\dot{m}$. The zero-equation models overestimate π_{T-T} by ~3 percent, whereas the two-equation models overestimate π_{T-T} by ~1.5 percent [103]. Grid convergence is important, as demonstrated by comparing the results using the $k-\varepsilon$ model of Chien [27] obtained by Hah and Loellbach [26] using $\sim1.9\times10^6$ points grid and by Arima et al. [59] using $\sim0.6\times10^6$ points. The latter grid was particularly coarse in the blade-to-blade direction, and as a consequence underestimated choke massflow $\dot{m}_{\mathrm{CH}}$ (20.77 kg s^{-1}

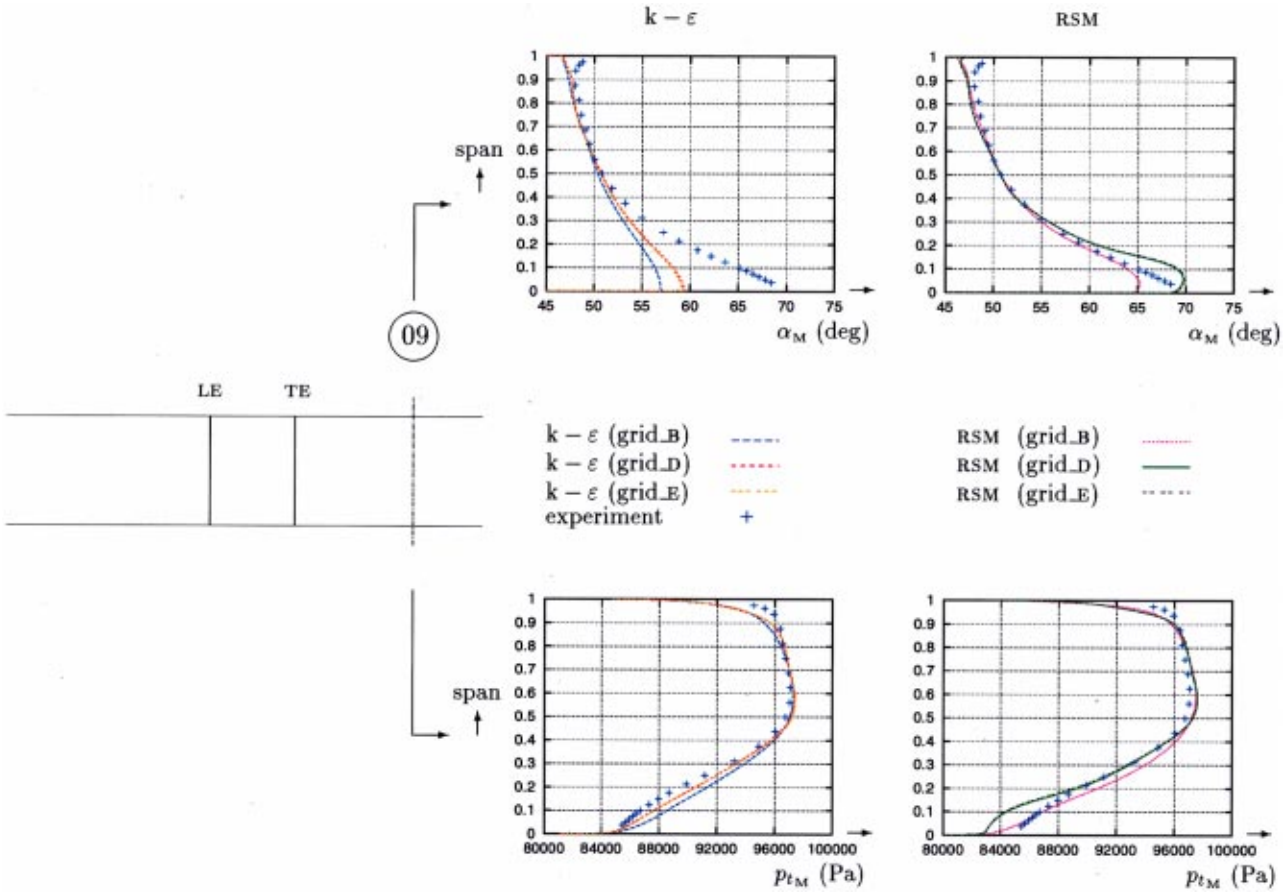

Fig. 3 Study of grid-convergence of computed (using the present RSM and the Launder-Sharma $k-\varepsilon$ [58]) pitchwise-averaged flow-angle α_M, and total-pressure p_{t_M}, at the exit of the NTUA_1 annular cascade ($\dot{m}=13.2$ kg s^{-1}; $T_u=4$ percent)

instead of the measured value of 20.93 kg s^{-1}), which was correctly predicted by the fine grid computations by Hah and Loellbach [26]. The associated increased blockage gave a seemingly good prediction of pressure-ratio in the coarse grid computations [59], but the characteristic is translated towards lower massflow (in terms of dimensional $\dot{m}$), and the results are not representative of the grid-converged model performance.

If the form of the spanwise distribution of the pitchwise averaged total pressure p_{t_M} downstream of the rotor is considered, there are two regions of discrepancy with measurements: 1) a local peak of p_{t_M} near the casing, corresponding to a too strong tip-clearance vortex, and 2) a p_{t_M} deficit near the hub (this deficit is attributed to both an underestimation of hub-corner stall by the models [26] and to massflow leakage emanating from a small gap between the stationary and rotating parts of the hub upstream of the rotor [13] which was not modelled in the computations).

Previous studies by the authors [55,56] using the same grid-generation methodology [92] and the same numerical scheme, but with the Launder-Sharma $k-\varepsilon$ turbulence model [58], include grid-convergence studies using 1, 2, and 3×10^6 points (Table 3), indicating that results with grid_C (2×10^6 points) are practically grid independent. Based on these results, all the computations presented here were run on grid_D of $\sim3\times10^6$ points (Table 3). The computational grid consists of an H-O-H grid with 161 radial stations. Tip clearance is discretized using an independent O-type grid with 41 radial stations [55,92]. Comparison of the measured characteristic (π_{T-T} between stations 1 and 4 versus $\dot{m}$) at nominal speed (Fig. 4) with computations using the new RSM closure [69] and the Launder-Sharma $k-\varepsilon$ turbulence model [58] indicate that the RSM results follow closely the experimental characteristic. The improvement of the agreement with measurements is substantial, compared to the $k-\varepsilon$ results (Fig. 4). Examination of the spanwise distribution of pitchwise-averaged total pressure p_{t_M} at station 4, for various operating points shows that the improvement is mainly due to the accurate prediction between 40 percent and 80 percent span (Fig. 4), where the RSM results closely follow the experimental data, improving upon the $k-\varepsilon$ computations. There is also noticeable improvement in predicting the p_{t_M} deficit near the hub (where the nonsimulated massflow leakage might account for the remaining discrepancy), for all operating points (Fig. 4). On the other hand, the RSM model fails to correct the parasite p_{t_M} peak near the casing, indicating that the relaxation behavior of the model must be improved. Comparison of computed and measured spanwise distributions of pitchwise-averaged absolute flow angle α_M at station 4 for the different operating points (Fig. 4) shows good agreement between the two models and the experiment. The RSM results underestimate α_M by ~1 deg, which is within measurement accuracy [78], whereas the $k-\varepsilon$ results are very close to the experimental data.

In order to understand the mechanism responsible for the improved agreement with measurements, the isentropic Mach-number distributions M_{is} [69] at 70 percent span (Fig. 5) are examined. At operating point 1, the RSM results predict a flow at the limit between started and unstarted regime [104], whereas the $k-\varepsilon$ computations indicate that the flow is started, with a clearly visible pressure-side shock-wave (Fig. 5). On the suction-side the RSM results predict a shock-wave location ~5 percent χ_x further upstream compared to the $k-\varepsilon$ computations (Fig. 5). This point is choked, so that the correspondence between experiment and computations is taken at the same pressure-ratio (and same mass-

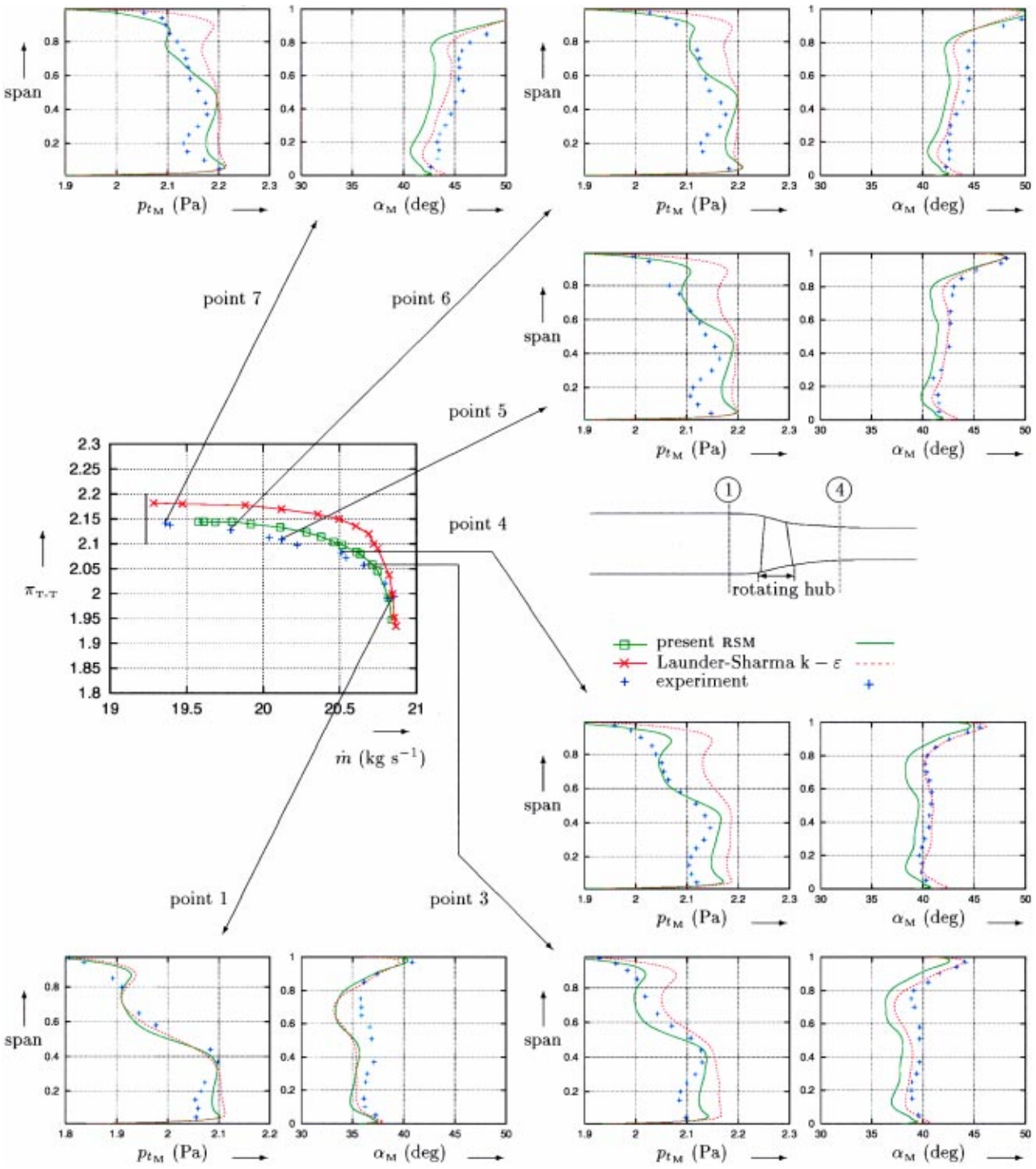

Fig. 4 Comparison of measured and computed (using the present RSM and the Launder-Sharma $k-\varepsilon$ [58]) radial distributions of pitchwise-averaged flow-angle $\alpha_{x\theta M}$, and total-pressure p_{t_M}, for various operating points at design-speed, for NASA_37 rotor ($\dot{m}$=20.85, 20.79, 20.65, 20.51, 20.12, 19.78, 19.36 kg s^{-1}; T_u=3 percent; δ_{TC}=0.356 mm; grid_D)

flow), corresponding to different shock-structures in the two models. For all the other operating points the flow is unstarted [104], with the RSM results predicting the suction-side shockwave systematically ~5 percent χ_x (χ_x=axial chord) upstream of the $k-\varepsilon$ location. Similar conclusions are drawn at other spanwise locations. It is plausible that the main improvement brought by the RSM closure is an improved prediction of the limit between started and unstarted flow, attributed to a better prediction of blockage [78], because of a better prediction of shock-wave/boundary-layer interaction. Another improvement of the RSM closure is a more pronounced p_{t_M} peak very near the hub (Fig. 4), for all operating points, indicating a better prediction of hub secondary flows.

Turbine 1 1/2 Stage. Finally computations were run for a 1 1/2 stage axial flow turbine, experimentally investigated at the Institut für Strahlantriebe und Turboarbeitsmaschinen of the RWTH [79,80]. Steady three-dimensional multistage computa-

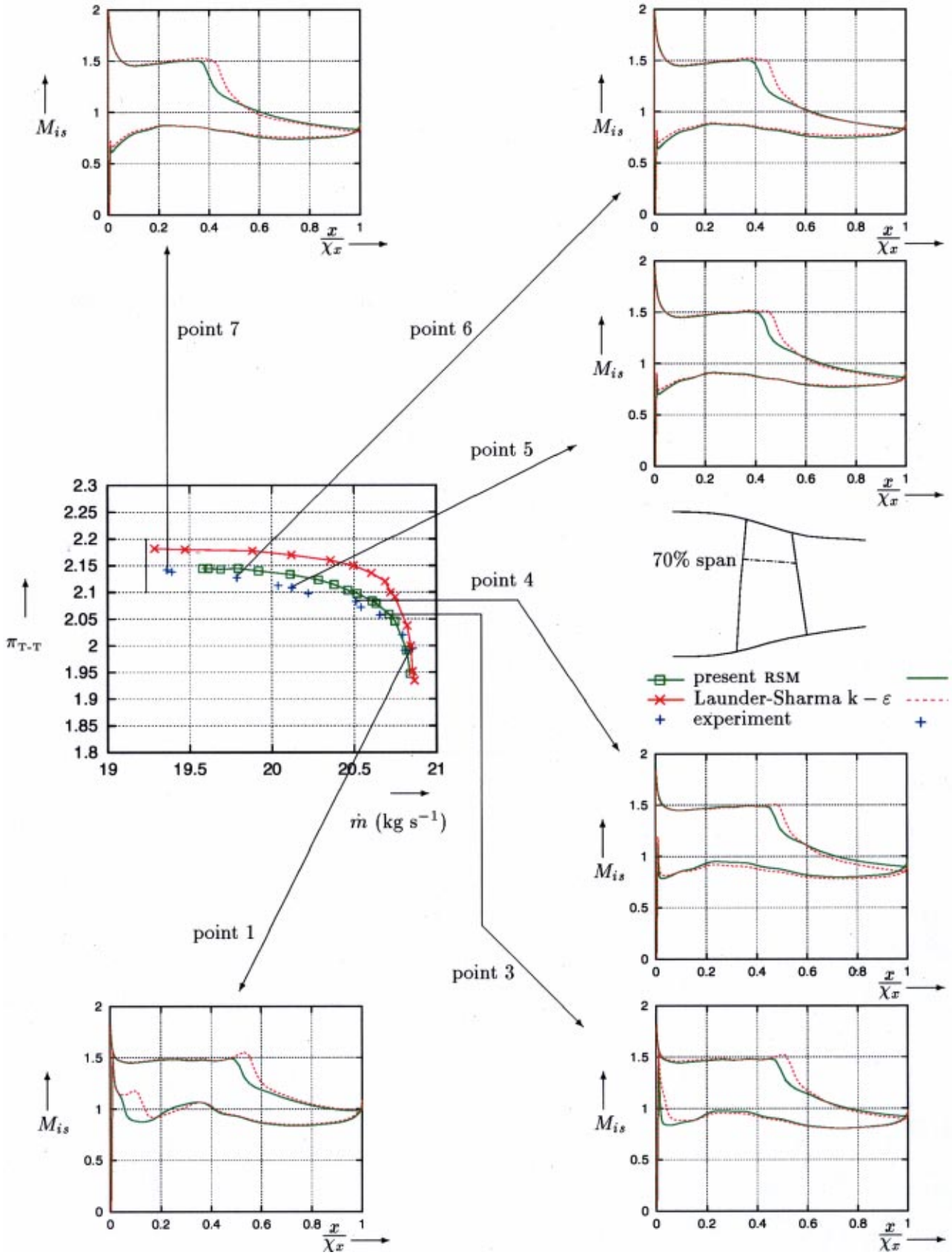

Fig. 5 Computed (using the present RSM and the Launder-Sharma $k-\varepsilon$ [58]) isentropic-Mach-number distributions at 70 percent span for various operating points at design-speed, for NASA_37 rotor ($\dot{m}$=20.85, 20.79, 20.65, 20.51, 20.12, 19.78, 19.36 kg s^{-1}; T_u=3 percent, δ_{TC}=0.356 mm; grid_D)

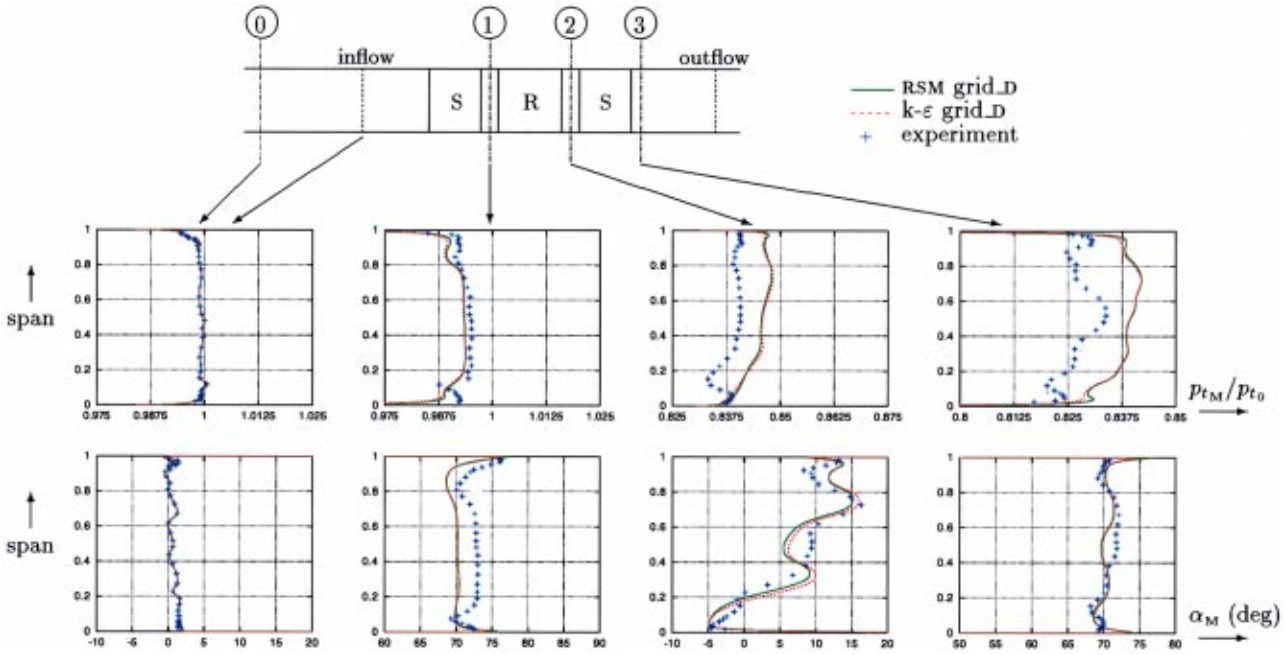

Fig. 6 Measured and computed (using the present RSM and the Launder-Sharma $k-\varepsilon$ [58]) radial distributions of pitchwise-averaged total pressure p_{t_M} and flow angle α_M for RWTH_1 turbine 1 1/2 stage ($\dot{m}=8.23$ kg s^{-1}; $T_u=3$ percent; $\delta_{TC}=0.4$ mm; grid_D)

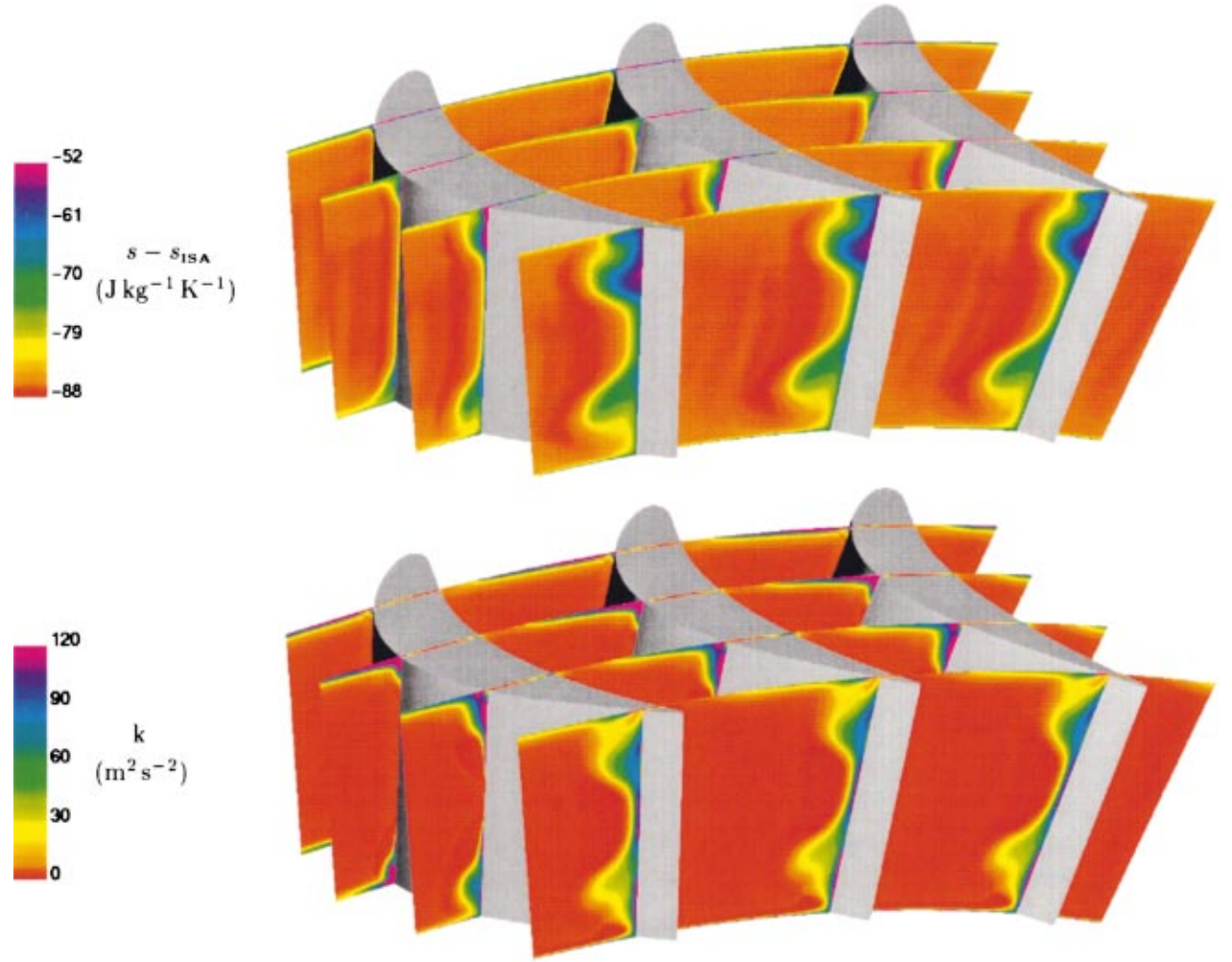

Fig. 7 Computed entropy and turbulent kinetic energy plots at various axial planes in the rotor of the RWTH_1 turbine 1 1/2 stage ($\dot{m}=8.23$ kg s^{-1}; $T_u=3$ percent; $\delta_{TC}=0.4$ mm; RSM grid_D)

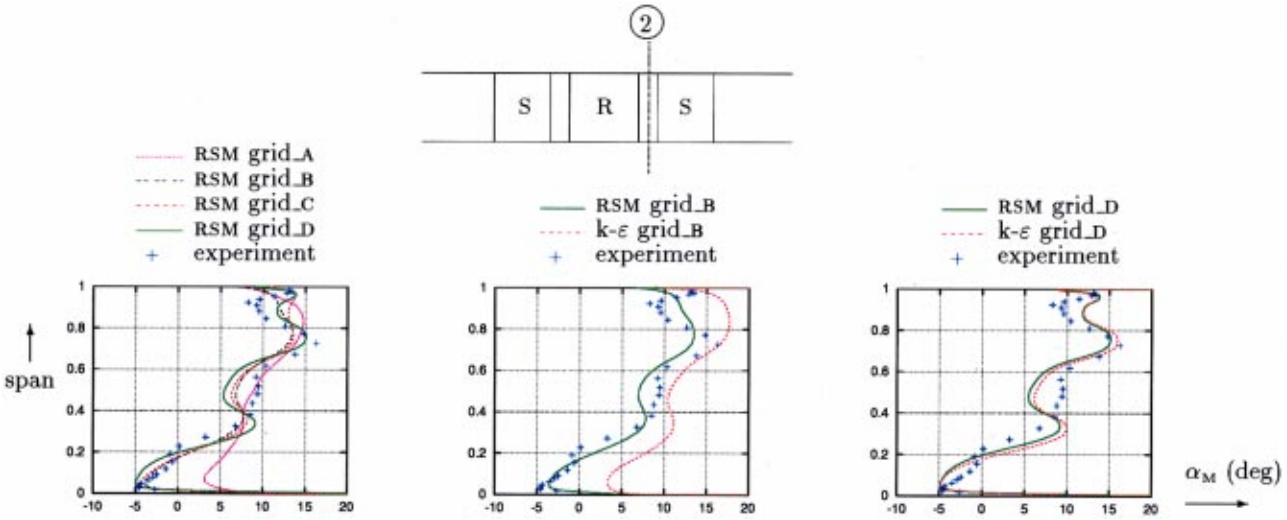

Fig. 8 Grid-influence on pitchwise-averaged absolute-flow angle α_M at rotor-exit of RWTH_1 1 1/2 stage turbine ($\dot{m}$ = 8.23 kg s^{-1}; T_u = 3 percent; δ_{TC} = 0.4 mm; grid_D)

tions for this configuration (Table 3) have been compared with measurements by Emunds et al. [105], who used a mixing-length turbulence model [23]. Volmar et al. [106] have performed unsteady computations with time-lagged pitchwise periodicity for this configuration, using a $k-\varepsilon$ model [27]. Gallus et al. [107] have performed both steady and unsteady computations, for the stage without the outlet-guide-vane, using a $k-\varepsilon$ model [27].

In the present work we have performed steady-multistage computations using four different grids of 1, 2.3, 3, and 4.4×10^6 points (Table 4) with 51, 65, 81, and 121 radial stations, respectively. The multistage method is based on a mixing-plane approach between blade-rows, and is described in detail in Gerolymos and Hanisch [57]. The meridional averages that are conserved across the interface are density, mass-weighted velocities, static pressure, Reynolds-stresses, and kinetic-energy-dissipation-rate [57]. The matching between rows is achieved using overlapping grids that allow matching of both values and throughflow-wise gradients of the conserved quantities, ensuring very good continuity at the interfaces [57].

Comparison of measured and computed pitchwise-averaged total pressure p_{t_M} and absolute flow-angle α_M at various axial stations (Fig. 6) indicates that there is close agreement between the RSM and the $k-\varepsilon$ computations on the fine grid_D (4.4×10^6 points). Agreement with measurements is good for the flow-angles α_M, but the computations slightly overestimate the total pressure p_{t_M} at rotor exit (plane 2), and as a consequence at the stage exit plane 3. This overestimation corresponds to a ~1.5 percent underestimation of turbine expansion ratio.

The form of the radial distribution of p_{t_M} is nonetheless very well predicted (Fig. 6). Volmar et al. [106] note that there are some slight inconsistencies in the experimental data (measurements were taken at different planes for slightly different values of $\dot{m}$, and different values of inlet total pressure p_{t_0}). In our computations the same problems were encountered. As there was some uncertainty concerning massflow, it was preferred to run the computations at a massflow $\dot{m}=8.23\,\mathrm{kg\,s^{-1}}$ slightly higher than the average experimental massflow $\dot{m}_{\mathrm{exp}}=8\,\mathrm{kg\,s^{-1}}$, so as to have good agreement in rotor outflow (plane 2) angle α_M (Fig. 6). This resulted in the slight difference in p_{t_M} level. This choice (instead of fitting p_{t_M} with a corresponding discrepancy in α_M) was taken because of our interest in the secondary flow phenomena at rotor exit (Fig. 7). Each peak on the rotor-exit α_M (Fig. 6) distribution can be identified with a secondary flow-peak in entropy and turbulence-kinetic energy distributions (Fig. 7). The overall agreement with measurements is quite good, for both turbulence models, except at ~20 percent span, where a slight dip in α_M, associated with an important dip in p_{t_M}, is not correctly predicted. Emunds et al. [105] argue that this location corresponds to the interaction between the nozzle-hub and the rotor-hub secondary vortices.

The grid influence on results is illustrated by comparing the results obtained using the different grids (Table 4) and the two turbulence models for the α_M distribution at rotor exit (Fig. 8). Concerning the RSM computations, it is seen that the coarsest grid_A with 51 radial stations fails to predict correctly the structure of the secondary flows. It should be noted that this grid has unacceptably high values of $n_w^+\cong5-10$ (Table 4). The RSM computations on grid_B with 65 radial stations and $n_w^+\sim3/2$ (Table 4) does a good job in predicting the structure of the secondary flows everywhere, except near the casing where it fails to correctly describe the tip-leakage vortex, associated with the α_M-peak at 96 percent span (Fig. 8). This is improved in the RSM computations on grid_C which has 81 radial stations, $n_w^+<1$, and a finer grid within the tip-clearance-gap (Table 4). This grid predicts the tip-leakage vortex α_M-peak at 96 percent span, but not the undulation at 90 percent span, corresponding to the interaction between tip-clearance and the casing secondary vortex (Fig. 8). Finally, the RSM computations on grid_D with 121 radial stations predict correctly the secondary flows. Examination of the $k-\varepsilon$ computations on grid_B and grid_D reveals the interesting feature that although both models give similar results on the fine grid_D, the RSM computations are substantially better on the coarse grid_B, compared to the $k-\varepsilon$ computations on the same grid (Fig. 8).

Conclusions and Perspectives in Turbulence Modelling

In the present work a new near-wall low-turbulence-Reynolds-number Reynolds-stress model (RSM), that has been designed to be completely independent of wall-topology (distance-from-the-wall and normal-to-the-wall orientation), has been evaluated by comparison with experimental measurements, and with results using the Launder-Sharma $k-\varepsilon$ model, for three turbomachinery configurations. To the authors knowledge, this is the first time that a full near-wall second-moment closure is applied to complex three-dimensional turbomachinery configurations.

For the NTUA_1 subsortic annular cascade, the RSM closure corrects the deficiency of the $k-\varepsilon$ model, by predicting the large suction-side hub-corner-stall observed experimentally. This results

in a substantially improved prediction of cascade-exit flow-angle distribution, resulting from a better prediction of the complex three-dimensional separated flow structure.

For the NASA_37 transonic compressor rotor, the RSM closure improves the massflow versus pressure-ratio operating-map prediction, by improving the prediction of the radial distribution of total-pressure, through a better prediction of rotor-shockwave structure (and of shock-wave/boundary-layer interaction). In particular, the rotor spill-point (where the flow at the tip becomes unstarted) is correctly predicted.

For the RWTH_1 1 1/2 stage axial flow turbine, both models give good prediction of the flow, with the RSM model being less-grid-sensitive than the $k-\varepsilon$ model, an important advantage for industrial applications on relatively coarse grids. In this case the $k-\varepsilon$ results on the fine grid are very satisfactory, because there is no substantial flow separation.

Globally, the present RSM closure yields invariably better results than the $k-\varepsilon$ closure, especially when flow separation dominates the flowfield. For flows with little separation, the improvement is marginal, but for all the configurations studied by the authors results are invariably better with the RSM closure. Experience with the model shows that it is as robust as the $k-\varepsilon$ model, and computing time-requirements are only 30 percent higher per iteration. When the RSM closure captures complex separated flow structures, convergence may be slower so that a factor 1.5 in overall computing-time requirements is estimated.

The basic drawback of the model, as established from comparisons with experimental data for basic shockwave/boundary-layer interaction flows, is a too slow relaxation after the interaction, and a delayed reattachment. As a consequence, blockage is slightly overpredicted. Furthermore, the model does not improve upon the $k-\varepsilon$ results in the prediction of the tip-clearance vortex mixing with the main flow, but this is again a problem of too slow relaxation (mainly observed in the p_{t_M}-peak near the casing for the NASA_37 rotor case). In summary, the new model correctly predicts separation, but should be improved in the prediction of reattachment. These are two different processes. The separation has been controlled in the model by an improved quasi-linear model of the rapid pressure-strain term. The control of reattachment (independently of separation) is currently under investigation (improved ε equation, or 2-scale model).

Despite the aforementioned drawbacks, the new RSM offers more confidence in CFD results than 2-equation closures, and also more possibilities for improvements, since it offers a better description of turbulence structure. It is believed that further validation work, and further developments in such advanced turbulence closures (as opposed to oversimplified 1-equation closures) will improve the state-of-the-art of turbomachinery CFD.

Acknowledgments

The computations presented were run at the Institut pour le Développement des Ressources en Informatique Scientifique (IDRIS), where computer ressources were made available by the Comité Scientifique. The research scholarships of V.C.S. and J.N. were funded through the APPACET project (BRITE project of the European Community). Authors are listed alphabetically.

References

[1] Adamczyk, J. J., 1985, "Model Equation for Simulating Flows in Multistage Turbomachinery," ASME Paper No. 85-GT-226.
[2] Dawes, W. N., 1992, "Toward Improved Throughflow Capability: The Use of 3-D Viscous Flow Solvers in a Multistage Environment," ASME J. Turbomach., **114**, pp. 8–17.
[3] Denton, J. D., 1992, "The Calculation of 3-D Viscous Flow through Multistage Turbomachines," ASME J. Turbomach., **114**, pp. 18–26.
[4] Erdos, J. I., Alzner, E., and McNally, W., 1977, "Numerical Solution of Periodic Transonic Flow through a Fan Stage," AIAA J., **15**, pp. 1559–1568.
[5] Giles, M. B., 1990, "Stator/Rotor Interaction in a Transonic Turbine," J. Propul. Power, **6**, pp. 621–627.
[6] He, L., 1992, "Method of Simulating Unsteady Turbomachinery Flows with Multiple Perturbations," AIAA J., **30**, pp. 2730–2735.
[7] Rieß, W., and Evers, B., 1985, "Die Strömung in mehrstufigen Turbinen mit langen Schaufeln bei Schwachlast- und Leerlaufbetrieb," VGB Kraftwerkstechnik, **65**, pp. 1020–1026.
[8] Leylek, J. H., and Wisler, D. C., 1991, "Mixing in Axial-Flow Compressors: Conclusions Drawn from 3-D Navier-Stokes Analyses and Experiments," ASME J. Turbomach., **113**, pp. 139–160.
[9] Suder, K. L., Chima, R. V., Strazisar, A. J., and Roberts, W. B., 1995, "The Effect of Adding Roughness and Thickness to a Transonic Axial Compressor Rotor," ASME J. Turbomach., **117**, pp. 491–505.
[10] Denton, J. D., 1993, "Loss Mechanisms in Turbomachines," ASME J. Turbomach., **115**, pp. 621–656.
[11] Adamczyk, J. J., 2000, "Aerodynamic Analysis of Multistage Turbomachinery Flows in Support of Aerodynamic Design," ASME J. Turbomach., **122**, pp. 189–217.
[12] Silkowski, P. D., and Hall, K. C., 1998, "A Coupled Mode Analysis of Unsteady Multistage Flows in Turbomachinery," ASME J. Turbomach., **120**, pp. 410–421.
[13] Shabbir, A., Celestina, M. L., Adamczyk, J. J., and Strazisar, A. J., 1997, "The Effect of Hub Leakage on 2 High Speed Axial Flow Compressor Rotors," ASME Paper No. 97-GT-346.
[14] Wellborn, S. R., and Okiishi, T. H., 1999, "The Influence of Shrouded Cavity Flows on Multistage Compressor Performance," ASME J. Turbomach., **121**, pp. 486–498.
[15] Wellborn, S. R., Tolchinsky, I., and Okiishi, T. H., 2000, "Modeling Shrouded Stator Cavity Flows in Axial-Flow Compressors," ASME J. Turbomach., **122**, pp. 55–61.
[16] Lakshminarayana, B., 1986, "Turbulence Modeling for Complex Shear Flows," AIAA J., **24**, pp. 1900–1917.
[17] Mayle, R. E., 1991, "The Role of Laminar-Turbulent Transition in Gas Turbine Engines," ASME J. Turbomach., **113**, pp. 509–537.
[18] Bradshaw, P., 1996, "Turbulence Modeling with Application to Turbomachinery," Prog. Aerosp. Sci., **32**, pp. 575–624.
[19] Hah, C., 1986, "A Numerical Modeling of Endwall and Tip-Clearance Flow of an Isolated Compressor Rotor," ASME J. Eng. Gas Turbines Power, **108**, pp. 15–21.
[20] Hah, C., 1987, "Calculation of 3-D Viscous Flows in Turbomachinery with an Implicit Relaxation Method," J. Propul. Power, **3**, pp. 415–422.
[21] Dawes, W. N., 1987, "A Numerical Analysis of the 3-D Viscous Flow in a Transonic Compressor Rotor and Comparison with Experiment," ASME J. Turbomach., **109**, pp. 83–90.
[22] Goyal, R. K., and Dawes, W. N., 1993, "A Comparison of the Measured and Predicted Flow Field in a Modern Fan-Bypass Configuration," ASME J. Turbomach., **115**, pp. 273–282.
[23] Baldwin, B., and Lomax, H., 1978, "Thin-Layer Approximation and Separated Algebraic Model for Separated Turbulent Flows," AIAA Paper No. 78–257.
[24] Hah, C., Bryans, A. C., Moussa, Z., and Tomsho, M. E., 1988, "Application of Viscous Flow Computations for the Aerodynamic Performance of a Backswept Impeller at Various Operating Conditions," ASME J. Turbomach., **110**, pp. 303–311.
[25] Copenhaver, W. W., Hah, C., and Puterbaugh, S. L., 1993, "3-D Flow Phenomena in a Transonic, High-Throughflow, Axial-Flow Compressor Stage," ASME J. Turbomach., **115**, pp. 240–248.
[26] Hah, C., and Loellbach, J., 1999, "Development of Hub Corner Stall and Its Influence on the Performance of Axial Compressor Blade Rows," ASME J. Turbomach., **121**, pp. 67–77.
[27] Chien, K. Y., 1982, "Predictions of Channel and Boundary-Layer Flows with a Low-Reynolds Number Turbulence Model," AIAA J., **20**, No. 1, pp. 33–38.
[28] Adamczyk, J. J., Celestina, M. L., Beach, T. A., and Barnett, M., 1990, "Simulation of 3-D Viscous Flow within a Multistage Turbine," ASME J. Turbomach., **112**, pp. 370–376.
[29] Mulac, R. A., and Adamczyk, J. J., 1992, "The Numerical Simulation of a High-Speed Axial Flow Compressor," ASME J. Turbomach., **114**, pp. 517–527.
[30] Adamczyk, J. J., Celestina, M. L., and Greitzer, E. M., 1993, "The Role of Tip Clearance in High-Speed Fan Stall," ASME J. Turbomach., **115**, pp. 28–39.
[31] Chima, R. V., and Yokota, J. W., 1990, "Numerical Analysis of 3-D Viscous Internal Flows," AIAA J., **28**, pp. 798–806.
[32] Chima, R. V., 1998, "Calculation of Tip Clearance Effects in a Transonic Compressor Rotor," ASME J. Turbomach., **120**, pp. 131–140.
[33] Kunz, R. F., and Lakshminarayana, B., 1992, "3-D Navier-Stokes Computation of Turbomachinery Flows using an Explicit Numerical Procedure and a Coupled $k-\varepsilon$ Turbulence Model," ASME J. Turbomach., **114**, pp. 627–642.
[34] Kunz, R. F., Lakshminarayana, B., and Basson, A. H., 1993, "Investigation of Tip-Clearance Phenomena in an Axial Compressor Cascade using Euler and Navier-Stokes Procedures," ASME J. Turbomach., **115**, pp. 453–467.
[35] Koiro, M., and Lakshminarayana, B., 1998, "Simulation and Validation of Mach-Number Effects on Secondary Flow in a Transonic Turbine Cascade using a Multigrid $k-\varepsilon$ Solver," ASME J. Turbomach., **120**, pp. 285–297.
[36] Dawes, W. N., 1992, "The Simulation of 3-D Viscous Flow in Turbomachinery Geometries using a Solution-Adaptive Unstructured Mesh Methodology," ASME J. Turbomach., **114**, pp. 528–537.
[37] Dawes, W. N., 1993, "The Extension of a Solutions-Adaptive 3-D Navier-Stokes Solver toward Geometries of Arbitrary Complexity," ASME J. Turbomach., **115**, pp. 283–295.
[38] Lam, C. K. G., and Bremhorst, K. A., 1981, "Modified Form of the $k-\varepsilon$

Model for Predicting Wall Turbulence,'' ASME J. Fluids Eng., **103**, pp. 456–460.
[39] Rizzi, A., Eliasson, P., Lindblad, I., Hirsch, C., Lacor, C., and Haeuser, J., 1993, ''The Engineering of Multiblock/Multigrid Software for Navier-Stokes Flows on Structured Meshes,'' Comput. Fluids, **22**, pp. 341–367.
[40] Kang, S., and Hirsch, C., 1996, ''Numerical Simulation of 3-D Viscous Flow in a Linear Compressor Cascade with Tip-Clearance,'' ASME J. Turbomach., **118**, pp. 492–505.
[41] Arnone, A., Liou, M. S., and Povinelli, L. A., 1993, ''Multigrid Calculation of 3-D Viscous Cascade Flows,'' J. Propul. Power, **9**, pp. 605–614.
[42] Ameri, A. A., and Arnone, A., 1996, ''Transition Modeling Effects on Turbine Rotor Blade Heat Transfer Predictions,'' ASME J. Turbomach., **118**, pp. 307–313.
[43] Arnone, A., 1994, ''Viscous Analysis of 3-D Rotor Flow using a Multigrid Method,'' ASME J. Turbomach., **116**, pp. 435–445.
[44] Turner, M. G., and Jennions, I. K., 1993, ''An Investigation of Turbulence Modeling in Transonic Fans Including a Novel Implementation of an Implicit $k-\varepsilon$ Turbulence Model,'' ASME J. Turbomach., **115**, pp. 249–260.
[45] Jennions, I. K., and Turner, M. G., 1993, ''3-D Navier-Stokes Computations of Transonic Fan Flow using an Explicit Flow Solver and an Implicit $k-\varepsilon$ Turbulence Model,'' ASME J. Turbomach., **115**, pp. 261–272.
[46] Launder, B. E., and Spalding, D. B., 1974, ''The Numerical Computation of Turbulent Flows,'' Comput. Methods Appl. Mech. Eng., **3**, pp. 269–289.
[47] Langowsky, C., and Vogel, D. T., 1997, ''Influence of Film-Cooling on the Secondary Flow in a Turbine Nozzle,'' AIAA J., **35**, pp. 111–118.
[48] Hildebrandt, T., and Fottner, L., 1999, ''A Numerical Study of the Influence of Grid Refinement and Turbulence Modeling on the Flow Field Inside a Highly Loaded Turbine Cascade,'' ASME J. Turbomach., **121**, pp. 709–716.
[49] Wilcox, D. C., 1994, ''Simulation of Transition with a 2-Equation Turbulence Model,'' AIAA J., **32**, pp. 247–255.
[50] Ameri, A. A., Steinthorsson, E., and Rigby, D. L., 1998, ''Effect of Squealer Tip on Rotor Heat Transfer and Efficiency,'' ASME J. Turbomach., **120**, pp. 753–759.
[51] Ameri, A. A., Steinthorsson, E., and Rigby, D. L., 1999, ''Effects of Tip-Clearance and Casing Recess on Heat Transfer and Stage Efficiency in Axial Turbines,'' ASME J. Turbomach., **121**, pp. 683–693.
[52] Furukawa, M., Inoue, M., Saiki, K., and Yamada, K., 1999, ''The Role of Tip Leakage Vortex Breakdown in Compressor Rotor Aerodynamics,'' ASME J. Turbomach., **121**, pp. 469–480.
[53] Rhie, C. M., Gleixner, A. J., Spear, D. A., Fischberg, C. J., and Zacharias, R. M., 1998, ''Development and Application of a Multistage Navier-Stokes Solver: Part I—Multistage Modeling using Bodyforces and Deterministic Stresses,'' ASME J. Turbomach., **120**, pp. 205–214.
[54] LeJambre, C. R., Zacharias, R. M., Biederman, B. P., Gleixner, A. J., and Yetka, C. J., 1998, ''Development and Application of a Multistage Navier-Stokes Solver: Part II—Application to a High-Pressure Compressor Design,'' ASME J. Turbomach., **120**, pp. 215–223.
[55] Gerolymos, G. A., Tsanga, G., and Vallet, I., 1998, ''Near-Wall $k-\varepsilon$ Computation of Transonic Turbomachinery Flows with Tip-Clearance,'' AIAA J., **36**, pp. 1769–1777.
[56] Gerolymos, G. A., and Vallet, I., 1999, ''Tip-Clearance and Secondary Flows in a Transonic Compressor Rotor,'' ASME J. Turbomach., **121**, pp. 751–762.
[57] Gerolymos, G. A., and Hanisch, C., 1999, ''Multistage 3-D Navier-Stokes Computation of Off-Design Operation of a 4-Stage Turbine,'' IMechE J. Power Energy, **213**, pp. 243–261.
[58] Launder, B. E., and Sharma, B. I., 1974, ''Application of the Energy Dissipation Model of Turbulence to the Calculation of Flows near a Spinning Disk,'' Lett. Heat Mass Transfer, **1**, pp. 131–138.
[59] Arima, T., Sonoda, T., Shirotori, M., Tamura, A., and Kikuchi, K., 1999, ''A Numerical Investigation of Transonic Axial Compressor Rotor Flow using a Low-Reynolds-Number $k-\varepsilon$ Turbulence Model,'' ASME J. Turbomach., **121**, pp. 44–58.
[60] Hoeger, M., Fritsch, G., and Bauer, D., 1999, ''Numerical Simulation of the Shock/Tip-Leakage-Vortex Interaction in a HPC Front Stage,'' ASME J. Turbomach., **121**, pp. 456–468.
[61] Fritsch, G., Hoeger, M., Blaha, C., and Bauer, D., 2000, ''Viscous 3-D Simulation of Transonic Compressor Stage on Parallel Hardware,'' J. Propul. Power, **16**, pp. 388–396.
[62] Sleiman, M., Tam, A., Robichaud, M. P., Peeters, M. F., and Habashi, W. G., 1999, ''Multistage Simulation by an Adaptive Finite Element Approach using Structured Grids,'' ASME J. Fluids Eng., **121**, pp. 450–459.
[63] Sayma, A. I., Vahdati, M., Sbardella, L., and Imregun, M., 2000, ''Modeling of 3-D Viscous Compressible Turbomachinery Flows using Unstructured Hybrid Grids,'' AIAA J., **38**, pp. 945–954.
[64] Baldwin, B. S., and Barth T. J., 1991, ''1-Equation Turbulence Transport Model for High-Reynolds-Number Wall-Bounded Flows,'' AIAA Paper No. 91–0610.
[65] Launder, B. E., 1989, ''2-Moment Closure: Present and Future?,'' Int. J. Heat Fluid Flow, **10**, pp. 282–300.
[66] Hanjalić, K., 1994, ''Advanced Turbulence Closure Models: A View of Current Status and Future Prospects,'' Int. J. Heat Fluid Flow, **15**, pp. 178–203.
[67] Leschziner, M. A., 1995, ''Computation of Aerodynamic Flows with Turbulence-Transport Models Based on 2-Moment Closure,'' Comput. Fluids, **24**, pp. 377–392.
[68] Gerolymos, G. A., and Vallet, I., ''Wall-Normal-Free Near-Wall Reynolds-Stress Closure for 3-D Compressible Separated Flows,'' AIAA J., **39**, 1833–1842.
[69] Gerolymos, G. A., and Vallet, I., , ''Wall-Normal-Free Reynolds-Stress Model for Rotating Flows Applied to Turbomachinery,'' AIAA J., to be published.
[70] Noussis, I., 2000, ''Validation d'une Fermeture RSM des sur des Profils d'Aile,'' DEA, Université Pierre-et-Marie-Curie, Paris.
[71] Filaire, F., 2000, ''Evaluation des Possibilités Prédictives es Modélisations de l'Interaction Choc/Couche-Limite,'' DEA, Université Pierre-et-Marie-Curie, Paris.
[72] Doukelis, A., Mathioudakis, K., Papailiou, K., 1998, ''The Effect of Tip Clearance Gap Size and Wall Rotation on the Performance of a High-Speed Annular Compressor Cascade,'' ASME Paper No. 98-GT-38.
[73] Doukelis, A., Mathioudakis, K., Papailiou, K., 1998, ''Investigation of the 3-D Flow Structure in a High-Speed Annular Compressor Cascade for Tip Clearance Effects,'' ASME Paper No. 98-GT-39.
[74] Doukelis, A., Mathioudakis, K., Papailiou, K., 2000, ''Detailed Flow and Overall Performance Measurements for Different Clearance Configurations in the NTUA Annular Cascade Facility,'' Chapter 3, Final Report, APPACET Project, EEC Contract BRPR-CT97-0610.
[75] Strazisar, A. J., 1994, ''Data Report and Data Diskette for NASA Transonic Compressor Rotor 37,'' NASA Lewis Research Center.
[76] Davis, R. L., Delaney, R. A., Denton, J. D., Giles, M. B., Strazisar, A. J., and Wisler, D. C., 1993, ''CFD Code Assessment in Turbomachinery—Author's Information Package,'' ASME Turbomachinery Committee.
[77] Denton, J. D., 1996, ''Lessons Learned from Rotor 37,'' *Int. Symp. on Experimental and Computational Aerothermodynamics of Internal Flows (ISAIF)*, Beijing, China, Sept.
[78] Suder, K. L., 1998, ''Blockage Development in a Transonic Axial Compressor Rotor,'' ASME J. Turbomach., **120**, pp. 465–476.
[79] Walraevens, R. E., and Gallus, H. E., 1996, ''Stator-Rotor-Stator Interaction in an Axial Flow Turbine and its Influence on Loss Mechanisms,'' *AGARD Conf. Proc.*, Vol. 571, pp. 39.1–39.14.
[80] Walraevens, R. E., Gallus, H. E., Jung, A. R., Mayer, J. F., and Stetter, H., 1998, ''Experimental and Computational Study of the Unsteady Flow in a 1 1/2 Stage Axial Turbine with Emphasis on the Secondary Flow in the Second Stator,'' ASME Paper No. 98-GT-254.
[81] Aris, R., 1962, *Vectors, Tensors, and the Basic Equations of Fluid Mechanics*, Dover, New York.
[82] Hanjalić, K., and Launder, B. E., 1972, ''A Reynolds Stress Model of Turbulence and its Application to Thin Shear Flows,'' J. Fluid Mech., **52**, pp. 609–638.
[83] Launder, B. E., and Shima, N., 1989, ''2-Moment Closure for the Near-Wall Sublayer: Development and Application,'' AIAA J., **27**, pp. 1319–1325.
[84] Launder, B. E., Tselepidakis, D. P., and Younis, B. A., 1987, ''A Second-Moment Closure Study of Rotating Channel Flow,'' J. Fluid Mech., **183**, pp. 63–75.
[85] Shima, N., 1993, ''Prediction of Turbulent Boundary-Layer Flows with a 2-Moment Closure: Part I—Effects of Periodic Pressure Gradient, Wall Transpiration, and Free-Stream Turbulence,'' ASME J. Fluids Eng., **115**, pp. 56–63.
[86] Shima, N., 1993, ''Prediction of Turbulent Boundary-Layer Flows with a 2-Moment Closure: Part II—Effects of Streamline Curvature and Spanwise Rotation,'' ASME J. Fluids Eng., **115**, pp. 64–69.
[87] Gibson, M. M., and Launder, B. E., 1978, ''Ground Effects on Pressure Fluctuations in the Atmospheric Boundary Layer,'' J. Fluid Mech., **86**, pp. 491–511.
[88] Lumley, J. L., 1978, ''Computational Modeling of Turbulent Flows,'' Adv. Appl. Mech., **18**, pp. 123–176.
[89] Launder, B. E., and Li, S. P., 1994, ''Elimination of Wall-Topography Parameters from 2-Moment Closure,'' Phys. Fluids, **6**, pp. 999–1006.
[90] Gerolymos, G. A., and Vallet, I., 1996, ''Implicit Computation of the 3-D Compressible Navier-Stokes Equations using $k-\varepsilon$ Turbulence Closure,'' AIAA J., **34**, pp. 1321–1330.
[91] Gerolymos, G. A., and Vallet, I., 1997, ''Near-Wall Reynolds-Stress 3-D Transonic Flows Computation,'' AIAA J., **35**, pp. 228–236.
[92] Gerolymos, G. A., and Tsanga, G., 1999, ''Biharmonic 3-D Grid Generation for Axial Turbomachinery with Tip-Clearance,'' J. Propul. Power, **15**, pp. 476–479.
[93] Jones, W. P., and Launder, B. E., 1972, ''The Prediction of Laminarization with a 2-Equation Model of Turbulence,'' Int. J. Heat Mass Transf., **15**, pp. 301–314.
[94] Van Driest, E. R., 1951, ''Turbulent Boundary-Layer in Compressible Fluids,'' J. Aerosp. Sci., **18**, pp. 145–160, 216.
[95] Spalding, D. B., 1961, ''A Single Formula for the Law-of-the-Wall,'' ASME J. Appl. Mech., **28**, pp. 455–458.
[96] Coles, D., 1956, ''The Law of the Wake in the Turbulent Boundary Layer,'' J. Fluid Mech., **1**, pp. 191–226.
[97] Clauser, F. H., 1956, ''The Turbulent Boundary-Layer,'' Adv. Appl. Mech., **4**, pp. 1–51.
[98] Harris, V. G., Graham, J. A. M., and Corrsin, S., 1977, ''Further experiments in nearly homogeneous turbulent shear flows,'' J. Fluid Mech., **81**, pp. 657–687.
[99] Gerolymos, G. A., 1990, ''Implicit Multiple-Grid Solution of the Compressible Navier-Stokes Equations using $k-\varepsilon$ Turbulence Closure,'' AIAA J., **28**, pp. 1707–1717.
[100] Vallet, I., 1995, ''Aérodynamique Numérique 3-D Instationnaire avec Fermeture Bas-Reynolds au Second Ordre,'' Doctorat, Université Pierre-et-Marie-Curie, Paris.
[101] Tsanga, G., 1997, ''Aérodynamique Numérique 3-D des Turbomachines Axi-

ales Multiétages avec Fermeture $k-\varepsilon$ Bas-Reynolds,'' Doctorat, Université Pierre-et-Marie-Curie, Paris.
[102] Shabbir, A., Zhu, J., and Celestina, M., 1996, ''Assessment of 3 Turbulence Models in a Compressor Rotor,'' ASME Paper No. 96-GT-198.
[103] Gregory-Smith, D. G., 2000, ''Synthesis of Calculations Performed on the NASA Rotor 37,'' Ch. 5, Final Report, APPACET Project, EEC Contract BRPR-CT97-0610.
[104] Lichtfuss, H. J., and Starken, H., 1974, ''Supersonic Cascade Flow,'' Prog. Aerosp. Sci., **15**, pp. 37–149.
[105] Emunds, R., Jennions, I. K., Bohn, D., and Gier, J., 1999, ''The Computation of Adjacent Blade-Row Effects in a 1 1/2-Stage Axial Flow Turbine,'' ASME J. Turbomach., **121**, pp. 1–10.
[106] Volmar, T. W., Brouillet, B., Gallus, H. E., and Benetschik, H., 2000, ''Time-Accurate 3-D Navier-Stokes Analysis of 1 1/2-Stage Axial-Flow Turbine,'' J. Propul. Power, **16**, pp. 327–335.
[107] Gallus, H. E., Zeschky, J., and Hah, C., 1995, ''Endwall and Unsteady Flow Phenomena in an Axial Turbine Stage,'' ASME J. Turbomach., **117**, pp. 562–570.

Measurements in a Turbine Cascade Flow Under Ultra Low Reynolds Number Conditions

Kenneth W. Van Treuren
Department of Engineering,
Baylor University,
Waco, TX 76798-7536

Terrence Simon
Department of Mechanical Engineering,
University of Minnesota,
Minneapolis, MN 55455

Marc von Koller
Bundesamt fur Wehrtechnik und Beschaffung,
Koblenz, Germany

Aaron R. Byerley
Department of Aeronautics,
USAF Academy,
Colorado Springs, CO 80840

James W. Baughn
Mechanical and Aeronautical Engineering,
University of California,
Davis, CA 95616

Richard Rivir
Aero Propulsion and Power Directorate,
Wright Laboratories,
Wright-Patterson AFB, OH 45433

With the new generation of gas turbine engines, low Reynolds number flows have become increasingly important. Designers must properly account for transition from laminar to turbulent flow and separation of the flow from the suction surface, which is strongly dependent upon transition. Of interest to industry are Reynolds numbers based upon suction surface length and flow exit velocity below 150,000 and as low as 25,000. In this paper, the extreme low end of this Reynolds number range is documented by way of pressure distributions, loss coefficients, and identification of separation zones. Reynolds numbers of 25,000 and 50,000 and with 1 percent and 8-9 percent turbulence intensity of the approach flow (free-stream turbulence intensity, FSTI) were investigated. At 25,000 Reynolds number and low FSTI, the suction surface displayed a strong and steady separation region. Raising the turbulence intensity resulted in a very unsteady separation region of nearly the same size on the suction surface. Vortex generators were added to the suction surface, but they appeared to do very little at this Reynolds number. At the higher Reynolds number of 50,000, the low-FSTI case was strongly separated on the downstream portion of the suction surface. The separation zone was eliminated when the turbulence level was increased to 8-9 percent. Vortex generators were added to the suction surface of the low-FSTI case. In this instance, the vortices were able to provide the mixing needed to re-establish flow attachment. This paper shows that massive separation at very low Reynolds numbers (25,000) is persistent, in spite of elevated FSTI and added vortices. However, at a higher Reynolds number, there is opportunity for flow reattachment either with elevated free-stream turbulence or with added vortices. This may be the first documentation of flow behavior at such low Reynolds numbers. Although it is undesirable to operate under these conditions, it is important to know what to expect and how performance may be improved if such conditions are unavoidable. [DOI: 10.1115/1.1415736]

Keywords: Turbine Cascade, Low Reynolds Number Flow

Introduction

Recent trends in engine development have led to increased interest in low Reynolds number flows in turbines. These trends include increased bypass ratios, resulting in lower core flows, higher stage loading to reduce weight and cost, and increased interest in higher efficiency at altitude to reduce emissions and fuel consumption and to increase payload. Low Reynolds numbers lead to increased concern on the part of designers about properly accounting for transition from laminar to turbulent flow and about separation of the flow from the suction surface, which is strongly dependent upon transition. Flow separation reduces the operating efficiency of the low-pressure turbine which results in increased fuel consumption. As noted by Rivir [1], ''unpredicted losses in the low pressure turbine during operation at high altitudes has stimulated current interest in transition and separation at low Reynolds numbers.'' The subject of separation and transition as it applies to the turbine was discussed at the Minnowbrook II Conference [2], Narasimha [3] summarized the conference proceedings and specifically stated that low Reynolds number flows in the turbine are particularly susceptible to what was termed short and long separation bubbles. The Minnowbrook III Conference [4] continued to explore a variety of topics related to turbine flow with laminar separation under low Reynolds number conditions still being a major topic of interest. The definition of Reynolds number varies among investigators. A common definition of Reynolds number is based on the upstream velocity and axial chord [5]. The research discussed in this paper uses a Reynolds number based on suction surface length and flow exit velocity as proposed by NASA Glenn. The question of how low a Reynolds number is important in low-pressure turbine applications is frequently addressed. Communication with industry indicates that the Reynolds numbers based upon suction surface length and flow exit velocity below 150,000 and as low as 25,000 are of interest [6].

While it has been of interest to investigators in recent years, little research has been done in methods of preventing this separation in the low pressure turbine situation. Bearman and Harvey [7] used dimples on a circular cylinder to control the flow successfully. Recently, Lake [5] and Lake et al. [8] proposed the use of dimples on the suction surface of a turbine blade to control low Reynolds number separation. Their research showed a decrease in loss coefficient at low Reynolds numbers with little aerodynamic penalty at the higher Reynolds numbers.

Another technique proposed to control separation is the use of a vortex generator jets (VGJs). This technique uses spanwise arrays of small skewed and pitched jets from holes in the surface. Johnston and Nishi [9] showed on a flat plate that stalled regions in a turbulent boundary layer might be eliminated by use of the VGJ method. This work continued by looking at the application of additional configurations of the VGJ method to the turbulent boundary layer [10]. Selby [11] applied the VGJ method to a flap configuration with good results. More recent work by Bons et al. [12] specifically applied the VGJ method to the low-pressure turbine. Work in a cascade facility showed that the separation region was almost totally eliminated with significant reductions in momentum loss downstream of the blade with jets. Also, significant

Contributed by the International Gas Turbine Institute and presented at the 46th International Gas Turbine and Aeroengine Congress and Exhibition, New Orleans, Louisiana, June 4–7, 2001. Manuscript received by the International Gas Turbine Institute February 2001. Paper No. 2001-GT-164. Review Chair: R. Natole.

was the finding that VGJs produce no significant adverse effects when used at higher, nonseparating Reynolds numbers.

Other control devices for separation include both grooves [13] and vortex generators. The vortex generators have been mainly applied to aircraft flaps or wind turbines [14–17]. No research has been conducted with passive vortex generators on actual turbine or cascade blades. The challenge is that, while energizing the boundary layer and preventing separation at low Reynolds numbers, the penalty associated with these devices at higher Reynolds numbers were considered to be unacceptable. Lin [14] showed that Micro-Vortex Generators, on the order of 20 percent of the boundary layer thickness, are effective in reducing separation with only a small drag penalty. The question of manufacturability must also be addressed, but it is outside the scope of this investigation. The use of vortex generators shows promise aerodynamically and is addressed as part of this investigation.

In this paper the extreme low end of the Reynolds number range of interest, 25,000–50,000, was investigated. Documentation of the flow included blade surface pressure distributions, loss coefficients, and identification of separation zones. Total and static pressures were measured with a precision transducer and a micromanometer and separation documentation was with a tuft tied with a double loop to a small rod. These investigations were accomplished at approximately 25,000 and 50,000 Re with both 1 percent and 8–9 percent FSTI. The blade shape is the profile often referred to as the Langston profile. The blade row aspect ratio was nearly 4:1 with a solidity ratio of 0.95.

Experimental Apparatus

Aero-Thermodynamic Cascade Facility. The test facility at the United States Air Force Academy (USAFA) is a closed-loop wind tunnel facility specifically designed for use as a linear cascade, as shown in Fig. 1 (see [18]). The tunnel is normally capable of velocities from 5 m/s up to approximately 75 m/s, which are adjusted by moving the variable pitch fan blades on the 200 hp electric motor. For these experiments, lower velocities to approximately 1 m/s were achieved by opening access panels to the closed-loop tunnel and by providing further restrictions to the flow in the tunnel loop upstream of the fan. The tunnel operates near ambient pressure of 78 kPa and temperature of 22–25°C. The tunnel temperature can be controlled by varying the flow rate of cooling water through a fin-and-tube heat exchanger. The geometry is shown in Figs. 1 and 2 and parameters are in Table 1. The USAFA tunnel was modified to accept seven blades (nine including sidewalls) with a high aspect ratio of nearly 4.0, which achieves uniform, two-dimensional flow over the test portion of the blades. The clean tunnel free-stream turbulence was measured with a hot-wire to be approximately 1 percent. Upstream hotwire

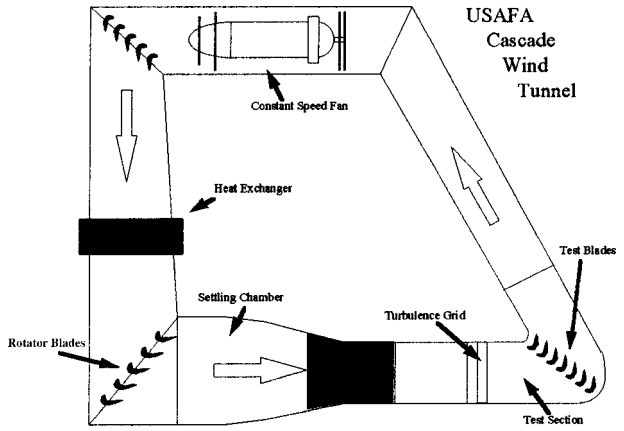

Fig. 1 Linear cascade facility at the United States Air Force Academy

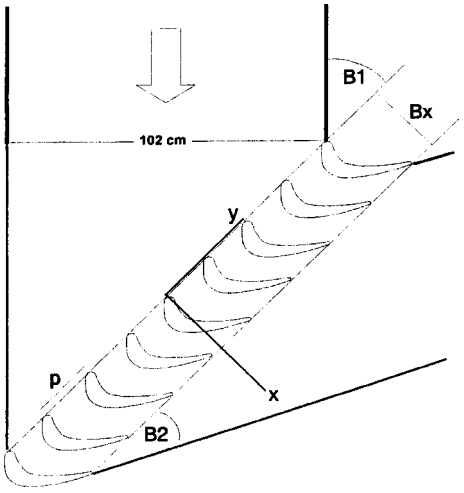

Fig. 2 Cascade geometry

and pitot static measurements were made at a location displaced outboard (to the right when facing the blade) of the measurement blade leading edge at a location that was the same distance downstream from the turbulence generation grid as that of the measurement blade. This location provided velocity and turbulence data using the same flow seen by the blade but kept the probes from influencing the flow over the test blade. The total pressure from this location was also used in the measurement of the loss coefficient.

The blades on either side of the center blade were tapped to measure static pressure over each blade. The inboard of these two was the test blade of this study and the other was used to show periodicity. Welsh et al. [18] showed the tunnel periodicity and demonstrated that the approach velocity is uniform to within 1 percent over the test region being studied.

Turbulence Generation Grid. The turbulence generation grid was modeled after that described by Roach [19] and placed in the tunnel so that it was perpendicular to the flow. An elevated turbulence level of approximately 8–9 percent was achieved using a passive biplanar lattice grid with square-bar widths of 1.27 cm. The grid was placed the appropriate distance upstream of the test

Table 1 Cascade parameters

Operation	Closed Loop
Axial Chord (B_x)	0.171m
Blade Pitch (p)	0.163m
Pitch/Axial Chord	0.95
Span/Axial Chord	3.86
Inlet Camber Angle	44°
Exit Camber Angle	26°
Air Inlet Angle (B_1)	46°
Air Exit Angle (B_2)	26°
Grid Orientation	Perpendicular to Freestream

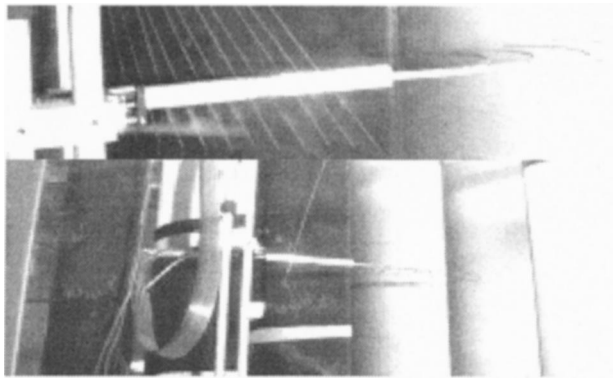

Fig. 3 Detail of loss coefficient pitot rake

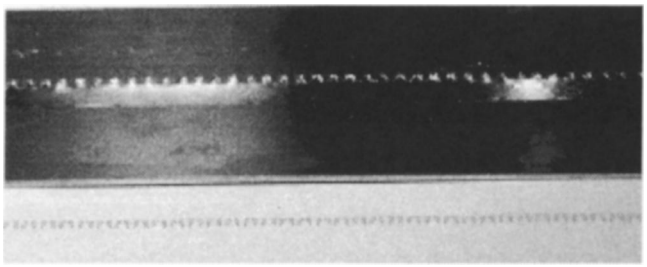

Fig. 4 Vortex generators and template

section to produce the 8–9 percent turbulence intensity at the inlet to the test passage under study. Turbulence length scales were measured previously by Butler et al. [20] for a slightly higher Reynolds number. They found the turbulence micro-scale to be approximately 16 mm and the turbulence macroscale to be 40 mm for this square bar width.

Loss Coefficient Pitot Rake. The loss coefficient pitot rake (see Fig. 3) was located 5 cm downstream of the test blade. The rake consists of seven 1.6-mm-dia tubes spaced 2.54 cm apart on the horizontal plane. The tubes were aligned with the camber exit angle. The center tube zero position is downstream of the trailing edge of the blade. The tubes extend downstream approximately 2.54 cm aligned with the flow and then bend 90 deg, merge together and exit the test region. The rake was mounted on a microtraverse that enabled it to be accurately translated horizontally. The rake tubes are connected with Tygon tubing to a Scani-valve and then to both an MKS Model 223 Differential Capacitance Manometer and a Dwyer Microtector Portable Electronic Point Gage.

Vortex Generator Fabrication. The counterrotating vortex generators (VG) of this experiment were fashioned after Lin [14] (see Fig. 4). They were fabricated from aluminum shim stock 0.0254 mm (0.001 in.) thick by bending the tabs individually to the proper angles. The VG tabs extend vertically approximately 1 mm, which is on order of the local boundary layer thickness. A height of 1 mm was chosen because it could be fabricated from the shim stock. The counterrotating VGs have a spacing of 1 mm and pairs repeat every 5 mm. The angle of the VG tabs to the flow is approximately 23 degrees. The strip was placed vertically at S/B_x of 0.5 on the blade suction surface and fastened with 0.0508 mm (0.002 in.) thick tape. This location was chosen because it was near the position of highest velocity on the suction surface according to the static pressure distribution.

Experimental Techniques

Measuring velocities and pressures to calculate loss coefficients and pressure coefficients in the flow associated with a Reynolds number of 25,000 proved to be challenging. The scale of the cascade tunnel (approximately 10× normal size) resulted in an approach velocity of 1 m/s. This corresponds to a pressure difference between pitot and static pressure of approximately 0.004 torr (0.0021 in. of water). When measuring the total pressure differential between the upstream total pressure and the wake total pressure, the numerical value can be even smaller. As a result, several methods were used to document the flow.

A pressure transducer was used to document the pressure differences for both the coefficient of pressure, C_p, and loss coefficient, γ, plots. This pressure transducer had a range of 0–0.2 torr and an accuracy of 0.3 percent full scale. The measurements taken, 0.004 torr and lower, are on the low end of this scale. This translates to approximately 15 percent bias error associated with the instrument at this velocity. To improve the stochastic uncertainty associated with this measurement, a data acquisition system was used and measurements were taken at a rate of 10 per s for 120 s. At 1 m/s, two standard deviations were approximately 28 percent of the overall measurement. These two contributors would combine to have an overall measurement error for the single sample of approximately 32 percent. This number highlights the challenge associated with measuring extremely low velocities. At a Reynolds number of 50,000, the signal is much stronger and these problems disappear. Even with the rather large uncertainty associated with this measurement, the repeatability was excellent when compared with subsequent data runs using the pressure transducer, the hotwire anemometer, or the micro-manometer. This applies to measurements of steady flow that will be discussed. Some cases had a very unsteady behavior at the separation zone and such repeatability was not possible, due to the flow unsteadiness.

A Dwyer Microtector Portable Electronic Point Gage micromanometer was used for pressure measurements. This instrument has a stated accuracy of 0.00025 in. of water. This reported accuracy results in an error of 12 percent in the measurement made under the present conditions. To reduce the uncertainty associated with measurements using this device, 20 samples were taken at each measurement point. As a result, the two standard deviation error associated with a typical measurement would be approximately 10 percent, with errors as high as 20 percent with smaller pressure differentials. At 1 m/s, the overall uncertainty would be on the order of 15.5 percent using the root sum squared method. This lower uncertainty prompted the use of this instrument in conjunction with the pressure transducer. Again, the repeatability of the measurement was extremely good and the comparison with the pressure transducer was excellent. While the micromanometer has a lower stated accuracy, comparing the two measurements gives confidence to pressure transducer data recorded previously. The transducer will likely be the instrument of choice in the future as the data can be taken and recorded electronically.

Using the method of Kline and McKlintock [21] yields uncertainties in loss coefficient measurement (for the range of data points) on the order of 16 to 60 percent when using the manometer and uncertainties on the order of 40 to 60 percent when using the transducer. For C_p, the uncertainties ranged from 15 to 48 percent using the manometer and were slightly higher for the transducer. These values reflect the difficulty in making measurements at such low velocities.

Measurements of mean velocity and turbulence were made with a hot-film anemometer driven by a TSI IFA-300 bridge and acquisition unit. Calibration was done using the TSI Calibration System with the proper choice of flow metering nozzles. The sensor could be calibrated to as low as 0.5 m/s with an uncertainty of less than 7–8 percent. A King's law relationship provided an excellent data fit over the range $0.5 < V < 3.0$ m/s. Below 0.5 m/s, data were not repeatable and errors due to natural convection were suspected.

Last, to gain additional insight into the data gathered with the pressure measurement instruments, a tuft was used to determine flow direction and to verify separated regions. A double-loop tuft

was used to eliminate any bias with the attachment of the string to the wand. The single wand was inserted through a slot in the top of the tunnel and moved to various locations on and around the blade. It proved extremely useful under the low flow conditions. It seemed to be intrusive only in the cases of unsteady separation.

Results and Discussion

Re_{NASA} 28,000 With low Free-Stream Turbulence Intensity (~1 Percent). As revealed by the tuft at Re=28,000 and low FSTI, the suction surface displayed a strong and steady separation region. As shown in Fig. 5, this region started approximately 65 percent of the suction surface length downstream of the leading edge (S/L_w). No reattachment was noted. On the pressure surface, a large separation region was noted at the leading edge with reattachment approximately 20 percent down the pressure surface. Figure 6 shows observations taken from the tuft visualization. Because gravity forces were important relative to drag forces, the attached flow is viewed as a tuft tilted downstream (40 percent S/L_w), whereas the separated flow is viewed as a vertical tuft position.

The C_p plot (Fig. 7) for a ReNASA of 28,000 shows reasonably good agreement between various data sets taken for this study using the micro-manometer and the MKS transducer (within the uncertainty). On the suction surface there is a peak at approximately 0.6 S/B_x. This would correspond to the highest velocity on the suction surface. Downstream is a region of separated flow at approximately $S/B_x=1$ which continues until close to the trailing edge of the blade. On the pressure surface, there is a region of low-velocity flow near the leading edge. The nonzero value of the flow is attributed to the unsteadiness or movement of the stagnation point, as observed with the tuft. The loss coefficient data are presented in Fig. 8 with the zero location being downstream of the trailing edge. Positive values are on the suction surface and negative values are on the pressure surface. The loss coefficient is the drop in total pressure from that of the approach flow, normalized by the departure flow velocity head. The departure flow velocity is computed from the approach flow velocity, as measured by a pitot-static tube, and the flow area ratio between the inlet and departure planes. The graph shows good agreement between the transducer and the micro-manometer. The overall loss coefficient (integrated area under the entire curve) is 0.156 for the micro-manometer and 0.174 for the transducer. The peak of the curve favors the suction surface at approximately 1.27 cm from the trailing edge indicating the large losses associated with the large separation zone on the suction surface. It also shows a nonzero value in the areas outside of the separation wake region. The mechanism for this value is not entirely understood but must be attributable to some shear causing losses throughout the channel when integrated over the measurement time of 120 s.

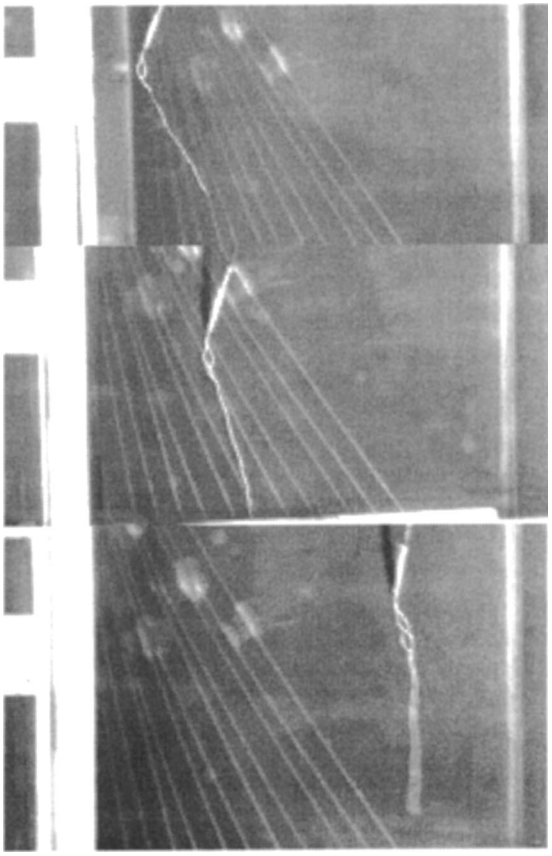

Fig. 6 Flow region shown by tufts located at the 40 (top), 70 (middle), and 90 percent (bottom) suction surface length positions as measured from the leading edge; Re_{NASA} ~28,000; 1 percent FSTI

Re_{NASA} 24,000 With High Free-Stream Turbulence Intensity (~9 Percent). Raising the turbulence intensity caused some tendency for reattachment; however, this resulted in a very unsteady separation region that reached a maximum size approximately equal to that of the previous case, diminished somewhat, then grew again. The dynamics could not be measured but were inferred from tuft visualization. See Figs. 9 and 10. The bottom photo in Fig. 10 shows the tuft in a low shear condition. The

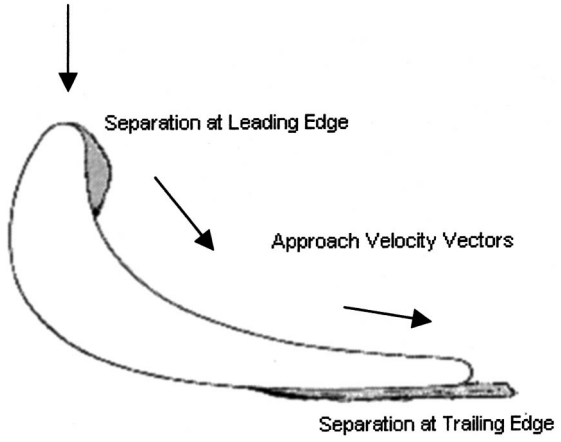

Fig. 5 Passage flow for Re_{NASA} 28 K and 1 percent FSTI—a sketch showing observations with tuft

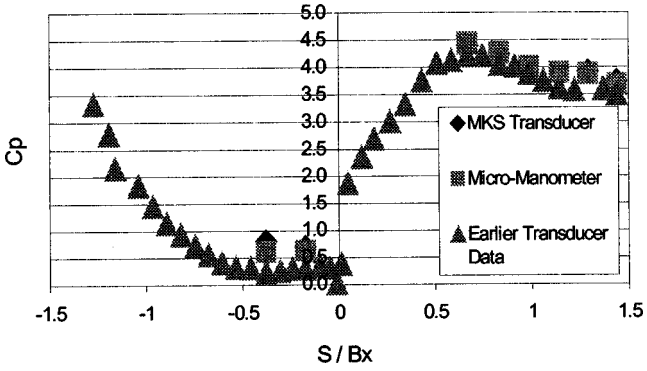

Fig. 7 C_p plot for Re_{NASA}=28,000, FSTI ~1 percent; the "earlier data" were taken under similar conditions but several months prior to the current tests

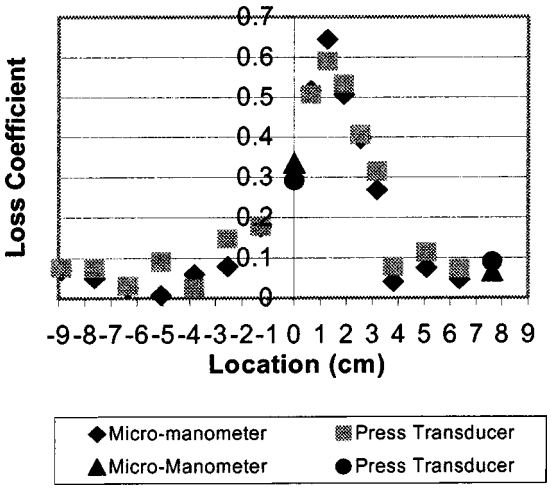

Fig. 8 Loss coefficient for Re_{NASA}=28 K, FSTI ~1 percent

unsteadiness at this location caused the tuft to oscillate between this condition and a complete separation. This unsteadiness appeared to propagate throughout the channel leading to an unsteady approach flow (velocity magnitude and angle) to the leading edge. This unsteadiness greatly influenced the leading edge region, preventing the establishment of a steady stagnation point. It also appears to be responsible for a very large separation zone on the upstream portion of the pressure surface, a much more pronounced separation zone than was present in the more steady, low-FSTI approach flow case at this Reynolds number. It is interesting to note that even with such strong separation, upstream on the pressure surface and downstream on the suction surface, the channel was effective in turning the flow. In fact, the flow appears to have the same turning as in high Reynolds number cases where separation is avoided. The role of the tailboards, which were set for high Reynolds number flow and not changed, is unknown. Also noteworthy for this extreme case is that the C_p distribution was not strongly changed from distributions for higher Reynolds number cases and other turbulence intensities even though the separation was noted. This would suggest that the separation zones are thinner in this case than in the low FSTI case. The peak in C_p remains approximately at 0.5 S/B_x and the separation region begins at approximately $S/B_x=1$ and continues to the trailing edge (at its largest). Figure 11 shows disagreement between

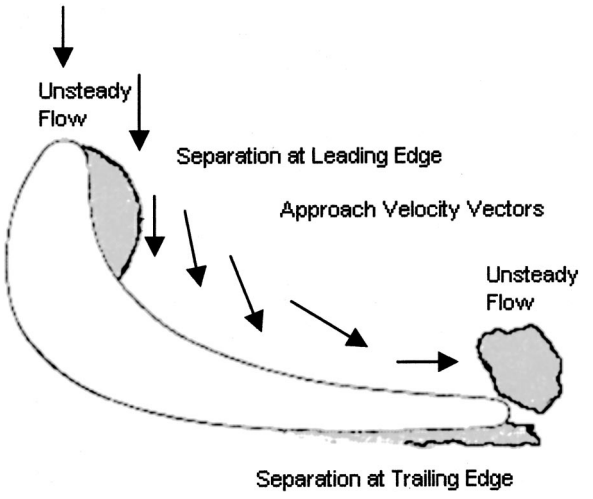

Fig. 9 Passage flow for Re_{NASA} 24 K and 9 percent FSTI—a sketch showing observations with tuft

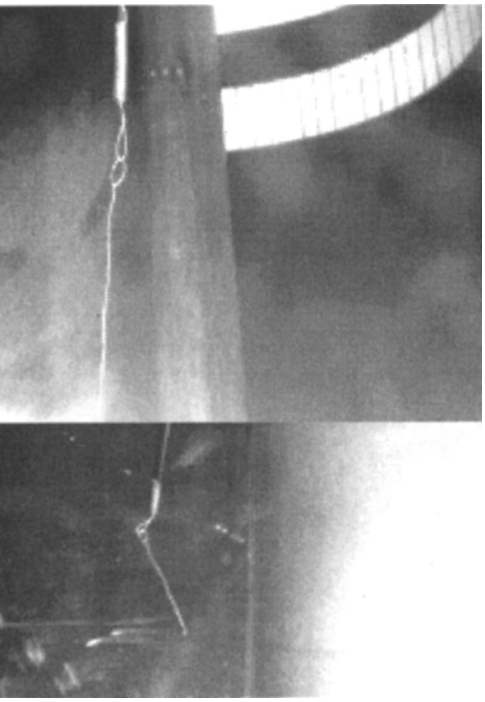

Fig. 10 Upper photo shows separated flow region on the pressure surface. Bottom photo shows the unsteady separated flow region near the trailing edge of the blade on the suction surface. Re_{NASA} ~24,000; FSTI ~1 percent.

vanes measured with the two pressure recording instruments, whereas Fig. 12 shows agreement. The normalizing quantity is the inlet flow head. The inlet velocity head is one of the weakest signals measured. Hence, the normalizing quantity is one of the most difficult quantities of the series to measure accurately. If the quantity is that measured by the upstream pitot tube as recorded by the micro-manometer or pressure transducer, for normalization of respective curves, the results of Fig. 11 are achieved. If the velocity measured by the hot-wire is used to normalize both curves (numerators recorded by transducer and micro-manometer), the curve of Fig. 12 is achieved. To conform with standard practice, all loss coefficient data, except for Fig. 12, are normalized by using velocities taken with their respective measurement instrument. Again the pressure coefficient on the pressure surface near the leading edge is not zero, indicating that all

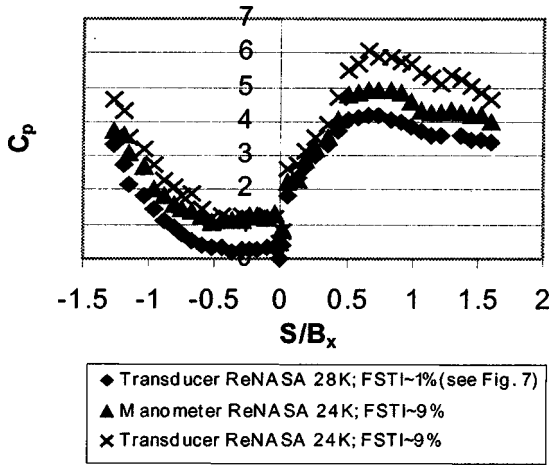

Fig. 11 C_p plot for low Re_{NASA} with FSTI 1 and 9 percent

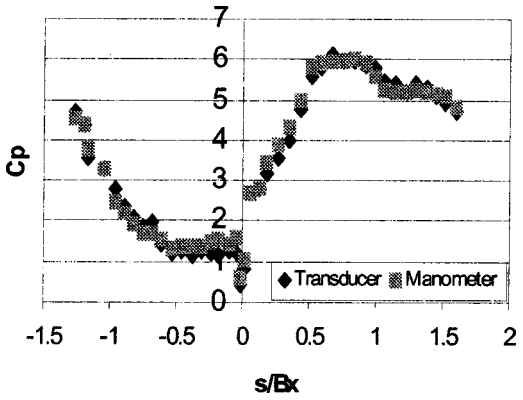

Fig. 12 C_p plot using hot-wire velocity to normalize C_p

stream tubes passing through the channel experienced some loss in total pressure. This is consistent with the observation that both pressure and suction side separation zones were large and appeared to fill much of the channel width. The loss coefficient plot, as shown in Fig. 13, illustrates the difficulty of measurement due to the unsteady nature of the flow. Consistent measurements were hard to make and the data scatter in a wide band.

Re_{NASA} 59,000 With Low and High Free-Stream Turbulence Intensity (~1 Percent, ~9 Percent)). At the higher Reynolds number of 58,000, the low-FSTI case was strongly separated on the downstream portion of the suction surface. When the turbulence level was increased to 8–9 percent, the separation zone was eliminated. It was found that flow through the center of the passage contained a very small drop in stagnation pressure. This is contrary to the higher losses across the entire passage in the low Reynolds number cases and somewhat different than the expectation based on experiences with high Reynolds number cases where no losses were observed over a considerable portion of the center of the channel. The C_p plot, as shown in Fig. 14, looks similar to that of the lower Reynolds number case complete with a maximum at 0.6 S/B_x and a separation region that appears slightly smaller. The loss coefficient plot, shown in Fig. 15, shows a reduction in magnitude and a shift in the peak towards the trailing edge when compared to the lower Reynolds number case. The loss coefficient distribution appears slightly smaller, especially on the pressure side. The loss coefficients for this Re_{NASA} were 0.084 for the micro-manometer measurements and 0.087 for the pressure transducer.

Vortex Generators. To investigate the opportunities for control, vortex generators were added to the suction surface as previ-

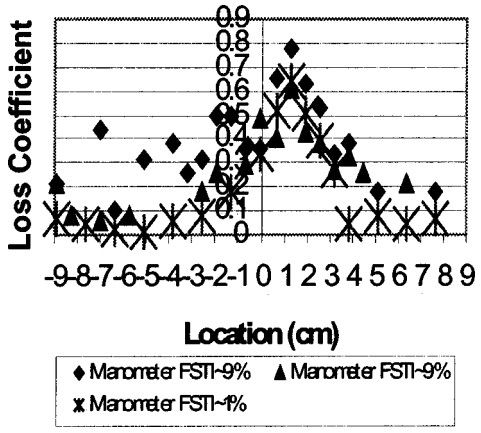

Fig. 13 Loss coefficient Re_{NASA}=24 K

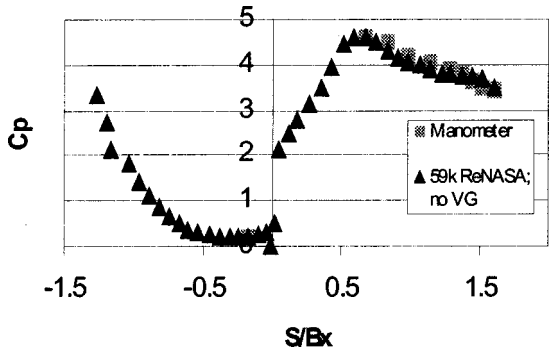

Fig. 14 C_p plot for Re_{NASA}=59 K; FSTI ~1 percent with vortex generators

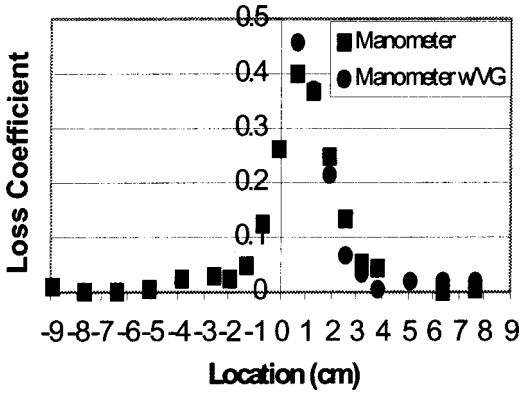

Fig. 15 Loss coefficient Re_{NASA}=54 K; FSTI ~1 percent

ously stated. For the case of the low Reynolds number of approximately 25,000, the 1-percent FSTI case was so massively separated that no effect of the vortex generators could be noted. For the low FSTI case, again, the separation was quite strong and unsteady. The vortex generators may have reduced the wake region downstream of the blade slightly, but the data were inconclusive.

For the high Reynolds number cases, the high FSTI eliminated separation and the effect of the vortex generators was not measured. For the low FSTI case, the vortices were able to provide the mixing needed to reestablish flow attachment. Figure 14 shows a continuous slope in the region of $S/B_x=1$ for the VG case indicating separation has been eliminated. Figure 15 shows that the loss coefficient distribution for the higher Reynolds number flow seems to be changed by the addition of vortex generators, indicating a narrowing of the wake region. Only one row of vortex generators was placed on one blade; therefore, only suction surface data are reported. VGs need to be applied to more than one blade to determine the effect that VGs on the suction surface may have on the pressure surface data.

Future Work

Further documentation of Re_{NASA} of 50,000 and 75,000 is necessary for the clean tunnel, 5 percent FSTI, and 10 percent FSTI configurations. The use of passive devices, such as vortex generators, dimples, and active control, will be evaluated for their impact on loss coefficient and coefficient of pressure. While passive devices do delay separation at lower Reynolds numbers, their influence on losses at the higher Reynolds numbers also should be explored.

In conjunction with the experimental testing, low Reynolds number CFD support should be conducted. This might add some insight on the extent of the separated regions and where transition is occurring.

Summary

This paper shows that massive separation at very low Reynolds numbers (25,000) is persistent, in spite of elevated FSTI and added vortices. However, at a higher Reynolds number of 50,000, there appears to be opportunity for flow reattachment either with elevated free-stream turbulence or with added vortices. This may be the first documentation of flow behavior at such low Reynolds numbers where massive separation zones are prevalent. Although it is undesirable to operate under these conditions, it is important to know what to expect and to have an idea of how performance may be improved if such conditions cannot be avoided.

Nomenclature

B_1 = air inlet angle
B_2 = air exit angle
B_x = axial chord, m
C_p = coefficient of pressure $=(P_{\text{totup}}-P_s)/(0.5\rho V^2_{\text{inlet}})$
FSTI = free-stream turbulence intensity
L_w = wetted length of suction/pressure surface, m
p = blade pitch, m
P = pressure, N/m^2
Re_{NASA} = Reynolds number based on suction surface length and passage exit velocity $=\rho V_{\text{exit}} S/\mu$
S = length along suction surface, m
V = velocity, m/s
γ = loss coefficient $=(P_{\text{totup}}-P_{\text{totdown}})/(0.5\rho V^2_{\text{exit}})$
μ = dynamic viscosity, kg/m s
ρ = density, kg/m^3

Subscripts

exit = exit to passage
inlet = approaching the airfoil row
s = local static
s-up = upstream static
totdown = downstream total
totup = upstream total

References

[1] Rivir, R. B., 1996, ''Transition on Turbine Blades and Cascades at Low Reynolds Numbers,'' AIAA Paper No. 96-2079.
[2] LeGraff, J. E., and Ashpis, D. E., eds., 1998, ''Minnowbrook II—Workshop on Boundary Layer Transition in Turbomachines,'' NASA Conference Publication 206958.
[3] Narasimha, R., 1998, ''Minnowbrook II—Workshop on Boundary Layer Transition in Turbomachines,'' NASA Conference Publication 206958, pp. 485–495.
[4] LeGraff, J. E., and Ashpis, D. E., eds., 2000, ''Minnowbrook III—Workshop on Boundary Layer Transition in Turbomachines,'' to be published as a NASA Conference Publication.
[5] Lake, J. P., 1999, ''Flow Separation Prevention on a Turbine Blade in Cascade at Low Reynolds Number,'' Ph.D. Dissertation, Graduate School of Engineering of the Air Force Institute of Technology, Air University, Wright-Patterson AFB, OH.
[6] Simon, X. X., 1999, private communication with industry.
[7] Bearman, P. W., and Harvey, J. K., 1993, ''Control of Circular Cylinder Flow by the Use of Dimples,'' AIAA J., **31**, No 10, pp. 1753–1756.
[8] Lake, J. P., King, P. I., and Rivir, R. B., 2000, ''Low Reynolds Number Loss Reduction on Turbine Blades With Dimples and V-Grooves,'' AIAA Paper No. 00-0738.
[9] Johnston, J., and Nishi, M., 1989, ''Vortex Generator Jets—A Means for Passive and Active Control of Boundary Layer Separation,'' AIAA Paper No. 89-0564.
[10] Compton, D. A., and Johnston, J. P., 1991, ''Streamwise Vortex Production by Pitched and Skewed Jets in a Turbulent Boundary Layer,'' AIAA Paper No. 91-0038.
[11] Selby, G., 1990, ''Experimental Parametric Study of Jet Vortex Generators for Flow Separation Control,'' NASA-CR-187836 (Library No N91-16296).
[12] Bons, J. P., Sondergaard, R., and Rivir, R. B., 1999, ''Control of Low Pressure Turbine Separation Using Vortex Generator Jets,'' AIAA Paper No. 99-0367.
[13] Lin, J. C., Howard, F. G., and Selby, G. V., 1989, ''Turbulent Flow Separation Control Through Passive Techniques,'' AIAA Paper No. 89-0976.
[14] Lin, J. C., 1999, ''Control of Turbulent Boundary-Layer Separation Using Micro-Vortex Generators,'' AIAA Paper No. 99-3404.
[15] Miller, G. E., 1995, ''Comparative Performance Tests on the MOD-2, 2.5-MW Wind Turbine With and Without Vortex Generators,'' N 95-27970, DASCON Engineering, Collected Papers on Wind Turbine Technology p. 67–77. Presented at the DOE/NASA Workshop on Horizontal Axis Wind Turbine Technology, May 8–10, 1984 in Cleveland, OH.
[16] Nickerson, J. D., 1986, ''A Study of Vortex Generators at Low Reynolds Numbers,'' AIAA Paper No. 86-0155
[17] Rao, D. M., and Kariya, T. T., 1988, ''Boundary-Layer Submerged Vortex Generators for Separation Control—An Exploratory Study,'' AIAA Paper No. 88-3546CP.
[18] Welsh, S. T., Barlow, D. N., Butler, R. J., Van Treuren, K. W., Byerley, A R., Baughn, J. W., and Rivir, R. B., 1997, ''Effect of Passive and Active Air-Jet Turbulence on Turbine Blade Heat Transfer,'' ASME Paper No. 97-GT-131.
[19] Roach, P. E., 1987, ''The Generation of Nearly Isotropic Turbulence by Means of Grids,'' Int. J. Heat Fluid Flow, **8**, No. 2, pp. 82–92.
[20] Butler, R. J., Byerley, A. R., Van Treuren, K. W., and Baughn, J. W., 2001, ''The Effect of Turbulence Intensity and Length Scale on Low Pressure Turbine Blade Aerodynamics,'' Int. J. Heat Fluid Flow, **20**, No. 2, pp. 123–133.
[21] Kline, S. J., and McKlintock, F. A., 1953, ''Describing Uncertainties in Single Sample Experiments,'' Mech. Eng. (Am. Soc. Mech. Eng.), **75**, Jan., pp. 3–8.

Detailed Boundary Layer Measurements on a Turbine Stator Vane at Elevated Freestream Turbulence Levels

R. W. Radomsky[1]
e-mail: roger_w_radomsky@raytheon.com

K. A. Thole
e-mail: thole@vt.edu

Mechanical Engineering Department,
Virginia Polytechnic Institute
and State University,
Blacksburg, VA 24060

High freestream turbulence levels have been shown to greatly augment the heat transfer on a gas turbine airfoil. To better understand these effects, this study has examined the effects elevated freestream turbulence levels have on the boundary layer development along a stator vane airfoil. Low freestream turbulence measurements (0.6 percent) were performed as a baseline for comparison to measurements at combustor simulated turbulence levels (19.5 percent). A two-component LDV system was used for detailed boundary layer measurements of both the mean and fluctuating velocities on the pressure and suction surfaces. Although the mean velocity profiles appeared to be more consistent with laminar profiles, large velocity fluctuations were measured in the boundary layer along the pressure side at the high freestream turbulence conditions. Along the suction side, transition occurred further upstream due to freestream turbulence.
[DOI: 10.1115/1.1424891]

Introduction

Accurate predictions of surface heat loads on an airfoil are made difficult by the complex flow structure surrounding the airfoil. Boundary layers developing on a vane or blade surface are subjected to a combination of variables including freestream turbulence, surface curvature, roughness, favorable and unfavorable pressure gradients, boundary layer transition, relaminarization, and stagnation point flow. Numerous investigations have been performed in the past that have addressed the isolated effects of most of these variables on boundary layer development with the majority of the studies being performed on simple flat plate or cylinders-in-crossflow geometries. To incorporate all of the variables affecting boundary layer development on gas turbine airfoils, studies need to be performed on geometries representative of those found along an airfoil. While there have been a few studies performing boundary layer measurements on an airfoil surface, these studies have been made at relatively low freestream turbulence conditions. To date, no studies have been performed on a turbine airfoil geometry at turbulence levels representative of those exiting current gas turbine combustors.

Turbulence measurements taken at the exit of a variety of gas turbine combustors have shown that the levels can range between 8 percent and 40 percent (Goldstein et al. [1]; Kuotmos and McGuirk [2]; and Goebel et al. [3]) with an indication that the integral length scale is dictated by the diameter of the dilution holes in the combustor (Moss [4]). Although the turbulent kinetic energy levels actually increase through the downstream airfoil passage due to the velocity gradients experienced by the flow (Radomsky and Thole [5]), the local turbulence levels, particularly along the suction side, decrease as the flow is accelerated. The effect that these high turbulence levels has on the airfoil is to significantly increase the heat transfer along the leading edge and pressure side surfaces as well as move the transition location forward on the suction side surface. Typically, the increase in turbulent kinetic energy in the passage is not accounted for in the current boundary layer codes, which assume decay rates similar to that occurring downstream of a grid. Thus, it is important to generate an experimental database to use as a benchmark for improving predictive tools for the purpose of more accurately capturing the physics of the flowfield.

Past Studies

As stated previously, most of the boundary layer studies examining various flowfield effects have used a flat plate geometry. These studies, which started as early as Kestin [6], are far too numerous to completely discuss in this paper. A few of the more relevant investigations in which boundary layer measurements have been made along an airfoil will be discussed in the following paragraphs.

Detailed boundary layer measurements have been made on an airfoil surface by Ubaldi et al. [7], Bario and Beral [8], and Lee and Kang [9]. Ubaldi et al. [7] performed detailed boundary layer measurements at low freestream turbulence conditions in a large-scale turbine vane cascade at low turbulence levels. The measurement technique that they used was a two-component LDV system with a probe volume size that ranged between a $10<D^+<40$. Ubaldi et al. [7] reported that the boundary layers on the pressure side of the vane remained ''laminar in shape'' along the majority of the pressure surface although large streamwise fluctuations were present inside the boundary layer.

Measurements reported by Bario and Beral [8] were for a scaled up stator vane geometry in which they used a two component LDV system. The freestream conditions included two turbulence levels at Tu=0.6 and 5 percent. For the turbulent profiles, the increased turbulence penetrated into the boundary layer causing elevated levels of streamwise fluctuations in the transition region. An increase in the correlation coefficient was also observed in the boundary layer for the higher turbulence levels, which was the opposite trend to that observed by Thole and Bogard [10] for flat plate boundary layers. They attributed these increases to the highly correlated turbulence outside of the boundary layer.

Lee and Kang [9] compared low freestream turbulence conditions to levels as high as 15 percent that they were able to simulate by placing their symmetric airfoil in the downstream wake of another airfoil. Note that the wake flowfield is fundamentally

[1]Presently at Raytheon, Tuscon, AZ 85734.

Contributed by the International Gas Turbine Institute and presented at the 46th International Gas Turbine and Aeroengine Congress and Exhibition, New Orleans, Louisiana, June 4–7, 2001. Manuscript received by the International Gas Turbine Institute February 2001. Paper No. 2001-GT-169. Review Chair: R. Natole.

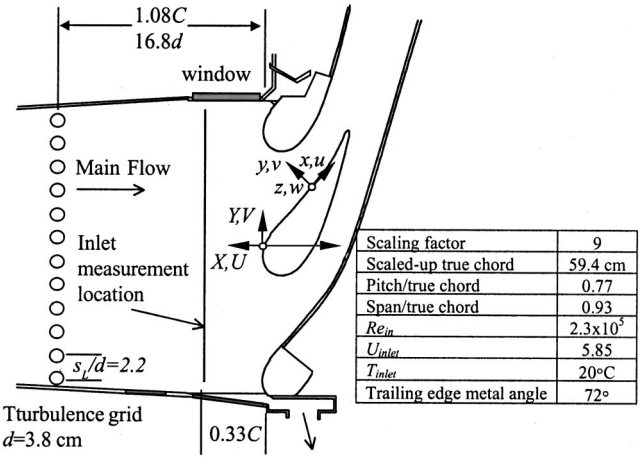

Scaling factor	9
Scaled-up true chord	59.4 cm
Pitch/true chord	0.77
Span/true chord	0.93
Re_{in}	2.3×10^5
U_{inlet}	5.85
T_{inlet}	20°C
Trailing edge metal angle	72°

Fig. 1 Schematic of stator vane test section

different from the one studied in our paper for the following two reasons: i) there exists a mean velocity deficit from the upstream airfoil wake that impacts the airfoil leading edge, and ii) the turbulence level outside of the wake region is low. At low freestream turbulence conditions, the measured streamwise velocity fluctuations near the wall appeared to go from a two-peaked profile to a single peaked profile as the mean velocity profiles transitioned from laminarlike to fully turbulent. At high freestream turbulence conditions, their results indicated the presence of high streamwise velocity fluctuations even though the mean profile appeared laminar in shape for the case with high freestream turbulence conditions.

Although these studies have given an indication of boundary layer development on an airfoil surface, there is a need for detailed measurements at turbulence levels representative of those exiting typical gas turbine combustors. This paper represents one in a series of papers that have documented highly turbulent flow through a first-stage vane passage. Midspan turbulence measurements and surface heat transfer measurements were reported by Radomsky and Thole [5] while the effects of freestream turbulence in the endwall region were reported by Radomsky and Thole [11]. These previous two papers in addition to the present paper provide a complete database for computational benchmarking.

Experimental Design

The details of the recirculating wind tunnel and design of the stator vane test section used in this study have been documented thoroughly in a number of previous studies including Kang et al. [12], Kang and Thole [13] and Radomsky and Thole [5,11,14]. A schematic of the stator vane test section and a table showing the relevant geometrical parameters and operating conditions are given in Fig. 1. Note that the metal angle is the average angle of the pressure and suction sides, which is 72 deg for our case, while the flow angle is the angle at which the flow leaves the passage relative to the inlet, which is 78 deg for our case. To allow for highly resolved boundary layer measurements, the vane cascade was geometrically scaled-up by a factor of nine. The inlet Reynolds number to the test section was matched to that of an engine; however, the inlet Mach number could not be matched due to the increased scale of the test section. It can be shown using the boundary layer equations that if the acceleration parameter and momentum thickness Reynolds numbers are matched, the flow field between the compressible and incompressible conditions will also be matched (Polanka [15]).

The test section consisted of an instrumented central vane in addition to the leading edges of two adjacent vanes. A flexible plexiglass sidewall, which allowed optical axis for LDV measurements, was attached to the leading edges of the vane. The flexible wall was placed to exactly match the geometry of an adjacent vane. Downstream of where the adjacent airfoil would end, the location of the flexible wall was placed to match the pressure distribution predicted by a two-dimensional, low-speed, inviscid calculation. Static pressure measurements on the vane were performed to insure the correct placement of the flexible wall in addition to insuring periodic flow was achieved between the two passages.

Heat transfer measurements were made on the polystyrene central vane, which was wrapped with five 50-micron-thick type 304 stainless steel foils. The metal foils provided a constant heat flux boundary condition. Beneath the stainless steel foil and embedded in the styrofoam 58 type E thermocouples were placed. The spanwise position for the thermocouples was at 40 percent of the span measured from the bottom endwall.

A few changes were implemented to the experimental setup that differed from the descriptions given in the aforementioned investigations. In order to accurately measure boundary layers with a laser Doppler velocimetry (LDV) system, which was the main objective of the investigation, a surface must be both smooth and nonreflective. For this reason, a new instrumented central vane was constructed to replace the original vane which had the metallic constant heat flux surface. As with the original vane, the new vane was also constructed from stacking pieces of 2-in. rigid Styrofoam insulation that was cut to shape using a template and an electrically heated wire. The Styrofoam cutouts were epoxied together to achieve the necessary span/chord ratio given in Fig. 1. The entire vane was sanded to achieve the correct profile and eliminate any steps between adjacent cutouts. Upon achieving a smooth surface, the entire vane was then covered with several layers of fiberglass. After the final layer of fiberglass was applied, the vane was sanded and painted repeatedly using progressively finer sand paper until a smooth, flat black surface was achieved. A description of the process is found in Radomsky [16].

The second change in the experimental setup involved the method for generating elevated freestream turbulence levels. Due to a change in the location of the experimental facility, the compressed air system required for the active-grid turbulence generator was no longer available. As a result, a different technique for generating turbulence levels of 20 percent was required. Previous work at the University of Texas showed that turbulence levels of 20 percent and length-scale-to-pitch ratios of $\Lambda_x/P=0.091$ could be obtained using a passive grid system (Polanka, [15]). Note that these are the same level and scale of the turbulence used in Radomsky and Thole [5,11]. The passive grid design consisted of a series of 3.8-cm-dia bars with a lateral spacing of $s_L/d=2.2$. The bar size and the close spacing between the bars was reported to eliminate the shedding from the bars in the region where measurements were performed. As will be shown later, good agreement in the turbulence level was achieved between the two turbulence generator techniques.

Methods Used for Boundary Layer Measurements

Boundary layers at nine streamwise locations were measured with the LDV system on the vane at the midspan location. The location of boundary layer measurements on the vane surface can be seen in Fig. 2. Boundary layer profiles were measured at four streamwise locations on the pressure surface. These locations correspond to streamwise distances of $s/C=-0.15$ (P1), -0.30 (P2), -0.45 (P3), and -0.60 (P4) from the vane stagnation location. Boundary layer profiles were measured at five streamwise locations on the suction surface corresponding to streamwise distances of $s/C=0.21$ (S1), 0.50 (S2), 0.75 (S3), 1.00 (S4), and 1.25 (S5). The boundary layer measurements used a local coordinate system, as shown in Fig. 1, where the origin was located at the vane surface at the desired streamwise location. One axis of the coordinate system was aligned parallel (x), while the other axis was

Name	Location	D^+
SP	$s/C=0$	stagnation
Pressure Side		
P1	-0.15	0.9
P2	-0.3	1.3
P3	-0.45	1.6
P4	-0.60	1.8
Suction Side		
S1	0.21	2.7
S2	0.5	3.1
S3	0.75	1.2
S4	1.0	1.3
S5	1.2	3.4

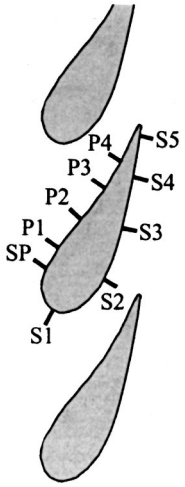

Fig. 2 Location of boundary layer measurements

normal (y) to the surface. To completely document the boundary layer structure, a minimum of 20 measurement locations were measured in each of the boundary layer profiles.

A two-component back-scatter fiber optic LDV system used in this study consisted of a 5 W laser and a TSI model 9201 Colorburst beam separator. Velocity data was processed using TSI model IFA 755 Digital Burst Correlator controlled using TSI's FIND software. To keep the measurement volume as small as possible, a beam expander and 450 mm focusing lens were used. This resulted in a probe diameter, which is the coordinate normal to the surface, of 44 μm and a probe volume length of 0.32 mm. In addition to the location of the measurements, Fig. 2 also shows the nondimensional diameter of the probe volume (D^+), in terms of inner wall coordinates, at each of the measurement locations. The LDV probe was tilted at the half-angle of the beams, $\kappa = 7.78$ deg, to allow for measurements very near the vane surface. For the noncoincident LDV measurements, each mean and rms velocity were averaged over 12,000 points, which took nominally 20 s to acquire. For coincident LDV measurements, using a coincidence window of 10 μs, each mean and rms velocity were averaged over 25,000 points to allow for accurate determination of higher order velocity statistics. All measurements were corrected for bias errors using the well-accepted time weighted average correction scheme.

The location of the wall during boundary layer measurements was estimated using two techniques. The first technique involved lowering the input power to the LDV system and visually monitoring the crossing of the beams on the vane surface. The second technique was to monitor the output from the photomultiplier tubes using an oscilloscope. Both methods for locating the wall produced nearly identical results. From numerous repeatability studies, it was determined that the location of the wall was known to within ± 20 μm. For the present investigation, this value corresponds to a distance from the wall in wall coordinates of at most a $y^+=2$ at a $s/C=1.2$.

Boundary layer measurements will be presented in terms of both freestream variables and inner variables. When presenting the data in terms of inner variables, knowledge of the shear velocity, $u_\tau = \sqrt{\tau_w/\rho}$, is required. For laminar, flat plate boundary layer flows, the shear velocity is typically determined by calculating the velocity gradient near the wall where the profile is linear. For a laminar boundary layer affected by a strong pressure gradient there is additional stress added by the pressure gradient, $\tau_w = \mu(du/dy) - y(dP/ds)$ (Kays and Crawford [17]). This relation, however, does not consider any momentum flux term. In analyzing the measured velocities close to the wall, we determined that the mean velocities indicated a linear relation with distance from the wall. This implies that the pressure gradient term is not affecting the velocities in the near wall region and that the additional pressure force is balanced by the momentum flux difference. For that reason, the wall shear stress used in the data presented in this paper was that calculated from the slope of the velocity at the wall.

Generally for turbulent boundary layers, the shear velocity is determined using a Clauser fit in the log-law region of the velocity profile. This is because the physical distance to the wall where $u^+=y^+$ is very small making it difficult to measure the viscous sub-layer velocities. The Clauser fit technique has been shown by Thole and Bogard [10] to be a valid method of estimating u_τ even at high freestream turbulence conditions of 20 percent.

The most difficult region for estimating u_τ is where a transitional boundary layer is present. In this region, as with the laminar profiles, measurements were performed in the viscous sublayer to allow the data to be fit to the $u^+=y^+$ relationship. This requires measurements very near the wall surface. For all of the measurements to be discussed, the closest measurement was typically 0.08 to 0.10 mm from the surface of the vane. For laminar boundary layers, this distance typically corresponded to y^+ values of $y^+ \sim 5$. For transitional and turbulent boundary layers the closest measurement location was a $y^+ \sim 8$ to 10.

Uncertainty Estimates

The partial derivative and sequential perturbation methods, described by Moffat [18], were used to estimate the uncertainties of the measured values. Uncertainties were calculated based on a 95 percent confidence interval. The estimate of bias and precision uncertainties for the mean velocities were 1 percent, while the precision of the rms velocities was 1.2 percent for u_{rms} and 1.7 percent for v_{rms}. The precision uncertainties of the Reynolds shear stress and correlation coefficient were 4.8 percent and 5.4 percent. Note that these uncertainty estimates were at the high freestream turbulence conditions near the surface on the suction side of the vane. The total uncertainty in the Stanton numbers was 4 percent at the leading edge and 5 percent at the trailing edge on the suction side of the vane. The total uncertainty in the friction factor was a maximum of 7.5 percent for a laminar boundary layer and 5 percent for a turbulent boundary layer.

Inlet Flow Conditions

Profiles of the mean velocity and turbulence components were measured at one-third chord upstream ($X/C=-0.33$) for inlet turbulence levels of Tu=19.5 percent. Figure 3(a) shows streamwise and pitchwise mean velocity profiles measured across the entire pitch of two vane passages using the passive-grid and previously reported active grid turbulence generators. These measurements were compared to a baseline case, measured at low freestream turbulence conditions of Tu=0.6 percent, and to a CFD prediction using the Reynolds stress turbulence model (RSM) at freestream turbulence levels of Tu=1 percent (Radomsky and Thole [5]). The mean velocities have been normalized by the inlet approach velocity, U_{inlet}. A global coordinate system, as shown in Figure 1 with the origin at the stagnation point of the center vane ($Y/P=0$), was maintained for the results shown in Fig. 3(a). At this upstream location, the mean velocity was just beginning to feel the effects of the stator vane, as is evident by the deceleration in U/U_{inlet} observed in front of the central vane ($Y/P=0$). As the streamlines turn around the vane, slightly positive pitchwise velocities (V/U_{inlet}) occurred near the stagnation point for $Y/P>0$ and slightly negative pitchwise velocities occurred near the stagnation for $Y/P<0$. Although the turbulence levels were very high, the good agreement with the low freestream turbulence case and CFD prediction shows the mean flowfield was unaffected by either of the turbulence generators.

Turbulence levels and length scales were measured across the entire pitch of the two passages at $X/C=-0.33$. Figure 3(b)

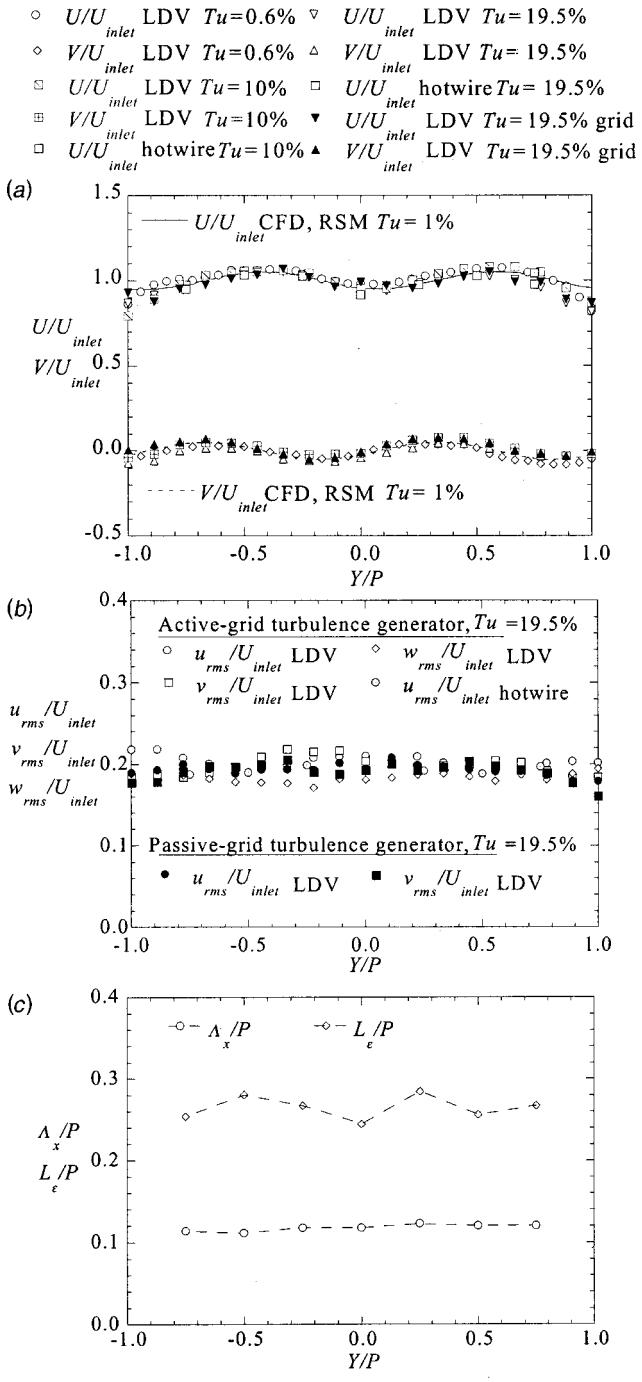

Fig. 3 Profiles of: (*a*) normalized streamwise, U/U_{inlet}, and pitchwise, V/U_{inlet}, velocities at various turbulence levels and measurement techniques, (*b*) streamwise (u_{rms}/U_{inlet}), pitchwise (v_{rms}/U_{inlet}) and spanwise (w_{rms}/U_{inlet}) turbulence levels, and (*c*) integral and dissipation length scales measured at $X/C=-0.33$

shows the streamwise ($u_{\rm rms}/U_{\rm inlet}$), pitchwise ($v_{\rm rms}/U_{\rm inlet}$), and spanwise ($w_{\rm rms}/U_{\rm inlet}$) rms levels at an inlet turbulence level of 19.5 percent using two different turbulence generators. The maximum deviations relative to the average for the streamwise and pitchwise rms levels were 7.8 percent and 7.6 percent for the 19.5-percent case. No noticeable difference was observed in the level or uniformity of the turbulence between the different turbulence generators. Fig. 3(*c*) shows the measured integral and dissipation length scales across the passages with the integral scale being approximately 11 percent of the pitch.

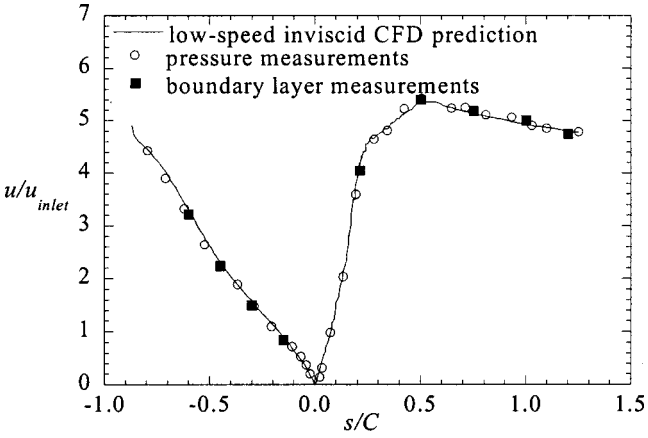

Fig. 4 Comparison of inviscid velocity distribution from static pressure and LDV boundary layer measurements to the low-speed inviscid CFD prediction

As a check for the boundary layer measurements, a comparison was made between measured edge velocities, the calculated velocities from the measured static pressure distribution, and the predicted velocities from an inviscid CFD simulation. Figure 4 shows this comparison and indicates good agreement between the two independent measurements. The positive values of s/C refer to the suction surface, while the negative values indicate the pressure surface. Figure 4 also illustrates the inviscid velocities affecting the boundary layer development. On the pressure side there is a constant acceleration, with an acceleration factor of $K=3.14\times10^{-6}$ over the majority of the surface, as the flow progresses from the stagnation to the end of the vane. The inviscid velocities along the suction side show a much different behavior with a rapid acceleration up to $s/C=0.2$ with very high acceleration parameters between $1.1\times10^{-6}<K<0.01$. From $s/C=0.2$ to 0.5, there is a continual acceleration but at a much lower rate having an average acceleration of $K=1.1\times10^{-6}$. Beyond $s/C=0.5$, there is a slight adverse pressure gradient giving a $K=-1.6\times10^{-8}$.

For computational benchmarking purposes, the tables shown in Appendix A1 and A2 of this paper indicate the local boundary layer edge velocities, local edge turbulence levels, and boundary layer parameters for each of the measurement locations. As can be seen by these levels, the local turbulence levels along the suction side decreased rapidly as the flow accelerates while the levels along the pressure side remained slightly higher.

Boundary Layer Parameters

In this section, comparisons will be made of the boundary layer parameters at low and high freestream turbulence levels. These parameters include the boundary layer and momentum thicknesses, the shape factor, friction coefficients, and Stanton numbers. When possible the values will be compared to correlation results using the Thwaites [19] method. The Thwaites method provides a correlation for laminar boundary layers when affected by a pressure gradient.

Figure 5(*a*) compares the measured boundary layer thickness, δ/C, at turbulence levels of 0.6 percent and 19.5 percent to the Thwaites prediction. On the pressure surface, for the 0.6 percent turbulence level, the constant flow acceleration resulted in nearly a constant boundary layer thickness. In contrast, the elevated turbulence level had a large impact on the size of the boundary layer on the pressure surface. At the trailing edge of the pressure surface, the boundary layer thicknesses at the 19.5-percent condition are nearly double those at the 0.6 percent level. On the suction surface, at both turbulence levels, the boundary layer thickness initially decreased in size to a minimum at an $s/C=0.21$ due to the large acceleration at this location. Downstream of location

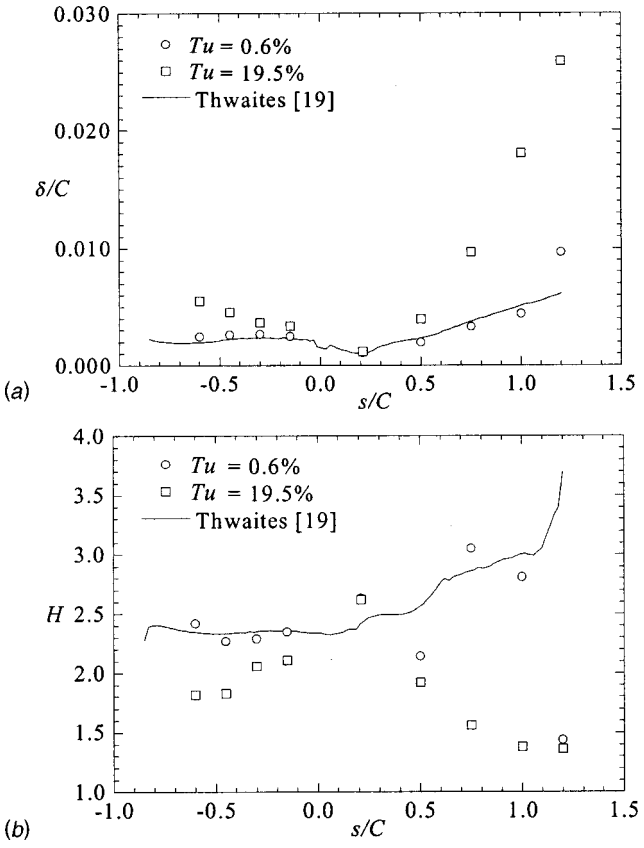

Fig. 5 Comparison of measured: (*a*) boundary layer thickness, δ/C, and (*b*) shape factor, *H*, at turbulence levels of 0.6 percent and 19.5 percent with predictions given by Thwaites [19]

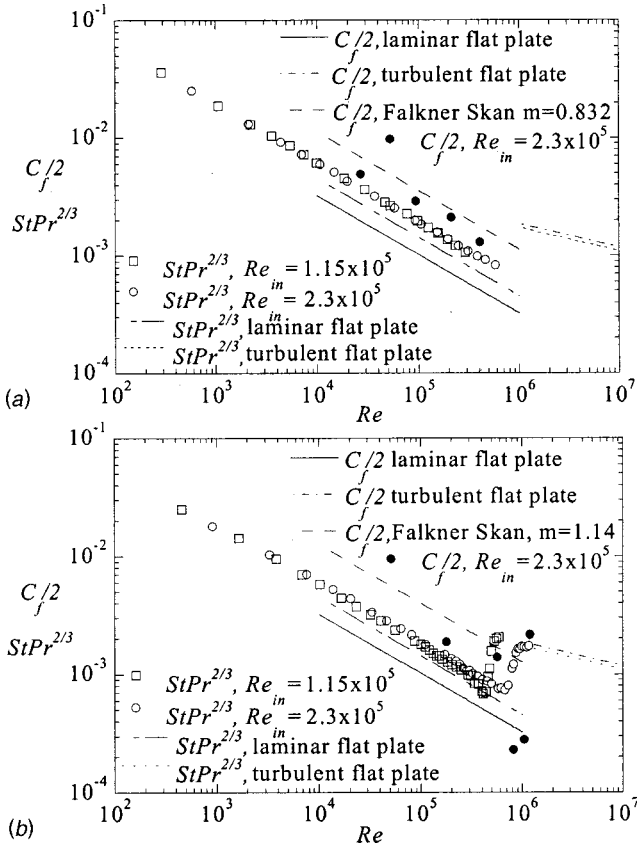

Fig. 6 Comparison of measured Stanton number and friction coefficients on: (*a*) the pressure surface, and (*b*) the suction surface at Tu=0.6 percent

$s/C=0.5$, in the adverse pressure gradient region, the thickness increased quickly. At the high freestream turbulence conditions, there was a sharp rise in the thickness of the suction side boundary layers due to earlier transition to a turbulent boundary layer. The Thwaites [19] method was able to accurately predict the boundary layer thickness over both surfaces at low turbulence conditions up to the point of transition.

The measured displacement and momentum thicknesses are given in Appendix A1 and A2 of this paper. On the pressure surface at low freestream turbulence the pressure gradient caused nearly a constant momentum thickness. At high turbulence conditions, the momentum thickness increased towards the trailing edge of the pressure surface. On the suction surface at low turbulence conditions, the momentum thickness grew steadily from a minimum that occurred at $s/C=0.21$. At high freestream turbulence conditions, the momentum thickness deviated quickly from the low freestream turbulence values as transition began near an $s/C=0.5$.

The ratio of the displacement thickness to the momentum thickness is defined as the shape factor, $H=\delta^*/\theta$. The shape factor for a laminar boundary layer along a flat plate is 2.6. In general, for a laminar boundary layer, favorable pressure gradients tend to steepen the mean velocity profile thereby decreasing the shape factor and adverse pressure gradients flatten the mean velocity profiles thereby increasing the shape factor (Schetz [20]). Figure 5(*b*) compares the measured and predicted shape factor for the 0.6 percent and 19.5 percent conditions. On the pressure surface at low freestream turbulence, the shape factor was essentially constant at a value near 2.4. On the suction surface, at low freestream turbulence levels, the shape factor was near 2.6 at an $s/C=0.21$. At location S2 ($s/C=0.5$), the shape factor decreased to 2.1 indicating that transition was beginning. Downstream at an $s/C=0.5$, the shape factor has decreased due to the favorable pressure gradient occurring up to this point. Farther downstream, the shape factor increased to a value near 3 due to the presence of the adverse pressure gradient. After transition the shape factor decreased to 1.4, which is typical of a turbulent boundary layer. At the elevated turbulence levels, the shape factor on the pressure surface decreased below 2. On the suction surface at elevated turbulence levels, the shape factor quickly fell below 2 at location S2 and reached the fully turbulent values of 1.4 at location S4.

The friction coefficient and the Stanton number distribution at the low turbulence level are plotted for the pressure surface as a function of surface Reynolds numbers in Fig. 6(*a*). Note that the local edge velocities are used as the velocity scales in Re, C_f, and St. The surface distance from the stagnation location is used in Re. In addition to the friction coefficient measurements, heat transfer data measured at identical operating conditions are also shown. Stanton numbers are given at two inlet Reynolds numbers of $\mathrm{Re_{in}}=1.15\times10^5$ and 2.3×10^5 at turbulence levels of 0.6 percent. The Stanton number curves for the two Reynolds numbers fall on the same curve for the pressure surface. Both the friction coefficient and heat transfer data indicate the boundary layer remained laminar over the entire surface.

Both data sets fell above their respective correlations for laminar boundary layer flow over a flat plate. The increased friction and heat transfer is a result of the presence of a favorable pressure gradient caused by the flow accelerating in the vane passage. These data were also compared with a prediction using the Falkner-Skan similarity approach for a laminar boundary layer, which accounts for the streamwise pressure gradients. The friction coefficients fell below the Falkner-Skan prediction, but the agreement was better than observed with the flat plate correlations.

The friction coefficient and the Stanton number distribution at

low turbulence level are plotted for the suction surface as a function of surface Reynolds numbers in Fig. 6(*b*). Both the friction coefficient and heat transfer data initially indicated a laminar boundary layer. As with the pressure surface, the data was above the respective flat plate correlations due to the favorable pressure gradient. The flow was accelerated up to the location of the second boundary layer measurement at an $s/C=0.5$ ($\mathrm{Re}=6\times10^5$). The friction coefficient at this location indicates an increase in the slope of the friction coefficient suggesting that transition was beginning at this location. This transition assertion is supported by the velocity measurements, which showed a mean profile that was beginning to appear turbulent (decrease in the boundary layer shape factor) and a turbulence profile that showed some fluctuations. Downstream of this location, the boundary layer was subjected to an adverse pressure gradient and the measured friction coefficient at locations S3 and S4 showed a dramatic decrease in magnitude. The adverse pressure gradient prevented a full transition from occurring. The decrease in the friction coefficient was the result of the adverse pressure gradient affecting the development of the boundary layer in the near wall region as will be shown later by the boundary layer measurements. Similar dramatic decreases in the friction coefficient for laminar boundary layer flows in the presence of an adverse pressure gradient have been observed by Mislevy and Wang [21]. Farther downstream, at a location of $s/C=1.2$ ($\mathrm{Re}=1.2\times10^6$), the measured friction coefficient indicated that transition from a laminar to turbulent boundary layer had been completed.

The Stanton number curve also indicated that transition began near location S2 ($\mathrm{Re}=5\times10^5$) where the friction coefficient initially started to increase. The heat transfer on the vane was not as affected by the adverse pressure gradient and transition proceeded normally. Greater effects on the friction coefficients as compared to the Stanton numbers were observed in transitioning boundary layers subjected to adverse pressure gradients in Mislevy and Wang [21]. The Stanton numbers for the two Reynolds numbers initially fell along the same curve in the favorable pressure gradient region. The presence of the adverse pressure gradient caused transition to occur at both Reynolds numbers near the trailing edge.

Figure 7(*a*) shows the friction coefficients at 19.5 percent and Stanton numbers on the pressure surface at 10-percent and 19.5-percent turbulence levels. Both the friction coefficient and Stanton numbers indicate that over a majority of the surface a laminar boundary layer was present, with magnitudes higher than those at 0.6 percent turbulence levels. At the higher Reynolds number (near the trailing edge), both the friction coefficients and Stanton numbers began to increase slightly, indicating the onset of transition.

Figure 7(*b*) displays the friction coefficient at 19.5 percent and Stanton numbers on the suction surface at 10-percent and 19.5-percent turbulence levels. Comparisons to Fig. 6(*b*) show that transition occurs at a lower Reynolds number near $\mathrm{Re}=4\times10^5$ as compared to $\mathrm{Re}=6\times10^5$ at low freestream turbulence conditions. The dip in the friction coefficient is not observed at high freestream turbulence conditions because the boundary layer transitioned prior to the onset of the adverse pressure gradient. This resulted in an increase in momentum in the near wall region which resulted in less of a decrease in the friction coefficient for the adverse pressure gradient under high freestream turbulence.

Figure 7(*c*) shows the augmentations of the Stanton number and skin friction due to high freestream turbulence. In general, the heat transfer augmentation was greater than the skin friction augmentation. The heat transfer was augmented by as much as 80 percent for the highest turbulence levels on the pressure side. The large spikes on the suction side are due to the upstream shift in the transition location.

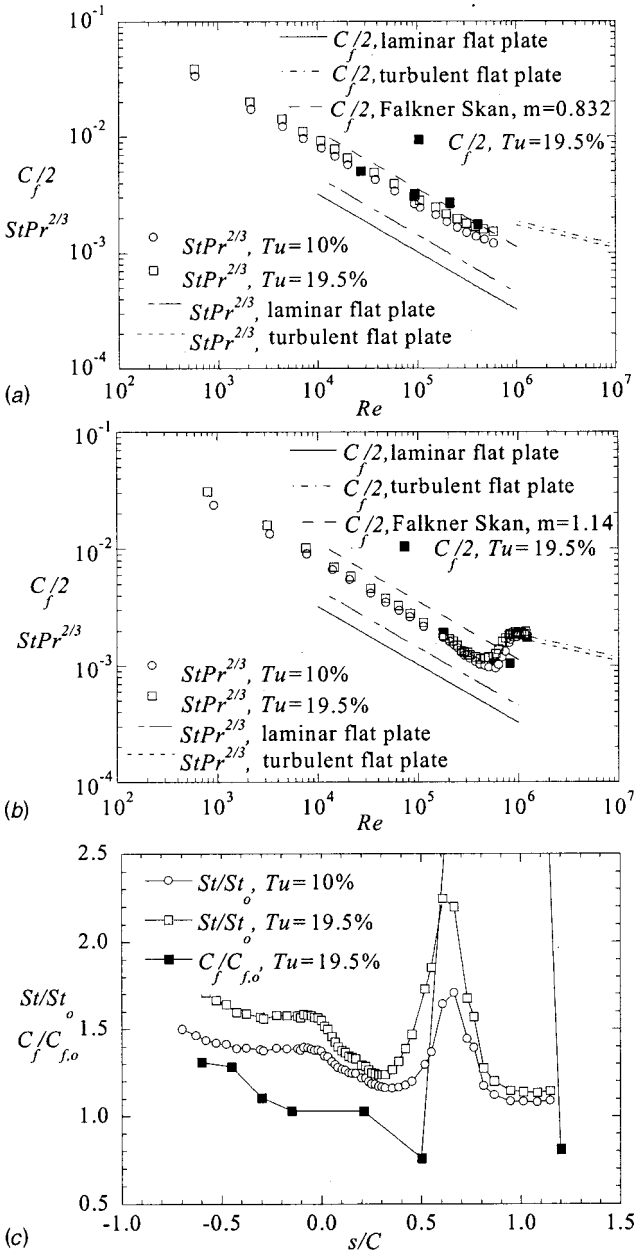

Fig. 7 Comparison of measured Stanton number and friction coefficients on: (*a*) the pressure surface, (*b*) the suction surface at Tu=19.5 percent, and (*c*) friction coefficient, Cf/Cf_o, and Stanton number augmentation, St/St_o, at turbulence levels of 10 percent and 19.5 percent at $\mathrm{Re}=2.3\times10^5$

Boundary Layer at Low Freestream Turbulence

The boundary layer profiles discussed in this section will be presented using two scaling methods. The first method uses outer variables for the normalization scheme. The distance from the surface is normalized by the boundary layer thickness, δ, and the velocity and turbulence statistics are normalized by the inviscid velocity at the edge of the boundary layer, U_{edge}. The second method uses inner wall scaling parameters, which are a function of the shear velocity, u_τ, and viscosity, ν.

Pressure Surface. Figure 8(*a*) shows the mean velocity profiles measured on the pressure surface plotted in terms of freestream parameters. Predictions at $s/C=-0.15$ and $s/C=-0.60$ using the method given by Pohlhausen [22] for laminar boundary layers are also given in Fig. 8(*a*). This boundary layer

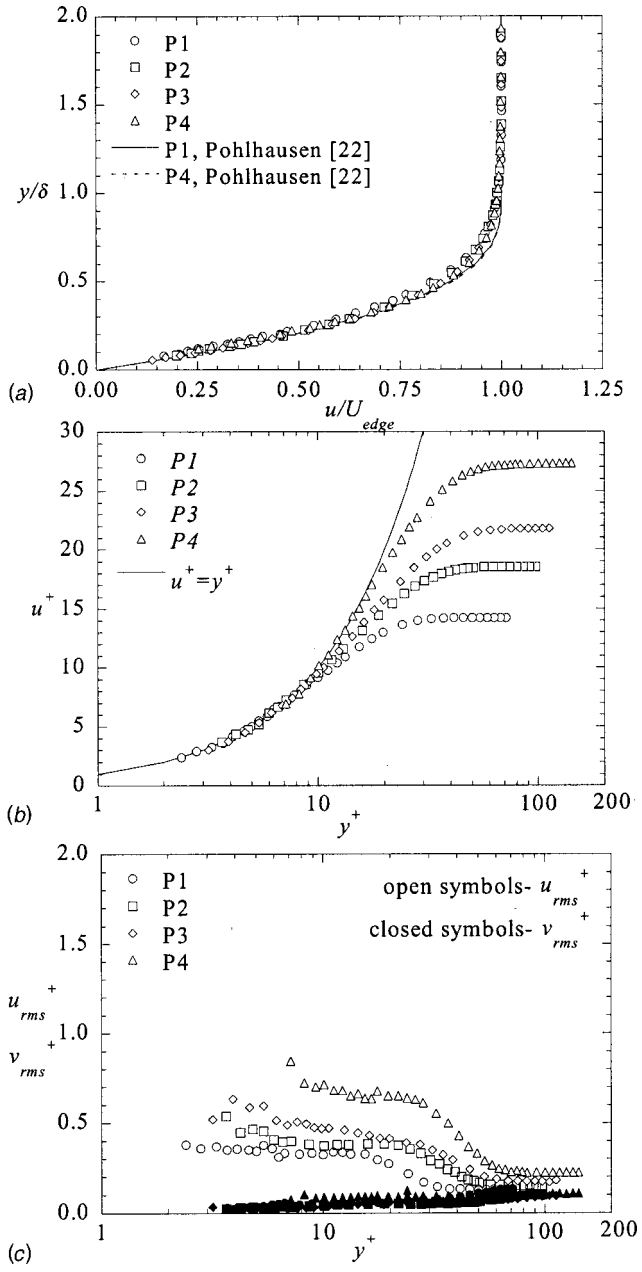

Fig. 8 Boundary layer profiles on the pressure surface at Tu = 0.6 percent plotted using: (*a*) freestream parameters, (*b*) inner wall scaling parameters, and (*c*) boundary layer profiles of streamwise (u^+_{rms}) and normal (v^+_{rms}) rms levels

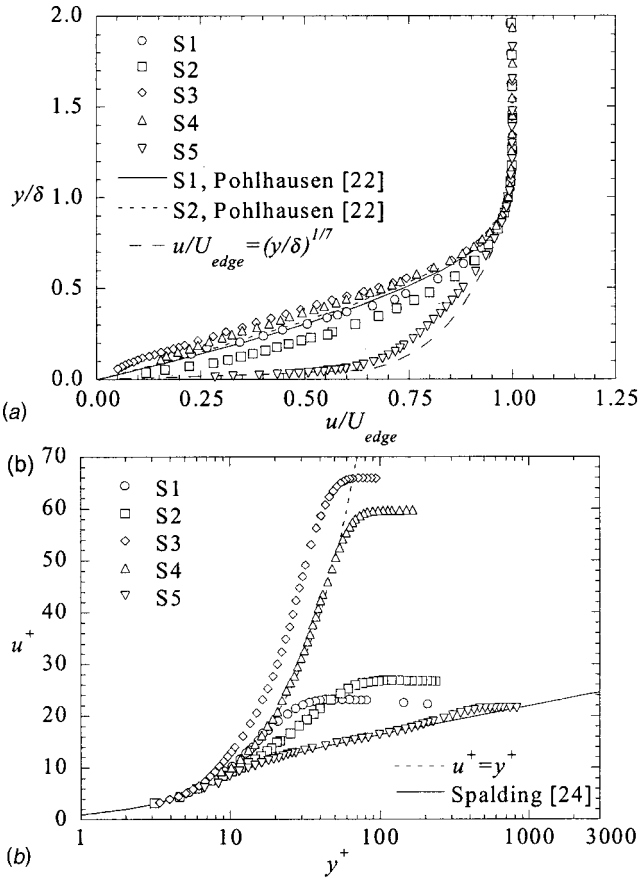

Fig. 9 Boundary layer profiles on the suction surface at Tu = 0.6 percent plotted using: (*a*) freestream parameters, and (*b*) inner wall scaling parameters

profile was generated using the WALZ program (Devenport et al. [23]). The Pohlhausen integral method is a function of the momentum thickness at each location. Only two profiles are displayed due to the similarity between the profiles on the pressure surface. As suggested by the agreement with the Pohlhausen [22] prediction, all four of the measured profiles on the pressure surface were laminar and collapsed onto a single curve when normalized by the boundary layer thickness and freestream velocity. The collapse of the mean velocity was a result of the constant favorable pressure gradient that caused similar boundary layer characteristics over the entire pressure surface. The linear portion of the profile, clearly indicated in Fig. 8(*a*) extended nearly 40 percent into the boundary layer from the wall for each of the profiles.

Figure 8(*b*) shows the mean velocity profiles plotted in terms of inner wall scaling parameters. Also presented in Fig. 8(*b*) is the linear relationship $u^+ = y^+$. As can be seen, for the laminar profiles the measurement location nearest the wall typically corresponded to $y^+ \sim 4$. Where the flow was linear in the near wall region, the use of inner wall scaling parameters collapsed the experimental data. As the flow progressed downstream, the decrease in the wall shear stress continually increased the u^+ values.

The streamwise (u^+_{rms}) and normal (v^+_{rms}) rms levels are given in Fig. 8(*c*). In general, the fluctuation levels are quite low with a maximum value of $u^+_{rms} = 0.9$ at the last streamwise location, $s/C = -0.6$. For a fully turbulent boundary layer at low freestream turbulence conditions the maximum streamwise rms levels reach a value of $u^+_{rms} = 2.8$ in the near wall region (Thole and Bogard [10]). The normal component is also given in Fig. 8(*c*) indicating essentially no fluctuations. As expected, the Reynolds shear stress profile, $\overline{u'v'}$, indicated no Reynolds shear stress was present in the boundary layers at low freestream turbulence conditions.

Suction Surface. Figure 9(*a*) shows the mean velocities measured on the suction surface using outer freestream scaling parameters. In addition to the measurements, a Pohlhausen [22] prediction for the boundary layers at an $s/C = 0.21$ and $s/C = 0.50$ are given along with a $1/7^{th}$ law turbulent boundary layer approximation. The friction coefficient and Stanton number curves indicated the start of transition at location S2. For this reason the Pohlhausen [22] prediction, which is valid for laminar flows, is only given at locations S1 and S2. The measured boundary layer at location S1 agreed well with the laminar boundary layer prediction. The boundary layer at location S2 in the near wall region was fuller than the boundary layer at S1 and disagreed with the Pohl-

hausen prediction at location at S2. This should be expected because the friction coefficients showed the boundary layer was beginning to transition at this location. Just downstream of location S2 the adverse pressure gradient began, as shown in Fig. 4. At location S3, the adverse pressure gradient caused a decrease in the streamwise momentum near the wall. The decrease in momentum near the wall was still observed at location S4. The measured velocity profile at location S5 is similar to the $1/7^{th}$ power law approximation for a turbulent boundary layer. This indicates that the boundary layer was either near the end or just downstream of transition.

Figure 9(*b*) displays the measured mean velocity profiles on the suction surface in addition to the $u^+=y^+$ curve and Spalding's law (Spalding [24]). The first streamwise locations (S1) showed the typical laminar boundary layer behavior and agreement with the $u^+=y^+$ curve in the near wall region. The favorable acceleration gradient caused the boundary layer at location S2 to fall below the $u^+=y^+$ curve indicating a start of transition to a turbulent boundary layer. At location S3, the measured boundary layer was above the $u^+=y^+$ curve, which is again the result of the adverse pressure gradient. This result is consistent with the results from Mislevy and Wang [21] who also showed that laminar boundary layers were above the $u^+=y^+$ curve when subjected to an adverse pressure gradient. Farther downstream at location S4, the boundary has moved back towards the $u^+=y^+$ curve. At the farthest downstream location, S5, the boundary layer was turbulent with a depressed wake and showed good agreement with Spalding's law for a turbulent boundary layer.

The streamwise ($u^+_{\rm rms}$) and normal ($v^+_{\rm rms}$) rms levels are presented in Figs. 10(*a*) and 10(*b*). The first three streamwise locations (S1, S2, and S3) had a peak streamwise rms level of 1.5. Large fluctuations were observed at location S4. As discussed previously, for a fully turbulent boundary layer at low freestream turbulence conditions the maximum values of reach a value of $u^+_{\rm rms}=2.8$ in the near wall region (Thole and Bogard [10]). The values of $u^+_{\rm rms}=8$ that occurred at S4 were the result of the elevated turbulence existing in a boundary layer with low wall shear stress due to the adverse pressure gradient. The peak rms level at position S3 is higher by 20 percent relative to the S5 position, while the wall shear stress at position S3 is lower by 29 percent relative to the S5 position. Thereby, the two almost equally contribute to having high $u^+_{\rm rms}$ peaks. Similar behavior is noted by Lee and Kang [9] and Mislevy and Wang [25] in their results at their highest inlet turbulence level of 7 percent. Farther downstream at location S5, the magnitude of the streamwise rms levels reached a value of $u^+_{\rm rms}=3$ which was near the typical value for a fully turbulent boundary layer.

The normal rms levels (Fig. 10(*b*)) for the first three locations (S1, S2, and S3) indicated low levels throughout the boundary layer. At location S4 a large increase was observed with a peak level of $v^+_{\rm rms}=1.8$. Again, the higher values were the result of the elevated turbulence levels being present in a region of low wall shear stress. Downstream at location S5, an increase in the normal rms level was observed in the outer portion of the boundary layer. Inside the boundary layer, these levels flattened out and began to decrease as the result of attenuation of the vane surface. Thole and Bogard [9] showed that for a boundary layer at low freestream turbulence conditions, the normal rms levels should reach a maximum near $v^+_{\rm rms}=1$.

The Reynolds shear stress profiles ($\overline{u'v'}$) are given in Fig. 10(*c*). The first two locations where coincident LDV measurements were performed (S2 and S3) showed the absence of Reynolds shear stress. At location S4, near the start of transition, a peak in the Reynolds stress was observed away from the surface of the vane. The level of the turbulent shear stress has been shown by Mislevy and Wang [23] to increase dramatically in transitional boundary layers being subjected to an adverse pressure gradient. At this location, the turbulent shear stress was approximately 300 percent of the wall-generated shear stress. Proceeding farther downstream to location S5, the peak stress moved closer to the vane surface. At this location, the peak turbulent shear stress was approximately equal to the wall shear stress as is typically the case for a fully turbulent boundary layer.

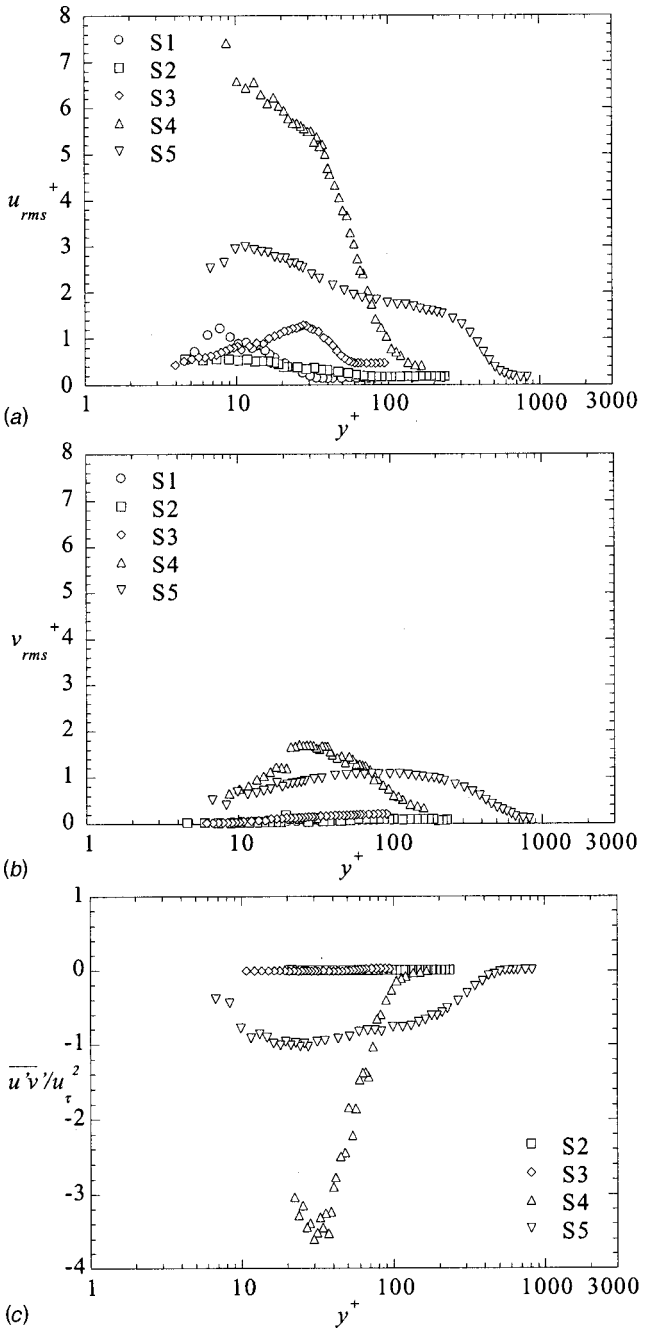

Fig. 10 Profiles of: (*a*) streamwise ($u^+_{\rm rms}$) (*b*) normal ($v^+_{\rm rms}$), and (*c*) Reynolds shear stress levels on the suction surface at Tu=0.6 percent plotted using inner wall scaling parameters

Boundary Layer at High Freestream Turbulence

Boundary layer measurements were performed at the same streamwise locations to allow for a direct determination of the effect of turbulence levels on boundary layer growth and development.

Pressure Surface. Figure 11(*a*) shows the mean velocity profiles measured on the pressure surface plotted in terms of

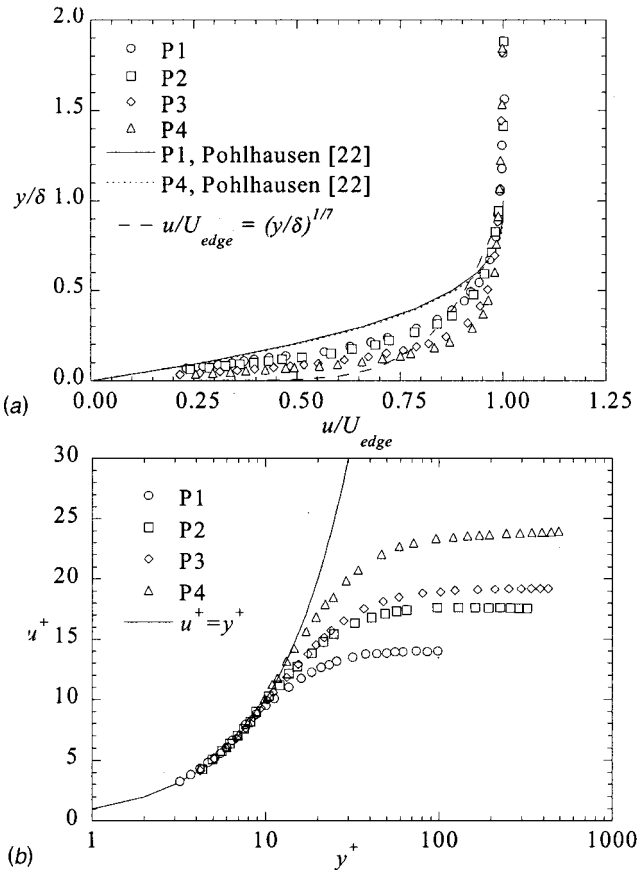

Fig. 11 Boundary layer profiles on the pressure surface at Tu=19.5 percent plotted using: (*a*) freestream parameters, and (*b*) inner wall scaling parameters

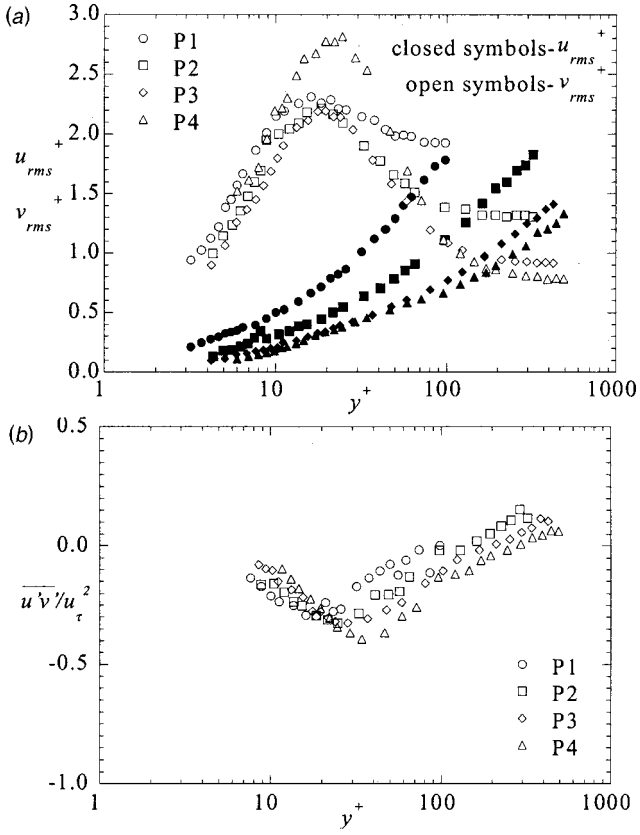

Fig. 12 Boundary layer profiles of: (*a*) streamwise (u_{rms}^+) and normal (v_{rms}^+) rms levels, and (*b*) Reynolds shear stress on the pressure surface at Tu=19.5 percent plotted using inner wall scaling parameters

freestream parameters at the 19.5-percent turbulence levels. Figure 11(*a*) also shows the Pohlhausen predictions at locations P1 and P4 as well as a $1/7^{th}$ turbulent profile. At low freestream turbulence conditions, shown previously in Fig. 8(*a*), all four of the measured profiles on the pressure surface were laminar and collapsed onto a single curve. At the high freestream turbulence conditions, the boundary layers did not agree with the Pohlhausen [21] predictions for a laminar boundary layer with no turbulence as shown by the discrepancy with the correlation given for the P1 and P4 locations. As expected from the increased shear stress, the velocity profiles in the near wall region were fuller than at low freestream turbulence levels. The first two streamwise locations (P1 and P2) showed a laminar velocity profile and still collapsed onto a single curve. At locations P3 and P4, where an increase in the friction coefficient was observed, the profiles had steeper velocity gradients in the near wall region.

Figure 11(*b*) presents the velocity profiles using inner wall scaling on the pressure side for the high freestream turbulence conditions. These boundary layer profiles are similar to the profiles displayed in Fig. 6(*b*) measured at 0.6 percent turbulence. The only noticeable difference between Fig. 8(*b*) and Fig. 11(*b*) was that the u^+ values level off to lower values for the 19.5-percent turbulence case as compared with the 0.6 percent turbulence case. This was the result of the high shear stress measured at the wall for the high freestream turbulence conditions as compared to the low freestream turbulence conditions.

The streamwise (u_{rms}^+) and normal (v_{rms}^+) rms levels are plotted using inner wall scaling parameters in Fig. 12(*a*). The streamwise rms levels increased from the values at the edge of the boundary layer to their maximum levels near a $y^+=20$. For a turbulent boundary layer, the maximum value of the streamwise rms levels were $u_{\text{rms}}^+=2.8$ and occur at a location near $y^+=10$. For the first three streamwise positions (P1, P2, and P3) the maximum level in the boundary layer reached levels of $u_{\text{rms}}^+=2.0$ at a location of $y^+\sim 20$. At location P4, the streamwise rms levels are higher reaching levels similar to those in a turbulent boundary layer. Moving closer to the wall, a sharp decrease in the streamwise rms levels was observed. Recall that the acceleration parameter was $K=3.4\times 10^{-6}$ along the pressure side of the airfoil. With such a large acceleration, one would expect that any boundary layer transition would be suppressed by the acceleration. The previously shown mean velocity profiles are in agreement with typical laminar profiles, but the large fluctuations indicate the presence of turbulence. The normal rms levels show a continual decrease in magnitude as the stator vane surface is approached as a result of being attenuated by the vane surface. It is interesting to note that the location of the peak fluctuating value is further away from the wall than that which would occur for a turbulent boundary layer profile along a flat plate. Figure 12(*a*) also indicates the anisotropy of the freestream turbulence outside the boundary layer, which is a result of the redistribution of the turbulence due to streamline curvature.

Normalized values of the Reynolds shear stress ($\overline{u'v'}/u_\tau^2$) are given in Fig. 12(*b*). For each of the cases the Reynolds stress was near zero at the edge of the boundary layer. At location P1 the Reynolds shear stress became negative in the boundary reaching a value of -0.3 at a $y^+=15$. Proceeding downstream the shear stress levels became increasingly negative reaching a value of $\overline{u'v'}/u_\tau^2=-0.4$ at a $y^+=30$ at location P4. The maximum Reynolds shear stress in the boundary layer was approximately 30 percent of the viscous shear stress measured at the wall for each of

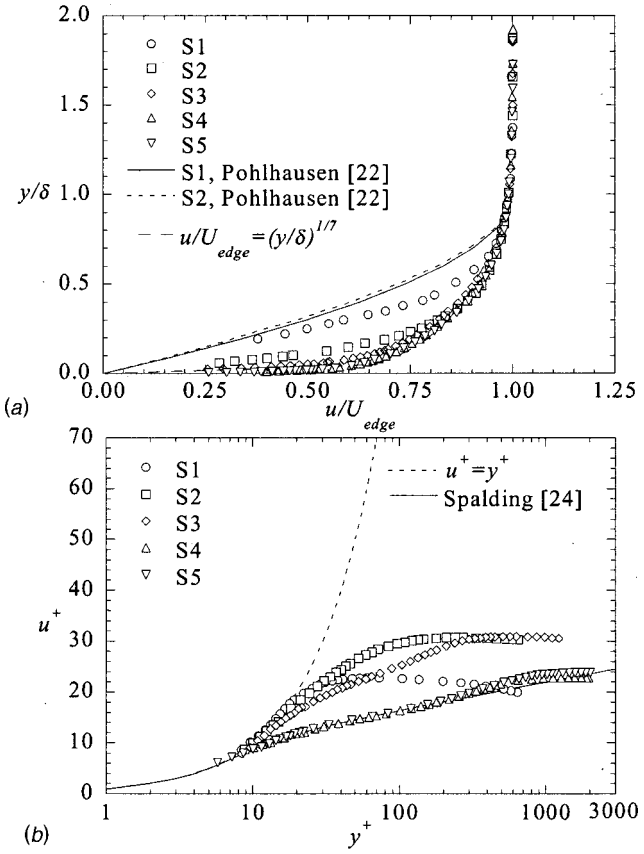

Fig. 13 Boundary layer profiles on the suction surface at Tu = 19.5 percent plotted using; (*a*) freestream parameters, and (*b*) inner wall scaling parameters

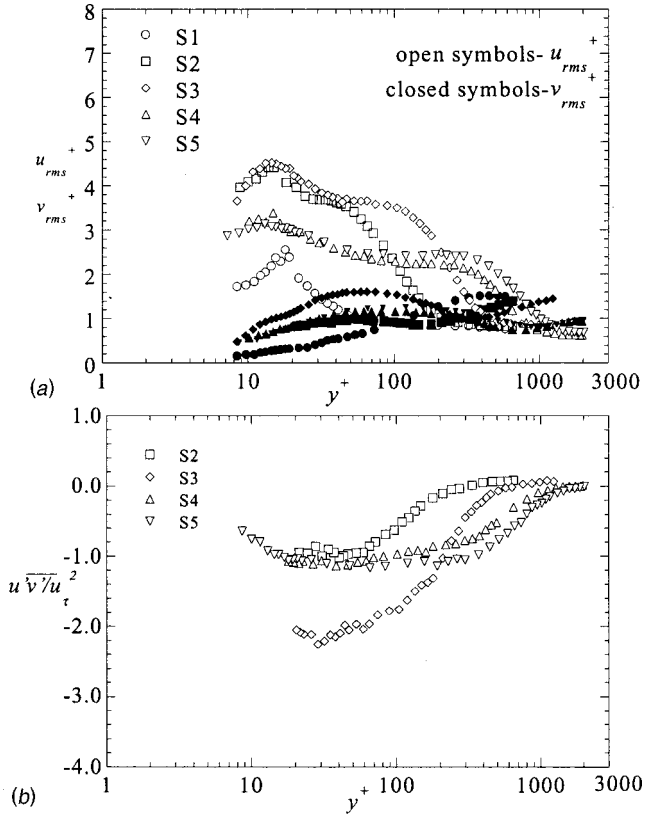

Fig. 14 Boundary layer profiles of: (*a*) streamwise (u^+_{rms}) and normal (v^+_{rms}) rms levels, and (*b*) Reynolds shear stress, on the suction surface at Tu = 19.5 percent plotted using inner scaling

the streamwise locations. Moving closer to the wall, the Reynolds shear stress approached zero for each of the streamwise locations. This was expected since the viscous shear dominates near the wall.

Suction Surface. The boundary layer profiles measured on the suction surface at 19.5-percent turbulence levels are plotted in Fig. 13(*a*) using boundary layer scaling parameters. The laminar profiles predicted by Pohlhausen [22] at locations S1 and S2 and the $1/7^{th}$ power law approximation for the turbulent boundary layer are also shown in Fig. 13(*a*). At location S1, the boundary layer was slightly fuller than the boundary layer measured at low freestream turbulence conditions. The measured boundary layers do not agree with the laminar profiles at S1 and S2 predicted by Pohlhausen [22] at high freestream turbulence levels. The profiles at S3 and S4 showed much fuller velocity profiles in the near wall region at higher turbulence than the low freestream turbulence conditions. This was the result of the earlier transition, which gave a higher momentum fluid in the boundary layer.

The streamwise velocity profiles on the suction surface are plotted using inner wall scaling parameters in Fig. 13(*b*). The boundary layer at location S1 was laminar, based upon the friction coefficients, and similar to the profiles measured at low freestream turbulence conditions shown in Fig. 10(*b*). The boundary layer started to transition from laminar to turbulent at locations S2 and S3. The transition at location S3 was obvious as shown by the deviation from the laminar profile for $50<y^+<200$. The boundary layers were fully turbulent at locations S4 and S5 and agreed well with Spalding's law. The strength of the wake, defined as the maximum deviation from the velocity distribution to the log-law in the outer region of the boundary layer, is larger at location S5 than S4. This is consistent with the higher momentum thickness Reynolds number at this location. The strength of the wake for these profiles was smaller than expected due to the presence of elevated turbulence in the freestream, but does indicate a negative wake strength. Negative wake strengths often occur for high freestream turbulence conditions (Thole and Bogard [10]).

The streamwise ($u^+_{\rm rms}$) and normal ($v^+_{\rm rms}$) rms levels are displayed using inner wall scaling parameters in Fig. 14(*a*). The $u^+_{\rm rms}$ levels at location S1, which was a laminar boundary layer, were high but lower than values for a fully turbulent boundary layer. At locations S2 and S3, the transitional boundary layer resulted in rms levels of $u^+_{\rm rms}=4$, which were higher than measured for a turbulent boundary layer. As discussed previously, this was due to the presence of the high turbulence levels in boundary layers with low wall shear stress. At locations S4 and S5, which were fully turbulent boundary layers, the maximum level in the boundary layers were $u^+_{\rm rms}=3$ which was only slightly higher than expected.

The normal rms ($v^+_{\rm rms}$) levels are also shown in Fig. 14(*a*). For the S1 location, the vrms+ levels showed a continuous decrease in magnitude through the boundary layer. At location S2, the levels in the boundary layer were higher than the levels for S1, indicating that the profile was on the onset of transition at this streamwise location. Farther downstream at S3, the normal fluctuations reached a maximum of $v^+_{\rm rms}=1.5$. These values are larger than the typical value of $v^+_{\rm rms}=1$ for a turbulent boundary layer, and were the result of the fluctuations being present in the boundary layer. The values at S4 and S5 agreed with the expected values for a turbulent boundary layer.

The Reynolds shear stress profiles are shown in Fig. 14(*b*). The boundary layer at location S2 contained Reynolds shear stress

indicating that it was at the onset of transition. At location S3, the maximum Reynolds shear stress in the boundary layer was approximately twice the measured viscous shear stress at the wall. For the fully turbulent boundary layers at locations S4 and S5, the maximum Reynolds stress in the boundary layer was approximately equal to the viscous shear stress deduced from the velocity gradient.

Conclusions

Detailed boundary layer measurements on a turbine vane geometry at combustor turbulence levels have been compared to boundary layer measurements at low turbulence levels. To date, this data has not been available in the literature and was made possible by using a large-scale test facility.

The integral boundary layer parameters at low freestream turbulence levels agreed well with those estimated using Thwaites' method when the boundary layer remained laminar. At high freestream turbulence levels, the integral parameters on the suction side indicated the transition location moved upstream of the transition location that had occurred at low freestream turbulence conditions. This upstream shift was also seen in the skin friction and heat transfer measurements. Overall lower shape factors occurred for the high freestream turbulence case as compared with the low freestream turbulence case indicating lower displacement to momentum thickness ratios. This is expected since lower shape parameters occur for turbulent boundary layers compared to laminar boundary layers.

At low freestream turbulence levels, the mean velocity profiles along the pressure side of the vane collapsed to a single curve using the edge velocity and boundary layer thicknesses as the scaling parameter. The profiles also indicated a linear behavior of velocity with distance from the wall in the near-wall region, even though the boundary layer is affected by a pressure gradient. At high turbulence levels, the outer scaling parameters did not collapse the profiles. At high freestream turbulence levels, fluctuations were measured in the boundary layer along the pressure side even though the mean profiles were more consistent with a laminar-like boundary layer. At the most downstream positions measured along the suction side, the mean velocity profiles indicated a fully turbulent profile with a depressed wake region.

The data presented in this paper provide the community with an understanding of the effects that high freestream turbulence can have on the development of an airfoil boundary layer. In addition, this data provides not only surface phenomena but also velocity field measurements to use for improving predictive turbulence models.

Appendix A1

Boundary Layer Parameters at Low Turbulence Conditions

Pressure Surface	U_{edge} (m/s)	Tu	$C_f/2$	δ/C	δ^*/C	θ/C	H
P1	4.99	0.8%	0.0049	0.0025	7.09E−4	3.01E−4	2.35
P2	8.69	0.8%	0.0029	0.0026	7.24E−4	3.17E−4	2.29
P3	13.11	0.6%	0.0021	0.0026	6.91E−4	3.04E−4	2.27
P4	18.65	0.7%	0.0013	0.0024	6.76E−4	2.80E−4	2.42
Suction Surface			$C_f/2$	δ/C	δ^*/C	θ/C	H
S1	23.54	0.5%	0.0019	0.0010	3.49E−4	1.33E−4	2.63
S2	31.23	0.6%	0.0014	0.0020	5.51E−4	2.58E−4	2.14
S3	30.04	0.6%	0.0002	0.0033	1.40E−4	4.58E−4	3.05
S4	28.97	2.1%	0.0003	0.0044	1.71E−4	6.08E−4	2.81
S5	27.56	2.2%	0.0022	0.0097	1.56E−4	1.08E−3	1.44

Appendix A2

Boundary Layer Parameters at High Turbulence Conditions

Pressure Surface	U_{edge} (m/s)	Tu	$C_f/2$	δ/C	δ^*/C	θ/C	H
P1	5.43	12.1%	0.0051	0.0034	6.80E−4	3.22E−4	2.11
P2	9.22	7.1%	0.0032	0.0037	6.79E−4	3.29E−4	2.06
P3	13.43	4.9%	0.0027	0.0046	6.55E−4	3.57E−4	1.83
P4	18.96	3.7%	0.0018	0.0055	6.89E−4	3.78E−4	1.82
Suction Surface			$C_f/2$	δ/C	δ^*/C	θ/C	H
S1	23.31	3.9%	0.0019	0.0012	3.41E−4	1.30E−4	2.62
S2	31.02	4.0%	0.0011	0.0040	7.25E−4	3.78E−4	1.92
S3	30.05	3.6%	0.0011	0.0097	1.52E−3	9.78E−4	1.56
S4	28.99	3.4%	0.0019	0.0180	2.41E−3	1.74E−3	1.38
S5	27.61	3.7%	0.0018	0.0259	3.34E−3	2.44E−3	1.36

Acknowledgments

The authors would like to acknowledge the Department of Energy-Advanced Gas Turbine Systems Research Program for their support. Partial support for this work also came from Pratt & Whitney.

Nomenclature

C = true chord of stator vane
$C_j(C_{fo})$ = friction coefficient (low turbulence case), $2(u_\tau^2/U_{edge}^2)$
C_p = specific heat
d = turbulence generator rod diameter
D^+ = probe volume diameter in inner coordinates, Du_τ/ν
h = convective heat transfer coefficient
H = shape factor, δ^*/θ
L_ε = dissipation length scale, $1.5u_{rms}^2/\varepsilon$
K = acceleration parameter, $\nu(dU_{edge}/ds)/U_{edge}^2$
P = vane pitch
Pr = Prandtl number
Re = Reynolds number defined as $Re=sU_{edge}/\nu$
Re_{in} = Reynolds number defined as $Re=CU_{in}/\nu$
s = surface distance along vane measured from stagnation
s_L = turbulence generator bar spacing
S = span of vane
$St(St_o)$ = Stanton number (low turbulence case) $St=h/\rho CpU_{edge}$
Tu = turbulence level $(0.5(u_{rms}{}^2+v_{rms}{}^2))^{0.5}/U_{edge}$
u_τ = shear velocity, $\sqrt{\tau_w/\rho}$
u^+ = velocity in inner coordinates, u/u_τ
u, v, w = mean local velocity in local coordinate system
U_{inlet} = incident upstream velocity
U_{edge} = local inviscid velocity
$U, \underline{V, W}$ = mean velocity in the X, Y, Z directions
$\overline{u'v'}$ = Reynolds shear stress
x, y, z = local coordinates defined at measurement location
X, Y, Z = global coordinates defined from stagnation location
y^+ = velocity in inner coordinates, yu_τ/ν
δ = boundary layer thickness
δ^* = displacement thickness
ε = turbulent dissipation rate
θ = momentum thickness
Λ_x = integral length scale

ρ = density
τ_w = wall shear stress
ν = viscosity

Subscripts

edge = local inviscid quantity
inlet = inlet
rms = root mean square

References

[1] Goldstein, R. J., Lau, K. Y., and Leung, C. C., 1983, ''Velocity and Turbulence Measurements in Combustion Systems,'' Exp. Fluids, **1**, pp. 93–99.
[2] Kuotmos, P., and McGuirk, J. J., 1989, ''Isothermal Flow in a Gas Turbine Combustor—A Benchmark Experimental Study,'' Exp. Fluids, **7**, pp. 344–354.
[3] Goebel, S. G., Abuaf, N., Lovett, J. A., and Lee, C. P., 1993, ''Measurements of Combustor Velocity and Turbulence Profiles,'' ASME Paper No. 93-GT-228.
[4] Moss, R. W., 1992, ''The Effects of Turbulence Length Scale on Heat Transfer,'' University of Oxford, Department of Engineering Science, Report No. OUEL 1924, Ph.D. dissertation.
[5] Radomsky, R., and Thole, K. A., 2000, ''Highly Turbulent Flowfield Measurements Around a Stator Vane,'' ASME J. Turbomach., **122**, pp. 255–262.
[6] Kestin, J., 1966, ''The Effect of Freestream Turbulence on Heat Transfer Rates,'' Advances in Heat Transfer, 3, New York, Academic Press.
[7] Ubaldi, M., Zunino, P., Campora, U., and Ghiglione, A., 1996, ''Detailed Velocity and Turbulence Measurements of the Profile Boundary Layer in a Large Scale Turbine Cascade,'' ASME Paper No. 96-GT-42.
[8] Bario, F., and Beral, C., 1998, ''Boundary Layer Measurements on the Pressure and Suction Sides of a Turbine Inlet Guide Vane,'' Exp. Therm. Fluid Sci., **17**, pp. 1–9.
[9] Lee, H., and Kang, S.-H., 2000, ''Flow Characteristics of Transitional Boundary Layers on an Airfoil in Wakes,'' ASME J. Fluids Eng., **122**, pp. 522–532.
[10] Thole, K. A., and Bogard, D. G., 1996, ''High Freestream Turbulence Effects on Turbulent Boundary Layers,'' ASME J. Fluids Eng., **118**, No. 2, pp. 276–284.
[11] Radomsky, R., and Thole, K. A., 2000, ''High Freestream Turbulence Effects in the Endwall Leading Edge Region,'' ASME J. Turbomach., **122**, pp. 699–708.
[12] Kang, M., Kohli, A., and Thole, K. A., 1999, ''Heat Transfer And Flowfield Measurements In The Leading Edge Region of a Stator Vane Endwall,'' ASME J. Turbomach., **121**, pp. 558–568.
[13] Kang, M., and Thole, K. A., 2000, ''Flowfield Measurements in the Endwall Region of a Stator Vane,'' ASME J. Turbomach., **122**, pp. 458–466.
[14] Radomsky, R., and Thole, K. A., 2000, ''Measurements and Predictions of a Highly Turbulent Flowfield in a Turbine Vane Passage,'' ASME J. Fluids Eng., **122**, pp. 666–676.
[15] Polanka, M., 1999, ''Detailed Film Cooling Effectiveness and Three Component Velocity Field Measurements on a First Stage Turbine Vane Subject to High Freestream Turbulence,'' Ph.D. dissertation, University of Texas-Austin.
[16] Radomsky, R. W., 2000, ''High Freestream Turbulence Studies on a Scaled-up Stator Vane,'' University of Wisconsin, Department of Mechanical Engineering, Ph.D. dissertation.
[17] Kays, W. M., and Crawford, M. E., 1991, *Convective Heat and Mass Transfer*, McGraw-Hill, New York, NY.
[18] Moffat, R. J., 1988, ''Describing the Uncertainties in Experimental Results,'' Exp. Therm. Fluid Sci., **1**, pp. 3–17.
[19] Thwaites, B., 1949, ''Approximate Calculation of the Laminar Boundary Layer,'' Aeronaut. Q., **1**, pp. 245–280.
[20] Schetz, J. A., 1993, *Boundary Layer Analysis*, Prentice-Hall, New York.
[21] Mislevy, S. P., and Wang, T., 1996, ''The Effects of Adverse Pressure Gradients on Momentum and Thermal Structures in Transitional Boundary Layers: Part 1-Mean Quantities,'' ASME J. Turbomach., **118**, pp. 717–727.
[22] Pohlhausen, K., 1921, ''On the Approximate Integration of the Differential Equations of Laminar Shear Layers,'' Z. Angew. Math. Mech., **1**, pp. 252–268.
[23] Devenport, W. J., Kapania, R., Rojiani, K., and Singh, K., ''Java Applets for Engineering Education,'' http://www.engapplets.vt.edu (Virginia Tech, 2000).
[24] Spalding, D. B., 1961, ASME J. Appl. Mech., **28**, pp. 455–457.
[25] Mislevy, S. P., and Wang, T., 1996b, ''The Effects of Adverse Pressure Gradients on Momentum and Thermal Structures in Transitional Boundary Layers: Part 2-Fluctuation Quantities,'' ASME J. Turbomach., **118**, pp. 728–736.

M. Dittmann
e-mail: Mario.Dittmann@its.uni-karlsruhe.de

T. Geis

V. Schramm

S. Kim

S. Wittig

Lehrstuhl und Institut für Thermische Strömungsmaschinen,
University of Karlsruhe,
76128 Karlsruhe, Germany

Discharge Coefficients of a Preswirl System in Secondary Air Systems

The discharge behavior of a "direct-transfer" preswirl system has been investigated experimentally. The influences of the pressure ratio and the swirl ratio as well as the influence of the receiver and stator geometry were investigated. The discharge coefficients of the preswirl nozzles are given in the absolute frame of reference. The definition of the discharge coefficient of the receiver holes is applied to the rotating system in order to consider the work done by the rotor. Numerical calculations carried out for a free expansion through the stationary preswirl nozzles show very good agreement with experimental data. [DOI: 10.1115/1.1413474]

Introduction

In high-efficiency gas turbine engines, the cooling air for the high-pressure turbine stage is expanded through stationary preswirl nozzles to the blade feed holes of the rotating disk. By accelerating the cooling air in the direction of rotation, the total temperature relative to the rotor disk and the pressure losses occurring at the receiver hole inlet can be reduced. According to Scricca and Moore [1], there are two different preswirl systems established in modern engines.

In a "cover-plate" system, the preswirl nozzles are located at a small radius to reduce seal leakage. The air flows radially outward between the turbine disk and the cover-plate attached to it. The preswirl nozzles of a "direct-transfer" system are positioned at a large pitch radius similar or equal to the pitch radius of the receiver holes. In such a system, lower cooling air temperatures can theoretically be achieved. In addition, the weight of the engine can be reduced if the cover-plate is omitted [1]. Meierhofer and Franklin [2] were the first to measure the cooling air temperature in the rotating blade feed holes of a "direct-transfer" system. They found the preswirl system effectiveness to be a function of the ratio of disk velocity to effective preswirl velocity. Unfortunately, the discharge behavior of the system was not considered in their study. Discharge coefficients for rotating holes without preswirl are presented by Samoilovich and Morozov [3], Meyfarth and Shine [4], McGreehan and Schotsch [5] in the absolute frame of reference plotting c_D against $u/c_{ax,id}$. Wittig et al. [6] presented a correlation in the relative frame of reference for different l/d and r/d ratios.

A combined experimental and numerical study is presented by El-Oun and Owen [7], where the effectiveness of a "direct-transfer" preswirl system was calculated with a simple theoretical model, based on the Reynolds analogy. Wilson et al. [8] used an axisymmetric elliptic flow solver to determine the flow structure and the heat transfer in a preswirl rotor–stator system. Popp et al. [9] introduced a plane model for a CFD analysis of a "cover-plate" system with several simplifications. Discharge coefficients and the temperature drop were calculated for different geometries. For low velocity ratios u/c good agreement between CFD and measured data was achieved.

To the authors' knowledge, no data are available describing the discharge behavior of a "direct-transfer" preswirl system. It is the subject of this paper to investigate the main parameters influencing the discharge coefficients of the preswirl nozzles and receiver holes.

Experimental Setup

A sectioned view of the "direct-transfer" preswirl rotor–stator system is shown in Fig. 1. Details of the test section are given in Fig. 2.

Compressor air was discharged from a settling chamber through the flange of the rig to the preswirl plate, which contained the preswirl nozzles. Four different preswirl plates were used in order to vary the axial distance s_1 between the stator and rotor. The number of preswirl nozzles N_N varied between 11 and 12. The nozzle centerlines were inclined at $\alpha = 20$ deg to the stator surface. In addition, the preswirl nozzles were oriented such that a jet following the extended nozzle centerline enters the receiver hole tangential to the pitch circle. In order to meet these geometric constraints, the radial position r_e of the nozzle exit had to be varied for each distance s_1. The corresponding values for s_1, s_0 and r_e are listed in the left part of Table 1. Thereby, s_0 indicates the distance between the stator and the casing, which changed with different preswirl plates installed.

The preswirled air entered an annulus, of 46.8 mm radial height, formed by an inner seal and the casing. A labyrinth seal placed between the rotor and the casing could be fed with sealing air to reduce the leakage flow. Two differential pressure transducers were located at different angular positions to monitor the leakage. During the experimental investigations, the pressure drop across the labyrinth seal was adjusted to be close to zero. The air left the test section through receiver holes located at a pitch radius of $r_m = 220$ mm.

In order to maintain the total cross-sectional area of the receiver holes while changing the length to diameter ratio, the number of receiver holes N_R had to be increased with decreasing diameter d. Thereby, the length of the receiver holes was kept constant at $l = 40$ mm. The number of holes, the l/d ratio, and the corresponding diameter are given in the right part of Table 1.

The rotor was driven up to $n = 7000$ rpm, which is equivalent to a circumferential velocity of the receiver holes of $u = 161$ m/s, or a rotational Reynolds number $\mathrm{Re}_\phi = 2.3 \times 10^6$. The rig offered the possibility to superimpose a radial outflow to the swirled mainflow. Therefore, air was fed into the rotor–stator wheelspace near the hub region. Passing the inner seal and mixing with the mainflow, the superimposed cooling air left the test section radially through a lip seal arrangement in the casing.

The mass flow rate discharged through the preswirl rig was measured by an orifice-metering system in accordance to European Standards with an uncertainty of 1 percent. The radially su-

Contributed by the International Gas Turbine Institute and presented at the 46th International Gas Turbine and Aeroengine Congress and Exhibition, New Orleans, Louisiana, June 4–7, 2001. Manuscript received by the International Gas Turbine Institute February 2001. Paper No. 2001-GT-122. Review Chair: R. Natole.

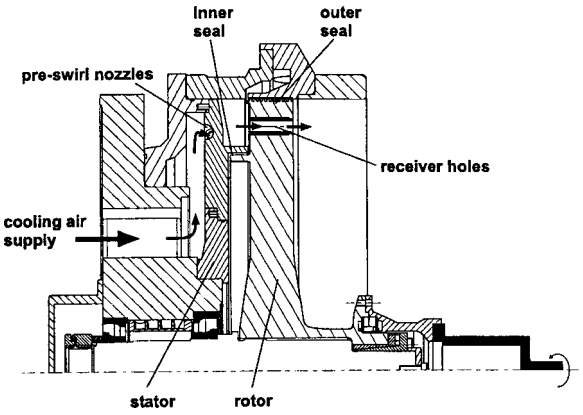

Fig. 1 Preswirl rig

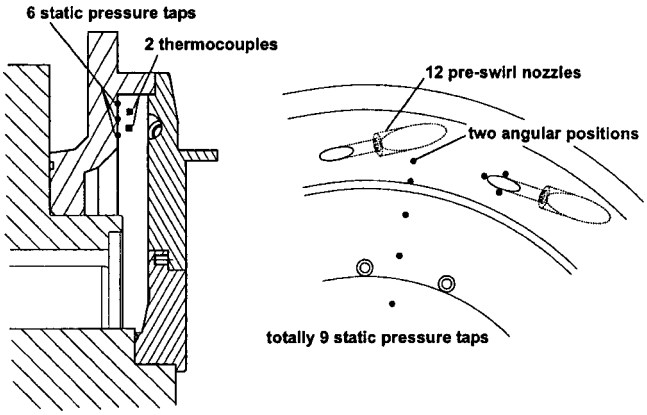

Fig. 3 Instrumentation of preswirl rig

perimposed outflow was measured with hot-film-sensors calibrated to an uncertainty of 1 percent. The overall pressure ratio π across the preswirl rig was varied from 1.05 to 2.00, resulting in Reynolds numbers in the range of $3.8\times10^4<\mathrm{Re}<1.3\times10^5$ for a subsonic flow through the preswirl nozzles.

The instrumentation inside the test section is shown in Fig. 3. Total pressure and total temperature sensors were installed inside the settling chamber to monitor the inlet conditions of the preswirl system. Between each preswirl plate and the opposite casing, six static pressure tappings and two thermocouples were located, which could measure the total pressure and the total temperature in front of the preswirl nozzles. Three out of six pressure tappings were located just opposite one nozzle inlet, while the other taps were placed at a different angular position in between two nozzle inlets. The thermocouples were arranged at one angular and two radial positions. The total number of static pressure taps downstream of the preswirl nozzles was nine. Six pressure tappings were arranged in the preswirl chamber. Three of them were located around the exit plane of one nozzle, while the other three were placed at two different radii on the bisecting line of two neighboring nozzles. The outmost tapping was placed at two different angular positions. The remaining three pressure tappings were placed on the bisecting line at different radial positions inside the inner wheelspace.

For the temperature measurements, type K thermocouples were employed. The temperature was recorded with an uncertainty of ±1K. The pressure measurements were accomplished by means of a pressure transducer in combination with a Scanivalve system. The pressure was measured with an accuracy of 0.5 percent in the range of $0-5.17\times10^5$ Pa.

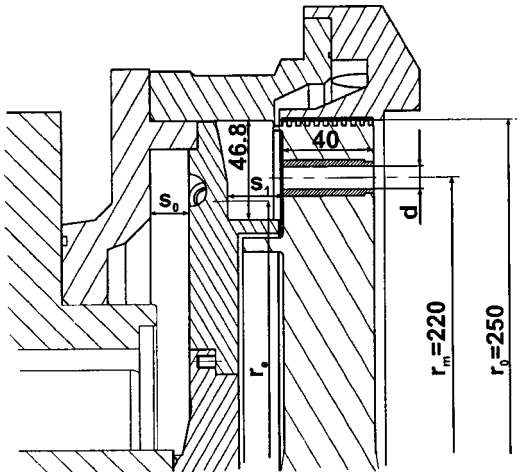

Fig. 2 Details of test section; dimensions in mm

Table 1 Geometric parameters; dimensions in mm

s_1	s_0	r_e	N_R	l/d	d
5	33.7	220.4	4	2.31	17.3
10	28.7	221.7	12	4.00	10.0
24	14.7	229.7	24	5.66	7.1

Definitions

In addition to all relevant temperatures and pressures, the characteristic absolute and relative velocities inside the preswirl system are sketched in Fig. 4. The arrows indicate the positive direction of the velocities in the absolute and relative frames of reference.

The total pressure p_{0t} and the total temperature T_{0t} are defined as the arithmetic average of the corresponding readings in front of the preswirl nozzles. The static pressure p_{1s} in the annulus is the mean average calculated from the six pressure tappings inside the preswirl chamber. Finally, p_{2s} was assumed to be equal to the ambient pressure measured downstream of the rig.

According to Zimmermann et al. [10], for investigations of the rotating part of rotor–stator systems, it is convenient to transfer the variables into the relative frame of reference. As the total properties of the air change with relative motion, total temperature and total pressure have to be transformed according to Eqs. (1) and (2)

$$\frac{T_{1t,\mathrm{rel}}}{T_{1t}}=1+\frac{u^2-2uc_t}{2c_pT_{1t}} \tag{1}$$

$$\frac{p_{1t,\mathrm{rel}}}{p_{1t}}=\left(1+\frac{u^2-2uc_t}{2c_pT_{1t}}\right)^{\kappa/(\kappa-1)} \tag{2}$$

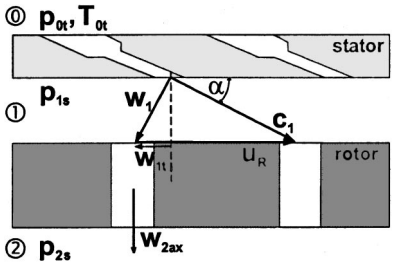

Fig. 4 Velocities in absolute and relative frames of reference

This transformation assumes that the cooling air attains solid body rotation before it leaves the receiver holes. Especially for relatively small l/d ratios of the receiver holes and a large relative tangential inlet velocity, this is unlikely to happen in the test rig. However, the resulting uncertainty in the total properties is estimated to be negligible for the receiver hole geometry and radial position chosen in this study. The total properties T_{1t} and p_{1t} as well as the velocity c_t in the preswirl chamber are calculated assuming isentropic flow through the preswirl nozzles and inside the preswirl chamber. Thus, these values equal T_{0t} and p_{0t}, respectively. Frictional effects inside the nozzles and inside the preswirl chamber as well as the interaction of the jet with the annulus flow are supposed to reduce c_t, but are difficult to quantify with the measuring techniques applied in this study. An iterative process might be used to calculate the polytropic nozzle exit velocity, but neither the mixing effects nor the frictional effects inside the preswirl chamber would be considered. An alternative would be to measure a representative velocity in the preswirl chamber. However, this can hardly be done for every test case. The accurate measurement of the total temperature T_{1t} and the total pressure p_{1t} inside the preswirl chamber is also difficult due to the turbulent three-dimensional unsteady flow structures existing in such systems.

The c_D value is defined as the ratio of the real mass flow rate to the ideal mass flow rate. While the discharge coefficient of the preswirl nozzles (Eq. (3)) is defined in the absolute frame of reference, the discharge coefficient for the receiver holes (Eq. (4)) is defined in the relative frame of reference. Neglecting the pressure losses and the frictional effects occurring upstream the receiver results in lower c_{DR} values. The assumption of a fully developed flow inside the receiver hole enhances or reduces the discharge coefficient of the receiver hole depending on the direction of the flow deflection in the hole.

A hypothetical discharge coefficient (Eq. (5)) can be used to describe the flow resistance of the receiver holes without considering the work done by the rotor [10]. In this definition, the real mass flow rate is compared to a ideal mass flow rate calculated for a free expansion to p_{2s}.

$$c_{DN}=\frac{\dot{m}}{\frac{A_N p_{0t}}{\sqrt{RT_{0t}}}\cdot\sqrt{\frac{2\kappa}{\kappa-1}\cdot\left(\left(\frac{p_{1s}}{p_{0t}}\right)^{2/\kappa}-\left(\frac{p_{1s}}{p_{0t}}\right)^{1+1/\kappa}\right)}} \tag{3}$$

$$c_{DR}=\frac{\dot{m}}{\frac{A_R p_{1t,\mathrm{rel}}}{\sqrt{RT_{1t,\mathrm{rel}}}}\cdot\sqrt{\frac{2\kappa}{\kappa-1}\cdot\left(\left(\frac{p_{2s}}{p_{1t,\mathrm{rel}}}\right)^{2/\kappa}-\left(\frac{p_{2s}}{p_{1t,\mathrm{rel}}}\right)^{1+1/\kappa}\right)}} \tag{4}$$

$$c_D=\frac{\dot{m}}{\frac{A_N p_{0t}}{\sqrt{RT_{0t}}}\cdot\sqrt{\frac{2\kappa}{\kappa-1}\cdot\left(\left(\frac{p_{2s}}{p_{0t}}\right)^{2/\kappa}-\left(\frac{p_{2s}}{p_{0t}}\right)^{1+1/\kappa}\right)}} \tag{5}$$

Results

Before the main investigation of the entire preswirl system started, its components, namely the preswirl nozzles and the receiver holes, were tested individually. After the discharge behavior for a free expansion through the preswirl nozzles was determined, the effect of the rotor on c_{DN} was investigated. With the preswirl plate not integrated in the rig, the discharge coefficient for rotating holes could be determined. These data can be compared with existing correlations to check the proper instrumentation of the rig.

Preswirl Nozzles. In order to determine the discharge behavior of the preswirl nozzles, the rotor disk was detached from the shaft. This simplified stationary system was also studied numerically and a CFD analysis was carried out for different pressure ratios p_{0t}/p_{1s} to predict the discharge coefficients. The commercial code TASCFLOW, incorporating the standard $k-\varepsilon$ turbulence model for a compressible flow, was used for the calculations. Figure 5 shows a comparison between the results obtained experimentally and numerically for the preswirl plate containing 12 nozzles and an axial distance to the casing $s_0=28.7$ mm. The discharge coefficient increases with the pressure ratio due to the compressibility effect [11]. With a deviation of less than 1 percent with respect to the experimental values, the experimental and numerical data show perfect agreement for the whole pressure ratio variation. In a subsequent experimental setup, the rotor was installed spinning at rather low speed ($n=60$ rpm) in order to investigate its effect on c_{DN}. As shown in Fig. 5, the presence of a slowly moving rotor disk obviously has little effect on the discharge behavior of the preswirl nozzles located upstream. For all three configurations with different numbers of radiused receiver holes, the maximum deviation is only 4 percent based on the setup without a rotor disk.

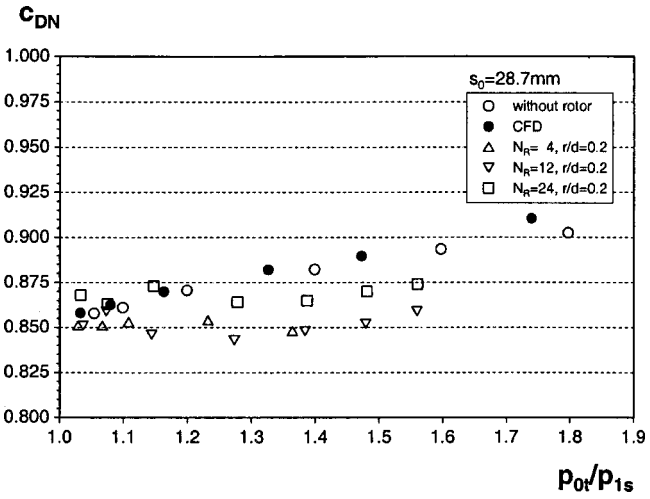

Fig. 5 Discharge coefficients for preswirl nozzles c_{DN}

Rotating Holes Without Preswirl. In order to separate the receiver holes from the entire system and to characterize the discharge behavior dependent on pressure ratio and disk circumferential velocity, the preswirl plate was detached from the rig. Similar investigations were performed earlier by Wittig et al. [6] using a different test rig. The experimental study was also assisted by

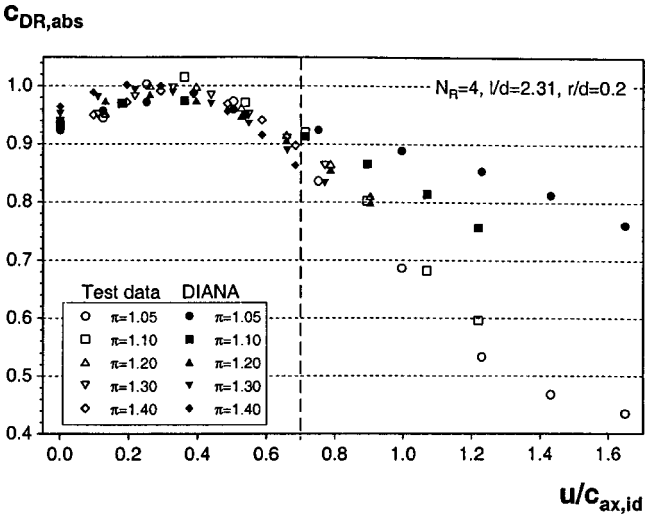

Fig. 6 $c_{DR,abs}$ without preswirl plate

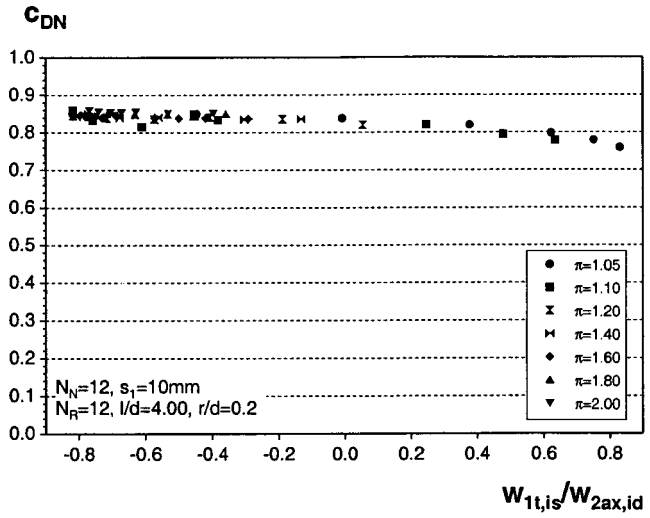

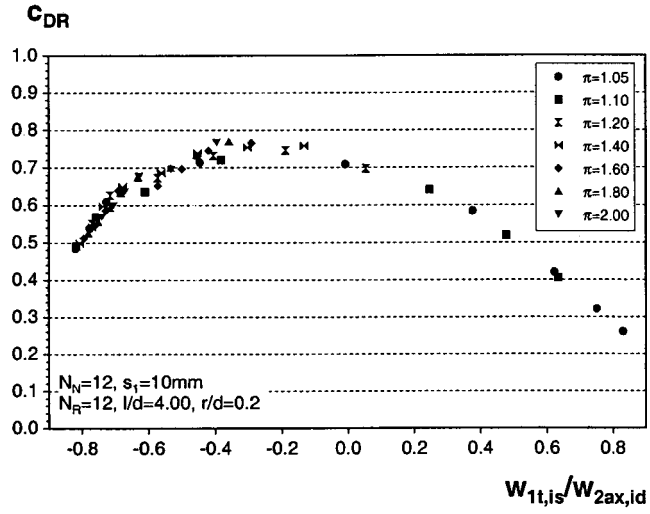

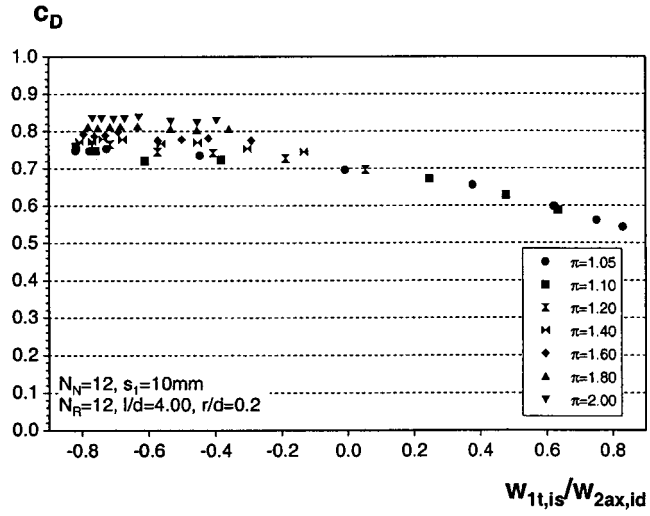

Fig. 7 Typical trends for c_{DN}, c_{DR}, and c_D

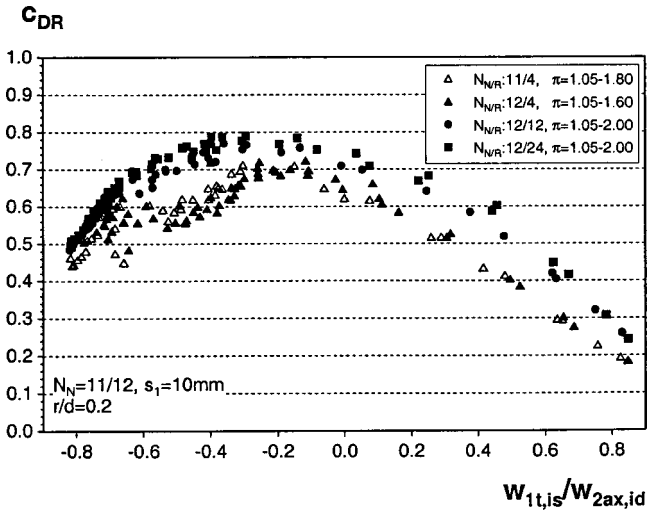

Fig. 8 Effect of N_R, l/d, and N_N

CFD work. The authors presented a correlation called DIANA, capable of predicting **Di**scharge coefficients **A**nd **N**usselt numbers for such an **A**ir system [6]. According to that correlation $c_{DR,\mathrm{abs}}$ was defined using the static pressure in front of the receiver hole. As the work term was not considered, values larger than unity were achieved. Although the geometries of both test rigs differ in respect to the pitch radius of the rotating holes and the inflow conditions, the new data fit very well within the validity range of the existing correlation, as shown in Fig. 6. However, it must be noticed that there is a considerable overprediction of $c_{DR,\mathrm{abs}}$ for $u/c_{\mathrm{ax,id}}>0.7$.

Preswirl System. For the investigation of the entire preswirl system, the number of preswirl nozzles N_N and the receiver holes N_R, the r/d ratio, the axial gap width s_1 between the stator and rotor, and the radial flow rate was varied for different rotating disk speeds and a wide range of overall pressure ratios $\pi=p_{0t}/p_{2s}$. All experimental tests were conducted at near adiabatic conditions.

Figure 7 shows typical trends for c_{DN} and c_D defined in the absolute frame of reference and for c_{DR} defined in the relative frame of reference. The discharge coefficients are plotted against the velocity ratio $w_{1t,\mathrm{is}}/w_{2\mathrm{ax,id}}$. Thereby, the tangential relative velocity $w_{1t,\mathrm{is}}$ is calculated assuming an isentropic expansion through the preswirl nozzle in the stationary system. $w_{2\mathrm{ax,id}}$ denotes the ideal axial velocity of the receiver flow in the relative frame of reference for an isentropic expansion from $p_{1t,\mathrm{rel}}$ to p_{2s}. To plot the c_{DR} value against $w_{1t,\mathrm{is}}/w_{2\mathrm{ax,id}}$ incorporates several advantages. The use of the velocity ratio $w_{1t,\mathrm{is}}/w_{2\mathrm{ax,id}}$ allows one to discuss the effects on c_{DR} resulting from over and underswirl, separately. In addition, $w_{1t,\mathrm{is}}/w_{2\mathrm{ax,id}}$ was found to equal unity if u approaches infinity. Vice versa, if the rotor were accelerated into the opposite direction of the preswirl jet, then the velocity ratio would be limited to $w_{1t,\mathrm{is}}/w_{2\mathrm{ax,id}}=1$. In addition, the discharge coefficient of the receiver holes c_{DR} equals zero for u approaching $\pm\infty$. With these two fixed points, extrapolations and correlations can be established that are more reliable.

The discharge coefficients for the preswirl nozzle c_{DN} show a linear behavior. Thereby, c_{DN} decreases with increasing rotor disk speed due to the increased momentum of the annulus flow. The discharge coefficient c_{DR} of the receiver hole is strongly dependent on the velocity ratio with a distinct maximum at $w_{1t,\mathrm{is}}/w_{2\mathrm{ax,id}}<0$. As the discharge coefficient should decrease with increasing flow angle, a symmetric progression of c_{DR} relative to $w_{1t,\mathrm{is}}/w_{2\mathrm{ax,id}}=0$ was expected. The position of the maximum at $w_{1t,\mathrm{is}}/w_{2\mathrm{ax,id}}<0$ can be explained by the definition of $w_{1t,is}$. As c_1 is determined for an isentropic expansion through the preswirl nozzle and neither mixing of the preswirl jet with the annulus flow nor frictional effects were taken into account, $w_{1t,\mathrm{is}}$ overpredicts the real inlet velocity for the receiver holes. Thus, perpendicular inflow into the rotating receiver holes occurs at smaller velocity ratios $w_{1t,\mathrm{is}}/w_{2\mathrm{ax,id}}$.

The hypothetical discharge coefficient c_D of the system decreases with increasing rotor speed and increases with the overall

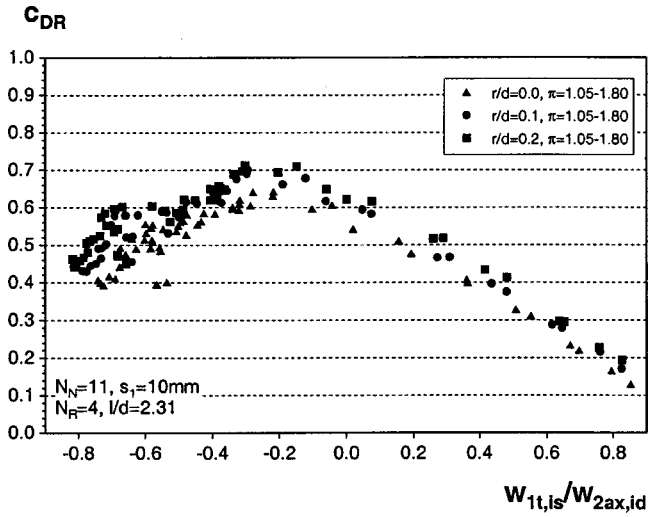

Fig. 9 Effect of r/d for $N_N=11$, $N_R=4$, and $s_1=10$ mm

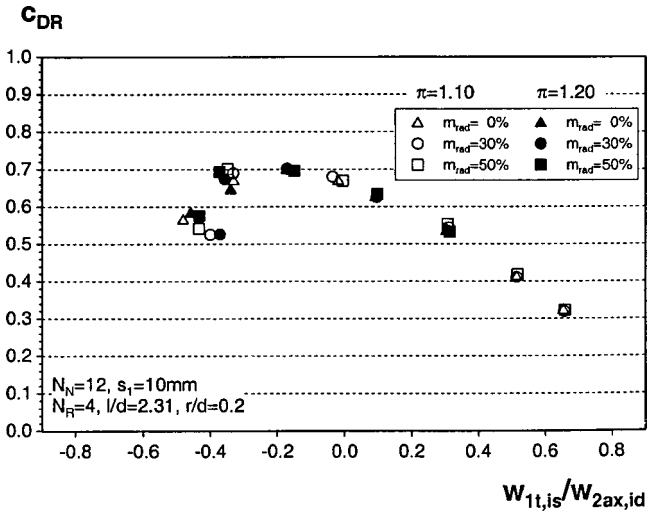

Fig. 11 Effect of a superposed radial outflow

pressure ratio. As the ideal mass flow rate (Eq. (5)) is constant at a specific overall pressure ratio, the graphs show the progression of the real mass flow rate, which was found to decrease with increasing rotor disk speed.

The number of receiver holes N_R and the l/d ratio were changed simultaneously due to the above-mentioned reasons. In Fig. 8, discharge coefficients of the receiver holes are given for different numbers of preswirl nozzles and receiver holes. For the setup with $N_N=12$, N_R was varied from 4 to 24. In addition, the number of preswirl nozzles was reduced to 11 for $N_R=4$. The discharge coefficient c_{DR} increases with the number of receiver holes although the l/d ratio exceeds 2.0. At $l/d>2.0$, frictional effects inside the hole should reduce c_{DR} according to McGreehan and Schotsch [5]. Therefore, it can be concluded that the number of receiver holes N_R seems to have a stronger impact on c_{DR} than the length-to-diameter ratio l/d.

The integral ratio of preswirl nozzles and receiver holes was chosen to facilitate numerical computations of such a complex system. In real engines such a symmetric configuration is always avoided to prevent periodic excitation. As a matter of fact, unstable flow occurred for a setup with 12 preswirl nozzles and 4 receiver holes, causing a severe decrease in c_{DR} in the range of $-0.7<w_{1t,is}/w_{2ax,id}<-0.3$. Therefore, the number of preswirl nozzles was reduced to 11 in a subsequent setup. Nevertheless, the flow stayed unsteady in the same range of $w_{1t,is}/w_{2ax,id}$, as shown in Fig. 8. Samoilovich and Morozov [3] observed a similar decrease in the discharge coefficient for a setup with fewer than six rotating holes. To be able to predict the occurrence of unstable flow, depending on the system geometry and the operating conditions, a more profound experimental investigation is necessary. A possible approach would also incorporate a more advanced data acquisition system, employing pressure transducers with a high-frequency response at several locations inside the rig. As a single pressure transducer in combination with a Scanivalve unit was used in the present setup, only time-averaged pressures could be measured. Study of the building mechanisms of the observed flow instabilities therefore was not within the realms of possibility.

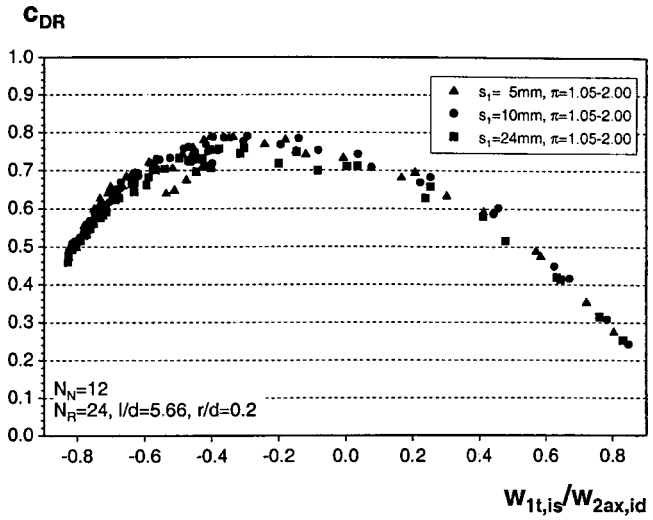

Fig. 10 Effect of s_1 for $N_N=12$, $N_R=24$, and $r/d=0.2$

Additional tests were run with 11 preswirl nozzles, 4 receiver holes, and an axial gap width of $s_1=10$ mm to find the influence of the inlet geometry of the receiver holes. The r/d ratio was varied from 0.0 to 0.2. As shown in Fig. 9, a radius at the inlet of the receiver hole enhanced the discharge coefficient c_{DR}.

The results obtained for a variation of the axial distance s_1 between the stator and rotor are shown in Fig. 10. For $N_R=24$ receiver holes, a variation of s_1 does not significantly influence the discharge coefficient c_{DR}. It can further be seen in Fig. 10 that unstable flow occurred for the smallest gap width $s_1=5$ mm in the vicinity of $w_{1t,is}/w_{2ax,id}=-0.5$.

In addition to the geometric variations, the flow pattern was changed by superimposing a radial outflow to the swirled main-flow. Thereby, the radial outflow was set to 30 and 50 percent of the original main mass flow rate, while the overall total pressure ratio was kept constant. According to Fig. 11, a radial outflow of coolant scarcely influences the discharge behavior of the receiver holes for the whole range of velocity ratios. A slight scatter of c_{DR} can be observed for $w_{1t,is}/w_{2ax,id}<-0.2$. However, in this particular region it is difficult to detect a definite trend.

Conclusions

The discharge behavior of a preswirl system and its main components were investigated experimentally. The discharge coefficients of the preswirl nozzles were determined in a simplified static setup without rotor. Experimental and numerical data show perfect agreement for different pressure ratios. The influence of a rotor spinning at rather low speed ($n=60$ rpm) on c_{DN} can be neglected. With increasing rotor speed, however, the discharge coefficient of the preswirl nozzles is slightly reduced. The discharge coefficients of the receiver holes in a setup without preswirl plate were compared with an existing correlation. Although

the geometries involved in both studies were different, good agreement was obtained within the range of validity. However, the data obtained in this study are severely overpredicted if the correlation is used out of its specified range. The discharge coefficients of the receiver holes c_{DR} were defined in the relative frame of reference taking into account the work that is required (or gained) if the fluid is brought up (or down) to disk speed. Thereby, c_{DR} was plotted against the velocity ratio $w_{1t,\mathrm{is}}/w_{2\mathrm{ax,id}}$, which estimates the flow angle relative to the receiver hole. The discharge behavior of the receiver holes was found to be strongly dependant on this ratio. The number of receiver holes N_R turned out to have a stronger impact on c_{DR} than the l/d ratio. A fillet radius at the receiver hole inlet improves the discharge behavior while the distance between the stator and rotor s_1 has no significant influence on c_{DR}. The occurrence of unstable flow, leading to a decrease of c_{DR} seemed to be more probable for small s_1 and small numbers of receiver holes. A radial outflow of coolant scarcely influences the discharge behavior of the receiver holes. Since neither the total temperature nor the total pressure in front of the receiver hole can be precisely measured owing to the existing complex flow structure, they had to be calculated assuming isentropic expansion through the nozzles. Friction on the stator walls and mixing of the preswirl jet with the annulus flow are believed actually to elevate the relative total temperature and to reduce the total pressure. As these effects are neglected by the theoretical approach, it also follows that $w_{1t,\mathrm{is}}$ overpredicts the real circumferential velocity relative to the rotor. This puts an error on the ''work term'' and finally on c_{DR}. As the discharge coefficient simply describes the ratio between real and ideal mass flow rate, it sums up the existing individual losses. Separating the loss mechanisms and quantifying their effects is worthwhile and would help to gain a more detailed physical understanding. The apparent lack of experimental data gives scope for future investigations.

Acknowledgments

The authors wish to thank the ''Forschungsvereinigung Verbrennungskraftmaschinen e.V.'' for supporting the work described in this paper. The work was also partly funded by the EU.

Nomenclature

A = cross-sectional area, m^2
c = velocity in absolute frame of reference, m/s
c_D = discharge coefficient
c_p = specific heat, J/(kg K)
d = diameter of receiver holes, m
l = length of receiver holes, m
$\dot{m}$ = mass flow rate, kg/s
n = revolutions per min, 1/min
N = number of holes
p = pressure, N/m^2
r = radius, m
r_0 = outer radius of rotor, m
r_e = pitch radius of preswirl nozzle exit, m
r_m = pitch radius of receiver holes, m
R = specific gas constant, J/(kg K)
Re = Reynolds number defined for preswirl nozzles $=cd_N/\nu$
Re_ϕ = rotational Reynolds number$=\omega r_m^2/\nu$
s = axial gap, m
T = temperature, K
u = circumferential velocity, m/s
w = velocity in relative frame of reference, m/s
α = inclination of preswirl nozzles, deg
κ = isentropic exponent
ν = kinematic viscosity, m^2/s
π = total pressure ratio$=p_{0t}/p_{2s}$
ω = angular velocity of rotor, 1/s

Subscripts

abs = absolute system
ax = axial
is = isentropic
id = ideal
N = preswirl nozzle
rad = radial
rel = relative system
R = receiver hole
s = static
t = total, tangential
0, 1, 2 = stages 0, 1, 2

References

[1] Scricca, J. A., and Moore, K. D., 1997, ''Effects of 'Cooled' Cooling Air on Pre-Swirl Nozzle Design,'' Tech. Rep. NASA/CP-98-208527, Pratt & Whitney, Oct.
[2] Meierhofer, B., and Franklin, C. J., 1981, ''An Investigation of a Preswirled Cooling Airflow to a Turbine Disc by Measuring the Air Temperature in the Rotating Channels,'' ASME Paper No. 81-GT-132.
[3] Samoilovich, G. S., and Morozov, B. I., 1957, ''Coefficients of Flow Through Pressure Equalizing Holes in Turbine Discs,'' Teploenergetica, **8**, pp. 16–23.
[4] Meyfarth, P. F., and Shine, A. J., 1965, ''Experimental Study of Flow Through Moving Orifices,'' ASME J. Basic Eng., **87**, pp. 1082–1083.
[5] McGreehan, W. F., and Schotsch, M. J., 1988, ''Flow Characteristics of Long Orifices With Rotation and Corner Radiusing,'' ASME J. Turbomach., **110**, pp. 213–217.
[6] Wittig, S., Kim, S., Scherer, T., Jakoby, R., and Weissert, I., 1995, ''Durchfluß an rotierenden Wellen und Scheibenbohrungen und Wärmeübergang an rotierenden Wellen,'' Forschungsvereinigung Verbrennungskraftmaschinen (FVV), Abschlußbericht, Vorhaben No. 465 and 536, Heft 574.
[7] El-Oun, Z. B., and Owen, J. M., 1988, ''Pre-Swirl Blade-Cooling Effectiveness in an Adiabatic Rotor–Stator System,'' ASME J. Turbomach., **111**, pp. 522–529.
[8] Wilson, M., Pilbrow, R., and Owen, J. M., 1997, ''Flow and Heat Transfer in a Pre-Swirl Rotor–Stator System,'' ASME J. Turbomach., **119**, pp. 364–373.
[9] Popp, O., Zimmermann, H., and Kutz, J., 1998, ''CFD Analysis of Coverplate Receiver Flow,'' ASME J. Turbomach., **120**, pp. 43–49.
[10] Zimmermann, H., Kutz, J., and Fischer, R., 1998, ''Air System Correlations: Part 2—Rotating Holes and Two Phase Flow,'' ASME Paper No. 98-GT-207.
[11] Bragg, S. L., 1960, ''Effect of Compressibility on the Discharge Coefficient of Orifices and Convergent Nozzles,'' J. Mech. Eng. Sci., **2**, No. 1, pp. 35–44.

Approach to Unidirectional Coupled CFD–FEM Analysis of Axial Turbocharger Turbine Blades

D. Filsinger

J. Szwedowicz

O. Schäfer

R & D Turbochargers,
ABB Turbo Systems Ltd.,
5401 Baden, Switzerland

This paper describes an approach to unidirectional coupled CFD–FEM analysis developed at ABB Turbo Systems Ltd. Results of numerical investigations concerning the vibration behavior of an axial turbocharger turbine are presented. To predict the excitation forces acting on the rotating blades, the time-resolved two-dimensional coupled stator–rotor flow field of the turbine stage was calculated. The unsteady pressure, imposed on the airfoil contour, leads to circumferentially nonuniform and pulsating excitation forces acting on the rotating bladed disk. A harmonic transformation of the excitation forces into the rotating coordinate system of a single blade was elaborated and the complex Fourier amplitudes were determined. The bladed rotor was modeled by a single symmetric segment with complex circumferential boundary conditions. With respect to different nodal diameter numbers, free vibration analyses of the disk assembly were then effectively performed. For calculated resonance conditions, the steady-state responses of the turbocharger bladed disk were computed. By using this coupled CFD–FEM analysis, the dynamic loading of the turbine blades can be determined in the design process.
[DOI: 10.1115/1.1415035]

Introduction

High cycle fatigue of rotating turbine components is a serious problem, causing substantial damage and high maintenance effort. Highly loaded compressor or turbine blades are damaged by alternating stresses resulting from the excitation forces. To improve the component reliability, this important technical aspect has initiated intensive research programs [1]. An understanding of the fluid–structure interaction is essential because excitation is mainly induced by the fluid flow. Phenomena like stator wakes, flutter, rotating stall, as well as acoustic resonance are numerically and experimentally under investigation [2–8], but the link between fluid dynamics and structural mechanics is still not well established. Numerical tools can help to close this gap, but there are only a few reports [9,10] describing the complete procedure, beginning with the flow evaluation and stepping on to the calculation of the resulting loading of the turbine blades.

Turbine blades of axial turbochargers operating with variable speed are exposed to extreme unsteady dynamic forces. These forces are caused by the stroke and the charging system of the engine, the gas inlet, and the nozzle guide vanes. In general, lack of experimental and numerical data does not allow the definition of the exciting forces required in the design process. Therefore, in current design procedures, the reliability of the already manufactured blade can only be proved experimentally for instance by applying expensive strain gauge measurements.

A research program, initiated at ABB Turbo Systems Ltd. in Switzerland, intends to support the expensive experimental work with numerical tools. In analogy to Srinivasan's [11] statement, progress could be achieved by close collaboration among experts in computational fluid dynamics (CFD), Finite Element methods (FEM), turbine design, and charging systems. This paper presents an approach to unidirectional coupled CFD–FEM analysis of axial turbocharger turbine blades.

Contributed by the International Gas Turbine Institute and presented at the 46th International Gas Turbine and Aeroengine Congress and Exhibition, New Orleans, Louisiana, June 4–7, 2001. Manuscript received by the International Gas Turbine Institute February 2001. Paper No. 2001-GT-288. Review Chair: R. Natole.

Numerical Procedure

The final goal of the research program is the calculation of dynamic stresses σ in rotating blades exposed to unsteady aerodynamic forces. This ambitious task requires reliable numerical tools. Firstly, the transient flow behavior in the turbine cascade has to be simulated requiring time-dependent pressure and temperature inlet boundary conditions. Finally, forced blade responses u have to be computed due to the pulsating pressure distribution $p(t)$ obtained from CFD analysis (Fig. 1). The coupling between these two numerical methods is achieved by a Fourier decomposition (amplitude P_k, phase delay β_k) of the time resolved excitation forces $F(t)$ acting on the rotating bladed disk. Figure 1 illustrates the unidirectional coupled procedure. Emphasis was on the issue not to exceed industrial standards for the turnaround time of a complete calculation cycle. Also the required computational memory and time had to be kept in mind and, therefore, some simplifications had to be accepted. Features of the applied numerical tools and assumed simplifications are described in the following.

Computational Fluid Dynamics. The program system developed in-house was already adjusted to the prediction of unsteady

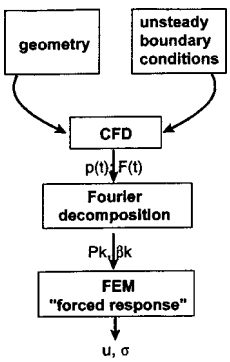

Fig. 1 Unidirectional coupled numerical procedure

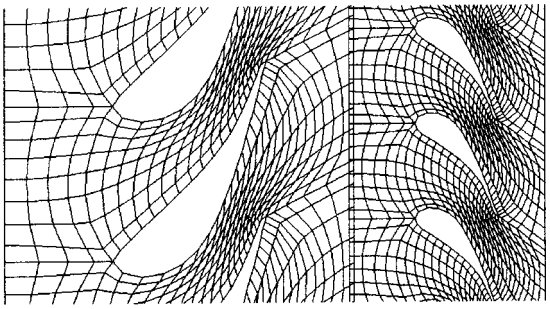

Fig. 2 Example of CFD grid

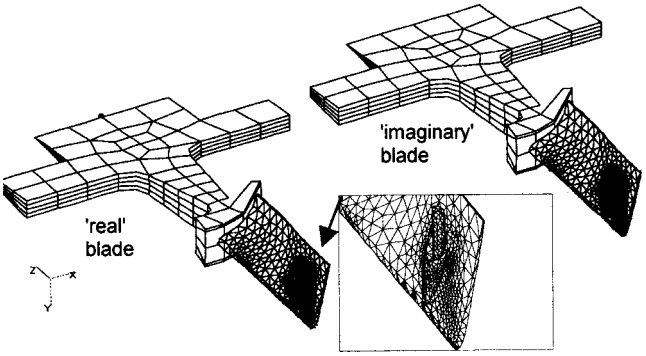

Fig. 3 Identical meshes to define complex bladed disk oscillations in the real domain

aerodynamic forces in pulse charged turbines of turbochargers [12]. It is based on a two-dimensional time accurate multiblock Euler/Navier–Stokes solver. The integrated postprocessing offers a close link to mechanical integrity codes by the determination of the blade forces. The calculations are done in the absolute frame of reference, using a moving grid for the rotor. At the intersection between the stator and the rotor grid, the cells have to overlap, and the so-called CHIMERA Interpolation is used [13]. The number of channels in the stage is between 60 and 70. For a fully three-dimensional simulation of the transient flow field, the amount of computational time and computer memory would be far beyond the capacity of standard computers used in design departments. Therefore, a simplified model was applied, based on two-dimensional Euler equations. These equations are valid for straight inviscid cascade flows and sufficient for the flow simulation on a circumferential stream plane of a chosen radius with constant radial thickness. Assuming thin boundary layers, the influence of friction and heat transfer are negligible and coarse computational grids could be used for the two-dimensional simulation without loss in accuracy. Figure 2 shows an example with only 29×9 grid points per block. A more detailed explanation of the CFD tool can be found in Schäfer [14].

Boundary Conditions. The unsteady inlet boundary conditions were determined by using the simulation system, SiSy, which was developed at ABB Turbo Systems, Ltd., by Bulaty et al. [15]. This code simulates Diesel engine behavior with respect to the exhaust pipe system and the turbocharger performance. The SiSy system fulfills the following requirements: (1) optimization of gas exchange processes, (2) simulation of engine performance under different ambient conditions, (3) analysis of the influence of turbocharger specifications, (4) comparison of different turbocharging systems, and (5) parameter studies for load acceptance. In the scope of the ''coupled CFD–FEM analysis'', the SiSy program delivers the transient total pressure and temperature at the inlet of the turbocharger turbine in terms of the operating conditions. Total temperature and pressure are highly unsteady due to the pressure pulses in the exhaust system of an alternating combustion engine (compare Fig. 6).

Finite Element Method: Dynamic Analysis. At ABB Turbo Systems, Ltd., the ABAQUS finite element code is already intensively used for structural and dynamic analyses. Valuable experience is available and, therefore, the ABAQUS program was integrated into the design procedure.

Disk assemblies containing N turbine blades coupled circumferentially through the elastic rotor and an optional lacing wire had to be analyzed. Blade mistuning effects (slight differences in geometry and/or in the damping properties among blades [16]) were neglected in the performed analyses. Under these conditions the disk assembly is a rotationally periodic structure of N identical blades and the cyclic wave theory could be applied. Thus, the static and dynamic deformations of the whole disk could be represented by a single blade with complex circumferential boundary conditions.

Free Vibration Computation. Neglecting dissipation effects, the harmonic free vibration of the single coupled blade is given by the complex matrix equation

$$\lfloor M(e^{jn\varphi})\rfloor\{\ddot{q}\}+\lfloor K(e^{jn\varphi},\Omega)\rfloor\{q\}=\{0\},\quad j=\sqrt{-1} \tag{1}$$

where $\varphi=2\pi/N$ is the circumferential periodicity angle of the disc sector and the nodal diameter number n varies according to

$$n=0,1,2,\ldots\begin{cases}N/2 & \text{for } N \text{ even}\\ (N-1)/2 & \text{for } N \text{ odd}\end{cases} \tag{2}$$

In Eq. (1), $[M(e^{jn\varphi})]$ and $[K(e^{jn\varphi},\Omega)]$ represent the blade mass and nonlinear stiffness matrices with respect to the rotational speed Ω Both complex matrices depend on the nodal diameter number n. The complex vectors $\{q\}$ and $\{\ddot{q}\}$ describe the nodal displacement and the acceleration of the blade vibration. Between nodes located on the right and left circumferential sector sides, cyclic kinematic constraints are imposed as

$$\{q\}_{\text{right}}=\{q\}_{\text{left}}e^{jn\varphi} \tag{3}$$

$$\{\ddot{q}\}_{\text{right}}=\{\ddot{q}\}_{\text{left}}e^{jn\varphi} \tag{4}$$

Rewriting the Euler function in trigonometric notation, eigenfrequencies of the cyclic finite element system can be computed in the real domain. Consequently, the cyclic model has to be represented by two identical finite element meshes (Fig. 3), whose nodal boundaries on the circumferential sector sides are constrained as shown in Eqs. (3) and (4). For each mode i and nodal diameter n (besides $n=0$ and $n=N/2$), two identical eigenfrequencies are computed, which refer to two possible orthogonal mode shapes of the disk assembly.

Static Calculation. By substituting n equal to 0 into Eq. (1) and Eqs. (3) and (4) as well as omitting the inertial term of Eq. (1), the static equation of the disk assembly rotating with the angular speed Ω is obtained in the following form:

$$[K(\Omega)]\{q\}=\{P_o\}+\{T\}+\{F(\Omega)\} \tag{5}$$

where $\{P_o\}$, $\{T\}$, and $\{F(\Omega)\}$ are stationary gas pressure (obtained from CFD), thermal loads (obtained from thermal FE simulation), and centrifugal forces, respectively. In turbocharger blisks the blades can be circumferentially coupled by a lacing wire, as shown in Fig. 3. In this case, an effective contact area between the airfoil and lacing wire is obtained from a nonlinear static computation by using contact elements [17]. In the free vibration analyses, the nodes located on the computed contact area are fixed rigidly to each other as demonstrated by Szwedowicz [18]. Finally, for the considered rotational speed Ω, the eigenfrequencies of the bladed disk can be computed.

Damping Properties of Turbocharger Disks. Gust-response and motion-dependent unsteady aerodynamics assure improve-

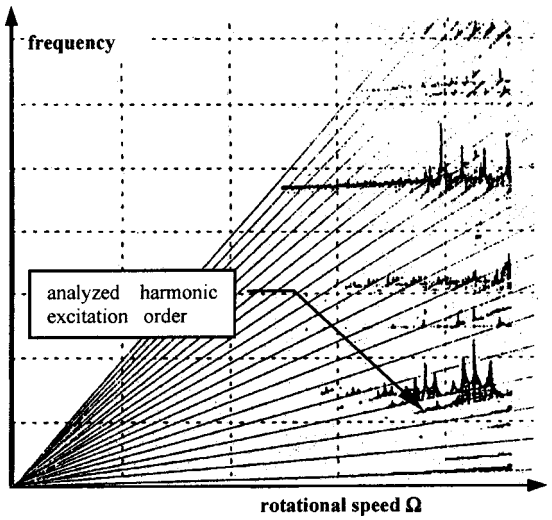

Fig. 4 Measured Campbell diagram of turbocharger disk with lacing wire in service

ments for calculations of aero-damping [19]. But their reliability is restricted due to hardware limitations and an excessive need of computational time.

For the numerical analyses, the total blade damping (material, micro-frictional, and aero-damping) was evaluated from measured resonance peaks. Vibrations of disk assemblies with (Fig. 4) and without lacing wire were measured under service conditions. With the help of the fractional-power bandwidth method [20], the magnitudes of the damping ratios were evaluated from the resonance peaks. The values obtained by means of fraction of the critical damping were in the range of between 0.15 and 0.4 percent.

CFD–FEM Coupling

Even for simplified models of disk assemblies, a time-marching structural finite element simulation of the bladed disk response is ineffective because of the need of the excessive computational time. Hence, the finite element calculations were performed in the frequency domain as mentioned before.

From CFD simulations (Fig. 1), the time-dependent two-dimensional pressure distribution on the blade midsection is obtained. To realize a quite simple first approach, a single excitation force, split into axial and circumferential direction, is calculated from the pressure distribution assuming a uniform radial distribution along the blade height. This force, acting on the center of gravity of the blade midsection, represents the blade stimulation in the forced response analyses. This simplification is acceptable since in the scope of this project, there is major interest in vibrations caused by the pressure pulses of the diesel engine exhaust system, which mainly excite low, simple bending blade modes [21].

Forced Response Analysis. In general, forced vibrations of a single coupled blade can be expressed in the Cartesian system by

$$\lfloor M(e^{jm\varphi})\rfloor\{\ddot{q}\}+[D]\{\dot{q}\}+\lfloor K(e^{jm\varphi},\Omega)\rfloor\{q\}=\{P\} \qquad (6)$$

where the damping matrix $[D]$ is determined by the Rayleigh dissipation model as a linear combination of the mass and stiffness matrices. The generalized vector $\{P\}$ describes the nonuniform pressure distribution along the circumference. For a blade rotating with the constant angular speed Ω, the pressure P is a periodic excitation function with the period of $\tau=2\pi/\Omega$. After applying the computed eigenfrequencies $\omega_{i,n}$ and mode shapes $\phi_{i,n}$ (see Eq. (1)), the steady state response of the disk rotating with constant angular speed Ω is given for each nodal diameter n in the rotating frame of reference as

$$m_{i,n}\ddot{u}_{i,n}+2\omega_{i,n}\xi_i\dot{u}_{i,n}+k_{i,n}u_{i,n}=\{\phi\}^{*T}_{i,n}\{P_k\}e^{j(k\alpha_l-\beta_k)}e^{jk\Omega t} \qquad (7)$$

[22] where $k=1,2,\ldots,\infty$ describes the engine order, $i=1,2,3$ indicates the number of the considered mode shapes, α_l denotes the circumferential position of the excited node of the cyclic finite element model (Figs. 3 and 11). In Eq. (7), $m_{i,n}=\{\phi\}^{*T}_{i,n}[M(e^{jn\varphi})]\{\phi\}_{i,n}$ and $k_{i,n}=\{\phi\}^{*T}_{i,n}[K(e^{jn\varphi})]\{\phi\}_{i,n}$ are the modal mass and modal stiffness of the cyclic FE model, respectively, (Fig. 3), and $\{\phi\}^{*T}_{i,n}$ is the conjugate transposed vector of the disk eigenform $\phi_{i,n}$. The nodal circumferential position α_l is determined from Cartesian coordinates of the excited node l. For each nodal diameter n, constant either minimum or maximum values of the damping ratio ξ_i evaluated from the experimental resonance curves (see Fig. 4) are only taken into account in Eq. (7). Therefore, the global damping matrix $[D]$ in the space-time differential Eq. (6) can be simplified by $2\omega_{i,n}\xi_i$ in the modal dynamic Eq. (7) of the cyclic FE blade model shown in Fig. 3.

Amplitudes P_k and phase delay β_k are obtained from the Fourier decomposition of the nonuniform pressure P. For the applied twin FE models (Fig. 3), excitation loads of each engine order k have to be imposed simultaneously on node l of the real and imaginary blade as shown by Szwedowicz [22]

$$F^{(\mathrm{real})}_{l,\chi}=P_{k,\chi}[\cos(k\alpha_l-\beta_{k,\chi})+j\,\sin(k\alpha_l-\beta_{k,\chi})] \qquad (8.1)$$

$$F^{(\mathrm{imag})}_{l,\chi}=P_{k,\chi}[\sin(k\alpha_l-\beta_{k,\chi})-j\,\cos(k\alpha_l-\beta_{k,\chi})] \qquad (8.2)$$

where χ refers either to the circumferential or the axial direction.

Due to the orthogonality condition between the disk mode $\phi_{i,n}$ and the circumferential pressure distribution P_k in Eq. (7), the disk assembly oscillating with nodal diameter number n is in resonance, if the excitation order k is equal to $\kappa\cdot N\mp n$ or $\kappa\cdot(N+2)\mp n$ where $\kappa=0,1,\ldots\infty$ for the even or odd number of the blades N of the turbine rotor [22].

Transformation of the Calculated Blade Forces Into the Rotating Blade System. For the analyzed pulse charged turbocharger, excitation amplitude $\{P_k\}$ in Eq. (7) varies in the time domain. For the forced response calculation, the excitation has to be transformed into the frequency domain. This is achieved by use of an ordinary Fourier decomposition. In this content, it is important not only to keep an eye on the amplitude (Fourier coefficients) but also on the phase relationship, which seems to be more uncertain to calculate [23], but influences the magnitude of the loading considerably.

It also has to be stated that the sampling interval of the time-resolved CFD plays an important role for the quality of the results [21]. Depending on the expected frequency contents and the desired resolution, the sampling interval was chosen according to the Nyquist sampling theorem given in Newland [24].

Results

With the help of these numerical tools, different turbine configurations under a variety of operating conditions were analyzed. This paper gives a summary of two loading cases of the turbine disk with the lacing wire. The first one was a turbine stage under constant pressure loading. The second example demonstrates the loading of a turbocharger turbine under pulse charging engine conditions. The numerical results were compared to experimental data as far as available.

Constant Pressure. For a first assessment of the CFD-calculations, three different turbine stages under full admission were analyzed. The output power P_T of the stages was calculated by means of the tangential blade forces F_1 multiplied with the rotational speed of the turbine n_{TC}, the Euler radius r, and the number of turbine blades N

$$P_T=2\cdot\pi\cdot n_{TC}\cdot r\cdot N\cdot F_t \qquad (9)$$

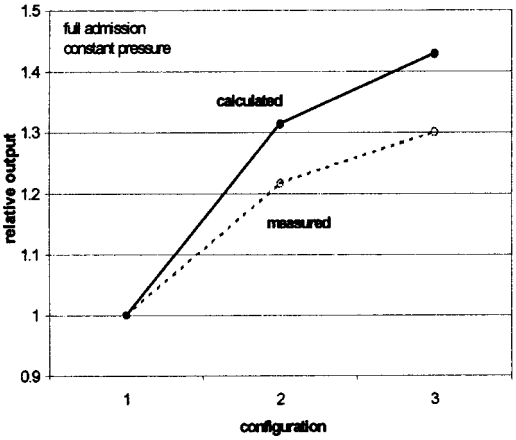

Fig. 5 Comparison of relative change in output power for different turbine configurations

The numerical results were compared to the measured values obtained from thermodynamic experiments. The relative difference is illustrated in Fig. 5. All values are related to the results for configuration 1. As expected, the calculated output power is higher than the corresponding measured values since the pressure distribution on the blade surface was calculated only for the midsection and was assumed to be constant along the total blade height. The difference between calculated and measured data for these calculations is maximal up to 10 percent, due to the applied simple Euler calculations.

Also, mass flow rates and the output power calculated from thermodynamic data are in a good agreement with the experimental results. This indicates that the CFD code is able to predict the flow fields for different turbine setups.

Pulse Charging. For this case, real engine conditions were modeled assuming a three-pulse charged six-cylinder diesel engine. This led to model an inlet casing with two separated gas inlets. Therefore, the inlet was divided along the circumferential direction into two parts. Each inlet segment was connected to an individual exhaust pipe serving three cylinders. Heavy pressure pulses from the exhaust system are directly led to the turbocharger turbine. This results in significant differences between the admissions of the two inlet segments and therefore high dynamic loads acting on the turbine blades had to be expected. Thus, the described test case is a good example to demonstrate the capability of the coupled CFD–FEM analysis.

Boundary Conditions. The unsteady inlet boundary conditions for the CFD analysis, namely the total pressure p and total temperature T, were obtained by the use of the SiSy code modeling the Diesel engine behavior with respect to the pipe system. The values for each of the two segments are displayed in Fig. 6. The six pulses of the cylinders (three per segment) can clearly be seen. With respect to the time, very high differences of the inflow

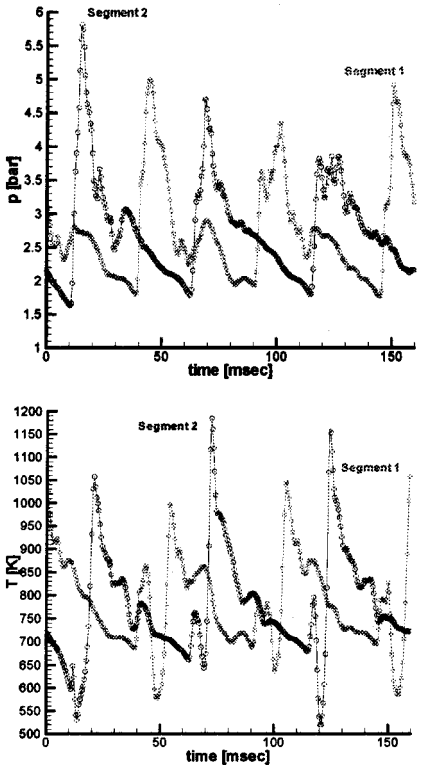

Fig. 6 Unsteady pressure p (upper) and temperature T (lower diagram) inlet boundary conditions

boundary conditions exist at the two separate gas inlets. The boundary conditions at the outlet were set to ambient conditions.

Blade Forces. The CFD calculation reveals snapshots of the unsteady pressure field of the turbine stage for each time step. An arbitrary example can be seen in the upper part of Fig. 7, which illustrates the significant difference in pressure distribution at turbine inlet and the pressure decrease over the stage. From the pressure distribution the pulsating forces acting on the rotating blade were calculated.

As mentioned before, only one single resulting force represents the loading on each blade. Figure 8 shows the calculated forces for a complete engine cycle, which equals two revolutions of the four-stroke diesel engine. In the graph, the forcing function is related to the time averaged value. Six pulses are detected and it can be stated that the blades are subjected to extreme dynamic loads. The turbocharger revolution can also be recognized, and in the lower part of Fig. 8 one turbocharger revolution is shown in detail. For reasons of clarity, the qualitative loading of the turbine blades during one revolution is also illustrated in the lower part of Fig. 7. The strong differences between the two segments and the influence of the turbine nozzles can be detected.

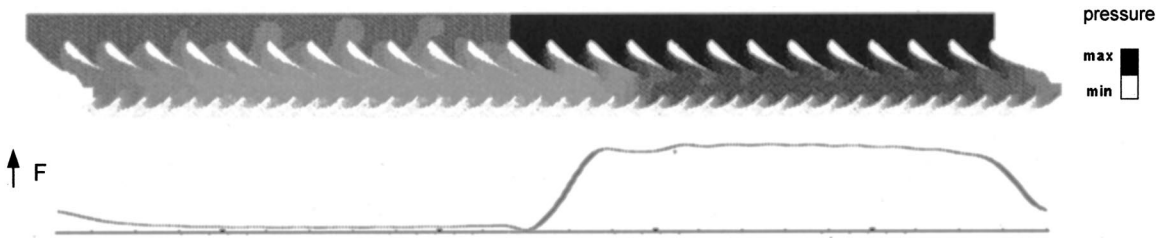

Fig. 7 Pressure distribution in the midsection of the turbine stage for a single time step (upper plot) and qualitative loading of the turbine blades (lower diagram)

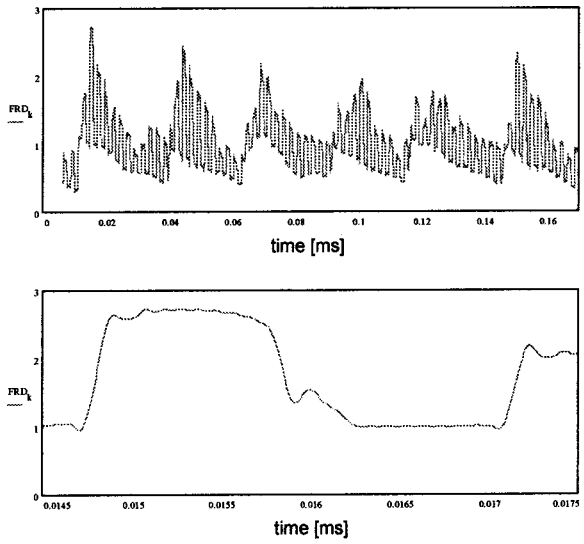

Fig. 8 Resulting blade force versus time

Figure 9 displays the power spectrum of the Fourier decomposition for the forces acting on the blade. The high values at frequencies below the first turbocharger order result from the charging system. Their frequencies are characterized by multiples of the speed of the Diesel engine n_{DE}. Further peaks are detected for multiples of the turbocharger rotation n_{TC}. Even turbocharger orders k are directly identified (see $k=2,4,6,\ldots$ in Fig. 9), because maximal peaks refer to the frequency $k\cdot n_{TC}$ as it is illustrated for the sixth engine order in the lower part of Fig. 9. For uneven turbocharger orders k (see $k=1,3,5,\ldots$ in Fig. 9), the highest peaks correspond to two particular frequencies $k\cdot n_{TC}-m\cdot n_{DE}$ and $k\cdot n_{TC}+m\cdot n_{DE}$ where m denotes the pulsation order ($m=1,2,\ldots$).

For each turbocharger order k, the excitation spectrum $k\cdot n_{TC}\pm m\cdot n_{DE}$ is obtained from the Fourier decomposition of the CFD results. An example for the sixth turbocharger order is shown in

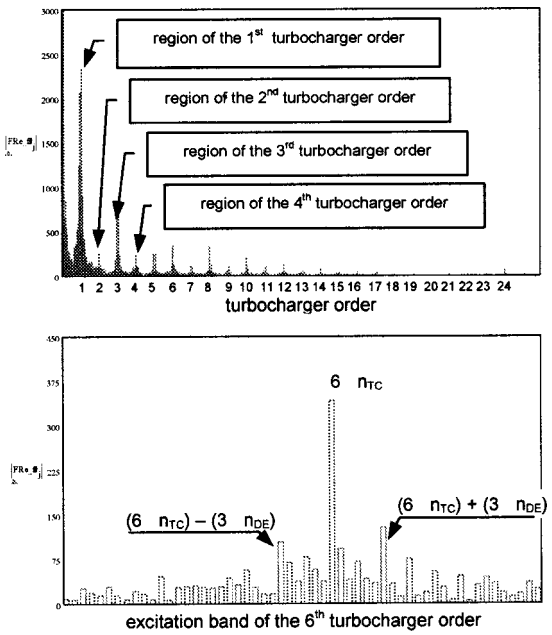

Fig. 9 Power excitation spectrum of the blade rotating with speed n_{TC}; upper diagram: full spectrum, lower diagram: zoomed spectrum for the sixth engine order

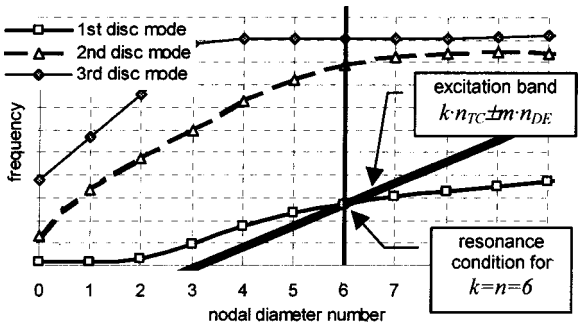

Fig. 10 Nodal diameter diagram of the bladed disk rotating with constant speed $n_{TC}=\Omega$ (compare Eq. (7))

the lower part of Fig. 9. For this particular excitation order, the unsteady excitation amplitude is about 3 percent of the steady load. These data compose the excitation input for the forced finite element response calculation.

Forced Response Calculations. Initially eigenfrequencies of the turbocharger assembly with respect to the different nodal diameter numbers n, characterizing the disk mode shapes, were calculated. As mentioned before, resonance can occur if the excitation order k is equal to the nodal diameter number n. Intersections between the calculated excitation bands and eigenfrequencies, which define possible resonance conditions, are found with the help of the well-known Campbell diagram (compare Fig. 4) in combination with the nodal diameter diagram given in Fig. 10. As an illustrative example, the sixth engine order was chosen to perform the FEM calculations.

In the CFD simulation, the rotor speed was adjusted to coincide with resonance of the first blade mode in the sixth engine order (compare Fig. 10). Using the ABAQUS finite element code, the forced response analysis was performed according to the excitation band of the sixth engine order shown in Fig. 9 (lower diagram). A constant equivalent damping ratio $\xi_{i=1}$ of 0.2 percent was assumed. As mentioned before, this value includes the energy dissipation effects of the vibrating blade caused by material, frictional, and aerodynamic damping (see Fig. 4). Considering only material damping, which can be obtained with the help of a hammer test, the value would be below 0.02 percent.

In the steady-state FE analysis, only the first blade mode was included, because the excitation spectra, which induce vibrations of the second and third blade modes (turbocharger orders above 12 in the upper diagram in Fig. 9), are much smaller in comparison to the spectrum of the sixth engine order. Additionally, the fundamental vibration mode of the analyzed nodal diameter 6 of the bladed disk is well separated and distinct from the higher modes (compare Fig. 11: $\omega_{i=2,n=6}=2.1\cdot\omega_{i=1,n=6}$ and $\omega_{i=3,n=6}=2.3\cdot\omega_{i=1,n=6}$).

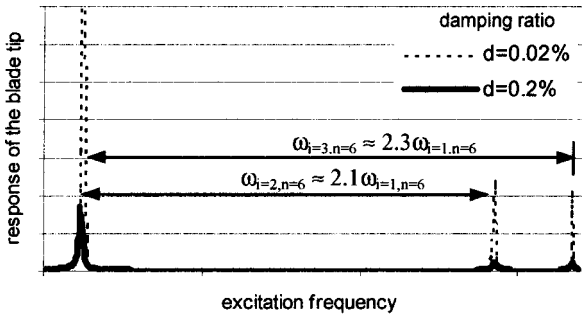

Fig. 11 Comparison among the resonance amplitudes of the lowest blade modes excited by the sixth engine order for two damping ratios ξ

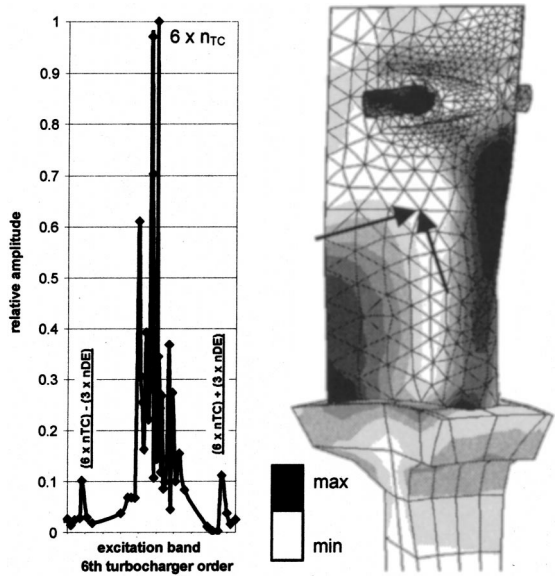

Fig. 12 Calculated blade amplitudes at the trailing edge versus exciting frequency (left); and contour plot of qualitative stress distribution in the turbine blade with the damping wire (right)

Fixed contact between the lacing wire and the airfoil was assumed in the steady state vibration analyses. The frictional as well as the aerodynamic energy dissipation are only included by the introduction of the equivalent damping ratio. To illustrate all this, Fig. 11 shows the computed minor resonance responses of the second and third blade modes related to the resonance of the fundamental blade mode.

The difference between the first computed and measured blade eigenfrequency was below 2 percent. To illustrate the results of the forced response analysis, the calculated relative amplitudes at the tip of the blade trailing edge are shown over the exciting frequencies on the left side of Fig. 12. The trailing edge was chosen because it exhibits the highest airfoil oscillations for the first blade mode. The right side of Fig. 12 displays the dynamic stress distribution. Additionally, the resulting circumferential and axial forces imposed on the blade are indicated in Fig. 12. The calculated peak stress was validated with the help of strain gage measurements. In spite of the simple model of the blade loading, fairly good agreements for the highest measured and computed stresses are obtained. The differences were below 25 percent. This

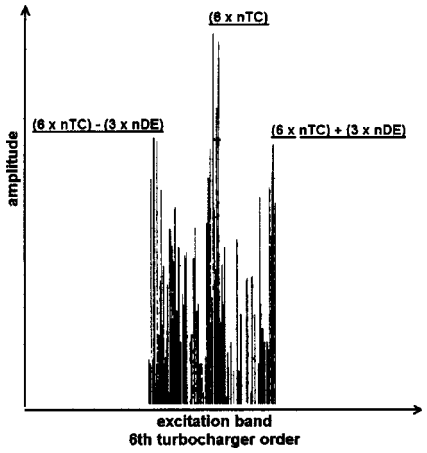

Fig. 13 Results of strain gage measurements around the sixth turbocharger order

leads to the conclusion, that for the described example case three-dimensional effects are small and the value of the damping ratio was well chosen.

To prove the numerical results (Fig. 12, left diagram), measured vibration amplitudes are shown in Fig. 13. The similarity between the measured and calculated spectrums is obvious and shows the capability of the unidirectional coupled numerical procedure to predict vibrations of turbocharger turbine blades.

Summary and Outlook

The described numerical procedure developed at ABB Turbo Systems, Ltd., is an approach to support turbocharger blade design for predicting dynamic stresses. With the help of this unidirectional coupled method, a structural optimization can be achieved with respect to the blade excitation resulting from the fluid flow. Costly experiments required within the design procedure of reliable turbine blades can then be reduced. In the first step the dynamic loads of pulse charged turbines were emphasized. A simple model of the blade loading was assumed because only fundamental blade mode shapes had to be considered. Qualitatively good agreement between experimental and numerical results was achieved. With respect to the simplifications, the quantitative agreement was satisfactory.

In the next step of the research program, the modeling of the blade loading and, therefore the CFD modeling, has to be improved to give quantitative better results. Higher resolution of the pressure loading takes torsional effects into account, and is therefore mandatory to be able to include higher mode shapes into the numerical design procedure. These mode shapes are possibly excited by the nozzle guide vanes and contribute to the dynamic load of turbocharger turbine blades.

Acknowledgments

The authors would like to thank ABB Turbo Systems Ltd. for the encouragement and the permission to publish this work. The authors are also in debt of Dr. P. Neuenschwander, who performed the ''SiSy'' calculations.

References

[1] Thompson, D. E., and Griffin, J. T., 1999, ''The National Turbine Engine High Cycle Fatigue Program,'' Global Gas Turbine News, **39**, No. 1, pp. 14–17.
[2] Feiereisen, J. M., Montgomery, M. D., and Fleeter, S., 1994, ''Unsteady Aerodynamic Forcing Functions: A Comparison Between Linear Theory and Experiment,'' ASME J. Turbomach., **116**, pp. 676–685.
[3] Fleeter, S., Feiereisen, J. M., and Johnston, R. T., 1995, ''Forced Response Wake and Potential Forcing Functions Including Blade Row Response,'' 12th Int'l Symposium of Air Breathing Engines, Melbourne, Australia, ISABE 95-7089, pp. 967–976.
[4] Kreuz-Ihli, T., Schulz, A., and Wittig, S., 1999, ''Aerodynamic Excitation and Vibration in Radial Inflow Turbines,'' 7th International Gas Turbines Congress, Kobe, Japan, Nov.
[5] Zaccaria, M. A., and Lakshminarayana, B., 1997, ''Unsteady Flow Field Due to Nozzle Wake Interaction With the Rotor in an Axial Flow Turbine: Part I—Rotor Passage Flow Field,'' ASME J. Turbomach., **119**, pp. 201–213.
[6] Zaccaria, M. A., and Lakshminarayana, B., 1997, ''Unsteady Flow Field Due to Nozzle Wake Interaction With the Rotor in an Axial Flow Turbine: Part II—Rotor Exit Flow Field,'' ASME J. Turbomach., **119**, pp. 214-224.
[7] Denos, R., Arts, T., Paniagua, G., Michelassi, V., and Martelli, F., 2001, ''Investigation of the Unsteady Rotor Aerodynamics in a Transonic Turbine Stage,'' ASME J. Turbomach., **123**, pp. 81–89.
[8] Gehrer, A., Lang, H., Mayrhofer, N., and Woisetschläger, J., 2000, ''Numerical and Experimental Investigation of Trailing Edge Vortex Shedding Downstream of Linear Turbine Cascade,'' ASME Paper No. 2000-GT-0434.
[9] Filsinger, D., Sekavcnik, M., Kreuz-Ihli, T., Schulz, A., and Wittig, S., 1999, ''Finite Element Analyses of the Vibration Characteristics of a Turbocharger Impeller,'' *Proc. 1st Int'l. Conference on Advances in Structural Engineering and Mechanics*, Seoul, Korea.
[10] Kreuz-Ihli, T., Filsinger, D., Schulz, A., and Wittig, S., 2000, ''Numerical and Experimental Study of Unsteady Flow Field and Vibration in Radial Inflow Turbines,'' ASME J. Turbomach., **122**, pp. 247–254.
[11] Srinivasan, A. V., 1997, ''Flutter and Resonant Vibration Characteristics of Engine Blades,'' ASME J. Eng. Gas Turbines Power, **119**, pp. 742–775.
[12] Schäfer, O., Phillipsen, B., and Breuhaus, P., 1998, ''Last Advances in Numerical Simulation of Aerodynamic Forces on Turbine Blades of Turbochargers for

Pulse Charged Engines,'' *Proc. CIMAC Congress*, Copenhagen, pp. 1705–1719.
[13] Steger, J., and Benek, J., 1987, ''On the Use of Composite Grid Schemes in Computational Aerodynamics,'' Comput. Methods Appl. Mech. Eng., **64**, No. 1–3.
[14] Schäfer, O., 1991, ''Application of a Navier–Stokes Analysis to Turbomachinery Blade-Cascade Flows,'' CIMAC Congress.
[15] Bulaty, T., Codan, E., and Skopil, M., 1996, ''A Flexible System for the Simulation of Turbocharged Diesel Engines and Turbocharging Systems,'' ASME ICE-Vol. 26-3, pp. 57–63.
[16] Lin, C. C., and Mignolet, M. P., 1996, ''Effects of Damping and Damping Mistuning on the Forced Vibration Response of Bladed Disks,'' J. Sound Vib., **193**, pp. 525–543.
[17] ABAQUS User's Manual Version 5.8, 1998, Hibbit, Karlsson and Sorenson Inc., 1080 Main Street, Pawtucket, RI 02860-4847.
[18] Szwedowicz, J., 1999, ''Cyclic Finite Element Modeling of Shrouded Turbine Blades Including Frictional Contacts,'' ASME Paper No. 99-GT-92.
[19] Aotsuka, M., Watanabe, T., and Machida, Y., 1999, ''Aerodynamic Damping Characteristics of a Transonic Turbine Cascade,'' ASME Paper No. 99-GT-50.
[20] Harris, C. M., and Crede, C. E., 1976, *Shock and Vibration Handbook*, 2nd Edition, McGraw-Hill Book Company, Inc., New York, NY.
[21] Filsinger, D., Szwedowicz, J., Schäfer, O., and Dickmann, H.-P., 2001, ''Pulse Charged Axial Turbocharger Turbines—A Challenge for Numerical Design Methods,'' *Proc. CIMAC World Congress on Combustion Engine Technology*, Vol. 2, pp. 712–722.
[22] Szwedowicz, J., 1996, ''Harmonic Forced Vibration Analyses of Blade Assemblies Modeled by Cyclic Systems, Part I—Theory and Verification,'' ABB Technical Reports HZX-ST 5849, Baden, Switzerland.
[23] Hoyniak, D., and Clarke, W. S., 1999, ''Aerodynamic Damping Predictions Using a Linearized Navier–Stokes Analysis,'' ASME Paper No. 99-GT-207.
[24] Newland, D. E., 1984, *Random Vibrations and Spectral Analysis*, Longman Scientific & Technical, Wiley, New York, NY.

Influence of Injection Type and Feed Arrangement on Flow and Heat Transfer in an Injection Slot

Hyung Hee Cho
Department of Mechanical Engineering,
Yonsei University,
Seoul 120-749, Korea
e-mail: hhcho@yonsei.ac.kr

Jin Ki Ham
Hyundai Heavy Industries Co., LTD.,
Ulsan 682-792, Korea

An experimental investigation is conducted to improve a slot film cooling system used for the cooling of a gas turbine combustor liner. The tangential slots are constructed of discrete holes with different injection types which are the parallel, vertical, and combined to the slot lip. The investigation is focused on the coolant supply systems of normal, inline, and counter-flow paths to the mainstream flow direction. A naphthalene sublimation technique has been employed to measure the local heat/mass transfer coefficients in a slot wall with various injection types and coolant feeding directions. A numerical simulation is also conducted to help understand the flow patterns inside the slot for different injection types. The velocity distributions at the exit of slot lip for the parallel and vertical injection types are fairly uniform with mild periodical patterns with respect to the injection hole positions. However, the combined injection type increases the nonuniformity of flow distribution with the period equaling twice that of hole-to-hole pitch due to splitting and merging of the ejected flows. The dimensionless temperature distributions at the slot exits differ little with blowing rates, injection types, and secondary flow conditions. In the results of heat/mass transfer measurements, the best cooling performance inside the slot is obtained with the vertical injection type among the three different injection types due to the effects of jet impingement. The lateral distributions of heat/mass transfer coefficients with the inline and counter-flow paths are more uniform than the normal-flow path. The average heat/mass transfer coefficients with the injection holes are about two to five times higher than that of a smooth two-dimensional slot path. [DOI: 10.1115/1.1424890]

Introduction

A slot film cooling has been used extensively for the cooling of a gas turbine combustor liner. A surface exposed to a hot gas stream can be protected by injecting a layer of cooling air along the surface. The injected coolant forms an insulating layer between the hot gas and the surface to be cooled. Generally, the liners of gas turbine combustors are film cooled by tangential slot injections of compressed air along their flame side surfaces. It is recognized that the best film cooling performance is achieved with a two-dimensional and uniform injection through continuous slots in the surface to be protected [1–3]. Extensive investigations, including numerical simulations, have been carried out in past years to determine the individual influences of the large number of parameters that can be of significance with slot film cooling [1,4–6]. Goldstein [7] provides an intensive summary of the film cooling works.

In actual slot film cooling application, a number of constraints such as structural strength, thermal expansion, cost of fabrication, and coolant metering often prevent the use of a two-dimensional continuous slot injection. Therefore, a practical combustor liner often uses discrete holes and three-dimensional film cooling slots to protect its wall from the hot gas stream. These film cooling slots consist of rows of parallel, vertical, and combined holes with or without slot lips. The cooling flow, which is admitted through discrete holes, impinges on the inside surface of a slot lip, and is mixed to form more or less uniform flows before ejection to the hot gas stream. The slot lip should be long enough to insure development of a uniform film, and the proper lip length is related to the hole size, hole-to-hole spacing, and slot height. However, an extremely long slot lip can be damaged because convection heat transfer inside the slot decreases gradually as the length of flow paths increases. Recently, as combustors develop into smaller sizes and higher temperature rises, it is essential to determine the detailed and accurate slot film cooling information. Many researchers [8–13] investigated slot film cooling, discharging flows through discrete injection holes, to obtain flow characteristics and cooling performances. Sivasegaram and Whitelaw [14] presented the flow characteristics affected by slot lip thickness and injection angles of 30 deg, 60 deg, and 90 deg to the direction of mainstream. Farmer et al. [15] investigated two geometries including a 35-deg inclined slot and a shaped 35-deg inclined slot. Hounslow et al. [16] reported the development of combustors for a power plant.

The present study is conducted experimentally and numerically to investigate flow and heat transfer characteristics of slot film cooling with discrete holes for changing blowing rates, injection types, and flow conditions at the slot exit. Especially, coolant feeding directions, which have inline and counter-flow directions to the mainstream flow, have the effect of secondary flows greatly being used. The investigation is focused on the heat transfer enhancement of the inside surface of a slot lip with changing the coolant flow paths. The mass transfer experiments by means of a naphthalene sublimation technique are conducted instead of heat transfer experiments to obtain detailed local transfer coefficients on the inside surface of the slot lip. The radiation and conduction errors that occur in heat transfer experiments are excluded in the naphthalene sublimation technique. Numerical simulations using a commercial code, FLUENT, are also conducted to help understand the flow patterns inside the slot for different injection types.

Experimental Apparatus and Procedure

1 Wind Tunnel and Secondary Injection System. The wind tunnel used for this experiment is an open circuit and blowing type. The test section is 300 mm wide by 195 mm high by 800 mm long and the area ratio of the contraction section is 9:1. A trip wire of diameter 2.5 mm is attached at the beginning of the test

Contributed by the International Gas Turbine Institute and presented at the ASME TURBO, Expo 2000, May 8–11, Munich, Germany. Manuscript received by the International Gas Turbine Institute February 2001. Paper No. 2000-GT-238. Review Chair: R. Natole.

section to ensure fully developed turbulent boundary layer in the test section. The nominal velocity of the mainstream is maintained at 8 m/s, which is the Reynolds number of 8000 based on the slot height, during the experimental tests. The turbulence intensity of the mainstream without secondary flow injection is measured within 0.7 percent. The boundary layer thickness based on 99 percent mainstream velocity at the location of slot exit is 11 mm.

The secondary injection system is composed of a blower, a heat exchanger, an orifice flow meter, and a plenum chamber. Secondary flow passes through fine screens in a plenum chamber and is injected through the slot holes into the boundary layer of the mainstream. The orifice flow meter between the blower and the plenum chamber is used to measure the mass flow rate of the secondary flow. For heat transfer experiments, the temperature of the secondary flow is raised above that of the mainstream with the aid of the heat exchanger supplied from an iso-thermal bath. A temperature difference of approximately 30°C is used and is measured by using J-type thermocouples which are attached to the inlet and outlet of system. For mass transfer experiments, the mainstream and secondary flows are maintained within 0.2°C.

2 Test Plates. The geometries of film cooling slots and coordinate system are shown schematically in Fig. 1. Parallel and vertical holes compared to the mainstream are punched linearly in the inside of slot. The configuration of the test plate is presented in Table 1. The coordinate system of the duct takes the streamwise, lateral, and vertical directions for *X*, *Y*, and *Z*, respectively, and its origin is located at the end point of the lip, the middle, and bottom point of the slot height. The geometries of slots with various injection types are presented schematically in Fig. 2 for a normal-feeding direction in which the secondary flow is supplied vertically from the bottom of plenum. Three injection types are used to study the effects of slot geometries. For a parallel injection, uniform velocity distribution can be obtained at the slot exit but convection heat transfer is the only method to cool the inside surface of the slot. For a vertical injection, jet impingement effect can be added to convection heat transfer and the inside surface of slot can be cooled intensively. For a combined injection, both advantages of the parallel and vertical injection are expected. Moreover, as shown in Figs. 3(*a*) and (*b*), the effects of feeding

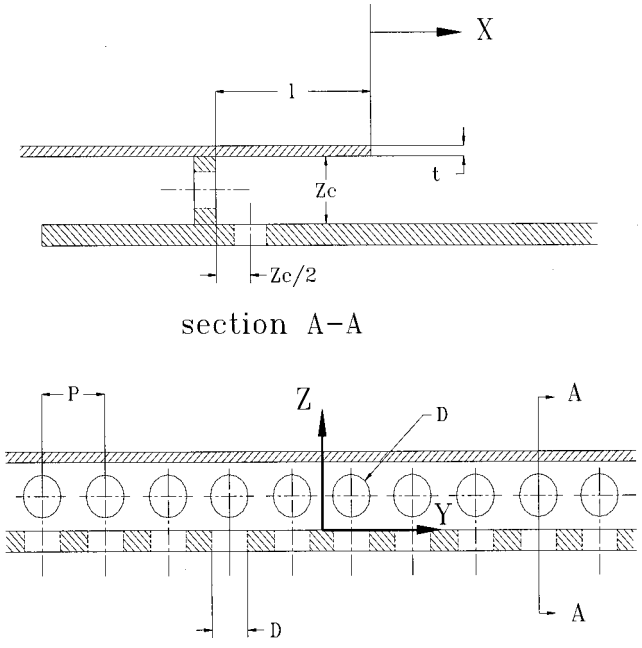

Fig. 1 Slot configuration and coordinate system

Table 1 Experimental configurations of the test plate

Slot Height (Z_c)	Lip Length (l)	Lip Thickness (t)	Pitch (P)	Diameter (D)
15 mm	45 mm	3 mm	15 mm	10.5 mm

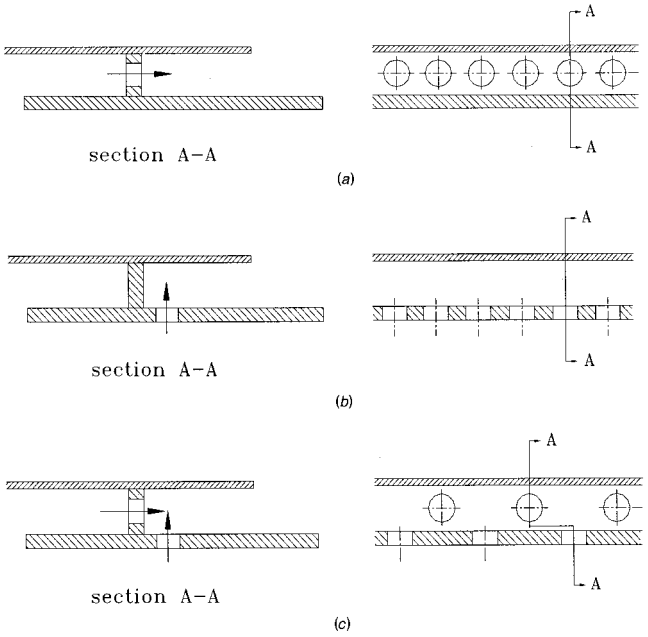

Fig. 2 Schematics of injection types—(*a*) parallel injection (PI); (*b*) vertical injection (VI); (*c*) combined injection (CI)

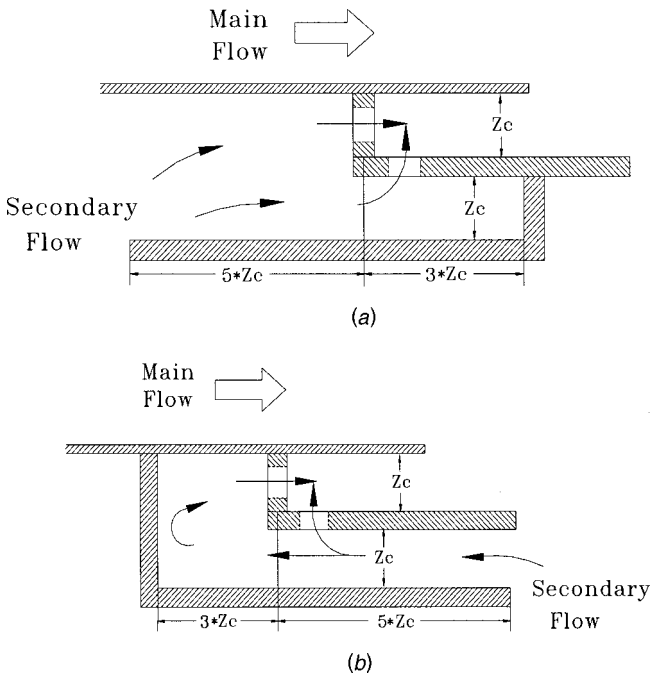

Fig. 3 Schematic view of different flow feeding directions—(*a*) parallel-feeding direction; (*b*) counter-feeding direction

directions of the secondary flow which have inline and counter-flow directions to the mainstream flow is investigated. The height of the guide vane is equal to that of the slot.

The mass transfer experiments are performed by using the naphthalene sublimation method instead of heat transfer experiments. The boundary of the naphthalene-coated surface corre-

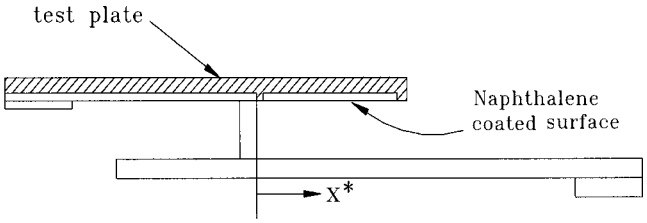

Fig. 4 Schematic diagram of test plate for mass transfer experiments

sponds to a constant temperature condition of heat transfer experiments. Detailed local heat/mass transfer coefficients are obtained in the present experiments. As shown in Fig. 4, the test plate including the naphthalene-coated surface is established like a slot lip. The coordinate system of the test plate takes the same lateral direction as *Y*, the vertical one as *Z* in Fig. 1. But the streamwise direction is defined newly as X^* at the start point of slot lip in Fig. 4. Therefore, the region to measure mass transfer coefficients is covered by $0.1 \leqslant X^*/Z_c \leqslant 2.8$ in the streamwise direction and $-2.0 \leqslant Y/Z_c \leqslant 2.0$ in the lateral direction and the naphthalene-coated surface includes four holes. A J-type thermocouple is positioned inside the naphthalene-coated layer near the exposed surface. The vapor pressure and density of naphthalene on the surface is calculated from this measured temperature.

A two-dimensional continuous slot test is conducted for reference values of the tested experimental results according to changing parameters (i.e., blowing rates, injection types, flow supply directions). The two-dimensional continuous slot is constructed with rounded approach duct sections at the front of slot and fine screens at the inlet of duct are used to minimize flow disturbance and to make a uniform flow condition at the slot exit.

Data Reduction. Velocity and turbulence intensity are measured by a hot-wire anemometer (TSI-IFA300) which is a constant temperature type with an *I*-type sensor. A three-axis traverse controlled by a PC is used to carry the hot-wire probe to various directions. The measured data are stored in the PC through a GPIB board.

Temperature distribution is measured by a J-type thermocouple rake which is composed of seven thermocouples arranged at intervals of 5 mm. The three-axis traverse is also used to move the rake. The dimensionless temperature coefficient is defined as

$$\Theta = \frac{T - T_\infty}{T_2 - T_\infty} \tag{1}$$

where T is the flow temperature at the measuring position, T_∞ is the mainstream temperature, and T_2 is the secondary flow temperature.

The test surface is cast with naphthalene using a set of molds composed of the test plate and the molding plate polished highly to a maximum smoothness. To obtain the local mass transfer rates, the sublimation depths of the naphthalene surface are measured at the numerous positions using an automated positioning table and an LVDT (linear variable differential transformer) made by Schaevitz Engineering (LBB-375TA-020). The LVDT has a resolution of 0.025 μm and the diameter of the measuring tip is 1.588 mm. An error of the LVDT measurements on the test plate is about 0.15 μm, which is within 0.5 percent of an averaged sublimation depth of 40 μm during the run.

The sublimation depths of the naphthalene-coated surface are measured before and after the test in the slot flow. Sherwood number (Sh), the dimensionless local mass transfer coefficient, is calculated from differences of the surface elevations (the naphthalene sublimation depths).

The local mass transfer coefficient is defined as

$$h_m = \frac{\dot{m}}{\rho_{v,w} - \rho_{v,\infty}} = \frac{\rho_s (dy/d\tau)}{\rho_{v,w}} \tag{2}$$

Since the approaching flow contains no naphthalene vapor, $\rho_{v,\infty} = 0$ in the present study. Therefore, the mass transfer coefficient is calculated from the local sublimation depth of naphthalene (dy), run time ($d\tau$), density of solid naphthalene (ρ_s), and naphthalene vapor density ($\rho_{v,w}$). The naphthalene vapor pressure is obtained from a correlation of Ambrose et al. [17].

The Sherwood number can be expressed as

$$\mathrm{Sh} = \frac{h_m d}{D_{\mathrm{naph}}} \tag{3}$$

D_{naph} is based on the discussion of naphthalene properties given by Goldstein and Cho [18].

Uncertainty Analysis. The uncertainty of the measured Sherwood number is estimated within 7.9 percent at the 95-percent confidence level by using Kline and McClintock's [19] uncertainty estimation method. This uncertainty is attributed mainly to the uncertainty of properties of naphthalene, such as the naphthalene saturated vapor pressure (3.8 percent), and diffusion coefficient of naphthalene vapor in the air (5.1 percent).

Numerical Simulations

The numerical simulations using a commercial package program (FLUENT) are accomplished to understand the flow patterns inside the slot lip with different injection types. The computation domains are modeled by the geometry used in the experimental study. The symmetry boundary conditions for one cell of injection holes are imposed to reduce the grid size and calculation time. The computation domain grids are created using the GAMBIT solid modeling, and the number of grids is about $80 \times 40 \times 150$. Different grids are used to verify the grid independence of the solution at the blowing rate of $M = 1.0$. The steady solutions for turbulent flow field in the slot cooling system are calculated using an RNG (re-normalization group) k-ϵ turbulence model. The flow characteristics with the variations of injection types are investigated in the present numerical simulation to support the experimental results.

Results and Discussion

1 Two-Dimensional Continuous Slot. Figure 5(*a*) shows the vertical velocity distribution of a two-dimensional continuous slot for $M = 1.0$ at $X/Z_c = 0.25$ (near the slot exit). As the secondary flow is injected through the two-dimensional continuous slot, the uniform velocity distributions are obtained laterally and the vertical velocity distribution is similar to a duct flow pattern. Therefore, this two-dimensional slot is expected to have a minimum entrainment of the mainstream into the coolant film with respect to shear mixing. Figure 5(*b*) shows the local variation of Sherwood numbers for M = 1.0 on the inside surface of slot lip at

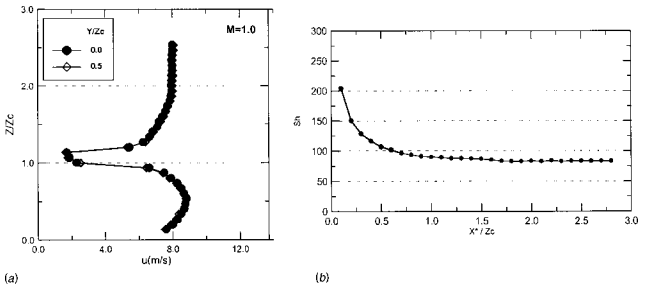

Fig. 5 Velocity and Sh distributions of 2-dimensional continuous slot for $M = 1.0$ — (*a*) vertical velocity distributions at X/Z_c-0.25; (*b*) local Sh along the slot lip

$Y/Z_c=0$. The heat/mass transfer decreases as the heat/mass transfer boundary layer develops from the root of slot lip and that is very uniform at the region of $X^*/Z_c \geq 0.7$. The lateral distributions of the local heat/mass transfer coefficients is fairly uniform over most parts of the slot lip. These results are used for a reference value evaluating experimental results obtained from other configurations.

2 Velocity Distributions. Figures 6–8 show lateral and vertical velocity distributions for $M=1.0$ at $X/Z_c=0.25$ according to the change of flow injection types and flow feeding directions. For the normal flow feeding direction, as shown in Fig. 6(*a*), the maximum and minimum velocities are repeated periodically at hole centers ($Y/Z_c=\pm 0.5, \pm 1.5$) and at middle points between holes ($Y/Z_c=0.0, \pm 1.0$) for the parallel injection (PI), respectively. The vertical velocity distribution shows that the maximum velocity appears near the bottom surface (Fig. 6(*d*)). This velocity distribution will produce high shear mixing with the mainstream due to a large velocity difference at the slot lip boundary.

For the vertical injection, maximum velocities appear at the middle points between injection holes due to the interaction of secondary flows inside the slot lip (Fig. 6(*b*)). The vertical velocity distribution presents that the maximum value exists near the slot lip, which is the reverse to that of the parallel injection case. The local velocity at $Z/Z_c \cong 0.9$ is much higher than that of the mainstream even though the average blowing rate equals 1.0. Therefore, the slot flow will produce a large shear mixing layer at the boundary in spite of $M=1.0$ for the vertical injection case.

For the combined injection as shown in Fig. 6(*c*), the period changes to twice that of hole-to-hole pitch due to the influence of splitting and merging of the parallel and vertical injection flows and its amplitude grows larger. This nonuniformity will affect the downstream region of the slot exit resulting in lower film cooling effectiveness values because the nonuniform velocity distribution enhances the entrainment-induced mixing between the mainstream and secondary flows.

For the inline-feeding direction, as shown in Figs. 7(*a–f*), the tendency of velocity distributions is similar to that of the normal flow feeding direction, except the parallel injection. The vertical velocity distributions are fairly uniform with the parallel injections, and will produce much less mixing with the mainstream.

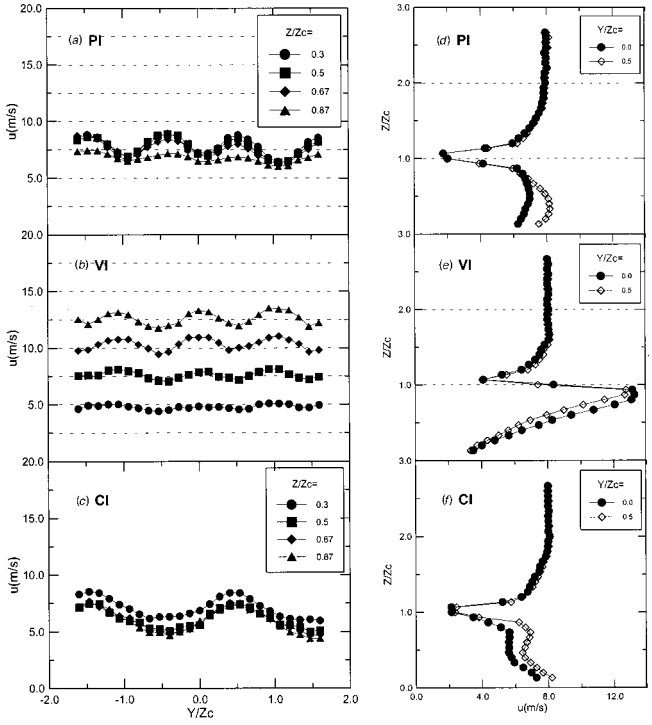

Fig. 7 Velocity distributions of inline-feeding direction for $M=1.0$ at $X/Z_c=0.25$: (*a*), (*b*), (*c*) lateral; (*d*), (*e*), (*f*) vertical distributions

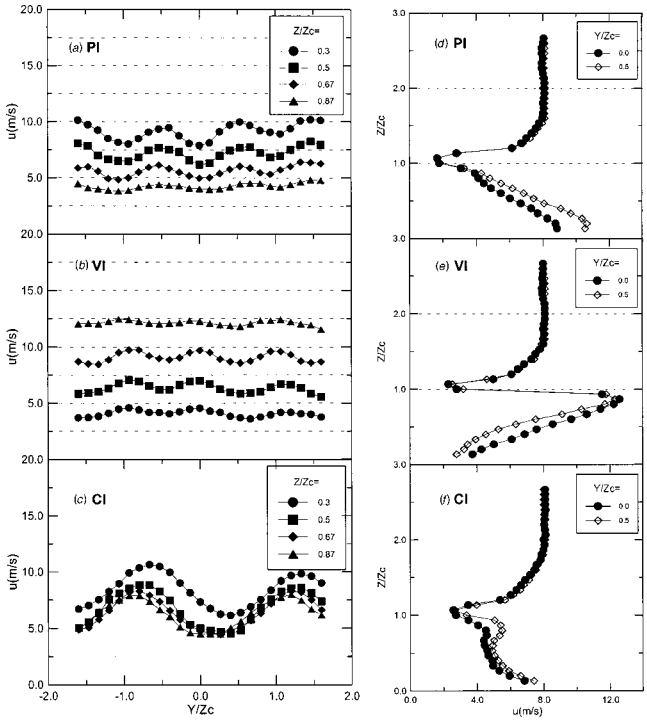

Fig. 6 Velocity distributions of normal-feeding direction for $M=1.0$ at $X/Z_c=0.25$: (*a*), (*b*), (*c*) lateral; (*d*), (*e*), (*f*) vertical distributions

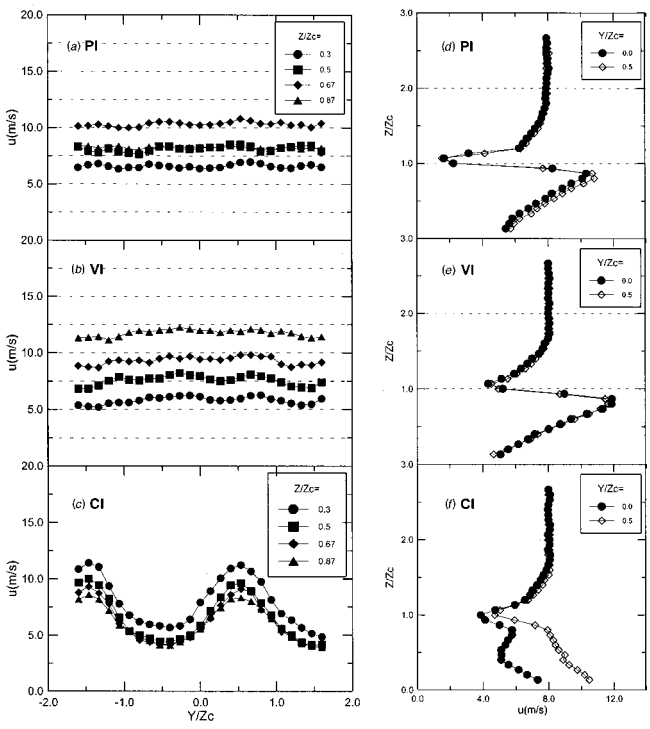

Fig. 8 Velocity distributions of counter-feeding direction for $M=1.0$ at $X/Z_c=0.25$: (*a*), (*b*), (*c*) lateral; (*d*), (*e*), (*f*) vertical distributions

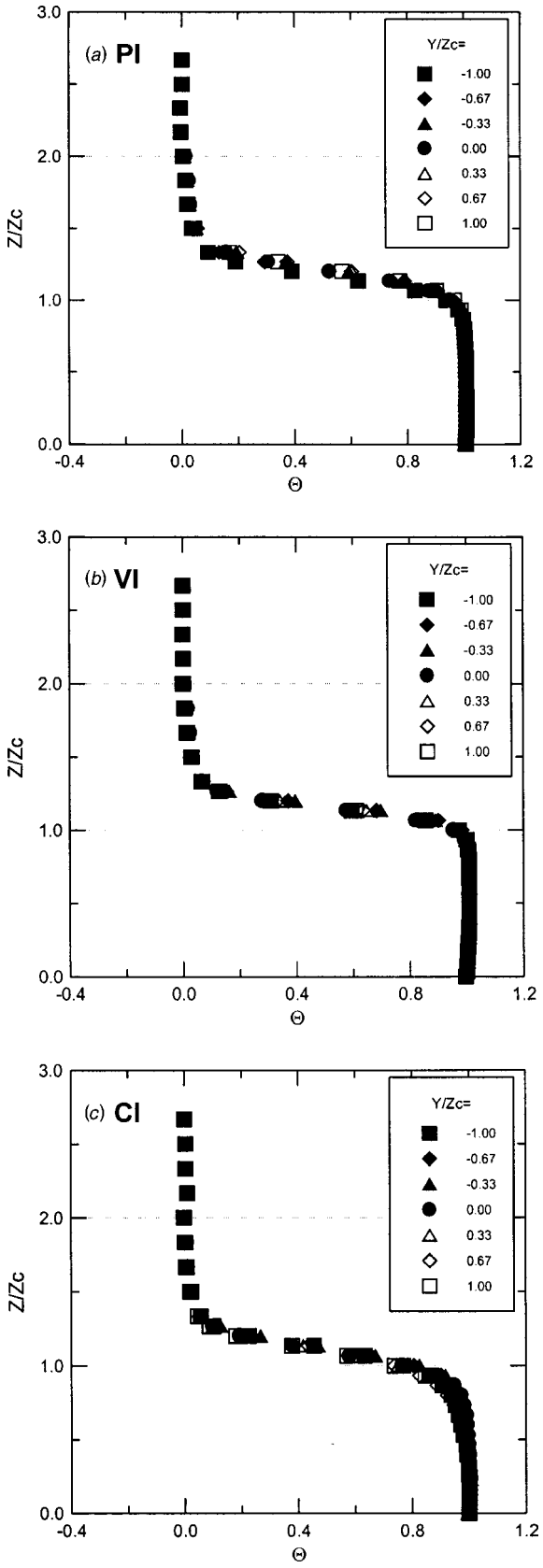

Fig. 9 Dimensionless temperature distributions for normal-feeding direction at $M=1.0$ and $X/Z_c=0.25$

For the combined injection, the difference of maximum and minimum velocities is considerably reduced owing to the change of secondary flow feeding direction. For the counter-feeding direction, as shown in Figs. 8(*a–f*), the velocity distributions have the most laterally uniform distributions at the parallel and vertical injection types, which are similar to the results of the two-dimensional continuous slot. However, the difference of maximum and minimum is highly amplified in the combined injection case. Therefore, the counter-feeding direction can be recommended for the parallel and vertical injections to obtain high film cooling effectiveness at the downstream region, but not for the combined injection.

3 Temperature Distributions. Figure 9 shows dimensionless temperature distributions for various injection types with the normal feeding direction. For the parallel injection, as shown in Fig. 9(*a*), the dimensionless temperature coefficients are fairly uniform and about $\Theta=1$ near the slot exit ($X/Z_c=0.25$) for M $=1.0$. As going downstream region ($X/Z_c=1.0$), the dimensionless temperature coefficients decrease ($\Theta=1$) maintained only in the region of $Z/Z_c\leqslant 0.6$) due to interaction of the mainstream and secondary flows. For the vertical injection, presented in Fig. 9(*b*), the distribution is similar to that of the parallel injection even though the coolant has different velocity distributions. For the combined injection (Fig. 9(*c*)), the dimensionless temperature coefficients are slightly lower and less uniform than the other cases due to the mixing of the mainstream and secondary flows with the large lateral variation of velocity distributions as shown in Fig. 6(*c*).

4 Heat/Mass Transfer. The contour plots of local heat/mass transfer coefficients (Sherwood number) are presented in Fig. 10 for various injection types with the normal-feeding direction. Different contour scales are used to show Sh distributions clearly for each case. For $M=0.5$ and the parallel injection, the high Sherwood number regions are observed along the lines of injection hole positions ($Y/Z_c=\pm 0.5,\pm 1.5$) and the maximum values appear approximately at $X^*/Z_c\cong 1.0$, as shown in Fig. 10(*a*). For the region of $X^*/Z_c\geqslant 1.5$, the heat/mass transfer decreases as the heat/mass transfer boundary layer develops. The lateral distribution of the local heat/mass transfer coefficients is fairly uniform over most parts of the slot lip regardless of hole positions. However, at the region of $X^*/Z_c\leqslant 0.5$, the heat/mass transfer coefficients have low values due to the recirculation flows which are blocked by diffused parallel injection flows.

For the vertical injection at $M=0.5$ (Fig. 10(*b*)), the injected flow from the plenum impinges on the inside surface of the slot lip and forms a cross-flow to the exit. The high heat/mass transfer coefficients are obtained in the area of $0.5\leqslant X^*/Z_c\leqslant 1.0$, where the jet is impinging on it. The impinged secondary flow spreads widely due to the interaction of neighboring jets with the close hole-to-hole spacing, and consequently high heat/mass transfer coefficients are obtained in the overall area including higher Sherwood numbers at $X^*/Z_c\leqslant 0.5$ than that of the parallel injection case. The lateral distribution of the local heat/mass transfer coefficients is fairly uniform due to the mixing of secondary flows inside the slot.

Figure 10(*c*) shows the results of the combined injection for $M=0.5$. Parallel and vertical hole positions are $Y/Z_c=-0.5$, 1.5 and $Y/Z_c=-1.5$, 0.5, respectively. For this case, the Sherwood number distributions are much different from those of the parallel and vertical injections. The lateral distributions of the local heat/mass transfer coefficients are nonuniform over most regions of the slot lip and it is expected from the lateral velocity distributions for the combined injection as presented in Fig. 6(*c*). This area would be subject to the excessive thermal stress load due to the nonuniform temperature distribution and including hot spots with lower cooling effectiveness regions. At increasing blowing rates, the distributions of Sherwood numbers have the similar trends in all three injection types. The heat/mass transfer coefficients increase continuously as the blowing rates increase.

The contour plots of local Sherwood numbers for different flow

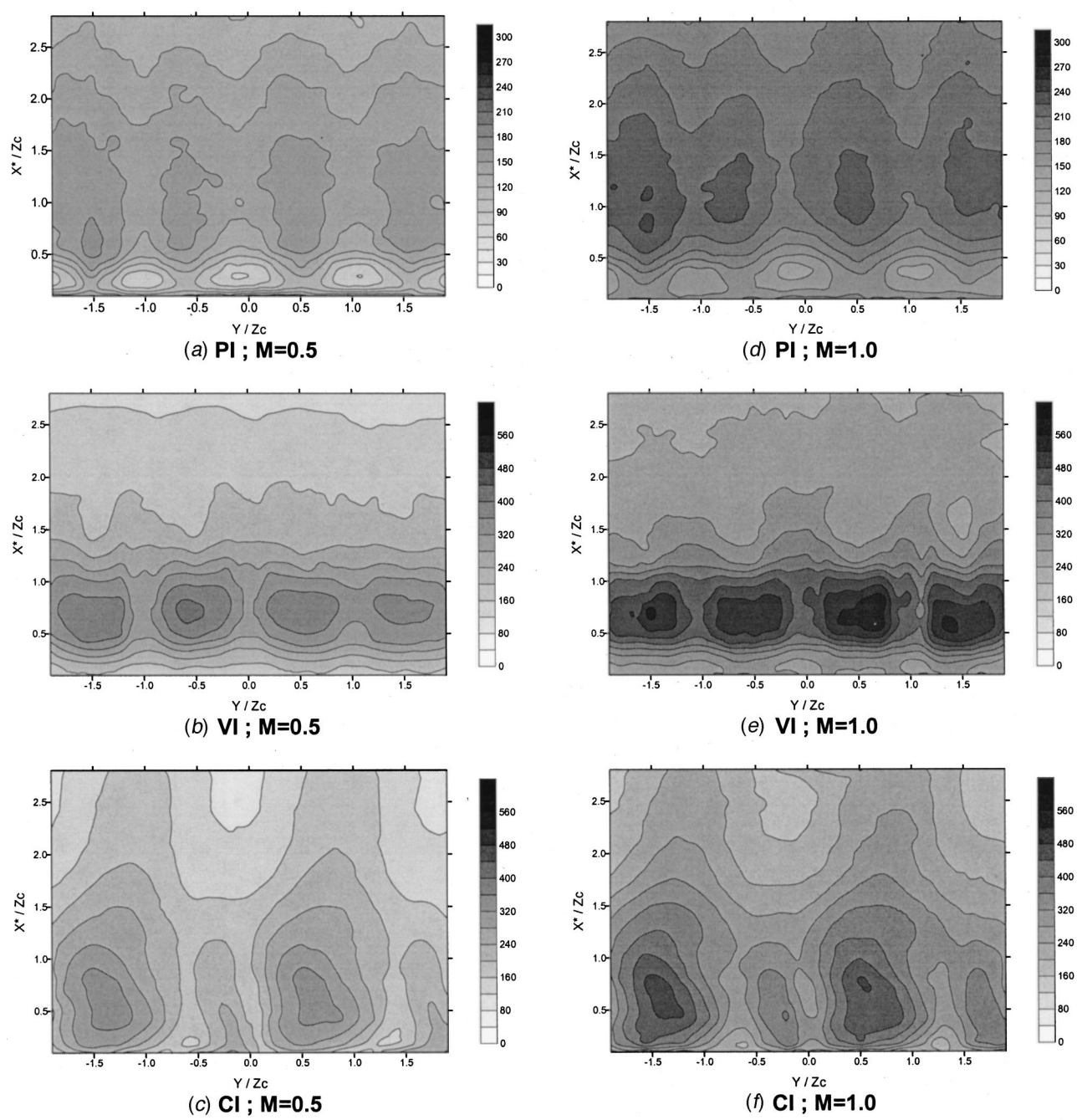

Fig. 10 Contour plots of Sh for various injection types with normal-feeding direction

feeding directions are presented in Fig. 11 for $M=1.0$; Figs. 11(*a-c*) for the inline-feeding direction and Figs. 11(*d–f*) for the counter-feeding direction. For the parallel injection with inline-feeding direction, although the overall trend is similar to that of the normal-feeding direction presented in Fig. 10(*d*), the increasing regime of local heat/mass transfer is widened and the effect of hole positions decreases. The reason is that the change of flow direction between the slot and plenum chamber results in the better mixing of secondary flows. Especially, the low transfer regions disappear at $X^*/Z_c \leqslant 0.5$ comparing with the results of normal-feeding direction (Fig. 10(*d*)). For the vertical injection, the jet flow impingement is the most important effect to augment heat/mass transfer on the slot lip. But, as changing of the flow feeding direction, the impinging region is slightly moved downstream rather than the normal flow feeding direction. Especially, the local heat/mass transfer coefficients at the region of $1.0 \leqslant X^*/Z_c \leqslant 1.5$ increases and that is more uniform in the lateral direction. For the combined injection, as the flow from parallel injection holes ($Y/Z_c = -0.5, 1.5$) is instantly divided into the vertical injection jets, the augmentation of heat/mass transfer appears along the vertical injection flows. It is confirmed that the peak values of lateral velocity distributions at the slot exit correspond to the vertical hole positions ($Y/Z_c = -1.5, 0.5$).

On the contrary, for the counter-flow feeding direction, the mass transfer enhanced area due to the injected secondary flows is moved upward compared with that of the normal flow feeding direction (Fig. 11(*d*)). For the parallel injection case, the high heat/mass transfer coefficient is seen in the region of $0.5 \leqslant X^*/Z_c \leqslant 1.0$ as shown in the vertical injection of other flow

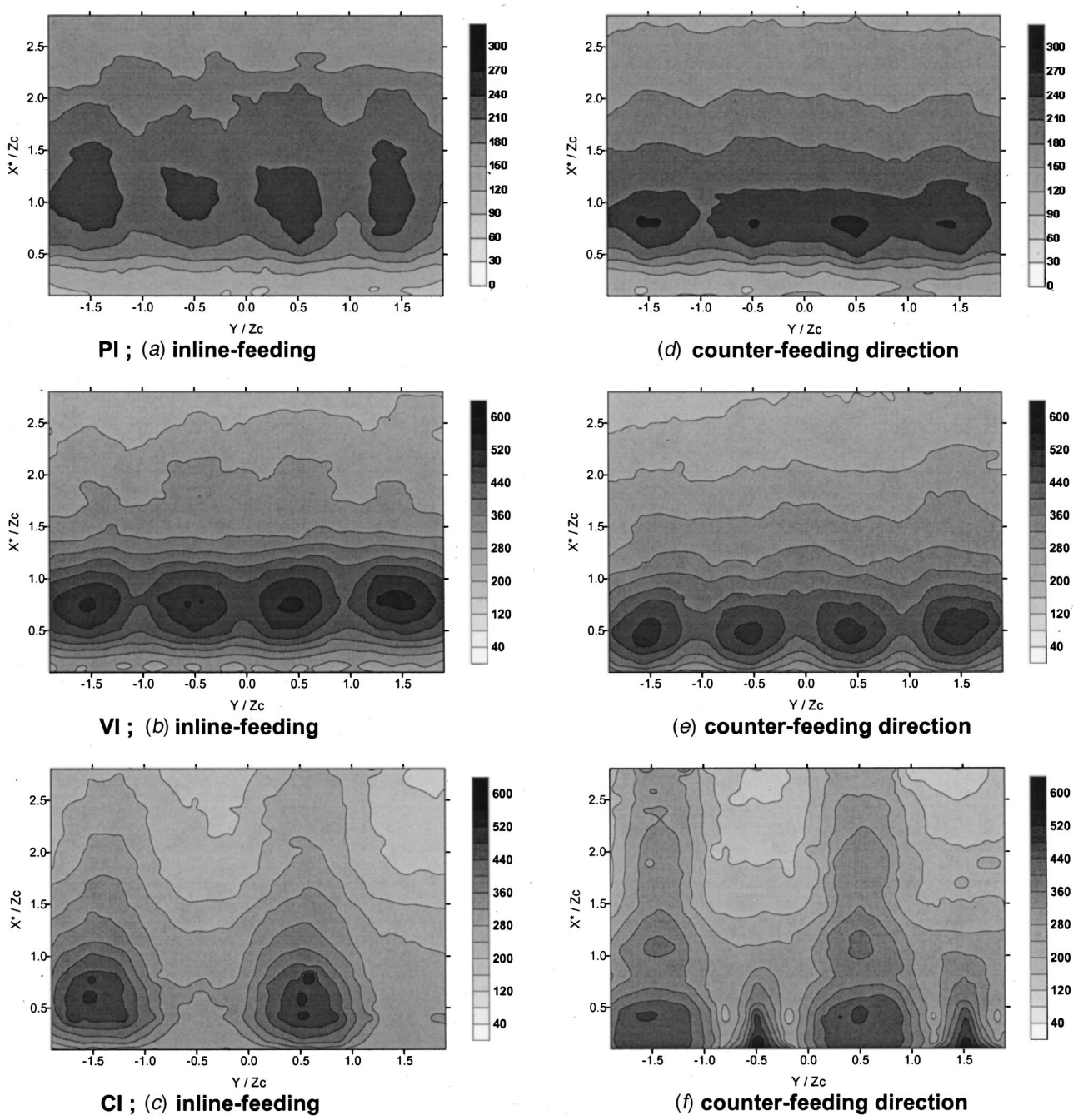

Fig. 11 Contour plots of Sh for various injection types at $M=1.0$

feeding directions. Since the flow feeding direction is changed, such as a counter direction to the mainstream, the secondary flow is injected obliquely through the parallel holes onto the slot lip. These trends are also distinctly observed in the vertical and combined injection results presented in Figs. 11(*e*) and (*f*), respectively. Therefore, the very high mass transfer coefficients are observed in the region of $X^*/Z_c \leqslant 0.5$.

The detailed local mass transfer coefficients are presented in Fig. 12 for $M=1.0$ at several lateral positions ($X^*/Z_c=0.2$, 0.7, and 1.5) for the inline-feeding direction. Generally, the periodical patterns correspond to the hole positions are observed mildly for the parallel and vertical injection types. As the secondary flow is moved downstream, the lateral distributions of heat/mass transfer coefficient are fairly uniform due to the large mixing of injection flows inside the slot. The best performance for the slot lip cooling is obtained with the vertical injection among the three types of injections due to the effects of jet impingement. In contrast, for the combined injection, high heat/mass transfer coefficients are observed periodically at $X^*/Z_c=0.2$ and 0.7. The lateral distributions of heat/mass transfer coefficients are extremely nonuniform due to the splitting and merging of flows between parallel and vertical injection jets regardless of the flow feeding directions.

5 Averaged Heat/Mass Transfer. Figure 13 shows the streamwise distributions of laterally averaged Sherwood numbers with different flow feeding directions for $M=1.0$. As discussed previously, the best performance is obtained by using the vertical injection type and the peak point of Sherwood numbers is about five times higher than that of the two-dimensional continuous slot. For the parallel injection type, the counter-flow feeding direction

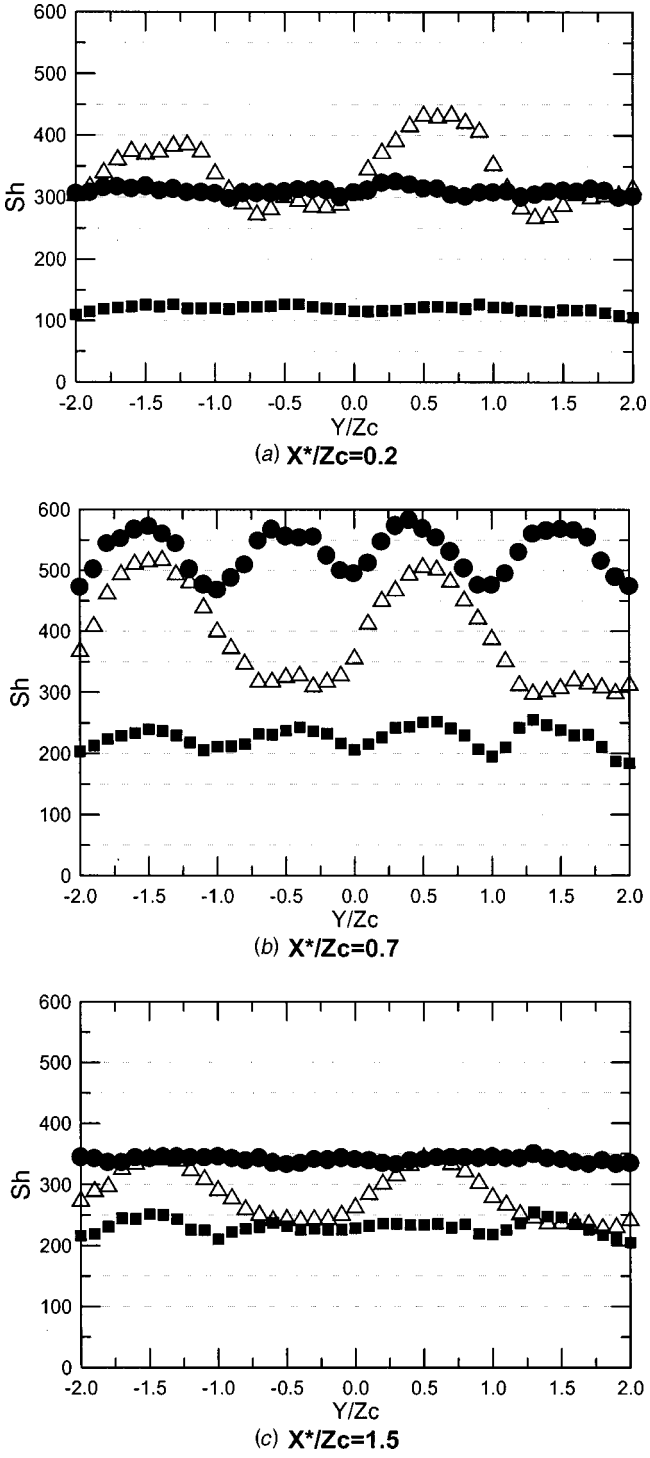

Fig. 12 Lateral distributions of Sh for various injection types with inline-feeding direction at $M=1.0$

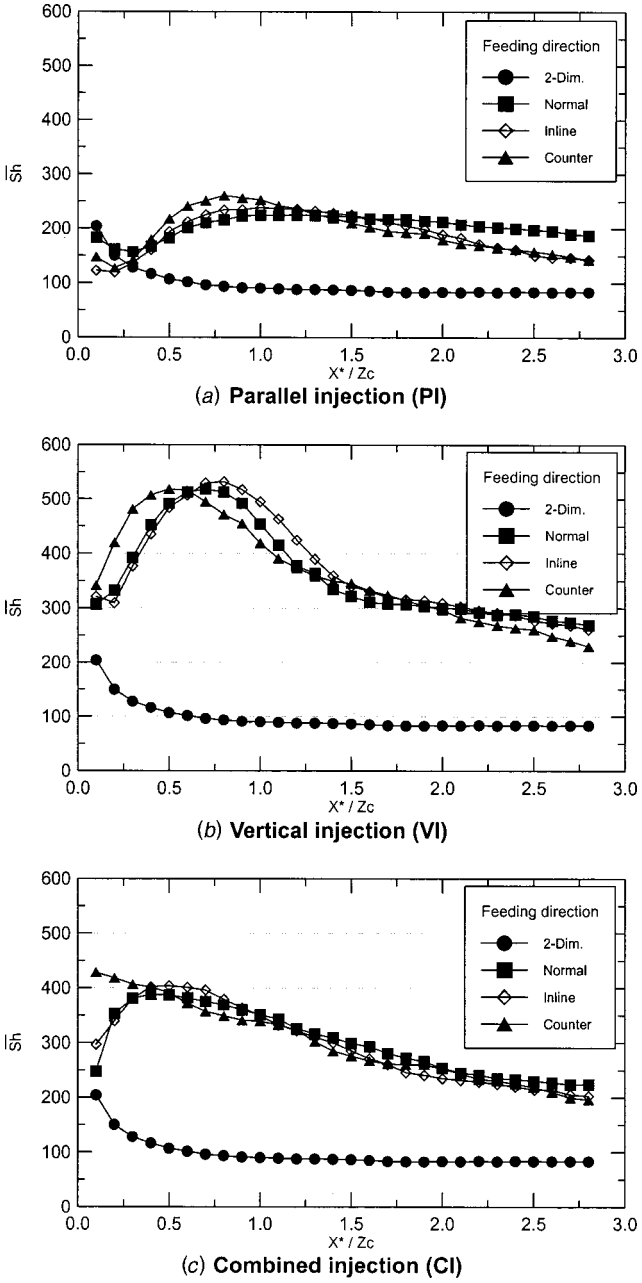

Fig. 13 Comparison of averaged Sh for flow feeding directions at $M=1.0$

has the highest averaged Sherwood numbers at the region of $0.5 \leqslant X^*/Z_c \leqslant 1.0$ because a kind of impinging effect is added to the parallel injection flows. Generally, the averaged Sherwood number is 2–5 times higher than that of the two-dimensional continuous slot injection. The patterns of the averaged Sh distributions for $M=0.5$ are similar to those for $M=1.0$ as partially shown in Fig. 10.

6 Numerical Simulation. Figures 14 and 15 show the velocity vector plots for different flow injection types with the inline-feeding direction. Those present only interested regions, even though the calculated domain includes a whole tested area, obtained from a numerical simulation using a commercial code, FLUENT. Figures 14(*a*) and (*b*) present the vector plots for a side view and a front view, respectively, with the parallel injection type. The flow ejected from the hole forms a separation bubble on the bottom surface (Fig. 14(*a*)) resulting in a down wash flow from the middle lines between holes (Fig. 14(*b*)). This flow pattern will produce the reverse velocity distribution near the bottom wall before the flow reattachment on the surface. Therefore, the flow structure ejected from the slot lip would be strongly dependent on the length of the slot lip. The numerically obtained flow patterns correspond fairly well with that measured from the experiments.

For the vertical injection case, the ejected jet impinges on the inside surface of the slot lip, as shown in Fig. 14(*c*), and enhances the heat transfer on the slot lip. The impinged jet inside the slot

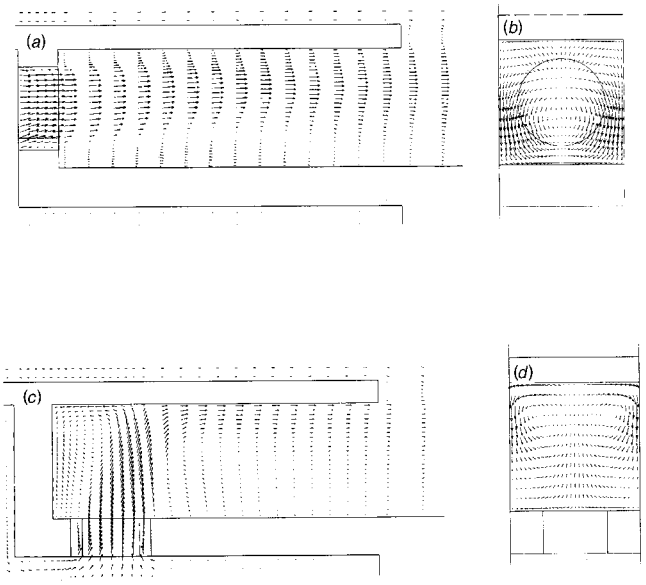

Fig. 14 Velocity vectors for inline-feeding direction (not in scale)—(*a*) side view of parallel injection at $Y/Z_c=0.5$; (*b*) front view of parallel injection at $X^*/Z_c=2.0$; (*c*) side view of vertical injection at $Y/Z_c=0.5$; (*d*) front view of vertical injection at $X^*/Z_c=2.0$

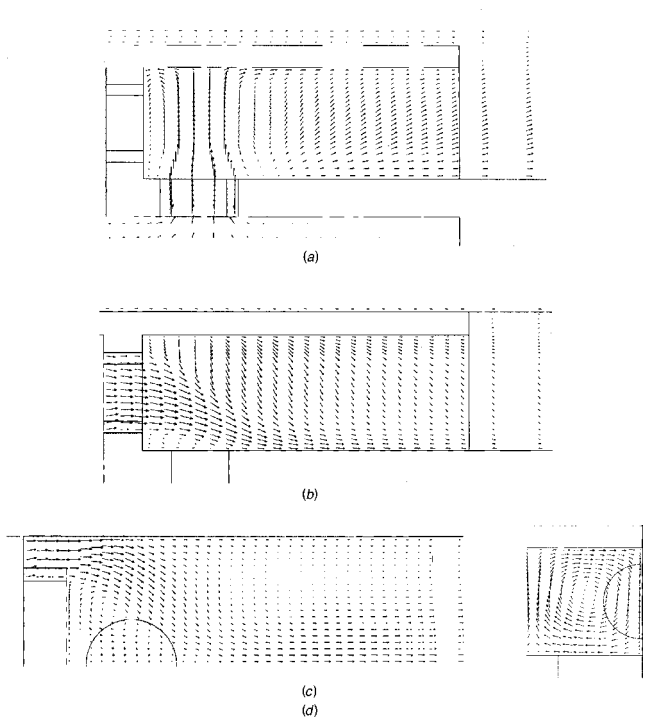

Fig. 15 Velocity vectors for the combined injection with inline-feeding direction (not in scale) — (*a*) side view at $Y/Z_c=0.5$; (*b*) side view at $Y/Z_c=0.5$; (*c*) top view at $Z/Z_c=0.5$; (*d*) front view at $X^*/Z_c=2.0$

develops quickly with a counter-rotating vortex resulting in a fairly uniform flow distribution in lateral directions before exposure to the mainstream. The maximum velocity is obtained near the slot lip and this result matches fairly well with the experimental data as shown in Fig. 7(*e*).

For the combined injection case, the flow pattern is different from those of the previous cases showing a large counter-rotating vortex (a double size of that in the vertical injection), as presented in Fig. 15. The flows ejected from the parallel holes split quickly and merge into the jet ejected from the vertical hole as shown in Fig. 15(*c*). Therefore, the nonuniform heat/mass transfer is obtained inside the slot lip and the flow velocity distribution is extremely nonuniform at the exit of slot lip. These results support strongly the heat/mass transfer and velocity data obtained from the experiments (Figs. (7) and (11)).

Conclusions

The present study has been conducted to investigate the velocity and temperature distributions in the slot and at the slot exit and local heat/mass transfer coefficients on the inside of the slot lip with various injection types and flow feeding directions. It is compared with the results of the two-dimensional continuous slot injection. The results are summarized as follows;

Velocity Distributions

- Generally, the parallel and vertical injection types have weak periodical flow patterns at the slot lip exit with respect to the hole positions, because the counter-rotating vortices mix the flow quickly inside the slot before exposure to the mainstream.
- For the combined injection type, the flow period changes to twice that of hole-to-hole pitch due to the splitting and merging of parallel and vertical injection flows.

Temperature Distributions

- The dimensionless temperature coefficients at the slot exit are little affected by variation of blowing rates and secondary flow injection types.

Heat/Mass Transfer

- The highest heat/mass transfer on the slot lip is obtained with the vertical injection among the three types of injections due to the effects of jet impingement.
- For the combined injection type, the lateral distribution of Sh is extremely nonuniform due to the splitting and merging of ejected jets.
- The inline and counter-flow feeding directions change slightly the flow pattern and the lateral distributions of Sh resulting in more uniform heat transfer distributions.
- As changing the injection types and flow feeding directions, the averaged Sherwood numbers increase about two to five times higher than that of the two-dimensional continuous slot injection.

Acknowledgment

The authors wish to acknowledge support for this study by the Korea Science and Engineering Foundation under the grant No. 98-0200-13-01-3 and the Ministry of Science and Technology through National Research Laboratory Program.

Nomenclature

D = diameter of slot film cooling hole
dy = sublimation depth of naphthalene
$d\tau$ = time interval during experiment
D_{naph} = naphthalene vapor diffusivity in air
h_m = local mass transfer coefficient
l = slot lip length
M = blowing rate, $\rho_2 U_2/\rho_\infty U_\infty$
$\dot{m}$ = mass transfer rate per unit area
P = hole-to-hole pitch
Sh = Sherwood number based on slot height $h_m Z_c/D_{\text{naph}}$
$\overline{\text{Sh}}$ = spanwise averaged Sherwood number
t = slot lip thickness

T = local temperature
T_2 = secondary flow temperature
T_∞ = mainstream temperature
u_2 = secondary flow velocity
u_∞ = mainstream velocity
X = streamwise distance from end of lip
X^* = streamwise distance from root of lip
Y = lateral distance from center of test plate
Z = vertical distance from bottom of test plate
Z_c = slot height
ρ_s = density of solid naphthalene
$\rho_{v,w}$ = naphthalene vapor density at wall
$\rho_{v,\infty}$ = naphthalene vapor density in mainstream
Θ = dimensionless temperature coefficient, $(T-T_\infty)/(T_2-T_\infty)$

References

[1] Seban, R. A., 1960, "Heat Transfer and Effectiveness for a Turbulent Boundary Layer with Tangential Fluid Injection," ASME J. Heat Transfer, **82**, pp. 303–312.

[2] Kacker, S. C., and Whitelaw, J. H., 1969, "An Experimental Investigation of the Influence of Slot Lip Thickness on the Imperious Wall Effectiveness of the Uniform-Density, Two-Dimensional Wall Jet," Int. J. Heat Mass Transf., **12**, pp. 1196–1201.

[3] Mayle, R. E., and Kopper, F. C., 1976, "Adiabatic Wall Effectiveness of a Turbulent Boundary Layer with Slot Injection," ASME J. Heat Transfer, **98**, pp. 240–244.

[4] Papell, S. S., 1960, "Effect on Gaseous Film Cooling of Coolant Injection through Angled Slots and Normal Holes," NASA Technical Note D–299.

[5] Metzger, D. E., Baltzer, R. T., Takeuchi, D. I., and Kuenstler, P. A., 1972, "Heat Transfer to Film-Cooled Combustion Chamber Liners," ASME Paper No. 72–WA/HT–32.

[6] Sturgess, G. J., 1980, "Account of Film Turbulence for Predicting Film Cooling Effectiveness in Gas Turbine Combustors," ASME J. Eng. Power, **102**, pp. 524–534.

[7] Goldstein, R. J., 1971, "Film Cooling," Adv. Heat Transfer, **7**, pp. 321–379.

[8] Nina, M. N. R., and Whitelaw, J. H., 1971, "The Effectiveness of Film Cooling with Three Dimensional Slot Geometries," ASME J. Eng. Power, **93**, pp. 425–430.

[9] Rastogi, A. K., and Whitelaw, J. H., 1973, "The Effectiveness of Three-Dimensional Film-Cooling Slots-I. Measurements," Int. J. Heat Mass Transf., **16**, pp. 1665–1672.

[10] Patankar, S. V., Rastogi, A. K., and Whitelaw, J. H., 1973, "The Effectiveness of Three-Dimensional Film-Cooling Slots-II. Predictions," Int. J. Heat Mass Transf., **16**, pp. 1673–1681.

[11] Folayan, C. O., and Whitelaw, J. H., 1976, "The Effectiveness of Combined Tangential and Normal Film-Cooling Slots with Finite Lip," ASME Paper No. 76–HT–30.

[12] Sturgess, G. J., 1986, "Design of Combustor Cooling Slots for High Film Effectiveness: Part I-Film General Development," ASME J. Eng. Gas Turbines Power, **108**, pp. 354–360.

[13] Sturgess, G. J., and Pfeifer, G. D., 1986, "Design of Combustor Cooling Slots for High Film Effectiveness: Part II-Film Initial Region," ASME J. Eng. Gas Turbines Power, **108**, pp. 361–369.

[14] Sivasegaram, S., and Whitelaw, J. H., 1969, "Film Cooling Slots: The Importance of Lip Thickness and Injection Angle," J. Mech. Eng. Sci., **11**, pp. 22–27.

[15] Farmer, J. P., Seager, D. J., and Liburdy, J. A., 1997, "The Effect of Shaping Inclined Slots on Film Cooling Effectiveness and Heat Transfer Coefficient," ASME Paper No. 97-GT-339.

[16] Hounslow, D. H., Grindley, W., Loughlin, R. M., and Daly, J., 1998, "The Development of a Combustion System for a 110 MW CAES Plant," ASME J. Eng. Gas Turbines Power, **120**, pp. 875–883.

[17] Ambrose, D., Lawrenson, I. J., and Sparke, C. H. S., 1975, "The Vapor Pressure of Naphthalene," J. Chem. Thermodyn., **7**, pp. 1173–1176.

[18] Goldstein, R. J., and Cho, H. H., 1995, "A Review of Mass Transfer Measurement Using Naphthalene Sublimation," Exp. Therm. Fluid Sci., **10**, pp. 416–434.

[19] Kline, S. J., and McClintock, F. A., 1953, "Describing Uncertainty in Single-Sample Experiments," Mech. Eng. (Am. Soc. Mech. Eng.), **75**, pp. 3–8.

Effects of Bulk Flow Pulsations on Film Cooling With Compound Angle Holes: Heat Transfer Coefficient Ratio and Heat Flux Ratio

In Sung Jung
Research Assistant

Joon Sik Lee
Professor

Turbo and Power Machinery Research Center,
School of Mechanical and Aerospace Engineering,
Seoul National University,
Seoul 151-742, Korea

P. M. Ligrani
Professor,
Convective Heat Transfer Laboratory,
Department of Mechanical Engineering,
University of Utah,
Salt Lake City, UT 84112-9208
Fellow ASME

Experiments are conducted to investigate the effects of bulk flow pulsations on film cooling from compound angle holes. A row of five film cooling holes is employed with orientation angles of 0, 30, 60, and 90 deg at a fixed inclination angle of 35 deg. Static pressure pulsations are generated using an array of six rotating shutter blades, which extend across the span of the exit of the wind tunnel test section. Pulsation frequencies of 0 Hz, 8 Hz, and 36 Hz, and time-averaged blowing ratios of 0.5, 1.0, and 2.0 are employed. Corresponding coolant Strouhal numbers based on these values then range from 0.20 to 3.6. Spatially resolved surface heat transfer coefficient distributions are measured (with the film and freestream at the same temperature) using thermochromic liquid crystals. Presented are ratios of surface heat transfer coefficients with and without film cooling, as well as ratios of surface heat flux with and without film cooling. These results, for compound angle injection, indicate that the pulsations cause the film to be spread more uniformly over the test surface than when no pulsations are employed. This is because the pulsations cause the film from compound angle holes to oscillate in both the normal and spanwise directions after it leaves the holes. As a result, the pulsations produce important changes to spatially resolved distributions of surface heat flux ratios, and surface heat transfer coefficient ratios. In spite of these alterations, only small changes to spatially averaged heat transfer coefficient ratios are produced by the pulsations. Spatially averaged surface heat flux ratios, on the other hand, increase considerably at coolant Strouhal numbers larger than unity, with higher rates of increase at larger orientation angles.
[DOI: 10.1115/1.1400110]

Introduction

It is well known that film cooling performance is affected by a number of parameters such as external boundary layer status, blowing ratio, blade curvature, and film hole arrangement and configuration, to name a few [1]. Flow unsteadiness in turbines has only recently been recognized to also affect film cooling performance in significant ways. Such unsteadiness develops from four different sources [2]: (*i*) potential flow interactions, (*ii*) shock waves, (*iii*) passing wakes, and (*iv*) random freestream turbulence from the combustion chamber. Potential flow pulsations are caused by the relative motion of a rotor blade row relative to an adjacent stator blade row. In transonic gas turbines, downstream rotor blades encounter shock waves which form at the trailing edges of upstream stator blades. As this happens, shock waves are often reflected, absorbed, or broken up near rotor blade surfaces. Such passing families of shock waves, along with potential flow interactions, result in periodic alterations to the static pressure on the surfaces of downstream rotor blades. When film cooling is employed, these surface static pressure variations are then present at the exit planes of the holes. As a result, coolant flow rates pulsate at film hole exits, and coolant trajectories and coverage vary with time downstream of the film holes. This often gives significant changes to the protection ordinarily provided by film cooling, as well as to the structural characteristics of film cooled boundary layers.

Contributed by the International Gas Turbine Institute and presented at the 46th International Gas Turbine and Aeroengine Congress and Exhibition, New Orleans, Louisiana, June 4–7, 2001. Manuscript received by the International Gas Turbine Institute February 2001. Paper No. 2001-GT-129. Review Chair: R. Natole.

The effects of potential flow interactions and passing shock waves are described by a number of investigators [2–9]. In an investigation of rotor heat transfer with a short-duration blowdown turbine test facility, Abhari and Epstein [3] indicated that these types of flow pulsations cause the time-averaged heat transfer rate to increase by 12 percent on the suction surface and to decrease by 5 percent on the pressure surface, compared with values measured with no pulsations. Flow visualization results in the recent experiments of Ligrani et al. [2,4,5] show two distinct coolant flow regimes: quasi-steady and nonquasi-steady. According to these authors, magnitudes of the coolant Strouhal number less than 1-2 correspond to quasi-steady behavior, and the magnitudes greater than 1-2 correspond to nonquasi-steady behavior, regardless of the blowing ratio. Quasi-steady film distributions are the same as the steady distribution which would exist at the same instantaneous flow condition. With the nonquasi-steady film behavior, multiple pulsations are imposed on the coolant over the time period required for it to pass through the film hole. As a result, portions of the film oscillate in ways different from adjacent portions, which gives a ''wavy'' appearance at each instant in time [2]. In many cases, nonquasi-steady film distributions lead to more important alterations to film effectiveness values and flow structure than when quasi-steady behavior is present [4,5]. More recently, Bell et al. [8] and Ligrani and Bell [9] present correlations which give the experimental conditions (for a single row of simple angle, round holes) when significant reductions in protection occur due to the imposed bulk flow pulsations.

Other recent investigations consider film cooling from holes with compound angle orientations (with no imposed pulsations) because lateral momentum components are produced which result

in more uniform film coverage along the surface. Of these investigations, Mehendale and Han [10] consider the effects of high freestream turbulence on leading edge film cooling. Heat transfer coefficients, measured downstream of holes with 90-deg orientation angles, increase as the ratio of coolant to crossflow mass flux increased. In a study which employs compound angle holes with 60 deg orientation angles, Sen et al. [11] present heat transfer rates which increase quite remarkably compared to simple angle injection, provided momentum ratios are large. They also report that the effect of the heat transfer coefficient on overall film cooling performance is stronger as the blowing ratio increases. The authors thus demonstrate that the film cooling performance should be evaluated using the surface heat flux rather than the adiabatic effectiveness alone.

Ligrani and Lee [12] present boundary layer temperature profiles, surface effectiveness distributions, and surface iso-energetic Stanton numbers at high blowing ratios ranging from 1.0 to 4.0 using holes with orientation angles of 50.5 deg. The authors show that overall film cooling performance, based on surface heat flux data, degrades considerably as the blowing ratio increases. Jung and Lee [13] report detailed boundary layer temperature and surface effectiveness measurements made downstream of compound angle holes with orientation angles of 30, 60, and 90 deg. Another recent study by Bell et al. [14] includes results measured downstream of shaped holes with compound angle orientations. According to the authors, the combination of less jet penetration, flow diffusion, and lower velocity gradients from *shaping*, and increased lateral spreading and greater injectant concentrations near the surface from *compound angles*, results in important local and spatially averaged protection benefits.

The present study is different from these other investigations because the combined effects of compound angle orientations and imposed bulk flow pulsations are considered together. Cylindrical film cooling holes with orientation angles of 0, 30, 60, and 90 deg are investigated. In all cases, the inclination angle is fixed at 35 deg. Blowing ratios are 0.5, 1.0, and 2.0, and pulsation frequencies are 0 Hz, 8 Hz, and 36 Hz. Corresponding coolant Strouhal numbers then range from 0.20 to 3.6. Surface heat transfer coefficient distributions are measured using thermochromic liquid crystals. This technique is employed because of its high spatial resolution, which allows detailed surface heat transfer coefficient distributions to be measured just downstream of the injection holes. Surface heat flux ratio distributions are subsequently obtained from these heat transfer coefficient data, along with surface effectiveness data, which are presented in a companion paper [15].

All of these data are valuable because they provide new information on means to prevent the thermal failure of turbine blades exposed to excessive, external heat loads. They are also valuable for the development of new prediction models for film cooling which are aimed at accounting for the combined effects of imposed, bulk flow pulsations, and compound angle orientations.

Experimental Apparatus and Procedures

Experimental apparatus and procedures are similar, in most cases, to ones described by Lee and Jung [15]. Many details are also presented here for the sake of completeness.

Wind Tunnel and Injectant Supply System. A schematic of the wind tunnel and the injectant supply system is shown in Fig. 1(*a*). The wind tunnel is an open-circuit and subsonic facility, with a 6.25 to 1 contraction ratio nozzle and an exit crosssection with dimensions of 0.40 m and 0.28 m. The nozzle leads to the test section, which is a rectangular duct 3.0 m long. At a freestream velocity of 10 m/s, flow at the test section inlet shows excellent spatial uniformity with spanwise velocity variation less than 0.3 percent and a turbulence level less than 0.2 percent. A boundary layer trip wire of 1.8 mm in diameter is located on the test plate just downstream of the nozzle exit. The air, used as the injectant, first flows through an orifice plate followed by two heat exchangers that control the injectant air temperature. The air is then ducted to a plenum chamber and is discharged through the injection holes.

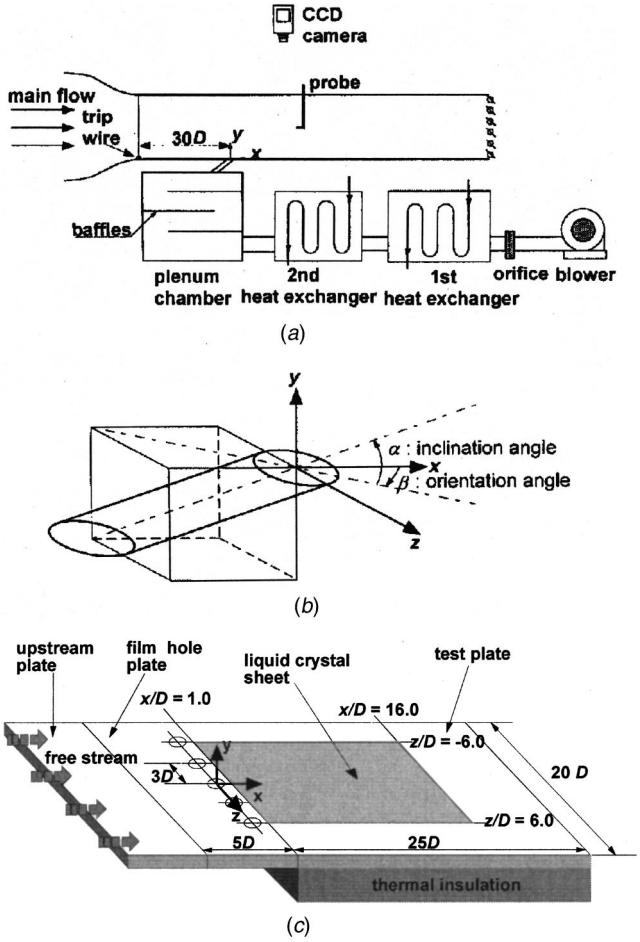

Fig. 1 Schematic diagrams of: (*a*) the experimental apparatus used for heat transfer coefficient measurements, (*b*) the film hole geometry, and (*c*) the test surface, including the coordinate system

Device Employed to Impose Bulk Flow Pulsations. Static pressure pulsations are produced in the test section using an array of rotating shutter blades located at the exit of the test section and driven by a system of timing belts and an electric motor. With bulk flow pulsations of 8 Hz, the coolant Strouhal number, $\mathrm{Sr}_c = 2\pi fL/U_c$, varies from 0.2 to 0.8, while the coolant Strouhal number with 36 Hz pulsations varies from 0.9 to 3.6, depending upon the blowing ratio. This Strouhal number definition gives the time required for the coolant to pass through each hole divided by the time period of one pulsation. Typical values for operating turbines range from 0.2 to 6.0. Coolant Strouhal numbers and non-dimensional pressure parameters at different blowing ratios are listed in Table 1. Here, the nondimensional pressure parameter is defined using

$$\psi = (\Delta P_{\max} - \Delta P_{\min})/\overline{\Delta P} \tag{1}$$

where ΔP is the instantaneous static pressure difference between the plenum and freestream, and $\overline{\Delta P}$ is the time-averaged magnitude of this value.

Experimental Conditions. Experiments are conducted at a fixed freestream velocity of 10 m/s. The injection hole diameter D is 20 mm and its length L is $4D$. The freestream Reynolds number Re_x, determined for a distance between the trip wire and the hole

Table 1 Coolant Strouhal number and pressure perameter values

m	Pulsation Frequency [Hz]			
	8		36	
	Sr_c	Ψ	Sr_c	Ψ
0.5	0.80	1.62	3.60	8.83
1.0	0.40	0.61	1.80	3.43
2.0	0.20	0.25	0.90	1.03

center, is 383,000. The boundary layer thickness (based on $0.99U_\infty$) at the hole center is $0.91D$, the displacement thickness is $0.14D$ and the momentum thickness is $0.10D$. The shape factor of the boundary layer is 1.4, which is typical for a fully developed turbulent boundary layer. Blowing ratios are 0.5, 1.0, and 2.0. Corresponding injectant Reynolds numbers Re_D are 6400, 12,700, and 25,400, respectively.

Injection Hole Configurations. Compound injection angle orientations are identified by two angles, as shown in Fig. 1(*b*). The inclination angle α is defined as the angle between the injection vector at the hole exits and its projection on the x-z plane. The orientation angle β is the angle between the streamwise direction and the projection of the injection vector onto the x-z plane. The inclination angle is fixed at 35 deg, and the orientation angle is positive in the $+z$ direction, as indicated in Fig. 1(*b*). A different injection plate is employed for each orientation angle of 0, 30, 60, and 90 deg. In each injection plate, a row of five holes is located $30D$ downstream of the trip wire as shown in Fig. 1(*c*). The spanwise spacing between the hole centers is $3D$.

Test Plate. As depicted in Fig. 1(*c*), the test plate consists of an upstream plate, one of the four injection plates and the measurement plate. The measurement plate starts at $x/D=1.0$. To prevent unwanted wall temperature variations near the downstream edges of the holes, injection holes are machined in the injection plate, not in the measurement plate. The triangular gap between the injection plate and the measurement plate is filled with polystyrene. The foamed polystyrene in the gap works as a thermal barrier that minimizes the conduction from the injection holes to the measurement plate.

Flow Visualization. To visualize the injectant and determine its distribution along and above the test surface, the injectant air is contaminated with fog. This is accomplished by pressurizing a 50-gal steel drum housing a Rosco model 1500 theatrical fog generator. Fog is produced from the vaporization of a water soluble liquid with this device, and subsequently fed into the diffuser and plenum of the injectant air supply system. The air is then photographed against a black background after it is ejected from the holes. This fog is employed to identify vortex structures and other secondary flow features produced by the compound angle, film cooling holes. Smoke patterns are illuminated using a thin sheet of light provided by a Colotran ellipsoidal No. 550, 1000-W spotlight, and light slits machined in two parallel metal plates, located between the spotlight and the test section. The illuminated, time-varying patterns are recorded at rates as high as 60 frames per second using a Dage-MTI CCD72 camera and control box with a Computar Inc. 12.5 mm, F1.8 lens, connected to a Panssonic AG-1960 type 4-head, multiplex video cassette recorder. The 16.7 ms exposure time of the camera is set by its 60 Hz vertical sweep rate. Recorded images are monitored using a Dage-MTI HR1000 monitor. Images recorded on video tape (in sequence) are then digitized using a Sony DCR-TRV 900 digital video camera recorder. The resulting images are then further processed using Adobe PhotoShop software on a Puwer Macintosh 7500 PC computer, and finally printed using a Panasonic PV-PD 2000 digital photo printer.

Surface Temperature Measurements Using Liquid Crystals. To measure the temperature distribution on the surface downstream of the injection holes, a thermochromic liquid crystal (THC) sheet is employed. The TLC sheet covers the test plate from $x/D=1.0$ to $x/D=16.0$, and from $z/D=-6.0$ to $z/D=+6.0$. The TLC sheet consists of 110-μm-thick polyester film, TLC coating, black paint, and an adhesive layer. The total thickness of the sheet is 240 μm. Beneath the TLC sheet, a 30-μm-thick stainless steel foil is used to generate a uniform surface heat flux. The stainless foil is heated using an AC electrical power supply. The current and voltage across the heating element are measured to calculate the input power. A 12.7-mm-thick polycarbonate plate is attached just beneath the stainless steel foil using adhesive tape. A layer of insulation then follows. Formed polystyrene, which is 50 mm thick, is then placed beneath the insulation. A CCD camera is used to capture the TLC color images, as it is aligned perpendicular to the TLC sheet and located about 1.2 m away. Two 150-W halogen lamps are used to illuminate the TLC sheet.

Various techniques of TLC are available for temperature measurement. Here, a steady-state, hue capturing method is utilized. The liquid crystals employed change color over the temperature range from 25°C to 45°C. With such a bandwidth, the liquid crystal sheet can map the entire isothermal pattern of the test surface from a single image. A robust TLC color-temperature response calibration is then necessary for high accuracy measurements. It is known that the perceived color of the TLC depends on the lighting/viewing arrangement, the spectrum of primary illuminant and background light, and the optical properties of the measurement path as well as temperature. For all measurements, extra care is taken to fix all conditions identical with calibration conditions to avoid unwanted color variations.

Measurement of Other Temperatures. The free-stream and the injectant temperatures are measured with T-type thermocouples that are calibrated in a constant temperature bath with a precision platinum resistance thermometer.

Heat Flux Ratio Determination. According to Eckert [16], the relationship between the heat flux and the heat transfer coefficient on a film-cooled surface is given by

$$q_f = h_f(T_{aw} - T_w) \tag{2}$$

where T_{aw}, T_w, h_f, and q_f denote adiabatic wall temperature, wall temperature, heat transfer coefficient with film cooling, and heat flux with film cooling, respectively. Another way of defining the heat transfer coefficient is given by

$$q_f = h(T_\infty - T_w) \tag{3}$$

Dividing both sides of Eq. (3) by both sides of Eq. (2), and rearranging, it follows that:

$$h/h_f = 1 - \eta[(T_c - T_\infty)/(T_w - T_\infty)] \tag{4}$$

where η is the adiabatic film cooling effectiveness, defined as

$$\eta = (T_{aw} - T_\infty)/(T_c - T_\infty) \tag{5}$$

From Eq. (4), h_f is identical with h when the coolant temperature and the freestream temperature are the same. In this study, the freestream temperature and the injectant temperature are both fixed at 20°C and the wall is heated with a uniform heat flux. The heat transfer coefficient h is then calculated using Eq. (3). Heat transfer coefficient data are then presented in terms of the heat transfer coefficient ratio (h_f/h_o). Here, h_f denotes the heat transfer coefficient with film cooling, whereas h_o is the heat transfer coefficient without film cooling at the same location and same Reynolds number.

To evaluate the reduction of thermal load due to film cooling, the thermal loads with and without film cooling are compared. The heat transfer coefficient without film cooling is expressed using

$$q_o = h_o(T_\infty - T_w) \tag{6}$$

The heat flux ratio can thus be expressed in the form given by

$$q_f/q_o = h_f(T_{aw} - T_w)/h_o(T_\infty - T_w) = (h_f/h_o)(1 - \eta/\theta) \tag{7}$$

where θ is the nondimensional temperature, which ranges from 0.5 to 0.7 for gas turbine blades with film cooling. A value of 0.6, which is typical of a film cooled turbine blade in operation, is used for the heat flux ratio calculation. This is the same θ value used to obtain the effectiveness values in the companion paper [15].

Uncertainty Estimates. Uncertainty estimates are based on 95 percent confidence levels, and determined using procedures described by Kline and McClintock [17] and Moffat [18]. The uncertainty of the heat transfer coefficient ratio is ± 9.5 percent at a typical h_f/h_o value of 1.2, and that of the heat flux ratio is ± 10.1 percent at a typical q_f/q_o of 0.8.

Experimental Results and Discussion

Bulk Flow Pulsation Characteristics. The periodic characteristics of the phase-averaged freestream static pressure are illustrated in Fig. 2. The data are presented for time-averaged blowing ratios of 0.5, 1.0 and 2.0 at pulsation frequencies of 8 and 36 Hz. Here, $\Delta\tilde{P}$ indicates the difference in the phase-averaged static pressure between the plenum and freestream, $\tilde{P}_c - \tilde{P}_\infty$. $\Delta\overline{P}$ is then the difference in the time-averaged static pressures. The pressure data show quantitative alterations to waveforms, which occur as blowing ratio and pulsation frequency are changed. Note that the peak-to-peak amplitude of the phase-averaged freestream velocity variation is fixed at 11 percent of the time-averaged velocity value, regardless of the magnitude of pulsation frequency.

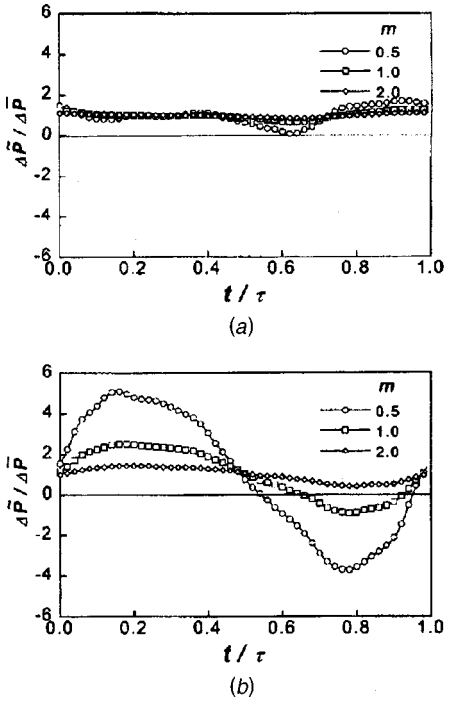

Fig. 2 Normalized, phase-averaged static pressure difference between the injectant plenum and the freestream: (*a*) $f=8$ Hz, (*b*) $f=36$ Hz

Normalized pressure differences $\Delta\tilde{P}/\Delta\overline{P}$ with pulsations imposed at 8 Hz show only slight variations in amplitude as m is changed (Fig. 2(*a*)), although the pressure parameter ψ varies widely from 0.25 to 1.62 (see Table 1). In this case, the coolant Strouhal numbers are less than unity (see Table 1), and thus, the pulsation conditions are located in the quasi-steady regime described by Ligrani et al. [2]. When the pulsation frequency is 36 Hz, Fig. 2(*b*) shows that the normalized pressure difference varies over a wider range of values. This is because the coolant Strouhal number is larger than unity and the injectant behavior is nonquasi-steady [2]. Such variations evidence important coupling between pulsations, and the injectant in the holes and within the plenum. The amplitude of the pressure difference thus increases as the blowing ratio decreases or the coolant Strouhal number increases. Another important feature of the data in Fig. 2(*b*) is apparent for blowing ratios of 0.5 and 1.0. Here, prolonged durations of negative values of $\Delta\tilde{P}$ are observed over the phase-averaged pulsation period. At $m=0.5$, negative values are present over almost half of the period from $t/\tau=0$ to $t/\tau=1$. This implies that the freestream static pressure is higher than the plenum pressure over this time interval, which might cause local ingestion of external boundary layer fluid into the holes.

Local Heat Transfer Coefficient Ratio Distributions. As expected from the pressure pulsation data shown in Fig. 2, the heat transfer coefficient ratio distributions measured with pulsations imposed at 8 Hz deviate little from ones measured with no pulsations. The heat transfer coefficient ratio distributions at 8 Hz pulsations are, therefore, not presented here. Instead, discussion is concentrated on the more interesting 36 Hz pulsations as they affect heat transfer coefficient ratio distributions. Note that baseline heat transfer coefficients used for normalization are measured on the same test surface with no pulsations imposed, and no film cooling.

Figure 3 shows detailed contours of the local heat transfer coefficient ratio (h_f/h_o) with 36 Hz pulsations when $m=0.5$ for four different orientation angles. The value of Sr_c is 3.6 and the dimensionless pressure parameter ψ is 8.83. The effect of 36 Hz pulsations on heat transfer is apparent by comparing with the heat transfer coefficient ratio distributions with no pulsations. For example, with simple angle injection ($\beta=0$ deg), Fig. 3(*a*) shows that heat transfer coefficient ratios are slightly augmented due to 36 Hz pulsations. This includes high heat transfer ratios along the geometrical centerline of each hole just downstream of each hole exit, which is caused by the periodic up-and-down motion of the injectant trajectory when pulsations are present.

When the orientation angle β is 30 deg, as shown in Fig. 3(*b*), the heat transfer coefficient ratio distribution is altered by the pulsations in the high heat transfer coefficient region near the injection holes ($1.5 \leqslant x/D \leqslant 5.0$). Without pulsations, the heat transfer coefficient ratio is high near the central hole in the region of $-1.0 \leqslant z/D \leqslant 0.0$. Whereas with pulsations, the high heat transfer coefficient ratio region near the central hole moves to $0.0 \leqslant z/D \leqslant 1.0$. This is because the injectant trajectory pulsates not only in the vertical direction (i.e., in the y-z plane), but also in the spanwise direction (i.e., in the x-z plane) when compound angle injection is employed. This is supported by results from an experiment on a flat plate with no film cooling holes, but with bulk flow pulsations, which show that pulsations do not affect the heat transfer on the surface because the freestream Strouhal number based on the boundary layer thickness is much less than unity. However, introduction of the injectant into pulsating flow creates increased disturbances and additional augmentations of heat transfer coefficient ratios in the near hole region.

Figures 3(*c*) and (*d*) illustrate additional important effects of the pulsations on local heat transfer coefficient ratios. Here, heat transfer coefficient ratios increase slightly with orientation angle. In addition, comparisons with distributions measured with no

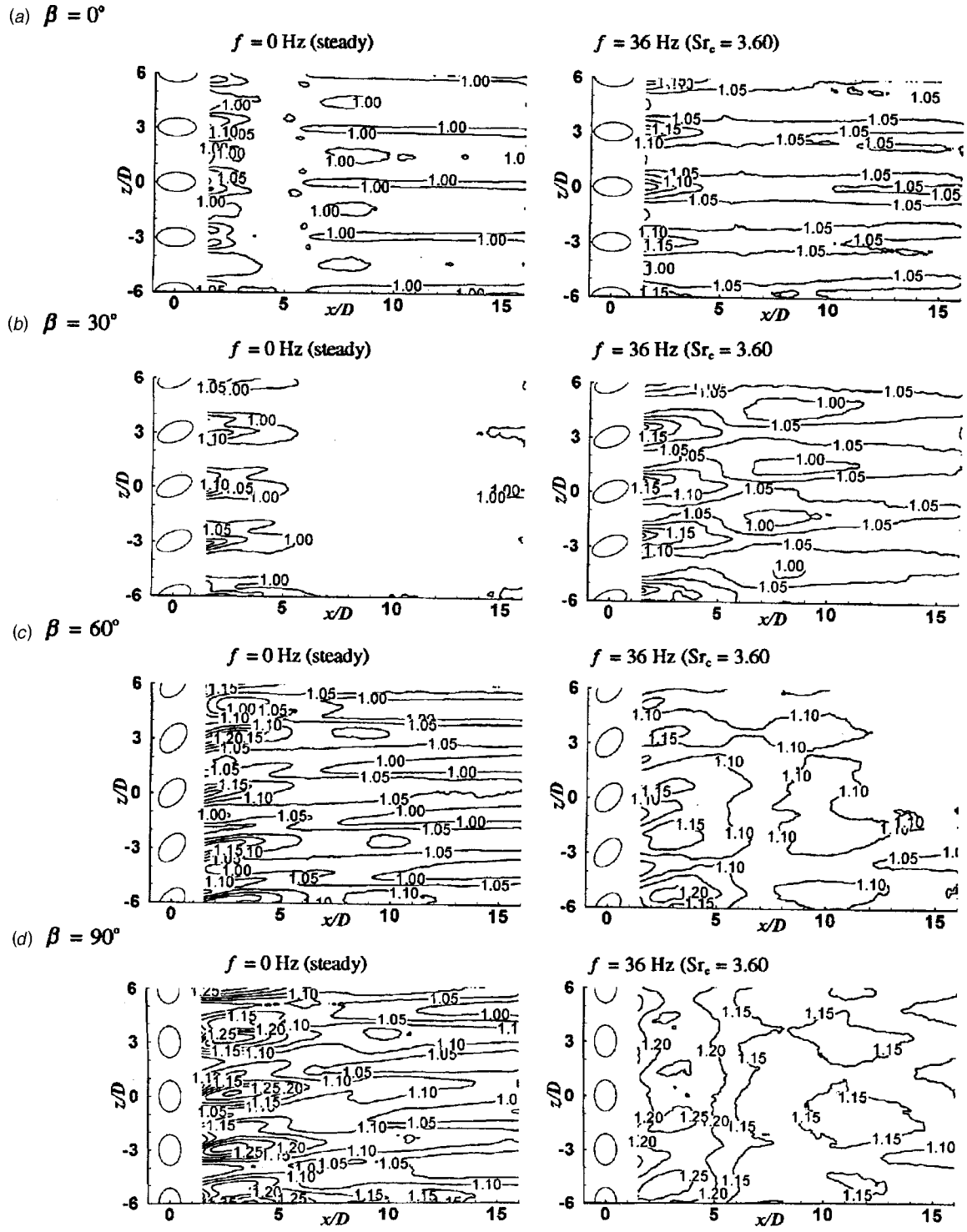

Fig. 3 Local surface heat transfer coefficient ratio distributions with and without imposed bulk flow pulsations at f=36 Hz for m=0.5: (*a*) β=0 deg, (*b*) β=30 deg, (*c*) β=60 deg, (*d*) β=90 deg

pulsations reveal that heat transfer coefficient ratio distributions become more uniform downstream of the holes when 36 Hz pulsations are present. The uniform distributions with large orientation angles also result from the swaying motion of the injectant. This is present because the injectant issued from compound angle holes contains significant spanwise momentum components. When large static pressure pulsations are applied to compound angle injection, the pressure difference behavior in Fig. 2 leads to changes of the injectant mass flow rate over each pulsation period. These changes in the injection rate cause alterations to the strength of the lateral momentum of the injectant over each pulsation period. The injectant trajectory then oscillates in the spanwise direction. As a result, the surface region covered by the injectant is widened, and the heat transfer coefficient ratio distribution becomes more uniform compared to the corresponding case with no pulsations. The smoothing effect is more prominent when the orientation angle is large because of higher magnitudes of lateral momentum.

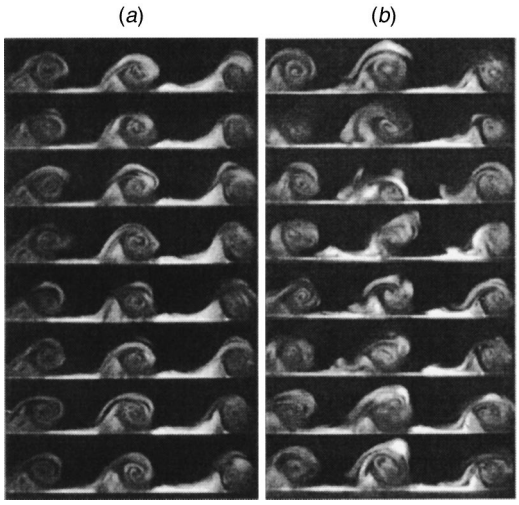

Fig. 4 Flow visualization results in an illuminated spanwise-normal plane located at $x/D=4.3$ for $\beta=30$-deg compound angle holes with $m=0.7$, (*a*) $f=0$ Hz, (*b*) $f=0.5$ Hz

Flow Visualization Results. The variations to injectant trajectories produced by pulsations are further illustrated by the flow visualization results in Figs. 4(*a*),(*b*). These are obtained in an illuminated spanwise-normal (y-z) plane located at $x/D=4.3$ downstream of the $\beta=30$ deg compound angle holes. As mentioned earlier, the injectant plenum is contaminated with fog so that injectant distributions are apparent during downstream advection. To increase the visibility and detail with the images, the fog patterns are videotaped at lower speeds and lower pulsation frequencies than used to obtain the heat transfer coefficient data. Freestream velocity is 0.5 m/s, and spatially-averaged film velocity in the holes is 0.35 m/s, giving a time-averaged blowing ratio m of 0.7. The data in Figs. 4(*a*),(*b*) are obtained using f of 0 Hz, and 0.5 Hz, respectively. Figures 4(*a*),(*b*) both show a time-sequence of flow images, arranged so that time increases as one proceeds down the page. With a 0.26-s time interval between adjacent images in the latter case, the eight sequential images then span one complete 2-s pulsation period.

In each image, fog patterns located just downstream of about three film cooling holes are apparent. A tilted and skewed vortex pair is then apparent in each fog pattern downstream of each of these holes. One vortex in each pair is large and readily apparent. The second is much smaller and located closer to the test surface. These differences are due to the orientations of the holes, the spanwise components of momentum that are produced by them, and the tilted orientation of the injectant as it emerges from each hole.

In Fig. 4(*a*) with no pulsations present, only small variations of vortex pair structure are evident as time increases. When 0.5 Hz pulsations are imposed, the coolant Strouhal number Sr_c is 0.72, and vortex pair changes with time in Fig. 4(*b*) are much more dramatic. These include convolutions and distortions of each vortex. Of particular interest are the changes to the distributions of film fluid near the test surface. In the first two images, most of this is concentrated beneath each vortex pair. However, substantial film concentrations are advected along the surface to the left of the each vortex pair (i.e., in the positive z direction) in the next four images (where all images are viewed looking upstream). This disappears in the last two images, as the cycle of events prepares to repeat itself. Such variations then lead to surface heat transfer coefficient distributions such as the ones shown in Fig. 3(*b*), except that the effects of the imposed pulsations (on local flow structure) are expected to be even much more dramatic and substantial when Sr_c increases to 3.6.

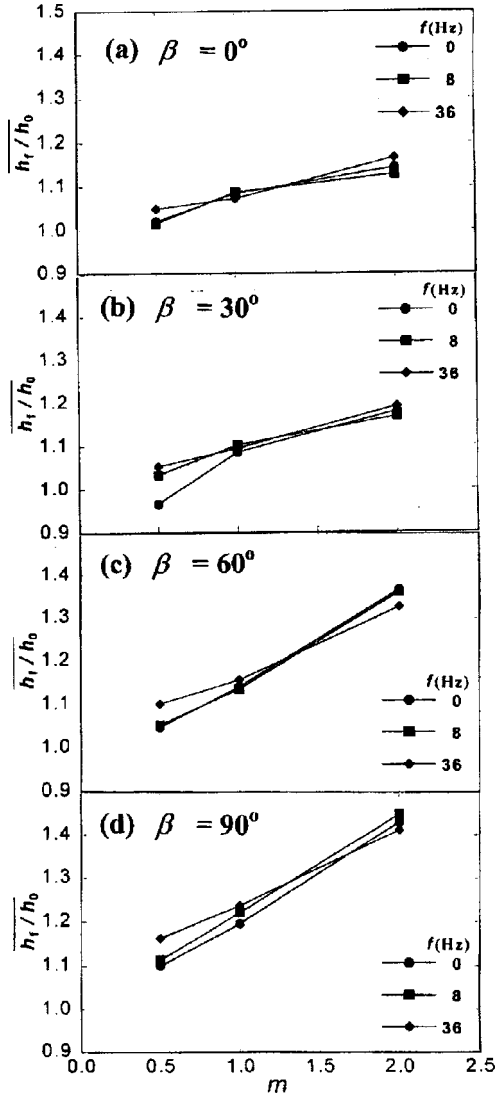

Fig. 5 Spatially averaged surface heat transfer coefficient ratios with imposed bulk flow pulsations at f of 0 Hz, 8 Hz, and 36 Hz for $m=0.5$: (*a*) $\beta=0$ deg, (*b*) $\beta=30$ deg, (*c*) $\beta=60$ deg, (*d*) $\beta=90$ deg

Spatially Averaged Heat Transfer Coefficient Ratio Distributions. Spatially averaged heat transfer coefficient ratios h_f/h_o are compared in Figs. 5 and 6. Note that all spatial averages are obtained over x/D from 2 to 16, and over z/D from -6 to $+6$.

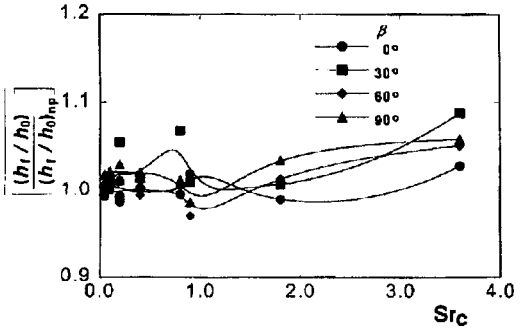

Fig. 6 Normalized spatially averaged surface heat transfer coefficient ratios as dependent upon coolant Strouhal number Sr_c and orientation angle β

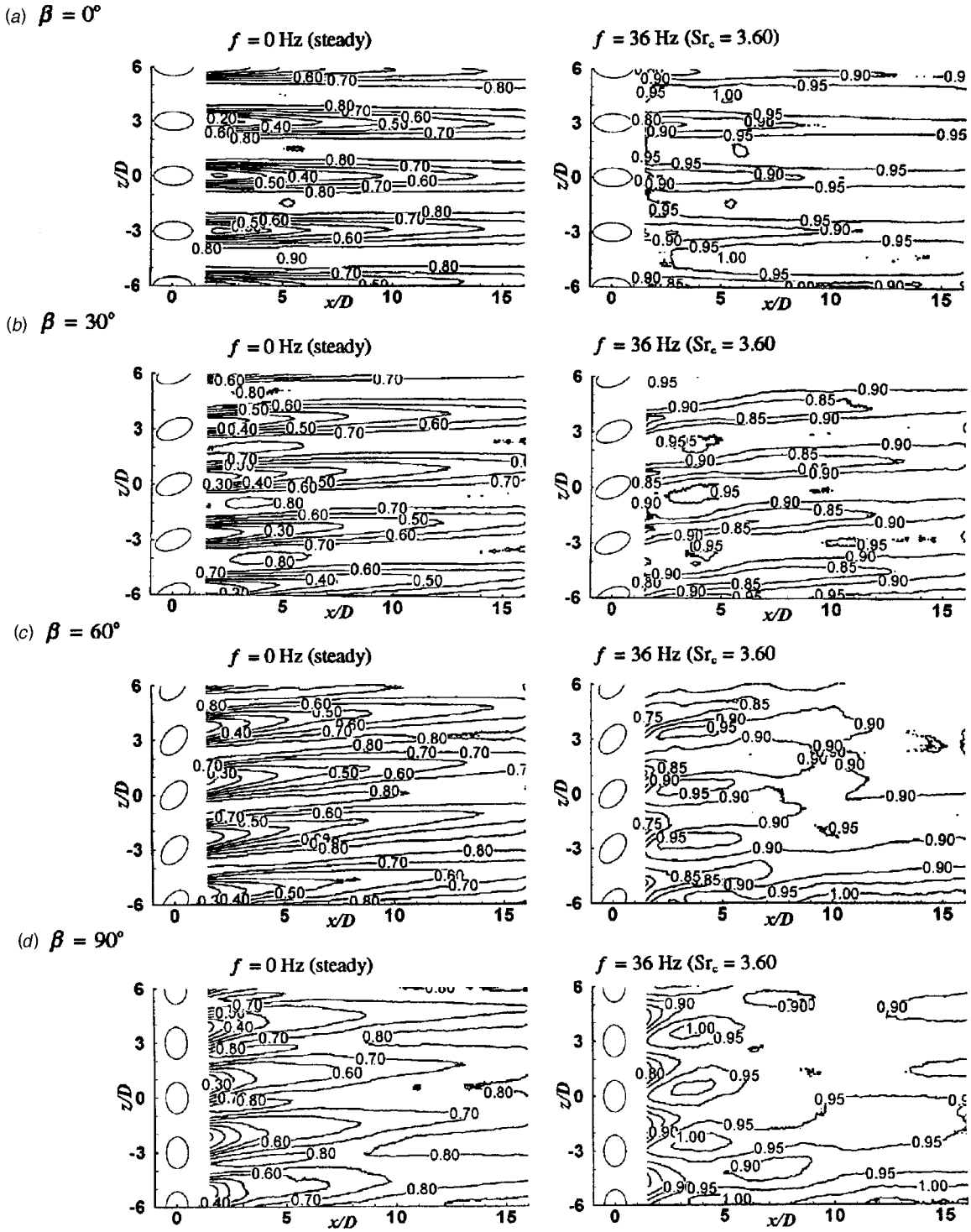

Fig. 7 Local surface heat flux ratio distributions with and without imposed bulk flow pulsations at $f=36$ Hz for $m=0.5$: (*a*) $\beta=0$ deg, (*b*) $\beta=30$ deg, (*c*) $\beta=60$ deg, (*d*) $\beta=90$ deg

From Fig. 5, it is evident that changing the orientation angle β plays a more dominant role than changing the pulsation frequency in augmenting magnitudes of spatially averaged heat transfer coefficients. Increasing the blowing ratio m also contributes to enhancement of h_f/h_o values, with more pronounced influences as the orientation angle increases.

Even though *local* heat transfer coefficient ratio distributions change considerably when the pulsation frequency changes, particularly at large orientation angles (see Fig. 3), the net result is more uniform distributions, with little changes to *spatially averaged* values. This is illustrated by the spatially averaged results in Fig. 5, where the only changes of any significance due to pulsations are measured when the blowing ratio m is 0.5. This is also shown by the results presented in Fig. 6, where ratios of film cooled heat transfer coefficients with pulsations, normalized by ratios with no pulsations, are presented. Here, changes to spatially averaged heat transfer coefficient ratios from flow pulsations are again relatively minor.

Local Heat Flux Ratio Distributions. Film cooling performance is best evaluated using the heat flux ratio q_f/q_o, which is the ratio of the heat flux with film cooling to that without film cooling [11]. A heat flux ratio value less than unity then indicates that the thermal load to the wall is reduced by film cooling.

According to Eq. (7), the adiabatic film cooling effectiveness and the heat transfer coefficient ratio are needed to determine the heat flux ratio. Adiabatic film cooling effectiveness magnitudes for the same hole geometries and experimental conditions investigated here are given by Lee and Jung [15]. For a ratio of coolant density to freestream density just less than 1, the effects of pulsations on adiabatic film cooling effectiveness distributions are also discussed by these authors, including dependence on the coolant Strouhal number. According to them, pulsations imposed at low coolant Strouhal numbers do not alter the effectiveness distributions by significant amounts. Minimal changes to heat flux ratios are thus expected for $f=8$ Hz, because heat transfer coefficients are also affected by only very small amounts when pulsations are imposed at this frequency. Consequently, heat flux ratio distributions are presented and discussed here only for an imposed pulsation frequency f of 36 Hz.

Such heat flux ratio data are presented and compared to data obtained with no bulk flow pulsations in Fig. 7 for a time-averaged blowing ratio m of 0.5. The corresponding coolant Strouhal number is 3.6, which is the highest value employed in the present investigation. From Fig. 7, it is evident that heat flux ratio distributions are altered significantly by the pulsations. With no pulsations present, heat flux ratio values are relatively small (which indicates good film protection), with lower magnitudes over regions where large injectant concentrations contact the surface, and higher values over z/D values positioned between the holes. Heat flux ratio values with no pulsations cover a wide range of values, but are less than unity over almost the entire surface. Such low heat flux ratios provide good film protection at a blowing ratio m of 0.5 (when no imposed pulsations are present) as a result of higher effectiveness magnitudes and lower heat transfer coefficients.

When imposed bulk flow pulsations at 36 Hz are present, Fig. 7 shows that heat flux ratio values are larger, with more uniform values over the test surface. For example, in Fig. 7(*a*) for $\beta=0$ deg, the difference between maximum and minimum values of the heat flux ratio is 0.36, compared to 0.78 when no pulsations are present. This is because of significant decreases of film cooling effectiveness magnitudes, as well as increased heat transfer coefficient ratios, which are distributed more uniformly over the surface. This occurs when pulsations are imposed regardless of the orientation angle of the film cooling holes, and results in significant local sugmentations of thermal loads to turbine blades.

Spatially Averaged Heat Flux Ratio Distributions. Spatially averaged heat flux ratios are presented in Figs. 8 and 9. In the first of these figures, q_f/q_0 values measured with pulsations imposed at 8 Hz are, in most cases, nearly the same as values measured when no pulsations are imposed ($f=0$ Hz), regardless of the values of β and m.

Much larger increases in heat flux ratio (and more significant reductions of film cooling protection relative to $f=0$ Hz data) are then present for $f=36$ Hz. In this case, heat flux ratio increases become larger as the blowing ratio m decreases for each value of the orientation angle β considered. This is also illustrated by the results in Fig. 9, where heat flux ratios with pulsations, normalized by ratios with no pulsations, are given. Such variations are also consistent with results described by Ligrani et al. [2], since coolant Stroubal numbers are greater than 1, ranging from 1.8 to 3.6 as m decreases from 1.0 to 0.5. Heat flux ratio increases with $f=36$ Hz are then quite small (relative to the $f=0$ Hz data) when m is equal to 2.0 because the coolant Strouhal number is 0.9, which is smaller than unity.

Figure 8 also shows that the pulsations imposed at 36 Hz

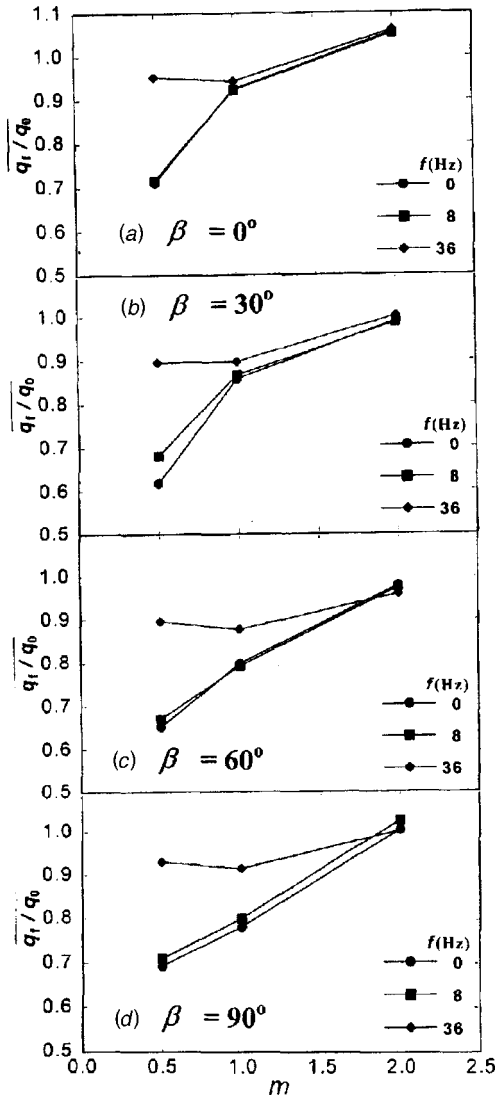

Fig. 8 Spatially-averaged surface heat flux ratios with imposed bulk flow pulsations at f of 0 Hz, 8 Hz, and 36 Hz for $m=0.5$: (*a*) $\beta=0$, (*b*) $\beta=30$, (*c*) $\beta=60$, (*d*) $\beta=90$ deg

have a more substantial effect on heat flux ratio increases (relative to $f=0$ Hz data) as the orientation angle increases. For example, for $m=1.0$, the incremental increase in $\overline{q_f/q_o}$ with simple angle injection is only 2 percent (Fig. 8*a*). It increases to 5, 10 and 18 percent as the orientation angle varies to 30, 60, and 90 deg, respectively, (Figs. 8(*b*),(*d*)). The indicates more severe pulsation effects, and greater reductions in protection, as the spanwise component of momentum from the film cooling holes increases.

With no pulsations present ($f=0$ Hz), Fig. 8 also shows heat flux ratios at $m=0.5$ which are much lower than values when $m=1.0$, especially at smaller orientation angles. However, with 36 Hz pulsations, heat flux ratio values at $m=1.0$ are about the same as or even slightly lower than values for $m=0.5$. This is partially due to static pressure variations like the ones shown in Fig. 2. For m of 0.5 and 1.0, this figure indicates that pulsations imposed at 36 Hz produce pressure differences between the plenum and freestream which can cause ingestion of external flow into the holes over substantial portions of each pulsation period.

Figure 9 provides additional insight into these effects. Here, heat flux ratios with pulsations, normalized by ratios with no pulsations, show a substantial increase as the coolant Strouhal num-

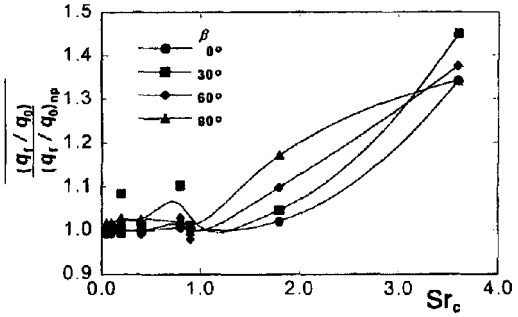

Fig. 9 Normalized spatially averaged surface heat flux ratios as dependent upon coolant Strouhal number Sr_c and orientation angle β

ber becomes greater than 1. Note that data for all four compound angle orientation angles, 0, 30, 60, and 90 deg, are included. Such behavior is thus consistent with other flow visualization and flow structure results [2,4,5], but over a wider range of experimental conditions and film hole geometries.

Summary and Conclusions

Presented are heat transfer coefficient and heat flux data on a surface film cooled with compound angle holes, and subject to imposed bulk flow pulsations. Film hole orientation angles are 0, 30, 60, and 90 deg. The film hole inclination angle is fixed at 35 deg. The frequencies of imposed bulk flow pulsations are 8 and 36 Hz at a peak-to-peak velocity amplitude of 11 percent of the time-averaged freestream velocity. The blowing ratios considered are 0.5, 1.0, and 2.0, which correspond to coolant Strouhal numbers from 0.2 to 3.6. Detailed surface heat transfer coefficient distributions are measured using thermochromic liquid crystals. Distributions of surface heat flux ratios are then evaluated from these heat transfer coefficient data, and adiabatic film cooling effectiveness values from another source [15]. Some important observations are noted and summarized in the following:

1 The pulsations produce important changes to *spatially resolved* distributions of surface heat flux ratios, and surface heat transfer coefficient ratios, mainly as a result of more uniform film coverage over the test surface (compared to situations when no pulsations are employed). This is a result of periodic changes to the magnitude of spanwise momentum in the injectant over each pulsation period. This then causes the film from compound angle holes to oscillate in both the normal and spanwise directions after it leaves the holes.

2 Only small changes to *spatially averaged* heat transfer coefficient ratios are produced by the pulsations, relative to distributions measured with no pulsations.

3 Spatially averaged surface heat flux ratios increase considerably at coolant Strouhal numbers larger than unity. Relative to values measured with no pulsations, rates of increase are higher for larger orientation angles and smaller blowing ratios.

4 Coolant Strouhal numbers greater than 1 generally indicate reductions in the protection provided by film cooling, relative to situations when no pulsations are imposed. This is consistent with other flow visualization and flow structure results [2,4,5], but over a wider range of experimental conditions and film hole geometries.

Acknowledgments

Mr. Brett Wagstaff and Mr. Venkata Krishnan are acknowledged because of their efforts in obtaining the flow visualization results presented in Figs. 4(*a*–*b*). The portions of this project conducted at the University of Utah were sponsored by the National Science Foundation (Grant No. CTS-9615196).

Nomenclature

D = film hole diameter
f = imposed pulsation frequency
h = heat transfer coefficient $=q/(T_w-T_\infty)$
L = film hole length
m = time-averaged blowing ratio $=\rho_c U_c/\rho_\infty U_\infty$
P = static pressure
q = local surface heat flux
Re_D = injectant Reynolds number $=DU_c/v$
Re_x = freestream Reynolds number $=XU_\infty/v$
Sr_c = coolant Strouhal number $=2\pi fL/U_c$
T = temperature
t = time
U = time-averaged velocity
X = streamwise coordinate, measured from trip wire
x = streamwise coordinate, measured from downstream edges of film cooling holes
y = normal coordinate, measured from test surface
z = spanwise coordinate, measured from spanwise centerline
α = inclination angle
β = orientation angle
η = local adiabatic film cooling effectiveness $=(T_{aw}-T_\infty)/(T_c-T_\infty)$
θ = nondimensional temperature $=(T_w-T_\infty)/(T_c-T_\infty)$
ν = kinematic viscosity
τ = imposed pulsation time period
ψ = pressure pulsation parameter $=(\Delta P_{\max}-\Delta P_{\min})/\overline{\Delta P}$
ΔP = instantaneous static pressure difference between plenum and freestream

Subscripts

aw = adiabatic wall value
c = coolant or plenum value
f = film cooling value
max = maximum value
min = minimum value
np = no pulsations value
o = no film cooling value
w = wall value
∞ = freestream value

Superscripts

$\tilde{}$ = phase-averaged value
$\bar{}$ = time-averaged, or space-averaged value

References

[1] Arts, T., and Bourguignon, A. E., 1990, "Behavior of a Coolant Film With Two Rows of Holes Along the Pressure Side of a High-Pressure Nozzle Guide Vane," ASME J. Turbomach., **112**, pp. 512–521.
[2] Ligrani, P. M., Gong, R., Cuthrell, J. M., and Lee, J. S., 1996, "Bulk Flow Pulsations and Film Cooling: Part 1, Injectant Behavior," Int. J. Heat Mass Transf., **39**, pp. 2271–2282.
[3] Abhari, R. S., and Epstein, A. H., 1994, "An Experimental Study of Film Cooling in a Rotating Transonic Turbine," ASME J. Turbomach., **116**, pp. 63–70.
[4] Ligrani, P. M., Gong, R., Cuthrell, J. M., and Lee, J. S., 1996, "Bulk Flow Pulsations and Film Cooling: Part 2, Flow Structure and Film Effectiveness," Int. J. Heat Mass Transf., **39**, pp. 2283–2292.
[5] Ligrani, P. M., Gong, R., Cuthrell, J. M., and Lee, J. S., 1997, "Effects of Bulk Flow Pulsations on Film-Cooled Boundary Layer Structure," ASME J. Fluids Eng., **119**, pp. 56–66.
[6] Sohn, D. K., and Lee, J. S., 1997, "The Effect of Bulk Flow Pulsations on Film Cooling from Two Rows of Holes," ASME Paper No. 97-GT-129.
[7] Jung, I. S., and Lee, J. S., 1998, "Effect of Bulk Flow Pulsations on Film Cooling From Spanwise Oriented Holes," ASME Paper No. 98-GT-211.
[8] Bell, C. M., Ligrani, P. M., Hull, W. A., and Norton, C. M., 1999, "Film Cooling Subject to Bulk Flow Pulsations: Effects of Blowing Ratio, Freestream Velocity, and Pulsation Frequency," Int. J. Heat Mass Transf., **42**, No. 23, pp. 4333–4344.
[9] Ligrani, P. M., and Bell, C. M., 2001, "Film Cooling Subject to Bulk Flow Pulsations: Effects of Density Ratio, Hole Length-to-Diameter Ratio, and Pulsation Frequency," Int. J. Heat Mass Transf., **44**, pp. 2005–2009.

[10] Mehendale, A. B., and Han, J.-C., 1992, ''Influence of High Mainstream Turbulence on Leading Edge Film Cooling Heat Transfer,'' ASME J. Turbomach., **114**, pp. 707–715.
[11] Sen, B., Schmidt, D. L., and Bogard, D. G., 1996, ''Film Cooling With Compound Angle Holes: Heat Transfer,'' ASME J. Turbomach., **118**, pp. 800–806.
[12] Ligrani, P. M., and Lee, J. S., 1996, ''Film Cooling From a Single Row of Compound Angle Holes at High Blowing Ratios,'' Int. J. Rotating Mach., **2**, pp. 259–267.
[13] Jung, I. S., and Lee, J. S., 2000, ''Effects of Orientation Angles on Film Cooling Over a Flat Plate: Boundary Layer Temperature Distributions and Adiabatic Film Cooling Effectiveness,'' ASME J. Turbomach., **122**, pp. 153–160.
[14] Bell, C. M., Hamakawa, H., and Ligrani, P. M., 2000, ''Film Cooling From Shaped Holes,'' ASME J. Heat Transfer, **122**, No. 2, pp. 224–232.
[15] Lee, J. S., and Jung, I. S., 2002, ''Effects of Bulk Flow Pulsations on Film Cooling With Compound Angle Holes,'' Int. J. Heat Mass Transf., accepted for publication.
[16] Eckert, E. R. G., 1984, ''Analysis of Film cooling and Full-Coverage Film Cooling of Gas Turbine Blades,'' ASME J. Eng. Gas Turbines Power, **106**, pp.206–213.
[17] Kline, S. J., and McClintock, F. A., 1953, ''Describing Uncertainties in Single Sample Experiments,'' Mech. Eng. (Am. Soc. Mech. Eng.), **75**, Jan., pp. 3–8.
[18] Moffat, R. J., 1988, ''Describing the Uncertainties in Experimental Results,'' Exp. Therm. Fluid Sci., **1**, No. 1, pp. 3–17.

Unsteady Flow/Quasi-Steady Heat Transfer Computations on a Turbine Rotor and Comparison With Experiments

T. Korakianitis
Department of Mechanical Engineering,
University of Glasgow,
Glasgow G12 8QQ, United Kingdom

P. Papagiannidis
Frigoglass,
Patras, Greece

N. E. Vlachopoulos
Panafon SA,
Athens, Greece

The unsteady flow in stator–rotor interactions affects the structural integrity, aerodynamic performance of the stages, and blade-surface heat transfer. Numerous viscous and inviscid computer programs are used for the prediction of unsteady flows in two-dimensional and three-dimensional stator–rotor interactions. The relative effects of the various components of flow unsteadiness on heat transfer are under investigation. In this paper it is shown that for subsonic cases, the reduced frequency parameter for boundary-layer calculations is about two orders of magnitude smaller than the reduced frequency parameter for the core flow. This means that for typical stator–rotor interactions, the unsteady flow terms are needed to resolve the location of disturbances in the core flow, but in many cases the instantaneous disturbances can be input in steady-flow boundary-layer computations to evaluate boundary-layer effects in a quasi-steady approximation. This hypothesis is tested by comparing computations with experimental data on a turbine rotor for which there are extensive experimental heat transfer data available in the open literature. An unsteady compressible inviscid two-dimensional computer program is used to predict the propagation of the upstream stator disturbances into the downstream rotor passages. The viscous wake (velocity defect) and potential flow (pressure fluctuation) perturbations from the upstream stator are modeled at the computational rotor–inlet boundary. The effects of these interactions on the unsteady rotor flow result in computed instantaneous velocity and pressure fields. The period of the rotor unsteadiness is one stator pitch. The instantaneous velocity fields on the rotor surfaces are input in a steady-flow differential boundary-layer program, which is used to compute the instantaneous heat transfer rate on the rotor blades. The results of these quasi-steady heat-transfer computations are compared with the results of unsteady heat transfer experiments and with the results of previous unsteady heat transfer computations. The unsteady flow fields explain the unsteady amplitudes and phases of the increases and decreases in instantaneous heat transfer rate. It is concluded that the present method is accurate for quantitative predictions of unsteady heat transfer in subsonic turbine flows.
[DOI: 10.1115/1.1405419]

Introduction

The flow between stator and rotor blade rows in turbomachinery cascades is inherently three-dimensional and unsteady. Demands for improved performance, fewer stages, and fewer blades per stage result in highly optimized and highly loaded airfoils that operate at continuously increasing gas and alloy temperatures. The sources of two-dimensional flow unsteadiness between the rotor and the stator are: viscous velocity wakes shed from the trailing edge of the stator; inviscid potential flow variations in time and space caused by the relative motion of the lifting surfaces; two-dimensional vortices shed at the stator trailing edge; flutter of both cascades; and the effect of flow changes due to cooling flows in high-pressure high-temperature turbine stages. Three-dimensional disturbances include the effects of passage vortices, end-wall effects, and radial flows. In order to analyze these flows and design reliable engines, we need to understand the effects of unsteady flow aerodynamics and unsteady heat transfer on airfoil and engine performance. This has resulted in a series of numerical and experimental investigations on unsteady flow and unsteady heat transfer. Stator–rotor computations are in common use [1–8]. Other investigators [9–17] have used unsteady flow programs to study the effect of upstream and downstream disturbances on blade flows, and have conducted experimental unsteady aerodynamic investigations [18–20]. Unsteady heat transfer experiments and computations, such as [21–31], are essential to understanding these processes.

Previous investigations [11–15] interpreted the aerodynamic effects of two-dimensional propagation of the combination of viscous wakes and potential flow (static pressure perturbation) in turbine passages. Incoming flow disturbances were modeled into the computational flow field of infinitely rigid uncooled downstream rotors, neglecting the effects of two-dimensional vortex shedding. The conclusion was that the aerodynamic unsteadiness (unsteady pressure and velocity fields) is a function of the stator-to-rotor pitch ratio R ($R \equiv N_{rb}/N_{sb} = S_{sb}/S_{rb}$) and of the axial gap d between blade rows. For typical gaps ($d \approx 0.30$) and for small values of R ($R < 1.5$), the wake disturbances dominated the unsteadiness onto the downstream cascade, while the potential-flow disturbance from the upstream cascade decays before it affects the downstream cascade significantly. For larger values of R ($R > 2.5$), the wake disturbance effect onto the downstream blades was dwarfed by the potential-flow disturbance. For intermediate values of R ($R \approx 2$), both disturbances influence the unsteady flow fields. The different mechanisms of propagation of the two disturbances and their phase effects on unsteady flow (functions of R

Contributed by the International Gas Turbine Institute and presented at the 38th International Gas Turbine and Aeroengine Congress and Exposition, Cincinnati, Ohio, May 24–27, 1993. Manuscript received at ASME Headquarters March, 1993; revised manuscript received August, 2001. Paper No. 93-GT-145. Associate Editor: H. Lukas.

and d) were explained. The combined interaction results in complex patterns of unsteady pressure and velocity regions influencing the forcing functions, stress levels, and blade heat transfer.

This paper shows theoretically, and demonstrates by comparing computations with experiments, that the amplitudes and phases of unsteady heat transfer in high subsonic turbines can be accurately predicted using unsteady-inviscid-flow and quasi-steady heat-transfer computations; and identifies the instantaneous (quasi-steady) convection as the major heat transfer mechanism. The unsteady two-dimensional inviscid computations predict the location of instantaneous disturbances in the rotor core flow using disturbance–rotor models of stator–rotor interactions. In order to predict the instantaneous location of the unsteady disturbances accurately, it is essential to model correctly the values of R and d, and the combined wake and potential-flow interactions. Three-dimensional unsteady inviscid flow computations would be required in cases where the flow has strong three-dimensional gradients. The resultant instantaneous velocities are input in a steady-flow finite-difference boundary-layer program, which is used to predict the instantaneous heat transfer rates at the corresponding times. The computed amplitudes and phases of unsteady heat transfer rates agree well with experimental measurements.

Theory and Hypothesis

The unsteady continuity, momenta, and energy equations are:

$$\frac{\partial \rho}{\partial t}+\nabla\cdot(\rho\vec{V})=0$$

$$\rho\frac{\partial \vec{V}}{\partial t}+\rho\vec{V}\cdot\nabla\vec{V}=-\nabla p+\nabla\cdot\tilde{\tau}+\rho\vec{f} \tag{1}$$

$$\rho\frac{\partial e_t}{\partial t}+\rho\vec{V}\cdot\nabla e_t=-p\nabla\vec{V}-\nabla\vec{q}+\varphi$$

Assuming that shearing in the core of the unsteady flow (outside the boundary layer) is less dominant than the core unsteady flow, the friction terms and dissipation function are dropped from Eq. (1). The resulting nondimensional equations for unsteady two-dimensional inviscid stator flows are

$$\Omega_{cf}\frac{\partial \mathbf{U}^*}{\partial t^*}+\frac{\partial \mathbf{F}^*}{\partial x^*}+\frac{\partial \mathbf{G}^*}{\partial y^*}=0 \tag{2}$$

where $\mathbf{U}^*$, $\mathbf{F}^*$, and $\mathbf{G}^*$ are four-component vectors given by

$$\mathbf{U}^*=\begin{pmatrix}\rho^*\\ \rho^*\mathrm{M}_x\\ \rho^*\mathrm{M}_y\\ \rho e_t^*\end{pmatrix};\quad \mathbf{F}^*=\begin{pmatrix}\rho^*\mathrm{M}_x\\ \rho^*\mathrm{M}_x^2+p^*\\ \rho^*\mathrm{M}_x\mathrm{M}_y\\ \rho\mathrm{M}_x h_t^*\end{pmatrix};$$

$$\mathbf{G}^*=\begin{pmatrix}\rho^*\mathrm{M}_y\\ \rho^*\mathrm{M}_x\mathrm{M}_y\\ \rho^*\mathrm{M}_y^2+p^*\\ \rho^*\mathrm{M}_y h_t^*\end{pmatrix} \tag{3}$$

For unsteady rotor flows, the equations are slightly modified to account for the centrifugal forces (the momentum equations) and for rotor work (the energy equation). Ω_{cf} is the reduced frequency parameter for the core flow. Many definitions of Ω_{cf} appear in the literature, but for the purposes of this paper it is a measure of the time required for a disturbance to pass through the rotor (modeled by b_{rb}/a_0), divided by the time between successive disturbances entering the rotor (or for the rotor to traverse the distance between two stator trailing edges, S_{sb}/V_{rb}). (This definition is slightly different from $\tilde{\omega}=2\pi\Omega_{cf}/\mathrm{M}_{x,0}$ used in our previous investigations.) Here

$$\Omega_{cf}\equiv\frac{b_{rb}}{a_0}\frac{V_{rb}}{S_{sb}}=\frac{V_{rb}}{a_0}\cdot\frac{b_{rb}}{S_{rb}}\cdot\frac{1}{R} \tag{4}$$

Starting from Eq. (1) and using the thin boundary layer approximation, the nondimensional unsteady boundary layer equations along the two-dimensional blade surface (along surface lengths s) become

$$\Omega_{bl}\frac{\partial \rho^*}{\partial t^*}+\frac{\partial(\rho^*\mathrm{M}_x)}{\partial x^*}+\frac{\partial(\rho^*\mathrm{M}_y)}{\partial y^*}=0$$

$$\Omega_{bl}\rho^*\frac{\partial \mathrm{M}_x}{\partial t^*}+\rho^*\mathrm{M}_x\frac{\partial \mathrm{M}_x}{\partial x^*}+\rho^*\mathrm{M}_y\frac{\partial \mathrm{M}_x}{\partial y^*}$$

$$=\rho_e^*\mathrm{M}_{x,e}\frac{d\mathrm{M}_{x,e}}{dx^*}+\frac{\mathrm{M}_{x,0}}{\mathrm{Re}_\theta}\frac{\partial \tau_{xy}^*}{\partial y^*} \tag{5}$$

$$\Omega_{bl}\rho^*\frac{\partial h_t^*}{\partial t^*}+\rho^*\mathrm{M}_x\frac{\partial h_t^*}{\partial x^*}+\rho^*\mathrm{M}_y\frac{\partial h_t^*}{\partial y^*}$$

$$=\frac{\mathrm{M}_{x,0}}{\mathrm{Re}_\theta}\left[\frac{\partial}{\partial y^*}\left(\frac{\dot{q}^*}{\mathrm{Pr}}+\mathrm{M}_x\tau_{xy}^*\right)\right]$$

where a_0 is the stagnation sonic velocity at inlet and

$$\mathrm{Re}_\theta\equiv\rho_0 c_x\theta/\mu_l$$

$$\mathrm{M}_{x,0}\equiv c_x/a_0$$

$$\tau_{xy}^*=\mu_{eq}^*\frac{\partial \mathrm{M}_x}{\partial y^*}$$

$$\mu_{\mathrm{eq}}^*=1+\lambda\mu_{\mathrm{tu}}/\mu_l=1+\lambda\,\mathrm{Pr}_{\mathrm{tu}}/\mathrm{Pr}_l$$

$$\dot{q}^*=\frac{\partial T^*}{\partial y^*}$$

$$\mathrm{Pr}_l=\frac{\mu_l c_{p,0}}{k}$$

$$\mathrm{Pr}_{\mathrm{tu}}=\frac{\mu_{\mathrm{tu}}c_{p,0}}{k}$$

Ω_{bl} is the reduced frequency parameter for the boundary layer. It is a measure of the time required for the disturbance to pass through the boundary layer thickness (modeled by θ/a_0), divided by the time between significant changes in properties at the boundary layer edge. The blade-passing frequency is the lowest frequency of unsteadiness for both disturbances (from potential flow interaction and from wake interaction). The unsteady amplitudes of higher harmonics from the wake interaction are orders of magnitude smaller than the first harmonic, and their downstream decay from the stator trailing edge is rapid [32]. The unsteady amplitudes of higher harmonics from the potential-flow interaction are several orders of magnitude smaller than the first harmonic, and their downstream decay is very rapid. As will be seen later in instantaneous velocity figures at points on the rotor surface, the dominant (highest amplitude) frequency of the core-flow unsteadiness is the blade-passing frequency. For subsonic cases, the amplitude of higher harmonics is much smaller than the amplitude of the first harmonic. For such cases we chose as characteristic time between significant changes in properties at the boundary layer edge the blade passing period (or for the rotor to traverse the distance between two stator trailing edges, S_{sb}/V_{rb}). Therefore, for these cases Ω_{bl} is given by

$$\Omega_{bl}\equiv\frac{\theta}{a_0}\frac{V_{rb}}{S_{sb}}=\frac{V_{rb}}{a_0}\cdot\frac{\theta}{S_{rb}}\cdot\frac{1}{R} \tag{6}$$

Comparison of Ω_{cf} and Ω_{bl}. Ω_{cf} and Ω_{bl} are strong functions of R. In Eq. (2), the second and third (inertia) terms are of the order of unity ($O(1)$). In most turbomachinery stator–rotor interactions, Ω_{cf} is of the order of or greater than unity, indicating that the unsteady terms cannot be neglected and that the flow is fully

unsteady. Unsteady-flow computations are required to predict the instantaneous location of the disturbances accurately. Direct comparison of Eqs. (4) and (6) results in

$$\Omega_{bl}=\left(\frac{\theta}{b_{rb}}\right)\Omega_{cf} \tag{7}$$

In many nonseparated turbine flows, the term (θ/b_{rb}) is between two and three orders of magnitude below unity ($O(10^{-2})$ to $O(10^{-3})$). (θ is defined as the average value of boundary-layer momentum thickness between the leading and trailing edge.) In Eq. (5) the inertia and viscous terms are one to two orders of magnitude larger than the unsteady terms (because Ω_{bl} is very small in comparison). In such cases, the unsteady terms multiplied by Ω_{bl} can be neglected from the boundary layer formulations without significant loss of accuracy.

This is not valid when the fifth or higher harmonics of local disturbances (with respect to the blade-passing frequency V_{rb}/S_{sb}) have a high amplitude, so that the corresponding Ω_{bl} becomes significant. In unsteady transonic flows this is valid away from the moving shocks, and is invalid in the temporal and spatial vicinity of the moving shocks, where an unsteady boundary layer computation with shock capturing is required. For example, in Fig. 8 of [31] and for the design case, the Nusselt number traces over the blade-passing period for most of the pressure surface have a dominant first harmonic amplitude, and negligible higher harmonics. This is because the flow solution for that case is not affected by shocks (see Fig. 9 of [31]). This idea is valid for most of the pressure surface in that case. It is clearly invalid in other cases shown in [31], where shocks significantly affect the flow solution on the blade surfaces.

Hypothesis. In subsonic turbines, while the core of the flow is unsteady and requires unsteady-flow computations, the boundary layer responds almost immediately to instantaneous changes in properties at its edge. The disturbance travels through the thickness of the compressible boundary layer (of order θ) with the local sonic velocity (of order a_0). Unsteady boundary-layer effects can be computed using a series of steady boundary-layer computations, in each of which the instantaneous properties at the edge of the boundary layer have been obtained from unsteady core-flow computations. This is true whenever the high-amplitude harmonics of the disturbances at the edge of the boundary layer have low frequency (up to about five times the blade-passing frequency), and the boundary-layer thickness and running length are small. In subsonic turbine cascades this is valid: near the leading edge because the boundary layers are thin; and farther downstream (where the boundary layers become a little thicker) because the amplitude of the high-frequency disturbances decay very fast.

Propagation of Two-Dimensional Disturbances

Giles' [6,7] computer program UNSFLO was used to compute the flow fields and the forces. The program can compute viscous stator–rotor flows, but we identified the propagation of the disturbances in the core of the flow using the inviscid dirturbance–rotor version of the program. Wakes are defined as the velocity defects generated by the surface boundary layers of upstream blade rows and propagating downstream. Since there is no static pressure jump at the trailing edge of blades, the wakes by this definition do not include a static pressure variation at the trailing edges where they are generated. Potential-flow interaction is defined as the static pressure variation generated by the existence of and relative motion between the lifting surfaces, propagating both upstream and downstream of the blade region that generates it.

The propagation mechanisms of wake and potential-flow interactions from upstream to downstream blades were examined in [14]. The wake is chopped, sheared, and rotated in the passages because the portion of the wake touching the pressure surface moves downstream with (lower) pressure-surface velocities, while the portion of the wake touching the suction surface moves downstream with (higher) suction-surface velocities. The resultant vortical unsteady flow patterns result in a region of increased pressure upstream of the wake centerline, and in a region of decreased pressure downstream of the wake centerline. The potential-flow interaction is chopped and propagates downstream with mechanisms similar to those of acoustic disturbances (pressure waves) in channels.

The phases of the unsteady pressures and velocities in stator–rotor interactions must be accurately computed in order to predict unsteady flows and heat transfer. Previous work [11–15,5] indicates that, in order to do that, one needs to model accurately both R and d. This last conclusion is evident if one considers the mechanisms of propagation of the unsteadiness for different geometries, and the limiting cases of $R=1$ (wake disturbances dominate the unsteadiness) and $R=3$, 4, and 6 (potential-interaction disturbances dominate the unsteadiness) [14,15].

Approach

Unsteady rotor heat transfer experimental data from stator–rotor interactions on the Garrett 731-2 HP rotor have been obtained by Dunn [21]. A previous investigation [29] performed unsteady inviscid flow combined with unsteady boundary layer (unsteady heat transfer) calculations on this rotor by approximating $R=78/41=1.90244\approx 2$ and by modeling only the wake interaction (neglecting the potential flow interaction). Their analyses reasonably predicted average values of heat flux but, because the location of unsteady flow disturbances was not modeled correctly [30], it missed unsteady amplitudes and phases.

The approach of this paper is to use UNSFLO in a disturbance-rotor interaction calculation to obtain the instantaneous velocities modeling the geometry and flow conditions of Dunn's experiments. The effects of both wake interaction and potential-flow interaction, and the correct values of stator-to-rotor-pitch ratio R and axial gap d are modeled at the computational rotor–inlet boundary. It is assumed that the instantaneous flow properties on the rotor surface (inviscid computation) are the same as the flow properties on the edge of the boundary layer. These properties (denoted by subscript e) are input in a series of steady-flow boundary-layer computations using a differential boundary-layer program [33]. The resultant amplitudes and phases of computed quasi-steady instantaneous heat transfer rates on the rotor surface are in better agreement with the experimental measurements than the earlier unsteady heat transfer study [29]. This is mainly because [29] did not predict correctly the location of the unsteady instantaneous disturbances from the wake in the core flow (and at the edge of the boundary layer).

Rotor-Inlet Boundary

The two disturbances (viscous wake and potential flow) from the stator have been modeled as inputs to the computational rotor–inlet boundary. This simplification provides accurate computational results only if one is extremely careful to specify the correct inlet boundary conditions. Details of the following derivations have been published elsewhere [6,7,11–15], but a summary has been included here because they are essential to understanding the model of the rotor–inlet boundary, and the following results and discussion.

The velocity disturbance due to the wake is characterized by the maximum amplitude of the velocity defect D, expressed as a fraction of the undisturbed velocity, and by the "width" W of the velocity defect. Most velocity wakes observed in experimental data have velocity distributions that resemble Gaussian distributions. For the wake model we assumed that: The velocity defect is a Gaussian distribution with characteristic width expressed as a fraction of the pitch of the blade cascade that generates the wake; in the stator frame the flow vectors in the wake are parallel to the undisturbed flow (a velocity deficit with no angle variation);

the static pressure is constant across the wake; and the stagnation enthalpy is constant across the wake. These assumptions are modeled by

$$u_{iw,q}=\left[1-D\cdot\exp\frac{1}{2}\left(\frac{\tan(\alpha_n)x-y}{S_{sb}W_q}\right)^2\right]c_n\cos(\alpha_n)$$
$$v_{iw,q}=\left[1-D\cdot\exp\frac{1}{2}\left(\frac{\tan(\alpha_n)x-y}{S_{sb}W_q}\right)^2\right]c_n\sin(\alpha_n) \tag{8}$$

where q is either s or p (suction or pressure surface). For the unsteady flow computations shown below the inputs were $D=0.10$ and $W_s=W_p=W=0.1100S_{sb}=0.2092S_{rb}$ based on a review of experimental data included in [15].

The model for the potential-flow disturbance is developed by observing measured and computed static pressure fields of various turbine-blade cascades. Across the line of the trailing edges there is a variation of static pressure with maxima at (or very near) the trailing edges and minima at (or very near) the middle of the passage. The exact location and shape of the pressure variation depends on the geometric shape of the passage (lift of blade). This static pressure disturbance is nearly sinusoidal in blades of various geometries and tangential lift coefficients, and the amplitude of the disturbance decays very fast with distance downstream.

The potential-flow model (in the stator frame) is derived as a two-dimensional, linear, isentropic, irrotational perturbation to uniform flow [34]

$$(u^2-a^2)\frac{\partial u}{\partial x}+(v^2-a^2)\frac{\partial v}{\partial y}+uv\left(\frac{\partial u}{\partial y}+\frac{\partial v}{\partial x}\right)=0 \tag{9}$$

The velocity–potential relationship is defined by

$$\frac{\partial\Phi}{\partial x}\equiv u \qquad \frac{\partial\Phi}{\partial y}\equiv v \tag{10}$$

For subsonic flows, one expects that the potential-flow disturbance from the upstream cascade is periodic (one period per stator pitch) in the y (circumferential or tangential) direction, and that it decays exponentially in the x (axial) direction. Thus, the general solution of Eq. (9) is of the form

$$\Phi(x,y)=B\cdot\exp\left[(\sqrt{-1})\frac{2\pi}{S_{sb}}y+\xi x\right] \tag{11}$$

where B is the amplitude, ξ is a complex parameter that depends on whether the flow is subsonic or transonic and governs the decay of the potential disturbance downstream, and $2\pi/S_{sb}$ dictates the periodicity of the potential Φ. Substituting these (with the negative root of ξ to make the potential disturbance decay downstream) in Eq. (9), solving for Φ, we derive the velocity disturbances δu_p and δv_p. These are coupled with the conditions of no variation in entropy and stagnation enthalpy to give a sinusoidal pressure perturbation Δp

$$\delta v_p=-\Delta v_p\cdot\exp\left[-\frac{2\pi}{S_{sb}}\frac{\sqrt{1-\mathrm{M}^2}}{1-\mathrm{M}_x^2}(x-x_{te})\right]\sin[2\pi(\epsilon+\Delta\epsilon)]$$
$$\delta u_p=-\tan(\alpha_{ip})\delta v-\frac{\sqrt{1-\mathrm{M}^2}}{1-\mathrm{M}_x^2}\Delta v_p$$
$$\cdot\exp\left[-\frac{2\pi}{S_{sb}}\frac{\sqrt{1-\mathrm{M}^2}}{1-\mathrm{M}_x^2}(x-x_{te})\right]\cdot\cos[2\pi(\epsilon+\Delta\epsilon)]$$
$$\Delta p=\Delta p_p\cos\left\{2\pi(\epsilon+\Delta\epsilon)-\tan^{-1}\left[\frac{\tan(\alpha_n)}{\sqrt{1-\mathrm{M}^2}}\right]\right\} \tag{12}$$
$$\Delta p_p=\frac{\rho c\mathrm{M}\Delta v_p}{\sqrt{1-\mathrm{M}_x^2}};\qquad \epsilon=\frac{y-\tan(\alpha_{ip})x}{S_{sb}}$$

$$\Delta\epsilon=\frac{1}{2\pi}\tan^{-1}\left[\frac{\tan(\alpha_n)}{\sqrt{1-\mathrm{M}^2}}\right]+\frac{[\tan(\alpha_{ip})-\tan(\alpha_n)]x_{te}}{S_{sb}}\tan(\alpha_{ip})$$
$$=-\frac{\mathrm{M}_x\mathrm{M}_y}{1-\mathrm{M}_x^2}.$$

where the phase-shifting ϵ and $\Delta\epsilon$ locate the maximum of the potential-flow variation at the trailing edge of the upstream stators, and $\tan(\alpha_{ip})$ is the direction of propagation of the potential field. Across the line of the trailing edges, Δp_p is typically between 4 and 5 percent of the average pressure [11,15]. In the computations presented in this paper we used $\Delta p_p=0.05$.

Unsteady Flow Calculations

The stage geometry and some pertinent values are shown in Fig. 1 and Table 1. Two-dimensional calculations were performed for the midspan location, at a radius of 4.92 in. The period of the rotor unsteadiness is one stator pitch, starting from phase $\phi=0.000$ (when the rotor leading edge is aligned with one stator trailing edge), and finishing at phase $\phi=8.780$ (Fig. 1). The results of the unsteady flow-disturbance/rotor calculations are illustrated in Fig. 2 for a series of ϕ. The computations have been performed on a relatively coarse 100×40 H-type Euler grid. This grid (with this solver) adequately resolves the location of the core-flow disturbances with minimum numerical diffusion. The figure

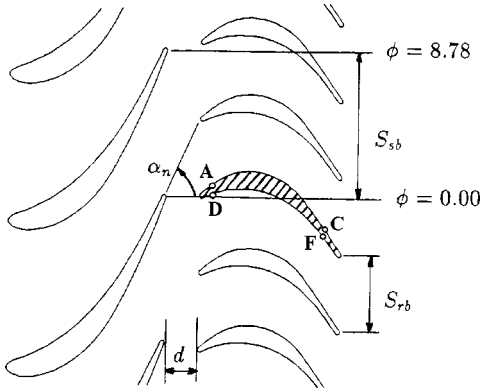

Fig. 1 Stator-rotor geometry, and periodic phase angle ϕ

Table 1 Rotor blade data

rotor solidity S_{rb}/b_{rb}	0.5497
rotor stagger angle	-23.7^o
$R=78/41$	1.902439
axial gap d (fraction of b_{rb})	0.23
stator absolute outlet flow angle α_n	69.19^o
rotor relative inlet Mach number	0.391
rotor relative inlet flow angle	36.29^o
rotor relative outlet flow angle	-58.96^o
rotor outlet p_{st}/p_t	0.7200
rotor surface $T_w=530^oR$	294.4 K
Turbine inlet $T_t=1007^oR$	559.4 K
assumed c_p	1039 $J/kg/K$
ratio of specific heats $\gamma=c_p/c_v$	1.3815

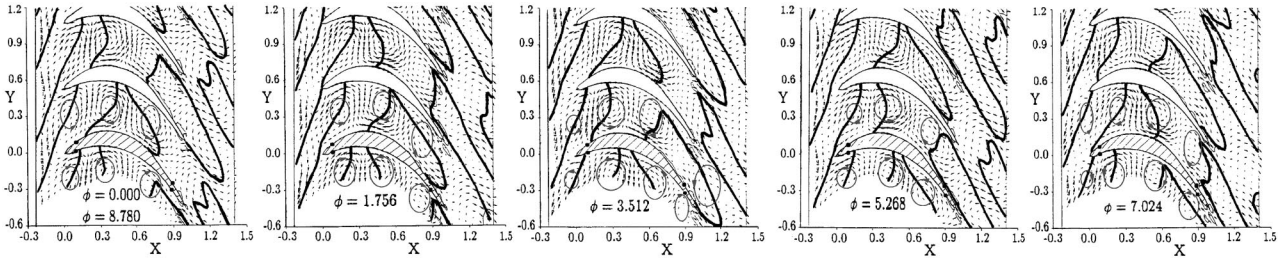

Fig. 2 Unsteady flow vectors superimposed on entropy contours for one full stator pitch from ϕ=0:000 to ϕ=8:780

shows unsteady flow vectors (instantaneous minus average vector at each grid point) superimposed on entropy contours. The stator trailing edges are along the lines of $X=-0.23$, and the centerlines of the wake contours can be used to identify the location of the stator trailing edges, as well as the chopping, shearing and rotation of the wakes in the rotor passages.

Since $R=1.9024$, the flow is approximately (but not exactly) periodic every second rotor. The results are obtained relative to the shaded rotor in Fig. 2, which is always shown in the same location with the wake centerlines moving in the negative y direction as ϕ increases. Counterrotating unsteady-flow vectors are located upstream and downstream of each wake centerline, resulting in a region of increased and decreased pressure, respectively, as discussed for general turbine geometries in [14,15].

Quasi-Steady Heat Transfer

The instantaneous Stanton number St for this case and at each point on the surface is defined by

$$\mathrm{St}\equiv\frac{\mathrm{Nu}}{\mathrm{Re\,Pr}}=\frac{\dot{q}}{\rho_e U_e c_p(T_e-T_w)} \tag{13}$$

where $\dot{q}$ is the heat transfer rate from the working fluid to the wall under the local conditions. The subscript e denotes properties on the blade surface (inviscid unsteady-flow computation), assumed equal to the properties at the boundary layer edge.

At every value of ϕ the instantaneous rotor-surface Mach number distribution (obtained for the rotor blade shown shaded in Fig. 2) was input for a boundary layer calculation using [33]. Other inputs to the boundary-layer calculations were the rotor blade geometry and its surface curvature, the stagnation pressure and temperature at the inlet, the ratio of specific heats, and the relative inlet Mach number.

The program starts from an initial velocity (and enthalpy) similarity solutions profile, and it recalculates the profile shape assuming either a stagnation point somewhere in the flow, or Blasius flat-plate flow, or some wedge flow. Stagnation-point profiles (about the leading-edge region stagnation point computed in the flow calculations) were used. For each quasi-steady boundary layer calculation the stagnation point moves about its nominal position as predicted by the unsteady-flow calculations (Fig. 2). The parabolized Navier–Stokes equations for the boundary layer are discretized in the s direction using a modification of Crank–Nicolson's finite-difference scheme. The resulting linearized ordinary (in the transverse direction) differential equations are numerically integrated at each s location. It was specified that the flow transitioned into turbulence as soon as it entered the rotor. The program calculates the boundary layer properties, and outputs the local St along the blade surfaces. This and the instantaneous and local Mach number distribution and the stagnation properties at rotor inlet are used to compute ρ_e, U_e and T_e are used to evaluate the instantaneous and local values of $\dot{q}$ on the surface of the rotor blade.

Figure 3 shows $\dot{q}$ (in units of btu/ft^2/s) as a function of ϕ for four points on the blade surface (near points A, C, D, F in Figs. 1 and 2). The computed quasi-steady $\dot{q}$ (solid lines without marks)

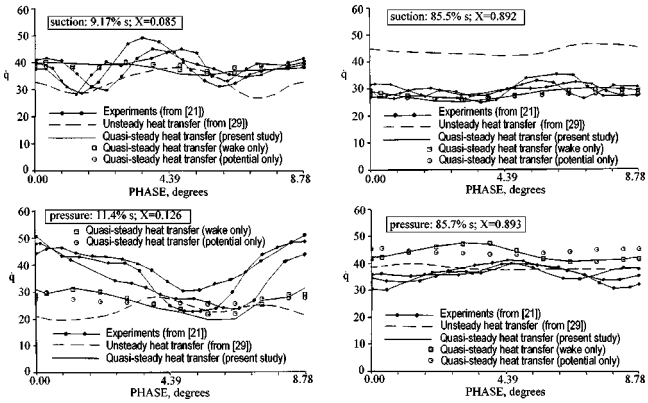

Fig. 3 Unsteady heat transfer rate ($\dot{q}$ [btu/ft^2/s]) measurements and calculations as a function of phase ϕ. Top left: point A; top right: point B; bottom left: point C; and bottom right: point D (cf. Figs. 1, 2).

are compared with experimental unsteady $\dot{q}$ data (solid tick marks and solid lines, from [21]) and with previous unsteady $\dot{q}$ computations (dashed line without tick marks, from [29]). The solid lines without tick marks represent the current calculations for the combined wake and potential-flow interaction; the open square tick marks indicate the results of similar computations to the foregoing considering the disturbances from the wake interaction alone (no potential-flow interaction); and the open round tick marks indicate the results of similar computations to the foregoing, considering the disturbances from the potential-flow interaction alone (no wake interaction).

Discussion

Figure 4 shows instantaneous local pressures and velocities for three points on the suction and pressure surfaces (normalized with their average values at each point) versus ϕ for one Ω_{cf} unsteadiness period. The upstream and downstream points on each surface in Fig. 4 are near points A, C, D, F in Figs. 1, 2, 3. The intermediate points are at $X=0.500$ (to show the propagation and diffusion of the disturbances and their higher harmonics from upstream to downstream, which post facto justify the hypothesis). For the unsteady flow computations $\Omega_{cf}\approx 0.6$, indicating the core flow is unsteady, as seen by the propagation of disturbances in Figs. 2 and 4. The wake and potential disturbances travel downstream with different mechanisms and they have different phases. As the disturbances pass a point on the rotor surface, each causes a local change in velocity and pressure agreeing with the explanations given in [14,15]. This is reflected in the unsteady flow computation in Fig. 2 and the quasi-steady heat transfer computation in Fig. 4. The pressure traces are not ''inverse'' to the velocity traces in Fig. 4 because the two interactions propagate downstream with different phases.

One way to interpret the unsteady flow vectors in Fig. 2 is as local and instantaneous perturbations from the average flow at that

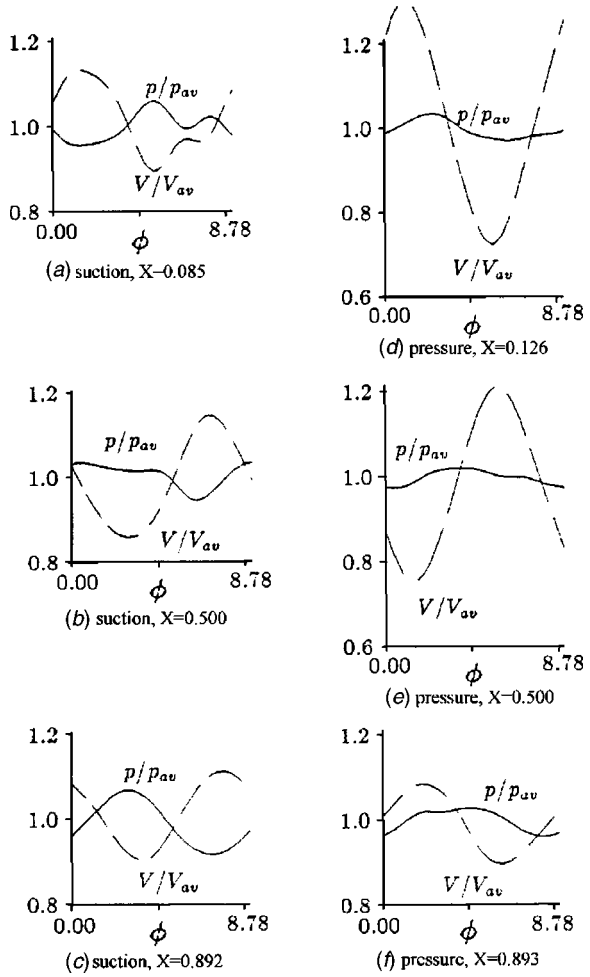

Fig. 4 Periodic local pressures and velocities versus ϕ for six points on the blade surfaces. On the suction surface: (*a*) at $X=0.085$; (*b*) at $X=0.50$; and (*c*) at $X=0.892$. On the pressure surface: (*d*) at $X=0.126$; (*e*) at $X=0.50$; and (*f*) at $X=0.893$.

surface point. Considering the unsteady flow vectors (counterrotating vortices) on the surfaces of the shaded blade, when the unsteady flow vector is pointing downstream, it indicates slightly increased velocity from the average conditions, and therefore slightly increased convective heat transfer at that instant and location. Conversely, when the unsteady flow vector is pointing upstream, it indicates slightly decreased velocity from the average conditions, and therefore slightly decreased convection at that instant and location. This matches the local velocity variations shown in Fig. 4. In the $\dot{q}$ figures in [29] there is a decrease and increase in $\dot{q}$ upstream and downstream of the wake centerlines, which was not explained in [29], but is better explained by the velocity increases and decreases from the average in Figs. 2, 3, and 4, and in [30].

With the exception of the upstream point on the suction surface (Fig. 4(*a*)), the velocity traces (Fig. 4(*b–f*)) are almost sinusoidal (implying the first harmonic of blade passing frequency is dominant). For the vicinity of points C, D, and F in Fig. 1 the traces of V/V_{av} in Fig. 4 are in phase agreement with the experimental data and the present-study quasi-steady heat transfer computations in Fig. 3. In contrast, the trace of computations of [29] in Fig. 3 disagree on the phase distribution of $\dot{q}$ with the experimental data. Even at the upstream point on the suction surface (Fig. 4(*a*)) the amplitude of the second harmonic is an order of magnitude smaller than the first, and the amplitudes of the third and higher harmonics are negligible. The frequency of the disturbances at the edge of the boundary layer is the blade-passing frequency. Therefore Ω_{bl} for Eqs. (5) can be computed using Eq. (6). Near the leading edge $\Omega_{bl}\approx 0.002$ and near the trailing edge $\Omega_{bl}\approx 0.005$. The hypothesis of this paper is valid in this case, and the boundary-layer flow is quasi-steady.

The current quasi-steady heat transfer computations for the combined wake and potential-flow interaction have predicted both the amplitude and the phase of the unsteady heat transfer rates better than the unsteady boundary layer computations of [29], and with less computational effort. Figures 3 and 4 show that the $\dot{q}$ variations follow the surface V/V_{av} variations, indicating that the hypothesis is valid. The normalized peak-to-peak heat transfer variation for each one of the four points is as follows: For point C, $X=0.126$ on the pressure surface: [21] 49, 74, 70 percent; present computation 45 percent; [29] 37 percent. For point F, $X=0.893$ on the pressure surface: [21] 31, 19, 15 percent, present computation 16 percent; [29] 6 percent. For point A, $X=0.085$ on the suction surface: [21] 44, 55, 40 percent; present computation 13 percent; [29] 35 percent. For point C, $X=0.892$ on the suction surface: [21] 20, 23, 34 percent; present computation 18 percent; [29] 9 percent.

The locations of the solid lines (combined wake and potential-flow interaction), the square tick marks (wake only), and the round tick marks (potential only) in Fig. 3 indicate the heat transfer effect of the two interactions is not additive. (Contrary to this, the unsteady flow pressure effects in the core of the flow are nearly additive [14,15].) The present method underpredicts the unsteady amplitude (although less than the unsteady boundary layer computation of [29]). The amplitude of the unsteady velocity depends on the amplitude of the wake input in the calculations. A larger-amplitude wake introduces larger velocity and heat transfer variations (with the same phases). There are no experimental wake data available for this geometry. A larger-amplitude wake was not used in computations because it is not supported by the average turbine-wake data in [15].

Near point A on the suction surface our calculations predict the average experimental $\dot{q}$ amplitude, and tend to follow the phase reasonably well, but they underpredict the unsteady amplitude. The direction of the unsteady flow vectors in Fig. 2 and the velocity trace in Fig. 4 indicate that the heat transfer rate should be decreasing at $\phi\approx 4.39$ and a little later, and increasing near $\phi\approx 0.00$ and 8.78. This is indeed the measured and computed trend in Fig. 3. The unsteady heat transfer calculations of [29] predict the amplitude of $\dot{q}$ better, but they do not follow the phases as well as the quasi-steady $\dot{q}$ computations (for example for $\phi>6$).

Near point C on the suction surface, and points D and F on the pressure surface, our calculations predict the steady and unsteady amplitude and phase of $\dot{q}$ reasonably well. The direction of the unsteady flow vectors in Fig. 2 and the velocity trace in Fig. 4 agree with the measured and quasi-steady $\dot{q}$ computed trends in Fig. 3, showing the expected increases and decreases. The unsteady heat transfer calculations of [29] do not follow the amplitudes and phases as well.

Similar trends (blade surface $\dot{q}$ is proportionately affected by local convection as measured by flow velocity at the edge of the local boundary layer) are observed by carefully examining the unsteady flow vectors, the instantaneous velocity traces, and the variations in unsteady heat transfer rates computed in [29]. This is a further indication that the unsteady terms in the boundary-layer equations (which they used in their computations) are negligible. However, the phases of their unsteady flow vectors and their velocity traces do not agree with ours, and this may be the reason for which they missed the phases of unsteady heat transfer rates.

In Fig. 3 the quasi-steady $\dot{q}$ from the wake interaction alone (square open tick marks) are reasonably close to the phase of the experimental results, indicating that in this case the wake interaction is dominant. The results from the potential-flow interaction alone (round open tick marks) frequently miss the phase of un-

steady heat transfer rates. However, in many cases the potential-flow interaction slightly, but critically, modulates the combined quasi-steady solution so that it predicts better the experimental $\dot{q}$. For example, at $X=0.126$ on the pressure surface and at $4.39<\phi<7.02$, the effect of the potential-flow interaction (round tick marks) on the wake interaction alone (square tick marks) is to further decrease the instantaneous heat transfer rate of the combined interaction (solid line) so that it matches better the unsteady amplitudes and phase of the experimental results. Similarly, at $X=0.892$ on the suction surface and at $5.26<\phi<8.78$, the effect of the potential-flow interaction (round tick marks) on the wake interaction alone (square tick marks) is to further increase the instantaneous heat-transfer rate of the combined interaction (solid line) so that it matches better the unsteady amplitudes and phase of the experimental results.

In Fig. 3 the experimental data and our computations show that on the suction surface the average heat transfer rates decrease downstream ($X=0.085$ versus $X=0.892$). This is a combined effect of: a decrease of working-fluid temperature due to work extraction; and a decrease of average relative flow vectors in the region of unguided diffusion [21]. Figures 8, 13, and 14 of [29] predict a slight increase of average heat transfer downstream, also shown in the present Fig. 3. On the pressure surface, the average heat transfer rates slightly increase downstream ($X=0.126$ versus $X=0.893$). This is a combined effect of: a decrease of working-fluid temperature due to work extraction; and an increase of average relative flow vectors downstream on the pressure surface [21]. Although the two effects are counteracting, the relative-flow acceleration that increases the convective heat transfer dominates the decrease due to reduction in working fluid temperature. Similar observations are shown in Figs. 5, 6, and 7 of [31].

For design studies, the time-averaged velocity distribution around the airfoil is approximately equal to the steady-state velocity distribution (a little less loading because of the effect of loss of momentum by the velocity deficit in the wake [14]). Since quasi-steady convection is the dominant heat transfer mechanism, the time-averaged (turbulent) heat transfer will be approximately equal to the (turbulent) steady-state heat transfer (as in Figs. 5, 6, and 7 of [31]). However, the local variation of heat transfer about its average depends on the variation of local velocity about its average, it is significant, and it can be reasonably predicted as illustrated above.

Conclusions

1 Using the concept of reduced frequency parameter it is theoretically demonstrated that:

- Unsteady core-flow computations are needed to predict the propagation of disturbances in blade-row interactions. Inviscid disturbance/blade-row computations can predict the core unsteadiness in many cases.
- Starting from the resultant unsteady properties on the blade surfaces, quasi-steady boundary-layer (heat transfer) computations are sufficient to predict the unsteady heat-transfer rates. This is valid whenever the boundary-layer reduced frequency parameter (evaluated using the maximum frequency of the dominant amplitudes in the frequency spectra of the unsteadiness and the boundary layer thickness) is small compared to the reduced frequency parameter of the core flow.
- This approach can be used in subsonic turbine cases and away from the location of the shocks in transonic turbine cases (which introduce large-amplitude high-frequency local disturbances).

2 The conclusions above are verified by comparing experiments with computations. A two-dimensional inviscid computer program is used to compute the instantaneous unsteady flow fields from disturbance–rotor interactions on a turbine rotor. The effects of the upstream stator on the rotor are modeled by carefully simulating: the stator-to-rotor-pitch ratio; the stator–rotor axial gap; the viscous wakes; and the potential-flow interaction between the stator and the rotor. The resultant unsteady rotor flow fields closely follow the explanations given in previous publications. The instantaneous unsteady velocities on the rotor surface and other pertinent stage data are input on a steady-flow differential boundary layer program, and the resultant heat transfer rates are computed. The results of these unsteady-flow/quasi-steady heat transfer computations are compared with experimental results for four points on the rotor surfaces. These computations predict the average amplitude of the heat transfer, the unsteady amplitude of the heat transfer, and the unsteady phase of the heat transfer well.

3 The unsteady flow fields in the core flow explain the phases and amplitudes of unsteady heat transfer rates. The unsteady flow instantaneous and local velocity variations on the rotor surface correspond to instantaneous variations of the convection heat transfer rate. The instantaneous velocity variations at the boundary layer edge cause instantaneous variations in convection that dominate unsteady heat transfer.

4 It is concluded that the present method can be used for quantitative predictions of unsteady heat transfer in subsonic turbines.

Acknowledgments

We thank Professor Michael B. Giles of Oxford University and Rolls Royce plc. for their permission to use UNSFLO; and David Winstanley of Garrett Corporation who supplied much useful data on the stator and rotor geometries.

Nomenclature

a = acoustic velocity (Eq. (9))
B = amplitude of potential variation (Eq. (11))
b = axial chord of rotor or stator cascade (lengths nondimensionalized with b_{rb})
c = local absolute-flow velocity (Eq. (8))
c_p = specific heat at constant pressure
D = wake amplitude, fraction of c_n (Eq. (8))
d = stator–rotor axial gap
e = energy
$\vec{f}$ = body forces (Eq. (1))
h = enthalpy
k = thermal conductivity
M, M_x, M_y = Mach number and its components
N = number of blades in row
Nu, Pr = Nusselt, Prandtl numbers
Re, St = Reynolds, Stanton numbers
$\dot{q}$ = heat transfer rate
R = $\equiv N_{rb}/N_{sb}=S_{sb}/S_{rb}$= stator-to-rotor-pitch ratio
S = pitch of blade row
s = surface length
T = temperature
t = time
u, v = velocity components in (x,y)
U = fluid relative velocity along rotor surface
V = velocity
W = characteristic width, fraction of S_{sb} (Eq. (8))
(x,y) = Cartesian coordinates
(X,Y) = coordinates nondimensionalized with b_{rb}
α = flow angle
Δ, δ = perturbation operators (on p, u, and v)
$\Delta\epsilon$, ϵ = angles locating the potential (Eq. (12))
θ = mean momentum thickness over s
λ = intermittency factor
μ = viscosity
ξ = complex parameter for x decay of Φ (Eq. (11))
ρ = density
$\tilde{\tau}$ = shear stress tensor (Eq. (1))
Φ = velocity potential (defined by Eq. (10))
ϕ = phase of unsteady rotor flow (Fig. 1)
φ = dissipation function (Eq. (1))

Ω = reduced frequency parameters (Eqs. (4), (6), (7))

Subscripts

0 = characteristic quantity
av = average
cf = core flow
bl = boundary layer
e = property at boundary layer edge
ip = flow property for potential flow model
iw = flow property in wake
l = laminar
n = absolute flow direction at stator outlet
p = perturbation value due to potential (Eq. (12))
q = suction (s) or pressure (p) side (Eq. (8))
rb, sb = rotor and stator blade row, respectively
t = stagnation property
te = location of upstream cascade trailing edge
tu = turbulent
w = wall (blade-surface) location
(x,y) = components in Cartesian coordinates

Superscript

$*$ = nondimensional quantity

References

[1] Erdos, J. I., and Lzner, E., 1977, ''Computation of Unsteady Transonic Flows Through Rotating and Stationary Cascades,'' NASA-CR-2900.
[2] Koya, M., and Kotake, S., 1985, ''Numerical Analysis of Fully Three-Dimensional Periodic Flows Through a Turbine Stage,'' ASME J. Fluids Eng., **107**, pp. 945–952.
[3] Fourmaux, A., 1986, ''Unsteady Flow Calculation in Cascades,'' ASME Paper No. 86-GT-178.
[4] Lewis, J. P., Delaney, R. A., and Hall, E. J., 1989, ''Numerical Prediction of Turbine Vane-Blade Aerodynamic Interaction,'' ASME J. Turbomach., **111**, pp. 387–393.
[5] Rai, M. M., and Madavan, N. K., 1990, ''Multi-Airfoil Navier–Stokes Simulations of Turbine Rotor–Stator Interaction,'' ASME J. Turbomach., **112**, pp. 377–384.
[6] Giles, M. B., 1988, ''Calculation of Unsteady Wake/Rotor Interactions,'' J. Propul. Power, **4**, No. 4, pp. 356–362.
[7] Giles, M. B., and Haimes, R., 1993, ''Validation of a Numerical Method for Unsteady Flow Calculations,'' ASME J. Turbomach., **115**, pp. 110–117.
[8] Richardson, S., 1990, ''Analysis of Unsteady Rotor–Stator Interaction Using a Viscous Explicit Method,'' AIAA Paper No. 90-0342.
[9] Hodson, H. P., 1985, ''An Inviscid Blade-to-Blade Prediction of a Wake-Generated Unsteady Flow,'' ASME J. Eng. Gas Turbines Power **107**, pp. 337–344.
[10] Scott, J. N., and Hankey, W. L., 1986, ''Navier–Stokes Solutions of Unsteady Flow in a Compressor Rotor,'' ASME J. Turbomach., **108**, pp. 206–215.
[11] Korakianitis, T., 1987, ''A Design Method for the Prediction of Unsteady Forces on Subsonic, Axial Gas-Turbine Blades,'' Doctoral Dissertation Sc.D. in Mechanical Engineering, Massachusetts Institute of Technology, Cambridge, MA.
[12] Korakianitis, T., 1992, ''On the Prediction of Unsteady Forces on Gas Turbine Blades: Part 1—Description of the Approach,'' ASME J. Turbomach., **114**, pp. 114–122.
[13] Korakianitis, T., 1992, ''On the Prediction of Unsteady Forces on Gas Turbine Blades: Part 2—Analysis of the Results,'' ASME J. Turbomach., **114**, pp. 123–131.
[14] Korakianitis, T., 1993, ''On the Propagation of Viscous Wakes and Potential-Flow in Axial-Turbine Cascades,'' ASME J. Turbomach., **115**, pp. 118–127.
[15] Korakianitis, T., 1993, ''The Influence of Stator-Rotor Gap on Axial-Turbine Unsteady Forcing Functions,'' AIAA J., **31**, No. 7, pp. 1256–1264, July.
[16] Hwang, C. J., and Liu, J. L., 1993, ''Analysis of Steady and Unsteady Turbine Cascade Flows by a Locally Implicit Hybrid Algorithm,'' ASME J. Turbomach., **115**, pp. 699–706.
[17] Manwaring, S. R., and Wisler, D. C., 1993, ''Unsteady Aerodynamics and Gust Response in Compressors and Turbines,'' ASME J. Turbomach., **115**, pp. 724–740.
[18] Gallus, H. E., Grollius, H., and Lambertz, J., 1982, ''The Influence of Blade Number Ratio and Blade Row Spacing on Axial-Flow Compressor Stator Blade Dynamic Load and Stage Sound Pressure Level,'' ASME J. Fluids Eng., **104**, pp. 633–641.
[19] Dring, R. P., Joslyn, H. D., Hardin, L. W., and Wagner, J. H., 1982, ''Turbine Rotor-Stator Interaction,'' ASME J. Eng. Power, **104**, pp. 729–742.
[20] Binder, A., Forster, W., Mach, K., and Rogge, H., 1987, ''Unsteady Flow Interaction Caused by Stator Secondary Vortices in a Turbine Rotor,'' ASME J. Turbomach., **109**, pp. 251–257.
[21] Dunn, M. G., 1990, ''Phase and Time-Resolved Measurements of Unsteady Heat-Transfer and Pressure in a Full-Stage Rotating Turbine,'' ASME J. Turbomach., **112**, pp. 531–538.
[22] Dunn, M. G., Kim, J., Civinskas, K. C., and Boyle, R. J., 1994, ''Time-Averaged Heart Transfer and Pressure Measurements and Comparison With Prediction for a Two-Stage Turbine,'' ASME J. Turbomach., **116**, pp. 14–22.
[23] Ashworth, D. A., Lagraff, J. E., Schultz, D. L., and Grindrod, K. J., 1985, ''Unsteady Aerodynamic and Heat Transfer Processes in a Transonic Turbine Stage,'' ASME J. Eng. Power, **107**, pp. 1022–1031.
[24] Blair, M. F., 1994, ''An Experimental Study of Heat Transfer in a Large-Scale Turbine Rotor Passage,'' ASME J. Turbomach., **116**, pp. 1–13.
[25] Liu, X., and Rodi, W., 1992, ''Measurement of Unsteady Flow and Heat Transfer in a Linear Turbine Cascade,'' ASME Paper No. 92-GT-323.
[26] Magari, P. J., and Legraff, L. E., 1994, ''Wake-Induced Unsteady Stagnation-Region Heat Transfer Measurements,'' ASME J. Turbomach., **116**, pp. 29–38.
[27] Krouthen, B., and Giles, M. B., 1988, ''Numerical Investigation of Hot Streaks in Turbines,'' AIAA Paper No. 88-3015.
[28] Griffin, L. W., and McConnaughey, H. V., 1989, ''Prediction of the Aerodynamic Environment and Heat Transfer for Rotor-Stator Configurations,'' ASME Paper No. 89-GT-89.
[29] Tran, L. T., and Taulbee, D. B., 1992, ''Prediction of Unsteady Rotor-Surface Pressure and Heat Transfer From Wake Passings,'' ASME J. Turbomach., **114**, pp. 807–817.
[30] Korakianitis, T., 1993, ''Discussion of 'Prediction of Unsteady Rotor-Surface and Heat Transfer From Wake Passings,''' ASME J. Turbomach., **115**, pp. 362–364.
[31] Abhari, R. S., Guenette, G. R., Epstein, A. H., and Giles, M. B., 1992, ''Comparison of Time-Resolved Turbine Rotor Blade Heat Transfer Measurements and Numerical Calculations,'' ASME J. Turbomach., **114**, pp. 818–827.
[32] Majjigi, R. K., and Gliebe, P. R., 1984, ''Development of a Rotor Wake/Vortex Model. Vol. I—Final Report,'' NASA-CR-174849.
[33] Albers, J. A., and Gregg, J. L., 1974, ''Computer Program for Calculating Laminar, Transitional, and Turbulent Boundary Layers for a Compressible Axisymmetric Flow,'' NASA TN D-7521, Apr.
[34] Liepmann, H. W., and Roshko, A., 1957, *Elements of Gasdynamics*, Wiley, New York, NY.